ICETI

ENGINEERING TECHNOLOGY INNOVATION

II INTERNATIONAL CONFERENCE ON ENGINEERING TECHNOLOGY AND INNOVATION

BOOK OF PROCEEDINGS 2018

www.iceti.org

March 07-11 2018 Budapest Hungary

ISBN: 978-605-67955-0-3

Organized by

Partners

II INTERNATIONAL CONFERENCE ON ENGINEERING TECHNOLOGY AND INNOVATION

ISBN 978-605-67955-1-0

II BOOK OF PROCEEDING OF THE INTERNATIONAL CONFERENCE ON ENGINEERING TECHNOLOGY AND INNOVATION 07-11 MARCH PUDAPEST

Edited by
Prof. Dr. Özer Çınar

Published, 2018

info@iceti.org
www.iceti.org

SCIENTIFIC COMMITTEE

1. Prof. Dr. Adisa Parić - University of Sarajevo - Bosnia and Herzegovina
2. Prof. Dr. Aleksandar Dimitrov - Ss. Cyril and Methodius University - Macedonia
3. Prof. Dr. Anita Grozdanov - Ss. Cyril and Methodius University - Macedonia
4. Prof. Dr. Asif Šabanović – International University of Sarajevo - Bosnia and Herzegovina
5. Prof. Dr. Christos Douligeris - University of Erlangen-Nurnberg - Germany
6. Prof. Dr. Dragutin T. Mihailović - University of Novi Sad - Serbia
7. Prof. Dr. Erkan Şahinkaya – İstanbul Medeniyet University - Turkey
8. Prof. Dr. Falko Dressler - University of Paderborn - Germany
9. Prof. Dr. Harry Miller – International University of Sarajevo - Bosnia and Herzegovina
10. Prof. Dr. Houssam Toutanji – Western Michigan University - USA
11. Prof. Dr. Ian F. Akyıldız – Georgia Institute of Technology - USA
12. Prof. Dr. İsmail Usta - Marmara University - Turkey
13. Prof. Dr. Liljana Gavrilovska - Ss Cyril and Methodius University - Macedonia
14. Prof. Dr. Lukman Thalib - Qatar University - Qatar
15. Prof. Dr. M. Asghar Fazel – University of Environment - Iran
16. Prof. Dr. Mehmet Akalin - Marmara University - Turkey
17. Prof. Dr. Mehmet Kitiş – Süleyman Demirel University - Turkey
18. Prof. Dr. Muammer Koç - Hamad bin Khalifa University - Qatar
19. Prof. Dr. Özer Çınar – Yıldız Technical University - Turkey
20. Prof. Dr. Perica Paunovik - Ss. Cyril and Methodius University - Macedonia
21. Prof. Dr. Rifat Škrijelj – University of Sarajevo - Bosnia and Herzegovina
22. Prof. Dr. Samir Đug - University of Sarajevo - Bosnia and Herzegovina
23. Prof. Dr. Tanju Karanfil – Clemson University - USA
24. Prof. Dr. Tibor Biro - National University of Public Service, Budapest - Hungary
25. Prof. Dr. Ümit Alver – Karadeniz Technical University - Turkey
26. Prof. Dr. Wolfgang Gerstacker - University of Erlangen-Nurnberg - Germany
27. Prof. Dr. Yılmaz Yıldırım - Bülent Ecevit University - Turkey
28. Prof. Dr. Yousef Haik - Hamad bin Khalifa University - Qatar
29. Assoc. Prof. Dr. Alaa Al Hawari - Qatar University - Qatar
30. Assoc. Prof. Dr. Izudin Dzafic - International University of Sarajevo - Bosnia and Herzegovina
31. Assoc. Prof. Dr. Muhamed Hadziabdic - International University of Sarajevo - Bosnia and Herzegovina
32. Assoc. Prof. Dr. Nusret Drešković - University of Sarajevo - Bosnia and Herzegovina
33. Assist. Prof. Dr. Faruk Berat Akçeşme - International University of Sarajevo - Bosnia and Herzegovina
34. Assist. Prof. Dr. Fouzi Tabet - German Biomass Research Center - Germany
35. Assist. Prof. Dr. Haris Gavranovic - International University of Sarajevo - Bosnia and Herzegovina
36. Assist. Prof. Dr. Murat Karakaya - Atılım University - Turkey
37. Assist. Prof. Dr. Sasan Rabieh - Shahid Beheshti University - Iran
38. Assist. Prof. Dr. Ševkija Okerić - University of Sarajevo - Bosnia and Herzegovina
39. Dr. Hasan Bora Usluer - Galatasaray University - Turkey
40. Dr. Muhammet Uzun - RWTH Aachen University - Germany
41. Dr. Zsolt Hetesi - National University of Public Service, Budapest - Hungary
42. Dr. Zsolt T. Németh - National University of Public Service, Budapest - Hungary

ORGANIZATION COMMITTEE

Chairman(s) of the Conference

Prof. Dr. Özer Çınar – Yıldız Technical University

Members of the Committee

Prof. Dr. M. Asghar Fazel – University of Environment - Iran
Prof. Dr. Ümit Alver - Karadeniz Technial University - Turkey
Assoc. Prof. Dr. Lukman Thalib - Qatar University - Qatar
Assoc. Prof. Dr. Nusret Drešković - University of Sarajevo - Bosnia and Herzegovina
Assist. Prof. Dr. Sasan Rabieh - Shahid Beheshti University - Iran
Alma Ligata - Zenith Group - Bosnia and Herzegovina

Ismet Uzun - Zenith Group - Bosnia and Herzegovina
Musa Kose - Zenith Group - Bosnia and Herzegovina

WELCOME TO ICETI 2018

On behalf of the organizing committee, we are pleased to announce that the International Conference On Engineering Technology And Innovation is held from March 07 to 11, 2018 in Budapest, Hungary.

ICETI 2018 provides an ideal academic platform for researchers to present the latest research findings and describe emerging technologies, and directions in Engineering Technology And Innovation. The conference seeks to contribute to presenting novel research results in all aspects of Engineering Technology And Innovation.

The conference aims to bring together leading academic scientists, researchers and research scholars to exchange and share their experiences and research results about all aspects of Engineering Technology And Innovation. It also provides the premier interdisciplinary forum for scientists, engineers, and practitioners to present their latest research results, ideas, developments, and applications in al lareas of Engineering Technology And Innovation. The conference will bring together leading academic scientists, researchers and scholars in the domain of interest from around the world. ICETI 2018 is the oncoming event of the successful conference series focusing on Engineering Technology And Innovation.

The International Conference on Engineering Technology and Innovation (ICETI 2018) aims to bring together leading academic scientists, researchers and research scholars to exchange and share their experiences and research results about all aspects of Engineering Technology and Innovation. It also provides the premier interdisciplinary forum for scientists, engineers, and practitioners to present their latest research results, ideas, developments, and applications in all areas of Engineering Technology and Innovation. The conference will bring together leading academic scientists, researchers and scholars in the domain of interest from around the world. The conference's goals are to provide a scientific forum for all international prestige scholars around the world and enable the interactive exchange of state-of-the-art knowledge. The conference will focus on evidence-based benefits proven in technology and innovation and engineering experiments.

Best regards,

Prof. Dr.Özer ÇINAR

CONTENT	PAGE

ICETI 2018 07-11 MARCH BUDAPEST HUNGARY www.iceti.org
II. INTERNATIONAL CONFERENCE ON ENGINEERING TECHNOLOGY AND INNOVATION

The Determination of Coastline Change Using Support Vector Machine in Berdan Dam Lake, Turkey

Tolga Kaynak[1], Sevim Yasemin Cicekli[2], Mustafa Hayri Kesikoglu[1], Coskun Ozkan[1]

Abstract

With the development of technology, new techniques have been developed to measure large areas. Remote sensing technique, which is one of them, is frequently used for monitoring the change of coastline areas. In this study, the coastline boundary changes of Berdan Dam Lake was detected in Mersin, Turkey. The dam lake was constructed between 1975 and 1984 for providing hydroelectric energy, drinking water and irrigation. The coastline boundary changes of Berdan Dam Lake was determined using Landsat 5 TM and Landsat 8 LDCM satellite images belonging to 2000 and 2017 years respectively. In first step, image to image registration process was performed to geometric corrections. In second step, each satellite image was classified into two classes, namely lake and other field by support vector machines method. The image classification accuracies were calculated by using post classification comparison method and the changes in coastline boundary were determined by image differencing method. The change image was created with the obtained classification images. It was observed that the lake area decreased while the other areas increased from 2000 to 2017. At the end of the study changes of coastline were detected in Berdan Dam Lake.

Keywords: *Support vector machines; post classification comparison; change detection; Landsat satellite images, remote sensing technology*

1. INTRODUCTION

Remote sensing method is frequently used in many disciplines. With the development of technology, Remote sensing technique is being used as one of the most successful methods in waterland management, ecological study, landcover and landuse determination, monitoring and determination of deformations.

Coastline is an intersection line with the land and sea, lake or river but it is invalid some situations such as water floods. From time to time, coastline can be change according to meteorological phenomena. The coast is a dynamic landscape. Coastal research is important component in some areas such as monitoring sea-level rise, coastal protection, land subsidence and erosion-sedimentation [1].

There are some studies met in literature about coastline change detection. Rasuly et al. [2] monitored Caspian Sea Coastline Changes by using Landsat images and determined increasement in height of water by using object-based classification method. Ghosh et al. [3] determined change of coastline Hatiya Island in Bangladesh by using Landsat image year of 1989,2000 and 2010 and monitored changes. Ciu and Liu [4] monitored Yellow River coastline change between 1976 and 2005 and determined relationships between the accretion–erosion of land and the runoff and sediment load of the Yellow River. Li et al. [5] determined coastline changes of Pearl River delta between 1966 and 2003 by using Landsat and Spot Satellite images and topographic map. Guney [6]determined coastline changes by using Landsat images year of 1975, 1987, 2000 and determined approximately 153 hectares in land acquired by filling the sea. Li and Gong [7], determined coastal changes in Florida by using Landsat image series from 1984 to 2013and detected coastline dynamics.

In this study, the aim is determine the change of coastline by using Landsat 5 TM and Landsat-8 LCDM satellite images of Berdan Dam Lake which were taken 2000 and 2017 years.

2. MATERIAL AND METHODS

2.1. Study Area

Berdan Dam, which is located in Eastern Mediterranean Basin and developed within the framework of Berdan Project to irrigation, flood control, energy and drinking water [8]. It was built in 1984 and today it is being used for the purpose of

[1] *Erciyes University, Department of Geomatics Engineering, Kayseri, Turkey.* tolgakaynak@erciyes.edu.tr, hayrikesikoglu@erciyes.edu.tr, cozkan@erciyes.edu.tr

Corresponding author: Cukurova University, Department of Geomatics Engineering, Adana, Turkey. yoturanc@cu.edu.tr

generating electricity, irrigation and drinking water [9]. Berdan Dam is one of the important dams for Cukurova region. The Landsat 8 image of the Berdan Dam Lake is shown in Figure 1.

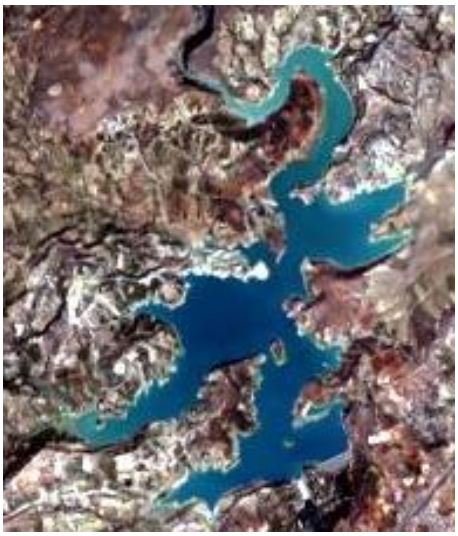

Figure 1. A Landsat 8 LDCM image on September 24, 2017 of the Berdan Dam Lake

2.2. Materials

In the study, Landsat 8 LDCM satellite images of Berdan Dam Lake in 2017 was used. Satellite image was taken on September 24th. In Table 1, Landsat 8 bands and their wavelength and resolution values are given in detail.

Table 1. Landsat-8 LDCM OLI / TIRS Satellite Bands And Features [10]

Band	Wavelength (micrometers)	Resolution (meters)
Band-1 Ultra Blue (Coastal Aerosol)	0.43-0.45	30
Band-2 Blue	0.45-0.51	30
Band-3 Green	0.53-0.59	30
Band-4 Red	0.64-0.67	30
Band-5 Near Infrared (NIR)	0.85-0.88	30
Band-6 Shortwave Infrared (SWIR-1)	1.57-1.65	30
Band-7 Shortwave Infrared(SWIR-2)	2.11-2.29	30
Band-8 Panchromatic	0.50-0.68	15
9 Cirrus	1.36-1.38	30
Band-10 Thermal Infrared (TIRS-1)	10.60-11.19	100*30
Band-11 Thermal Infrared(TIRS-2)	11.50-12.51	100*30

In the study, Landsat 5 TM satellite images of Berdan Dam Lake in 2000 was used. Satellite image was taken on June 21th. In Table 2, Landsat 5 bands and their wavelength and resolution values are given in detail.

Table 2. Landsat-5 TM Satellite Image Bands And Features [10]

Bands	Wavelength (micrometers)	Resolution (meters)
Band-1 Blue	0.45-0.52	30
Band-2 Green	0.52-0.60	30
Band-3 Red	0.63-0.69	30
Band-4 Near Infrared (NIR)	0.76-0.90	30
Band-5 Shortwave Infrared (SWIR) 1	1.55-1.75	30
Band-6 Thermal	10.40-12.50	120*30
Band-7 Shortwave Infrared(SWIR-2)	2.08-2.35	30

2.3. Methods

2.3.1. Support Vector Machines

In this study, support vector machines method are used in the classification of satellite images. Support vector machines (SVMs) is a learning technique and it is a supervised non-parametric statistical method which requires training samples [11]. This algorithm use with a set of labeled data instances and aims to find a hyperplane that separates the dataset into a discrete

predefined number of classes in a fashion consistent with the training examples [11]. Support vector machines method produced a k-1 dimensional hyperplane , for the classification of k dimensional data sets [12].

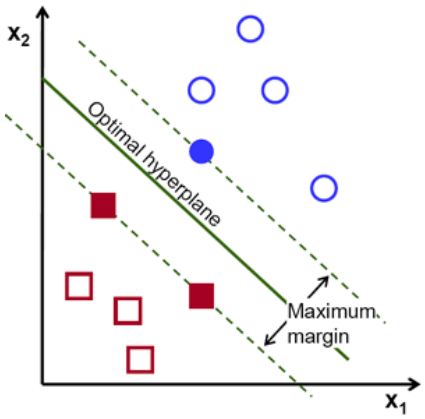

Figure 2. Support Vector Machines Classification Method[13]

Datasets are $\{x_i y_i\}$ $(i = 1, \ldots . k)$ for $x \in R^N$ is an N-dimensional space and $y \in \{-1 + 1\}$. For x is point on hyperplane, this hyperplane is defined as

$$w \times x_i + b = 0 \quad (1)$$

A separating hyper plane can be defined for two classes as [12]:

$$w \times x_i + b \geq 1 \text{ for all } y = +1 \quad (2)$$

$$w \times x_i + b \leq 1 \text{ for all } y = -1 \quad (3)$$

Support Vector Machines method detects boundaries between classes in an n-dimensional spectral space, rather than a class based on mean values, and thus differs from classic classification techniques [14]. There are some studies met in literature about using support vector machines. Heumann. [14] use object-based image analysis (OBIA), and support vector machine classification to monitoring mangroves vegetation. Pouteau et al. [15] use high quality quickbird images of Pasific islands and support vector machines method for classification of rare and endangered native plants.

2.3.2. Post Classification Comparison

In this study, post classification comparison was done for detection change of coastline dam lake. In this method, classified satellite images which taken two different times are compared with each other. Finally, the change direction and amount are calculated.

3. APPLICATION AND RESULTS

The flowchart of the study was shown in Figure 3.

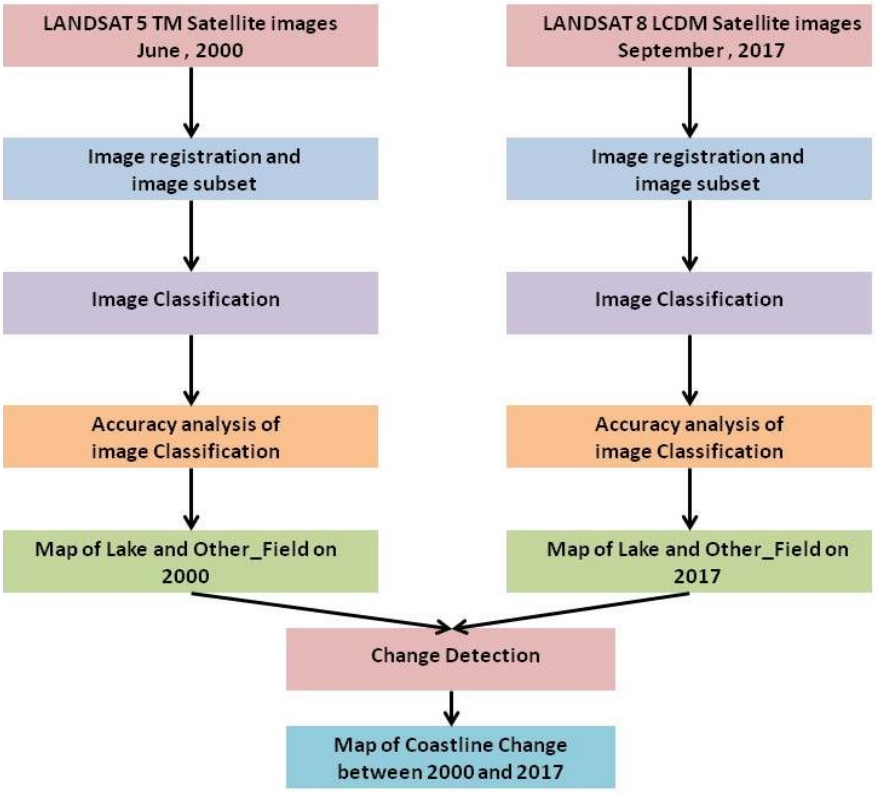

Figure 3. Flow chart of methodogy

In first step, "Image to Image Registration" was done for all satellite images. satellite image which was taken June 2000 was selected as reference image. Image which was taken September 2017 was registered in that image. In this step main goal is correct to meaningful nonsystematic errors which were occurred because of satellites position. These errors called geometric distortion. The images were cut based on the specified study area after registration. The registered and subset images are shown in Figure 4.

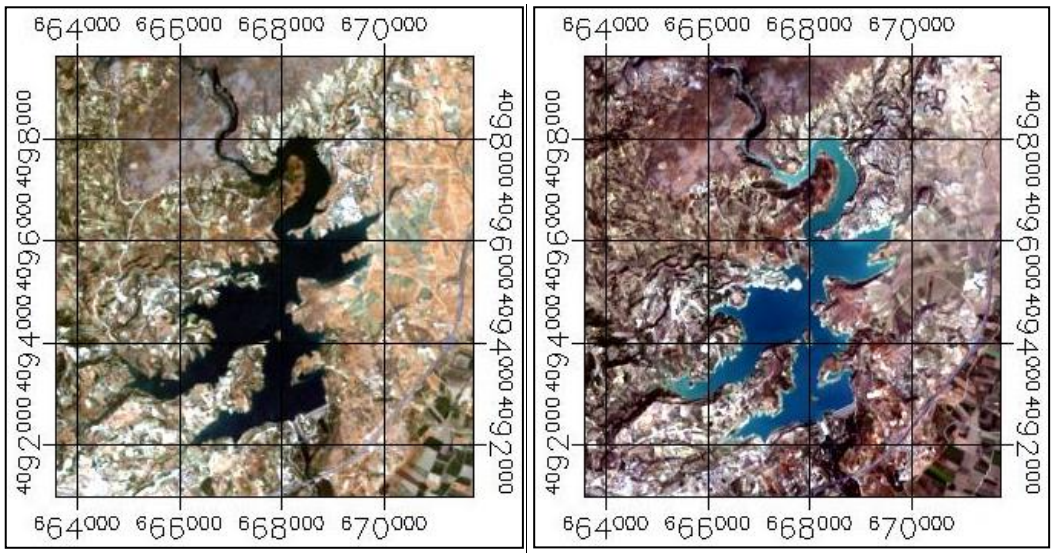

Figure 4. (a) June 2000 registration image (b) September 2017 registration image

In the second step, image classification was done. Support vector machines method was used in this step. By this classification, two classes were created which were called "Lake" and "Other_Field". Classified images of Berdan Dam Lake are shown in Figure 5.

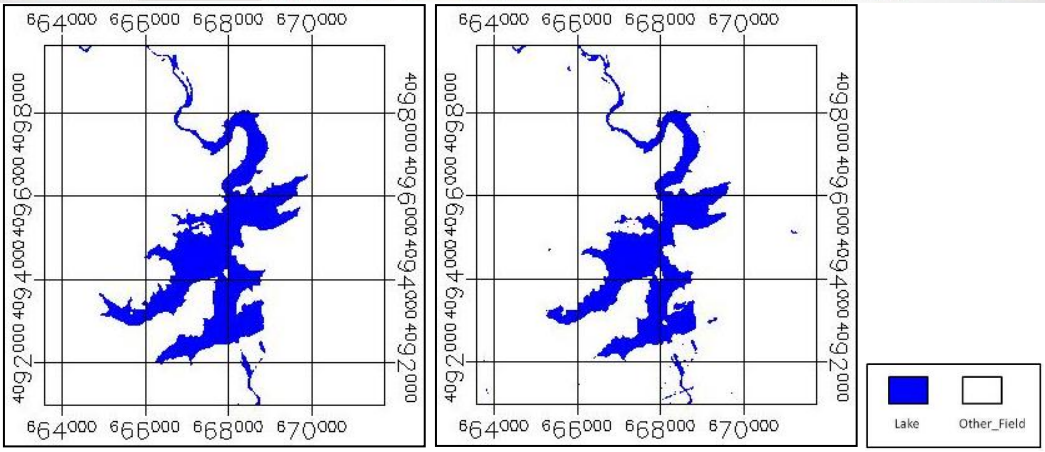

Figure 5. (a) June 2000 classification image (b) September 2017 classification image

In the third step, the image classification accuracies were determined. It was observed 99.33% overall accuracy for June,2000 image, 99.91% overall accuracy for June,2000 image. Kappa Coefficients were calculated 0.9742 for June 2000 image and 0.9962 for september 2017.

In the fourth step, changes were determined with the help of classified images. By using post classification comparison method change detection maps were created. Change detection map is shown in Figure 6.

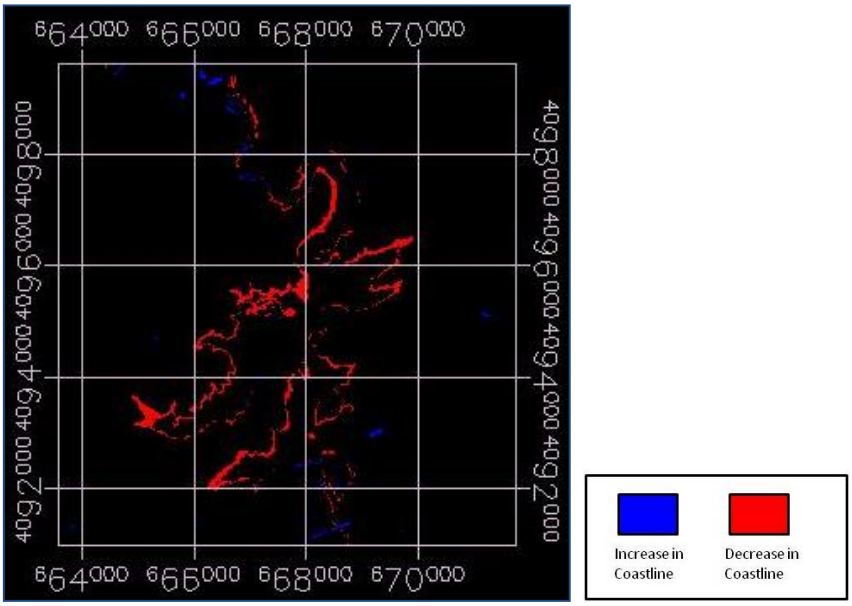

Figure 6. Map of Change 2000 and 2017

At the end of the study,1504 pixel decrease on the lake area was determined. Lake area was calculated 1.35 km^2 decrease.

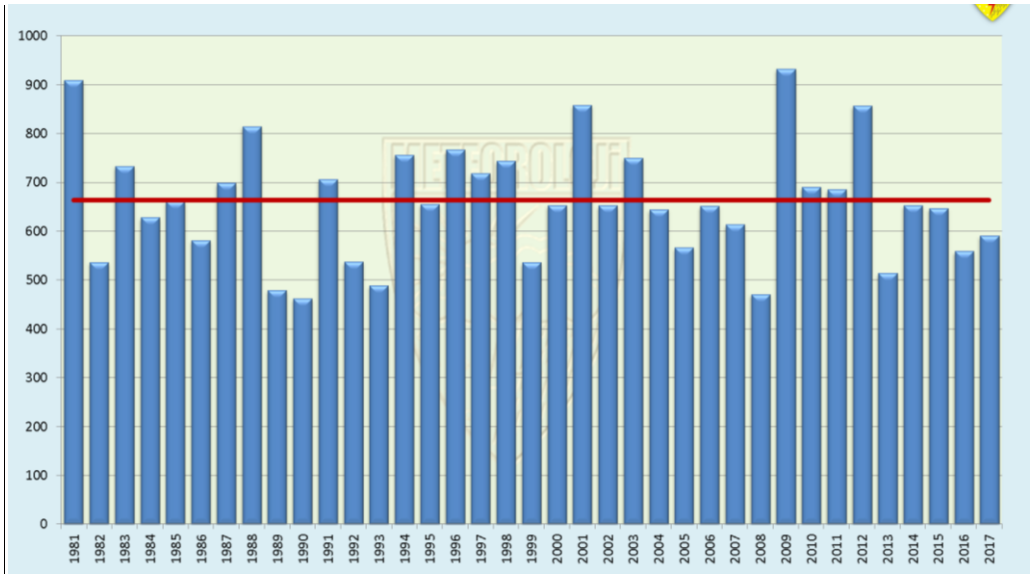

Figure 7. Annual total precipitation graphic of Mediterranean Reigon mm/year[16]

At the figure 7, precipitation graphic of Mediterranean Reigon is shown. Precipitation was about 650 mm in year of 2000 and precipitation was nearly 570 mm in year of 2017. In Mediterranean Region normal precipitation 663 mm. In 2017 precipitation is below the normal value. In 2000 precipitation is near the normal value.

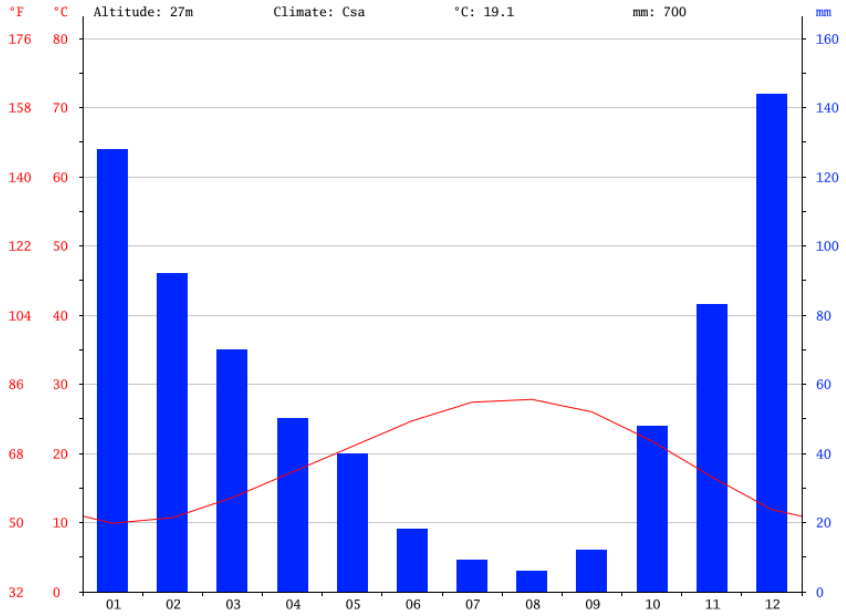

Figure 8. Annual precipitation and temperature of Tarsus,Mersin [17]

After the snow falling in the Taurus Mountains in the winter, the water in the Tarsus Berdan Dam reaches its maximum level in June. Since there is no snow in summer, in September the dam is at the lowest level. In Tarsus, precipitation l is maximum level in January, and minimum level in August. Berdan Dam Lake coastline was affected climate changes. Also, dams occupancy rate varies according to the amount of annual precipitation.

4. CONCLUSION

Coastline changes analyzing has a big important for environmental studies and wetland areas management. Coastlines can be change because of climatic changes, agricultural irrigation and use of water.

Precipitation is important factor for changes of waterland area. Low precipitation affected coastline of dam lake. This study shown that support vector machines method produced meaningful results in satellite images of different years.

In this study, image registrations, classification and change detection analysis were done. post classification comparison method was used to determine the change between 2000 and 2017 years by using classified Landsat 8 LDCM and Landsat 5 TM satellite images with support vector machines.

REFERENCES

[1]. T. Tochamnanvita, W. Muttitanon, "Investigation of coastline changes in three provinces of Thailand using remote sensing", *The International Archives of Photogrammetry, Remote Sensing and Spatial Information Sciences*, 40(8), 1079, 2014.
[2]. A. Rasulya, R. Naghdifarb and M. Rasoli, " Monitoring of Caspian Sea Coastline Changes Using Object-Oriented Techniques", *Procedia Environmental Sciences*, Vol. 2, pp. 416–426, 2010.
[3]. M. K. Ghosh, L. Kumar and C. Roy, "Monitoring the coastline change of Hatiya Island in Bangladesh using remote sensing techniques", *ISPRS Journal of Photogrammetry and Remote Sensing*, Vol. 101, pp. 137–144, 2015.
[4]. B. L. Cui, X. Y. Li, "Coastline change of the Yellow River estuary and its response to the sediment and runoff (1976–2005)", *Geomorphology*, Vol. 127, pp. 32–40, 2011.
[5]. X. Li, M. C.J. Damen, "Coastline change detection with satellite remote sensing for environmental management of the Pearl River Estuary, China", *Journal of Marine Systems*, Vol. 82, pp. 54–61, 2010.
[6]. Y. Guney, S. Polat, " Uzaktan Algilama Verileri Ile Kiyi Cizgisi Degisiminin Belirlenmesi: Aliaga Ve Candarli Ornegi", *Havacilik Ve Uzay Teknolojileri Dergisi* , Vol 8/1 , pp11-17, 2015.
[7]. W. Li, ,P.Gong, "Continuous monitoring of coastline dynamics in western Florida with a 30-year time series of Landsat imagery", *Remote Sensing of Environment*, vol. 179, pp.196–209, 2016.
[8]. S. P. Guvel, B. Selek, G. Seckin, "Baraj Rezervuarlarina Sediment Etkisinin Arastirilmasi: Berdan Baraji Ornegi", *Cukurova Universitesi Muhendislik-Mimarlik Fakultesi Dergisi*, 32(1), pp. 89-98,2017.
[9]. N. Koyuncu, F. Cevik, "Berdan Baraj Golu (Mersin) Fitoplankton Kompozisyonu ve Ekolojisi", *C. U. Fen ve Muhendislik Bilimleri Dergisi*, Vol. 31-3 pp. 63-74, 2014.
[10]. (2017) The USGS website. [Online]. Available: https://landsat.usgs.gov/what-are-band-designations-landsat-satellites/
[11]. G. Mountrakis, J. Im, C. Ogole, "Support vector machines in remote sensing: A review", ISPRS Journal of Photogrammetry and Remote Sensing, Vol. 66, pp. 247–259,2011.
[12]. T. Kavzoglu and I. Colkesen, "A kernel functions analysis for support vector machines for land cover classification", *International Journal of Applied Earth Observation and Geoinformation*, Vol. 11, pp.352–359,2009.
[13]. (2018) Introduction To Support Vector Machines . [online]. Available: https://docs.opencv.org/2.4/doc/tutorials/ml/introduction_to_svm/introduction_to_svm.html
[14]. B. W. Heumann, "An object-based classification of mangroves using a hybrid decision tree—Support vector machine approach", *Remote Sensing*, *3*(11), 2440-2460, 2011.
[15]. R. Pouteau, J. Y. Meyer, R. Taputuarai, B. Stoll, " Support vector machines to map rare and endangered native plants in Pacific islands forests", *Ecological Informatics*, *9*, pp. 37-46, 2012.
[16]. (2018) Yillik Toplam Yagis Verileri [Online]. Available: https://www.mgm.gov.tr/veridegerlendirme/yillik-toplam-yagis-verileri.aspx
[17]. (2017) Climate: Tarsus [Online]. available: https://en.climate-data.org/location/19373/

ICETI 2018 07-11 MARCH BUDAPEST HUNGARY www.iceti.org
II. INTERNATIONAL CONFERENCE ON ENGINEERING TECHNOLOGY AND INNOVATION

Experimental Analysis for the Thermal Performance of a Double Pipe Heat Exchanger with SiO_2-water Nanofluid

Fatih Selimefendigil[1], Hakan F. Oztop[2]

Abstract

Thermal performance of a double pipe heat exchanger with SiO2-water nanofluid was experimentally investigated. A double pipe heat exchanger with length of 0.5m was considered. SiO2-water nanofluid with various solid particle volume fractions between 0% and 2.5% were used as the hot fluid through the inner tube of the heat exchanger. Experimental analysis was performed for various flow rates and for different inlet temperatures of the nanofluid. Two turbine type flow meters was used to measure the flow rates of the inner tube and annulus while the inlet temperature for the hot water was controlled by using an electrical resistance heater. It was observed that the overall heat transfer coefficient enhances when the solid particle volume fraction of the nanofluid increases. The increment in the mass flow rate of the hot fluid through the inner tube results in overall heat transfer coefficient enhancement. The difference between overall heat transfer coefficient, for water and nanofluid with highest particle volume fraction enhances for higher flow rates of the hot fluid. For flow rate of 0.87 lt/min there is a difference of 20.60% while for flow rate of 2.37 lt/min, the difference becomes 83.26%. There is very slight effect of inlet temperature for the enhancement of the overall heat transfer coefficient when considering nanofluid at different particle volume fractions.

Keywords: double pipe heat exchanger, nanofluid, SiO2 nanoparticles, heat transfer coefficient

1. INTRODUCTION

Use of nanofluids in thermal engineering systems captures great attention recently. Metallic or non-metallic additives to the base fluid enhance the thermal conductivity of base fluid. The conductivity of heat transfer fluids such as water or ethylene glycol is very low when compared to metallic nanoparticles. When nanoparticles are added to the base fluid in very low amount, thermal conductivity increases significantly. Thus, it is possible to obtain compact, low weight thermal engineering systems. The environmental side effects can be reduced as a result of low energy consumption [1-3].

Demir et al. [3] performed numerical analysis for the hydrothermal behavior of a double pipe heat exchanger containing nanofluids. They used water and TiO_2 and Al_2O_3 nanoparticles. It was shown that the increase in heat transfer is much greater than the increase in pressure loss. In another study, Mahbubul et al. [4] investigated the heat transfer and pressure loss in a horizontal smooth pipe by using nano-refrigerants containing alumina nanoparticles. They used various solid nanoparticle volume fraction between 1% and 5%. They showed that an optimum solid particle volume fraction is achieved to obtain the best performance in a cooling system.

Chun et al. [5] examined the laminar heat transfer in a double-pipe heat exchanger with nanofluids. Form the experimental study they showed that the surface properties of nanoparticles are the main factors in the enhancement of the heat transfer. They obtained higher heat transfer coefficient as the solid particle volume fraction increases.

In many studies, it is shown that a compact lightweight heat exchanger can be obtained when nanoparticles are added to the base fluid. The heat transfer performance depends on many factors such as nanoparticle type, nanoparticle shape, solid volume fraction of the nanoparticles. The thermal conductivity enhancement of the base fluid when nanoparticles are added depends on some of those factors. In the application, many metallic or non-metallic nanoparticles are used which have spherical shape and have average particle diameter between 10 and 50 nm.

In this study, an experimental study foe the thermal performance improvement of a double pipe heat exchanger with SiO_2 nanoparticles inclusion to the water was performed. Various solid particle volume fraction of nanoparticles is tested for different mass flow rate and temperatures.

2. METHODOLGY

In this study, various solid particle volume fraction of SiO2 nanoparticles are used added in the water which is used in the double pipe heat exchanger. The nanofluid was obtained by using 2 step method. A TEM image of SiO2 nanoparticle is shown in Figure 1. Table 1 shows the thermophysical properties of SiO_2 nanoparticle.

[1] *Corresponding author: Department of Mechanical Engineering, Celal Bayar University, 45140 Manisa,Turkey. fthsel@yahoo.com*

[2] *Department of Mechanical Engineering, Technology Faculty, Firat University, 23119 Elazig, Turkey*

hfoztop1@gmail.com

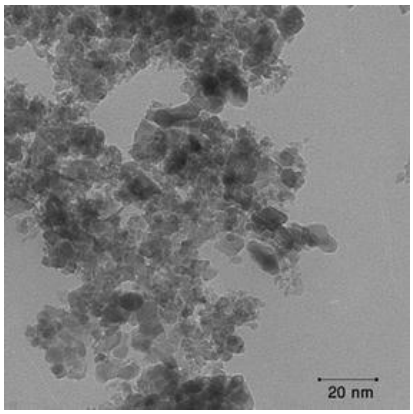

Figure 1 – TEM image of SiO_2 nanoparticles

Table 1 - Thermophysical properties of SiO_2

	Density kg m^{-3}	**Specific heat J kg^{-1} K^{-1}**	**Thermal conductivity W m^{-1} K^{-1}**
SiO_2	2400	691	8.4

Figure 2– Double pipe heat exchanger experimental setup

A double pipe heat exchanger was used which is shown in Figure 2. The measurement system consists of 2 turbine type flowmeter, 4 temperature sensors. The setup is composed of control panel, hot and cold water feed units and heat exchanger. The flow rates and temperatures can be read from the control panel. The hot water is obtained by using a resistance type heater

which is 2.5 kW. The water tank has a capacity of 15 t and is made of stainless steel. The inner pipe has an inner diameter of 14 mm and outer diameter of 16 mm. The length of the pipe is 500 mm. The outer pipe (the annulus side) has inner and outer diameters of 20 mm and 30 mm. The thermal conductivities of inner and outer pipes are 16 W/mK and 1.2 W/mK, respectively. The hot water is flowing through the inner pipe while the cold water is circulated thorough the annulus side of the heat exchanger. The hot water temperature of the inner pipe is controlled by using the resistance heater and the flow rates area also controlled. The SiO_2 nanoparticles are included in the hot water.

Following formulations are used to evaluate the heat transfer capacity and to find the overall coefficient of the double pipe heat exchanger:

Amount of heat transfer; $$Q = mc_p(T_2 - T_1) \quad (1)$$

Overall heat transfer coefficient; $$U = \frac{1}{\frac{1}{h_i} + \frac{1}{h_o} + R_{fi} + R_{fo}} \quad (2)$$

Logarithmic temperature difference; $$\Delta T_{lm} = \frac{\Delta T_1 - \Delta T_2}{\ln\left(\frac{\Delta T_1}{\Delta T_2}\right)} \quad (3)$$

Total heat transfer; $$Q = \frac{2\pi L \Delta T_{lm}}{\frac{1}{r_i h_i} + \frac{1}{r_o h_o} + \frac{\ln(r_2 / r_1)}{k}} \quad (4)$$

Following correlations can be used to find the heat transfer coefficient for the inner pipe and for the annulus side of the double pipe heat exchanger:

$$\mathrm{Nu} = \frac{(f/2)(\mathrm{Re})\,\mathrm{Pr}}{1 + 8.7(f/2)^{1/2}(\mathrm{Pr}-1)}, \qquad f = \left(1.58\ln(\mathrm{Re}) - 3.28\right)^{-2} \quad (5)$$

For the laminar flow configuration, Sieder –Tate correlation can be used:

$$\mathrm{Nu} = 1.86\left(\mathrm{Re}\,\mathrm{Pr}\frac{Dh}{L}\right)^{1/3}\left(\frac{\mu_b}{\mu_w}\right)^{0.14} \quad (6)$$

3. RESULTS AND DISCUSSIONS

In order the validate the experimental study, the size of the heat exchanger was determined by using the values from the control panel for the inner and outer flow rates and temperature of the inner pipe and annulus. By using the correlations given in Eq. (5) or (6) and expressions given by Eqs. (1)- (4), the length of heat exchanger was found to be 517 mmm and the actual length is 500 mm.

Figure 3 shows the heat transfer rate versus solid particle volume fraction of the nanoparticle for various flow rates of the hot water flowing through inner pipe. The flow rate of cold water in the annulus is fixed at 2.36 lt/min. It is seen that heat transfer rate enhances with solid particle volume fraction for all flow rates. The heat transfer rate is also increasing for higher values of flow rates. The rate of increment is higher when solid nanoparticle is increased from 0 to 1%. The heat transfer enhances by about 17.25%, 26.57% and 34.59% when solid particle volume fraction of nanofluid is increased from 0 to 1% for flow rates of 0.87, 1.44 and 2.16 lt /min.

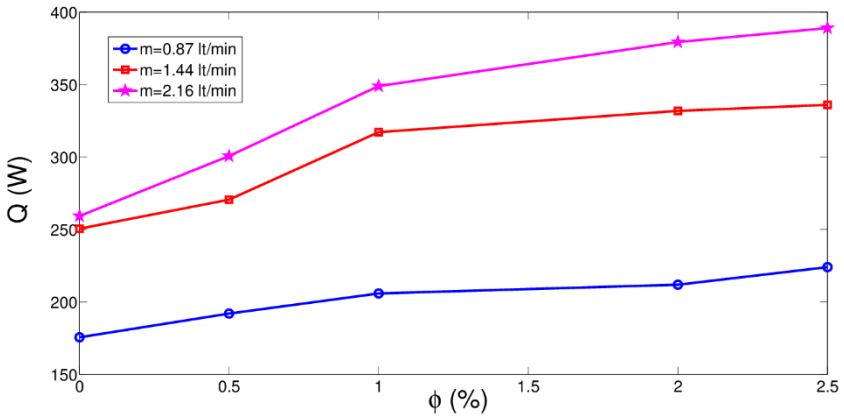

Figure 3 – Heat transfer rate versus nanoparticle volume fraction for various flow rates (T=30ºC)

Figure 4 shows the variation of overall heat transfer coefficient versus mass flow rate of the hot water considering various nanoparticle solid volume fractions. When the mass flow rate increases, the value of *U* increases as well. Adding nanoparticle results in enhancement of the overall heat transfer coefficient and this is significant for higher values of flow rate. For flow rate 0.87lt/min, the difference for overall heat transfer coefficient between the nanofluid and base fluid is 20.60% whereas its value becomes 83.26% when nanoparticle flow rate is increased to 2.37 lt/min.

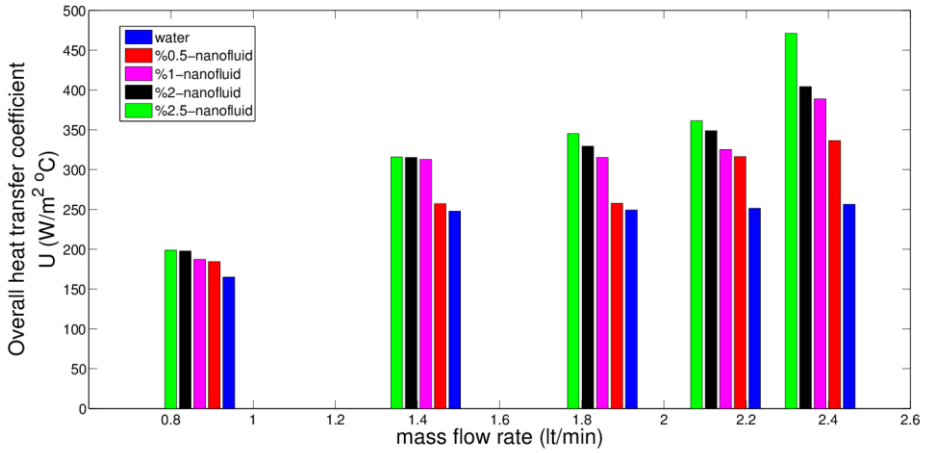

Figure 4- Variation of overall heat transfer coefficient for various mass flow rates and for different nanoparticle solid volume fraction (T=30ºC)

Figure 5 demonstrates the effect of hot water inlet temperature entering the inner pipe for various solid particle volume fraction. There is some slight enhancement in the heat transfer coefficient when water temperature is increased for all solid particle volume fractions. This value is 2.78% for pure water and 2.49% for nanofluid with the highest particle volume fraction.

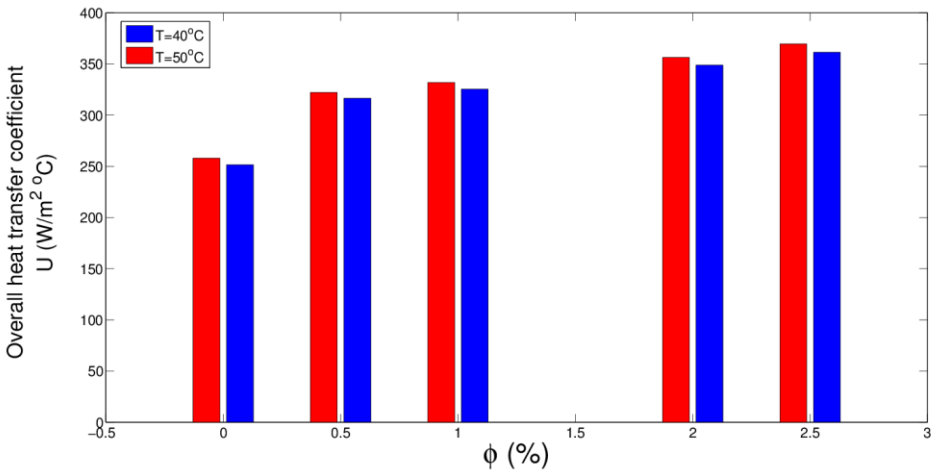

Figure 5- Variation of overall heat transfer coefficient versus solid particle volume fraction for two different values of hot water temperature entering the inner pipe (1.44 lt /min)

4. CONCULSIONS

Thermal performance enhancement within a double pipe heat exchanger with SiO_2-water nanofluid was demonstrated experimentally. It was observed that the thermal performed improves with nanoparticle inclusion and this effect is significant for higher values of flow rates. Enhancements of the overall heat transfer coefficient up to 83% was achieved for the nanofluid with the highest particle concentration. Pressure drop studies are needed to complete the hydrothermal performance of the double pipe heat exchanger.

ACKNOWLEDGMENT

This study is supported by Scientific Research Projects Unit (**BAP**) of Manisa Celal Bayar University for the project no: **2017-010** whose support is gratefully acknowledged.

REFERENCES

[1] F. Selimefendigil and Hakan F. Oztop, ‘’Mixed convection of nanofluids in a three dimensional cavity with two adiabatic inner rotating cylinders’’,*International Journal of Heat and Mass Transfer*, vol. 117, pp. 331-343, 2018.
[2] F. Selimefendigil and Hakan F. Oztop, ‘’ Modeling and optimization of MHD mixed convection in a lid-driven trapezoidal cavity filled with alumina–water nanofluid: Effects of electrical conductivity models’’, *International Journal of Mechanical Sciences*, vol. 136, pp. 264-278, 2018.
[3] H. Demir A.S, Dalkilic, N. A. Kurekci, W. Duangthongsuk and S. Wongwises . ‘’Numerical investigation on the single phase forced convection heat transfer characteristics of TiO_2 nanofluids in a double-tube counter flow heat exchanger’’, *International Communications in Heat and Mass Transfer*, vol. 38 (2), pp. 218–228, 2011
[4] I.M. Mahbubul, S.A. Fadhilah, R. Saidur, K.Y. Leong and M. A. Amalina,. ‘’Thermophysical properties and heat transfer performance of Al2O3/R-134a nanorefrigerants‘’, *International Journal of Heat and Mass Transfer*, vol.57, pp.100–108, 2013.
[5] B.H. Chun, H.U. Kang and S. H. Kim 2008, Effect of alumina nanoparticles in the fluid on heat transfer in double-pipe heat exchanger system, *Korean Journal of Chemical Engineering*, vol. 25 (5), pp. 966–971, 2008

ICETI 2018 www.iceti.org 07-11 MARCH BUDAPEST HUNGARY
II. INTERNATIONAL CONFERENCE ON ENGINEERING TECHNOLOGY AND INNOVATION

Welding of AA7075 to Galvanized Steel by Cold Metal Transfer Method

Hulya Durmus[1], Nilay Comez[1]

Abstract

The need for hybrid structures gains importance especially in vehicle industry in order to provide lightness. Hybrid structures of metals can be built by detachable joints or welding processes. The common problem in welding of dissimilar materials lies behind the formation of intermetallic phases and different thermal and electrical properties of these materials. In this study, cold metal transfer welding was applied to obtain AA7075-galvanized steel joints. The effect of arc energy on tensile strength of dissimilar joints and on thickness and mechanical properties of intermetallic layer was investigated. Formation of intermetallic phase layer was observed by microstructural investigations. Intermetallic phases were identified by SEM-EDX and XRD analyses. Mechanical properties of AA7075-galvanized steel joints were determined by tensile testing. Hardness and elastic modulus of intermetallic phases were determined by nano indentation technique. The outcomes showed that increasing arc energy increased the intermetallic layer thickness and tensile strength. However, brittle fracture occurred in intermetallic layer between aluminum and galvanized steel due to the increasing layer thickness.

Keywords: AA7075, intermetallic, nano indentation, steel, strength, welding,

1. INTRODUCTION

In recent years, vehicles have to meet the expectations of lightweight structure and high strength. Hereby, hybrid structure of aluminum (Al) and steel comes forward as a proper solution to provide lightness without sacrificing strength [1, 2]. Formation of intermetallic compounds and also difference in chemical and physical properties should be considered in welding of aluminum and steel [1, 3]. Al and steel can be welded by several techniques such as laser welding and friction stir welding which are characterized with low-heat input [1]. Especially, laser welding is found suitable for welding of Al and steel, however its high investment cost canalized the researchers to develop both economic and low-heat-input arc welding processes such as cold metal transfer (CMT) welding [4].

CMT process which relies on short circuiting principle can be defined as a modified MIG welding. In CMT process, the motion of filler wire is integrated into welding process and controlled by a digital system. When the short circuit occurs, the current is pulled down to zero and wire is drawn back by control system. The wire motion helps detachment of molten droplet and material transfer to weld pool. With controlled arc and wire motion, heat input and spatter can be reduced significantly [5, 6].

In addition to aircraft applications, investigations are necessary to adapt AA7075 Al alloy into automotive body panels because, AA7075 exhibits superior mechanical properties than 6XXX and 5XXX series which are widely employed in automotive [2, 7, 8]. However, studies about CMT welding of Al alloys and steel up to now have focused on 6XXX-steel [9]-[11] and 5XXX-steel [4] joints. Thus, the purpose of present study is to investigate the mechanical properties of AA7075-galvanized steel joints produced by CMT welding.

2. EXPERIMENTAL STUDY

2.1. CMT Welding Process and Sample Preparation

AA7075 (Table 1) and galvanized steel (Table 2) sheets with dimensions of 2x200x500 mm^3 were fixed by clamps before welding process. ER4043 (AlSi5) was used as filler wire (Table 1) and argon was employed as shielding gas. The cold metal transfer overlap welding was applied to AA7075-galvanized steel couples using a Fronius CMT-Advanced welding machine with the aid of a robotic arm (Table 3). Arc energy was calculated according to Equation (1) [12].

$$Q = V.I.60/S \quad (1)$$

Here;

Q : Arc energy (J/mm)

V : Voltage (V)

I : Current (A)

S : Welding speed (mm/min)

[1] *Corresponding author: Manisa Celal Bayar University, Department of Metallurgical and Materials Engineering, 45140, Yunusemre/Manisa, Turkey.* nilay.comez@cbu.edu.tr

Table 1. Chemical compositions of AA7075 aluminum alloy and ER4043 filler wire

Element	Mg	Si	Cr	Cu	Fe	Zn	Mn	Al
AA7075 (T6)	2.43	0.071	0.187	1.675	0.173	6.365	0.029	Rest
ER4043	-	5	-	<0.01	<0.3	<0.01	<0.01	

Table 2. Chemical composition of galvanized steel

C	Mn	P	S	Si	Ti	Fe
0.051	0.216	0.018	0.013	0.014	0.001	Rest

Table 3. CMT welding parameters

Sample	Current (A)	Voltage (V)	Welding speed (m/min)	Wire feed rate (m/min)	Arc energy (J/mm)
A	81	11	1	4.8	53.46
B	86	12.3	0.5	4.6	126.93

2.2. Microstructural Investigations

The samples were cut and polished for microstructural investigations. After polishing, AA7075 aluminum alloy was etched with Keller solution and Nital solution was used for steel. Microstructure images were obtained using Nikon Eclipse LV150 optical microscope and Clemex software. Identification of intermetallic phases was executed by SEM-EDX analyses.

2.3. Mechanical Tests

The tensile test of welded samples was carried out at a speed of 1 mm/min using Shimadzu Autograph (250 kN) equipment. Since CMT welding of aluminum-galvanized steel sheets is carried out in overlap position, additional parts were attached to the specimen ends in order to prevent axis misalignment during the tensile test.

The micro hardness measurements of AA7075-galvanized steel joints along the AA7075-weld metal-galvanized steel line were performed under a load of 100 gf applied for 10 seconds with a Future-Tech FM700 instrument.

In order to determine the elastic modulus and hardness of the intermetallic compounds formed between the aluminum weld metal and steel, nano indentation test was applied under load of 5 mN using Berkovich tip.

3. RESULTS AND DISCUSSIONS

3.1. Macro/Microstructural Investigations and SEM-EDX Analyses

Macrostructural examinations showed that weld beads have wavy edge which might occur due to the vaporization of zinc during welding process (Figure 1). Thomas et al., 2017 [13] stated that erratic zinc vapor which attempts to escape from weld zone changes both arc stability and wetting behavior of molten metal, thus it forms a wavy edge in weld bead.

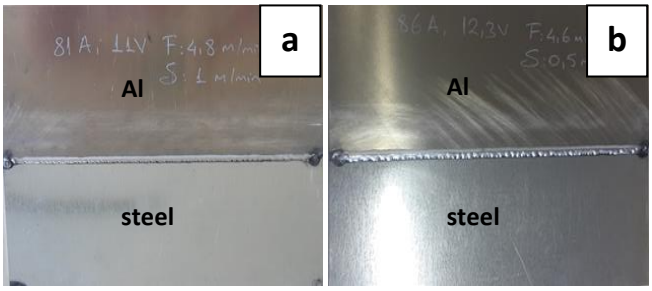

Figure 1. Macro images of AA7075-galvanized steel joints: a) Sample A, b) Sample B

Figure 2 presents microstructure of the interface of aluminum weld metal and galvanized steel. Intermetallic compound layer thickness was measured from microstructure images and it was observed that increasing arc energy increased the layer thickness and it caused grain coarsening in weld metal. The average thicknesses of intermetallic compound layers were found to be 1.83 µm and 2.65 µm for sample A and sample B, respectively. The effect of arc energy on AA7075 base metal can be clearly seen in Figure 3. Secondary phases tended to precipitate along the grain boundaries in heat affected zone (HAZ) and grains became coarse in sample B by virtue of increasing arc energy.

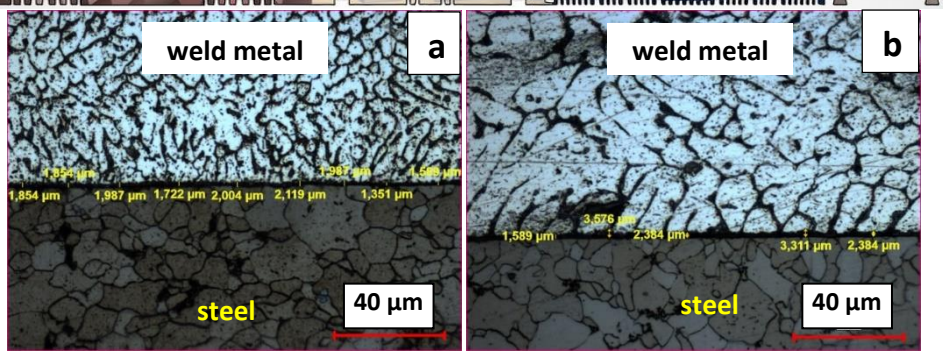

Figure 2. Microstructure of AA7075-galvanized steel joints: a) Sample A, b) Sample B

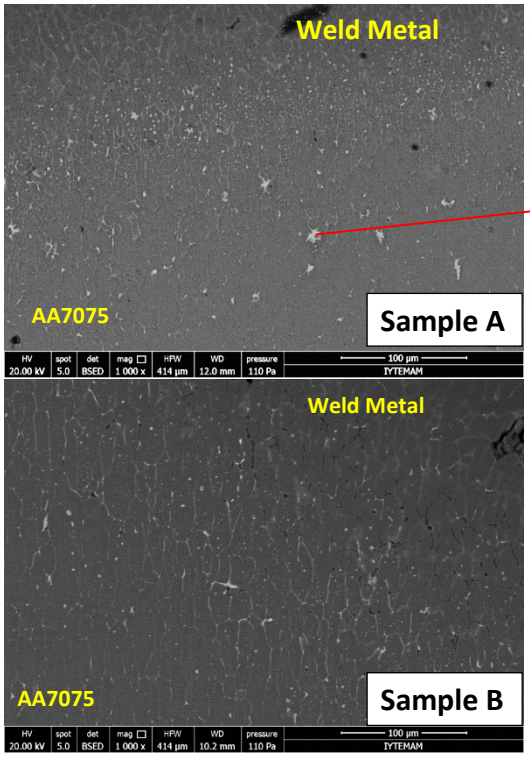

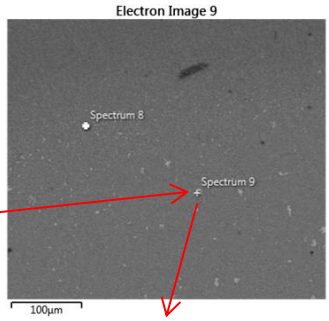

Element	Wt%	Atomic %
Al	69.44	80.85
Zn	12.45	5.58
Cu	9.23	4.26
Mg	6.51	7.85
Fe	1.97	1.04
Si	0.39	0.41
Total:	100.00	100.00

Figure 3. SEM image of AA7075/weld metal interface

SEM-EDX analyses of intermetallic compounds are given in Figure 4. According to Al-Fe binary [14] and Al-Fe-Si ternary [15] phase diagrams, $FeAl_2$ and Fe_2Al_5 intermetallic compounds formed in the sample A and intermetallic layer of sample B is composed of Al, τ_5 ($Al_{7.2}Fe_{1.8}Si$) and $FeAl_3$ (Table 4). XRD was applied only to intermetallic layer of sample B, because this sample fractured from intermetallic compound layer during tensile testing and the fracture surface of intermetallic layer was suitable for XRD analysis. XRD result of sample B is given in Figure 5. In addition to the SEM-EDX findings, Fe_2Al_5 phase in intermetallic compound layer of sample B was also detected by XRD (Table 4).

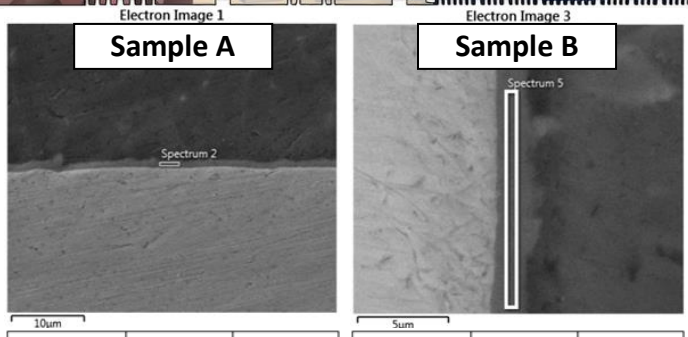

Element	Wt.%	At.%
Al	53.67	68.46
Fe	41.03	25.28
Si	4.97	6.09
Zn	0.33	0.17
Total	100.00	100.00

Element	Wt.%	At.%
Al	64.63	75.78
Fe	27.02	15.30
Si	7.59	8.55
Zn	0.76	0.37
Total	100.00	100.00

Figure 4. SEM-EDX analysis of intermetallic compound layers

Table 4. Detected intermetallic compounds

Sample	Intermetallic compound	XRD findings
A	$FeAl_2$+Fe_2Al_5	-
B	Al+τ_5+$FeAl_3$	Fe_2Al_5+$FeAl_3$

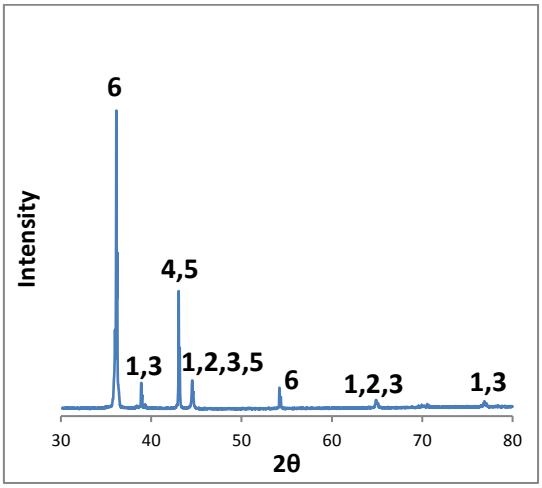

Figure 5. XRD analysis from intermetallic layer of sample B; 1: Al, 2: Fe, 3: AlZn, 4: $FeAl_3$, 5: Fe_2Al_5, 6: Zn

Elemental mapping of sample B shows that silicon and zinc elements accumulated along the intermetallic compound layer (Figure 6). Due to the vacancies in its lattice structure, Fe_2Al_5 phase has a high growth rate. Silicon atoms prevent diffusion of aluminum atoms into the Fe_2Al_5 phase by occupying these vacancies and accordingly suppress its growth [16]. In the intermetallic layer of the sample B, the silicon and zinc elements were able to keep the layer thickness below 5 microns despite the increased arc energy by placing in the vacancies during the formation of Al/Fe intermetallics.

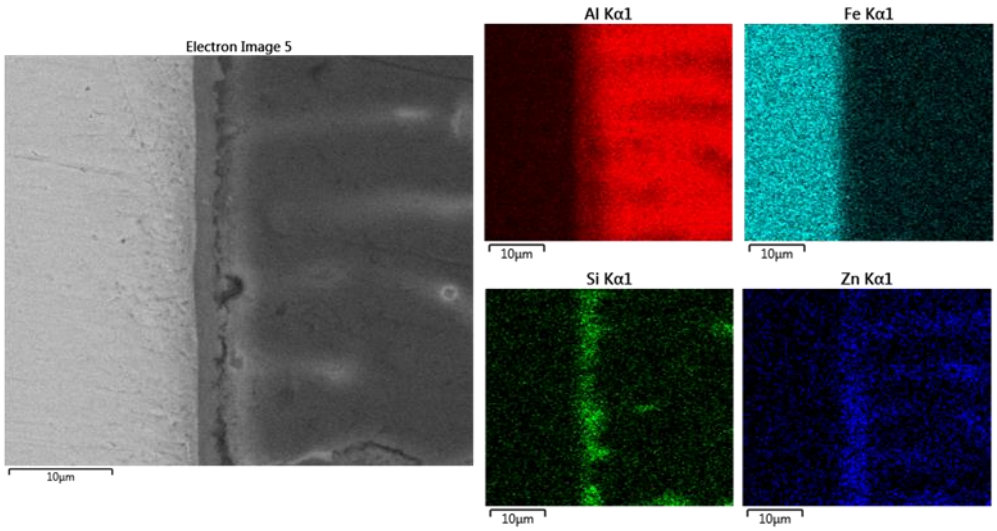

Figure 6. Elemental mapping analysis of sample B

3.2. Tensile, Hardness and Nano Indentation Tests

Micro hardness distributions of AA7075-galvanized steel joints are given in Figure 7. Hardness values of AA7075 and galvanized steel base metals were found to be close to each other. Minimum hardness values were obtained in aluminum based weld metal which has less alloying elements in comparison with AA7075. Heat affected zone of AA7075 base metal which was revealed by hardness measurements shows that increased arc energy caused grain coarsening (Figure 3) and also over aging in AA7075 base metal (Figure 7).

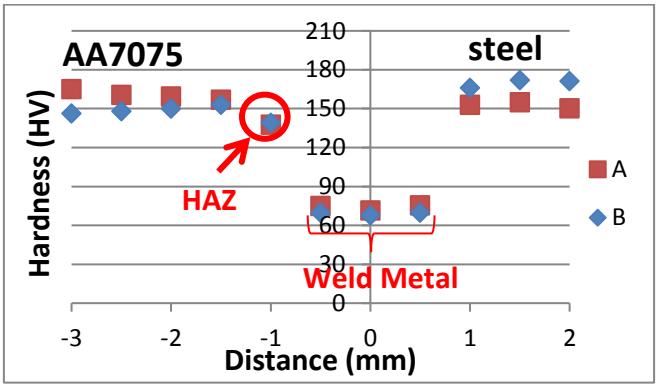

Figure 7. Micro hardness distribution of AA7075-galvanized steel joints

Hybrid structures, such as aluminum and steel welded joints, have various phases that exhibit different physical and chemical properties. For example, intermetallic compound layer between the aluminum weld metal and steel is composed of $FeAl_2$ and Fe_2Al_5 intermetallics in sample A and τ_5 ($Al_{7.2}Fe_{1.8}Si$), $FeAl_3$ and Fe_2Al_5 intermetallics in sample B (Table 4). Therefore, the tensile strength and fracture mechanism of Al-steel hybrid joints should be explained taking into account the type and mechanical properties of the intermetallic compound layer. For this purpose, elastic modulus and hardness of intermetallic layers were measured by nano indentation test. Hardness and elastic modulus values of intermetallic layers are given in Table 5. Unit of hardness values were converted from GPa to Vickers. Intermetallic layer hardness of sample B was found to be less than that of sample A due to the τ_5 ($Al_{7.2}Fe_{1.8}Si$) phase. Although the formation of Fe_xAl_y phases is necessary for an effective connection between aluminum and steel, excessive formation of these phases, especially those rich in aluminum, leads to susceptibility to crack formation and brittleness of the intermetallic compound layer under tensile stresses [17, 18]. With the addition of silicon, formation of brittle Al/Fe intermetallic compounds can be replaced by Al/Fe/Si phases, which are less detrimental [19]. As it was mentioned before, silicon inhibits the growth of Al-Fe phases by occupying the vacancies in the Al/Fe intermetallic compound and can form $Fe_xAl_ySi_z$ phases with lower growth rates than Fe_xAl_y phases [16, 20].

Table 5. Hardness and elastic modulus values of intermetallic compound layers

Sample	Phase	Hardness	Elastic Modulus
A	$FeAl_2$+Fe_2Al_5	11.4 GPa / 1161.5 HV	176.35 GPa
B	Al+τ_5+$FeAl_3$	8.74 GPa / 891.6 HV	197.7 GPa

Figure 8 helps to compare elastic and plastic behavior of intermetallic layers and aluminum weld metal. Maximum penetration depth (h_{max}) states the elastic + plastic deformation. Hardness is related to the grade of plastic deformation. The area bordered by P-h curves shows the work which plastic deformation did [21, 22]. Smaller plastic deformation area of intermetallic layers than that of weld metal means that they are harder than weld metal and were subjected to plastic deformation less than weld metal.

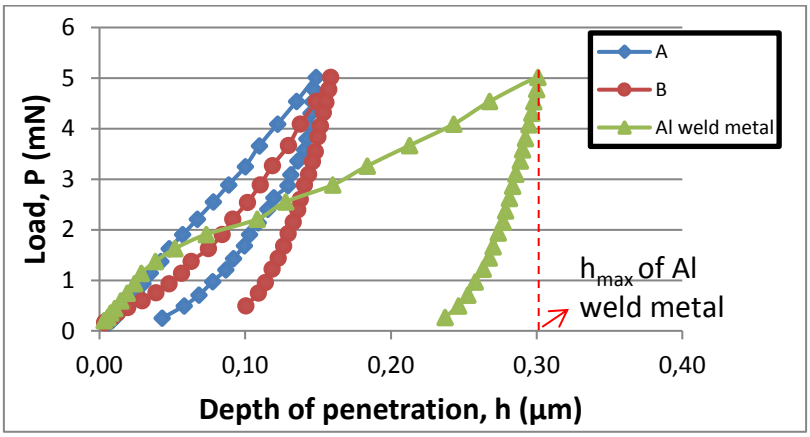

Figure 8. P-h curves of intermetallic compound layers and aluminium weld metal

The plastic deformation of AA7075-steel joints was found to be quite low as it can be seen in stress-strain curves (Figure 9). Fracture of tensile testing specimens showed brittle characteristic. Although sample B exhibited higher average tensile strength and strain in comparison with sample A, fracture occurred at its intermetallic compound layer (Table 6). Higher elastic modulus of sample B might provide more elastic deformation than sample A. However due to its thicker intermetallic layer, sample B ruptured from intermetallic layer. Sample A presented a stronger bond between Al, intermetallic compound layer and steel but the formation of pores in AA7075 base metal/weld metal interface caused brittle fracture (Figure 10).

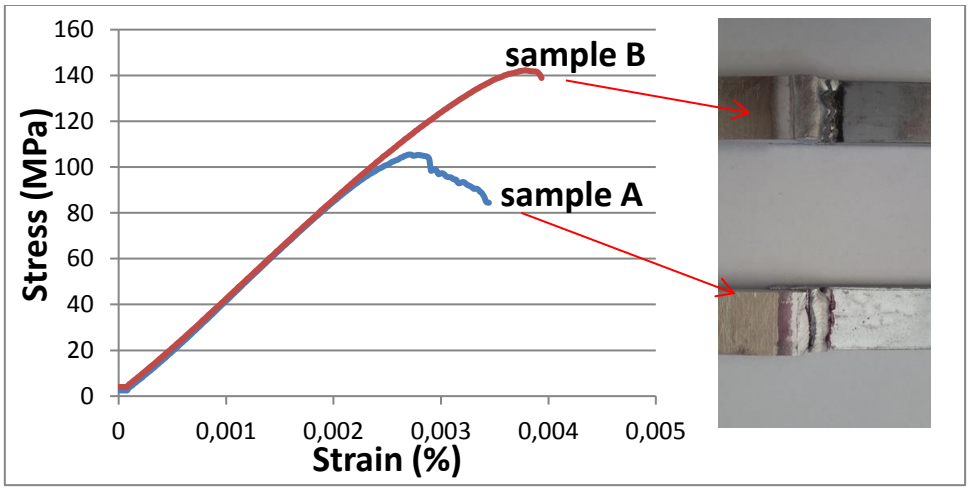

Figure 9. Stress-strain curves of AA7075-steel joints

Table 6. Average tensile strenght and e % values of AA7075-galvanized steel joints

Sample	Average tensile strength (MPa)	Average strain % (mm/mm)
A	113.81±2.45	0.42±0.10
B	139.83±11.80	0.51±0.12

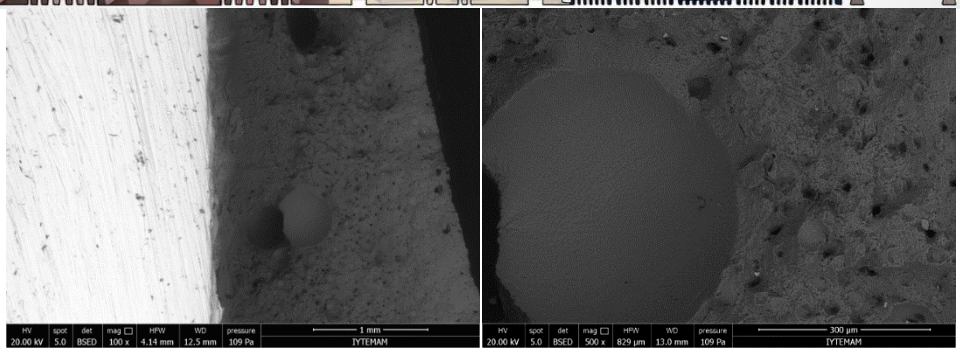

Figure 10. Fracture surface of sample A

4. CONCLUSIONS

2 mm thick AA7075 and galvanized steel plates were welded by CMT method. Findings of microstructural investigations and mechanical test applied to AA7075-steel joints are summarized as follows:

1) Increased arc energy supported the growth of intermetallic compound layer hereby increased its thickness and caused grain coarsening in weld metal and AA7075 base metal.

2) Al-Fe ($FeAl_2$, Fe_2Al_5, $FeAl_3$) and Al-Fe-Si (τ_5-$Al_{7.2}Fe_{1.8}Si$) intermetallic compounds were detected between aluminum weld metal/steel interface. Formation of $Al_{7.2}Fe_{1.8}Si$ phase decreased the hardness of intermetallic compound layer, whilst it increased the elastic modulus.

3) Hardness of thicker intermetallic compound layer composed of $Al_{7.2}Fe_{1.8}Si$ + $FeAl_3$ phases was found higher than that of thinner intermetallic compound layer composed of $FeAl_2$+Fe_2Al_5. Thick intermetallic compound layer provided superior tensile strength but fracture occurred at this layer during tensile test due to its thickness.

ACKNOWLEDGMENT

The authors would like to thank both Scientific and Technological Research Council of Turkey (Project Number: TUBITAK-215M623) and Manisa Celal Bayar University Coordination Department of Scientific Research Projects (Project Number: CBU-BAP 2015-130) which were financially supported this study.

REFERENCES

[1]. Y. C. Lim, L. Squires, T. Y. Pan, M. Miles, J. K. Keum, G. L. Song, Y. Wang, and Z. Feng, “Corrosion behaviour of friction-bit-joined and weld-bonded AA7075-T6/galvannealed DP980”, Sci. Technol. Weld. Joi., vol. 22, pp. 455-464, 2017.
[2]. L. Squires, Y. C. Lim, M. P. Miles, and Z. Feng, “Mechanical properties of dissimilar metal joints composed of DP 980 steel and AA 7075-T6”, Sci. Technol. Weld. Joi., vol. 20, pp. 242-248, 2015.
[3]. E. E. Patterson, Y. Hovanski, and D. P. Field, “Microstructural characterization of friction stir welded aluminum-steel joints”, Metall. Mater. Trans. A., vol. 47, pp. 2815-2829, 2016.
[4]. M. Kang, C. Kim, “Joining Al 5052 alloy to aluminized steel sheet using cold metal transfer process”, Mater. Design, vol. 81, pp. 95-103, 2015.
[5]. H. Liu, S. Yang, C. Xie, Q. Zhang, and Y. Cao, “Mechanisms of fatigue crack initiation and propagation in 6005A CMT welded joint”, J. Alloy. Compd., vol. 741, pp. 188-196, 2018.
[6]. H. Lei, Y. Li, B. E. Carlson, and Z. Lin, “Cold Metal Transfer Spot Joining of AA6061-T6 to Galvanized DP590 Under Different Modes”, J. Manuf. Sci. E.-T. ASME, vol. 137, pp. 051028 (1-10). 2015.
[7]. A. P. Singh, G. Elatharasan, “Friction stir welding optimization of AA7075 and AISI 1045 steel using grey-fuzzy logic approach”, Advances in Natural and Applied Sciences, vol. 11, pp. 263-271, 2017.
[8]. P. V. Kumar, G. M. Reddy, and K. S. Rao, “Microstructure, mechanical and corrosion behavior of high strength AA7075 aluminium alloy friction stir welds–Effect of post weld heat treatment”, Defence Technology, vol. 11, pp. 362-369, 2015.
[9]. R. Cao, G. Yu, J. H. Chen, and P. C. Wang, “Cold metal transfer joining aluminum alloys-to-galvanized mild steel”, J. Mater. Process. Tech., vol. 213, pp. 1753-1763, 2013.
[10]. S. Yang, J. Zhang, J. Lian, and Y. Lei, “Welding of aluminum alloy to zinc coated steel by cold metal transfer”, Mater. Design, vol. 49, pp. 602-612, 2013.
[11]. J. Lin, N. Ma, Y. Lei, and H. Murakawa, “Shear strength of CMT brazed lap joints between aluminum and zinc-coated steel”, J. Mater. Process. Tech., vol. 213, pp. 1303-1310, 2013.
[12]. S. S. Abed-Alkareem, “Determination of Welding Velocity and Arc Energy for Fusion MAG Welding Joint”, Al-Khawarizmi Engineering Journal, vol. 10, pp. 64-80, 2017.
[13]. K. R. Thomas, S. Unnikrishnakurup, P. V. Nithin, K. Balasubramaniam, P. Rajagopal, K. V. P. Prabhakar, “Online monitoring of Cold Metal Transfer (CMT) process using Infrared Thermography”, Quant. Infr. Therm. J., vol. 14, pp. 68-78, 2017.
[14]. H. Okamoto, M. E. Schlesinger, and E. M. Mueller, *ASM Handbook Volume 3: Alloy Phase Diagrams*, ASM International, 1992.
[15]. M. M. Atabaki, M. Nikodinovsk, P. Chenier, J. Ma, M. Harooni, and R. Kovacevic, “Welding of Aluminum Alloys to Steels: An Overview”, Journal for Manufacturing Science and Production, vol. 14, pp. 59-78, 2014.
[16]. G. Eggeler, W. Auer, and H. Kaesche, “On the Influence of Silicon on the Growth of the Alloy Layer During Hot Dip Aluminizing”, J. Mater. Sci., vol. 21, pp. 3348-3350, 1986.
[17]. L. Agudo, D. Eyidi, C. H. Schmaranzer, E. Arenholz, N. Jank, J. Bruckner, and A. R. Pyzalla, “Intermetallic FexAly -phases in a steel/Al-alloy fusion weld”, J. Mater. Sci., vol. 42, pp. 4205–4214, 2007.

[18]. Y. Su, X. Hua, and Y. Wu, "Influence of alloy elements on microstructure and mechanical property of aluminum–steel lap joint made by gas metal arc welding", J. Mater. Process. Tech., vol. 214, pp. 750– 755, 2014.
[19]. J. L. Song, S. B. Lin, C. L. Yang, and C. L. Fan, "Effects of Si additions on intermetallic compound layer of aluminum–steel TIG welding–brazing joint", J. Alloy. Compd., vol. 488, pp. 217–222, 2009.
[20]. L. A. Jácome, S. Weber, A. Leitner, E. Arenholz, J. Bruckner, H. Hackl, A. R. Pyzalla, "Influence of Filler Composition on the Microstructure and Mechanical Properties of Steel-Aluminum Joints Produced by Metal Arc Joining", Advanced Engineering Materials, vol. 11, pp. 350–358, 2009.
[21]. C. L. Chen, A. Richter, and R. C. Thomson, "Mechanical properties of intermetallic phases in multi-component Al–Si alloys using nanoindentation". Intermetallics, vol. 17, pp. 634–641, 2009.
[22]. M. Seo, *Analytical Methods in Corrosion Science and Engineering (Chapter 10)*, P. Marcus, F. B. Mansfeld, Ed. Florida, U.S.A.: CRC Press, 2005.

Biography of presenting author: Nilay COMEZ received bachelor's degree in Manisa Celal Bayar University, Department of Mechanical Engineering in 2010. She continued her graduate education in Manisa Celal Bayar University Department of Mechanical Engineering and got her Master of Science degree in 2012 and PhD in 2017.

ICETI
www.iceti.org
2018
07-11 MARCH
BUDAPEST
HUNGARY
II. INTERNATIONAL CONFERENCE ON ENGINEERING TECHNOLOGY AND INNOVATION

Parking Nearest to Light Tracking Vehicle with Microprocessor-Based Smart Parking System

Rukiye Uzun[1], Abdullah Cihad Ugur[1], Bayram Aran[1], Murat Sarikaya[1], Irem Senyer Yapici[1]

Abstract

With the increasing number of vehicles in the cities, the needs of the drivers for the parking spaces have increased and the intelligent parking systems developed have contributed to the solution of this problem. In this study, it was aimed that the drivers would identify the nearest free parking area on an area and, as soon as possible, determine the appropriate parking place with less fuel consumption. In this direction, a smart parking system designed to be installed in open or closed areas has been established. Drivers coming to the car park entrance in the designed system; the number of vacant parking spaces is displayed on an information screen, as well as the nearest parking is provided by means of light emitting diodes (LEDs). In addition, in case of emergencies such as possible fire in parking lots, in order to expel the drivers quickly from the car park area, the entrance and exit barriers are opened with audible warning and the evacuation routes with LEDs are drawn.

Keywords: *Arduino, Automatic Parking, Smart Parking System*

1. INTRODUCTION

In parallel with increasing human population, the number of vehicles has been arising day by day. According to the data obtained from Turkish Statistical Institute, while the number of registered vehicles was 21.090.424 by December 2016, it reached to 21.362.512 by March 2017 [1]. This increase in the number of the vehicles brought about many problems. Parking is one of these problems and this has become more significant than ever. In literature, there are many schematic studies centered on parking problem. For example, Uzkent at al. developed a new method for parking mobile robots like cars having holonomic limits. In the study, whether the parking area was enough or not was confirmed by ultrasonic detector placed on the robot and then planning of necessary maneuvers was carried out. Circular orbits to be followed by the moves in accordance with the dimension of parking place were established. The success of developed method for the parking areas in different dimensions was tested by MATLAB and it was shown that parking was carried out successfully [2]. Bingol et al. designed a prototype of automatic parking area system with programmable logic controller. The design has a capacity of 9 vehicles and also it can be used for educational purposes. Programmable logic controller limit switch was used for identifying the location of automatic transporters. Parking of the cars was carried out with user passwords [3]. In a study carried out recently, a vehicle prototype was developed to provide parking for cars and similar vehicles. The vehicle prototype provides parking with sensors on it without the user's help when it finds enough space after parking place calculation. Apart from automatic parking, remote controlling of prototype vehicle was carried out by developing an interface based on a mobile platform [4]. Also, finding a proper parking place in a short time in places having enormous parking areas (for example, multi-storey car parks, big shopping centers and airports) will provide drivers with many advantages. Smart car park system was developed to decrease the cost of fuel and time while looking for a proper parking place. In the system having a capacity of 9 vehicles, the transportation of the drivers coming to the entrance of the car park was carried out with light emitting diodes. Moreover, the number of available parking places was shown on a parking screen. It was provided in the design that car park exits were opened with a sound alarm in emergencies. The general structure of the study is as follows: used elements and their aims were explained in Section 2 by giving information about the car park system. Conclusions and future studies were explained in Section 3 by showing the success of the system.

2. MATERIAL AND METHOD

In the design, when a vehicle came to the entrance of the car park, entrance barrier was opened. Finding the closest place among available parking areas was carried out by light emitting diodes. Also, barriers in the entrance and exits of the car park were opened in emergencies. Moreover, the number of available parking places and emergency exits were shown on a digital screen. General schema of the car park system was given in Table 1.

[1] *Corresponding author: Bulent Ecevit University, Department of Electrical and Electronics Engineering, 67100, Zonguldak, Turkey. rukiyeuzun67@gmail.com*

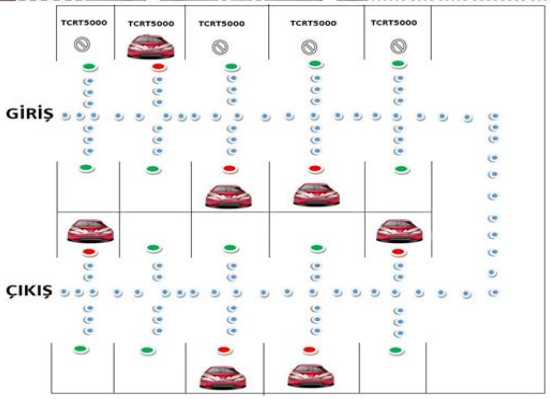

Figure 1. General diagram of smart parking system

In the design of smart car park system, direct electric servo motor, liquid crystal screen and key pad module, buzzer card, ULN-2003 DIP16 integrate, fire sensor, TCRT500 and MZ-80 sensor and light emitting diodes with chips were used. The control of these elements was provided by Arduino operator.

2.1. Arduino Mega 2560 R3

Arduino is an open-sourced physical programming platform providing basic input and output applications with the relevant elements by using Processing/Wiring language [5]. ATmega2560 microcontroller is available in Arduino Mega 2560 R3 and it is the latest model of Arduino. It has 54 digital input/output pins and 15 of these can be used as PWM outputs. Also, there are 16 analog outputs, 4 UART (serial port), a 16 MHz crystal oscillator, a USB connection, a power jack (2.1 mm), a ICSP head and a reset button [6]. Identifying available parking places was provided by transferring the information obtained from infrared sensor to Arduino microprocessor. Available areas were compared with each other and the closest area was marked and then the way was shown with LED.

2.2. DC Servo Motor

Servo motor is a motor rotating the shafts in an angular position with signals sent through the codes. This motor type is used when position and speed control are of importance. It can be adjusted according to requested position and speed [7]. This motor was used for opening and closing the barrier in the entrance of the car park.

2.3. Liquid Crystal Screen (LCD) and Key Pad Module

2x16 liquid crystal screen, 5 programmable push buttons and a reset button are available on the module. All buttons can be read through a pin by connecting 5 buttons to A0 pin of Arduino [8]. LCD placed upon the entrance of the carp park was used to show available parking places and warning sign when a fire is detected by the fire sensors.

2.4. Buzzer Card

Buzzer card is a basic electronic module having a buzzer and this buzzer can be used for audio output. Buzzer will start to alarm when an input/output pin is triggered by 5V or 3V. Card operating voltage is supported by 3.3-5V [9]. When a vehicle enters into or exits from the car park, sound signaling is given by the buzzer.

2.5. ULN-2003 DIP16 Integrate

ULN2003 integrate is used as a buffer integrate having a shared emitter and 7 open-collector darlington connected transistors. Each has a flow capacity of 500 mA from 7 channels. Diodes to prevent counter-electromotive force when inductive loads are run are connected to each channel [10]. Generally, it is a proper buffer for relay, DC motor, step motor, LED indicator and fleming light running.

2.6. Fire Sensor Card

Fire sensor card is a sensor card used to find the fire having a wave length between 760 nm and 1100 nm [9]. All barriers are opened thanks to these sensors placed in the system and also exits are shown.

2.7. MZ-80 Sensor

MZ-80 is one of infrared sensors. While the transmitter of this sensor sends infrared beams, reflected beams are taken by the receiver and distance measuring is performed. The sensor used during overtaking is MZ-80 sensor. This sensor gives logic 0 output when it sees an object and it gives logic 1 output when it doesn't see an object [11]. The entrance and exit of the vehicles are identified by using these distance measuring sensors.

2.8. TCRT5000 Sensor

TCRT5000 is an infrared sensor and it has an infrared transmitter and receiver on it. Infrared light in the sensor sent by the transmitter reaches to the receiver after reflected from a surface. The receiver gives output according to the number of coming lights [12]. In the study, this sensor was placed in lower parts of parking areas and it was used for identifying available places.

2.9. Light Emitting Diodes with Chips

Light Emitting Diodes are semi-conductive materials giving light by releasing a photon when there is a flow over it. It operates under LED 12V supply voltage and it has 60 LEDs in one meter [13]. In the study, parking areas were numbered from the entrance to the exits as the closest and the furthest ones and the closest way according to the parking places were shown by LEDs.

3. CONCLUSIONS AND RECOMMENDATIONS

In smart car park system, entrance barrier was opened when a vehicle came to the entrance of the car park. During this time, the closest parking area was identified among the parking areas. LED lights were benefited for the transportation of the driver to the closest available parking area. Therefore, the driver could find the opportunity of parking his vehicle through the closest way. An example showing the identification of the closest parking area for designed system was given in Table 2.

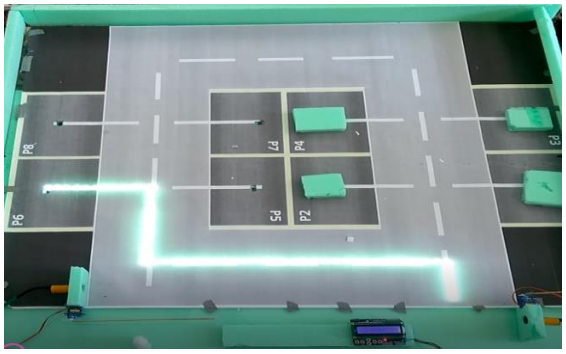

Figure 2. Design of the designed system

Thanks to this smart car park system, loss of fuel and time for searching an available parking area was prevented. Also, when there was a fire within the car park, fire sensors got activated with a sound alarm. Then entrance and exit barriers were opened and the vehicles were quickly discharged through designed evacuation road. On future studies, information like the plates of the vehicles entering into the car park, parking number and entrance/exit hour are recorded on an interface program and security level of the car park will be increased accordingly. Moreover, the system will be developed to find the parking place easily in enormous parking areas such as shopping stores.

REFERENCES

[1]. (2017) Turkiye Istatistik Kurumu, Motorlu Kara Tasitlari website. [Online]. Available: http://www.tuik.gov.tr/PreHaberBultenleri.do?id=24598
[2]. Uzkent B., and Parlaktuna O., "Araba Benzeri Gezgin Robotun Otomatik Park Etmesi Icin Bir Yontem", *Elektrik-Elektronik-Bilgisayar Ve Biyomedikal Muhendisligi 13. Ulusal Kongresi*, 2009.
[3]. Bingol O., Aydogan T., Didin H.R., Yalciner A.S., and Duygulu K., "PLC kontrollu otomatik katli otopark sistemi", *SDU International Technologic Science*, vol. 2, pp.65-76, 2010.
[4]. Yuzgec, U., and Sahin, S., "Mobil Otonom Park Etme (MOPA) Uygulamasi Gelistirilmesi Mobile", *Turkiye Bilisim Vakfi Bilgisayar Bilimleri Ve Muhendisligi Dergisi*, vol. 9, pp. 27-34, 2016.
[5]. Bergquist, K., and Abeysekera, J., "Quality function deployment (QFD)-A means for developing usable products", *International Journal of Industrial Ergonomics*, vol.18, pp.269- 275, 1996.
[6]. Jiang, L., Liu, D.Y., and Yang, B., "Smart home research", *Proceedings of the Third International Conference on Machine Learning and Cybernetics*,2004, p. 659- 663.
[7]. Sevinc, A., "A Full Adaptive Observer for DC Servo Motors", *Turk J. Elec. Engin*., vol. 11, pp. 117-130, 2003.
[8]. Akcayol, M. A., "Bulanik Mantik Denetimli Katodik Koruma Devresi Tasarimi", *G.U. Journal of Science*, vol. 17, pp.111-127, 2004.
[9]. Yuzgec, U., and Aba, O., "Raspberry Pi Kullanilarak bir Akilli Ev Uygulamasi Gelistirilmesi", *Bilecik Seyh Edebali Universitesi Fen Bilimleri Dergisi*, vol. 4, pp. 21-29, 2017.
[10]. Odeh, S., and Abdelghani, E., "Laboratory Experimentation for Supporting Collaborative Working in Engineering Education over the Internet", *World Academy of Science, Engineering and Technology International Journal of Computer, Electrical, Automation, Control and Information Engineering*, vol. 3, pp. 1868-1874, 2009.
[11]. Atas, M., "Fistik siniflandirma sistemi icin Siirt fistigi imgelerinden gurbuz ozniteliklerin cikarilmasi", *Dicle Muhendislik Fakultesi Dergisi*, vol. 7, pp. 93-102, 2016.
[12]. Song, W., Zhao, S., Jiang, F., Zhu, K., Cao, L., and Shi, Y., "Teleoperation Robot Control System Based on Mindband Sensor", *In Computational Intelligence and Design (ISCID), 2012 Fifth International Symposium*, vol.2, pp.299-302, 2012.
[13]. Mercan, M., Ongun, R., Dincer, K., and Tosun, M., "Selcuk Universitesi Kosullarinda Led Renklerinin Aydinlatmada Gunes Enerjisi Guc Performansina Etkisinin Incelenmesi", *Selcuk-Teknik Dergisi*, vol. 12, pp. 12-24, 2013.

ICETI
www.iceti.org
2018
07-11 MARCH
BUDAPEST
II. INTERNATIONAL CONFERENCE ON ENGINEERING TECHNOLOGY AND INNOVATION

Surface Characterization of Boronized Pure Tungsten

Ibrahim Gunes[1], Tayfun Uygunoglu[2]

Abstract

In the present study, effect of the boriding process on surface properties of pure Tungsten has been investigated. Boriding was performed in a solid medium consisting of Ekabor-II powders at 1173 and 1273K for 2 and 6 h. The boride layer was characterized by optical microscopy, X-ray diffraction technique and the micro-Vickers hardness tester. X-ray diffraction analysis of boride layers on the surface of the steels revealed the existence of WB_2, WB_3, WB_4 and W_2B_5 compounds. Depending on the chemical composition of substrates, the boride layer thickness on the surface of the Only parameter that changes is boronizing time. Thus, thickness of boride layer changes with boronizing time. WB boride layers ranged in thickness from 18 to 184 μm. The hardness of the boride compounds formed on the surface of the Tungsten ranged from 2185 to 4292 $HV_{0,1}$, whereas Vickers hardness values of the untreated Tungsten were 468 $HV_{0,1}$.

Keywords: Tungsten, Boride layer, XRD, Micro-hardness

1. INTRODUCTION

Boriding is a thermo chemical surface hardening method which can be applied to practically any ferrous material, as well as some nonferrous materials (W, Mo, Nb, Ti alloys). The boriding process is applied in order to increase the hardness and the wear resistance of the surfaces of metals and alloys, and in order to retain these properties at high temperatures and increase erosion resistance. The process can be carried out in solid, liquid, gaseous or plasma medium. The most useful boriding method is box boriding, which is easier to apply and more cost effective than other methods. Through boriding a very hard boride layer which has the properties of good friction and wear and corrosion resistance is obtained on the surface of the metal. The method applied during boriding, boron powder, type of borided material and process parameters are the factors which affect the shape of the boride layer and its mechanical properties. The thickness of the boride layer formed on the surface of the metal by the boriding process is affected by the composition of the boriding medium, degree of purity, treatment temperature and time and metal composition subjected to boriding. In general, the presence of alloying elements reduces the diffusivity of boron in the steel and consequently decreases the thickness of the borided layer. For example, while carbon, molybdenum and tungsten dramatically reduce the borided layer thickness; silicon, chromium and aluminum have moderate influence, and nickel, manganese and cobalt have only marginal influence [1-8]

In the present study, effect of the boriding process on surface properties of pure Tungsten has been investigated. For this reason, structural properties of each sample were investigated using optical microscopy, XRD, SEM, EDS, microhardness tests.

2. EXPERIMENTAL STUDIES

This study uses pure tungsten. The samples were sized to 20x8 mm and polished progressively with 1000-grit emery paper before boronizing process. The boriding heat treatment was carried out in solid medium containing a B_4C and KBF_4 powder mixture placed in an electrical resistance furnace operated at temperatures of 1173 and 1273 K for 2 and 6 h under atmospheric pressure.

The microstructures of polished and etched cross-sections of the specimens were observed under a Nikon MA100 optical microscope. The X-ray diffractograms were obtained by using a copper tube source as dictated by the conventional bragg-brentano (θ-2θ) technique having symmetric geometry with monochromatized radiation (Cu Kα, λ=0.15418 nm). The thickness of the layers formed on the steels was measured by an optical micrometer attached to the optical microscope. The hardness of the boride layers was measured on the cross-sections using the Micro-Vickers indenter (Shimadzu HMV-2) with 100 g loads.

Figure 1. Boriding heat treatment of Tungsten

3. RESULTS AND DISCUSSIONS

The cross-sections of optical micrographs of the borided pure tungsten at temperatures of 1173 and 1273 K for 2 and 6 h are shown in Figures 1a-c. It is seen that the formed boride layers on the borided pure tungsten appear to be compact and regular and having a smooth interface. Depending on the boriding parameter (temperature), the boride layer thickness on the surface of borided pure tungsten ranged from 18.65 µm and 184.78 µm.

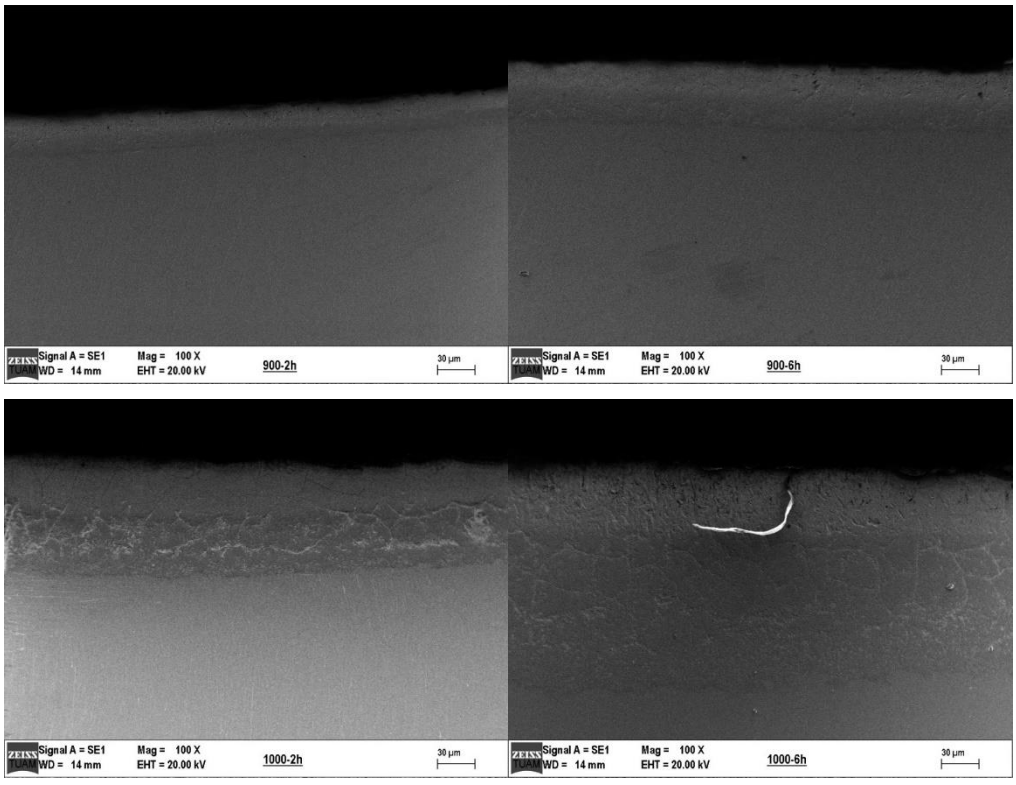

Figure 2. The SEM micrograph of the cross-sections of the borided tungsten a) 1173 K - 2h, b) 1173 K - 6h, c) 1273 K - 2h, d) 1273 K - 6h.

XRD results showed that the boride layers formed on the pure tungsten contained WB, WB_2, WB_3, WB_4 and W_2B_5 phases in Fig. 3. Micro-hardness measurements were carried out on the cross-sections from the surface to the interior along a line, as can be seen in Figure 3. The hardness of the borided tungsten varied between 2185 and 4292 $HV_{0,1}$.

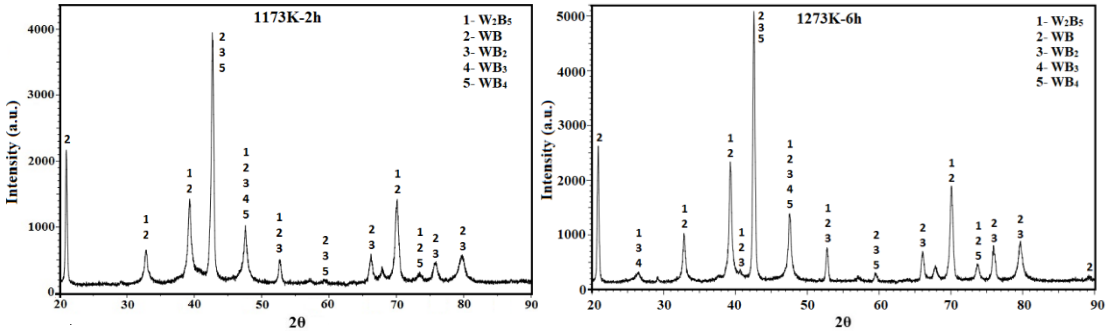

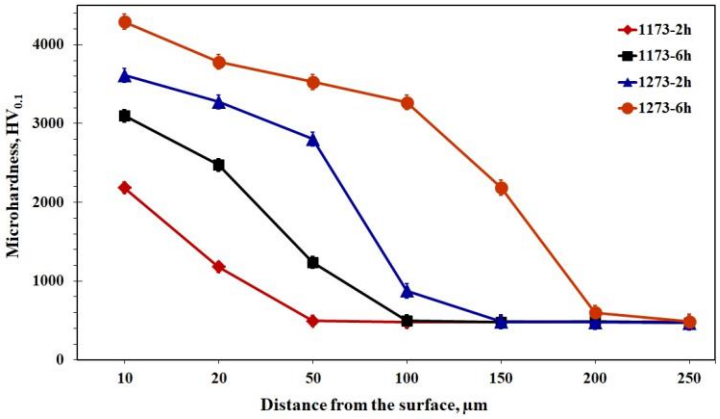

Figure 3 gives the XRD pattern and hardness recorded at the surface of borided tungsten at the two temperatures 1173 and 1273 K for 2 and 6 h.

4. CONCLUSIONS

The following conclusions may be derived from the present study.

- Boride types formed on the surface of the tungsten has a smooth and flat morphology.
- The multiphase boride coatings that were thermo chemically grown on the pure tungsten were constituted by the W_2B_5 WB, W_2B, W_3B and W_4B phases.
- Depending on the boriding parameters, the boride layer thickness formed on the borided pure tungsten was ranged from 18,65 µm to 184.78 µm.
- Depending on the boriding temperature and time, the hardness of the boride layer formed on the pure tungsten varied between 2185 and 4292 $HV_{0.1}$, whereas Vickers hardness value of the untreated pure tungsten was 475 $HV_{0.05}$.
- As a result of boriding, the high surface hardness of the pure tungsten was improved.

ACKNOWLEDGEMENT

The authors are grateful to the Scientific Research Project (16.KARIYER.37) Council of Afyon Kocatepe University. The authors wish to express their gratitude to the AKU-BAPK for its financial assistance.

REFERENCES

[1] B. Bhushan, B.K. Gupta: Handbook of tribology: materials, coatings, and surface treatments. McGraw-Hill (New York), 1991.
[2] A. K. Sinha: Boriding (Boronizing). ASM Int. Handbook, Vol 4, The Materials International Society, 1991, 437–447.
[3] C. Bindal, A. H. Ucisik: Characterization of borides formed on impurity-controlled chromium-based low alloy steels. Surf. Coat. Technol., 122, 208, 1999.
[4] I. Gunes: Tribological Properties and Characterisation of Plasma Paste Borided AISI 5120 Steel. Journal of the Balkan Tribological Association, 20, 351, 2014.
[5] M. Usta, I. Ozbek, C. Bindal, A. H. Ucisik, S. Ingole, H. Liang: A comparative study of borided pure niobium, tungsten and chromium. Vacuum, 80, 1321, (2006).
[6] H. Dinc, A.Motellabzadeh, H. Cimenoglu, M. Baydogan: Thermochemical boriding of inconel 718 superalloy, Academic Journal of Science, ISSN: 2165-6282, 2, 385, 2013.
[7] I. Gunes: Wear Behaviour of Plasma Paste Boronized of AISI 8620 Steel with Borax and B_2O_3 Paste Mixtures. J. Mater. Sci. Technol., 29, 662, 2013.
[8] A. G. Von Matuschka: Boronizing. Heyden and Son Inc., Philadelphia, 1980.

ICETI
www.iceti.org
2018
07-11 MARCH
BUDAPEST
HUNGARY
II. INTERNATIONAL CONFERENCE ON ENGINEERING TECHNOLOGY AND INNOVATION

The Properties of Yarns Containing Recycle Polyester Fiber in Different Yarn Number

***Seval Uyanik*[1]**

Abstract

Recycling is not new to the textile and apparel industry. Recycling 'refers to the breakdown of product into its raw materials in order for the raw material to be reclaimed and used in new products. In textile when recycling is mentioned, recycle fibers come first. The using of recycle fibers increases day by day in the yarn manufacturing. Cotton and polyester are especially the most common fibers recycled, but other fibers including wool, nylon, and even aramids are being recycled in yarn production. In this study, it is aimed to determine the properties of yarns containing recycle polyester fiber in different yarn number. For this purpose, the yarns containing viscose fiber and recycle polyester fiber were produced at different blend ratios and different yarn numbers. After, the produced yarns were tested to determine of their physical and mechanical properties considering relevant standards. Test results showed that recycle polyester fibers cause worsening in yarn quality. On the other hand, these negative effects are more clearly observed in terms of yarn physical properties which are unevenness, imperfection and hairiness in comparison to yarn mechanical properties which are tenacity and elongation. When the usage of recycle polyester fiber examined in terms of yarn number, RPET fiber is suitable for thick yarns which are Ne 20 and thicker yarns in all ratios. RPET fiber is suitable for Ne 30 yarns if it is used in 65% ratio and lower than this ratio whereas it is suitable for Ne 40 yarns if it is used in lower ratios than 50%.

Keywords: Recycle polyester fiber, viscose fiber, yarn manufacturing, yarn number, yarn properties, yarn tensile properties

1. INTRODUCTION

The increasing industrialization, urbanization and the technological development have caused to increase depletion of the natural resources and environmental pollution's problem. Especially, for the countries which have not enough space recycling of the waste eliminating waste on regular basis or decreasing the amount and volume of waste have provided the important advantages. For this purpose, usage areas of recycled PET have been developed rapidly. Although recycled PET is used in plastic industry, composite industry also provides usage alternatives of recycled PET. Textile is a suitable sector for recycling of some plastics made of polymers too [1].

Recycling has a lot of advantages which are supply of the raw materials needed to make new products, new working areas opportunities, decrease in waste, less natural resource consumption, energy saving to obtain virgin product, protection of available storage space, global warming prevention, water pollution reduction, protection of wildlife, and contribution to the economy [2].

Recycling and reuse of materials is not new to the textile and apparel industry. Recycling refers to the breakdown of product into its raw materials in order for the raw material to be reclaimed and used in new products. In contrast, reuse refers to an existing product being used again within the same production chain [3].

Textile recycling may involve reclaiming pre-consumer waste or post-consumer waste [4].

Recycle polyester fibers are produced from post-consumer pet bottles according to melt spinning technology (Figure 1). The plastic bottles are stripped of caps and labels cleaned. They are processed into flakes and washed. The clean flakes are transformed into chips. Yarn is pulled from the melted chips. 100% recycled polyester yarn can be used directly or blended with other fibers to produce new products [5].

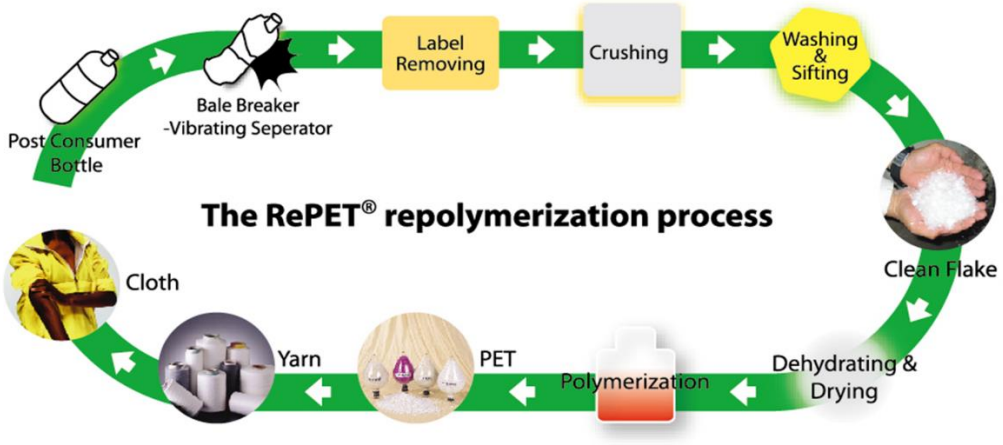

Figure 1. Recycle polyester fiber production process [6]

It can be given a lot of examples as recycling facts that 10 plastic bottles equal 1 pound of polyester fiber, 1 ton (2000) lbs of plastic bottles recycled saves 3.8 barrels of oil, 1 million plastic bottles recycled saves 250 barrels of oil, 1 million plastic bottles recycled eliminates 180 metric tons of CO_2 emissions from being released into the atmosphere, recycling plastic bottles takes 8 times less energy than to produce an equivalent amount of new ones, 150 fleece garments or 500 t-shirts or 50 back packs made from recycled plastic bottles save 1 barrel of oil [7].

Although there are many studies about recycle polyester production process, not many studies about yarn production parameters and fabric properties produced from recycle polyester and their blend yarns. In this study which is thought to contribute to the literature, it is aimed to determine the properties of yarns containing recycle polyester fiber in different yarn number.

2. MATERIALS AND METHOD

As raw materials, recycle polyester (RPET) fiber having 1.2 dtex fineness and 38 mm length, and viscose fiber (CV) having 1.4 dtex fineness and 38 mm length were used. 15 yarns were produced in different yarn numbers which are Ne 20, Ne 30 and Ne 40, and in different blend ratios which are 100% RPET, 65-35% RPET-CV, 50-50% RPET-CV, 35-65% RPET-CV, 100% CV by using these fibers. Machine parameters for spinning were given in Table 1.

Table 1. Machine parameters

Blow Room	Rieter Unifloc A11 Rieter Uniclean B12 Rieter Unimix B70 Rieter Unistore A79		
Card	Rieter C70	40 kg/h	Ne 0.100
Draw Frame-1	Rieter SDB 40	650 rpm	Ne 0.120
Draw Frame-2	Rieter RSB 40	550 rpm	Ne 0.120
Roving	Marzoli F10	1100 rpm	Ne 0.80
Ring-Compact	Rieter K45	18000 rpm	Ne 20, Ne 30, Ne 40
Autoconer	Schlafhorst X5	1200 rpm	

The obtained yarns were applied yarn unevenness, imperfection, hairiness tests in Uster Tester 6, and yarn tenacity and elongation tests in Uster Tensorapid 5.

3. RESULTS AND DISCUSSION

The test results were investigated in two headings including structural properties and tensile properties.

3.1. Structural Properties

The graphic by composed of yarn unevenness values is seen in Figure 2. There is no clear differences between yarns for Ne 20 yarns,. Also, 100% RPET yarn has the lowest unevenness. For Ne 30 and Ne 40 yarns, unevenness values increase parallel with increasing RPET ratio. On the other hand for Ne 30 yarn containing 100% RPET has very higher unevenness, for Ne 40 yarns, unevenness values are close to each other in the yarns containing RPET. Expectedly, unevenness values increase from thick yarn to thin yarn.

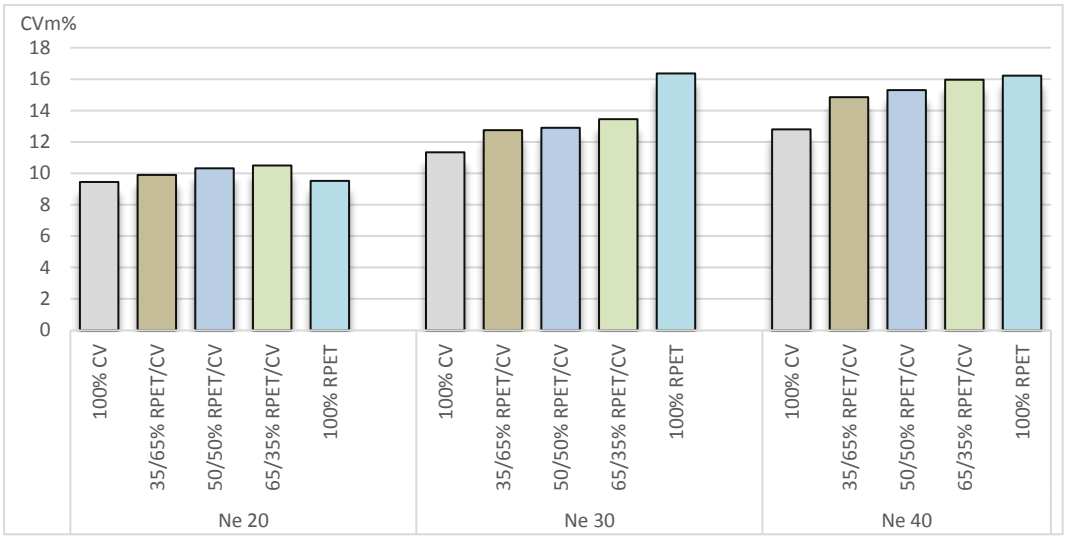

Figure 2. Unevenness

According to the graphic given in Figure 3, all Ne 20 yarns have not thin -50% places. For Ne 30 yarns, there is no differences in terms of thin places except 100% RPET yarn. Thin places increase parallel with increasing RPET ratio for Ne 40 yarns, Ne 40 yarns have higher thin places than Ne 30 yarns.

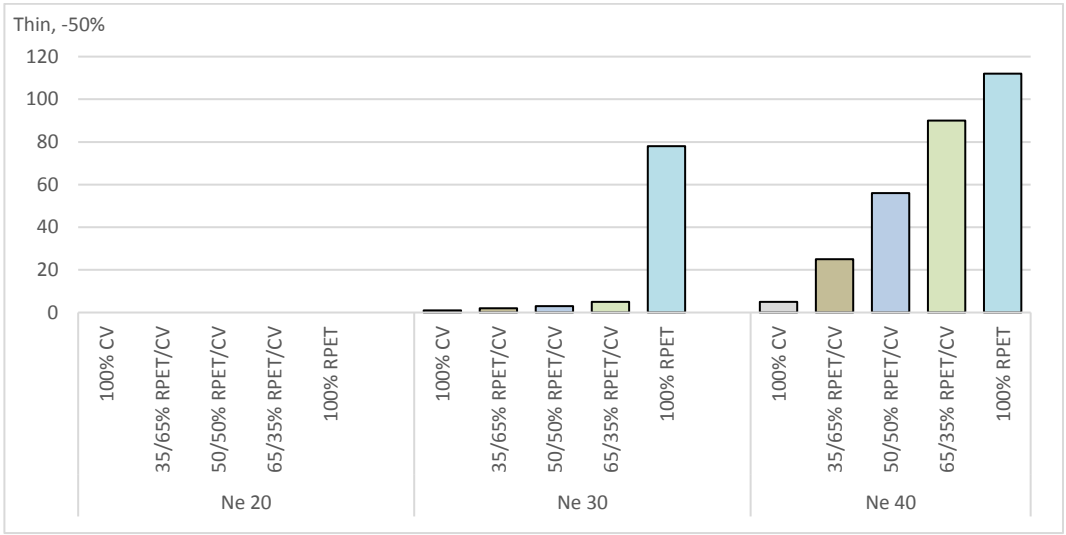

Figure 3. Thin places

From Figure 4 it is seen that thick places are very low for all Ne 20 yarns. The number of thick places are close to each other except 100% RPET yarn for Ne 30 yarns. For Ne 40 yarns, the number of thick places for the yarns containing 35% RPET and 65% RPET higher than that of the other yarns. Thick values are almost same for the yarns containing 50% RPET and 100%RPET. Ne 30 yarns have lower thick places than Ne 40 yarns except Ne 30 yarn having 100% RPET.

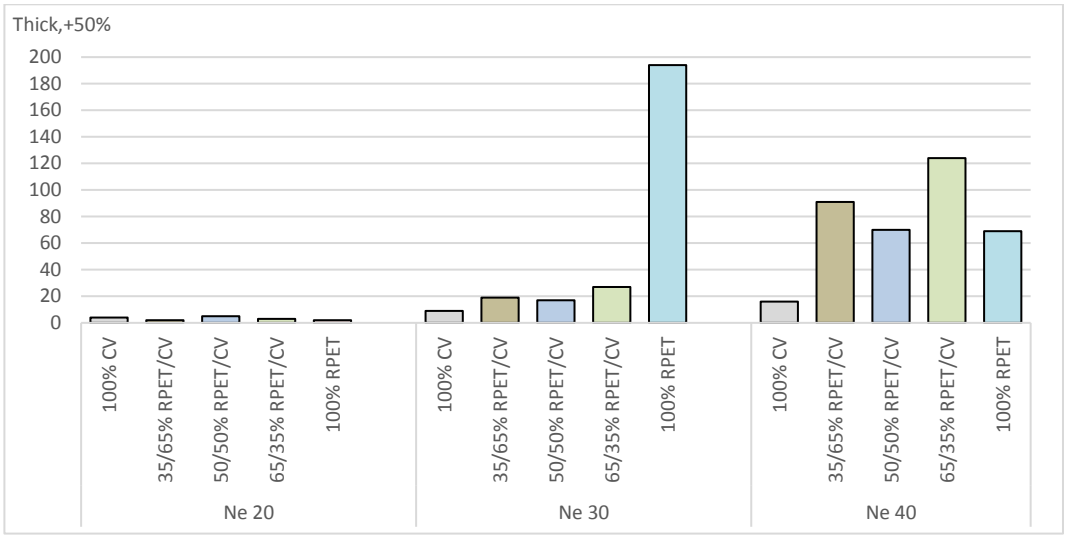

Figure 4. Thick places

As become in thin and thick places neps are very low and almost same for all Ne 20 yarns (Figure 5). Except 100% RPET yarn for Ne 30 yarns the number of neps are very low and close to each other. The number of neps is the highest in 100% RPET yarn. For Ne 40 yarns, the number of neps in the yarns containing 35% RPET and 65% RPET higher than that of the other yarns. 100% CV yarn and 100% RPET yarn have low neps. Ne 40 yarns have usually higher neps than Ne 30 yarns.

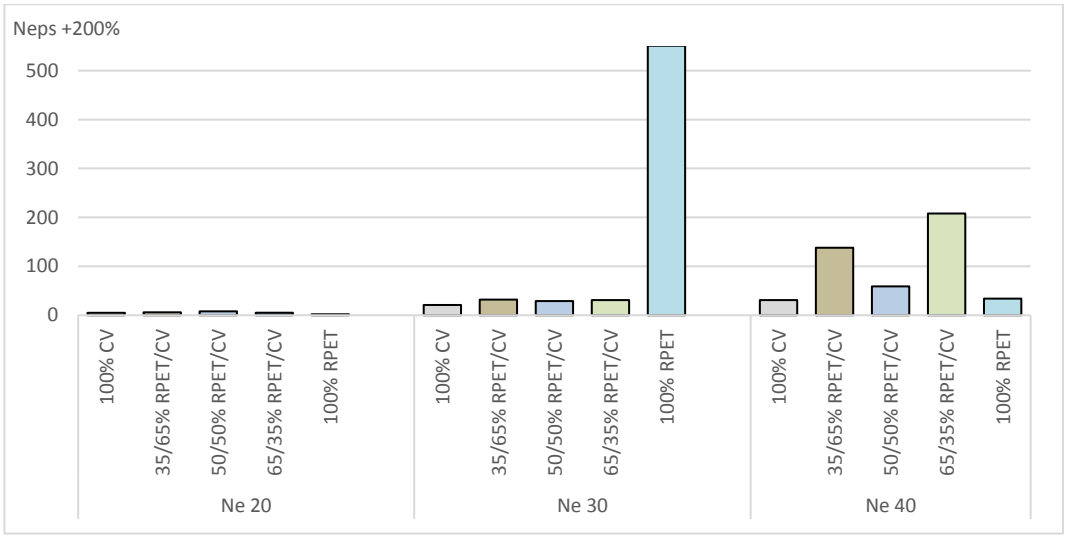

Figure 5. Neps

As seen in Figure 6, there is an increase tendency parallel with increasing RPET ratio in hairiness for all yarns. Hence, hairiness values decrease by increasing yarn number. In other way, thin yarns have lower hairiness than thick yarns. Ne 30 yarn with 100% RPET has the highest hairiness value.

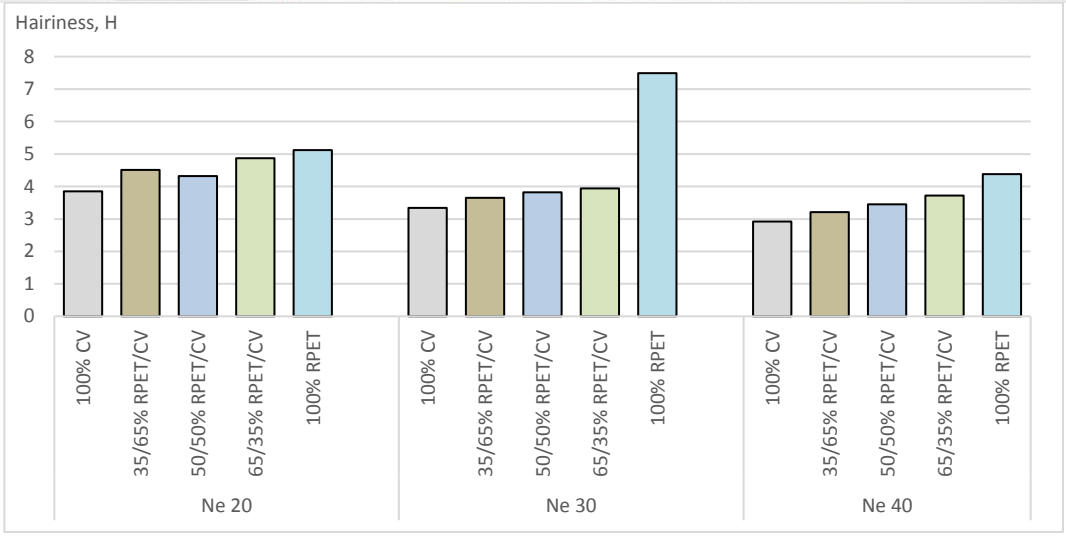

Figure 6. Hairiness

3.2. Tensile Properties

According to Figure 7 for all yarn numbers, 100% RPET yarns have the highest tenacity. The tenacity values are very close to each other for Ne 20 and Ne 30, whereas these values decrease parallel with RPET ratio for Ne 40. At the same time, the tenacity values decrease by increasing yarn number.

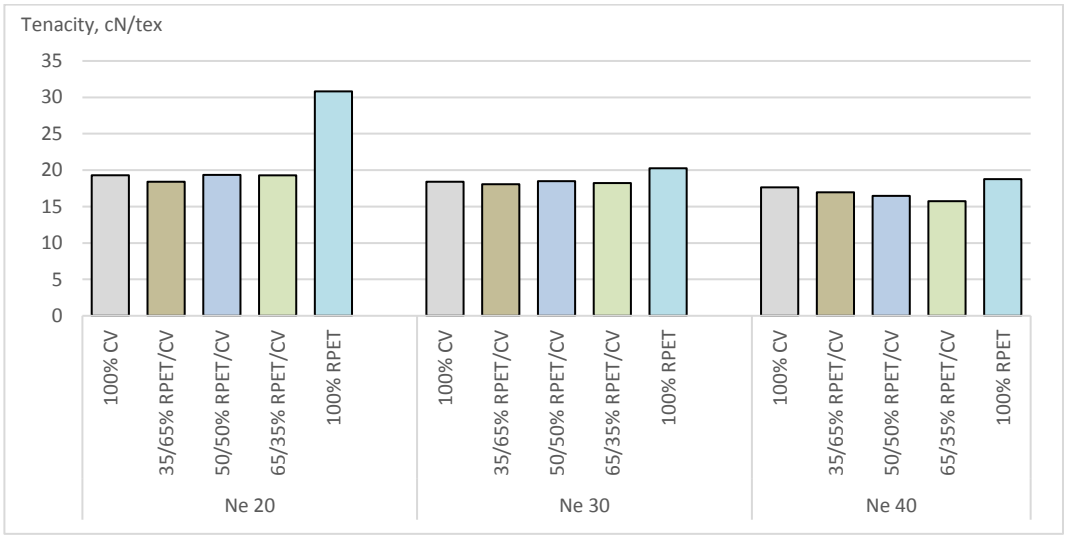

Figure 7. Tenacity

It is observed that there is usually the same tendency for Ne 30 and Ne 40 from Figure 8. So the yarns having 100% CV higher elongation than the other yarns, and elongation values increase parallel with increasing RPET ratio. For Ne 20 yarns, the yarn containing 65% RPET has the highest elongation whereas the yarn containing 100% RPET has the lowest elongation. Nevertheless, increase tendency is seen by increasing RPET ratio in elongation. The elongation values decrease from thick yarn to thin yarn.

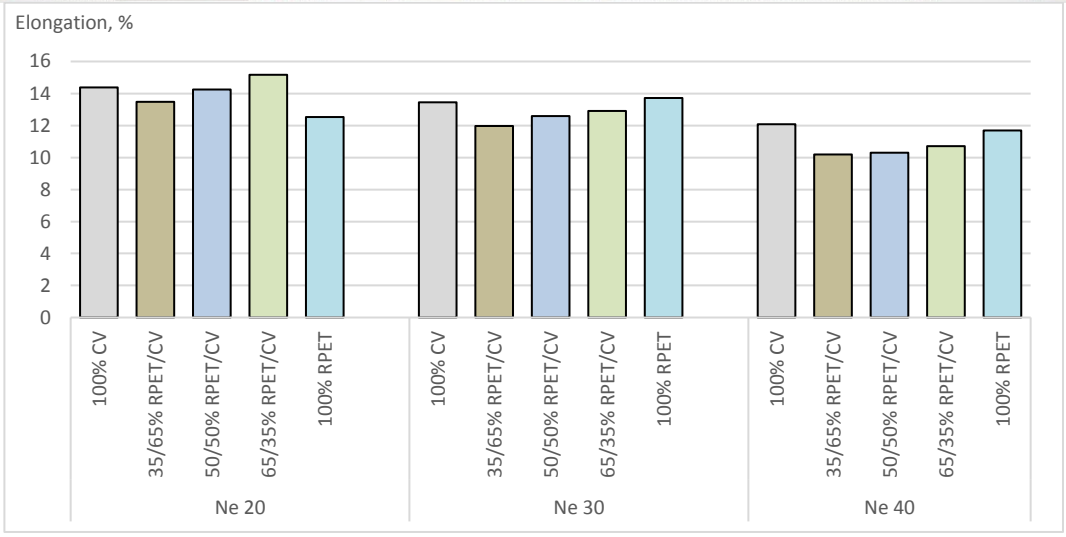

Figure 8.Elongation

4. CONCLUSION

The study results can be summarized:

- The values of unevenness, thin places, thick places, and neps increase by increasing RPET fiber ratio in all yarn numbers.
- The values of unevenness, thin places, thick places, and neps increase from thick yarn to thin yarn.
- The hairiness values increase by increasing RPET ratio whereas these values decrease by increasing yarn number.
- The elongation values usually increase by increasing RPET fiber ratio and decreasing yarn number.
- Pure RPET yarns have the highest tenacity values.
- In blend yarns, the tenacity values do not change for thick yarns, they decrease by increasing RPET fiber ratio for thin yarns.

As a conclusion of these it can be said that RPET fiber is suitable for thick yarns which are Ne 20 and thicker yarns in all ratios. RPET fiber is suitable for Ne 30 yarns if it is used in 65% ratio and lower than this ratio whereas it is suitable for Ne 40 yarns if it is used in lower ratios than 50%.

ACKNOWLEDGMENT

The author thanks to **Gama Recycle Mill** for yarn producing and testing.

REFERENCES

[1]. A. E. Tayyar, and S. Ustun, *Usage of Recycled Pet*, Pamukkale University, Journal of Engineering Sciences, Vol. 16, No. 1, pp.53-62, 2010.
[2]. Conserve Energy Future, Available: https://www.conserve-energy-future.com/advantages-and-disadvantages-of-recycling.php
[3]. K.K. Leonas, *The Use of Recycled Fibers in Fashion and Home Products*, Springer Science+Business Media Singapore S.S. Muthu (ed.), Textiles and Clothing Sustainability, Textile Science and Clothing Technology, DOI 10.1007/978-981-10-2146-6_2, 2017.
[4]. A. Payne, *Open and Closed-Loop Recycling of Textile and Apparel Products*, Handbook of Life Cycle Assessment (LCA) of Textiles and Clothing, 103–123, 2015
[5]. RPET-Fibers_Filament_August_2013 Available: https://tr.scribd.com/document/283190851/Fibers-Filament-August-2013-3
[6]. http://www.libolon.com/product273
[7]. Recycling of Plastic Bottles into Yarn & Fabric, Available: http://www.textilevaluechain.com/index.php/article/technical/item/247-recycling-of-plastic-bottles-into-yarn-fabric

Biography: Seval Uyanik received the B.Sc. degree in Department of Textile Engineering from Ege University in 1992. She is currently working as an Instructor, Department of Textile, Technical Sciences Vocational High School, University of Gaziantep, Turkey.

ICETI 2018 07-11 MARCH BUDAPEST HUNGARY www.iceti.org
II. INTERNATIONAL CONFERENCE ON ENGINEERING TECHNOLOGY AND INNOVATION

An Investigation of Injection Moulded Products Development

M. S. Abdul Karim[1], H. A. Al Shehri.[1]

Abstract

This research paper describes a proposal for the methodology or process of injection moulded parts and product development. Plastics i.e. thermoplastics, thermosets and elastomers products market is huge and the global plastics market is expected to reach USD 654.38 billion by 2020 [1]. Injection moulding is the most widely used moulding process for thermoplastics, and in few applications through equipment modifications thermosets and elastomers are also injection moulded [2]. In this paper, an injection moulded part product development process is suggested, and two real engineering case studies have been selected and investigated based on the suggested product development process. The first case study studied, proposed and validated the design and processability of an innovative and cost effective High Density Polyethylene (HDPE) industrial pallet design. The design criteria for the pallet were first outlined and iterations of designs were made to achieve and comply with the desired criteria. HDPE industrial pallets need to be designed in such a way it can withstand similar or better static and dynamic loadings than wooden pallets, have high stackability for maximum shipping quantity, consumed minimum volume of plastic materials and have comfortable processing window for injection mouldability. The second case study describes the investigation of failed paint buckets that happened in a paint factory. According to the data provided by the manufacturer, the design and the material of the buckets should be able to absorb the intended design loads. However, some buckets in the bottom of the bucket stacks have buckled and raise concerns to the company. Several potential reasons have been presented and investigated. An FEA mechanical load simulation has been designed and run to evaluate different cases and conditions.

Keywords: Injection Moulding, Plastics, CAD, CAE, Moldflow, Product Design, High Density Polyethylene

1. INTRODUCTION

This research work describes a proposal for the methodology or product development process for injection moulded parts. Plastics i.e. thermoplastics, thermosets and elastomers products market is huge and the global plastics market is expected to reach USD 654.38 billion by 2020 [1]. Injection moulding is the most widely used moulding process for thermoplastics, and in few applications through equipment modifications thermosets and elastomers are also injection moulded [2].

In this paper, an injection moulded part product development process is suggested and two real engineering case studies have been selected and investigated based on the suggested product development process. The first case study is for a new product development from ideas to realization and the second case study investigates failure that occurs on current injection moulded product.

2. METHODOLOGY

This research paper has propoesed two porcess design methodologies. One for new product development and the other one is for an exisiting product failure investigation. These methodologies are based on few case studies. One case study each is shown later to illustrate the design process.

[1]*Corresponding author: Higher Colleges of Technology, Abu Dhabi Men's Campus, Abu Dhabi, United Arab Emirates.* *mshairs@hct.ac.ae*

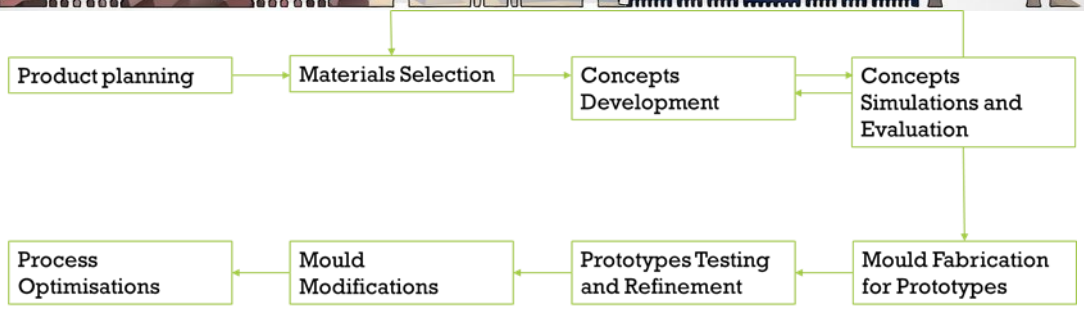

Figure 2. Methodology For New Development of Injection Moulded Product.

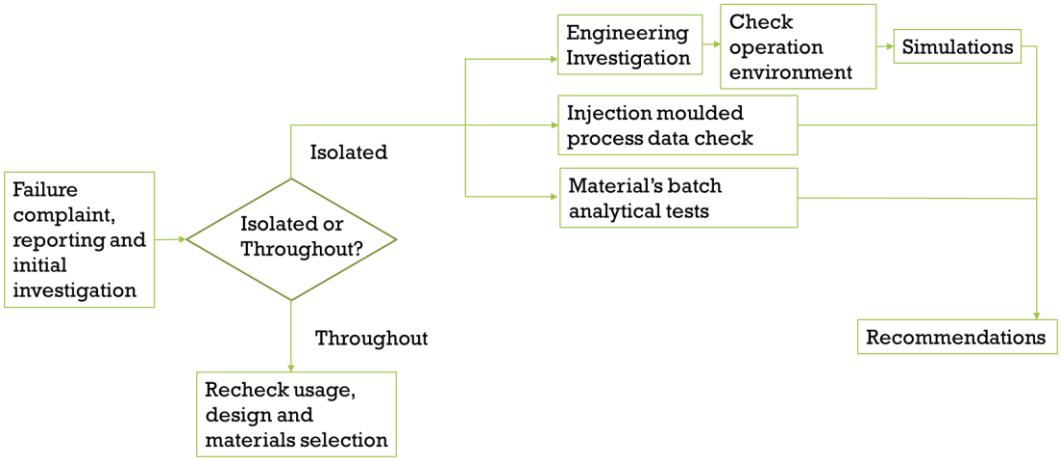

Figure 2. Methodology For Failure Investigation of Injection Moulded Product

3. CASE STUDY I: NEW PRODUCT DEVELOPMENT

During the design stage, the problem statement should be well understood that an industrial pallet of the size approximately 1100 mm x 1300 mm that can bear the static load of 3 tonnes and dynamic load of 1.5 tonne. Several designs have been considered and developed in-house and also outsourced from potential technology partners. Figure 2 below shows some of the designs considered during this stage. Prototypes were also made using our Fused Deposition Modelling (FDM) machine to understand better the functionality. Some designs needed to be reverse engineered to get the CAD data as the potential technology partners gave the physical prototypes.

These designs were then simulated in Autodesk Inventor to determine particularly the stress, strain and deformation analysis results (See Figure 3). In general, plastics strengths; in this case HDPE or PP, decreases tremendously over heat and time unlike metals. The individual molecules that make up polymeric materials are very large and have an extended chain-like shape that results in an entangled structure. This lack of a predictable and repeatable structure gives rise to a situation where changes in temperature always influence the mechanical properties of these materials [3]. Thus, in plastic product design for such an application like the industrial pallet that will be operating in hot weather of Saudi Arabia, very high safety factors needed to be considered during the design stage.

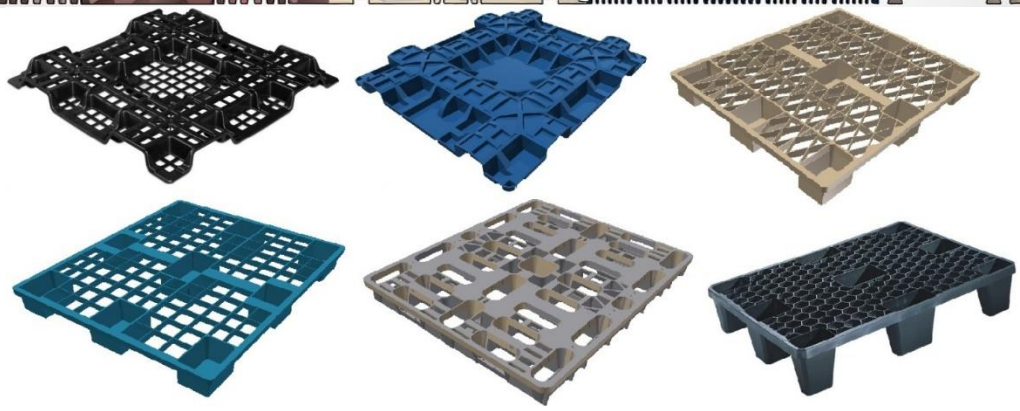

Figure 3. Samples of Industrial Pallet Designs Considered.

Based on the results simulated, a patent pending design from Scholler Allibert of 3 mm wall thickness was selected to be further investigated and tested. The design was selected based on the low stress, strain and deformation analysis results. The favored material was HDPE over PP because of extra strength that HDPE offers. This resulted in a lower internal stress and deformation of the pallet. The consumption of only 0.0083 m^3 of material makes the design in terms of price competitive to the wooden pallets. .Furthermore, the design allows for high stackability of empty pallets, thus, can decrease the cost of shipping of empty pallets compared to unit price. Incremental nest height of about 26 mm allows the pallets to be shipped more than 1400 pieces per 40 foot container.

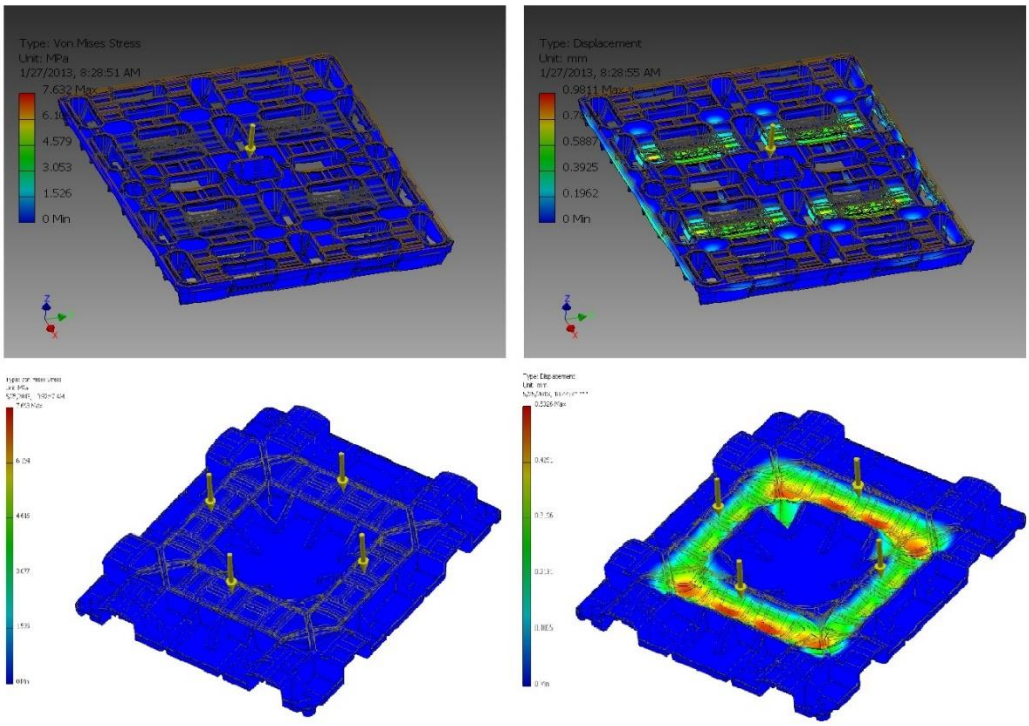

Figure 4. Stress and Deformation Analysis Results Obtained from Autodesk Inventor.

The HDPE pallet is mostly suitable to be produced by injection moulding process. The next stage is to put the selected design into Autodesk Moldflow to evaluate the processing parameters and machine conditions. Autodesk

Moldflow is an in-depth plastic injection moulding process simulation tool and has an extensive material library. Having such a simulation tool allows designers to optimize part design, mould design and the moulding process itself [4].

Although HDPE material is preferred, both HDPE and PP were simulated to see how the processing parameters would be and accordingly the machine sizing. Figure 4 below shows the meshed elements of the pallet and an example of the fill time result from the Autodesk Moldflow. Table 1 and Table 2 shows selected results obtained from the simulation for different PP and HDPE grades. These results are important for sizing of the injection moulding machine.

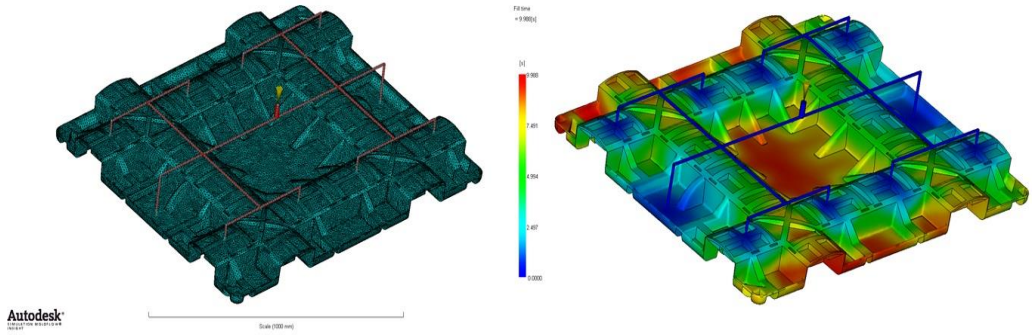

Figure 5. Moldflow Simulation Setup and Results

Table 1. Results for different PP grades.

Materials	**Melt Flow Rate**	**Required Clamp Force at Filling (ton)**	**Required Clamp Force at Packing (ton)**
PP	6	1154	1882
PP	8	1675	3241
PP	10	1357	2370
PP	15	1100	2226
PP	25	1196	2435

Table 2. Results for different HDPE grades.

Materials	**Melt Flow Rate**	**Required Clamp Force at Filling (ton)**	**Required Clamp Force at Packing (ton)**
HDPE	6	2065	3729
HDPE	8	1732	4865
HDPE	10	2034	4988
HDPE	15	1533	3663
HDPE	25	1182	2593

Prototypes units were given by the company who designed the industrial pallet for testing purposes. As in Figure 5 below, the physical prototypes were stacked excellently, and it showed good functionality in real application in the storage warehouse. Forklift movements were also tested for practicality.

Some observations and suggestions for improvement were made. Particularly wider fork channels could be redesigned to allow regular pallet jack to be used and addition of few ribs to make it more rigid for double stacking.

Figure 6. Physical Prototypes and Testing Activities in the Warehouse.

4. CASE STUDY II: EXISTING PRODUCT FAILURE INVESTIGATION

An injection moulded bucket manufacturing company produces injection molded paint pails of capacity of 17/18/20 and 21 litres with in-mold labeling as per the designs and requirements of the customers. These pails are made of an impact copolymer of polypropylene (PPCP) and lids are made of blends of PPCP and linear low density polyethylene (LLDPE). A lasting problem of buckling/ deformation of the pails under load had been reported when stacked at customers end; often this problem lead to unstable stack leading to damage and loss of contents.

The objective was on the improvement of material properties at no additional cost to the former. The stacking matrix of the pails is depicted in Fig.1. given below, and described in Table-3. The dynamic and static load requirements of different fill-capacities pails are shown in Table-4. The compressive strength of empty plastic pails measured in-house are shown in Table-5.

Figure 7. Pails stacking matrix and the visible deformation.

Table-3. Typical description of stacking matrix of pails

Stacking Matrix	Wooden Pallet + 3 layers + Wooden Pallet + 3 layers Each layer comprises 4 x 3 = 12 pails
Dynamic Load	Load on the pail during transportation. The matrix is usually 1+2 pails
Static Load	Load at customer warehouse with a stacking matrix of "pallet+3 pails + pallet + 3 pails".

Table-4. Dynamic and static load requirement of plastic pails

	17L	**18L-A**	**18L-B**	**20L**	**21L**
Fill capacity, kg.	27	30	30	32	35
Static load, kg.	150	165	165	175	190
Dynamic load, kg.	54	60	60	64	70
Empty pail weight, kg.	0.580	0.683	0.597	0.640	0.750
Pail lid weight, kg.	0.178	0.229	0.178	0.178	0.229

Table-5. Compression strength of empty plastic pails measured in-house using top load tester.

	17L	18L A-Type	18L B-Type	Benchmark*
single pail				
Yield force - kgf	820	1100	890	1200-1300
Max force - kgf	920	1250	1000	1300-1450
double (pail over pail)				
Yield force - kgf	590	775	640	NR**
Max force - kgf	650	850	720	

* Competitor pail which corresponds to Rowad 18Liter Pail

** Test terminates before pail collapse due to the design of the ribs

The objective of this work was to simulate the stress distribution and displacement in a selected part design under static load conditions provided by the bucket manufacturing company

An injection molded pail of 18 L was studied for possible deformation under a static load of 1620 N (165 kg) on the rim of the pail. The simulation was based finite element analysis (FEA) and was carried out with Autodesk® Inventor for a typical PPCP material. Two scenarios were considered: a) the base of the pail is fully supported on the pallet and b) half of the pail base was supported on the pallet and rest half is out of pallet with full load on entire rim (to simulate a case when the loaded pail moves out partly from the pallet as they are not wrapped with shrink film).

In the first case, the displacements are more prominent around the rim (A) and till the down portion of the satellite ring (B). However, the container sidewall (C) shows no displacement suggesting that under the static load the container with full supported base would not buckle.

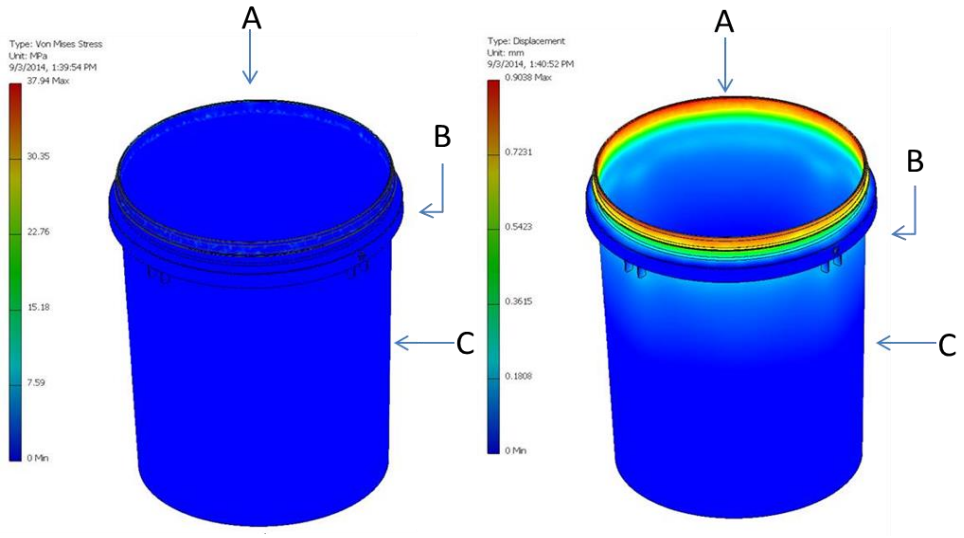

Figure 8. Fully Supported base buckets

In the second case, we considered a half supported base i.e. when the bottom container has moved out half the way of the pallet side with full static load on it (D). This scenario may arise when such displacement happens during transit or handling. Here one can observe that the container undergoes a significant displacement (the black outline is the container before loading). The displacement is more on the half of the supported top rim (A) and unsupported half of satellite ring (B) and container sidewall (C). The Von Mises Stress figure shows the location of high stress field at point D on the bottom wall (E).

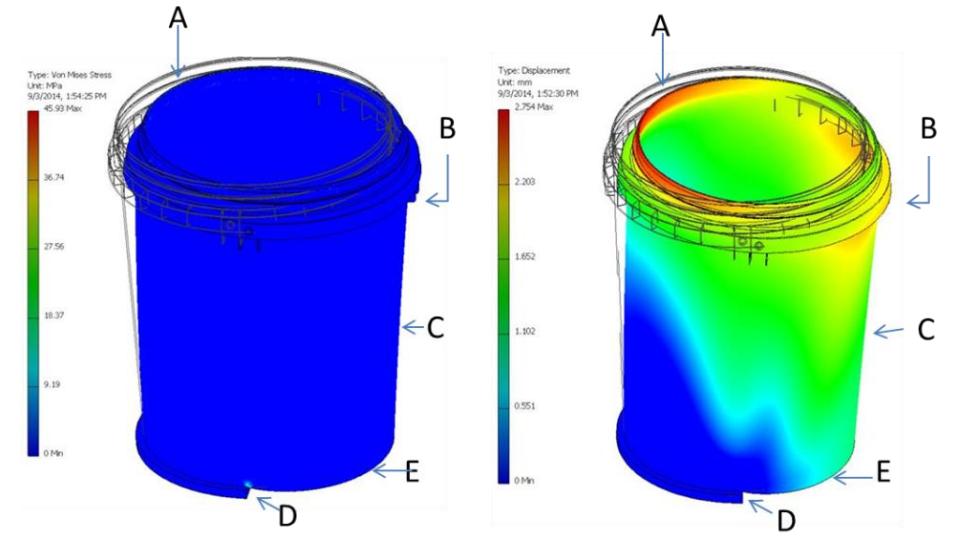

Figure 9. Half supported buckets.

The finite element analysis of the injection molded part clearly showed that extensive deformation could take place when the pail under static load was not fully supported. Thus, to minimize the buckling issue, the pails should always be fully supported or rested on even surface of a pallet.

5. CONCLUSION

This works of industrial case studies have suggested two design processes for new product development and existing product failure investigation of injection moulded products or parts. Industrial considerations are normally far from ideal where constraints on materials, costs, machines are present most of the time. These considerations cannot be sidelined and have to be incorporated in the design process. It is also found that time is very precious in the industry and some processes or tasks although seems duplicate and unnecessary, have to be executed simlutaneously considering customer urgency and the risk of losing the market.

REFERENCES

[1]. Market Research Report, "Plastics Market Analysis By Product (PE, PP, PVC, PET, Polystyrene, Engineering Thermoplastics), By Application (Film & Sheet, Injection Molding, Textiles, Packaging, Transportation, Construction) And Segment Forecasts To 2020", August 2015, 978-1-68038-232-7, Grand View Research Inc., San Francisco, U.S.A.

[2]. M.P. Groover (2013), "Principles of Modern Manufacturing", 5th Edition, John Wiley & Sons, ISBN 978-1-1-118-47420-4, Singapore.

[3]. Michael Sepe, Know How- The Effects of Temperature, Plastics Technology, Issue August (2011). Ascent, Autodesk Moldflow Insight Basic 2012 – Theory and Concept Plastic, Autodesk, Inc., (2011)

ICETI 2018 07-11 MARCH BUDAPEST HUNGARY
www.iceti.org
II. INTERNATIONAL CONFERENCE ON ENGINEERING TECHNOLOGY AND INNOVATION

Product Innovation in Sewing Machines

Emine Utkun[1], Nezla Unal[2]

Abstract

With the globalization in the world the extent of competing is increasing. In these conditions, companies or firms need innovation to be more efficient and productive and to give what is needed from them. Innovation is a concept that has existed for centuries and expresses novelty and creativity. It is known that development and progress without innovation and creativity is not possible. Innovation can be in the features of a product and service, in process or in marketing fields. Product innovation is the introduction of a product or service that is new or considerably improved in terms of its features or intended uses into the market. Product innovation includes significant improvements/developments in technical specifications, parts and materials, firmware, ease of use, or other functional features. In this study, the product innovations that sewing machines used in the apparel industry underwent were examined in the historical process.

Keywords: *Apparel industry, Product innovation, Sewing machine.*

1. INTRODUCTION

Innovation, in the simplest term, is to find different, marginal, and new ideas and implement these ideas (1, 2). Innovation involves the development of new or improved products, services or production methods, and all stages in which financial income can be obtained (3).

Innovation is divided into 4 groups (1, 4, 5). These can be explained as follows.

1. Product Innovation: While concrete objects presented to consumers through a company is called a product, a company's developing a different, new and creative product and introducing this product into the market is defined as product innovation.

2. Service Innovation: Utilities provided by a company to the consumer is defined as service innovation. It is service innovation when a company develops a new, different and creative service and offers it to customers.

3. Marketing Innovation: Marketing innovation is defined as the development and use of different, creative and new designs, packages, and marketing styles for the product created or the service offered.

4. Organizational Innovation: A company's methods of making innovation and doing business in order to gain and maintain competitive advantages over competitors operating in the same field.

This study investigated the product innovation that sewing machines undergone in the historical process.

[1,2] Program of Fashion Design, Buldan Vocational Training School, Pamukkale University, Denizli, 20400, Turkey.

2. SEWING MACHINES AND PRODUCT INNOVATION

The definition of first sewing machine that has reached the present day was made towards the mid-18th century. According to this definition, a sewing machine makes a stitch similar to basting stitch. In 1790, the British Thomas Saint invented the first sewing machine to make chain stitch. The most important feature of the chain stitch machine invented by Krems in 1800s was the use of the first sewing machine needle with an eye in its point (6).

The first lockstitch machine (straight stitch machine) was literally invented by Elias Howe in 1846, but he could not turn his invention into innovation. Having succeeded in transforming this invention into innovation, Isaac SINGER gave the product his name and was branded. The first Singer sewing machines were sold in Turkey in 1886. The company opened its first store in 1904 and its factory in 1959 (9). This emphasizes the importance of examining patents in the area in which entrepreneurs want to do business. Inventions and patents give important ideas for innovation (7).

Sewing machines that improved in time can be categorized in different ways. Some of these categorizations are as follows.

2.1. Types of Sewing Machines According to Stitch Types

Lockstitch Sewing Machine: It is a kind of stitch made by a vibrating shuttle or a hook in a sewing machine.

Single Thread Chain Stitch Sewing Machine: This is the kind of stitch in which the looper that creates the loop makes the stitch by using a single thread.

Double Thread Chain Stitch Sewing Machine: This is the kind of stitch in which the needle pricks the fabric, and the thread that is lowered by the looper is held, then the needle goes up, and when it comes down again, it creates the new loop by passing through the loop that is expanded by the looper.

2.2. Types of Sewing Machines According to Working System

Sewing Machines in Manual System: The individual who uses the machine does operations such as starting, stopping, stiffening the machine by himself/herself.

High Speed Electronic Programmable Sewing Machines: Functions of the machine (thread trimming, stiffening, etc.) are digitally programmed. The programmed stitching starts when the machine user presses the pedal, and the machine automatically stops when the program finishes (8).

2.3. Product Innovations in Sewing Machines

The innovation that sewing machines have undergone over time is visually given in Figure 1.

Figure 1. Sewing Machines from Past to Present (9).

Sewing machines that could do straight stitching were invented after sewing machines that could only do chain stitching at first. Over time, lockstitch sewing machines have had many different features. Some of them are as in the following;

- ✓ Feature of being able to write by using font characters,
- ✓ Feature of being able to turn a photo into stitch,
- ✓ Feature of being able to stitch decorative materials such as beads, spangle, and sequins,
- ✓ Feature of being able to apply patterns,
- ✓ Feature of being able to mirror patterns,
- ✓ Feature of unlimited embroidery frame,
- ✓ Feature of being able to operate without a pedal (10).

Computer-aided systems have been added to most of the sewing machines used in the textile and apparel industry in this century. Thanks to these systems added to sewing machines, they have become multifunctional and easy to use.

Some of the functional features in these computer-aided systems are;

- ✓ Automatic thread trimming
- ✓ Automatic presser foot lifting
- ✓ Reinforcement stitching at the top and bottom (lockstitch sewing machine)
- ✓ Electronic control panel
- ✓ Speed adjustment feature on electronic panel
- ✓ Milimetric presser foot pressure setting feature
- ✓ Milimetric stitch length setting feature
- ✓ Automatic sewing programs (11).

The sewing machines used in the textile and apparel sector have pedals that allow the machine's stitching steps to move by the machine user's using his/her foot to move the machine. To be able to use these machines, individuals must not have walking disabilities. Starting from this point; Sumbul and Yakut (2016) developed a control wristband system (KBS) that can provide the control of these machines at a distance, and thus enable people with walking disabilities to use such machines by adding the system to all sewing machines that can be controlled with a foot pedal in the textile and ready-to-wear sectors.

3. CONCLUSIONS

Product innovation includes significant improvements/developments in technical specifications, parts and materials, firmware, ease of use, or other functional features.

In this study, the product innovations that sewing machines used in the apparel industry underwent were examined in the historical process. With the advancement of technology, sewing machines continue to develop and attempt to respond to changing market conditions each passing day.

ACKNOWLEDGMENT

This study was submitted with the support of Pamukkale University Scientific Research Projects (BAP) Coordination Unit.

REFERENCES

[1]. E. Utkun and T. Atilgan, "Marketing Innovation in the Apparel Industry: Turkey", *Fibres&Textiles in Eastern Europe*, vol. 18(6), pp. 26-31, 2010.
[2]. (2018) Website. [Online]. Available: http://www.teknolojide.com/inovasyon-nedir_4929.aspx
[3]. (2018) Website. [Online]. Available: http://www.inomer.org/Inovasyon/%C4%B0novasyon-Nedir-Ne-Degildir
[4]. (2018) Website. [Online]. Available: http://www.gelisenbeyin.net/inovasyon-cesitleri.html
[5]. (2018) Website. [Online]. Available: https://sercanmedia.tr.gg/%26%23304%3Bnovasyon-%C7e%26%23351%3Bitleri.htm
[6]. Makine bilgisi 1-2 Komisyon Kitabi, Milli Egitim Bakanligi Yayinevi, p. 291, 1999.
[7]. (2018) Website. [Online]. Available: https://scholar.google.com.tr/scholar?hl=tr&as_sdt=0%2C5&q=diki%C5%9F+makineler+geli%C5%9Fimi&oq,
[8]. Megep (Meslekî Egitim Ve Ogretim Sisteminin Guclendirilmesi Projesi) Giyim Uretim Teknolojisi 1- Makinede Duz Dikis, ANKARA 2007, 65
[9]. (2018) Website. [Online]. Available: https://www.tekstilbilgi.net/dikis-makinesinin-icadi.html
[10]. (2018) Website. [Online]. Available: https://www.dunya.com/tekno-trend/yeni-nesil-dikis-makineleri-fotograftaki-desenleri-isleyebiliyor-haberi-397556
[11]. E. Utkun and Z. Ondogan, "Konfeksiyon Sektorunde Kullanilan CAD-CAM Sistemleri", in 2nd International 6th National Vocational Schools Symposium, May 2011.
[12]. H. Sumbul and Y. Yakut, "Yurume Engelli Bireyler icin Pedaldan Kumandali Dikis Makinelerinin Kumanda Bileklik Sistemi ile Kontrolu", Politeknik Dergisi, vol. 19 (3) , pp. 245-249, 2016.

ICETI 2018 07-11 MARCH BUDAPEST HUNGARY
www.iceti.org
II. INTERNATIONAL CONFERENCE ON ENGINEERING TECHNOLOGY AND INNOVATION

Investigating the Corrosion Behaviour of AA6060 Alloy in NaOH-Na_2SiO_3 Solution

***Alptekin Kisasoz*[1]**

Abstract

Aluminium alloys have been widely used in automotive and aeronautical industries owing to their relative lightness, specific strength, and corrosion resistance in various environment. The mechanical properties of the AA6XXX alloy can be increased with age hardening process by the formation of intermetallic particulates in the matrix structure. Unfortunately, these particulates have a negative influence on the corrosion resistance of AA6XXX alloy. Especially, the corrosion resistance of the AA6XXX alloys decreases drastically in alkaline media. Also, inhibitors can slow down the corrosion rate of aluminium alloys in alkaline media. In this study, corrosion behaviour of overaged AA6060 alloy in NaOH solution was investigated. Corrosion tests were carried out in 0.01 and 0.1M NaOH solutions and also, Na_2SiO_3 was used as an inhibitor to slow down the corrosion rate of AA6060 alloy in NaOH solutions. Moreover, corrosion properties were determined by measuring weight loss of the samples, pH values of the solution and also, microstructure analysis..

Keywords: AA6060, Heat Treatment, Corrosion

1. INTRODUCTION

AA6XXX aluminium alloys have a relatively satisfactory strength, good corrosion resistance and a low cost. Mechanical properties of the AA6XXX alloys can be enhanced with aging process by the formation of intermetallic precipitates. Also, intermetallic precipitates become larger and incoherent with the matrix by the overaging process. Thus, the corrosion resistance of AA6XXX alloys can be altered together with the mechanical properties in overaging process [1]-[6].

AA6XXX alloys have good corrosion resistance in various aqueous environment by the formation of protective oxide layer. For this reason, AA6XXX alloys are used in applications that require corrosion resistance. On the other hand, severe alkaline environments can destroy the protective oxide layer and corrosion of the metal occurs. Various protection methods have been used to prevent or slow down the corrosion of aluminium alloys. Using inhibitors is one of the protection method for corrosion of aluminium alloys. Especially, Na_2SiO_3 inhibits the corrosion of aluminium alloys in alkaline environments [7]-[11].

In this study, effect of Na_2SiO_3 on the corrosion resistance of overaged AA6060 alloy in alkaline environment was investigated. Corrosion tests were carried out in 0.01M and 0.1M NaOH solutions. Corrosion behavior of AA6060 samples were characterized by corrosion rate calculation and microstructural analysis.

2. EXPERIMENTAL

Chemical composition of the AA6060 alloy was given in Table 1. Solution treatment was applied at 530˚C for an hour. Also, solution treated AA6060 samples were overaged at 200˚C for 24 hours.

Table 2. Chemical composition of AA6060 alloy (wt.%)

Si	*Fe*	*Cu*	*Mn*	*Mg*	*Cr*	*Zn*	*Ti*	*Al*
0.35	0.14	0.10	0.10	0.42	0.05	0.10	0.10	Bal.

[1]Corresponding author: Yildiz Technical University, Department of Metallurgical and Materials Engineering, 34210, Esenler/Istanbul, Turkey. akisasoz@yildiz.edu.tr

Corrosion behaviour of AA6060 alloy was investigated in 0.1M NaOH and 0.01M NaOH solutions. Moreover, 1.5 g/l Na_2SiO_3 was added as an inhibitor to each solution. Corrosion tests were applied in 4 different solutions for 168

hours. Specimens were taken out after 24, 75 and 168 hours during the corrosion test from each solution. Corrosion behaviour of the samples were characterized with stereo microscope and weight loss measurements. Also, corrosion rates were calculated for each sample, initial and final pH values of the solutions were determined.

3. RESULTS AND DISCUSSION

Different NaOH solutions (0.1M and 0.01M) were used to determine the corrosion behaviour of AA6060 alloy. In addition, Na_2SiO_3 was added to solutions to investigate the inhibitor effect. The initial and final pH values were determined before and after the corrosion tests. In Figure 1, the pH value changes were given for each of the corrosion environment. The initial pH value of the solution containing 0.1 M NaOH was 12.85, while the pH value of the solution containing 0.01 M NaOH was 12.17. A slight decrease in pH values of 0.1M NaOH solutions occurred. However, pH values of the 0.01M solutions decreased to 9. The accumulation of the corrosion products in the corrosion environment was one of the main reason for the pH drop.

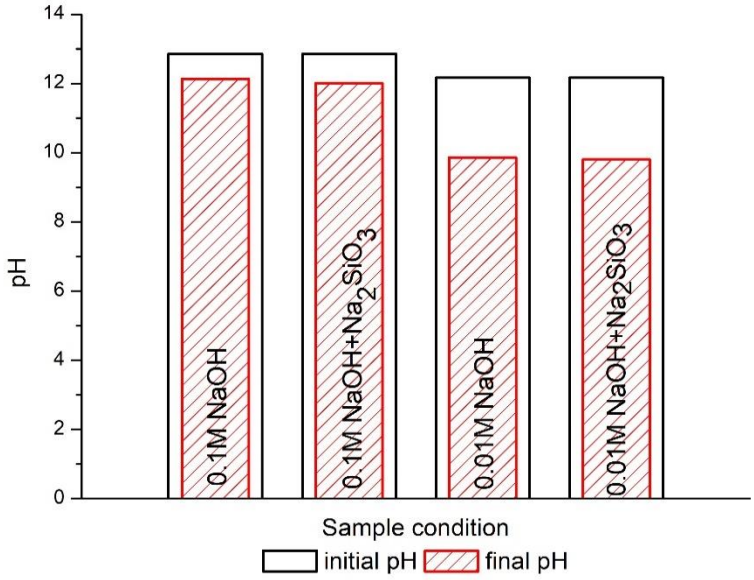

Figure 3. Initial and final pH values of the corrosion environments

Corrosion rate (mm/year) of the samples were calculated according to Equation 1.

$$Corrosion\ rate = 87.6\ (\frac{w}{d\ A\ t})$$

(1)

Where; *w* is weight loss in milligrams, *d* is metal density in g/cm^3, *A* is an area of the sample in cm^2 and *t* is the time of exposure of the metal sample in hours [12].

Corrosion rates were given in Figure 2. The corrosion rates were reduced with increasing test duration for the all corrosion solutions due to the accumulation of corrosion products in the corrosion environment. Corrosion rates corresponded to the pH changes given in Figure 1. The samples in the solutions containing 0.1M NaOH were corroded at higher corrosion rates. The addition of the Na_2SiO_3 as an inhibitor reduced the corrosion rate in the solution

containing 0.1M NaOH, but still resulted in a higher corrosion rate than the 0.01M NaOH containing solution. In the solution containing 0.01M NaOH, a lower corrosion rate was obtained and the corrosion rate was nearly zero with the addition of Na_2SiO_3.

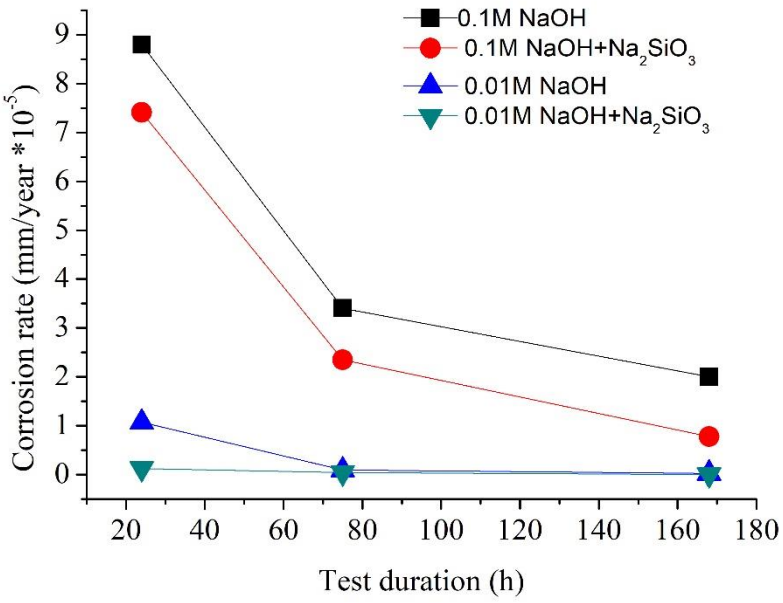

Figure 2. Corrosion rates of the samples

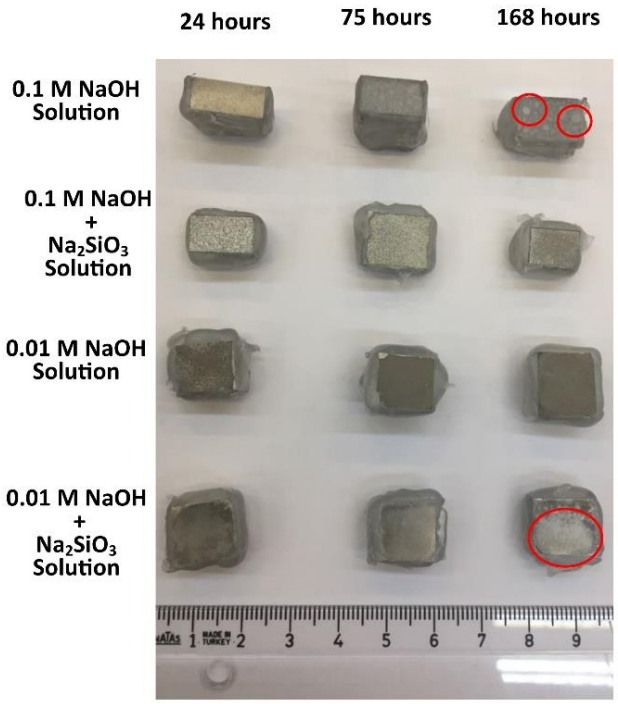

Figure 3. Macrostructure of the corroded samples

Macrostructures of the corroded samples were given in Figure 3. A significant corrosion damage occurred in the 0.1M NaOH solution, which has a higher aggressiveness. In particular, blisters were formed on the sample surface and surface damage occurred after 168 hours in 0.1M NaOH solution. On the other hand, Na_2SiO_3 added 0.01M NaOH solution caused almost no damage on the surface of samples. A slight amount of nigrescence was seen on the surface, but as can be seen, even the sample tested for 168 hours can be seen with a polished surface.

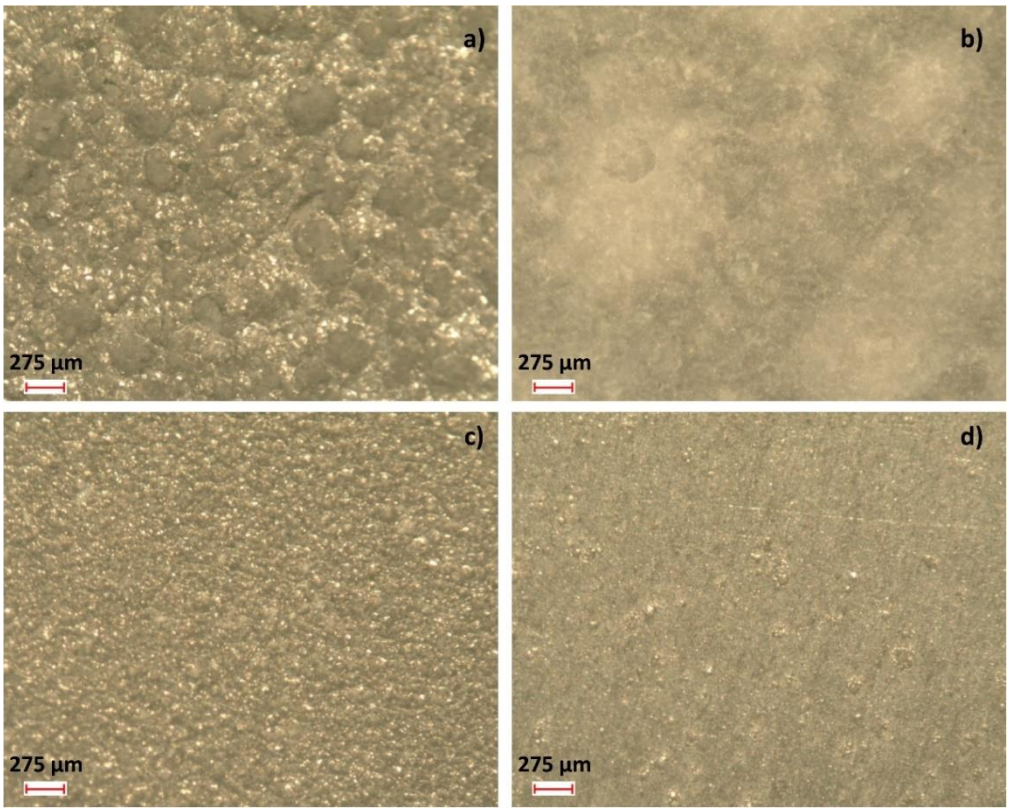

Figure 4. Microstructure of the sample surfaces after 168 hours corrosion test in various solutions a) 0.1M NaOH b) 0.1M NaOH+Na_2SiO_3 c) 0.01M NaOH d) 0.1M NaOH+Na_2SiO_3

Microstructure of the samples taken with stereo microscope after the corrosion tests were given in Figure 4. Craters and cavities formed on the sample surfaces after 168 hours in the absence of Na_2SiO_3. Cavities were larger due to the higher aggressiveness of the 0.1M NaOH solution and also, the surface damage was more severe as shown in Figure 3. Presence of Na_2SiO_3 reduced the corrosion rate, surface roughness and surface damage in both corrosion environments. Thus, usage of Na_2SiO_3 ensured smoother surface for the sample corroded in 0.01M solution.

4. CONCLUSION

In this study, the effect of Na_2SiO_3 addition on the corrosion behavior of the overaged AA6060 alloy in NaOH environment was investigated. For this aim, corrosion tests were carried out with and without addition of Na_2SiO_3 in solutions containing 0.1M and 0.01M NaOH.

As expected, the corrosion rate increased with increasing NaOH concentration. The addition of Na_2SiO_3 reduced the corrosion rate in both solutions, whereas the corrosion was almost stopped in the solution containing 0.01M NaOH. The addition of Na_2SiO_3 to the corrosion environment was more effective with the reduction of the NaOH concentration.

REFERENCES

[1]. B. A. Cieslak, J. Mizera and K. J. Kurzydlowski, "Microstructures in the 6060 aluminium alloy after various severe plastic deformation treatments," *Mater. Charac.*, vol. 62, pp. 327-332, 2011.
[2]. R. G. Kamat, J. F. Butler, S. J. Murtha and F. S. Bovard, "Alloy 6022-T4E29 for automotive sheet applications," *Mater. Sci. Forum*, vol.396, pp. 1591-1596, 2002.
[3]. I. N. Fridlyander, V. G. Sister, O. E. Grushko, V. V. Berstenev, L. M. Sheveleva and L. A. Ivanova, "Aluminium alloys: promising materials in the automotive industry," *Met. Sci. Heat. Treat.*, vol. 44, pp. 365-370, 2002.
[4]. W. S. Miller, L. Zhuang, J. Bottema, A. J. Wittebrood, P. De Smet and A. Haszler, "Recent development in aluminium alloys for the automotive industry," *Mater. Sci. Eng. A*, vol. 280, pp. 37-49, 2000.
[5]. C. D. Marioara, H. Nordmark, S. J. Andersen and R. Holmestad, "Post-beta" phases and their influence on microstructure and hardness in 6xxx Al–Mg–Si alloys," *J. Mater. Sci.*, vol. 41, pp. 471-478, 2006.
[6]. P. J. Apps, M. Berta and P. B. Prangnell, "The effect of dispersoids on the grain refinement mechanisms during deformation of aluminium alloys to ultra-high strains,". *Acta. Mater.*, vol. 53, pp. 499-511, 2005.
[7]. C. Vargel, *Corrosion of Aluminium*, Oxford: Elsevier, 2004.
[8]. Y. T. Du, H. L. Wang, Y. R. Chen, H. P. Qi and W. F. Jiang, "Synthesis of baicalin derivatives as eco-friendly green corrosion inhibitors for aluminum in hydrochloric acid solution," *J. Environ. Chem. Eng.*, vol. 5, pp. 5891-5901, 2017.
[9]. K. Xhanari and M. Finsgar, "Organic corrosion inhibitors for aluminum and its alloys in chloride and alkaline solutions: A review," *Arab. J. Chem.*, 2016. http://dx.doi.org/10.1016/j.arabjc.2016.08.009
[10]. N.A.F. Al-Rawashdeh and A.K. Maayta, "Cationic surfactant as corrosion inhibitor for aluminum in acidic and basic solutions," *Anti-Corros. Methods Mater.*, vol. 52, pp. 160-166, 2005.
[11]. S. Pyum and S. M. Moon, "Corrosion mechanism of pure aluminium in aqueous alkaline solution," *J. Solid. State Electrochem.*, vol. 4, pp. 267-272, 2000.
[12]. ASM International Handbook Committee, *ASM Handbook Volume 13A Corrosion: Fundamentals, Testing, and Protection,* Ohio: ASM International, 2003.

ICETI
www.iceti.org
2018
07-11 MARCH
BUDAPEST
HUNGARY
II. INTERNATIONAL CONFERENCE ON ENGINEERING TECHNOLOGY AND INNOVATION

Investigation of the Change of Mechanical and Physical Properties of AA7075 Alloy by RRA Heat Treatment Applied at Different Time and Temperature

Gokhan Ozer[1], Ahmet Karaaslan[2]

Abstract

The AA7075 alloy is an important material that is widely used today with its high strength and low weight. The heat treatment of this alloy plays an important role especially in the aerospace industry and high strength parts. T6 heat treatment is applied to give the AA7075 alloy strength, but as a result of this heat treatment, the material becomes susceptible to corrosion. The heat treatment to obtain the corrosion resistance decreases the mechanical strength. At this point, a special heat treatment, called RRA heat treatment, improves both the mechanical and corrosion properties of the AA7075 alloy.

In this study, an AA7075 alloy in T651 condition was retrograded at 180, 280 and 370°C for 1, 30, 50, 90 and 120 minutes. After retrogression, the samples were aged again under T6 conditions. The mechanical properties of the samples were determined by V-Charpy, hardness, and their physical properties by electrical conductivity tests. Microstructures of the samples were determined by light metal microscope and SEM. The results showed that the effect of the temperature and the duration of the RRA on the mechanical and physical properties is related to the precipitates at the grain boundary.

Keywords: AA7075, RRA, mechanical properties, physical properties

1. INTRODUCTION

Al-Zn-Mg-Cu alloys (7xxx series) are widely applied in aerospace and transport industries with high strength and toughness. The overall properties of these alloys are linked to the microstructure of the material, especially stable and metastable phases. Thus, the balance of properties of 7xxx alloys can be optimized by microstructural modifications via alloy compositional variations and heat treatment changes [1-3].

These alloys are known to be susceptible to corrosion in the peak strength state (T6 temper condition). The susceptibility of T6 temper to corrosion is alleviated through the use of over-aged T73 temper, which provides improved corrosion resistance, but with a 10%-15% reduction in strength [4-6].

A new heat treatment, known as the retrogression and reaging process (RRA), has been shown to produce the high corrosion resistance with retention of the high strength [7-10]. The RRA treatment normally involves reheating material under the near peak aged condition to a temperature between 180 and 240℃ for short periods of time, cooling back to room temperature and then reaging. RRA could offer the promise combination of good strength and corrosion resistance [11-13].

In this study, the effects of different RRA temperatures and durations on the hardness, impact toughness and electrical conductivity of AA7075 alloy were investigated. According to the results obtained, it has been found that the RRA

[1] *Corresponding author: Aluminium Test, Training and Research Center (ALUTEAM), FSMVU Halic Campus, Turkey, gozer@fsm.edu.tr*

[2] *Yildiz Technical University, Department of Metallurgical and Materials Science Engineering, 34220, Esenler/Istanbul, Turkey. karaas@yildiz.edu.tr*

process alters the physical and mechanical properties of the material by altering the microstructure formation of the alloy.

2. MATERIALS AND METHODS

2.1. Materials

A certified AA7075 aluminium alloy that underwent T651 condition was used in this study. The samples were taken from 10 mm thick plate. The chemical composition of the alloy is shown in Table 1.

Table 1. Chemical composition of AA7075 (wt %)

Si	Fe	Cu	Mn	Mg	Cr	Ni	Zn	Ti	Al
0.1	0.19	1.53	0.07	2.55	0.18	0.0058	5.89	0.024	Rest

2.2. Heat Treatments

Because the alloy was in the T651 temper the heat treatment started directly from retrogression stage. RRA heat treatment was conducted according to conditions determined by Table 2.

Table 2. RRA parameters

Starting condition	RRA			
	Retrogression			Re-aging
	Temperature (°C)	Time (minutes)	Cooling time (second)	
T651	180, 280, 370	15, 30, 50, 90, 120	1-3	120°C 24 hours

2.3. Microstructure

Samples for metallographic studies were prepared according to the standard sample preparation procedure and are etched for 1-4 minutes with Keller Solvent (95 ml of purified water, 2.5 ml of HNO_3, 1 ml of HF and 1.5 ml of HCl). The prepared specimens were examined on a NIKON Eclipse MA100 light metal microscope and microstructures were visualized using the NIS Elements BR Analysis program. The effect of different RRA temperatures and time periods on the precipitate size and distribution in the AA7075 alloy was determined using Hitachi SU3500 SEM.

2.4. Hardness Test

Hardness measurements were made by Brinell (BSD) hardness measurement method. The load was 62.5 kp and the ball diameter was 2.5 mm.

2.5. Notch Impact Test

Notch impact tests were carried out on a Mohr-Federhaff notch impact device with a 300 J breaking energy capacity.

2.6. Electrical Conductivity

Electrical conductivity measurements were made with a portable conductivity meter operating according to the GE Inspection 40I001 type Eddy current principle and the results are given in% IACS-International Annealed Copper Standard.

3. RESULTS AND DISCUSSION

3.1. Microstructure

Metallographically, the microstructures formed as a result of AA7075-T651 and RRA processes prepared in the direction of the roll are shown in Figure 1.

According to the examination results with an optical microscope, the intermetallics in the structure can be seen and it can be said that the precipitates become rough when the temperature increases. There is no significant effect of RRA treatment on grain size and orientation patterns.

When the precipitate structure in grain boundaries of AA7075 alloy in T651 state is examined, stable equilibrium precipitate (η) in the form of a relatively thin and continuous net structure is observed; while homogeneously distributed $\acute{\eta}$ precipitate is observed inside the grains (Figure 2a). It was determined that with the RRA temper the precipitate in grain boundaries coarsens and becomes discontinuous, while the $\acute{\eta}$ precipitate inside the grains is formed again in densely distributed and thin form (Figure 2b).

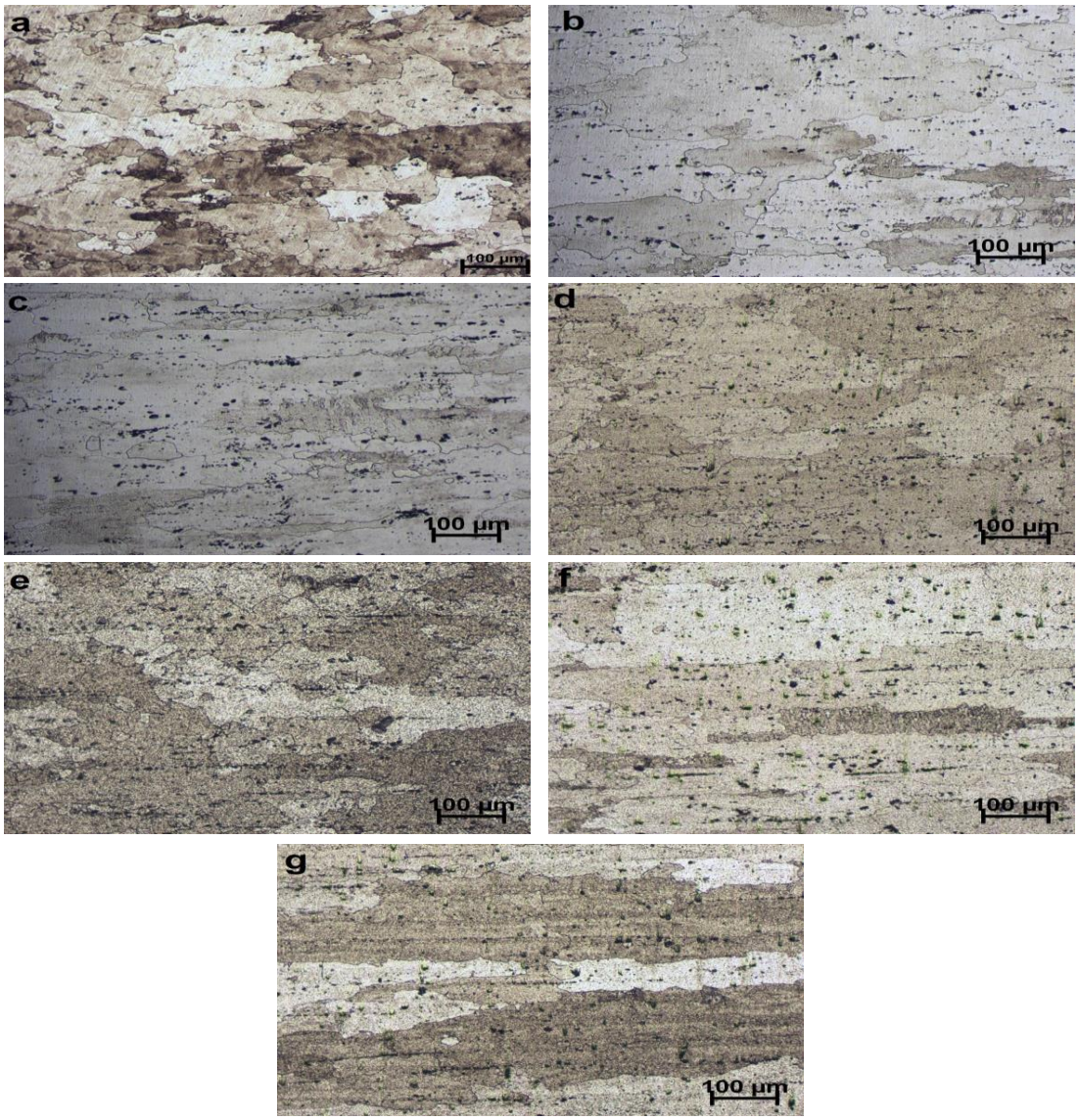

Figure 1 a) T651, b) 180ºC 30 minutes, c) 180ºC 90 minutes, d) 280ºC 30 minutes, e) 280ºC 90 minutes, f) 370ºC 30 minutes and g) 370ºC 90 minutes microstructure images of samples subjected to retrogression and re-aging (RRA).

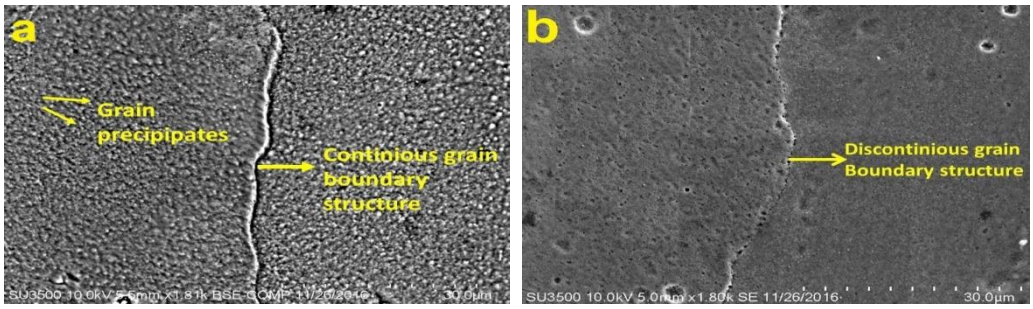

Figure 2 (a) grain boundary structure in the continuous net structure of the AA7075 alloy in T651 state, (b) decomposition of continuous net structure in the grain boundary and coarsened precipitate after the RRA temper

3.2. Hardness

Hardness changes of the material according to the RRA condition conducted with different heat levels and time periods can be seen in Figure 3.

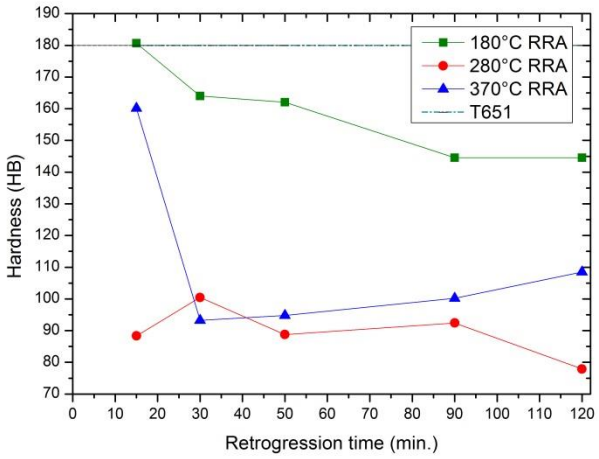

Figure 3 Hardness values obtained after RRA in AA7075 alloy depending on temperature and duration

It was determined that the hardness values exceeded the T651 hardness value (180 HB) during the short retrogression times under the RRA heat treatment conditions at low temperatures (180°C), but then decreased continuously with increasing retrogression time. In the RRA processes at higher temperatures, the hardness value was found to be lower than the hardness value of T651 and the hardness decreased with increasing retrogression time (Figure 3).

The initial reduction of the hardness is related to the beginning of the dissolution of the fully coherent (GP zones) and semi-coherent phase ($\acute{\eta}$) in the structure. However, at the beginning of retrogression (up to the first 10 minutes), there is a recurrence of stiffness. This is due to the formation of a new phase $\acute{\eta}$ nucleated on the dissolved GP zones. The increase in a volume ratio of this phase is much higher than in the case of T651 so that the hardness is higher than the T651 hardness. As the retrogression process continues to increase in time, the $\acute{\eta}$ phase becomes η phase, which is the stable phase of equilibrium, and this discordant phase causes the hardness to fall again. This condition, which is seen in hardness, can also be explained by it's over aging.

3.3. Impact Toughness

Figure 4 shows the change in impact strength of the material according to the RRA procedures applied at different temperatures and durations.

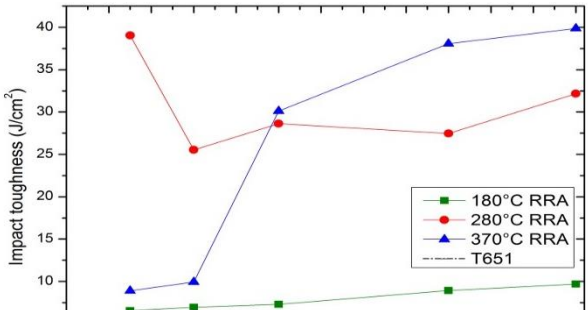

Figure 4 Variation of impact toughness with retrogression time

At relatively low RRA temperatures (180°C), impact strengths were close to T651. The increase in the RRA duration at low temperatures indicated that there was not very different change in impact strength values. With increasing duration, the formation and distribution of precipitates in the microstructure causes the impact strength to increase. As a result of the RRA process, the continuous network phase at the grain boundary becomes fragmented and discontinuous. In this way, while the removal of the continuous net phase from the high energy grain boundaries increases free energy values, the spherical precipitate decreases the notch effect in the structure.

3.4. Electrical Conductivity

The relationship between electrical conductivity and RRA conditions is shown in Figure 6.

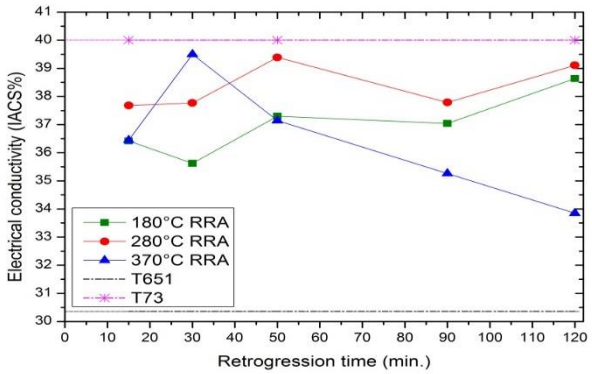

Figure 6 Variation of electrical conductivity with retrogression time

It has been observed that at all retrogression temperatures, the electrical conductivity of the material increases with increasing retrogression times in general. In the applied RRA processes, it was found that the conductivity of the alloy increased significantly in the 30-minute process, especially at 370°C, and the conductivity decreased dramatically in the RRA processes applied for a longer time.

As the result of increased retrogression time, the precipitates starts to become coarse and the distances between them start to increase. As a result, the electron conductivity in the structure becomes easier and the electrical conductivity also increases.

4. CONCLUSIONS

According to the findings obtained in this study;

- When RRA heat treatment is conducted in relatively low temperatures (180°C) and in short retrogression periods the hardness is higher compared to the T651 hardness value (180 HB), but with the increase of retrogression periods, it constantly decreases. At higher temperatures and with increased retrogression the hardness is continuously decreasing. The phases providing the highest strength of the AA7075 alloy are

compatible and semi-compatible components. It has been determined that the dissolution of these phases reduces the hardness.

- At relatively low temperatures (180°C), the impact toughness is close to the T651 level. The impact toughness increased with RRA temperature and time. Depending on the RRA temperature and duration, the impact toughness increase is explained by the morphology of the grain boundaries. According to that, the increase in temperature and duration of the RRA treatments broke the continuous net phase structure and the notch effect in the structure was diminished. As a result, the impact strength increased and the hardness decreased.

- It has been determined that the electrical conductivity increases due to increased retrogression temperature and duration. All electrical conductivity values found in the RRA applied samples are higher than in the initial state of the alloy (T651). The coarsening of the precipitate caused by the prolonged time in the heat facilitates the electron flow in the matrix which increases the electrical conductivity.

ACKNOWLEDGMENT

The authors are grateful to Yildiz Technical University and Fatih Sultan Mehmet Vakif University-Aluminium Test Training and Research Center (ALUTEAM) for their supports.

REFERENCES

[1] T. Marlaud, A. Deschamps, F. Bley, W. Lefebvre, and B. Baroux, "Evolution of precipitate microstructures during the retrogression and re-ageing heat treatment of an Al-Zn-Mg-Cu alloy", *Acta Mater.*, vol. 58, no. 14, pp. 4814–4826, 2010.

[2] J. Yu and X. Li, "Modelling of the precipitated phases and properties of Al-Zn-Mg-Cu alloys", *J. Phase Equilibria Diffus.*, vol. 32, no. 4, pp. 350–360, 2011.

[3] P. A. Rometsch, Y. Zhang, and S. Knight, "Heat treatment of 7xxx series aluminium alloys - Some recent developments", *Trans. Nonferrous Met. Soc. Chin.*, vol. 24, no. 7, pp. 2003–2017, 2014.

[4] R. Ranganatha, V. Anil Kumar, V. S. Nandi, R. R. Bhat, and B. K. Muralidhara, "Multi-stage heat treatment of aluminum alloy AA7049", *Trans. Nonferrous Met. Soc. Chin.*, vol. 23, no. 6, pp. 1570–1575, 2013.

[5] N. C. Danh, K. Rajan, and W. Wallace, "A TEM study of microstructural changes during retrogression and reaging in 7075 aluminum", *Metall. Trans. A*, vol. 14, no. 9, pp. 1843–1850, 1983.

[6] A. F. Oliveira, M. C. de Barros, K. R. Cardoso, and D. N. Travessa, "The effect of RRA on the strength and SCC resistance on AA7050 and AA7150 aluminium alloys", *Mater. Sci. Eng. A*, vol. 379, no. 1–2, pp. 321–326, 2004.

[7] T. Ohnishi, Y. Ibaraki, and T. Ito, '"Improvement of fracture tougness in 7475 aluminium alloy by the RRA (Retrogresssion and Re-Ageing) process", Mater. Trans., JIM, vol. 30, no. 8, pp. 601-607 1989.

[8] S. A. Mahmoud and M. Tash, 'Aging and Mechanical Behavior of Be-treated 7075 Aluminum alloys', *Int. J. Chem. Mol. Nucl. Mater. Metall. Eng.* , vol. 8, no. 3, pp. 252–256, 2014.

[9] G. Ozer and A. Karaaslan, "Relationship of RRA heat treatment with exfoliation corrosion, electrical conductivity and microstructure of AA7075 alloy", *Mater. Corros.*, vol. 68, no. 11,pp. 1260-1267, 2017.

[10] G. Ozer and A. Karaaslan, "The effect of RRA heat treatment on the intergranular corrosion (IGC) of the AA7075 alloy", *Prakt. Metallogr. Metallogr.*, vol. 54, no. 4, . 256-266, 2017.

[11] H. Li, J. Geng, X. Dong, C. Wang, and F. Zheng, "Effect of aging on fracture toughness and stress corrosion cracking resistance of forged 7475 aluminum alloy", *J. Wuhan Univ. Technol. Sci. Ed.*, vol. 22, no. 2, pp. 191–195, 2007.

[12] F. Andreatta, H. Terryn, and J. H. W. de Wit, "Effect of solution heat treatment on galvanic coupling between intermetallics and matrix in AA7075-T6", *Corros. Sci.*, vol. 45, no. 8, pp. 1733–1746, 2003.

[13] G. Ozer and A. Karaaslan, "Properties of AA7075 aluminum alloy in aging and retrogression and reaging process", *Trans. Nonferrous Met. Soc. China*, vol. 27, no. 11, pp. 2357-2362, 2017.

ICETI
www.iceti.org
2018
07-11 MARCH
BUDAPEST
HUNGARY
II. INTERNATIONAL CONFERENCE ON ENGINEERING TECHNOLOGY AND INNOVATION

Cooling Slope Casting and Thixoforging of A319 Alloy

Serhat Acar[1], Kerem Altug Guler[1]

Abstract

Semi-solid metal forming techniques have become more remarkable in recent decades due to advantages of both process and product properties. This technique principally relies on feedstocks with non-dendritic microstructure and well-studied for common aluminum casting alloys like A356 and A380 which are used for diverse industries such as automotive, aviation and marine. In order to obtain globular microstructure different routes are developed and these routes can be classified in two different branch: liquid metal and solid state routes. In this study, cooling slope casting, which is one of the liquid metal route, was chosen as feedstock production method for A319 alloy and a copper tube with the length of 650 mm was used as a cooling slope without water circulation. Castings were carried out at 635 °C and the tilt angle was 60° for copper tube. Obtained billets were cut into pieces with 40 mm height. One specimen was kept as reference without being exposed to any further treatment. Two specimens for each reheating time were reheated at 585 °C for 20, 40, 60 and 80 minutes. One of the each duplicates was quenched in water in order to freeze the present microstructure and the other one was thixoforged with 50% deformation via a hydraulic press. Microstructural investigation was performed with the evaluation of spheroidization index and average globule size for every sample. Brinell hardness test was carried out to examine the relation between microstructure and mechanical properties. Reheated for 40 minutes and quenched sample displayed the highest spheroidization index with 0.951, which is one of the most important feature for thixoforming feedstocks. On the other hand, maximum hardness value was observed on the sample with 20 minutes reheating time due to finer microstructure.

Keywords: A319, cooling slope casting, thixoforging

1. INTRODUCTION

Semi-solid metal processing (SSMP) techniques are almost 50 years old yet still attractive for manufacturing near net shaped products [1]. These methods offer a lot of advantages with combining the properties of both casting and forging/extrusion processes. More laminar die filling and extended mould life comparing to conventional casting methods, better mechanical properties with lesser shrinkage porosities are some of these advantages [2,3]. Industries such as aviation and automotive always continue their requirements for materials with better mechanical integrity. These needs keep the interests of both researchers and manufacturers in SSMP techniques on high levels [4,5].

SSMP methods are conducted by two main directions which are rheo- and thixo- routes. In thixoforming route special feedstocks with globular microstructure, rather than conventionally solidified dendritic counterpart, are needed in further forming steps. Several methods were developed to obtain feedstocks with spherical microstructure. Cooling slope casting is promising one among them. In this technique selected alloy is cast with a mild superheat through a cooling plate with a tilt angle. Cooling effect of the plate and shear forces due to tilt of plate suppresses dendritic growth during solidification. When the solidified billets are reheated to semi-solid state, globular microstructure is formed with high spheroidization index. Low equipment need makes this process favorable among other feedstock production techniques [4,6].

In this study, thixoforming feedstocks of A319 alloy which is commonly used in automotive industry due to its high strength, light weight and good machinability [7], produced by cooling slope casting method using a copper tube and thixoforging processes were carried out in open die with %50 deformation. Effects of different reheating times were investigated with the evaluation of microstructures and hardness values.

[1] *Corresponding author: Yildiz Technical University, Department of Metallurgical and Materials Engineering, 34210, Esenler/Istanbul, Turkey.* seacar@yildiz.edu.tr

2. EXPERIMENTAL

A319 alloy with chemical composition as given in Table 1 was melt at 635 °C in electric resistance melting furnace and cast through a copper cooling slope with 650 mm length and 60° tilt angle into a metal mould. Copper tube was coated with hexagonal boron-nitride before casting procedure in order to avoid metal adhesion. Cast billets were machined into nine specimens with 4 cm height and 2 cm diameter. One specimen was kept as reference and the others were reheated for 20, 40, 60 and 80 minutes as couples at 585 °C. After reheating step, one of the each duplicates was quenched in water and the other one thixoforged in open die with 50% deformation.

Table 3. Chemical composition of selected A319 alloy

Alloying Element	**Cu**	**Si**	**Zn**	**Fe**	**Mg**	**Mn**	**Ti**	**Al**
% Content	3.46	5.91	1.92	0.41	0.08	0.23	0.16	87.83

All specimens were ground up to 1200 grit SiC grinding paper, polished with 1 µm diamond paste and then etched with 0.5% HF solution. Microstructural examinations were carried out with image analyser assisted Nicon Eclipse MA100 optic microscope. Brinell hardness test was applied on each specimen with 62.5 kgF load and 2.5 mm tip diameter.

3. RESULTS AND DISCUSSION

Due to low Si content of A319 alloy comparing to well-studied casting Al alloys like A356 and A380, low fluidity during casting was observed thus, cooling slope casting procedures could be performed at 30 °C above the alloy's liquidus temperature. Microstructures of cooling slope as-cast specimen is given in *Figure 1*. It can be easily seen that near equiaxed grains were formed rather than dendritic formation due to combined effects of moderate super heating before casting, rapid cooling and shear effect of the slope.

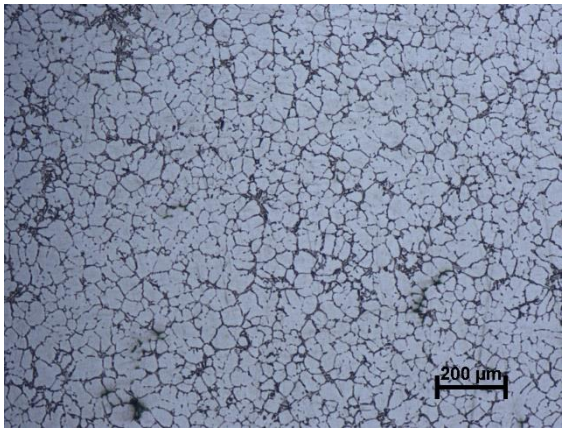

Figure 4. Microstructure of cooling slope as-cast specimen

As it was mentioned in experimental section, all other specimens were reheated below 20 °C of liquidus temperature and either quenched in water in order to freeze present microstructure or thixoforged with %50 deformation. Microstructures of quenched and thixoforged samples are given in *Figure 2*. It can be obviously seen that spheoridization of the grains were scaled up by increasing isothermal reheating time. Partial melting and re-solidification of eutectic phase around globular α grain boundaries with increasing ratio can be observed in quenched specimens' microstructures. Increase with the eutectic component can be explained by the migration of silicon content from polyhedral Si phases to the eutectic phase with increasing reheating time. Increase in the average grain size was also observed with increased reheating times. This situation can be explained by coalescence and Ostwald ripening mechanisms. Low reheating time causes rather low fraction of liquid and under this circumstances different grains tend to combine a larger agglomerate. On the other hand, Ostwald ripening mechanism takes place with higher reheating time or temperature. In this case as a result of high reheating times, alloying elements moved to larger grains therefore small grains were vanished and the larger ones grew even more.

Throughout the thixoforging process solid grains deform and liquid component flows. In this way semi-solid materials are able to be formed. This phenomenon can be seen in thixoforged microstructures. The deformation texture arises

with the deterioration on grain morphology during forging process at semi-solid state. Eutectic phase was spread around from grain boundaries because of deformation and equiaxed grains were begun to disrupt in thixoforged specimens.

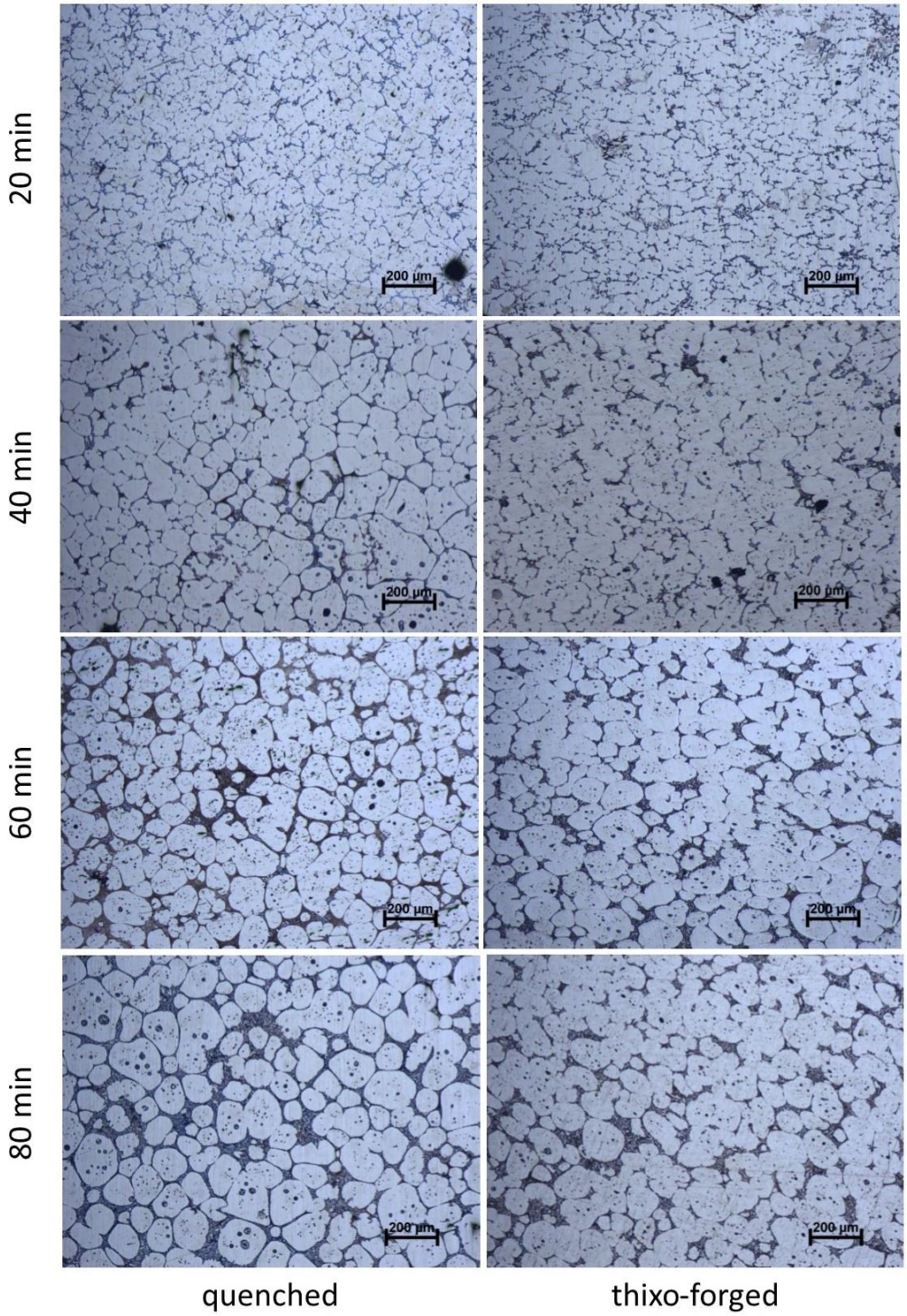

Figure 2. Microstructures of quenched and thixoforged specimens after reheating

In order to better understanding of the thixoformability of specimens, furthermore to realize the relation between microstructure and hardness property; spherodization indexes (SI) and average grain sizes which were calculated from

microstructures are given in Table 2 and Figure 3 respectively. Brinell hardness of the specimens are also given in Figure 4.

Table 2. Spherodization Index of As-Cast and Quenched Samples

	CS As-Cast	20 min quenched	40 min quenched	60 min quenched	80 min quenched
Spherodization Index	0.871	0.907	0.951	0.911	0.926

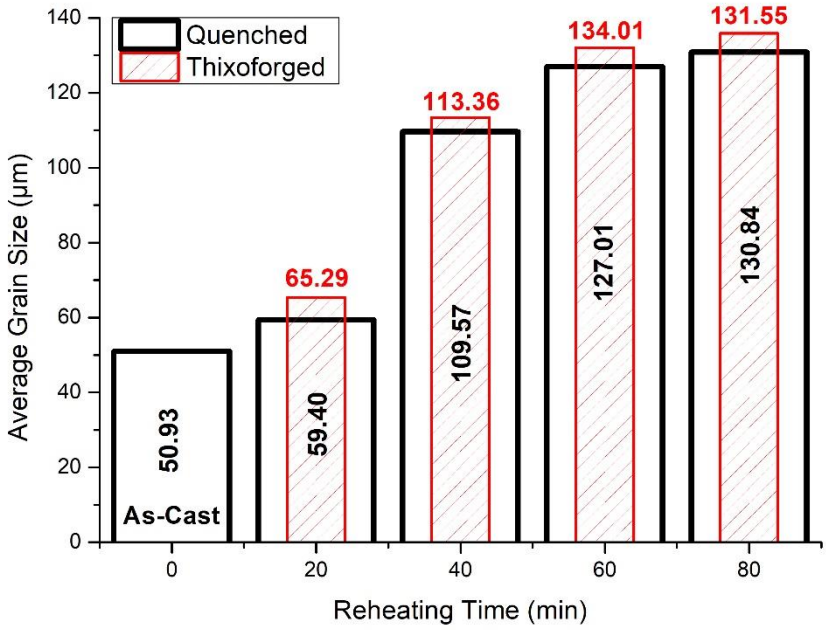

Figure 3. Average grain sizes

According to obtained data, 40 minutes reheated and quenched sample has the most globular microstructure with 0,951 SI. Spherodization decreases by the increasing reheating times because merging of former grains causes new grains with high diameter/perimeter ratio. Apart from the optimum liquid fraction, sufficient spheroidization rate is another crucial parameter for an effective thixoforming process. Therefore, more globular microstructures are expected from thixoforming feedstocks.

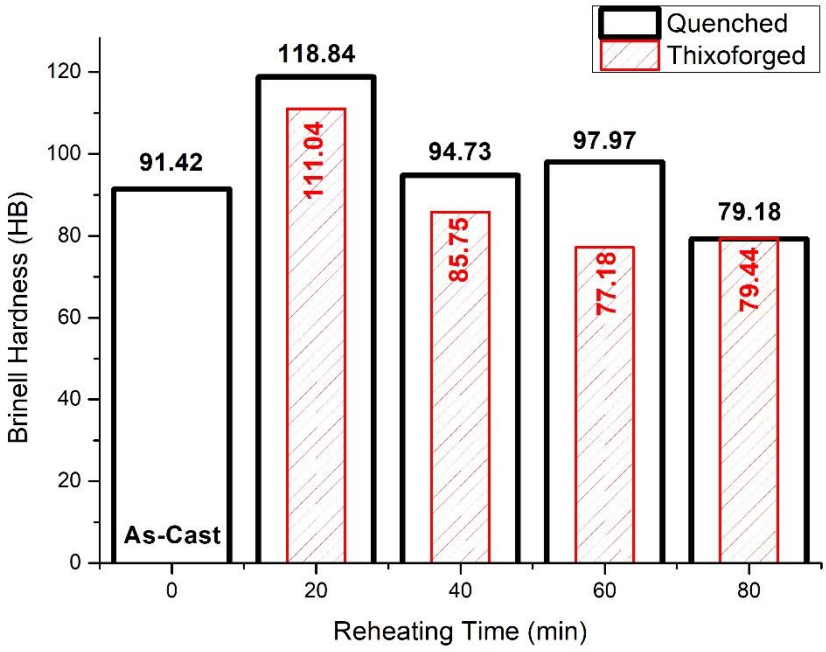

Figure 4. Brinell hardness values for all samples

Maximum hardness values were obtained for 20 minutes reheated samples. In spite of increased grain size comparing to as-cast specimen, reorganization of eutectic phase in finer morphology after partial melting and fast solidification along reheating-quenching may have caused that increment. 40 minutes and 60 minutes reheated and quenched samples were showed close hardness values with little difference in grain sizes. On the other hand thixoforged specimens displayed lower hardness values in a consequence of coarsened grain morphology due to random dispersion of secondary phases from grain boundaries. This deformation sourced new formation were accompanied with disappearance of grain boundaries and thusly reduction in hardness values. Hardness values obtained from 80 minutes reheated samples were quite low due to extreme increase in grain size for both quenched and thixoforged specimens.

4. CONCLUSION

Cooling slope casting method was employed to produce thixoforging feedstock for A319 aluminum casting alloy. Listed conclusions can be made according to obtained results.

1) 20 °C of super-heating in cooling slope casting procedure for common A3xx series alloys such as A356 and A380 was found sufficient in previous studies. However relative low fluidity of A319 alloy due to relative low silicone content was observed during casting procedure therefore castings were carried out at 635 °C with 30 °C of superheating.
2) Maximum sphericity was obtained in 40 minutes reheated sample with 0.951 SI.
3) Maximum hardness was obtained on 20 minutes reheated samples owing to finer microstructure.
4) Grain coarsening throughout increasing isothermal reheating times was observed up to x2.5 times comparing to as cast specimen.

REFERENCES

[1] D. Liu, H. V. Atkinson, P. Kapranos, W. Jirattiticharoean, and H. Jones, "Microstructural evolution and tensile mechanical properties of thixoformed high performance aluminium alloys," *Mater. Sci. Eng. A*, vol. 361, no. 1–2, pp. 213–224, 2003.

[2] M. Z. Omar, H. V. Atkinson, E. J. Palmiere, A. A. Howe, and P. Kapranos, "Microstructural Development of HP9/4/30 Steel During Partial Remelting," *steel Res. Int.*, vol. 75, no. 8–9, pp. 552–560, Aug. 2004.

[3] D. Abolhasani, H. R. Ezatpour, S. A. Sajjadi, and Q. Abolhasani, "Microstructure and mechanical properties evolution of 6061 aluminum alloy formed by forward thixoextrusion process,", *Mater. Des.*, vol. 49, pp. 784-790, 2013.

[4] Y. Birol, "A357 thixoforming feedstock produced by cooling slope casting," *J. Mater. Process. Technol.*, vol. 186, no. 1–3, pp. 94–101, 2007.

[5] S. D. Kumar, A. Mandal, and M. Chakraborty, "Cooling Slope Casting Process of Semi-solid Aluminum Alloys: A Review," *Int. J. Eng. Res. Technol.*, vol. 3, no. 7, pp. 269–283, 2014.

[6] H. V. Atkinson, "Semisolid processing of metallic materials", *Mater. Sci Technol.*, vol. 26, no. 12, pp. 1401-1413, 2010.

[7] M. S. Salleh, M. Z. Omar, J. Syarif, K. S. Alhawari, and M. N. Mohammed, "Microstructure and mechanical properties of thixoformed A319 aluminium alloy," *Mater. Des.*, vol. 64, pp. 142–152, Dec. 2014.

ICETI
www.iceti.org
2018
07-11 MARCH
BUDAPEST
HUNGARY
II. INTERNATIONAL CONFERENCE ON ENGINEERING TECHNOLOGY AND INNOVATION

Comparison of Method A1 and B of Tensile Test on Aluminium Specimens

Ramakumar Jayachandran[1];Christian Weißmuller[1]

Abstract

Tensile test is the predominant test method used in extrusion industry to check if the minimum mechanical properties required by the product are met test. The two most governing standards to perform the tensile test are the ISO – EN 6892-1 (2016) and the ASTM–E8.16. The new version of the tensile test standard ISO – EN 6892-1 (2016) strongly recommends using method A of the tensile test. A set of pre-machined specimen were sent to eighteen different labs to test both Method A1 and Method B of the tensile test. This paper presents the comparison of the test results from the two different test methods. Each method was evaluated for four specific criteria

1.Determination of 0,2 %-proof strength Rp0,2

2.Determination of the tensile strength Rm

3.Determination of percentage elongation after fracture A manually

4.Determination of percentage elongation after fracture A extensomer

The evaluation of the results shows no significant difference between the two test methods on 6061 aluminium alloy.

Keywords: Aluminium, Extrusion, Method A1, Method B, Strain, Stress, Tensile Test.

1. INTRODUCTION

Tensile test is the predominant test method used in extrusion industry to check if the minimum mechanical properties required by the product are met. The two most governing standards to perform tensile test are the ISO – EN 6892-1 (2016) [1] and the ASTM–E8.16 [2]. The tensile test provides valuable information on the material properties such as tensile strength (Rm), elongation (A), yield strength ($R_{p0,2}$) and reduction in area (Z). The new version of the tensile test standard [1] offers three different test methods to perform tensile test, namely; Method A1 (test based on closed loop strain rate), Method A2 (test based on estimated strain rates) and Method B (test based on stress rate).

As shown in figure 1, nearly all the existing tensile test equipment in use are capable to perform Method A2 and Method B of the tensile test. Most of the test equipment in use, are not capable to perform the test Method A1. In addition, the cost of purchasing a new equipment to perform Method A1 of the tensile test is almost twice the cost of purchasing a new equipment capable to perform Method B and Method A2 of the tensile test.

This paper compares the test results from the Method A1 and Method B of the tensile test from a pre-machined 6061-T6 aluminium alloy. ,

[1] *Corresponding author: Hydro- Extruded Solutions, Operational Excellence -Europe, Drammensveien, 264 Oslo, Norway ,* *Ramakumar.Jayachandran@hydro.com*

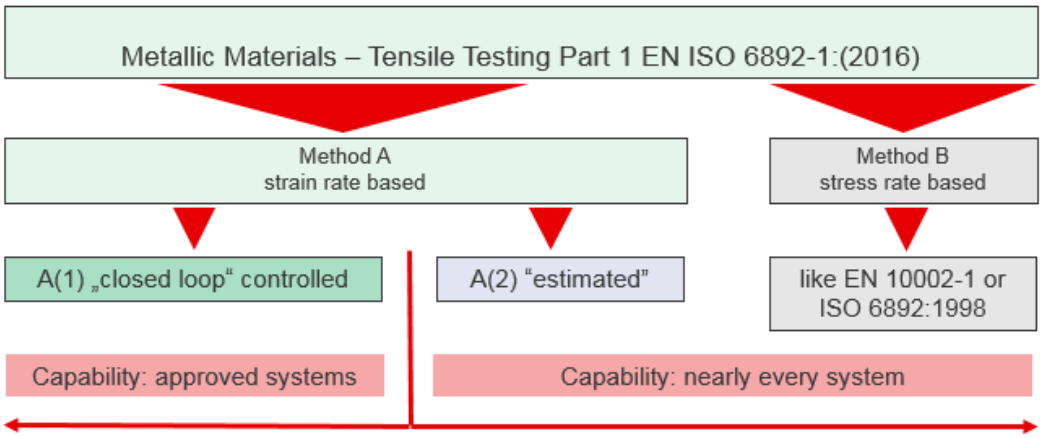

Figure 5. Three tensile test methods and capability of the equipment. [3]

2. EXPERIMENTAL

4.1. 2.1 Material

The material selected for the experiment was 6061 T6 aluminium alloy, from which a rectangular aluminium specimen was made according to ISO 6892-1 [1]. To eliminate the impact of machining quality on the final test results, the specimens were machined by a proficiency test provider – The Institute for Proficiency Tests (IfEP) [4]. A total of 250 specimens were made in batches of 25. Each specimen was 3mm thick and was machined to 12,5mm width. The specimens were sent to several Hydro Extruded Solutions laboratories in Europe for testing.

4.2. 2.2 Homogeneity Test

To ensure if the material was homogenous, the proficiency test provider also performed a homogeneous testing. The primary aim of a homogeneity testing is to verify, on a reasonable number of units, that all units of the reference material may be considered as being “identical” (between-unit homogeneity testing) when a batch certification is envisaged [5]. One specimen from a batch of 25 was selected for homogeneity test and every batch was tested.

Table 1 summarizes the results of seventeen specimens tested for homogeneity using method B of tensile test. In terms of the proficiency test the specimens were sufficiently homogeneous as the specific value *R*m presents a standard deviation within the homogeneity test of less than 1 % [6].

Table 4. Results from homogeneity testing

Series n=17	Thickness-mm	Width-mm	mE GPa	Rp0,2 MPa	Rm MPa	A50mm %
x̄	3,002	12,48	70,2	252	318	17,4
S	0,000655	0,004657	1,4	1,1	0,93	0,6
V [%]	0,00	0,04	1,98	0,43	0,29	3,43

x̄ - Mean; S – Standard deviation, V [%]- Coefficient of variation

4.3. 2.3 Test Protocol

Each specimen was given a unique number by the proficiency test provider, so that the specimen could be traced back to the homogeneity test group. Once the specimens passed the homogeneity testing, the specimens were packed into two sets clearly marked as Task A (for Method A1 test) and Task B (for Method B test) as shown in figure 2. Special care was taken that no more than two specimens from the same homogeneity group (from a batch of 25 specimens) were sent to one test laboratory for a given task.

The labs were asked to perform the tensile test according to the test speed provided by the proficiency test provider, for Method A1 being 0,00025 s−1 within the yield range and 0,00067 s-1 after the yield point was established, for Method B being 10 MPa/s.

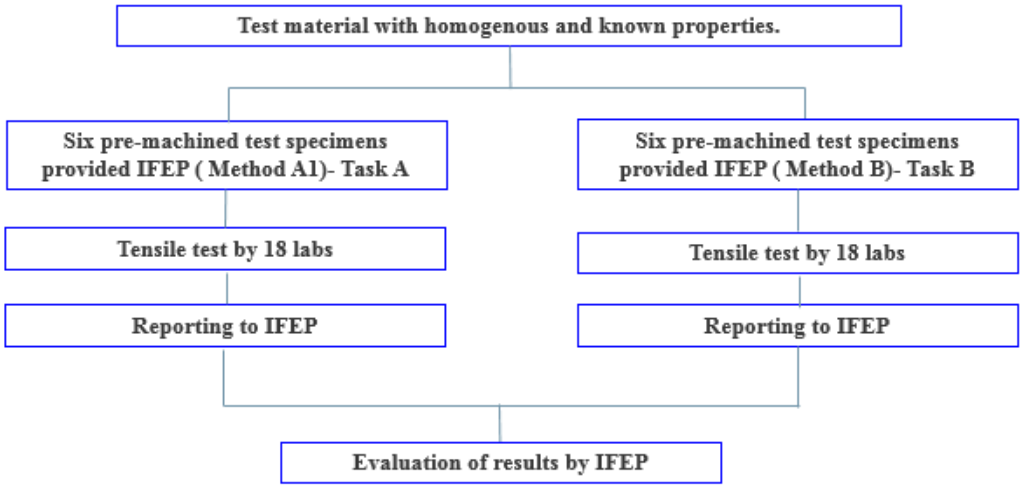

Figure 6. Test Protocol

4.4. 2.4 Test Equipment and Method

There are many sources of uncertainty during the tensile testing process, particularly stiffness of the equipment, the type of grips, test speeds, class (accuracy) of the extensometer used, operator's skills. A recent study [7] showed that the difference in the yield strength was around 5% when the specimens were tested at the same speed on low and high stiffness machine. Figure 3 shows other factors that influence the outcome of the test results.

To avoid these uncertainties all the equipment used in the evaluation were either 100KN Zwick tensile machine or 250KN Zwick tensile machine. All the test machines were equipped with hydraulic grips and with a high accuracy contact Zwick makroXtens extensometer. The cross-sectional dimensions of the specimens were measured with a Cross-sectional Measuring Unit (CMU) to eliminate the impact of human measurement error. The standard deviation on thickness measurement from all the labs was 0,06mm and the standard deviation on width measurement from all the labs was 0,02mm.

To minimize the factors influencing the test results, the following factors were addressed:

- Specimens were pre-machined
- Specimens were tested for homogeneity
- All the laboratories used cross sectional measurement unit to measure the dimensions
- Only Zwick 100KN and 250KN equipment were used.
- The test speeds were specified for both test methods
- Tensile test software was configured with identical parameters in all laboratories
- All the test equipment used hydraulic grips.
- All the users were given detailed training on equipment and methods.
- The test was done at a controlled temperature condition 23 °C ± 5 °C.

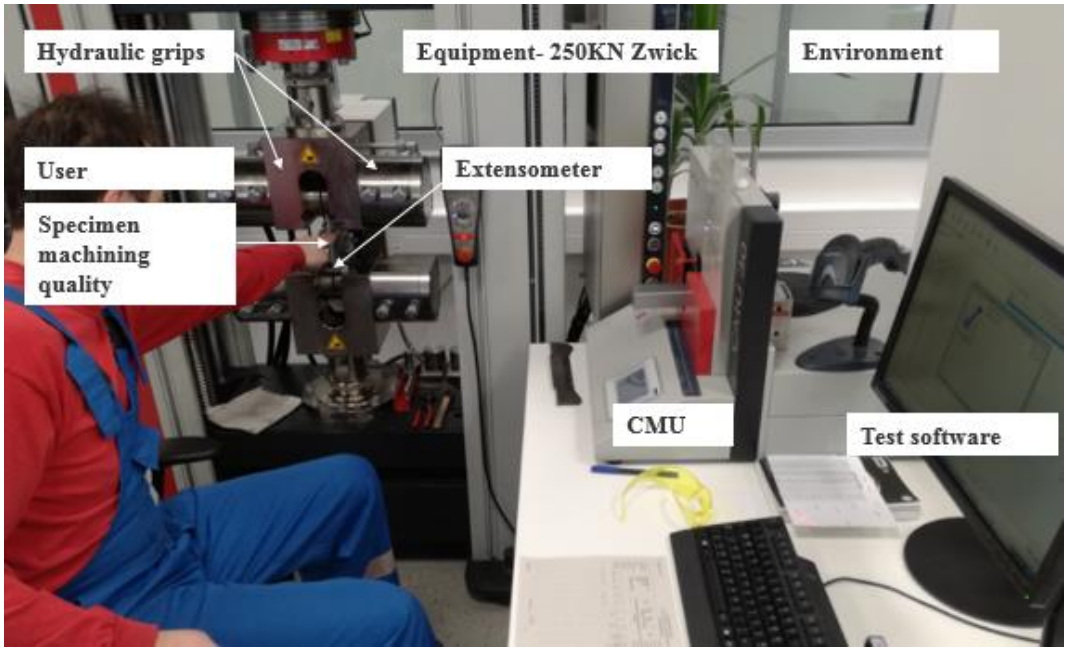

Figure 7: Factors affecting the test results

3. RESULTS AND DISCUSSION

The laboratories in Hydro Extruded Solutions tested six specimens for Method A1 and six specimens for Method B. The laboratories reported the test results through an online reporting system provided by the proficiency test provider [6]. Figure 4 shows the average of the results of the six specimens tested with Method A1 and B for their yield strength. The results show that there is no significant difference on the yield strength with method A1 and B tensile test. For lab numbers, 1,4,5,6,7 and 17, the yield strength values were identical from both test methods.

The tensile test standard [1] also provides an indication of expected scatter in tensile test tensile test results for a variety of materials including aluminium that have been reported during laboratory inter-comparison exercises, including both material scatter and measurement uncertainty - Annex L [1]. The results for the reproducibility are expressed as percentages calculated by multiplying by 2 the standard deviation of the respective parameter, e.g. Rp0,2, Rm, Z, and A, and dividing the result by the mean value of the parameter, thereby giving reproducibility values, which represent the 95 % confidence level. The evaluation of reproducibility values for Rp0,2 and Rm were less than 1,2% which is significantly less than reported values from the standard [1].

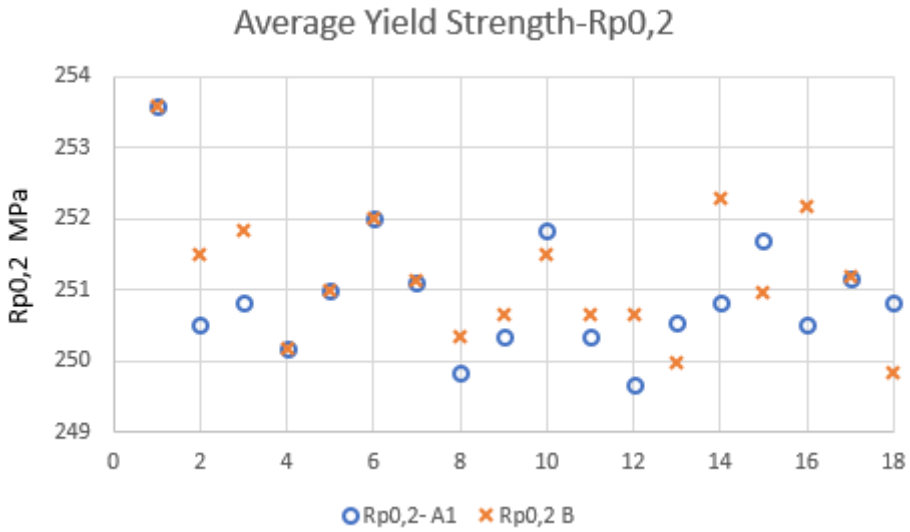

Figure 8 Average yield strength values from each lab

Table 2 shows the mean and standard deviation from Method A1 and B for the yield strength. The first two columns in Table 2 show the data from both types of test equipment and the next two columns show the data from the 100KN Zwick machine only. The variability between these two methods is insignificant.

Table 5. Statistical evaluation of test results- Yield strength -Rp0,2

n= 108	Rp0,2- MPa Method A1	Rp0,2- MPa Method B	Rp0,2- MPa * Method A1	Rp0,2-MPa * Method B	Rp0,2 # MPa
$\bar{x}$	250,93	251,13	250,62	250.92	252
s	1,56	1,39	1,3	1,21	1,1
V%	0,62	0,55	0,52	0,48	0,43

** Data from 100KN Zwick machine only, n=66*

 # Data from homogeneity test

Figure 5 shows the average of the results of the six specimens tested with Method A1 and B for their ultimate tensile strength. The results show that there is no significant difference on the tensile strength with Method A1 and B of tensile test. For lab numbers, 2, 7 and 11 the tensile strength values were identical from both the test methods.

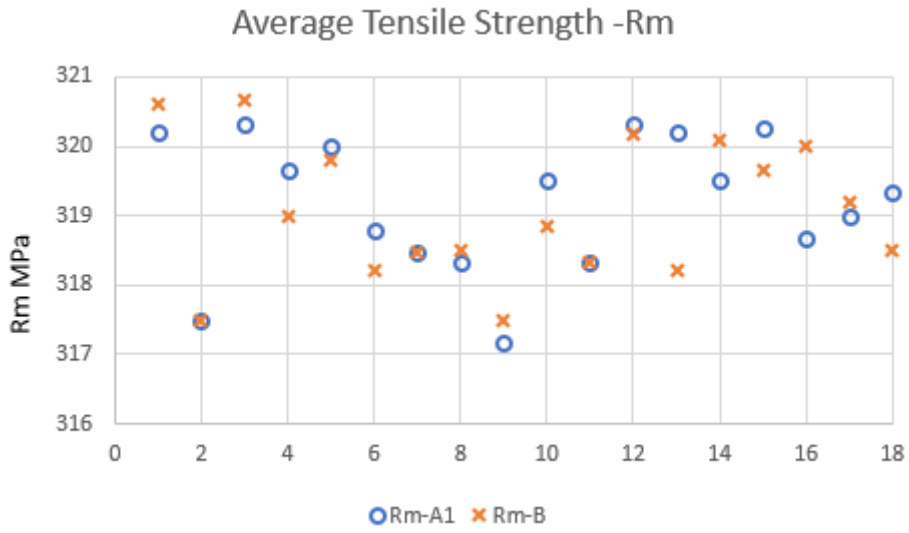

Figure 9 Average tensile strength values from each lab

Table 3 shows the mean and standard deviation from Method A1 and B for the tensile strength. The first two columns in table 3 show the data from both the test equipment and the next two columns show the data from the 100KN Zwick machine only. The variability between these two methods is insignificant.

Table 6. Statistical evaluation of test results- Tensile strength Rm

n= 108	Rm- MPa Method A1	Rm- MPa Method B	Rm- MPa * Method A1	Rm- MPa * Method B	Rm- MPa #
x̄	319,16	319,07	319,12	318,97	318
s	1,44	1,40	1,53	1,42	0,93
V%	0,45	0,44	0,47	0,44	0,29

** Data from 100KN Zwick machine only, n=66*

 # Data from homogeneity test

Figures 6 and 7 show the average of the results of the six specimens tested with Method A1 and B for elongation, measured by an extensometer and manual method respectively. The results show that there is no significant difference on the elongation measured for Method A1 and B. It can also be seen that the manual measurements of elongation from all the labs is marginally higher than the elongation values reported by the extensometer. One of the reasons could be is the difficulty in placing the fractured specimen together and measuring the elongation values.

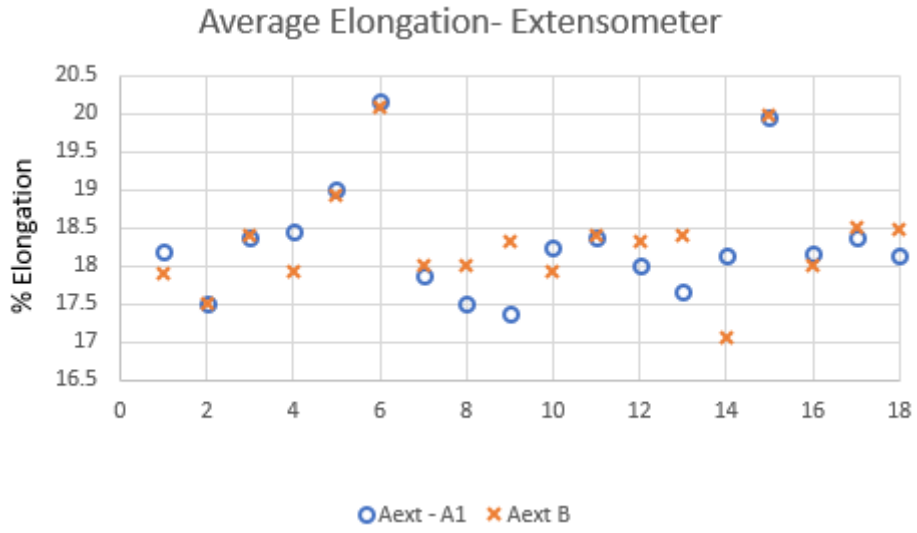

Figure 10 Average elongation measurement by extensometer

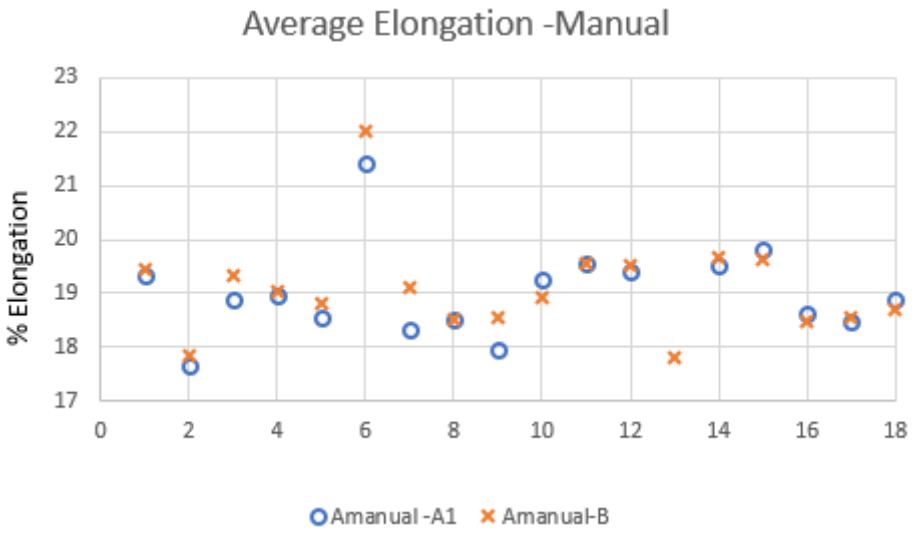

Figure 11 Average elongation -by manual measurement

Table 4 shows the statistical evaluation of elongation measurements from method A1 and B. Again, no difference in mean or standard deviation can be seen between these two methods.

Table 7. Statistical evaluation of test results-Elongation

n= 108	A Ext Method A1	A Ext Method B	A manual Method A1	A manual Method B	A manual Homogeneity test
$\bar{x}$	18,3	18,32	18,93	19,06	17,4
s	0,96	1,06	1,02	1,0	0,6
V%	5,24	5,78	5,39	5,24	3,45

To further evaluate the difference between these two test methods a T-test [8] was conducted for all the four parameters; yield strength, tensile strength, elongation by extensometer and by manual method. A T- test is typically used to evaluate whether the results are statistically different or not. Due to the large number of test data (108), showing a normal distribution and less variance in the results, an unpaired T-test analysis was performed. Table 5 shows the p values from the T-test evaluation. The T-test evaluation indicated (as p value is >0,05) no significant difference between the two tensile test methods A1 and B at 95% significance level.

Table 8. Unpaired T -test evaluation

Criteria	$Rp_{0,2}$	Rm	A extensometer	Amanual
p value	0,32	0,63	0,88	0,30

4. CONCLUSIONS

Tensile test was performed on pre-machined 6061 aluminium alloy with two different test methods (Method A1 and B). From this study, the difference in average tensile strength from the two test methods and average yield strength from the two test methods is less than 1MPa, which indicates that there is no difference between the two test methods for the 6061 aluminium alloy. To support the findings a T-test was performed, which also demonstrated no significant difference between the two-tensile test methods A1 and B. Similarly, the difference in elongation values from the two test methods was insignificant. Further work should focus on evaluating the effect of these two test methods on other aluminium alloys such as 6082, 6005 etc. commonly used in the extrusion industry.

ACKNOWLEDGMENT

The authors thank Quality and Lab managers from Hydro Extruded solutions for their support in the study.

REFERENCES

[1]. ISO 6892-1 :2016 (E), *Metallic Materials – Tensile Testing, Part 1 Method of test at room temperature*, 2nd ed., 2016 , www.iso.org

[2]. ASTM E8 / E8M-16a, *Standard Test Methods for Tension Testing of Metallic Materials*, ASTM International, West Conshohocken, PA, 2016, www.astm.org

[3]. E. Schenuit**,** *Strain Rate Control according to ISO 6892-1: 2016*, Quality conference Guest lecture, Hydro Extruded solutions, 2016

[4]. C.Weibmuller, H. Frenz and S. Wiler, "Proficiency tests in the field of mechanical testing and related areas", *The First International Proficiency Testing Conference*, 2007, Paper, pp-118-124

[5]. J. Pauwels, A. Lamberty and H.Schimmel, Homogenity testing of reference material , *Accreditation and Quality Assurance* , Vol 3, pp 51-55, Springer-Verlag, 1998.

[6]. C.Weibmuller, Proficiency Test -Tensile test aluminium- flat tensile specimens-*1780, Report-Hydro Extruded solutions*, Nov 2017

[7]. Ambient Tensile Testing of metallic materials. [Online]. Available http://www.instron.in/-/media/literature-library/whitepapers/2016/04/iso6892.pdf

[8]. T Test calculator [Online] https://www.graphpad.com/quickcalcs/ttest2/

ICETI
www.iceti.org
2018
07-11 MARCH
BUDAPEST
HUNGARY
II. INTERNATIONAL CONFERENCE ON ENGINEERING TECHNOLOGY AND INNOVATION

Performance of Zero-Forcing Receive Beamforming with Signal Space Diversity in the Presence of Channel Estimation Errors

Serdar Ozyurt [1]

Abstract

The performance of zero-forcing receive beamforming (ZFRBF) with signal space diversity (SSD) is examined under binary phase shift keying (BPSK) modulation. No channel state information (CSI) is available at the transmit side and the receiver has CSI under channel estimation errors. Such a scenario is quite practical and reflects an important practical impairment. Using a π/4-radian rotated BPSK signal constellation, we show that the inclusion of SSD considerably increases the immunity of the original ZFRBF system against the channel estimation errors. The capability of the proposed system to lower the error floor is also demonstrated.

Keywords: Wireless communications, multiple-input multiple-output, zero-forcing receive beamforming, signal space diversity, channel state information, channel estimation errors.

1. INTRODUCTION

This work considers a wireless communication scenario with 2 and M ($M \geq 2$) antennas at the transmitter and receiver, respectively. Such a system is known as a 2-by-M multiple-input multiple-output (MIMO) system and has the potential to double the channel capacity without additional bandwidth/time/power resources [1]. One of the spatial multiplexing techniques that can be used for this purpose is zero-forcing receive beamforming (ZFRBF) [2]. ZFRBF has the advantage of achieving full spatial multiplexing gain with relatively low complexity. However, it is seriously vulnerable to any kind of additive noise and thus offers a limited error performance. As a solution to this problem, we here study a combination of ZFRBF with signal space diversity (SSD) assuming that the number of simultaneous substreams is two. SSD provides error performance enhancement with no extra use of bandwidth/time slots and almost no additional complexity [3]. In [4], a zero-forcing transmit beamforming (ZFTBF) scheme is combined with SSD assuming perfect channel state information (CSI) both at the transmitter and receiver. SSD is integrated into ZFRBF in [5] where perfect CSI is assumed to be available only at the receiver. ZFTBF is studied with SSD in [6] by assuming a possibly imperfect CSI at the transmitter. For a literature review on the inclusion of SSD into spatial multiplexing techniques, interested reader may consult to the studies in [4, 5] and the references therein. In this work, we examine the performance of ZFRBF with SSD for binary phase shift keying (BPSK) modulation over slow flat Rayleigh fading channels. No CSI is available at the transmitter and the receiver has CSI with channel estimation errors as different from [5]. Such a scenario is quite practical and reflects an important practical impairment. The estimation errors are modeled by using a statistical error model parameterized by the correlation between the actual and estimated channel vectors. We show that the inclusion of SSD increases the immunity of the original ZFRBF system against the additive impairments to a great extent. Moreover, the proposed technique (ZFRBF/SSD) is shown to yield substantial signal-to-noise ratio (SNR) gains beyond the original ZFRBF scheme without SSD. SYSTEM MODEL

We investigate a single-user MIMO communication system with 2 and M antennas at the transmitter and receiver, respectively. At the receiver, the received complex baseband signal is given by;

[1] *Ankara Yildirim Beyazit University, Faculty of Engineering and Natural Sciences, 06010, Kecioren/Ankara, Turkey. sozyurt@ybu.edu.tr*

$$\mathbf{y} = \mathbf{H}\mathbf{x} + \mathbf{n} \tag{1}$$

where $\mathbf{H} \in \mathbb{C}^{M\times 2}$ is the M-by-2 channel matrix. The (i, k) element of $\mathbf{H}$, i.e., $[\mathbf{H}]_{ik} \in \mathbb{C}$, denotes the fading coefficient between the kth transmit antenna and ith receive antenna. Additionally, the vector $\mathbf{x} \in \mathbb{C}^{2\times 1}$ represents the transmitted baseband signal. Our target is to transmit two independently modulated symbols $s_i = s_{iI} + js_{iQ}$ $\left(i \in \{1,2\}\right)$ in a simultaneous fashion. The modulated symbols are obtained from a π/4-radian rotated BPSK signal constellation with the subscripts I and Q referring to the corresponding in-phase and quadrature components, respectively. We have a per-bit energy constraint such that $|s_i|^2 = E_b$ with E_b standing for the energy per bit. The vector $\mathbf{n} \in \mathbb{C}^{M\times 1}$ represents additive white Gaussian noise (AWGN) at the receiver. We have $\mathrm{E}\left[\mathbf{n}\mathbf{n}^H\right] = N_0\mathbf{I}$ where $\mathbf{I}$ stands for the identity matrix. Also, N_0 is the one-sided power spectral density of the AWGN at each receive antenna. It is assumed that the antennas are uncorrelated both at the transmit and receive sides. Accordingly, the elements of the matrix $\mathbf{H}$ are independent and identically distributed (IID) zero-mean complex Gaussian random variables with unit variance. A slow flat Rayleigh fading scenario is studied. The transmitter does not have CSI and an imperfect CSI is available at the receiver. The imperfection in CSI is captured by the following identity

$$\mathbf{H} = \rho\,\tilde{\mathbf{H}} + \sqrt{1-\rho^2}\;\mathbf{E} \tag{2}$$

where $\tilde{\mathbf{H}}$ is the estimated channel matrix and $\mathbf{E}$ represents its estimation error [1]. The matrices $\tilde{\mathbf{H}}$ and $\mathbf{E}$ are uncorrelated and the entries of both $\tilde{\mathbf{H}}$ and $\mathbf{E}$ are IID zero-mean complex Gaussian random variables with variance of one.

2. ZERO-FORCING RECEIVE BEAMFORMING WITH SIGNAL SPACE DIVERSITY

In this section, we show how SSD is integrated into the original ZFRBF scheme. The transmitter has a relatively simple architecture. The real parts of two modulated symbols s_1 and s_2 are joined together to form a complex number β_1 as $\beta_1 = s_{1I} + j\,s_{2I}$. Applying the same process on the imaginary parts of the two modulated symbols, the complex number β_2 is built as $\beta_2 = s_{1Q} + j\,s_{2Q}$. After digital-to-analog conversion operations on β_1 and β_2, the transmitted signals from the first and second transmit antennas are respectively acquired. Note that $\mathbf{x} = \left[\beta_1 \;\; \beta_2\right]^T$ and with this, (2) can be rephrased as

$$\mathbf{y} = \mathbf{h}_1\beta_1 + \mathbf{h}_2\beta_2 + \mathbf{n} \tag{3}$$

where $\mathbf{h}_1, \mathbf{h}_2 \in \mathbb{C}^{M\times 1}$ stand for the first and second columns of the channel matrix $\mathbf{H}$, respectively. In the same manner, let $\tilde{\mathbf{h}}_1$ and $\tilde{\mathbf{h}}_2$ denote the first and second columns of the estimated channel matrix $\tilde{\mathbf{H}}$, respectively. We have $\mathbf{h}_i = \rho\,\tilde{\mathbf{h}}_i + \sqrt{1-\rho^2}\;\mathbf{e}_i$ where $\mathbf{e}_i$ for i ∈ {1, 2} respectively represent the first and second columns of $\mathbf{E}$. As per ZFRBF, we first project $\mathbf{y} \in \mathbb{C}^{M\times 1}$ onto the vector $\tilde{\mathbf{h}}_1^H\mathbf{P}_{\tilde{\mathbf{h}}_2}^{\perp} \in \mathbb{C}^{1\times M}$. Here, $\mathbf{P}_{\tilde{\mathbf{h}}_i}^{\perp}$ is the projection matrix onto the null space of the vector $\tilde{\mathbf{h}}_i$, i.e., $\mathbf{P}_{\tilde{\mathbf{h}}_i}^{\perp} = \mathbf{I} - \tilde{\mathbf{h}}_i\tilde{\mathbf{h}}_i^H / \left\|\tilde{\mathbf{h}}_i\right\|^2$. This operation results in

$$\frac{\tilde{\mathbf{h}}_1^H\mathbf{P}_{\tilde{\mathbf{h}}_2}^{\perp}}{\left\|\tilde{\mathbf{h}}_1^H\mathbf{P}_{\tilde{\mathbf{h}}_2}^{\perp}\right\|}\mathbf{y} = \rho\left\|\tilde{\mathbf{h}}_1^H\mathbf{P}_{\tilde{\mathbf{h}}_2}^{\perp}\right\|\beta_1 + \hat{n}_1 \tag{4}$$

where the noise-plus-interference term $\hat{n}_1$ equals

$$\hat{n}_1 = \frac{\tilde{\mathbf{h}}_1^H \mathbf{P}_{\tilde{\mathbf{h}}_2}^{\perp} \mathbf{e}_1}{\left\| \tilde{\mathbf{h}}_1^H \mathbf{P}_{\tilde{\mathbf{h}}_2}^{\perp} \right\|} \sqrt{1-\rho^2}\ \beta_1 + \frac{\tilde{\mathbf{h}}_1^H \mathbf{P}_{\tilde{\mathbf{h}}_2}^{\perp} \mathbf{e}_2}{\left\| \tilde{\mathbf{h}}_1^H \mathbf{P}_{\tilde{\mathbf{h}}_2}^{\perp} \right\|} \sqrt{1-\rho^2}\ \beta_2 + \frac{\tilde{\mathbf{h}}_1^H \mathbf{P}_{\tilde{\mathbf{h}}_2}^{\perp} \mathbf{n}}{\left\| \tilde{\mathbf{h}}_1^H \mathbf{P}_{\tilde{\mathbf{h}}_2}^{\perp} \right\|}.$$

In the same manner, $\mathbf{y}$ is projected onto $\tilde{\mathbf{h}}_2^H \mathbf{P}_{\tilde{\mathbf{h}}_1}^{\perp} \in \mathbb{C}^{1\times M}$ as

$$\frac{\tilde{\mathbf{h}}_2^H \mathbf{P}_{\tilde{\mathbf{h}}_1}^{\perp}}{\left\| \tilde{\mathbf{h}}_2^H \mathbf{P}_{\tilde{\mathbf{h}}_1}^{\perp} \right\|} \mathbf{y} = \rho \left\| \tilde{\mathbf{h}}_2^H \mathbf{P}_{\tilde{\mathbf{h}}_1}^{\perp} \right\| \beta_2 + \hat{n}_2 \tag{5}$$

where

$$\hat{n}_2 = \frac{\tilde{\mathbf{h}}_2^H \mathbf{P}_{\tilde{\mathbf{h}}_1}^{\perp} \mathbf{e}_1}{\left\| \tilde{\mathbf{h}}_2^H \mathbf{P}_{\tilde{\mathbf{h}}_1}^{\perp} \right\|} \sqrt{1-\rho^2}\ \beta_1 + \frac{\tilde{\mathbf{h}}_2^H \mathbf{P}_{\tilde{\mathbf{h}}_1}^{\perp} \mathbf{e}_2}{\left\| \tilde{\mathbf{h}}_2^H \mathbf{P}_{\tilde{\mathbf{h}}_1}^{\perp} \right\|} \sqrt{1-\rho^2}\ \beta_2 + \frac{\tilde{\mathbf{h}}_2^H \mathbf{P}_{\tilde{\mathbf{h}}_1}^{\perp} \mathbf{n}}{\left\| \tilde{\mathbf{h}}_2^H \mathbf{P}_{\tilde{\mathbf{h}}_1}^{\perp} \right\|}.$$

It is straightforward to show that $\hat{n}_1$ and $\hat{n}_2$ are correlated and identically distributed circularly symmetric zero-mean complex Gaussian random variables both with a variance of $\left(2\left(1-\rho^2\right)E_b + N_o\right)$. Conditioned on the estimated channel vectors, the correlation coefficient between $\hat{n}_1$ and $\hat{n}_2$, i.e., $\mathrm{E}\left[\hat{n}_1 \hat{n}_2^* \middle| \tilde{\mathbf{h}}_1, \tilde{\mathbf{h}}_2\right]$, is given by

$$\mathrm{E}\left[\hat{n}_1 \hat{n}_2^* \middle| \tilde{\mathbf{h}}_1, \tilde{\mathbf{h}}_2\right] = \frac{\tilde{\mathbf{h}}_1^H \mathbf{P}_{\tilde{\mathbf{h}}_2}^{\perp} \mathbf{P}_{\tilde{\mathbf{h}}_1}^{\perp} \tilde{\mathbf{h}}_2}{\left\| \tilde{\mathbf{h}}_1^H \mathbf{P}_{\tilde{\mathbf{h}}_2}^{\perp} \right\| \left\| \tilde{\mathbf{h}}_2^H \mathbf{P}_{\tilde{\mathbf{h}}_1}^{\perp} \right\|} \left(2\left(1-\rho^2\right)E_b + N_o\right).$$

At the receiver, the maximum likelihood (ML) detector makes its decision on the two modulated symbols using

$$\upsilon_1 = \Re\left\{ \frac{\tilde{\mathbf{h}}_1^H \mathbf{P}_{\tilde{\mathbf{h}}_2}^{\perp}}{\left\| \tilde{\mathbf{h}}_1^H \mathbf{P}_{\tilde{\mathbf{h}}_2}^{\perp} \right\|} \mathbf{y} \right\} + j\ \Re\left\{ \frac{\tilde{\mathbf{h}}_2^H \mathbf{P}_{\tilde{\mathbf{h}}_1}^{\perp}}{\left\| \tilde{\mathbf{h}}_2^H \mathbf{P}_{\tilde{\mathbf{h}}_1}^{\perp} \right\|} \mathbf{y} \right\} \tag{6}$$

for the first modulated symbol and

$$\upsilon_2 = \Im\left\{ \frac{\tilde{\mathbf{h}}_1^H \mathbf{P}_{\tilde{\mathbf{h}}_2}^{\perp}}{\left\| \tilde{\mathbf{h}}_1^H \mathbf{P}_{\tilde{\mathbf{h}}_2}^{\perp} \right\|} \mathbf{y} \right\} + j\ \Im\left\{ \frac{\tilde{\mathbf{h}}_2^H \mathbf{P}_{\tilde{\mathbf{h}}_1}^{\perp}}{\left\| \tilde{\mathbf{h}}_2^H \mathbf{P}_{\tilde{\mathbf{h}}_1}^{\perp} \right\|} \mathbf{y} \right\} \tag{7}$$

for the second modulated symbol. Let $\left\| \tilde{\mathbf{h}}_1^H \mathbf{P}_{\tilde{\mathbf{h}}_2}^{\perp} \right\| = \gamma_1$ and $\left\| \tilde{\mathbf{h}}_2^H \mathbf{P}_{\tilde{\mathbf{h}}_1}^{\perp} \right\| = \gamma_2$. Then, υ_1 and υ_2 can also be written as

$$\upsilon_1 = \rho\ \gamma_1\ s_{1I}\ + j\rho\ \gamma_2\ s_{1Q}\ + \Re\left\{\hat{n}_1\right\} + j\ \Re\left\{\hat{n}_2\right\}$$

and

$$\upsilon_2 = \rho\ \gamma_1\ s_{2I}\ + j\rho\ \gamma_2\ s_{2Q}\ + \Im\left\{\hat{n}_1\right\} + j\ \Im\left\{\hat{n}_2\right\}.$$

The ML detector designates its decision in favor of the point that is nearest to $\upsilon_i\ \ (i \in \{1,2\})$ in the signal constellation where the in-phase and quadrature components of each point are respectively scaled by $\rho\ \gamma_1$ and $\rho\ \gamma_2$.

The recommended approach described above for the 2-by-M scenario can be extended to include the case of any number of transmit antennas ($t \geq 2$) and any number of receive antennas ($r \geq t$) using the technique described in [4,5]. For any t and r with $2 \leq t \leq r$, SSD can be inserted into the original system by employing the following baseband transmit signals

$$\mathbf{x} = \begin{bmatrix} s_{1I} + j\ s_{2I} \\ s_{1Q} + j\ s_{2Q} \\ s_{3I} + j\ s_{4I} \\ s_{3Q} + j\ s_{4Q} \\ \mathrm{M} \\ s_{t-1,I} + j\ s_{tI} \\ s_{t-1,Q} + j\ s_{tQ} \end{bmatrix} \quad \text{for even t} \tag{8}$$

and

$$\mathbf{x} = \begin{bmatrix} s_{tI} + j\ s_{2I} \\ s_{1Q} + j\ s_{2Q} \\ s_{3I} + j\ s_{4I} \\ s_{3Q} + j\ s_{4Q} \\ \mathrm{M} \\ s_{t-2,I} + j\ s_{t-1,I} \\ s_{t-2,Q} + j\ s_{t-1,Q} \\ s_{1I} + j\ s_{tQ} \end{bmatrix} \quad \text{for odd t.} \tag{9}$$

The detector constructs its decision on the t modulated symbols using the decision variables, i.e., υ_i for $i \in \{1, 2, \mathrm{K}\ , t\}$, which are formed as similar to (6) and (7).

3. NUMERICAL RESULTS

A number of numerical results on bit error probability (BEP) are provided in this section. In Figure 1, the proposed technique is compared with the original ZFRBF scheme without SSD for M = {5, 6} with $\rho = 0.9$. When M = 5, the proposed technique considerably lowers the error floor induced by the channel estimation errors. This in turn brings about serious SNR gains. For instance, the proposed approach attains an SNR gain of around 7 dB at a BEP of 2×10^{-3} when M = 5. The obtained SNR gain is about 5 dB at a BEP of 5×10^{-4} for M = 6. It can be observed that the error floor is noticeably lowered under this scenario as well. The two techniques are compared in Figure 2 for M = {4, 5} with $\rho = 0.95$. Some similar conclusions as above can also be drawn for these cases. For example, the proposed approach achieves an SNR gain of around 3 dB at a BEP of 2×10^{-3} when M = 4. The SNR gain is about 4 dB at a BEP of 2×10^{-4} for M = 5. The effect of the error floor's lowering can be seen also under these scenarios.

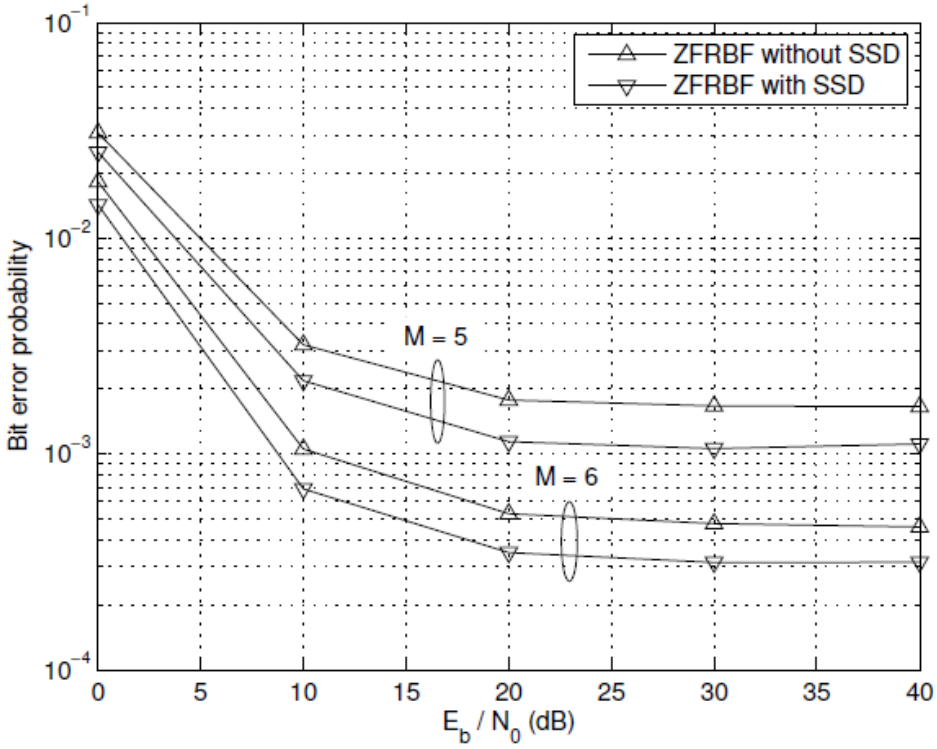

Figure 12. The performances of the proposed and original schemes when $\rho = 0.9$.

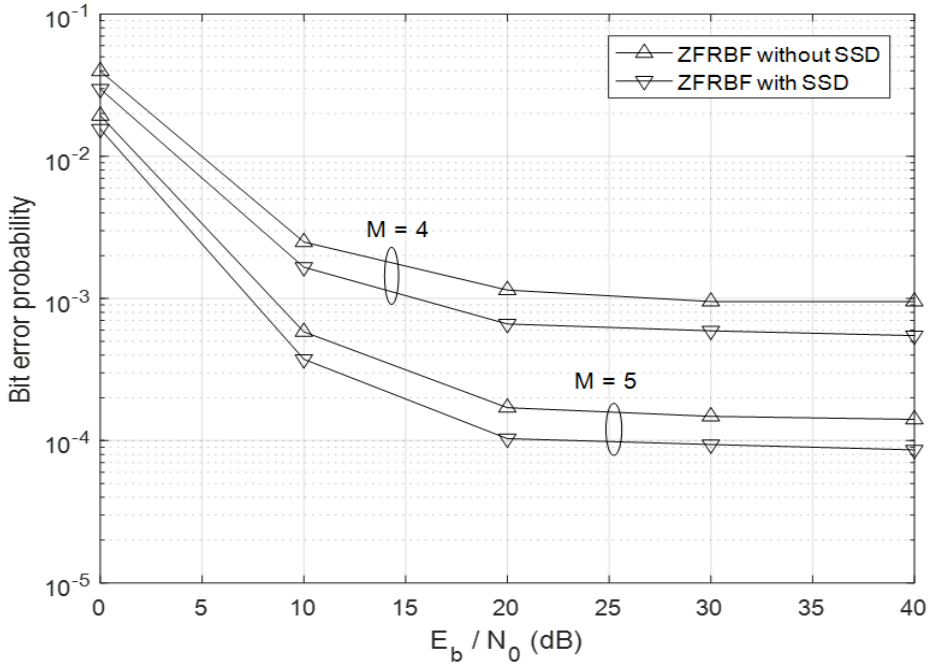

Figure 2. The performances of the proposed and original schemes when $\rho = 0.95$.

4. CONCLUSION

We have examined the performance of ZFRBF with SSD under BPSK modulation over slow flat Rayleigh fading channels. The transmitter does not have any CSI and the receiver possesses an imperfect CSI due to some channel estimation errors. We have shown that the error performance of ZFRBF can be enhanced considerably by incorporating SSD with only a small increase in the system complexity and no additional use of bandwidth/time resources. Additionally, it has been demonstrated that the proposed approach has the effect of lowering the error floor thus increasing the strength of the system against the estimation errors.

REFERENCES

[1]. I. E. Telatar, "Capacity of multi-antenna Gaussian channels," *European Trans. Telecommun.*, vol. 10, no. 6, pp. 585-595, Dec. 1999.
[2]. D. Tse and P. Viswanath, Fundamentals of Wireless Communications, NY: Cambridge Univ. Press, 2005.
[3]. G. Taricco and E. Viterbo, "Performance of component interleaved signal sets for fading channels," *Electron. Lett.*, vol. 32, no. 13, pp. 1170-1172, Apr. 1996.
[4]. S. Ozyurt and O. Kucur, "Zero-forcing beamforming with signal space diversity," *IEEE Trans. Veh. Technol.*, vol. 67, no. 1, pp. 812-816, Jan. 2018.
[5]. S. Ozyurt and O. Kucur, "Performance of zero-forcing receive beamforming with signal space diversity over Rayleigh fading channels," in Proc. *IEEE Adv. Wireless Optical Commun. (RTUWO)*, Riga, Latvia, Nov. 2017.
[6]. S. Ozyurt, "Performance analysis of zero-forcing precoding with signal space diversity under antenna correlation," submitted to *IEEE Access*, Feb. 2018

ICETI
www.iceti.org
2018
07-11 MARCH
BUDAPEST
HUNGARY
II. INTERNATIONAL CONFERENCE ON ENGINEERING TECHNOLOGY AND INNOVATION

Deformation of Soil at Tunnel Construction

Utkan Mutman[1], Merve Bulut[1]

Abstract

It is critical that the deformations that occur in and around the tunnels during and after the excavation are not a threat to the safety of life. The deformations must be inspected to ensure they are within the allowed limits. Engineering does not apply the principles of safety and economy from the 3E rule. A tunnel opened by the New Austrian Tunneling Method was modeled using the finite element method and the expected deformation after the construction was analyzed using PLAXIS 2D. The analysis results and the post-tunnel deformation measurements were compared and the model was found to be consistent with the actual data. The results of the deformation analysis calculated by the model were investigated for their divergence from the actual values measured after the construction. The effects of deformation of support elements, tunnel shape and soil parameters in the tunnel examined were also investigated.

Keywords: Deformation, FEM, NATM, Plaxis 2D, Tunnel

1. INTRODUCTION

Due to constant challenges facing transportation, the use of the underground became more and more a must. Some examples of underground structures that are being built are transportation tunnels, clean water-waste water tunnels, derivation tunnels, storage tunnels, military structures and mining structures. People in large cities are faced with problems such as air pollution, environmental pollution, water pollution, health and infrastructure problems, and traffic problems. Traffic and transportation problems are by far the largest problem that is being faced, 29% of cities face this problem. [1] Tunnels are a very efficient problem to this problem, in fact sometimes it is the only solution. The goal is to reduce load on above ground infrastructure by utilizing alternative channels underground.

Tunneling is a process that needs to be planned in detail starting from the project before tunnel opening to the process after excavation and excavation. Tunnel construction involve the selection of the route to be opened, the examination of the route base, the design of the tunnel, the selection of the construction method and support systems, the design with the right crew and equipment, the location monitoring and deformation measurements. Any misinformation during any of these steps has a great risk of involving economical and life loss. All possible side effects must be anticipated due to this great risk. With accurate ground analysis, deformations that may occur in and around engineering structures can be estimated before construction by various methods. Good tunneling is tunneling where deformations can be predicted and limited. These limit values are not as wide as the mining galleries in metro tunnels due to metro tunnels being usually built to a great extent under residential areas and buildings. In this study, a sample tunnel was examined on the basis of the fact if the deformation estimations before construction reflect the reality and the effects of deformation of tunnel support systems, shape and soil properties were investigated.

2. PROJECT AND METHOD DETAILS

2.1. New Austrian tunneling method (NATM)

The New Austrian Tunneling Method (NATM) was a concept first introduced by Prof. L.v. Rabcewicz. He applied for a patent in 1948 for this process and defined it as "by placing a fine temporary support and allowing deformations, the rock pressure is reduced and distributed to the surrounding rock. Thus, the last support will be loaded less and then the

[1] *Corresponding author: Kocaeli University, Department of Civil Engineering, 41380, Kocaeli/Istanbul, Turkey.*

last support will be placed in a thinner structure. Deformations should be observed with measurements and the results should be evaluated together with structural analysis and design."[2]

The principle of NATM is to make the rocky environment surrounding the tunnel carry its load. Thus, the rock environment in which the gap is opened becomes a load, and the system will serve as the carrier element. This method is distinguished from other tunneling methods in that it is compatible with different geometry and different geological conditions. As a result, tunnel constructions can be carried out at low cost and without interruption.

In November 1964 Professor Dr. L. V. Rabcewicz described NATM as "... a new method of covering the deformation as a function of time until deformation balance is achieved by a complete ring consisting of a thin shot of concrete and as soon as possible called an auxiliary belt". [3] In this definition, three main points are emphasized; the first is the application of the thin shotcrete coating, the second is the closure of the ring as quickly as possible, and the third is the systematic deformation measurement.

Deformation as a word means to change shape or distortion from the original shape. Observations made with various measurements are also referred to as deformation measurements. The step of determining and interpreting the changes of these measurements according to the parameters of location, time and size is the analysis of deformation measurements. Deformations can be observed by many geodetic and non-geodetic methods. [4]

2.2. Basic steps to monitor deformation levels

First, the possible maximum values of the expected deformations and deformations must be estimated. For this, the necessary measurement accuracy and methods must be determined. Then, the design of the measuring web and the measurement of the appropriate measurement methods is completed. At the last stage, evaluation of the collected data and modeling of the determined deformations is done. The basic process steps to follow in dealing with the deformations of the engineering structures are;

- Determination of the state of the work to be followed by the deformation
- The need for location accuracy and the appropriate method selection
- Type and number of measurements
- Selection of tools and equipment to be used in measurements
- Determination of measurements and determination of deformations
- Evaluation and analysis of data
- Establishing the behavior of deformations in terms of time, position and frequency
- Modeling
- Reporting [4]

2.3. The project location

This study covers the Sirkeci route of the Istanbul-Marmaray project. The total line length of the Marmaray project is 76.3 km. With this project, railways on both sides of Istanbul are connected to each other by a railway tunnel connection that goes under the strait. Various tunneling techniques have been used along the Marmaray project route. [5] The route section is given below;

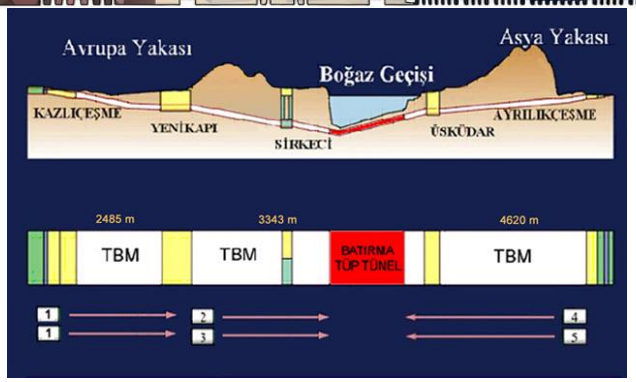

Figure 13. Marmaray project route section

The red part of the route are the immersed tunnels. The white sections are mostly constructed as drilling tunnels using tunneling machines (TBM), and yellow sections are made using the cut-cover technique (C & C) and the New Austrian Tunneling Method (NATM) or other conventional methods. Figures 1, 2, 3, 4 and 5 show Tunnel Boring Machines (TBM). The Sirkeci route, where the work was done, is the first station to move from Asia to Europe. 135 buildings on this route were examined by observation before excavation. According to these determinations, the risk of existing buildings before the excavation started and the damage distributions after the excavation are shown in Fig. 2 and Fig. 3, respectively. [6]

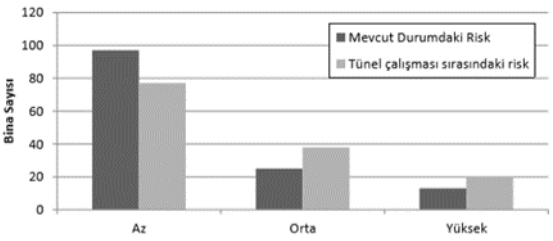

Figure 2. Risk of existing buildings

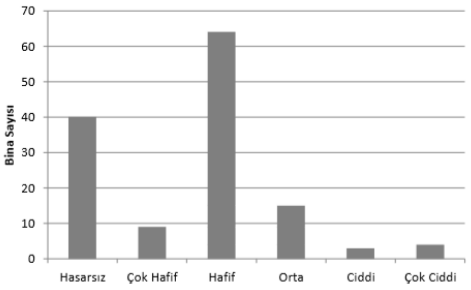

Figure 3. Damage after excavation

There are two entrances to the Sirkeci station. The station entrances were built using the Cut-Cover method, and the main line tunnel excavations were carried out by NATM. [5]

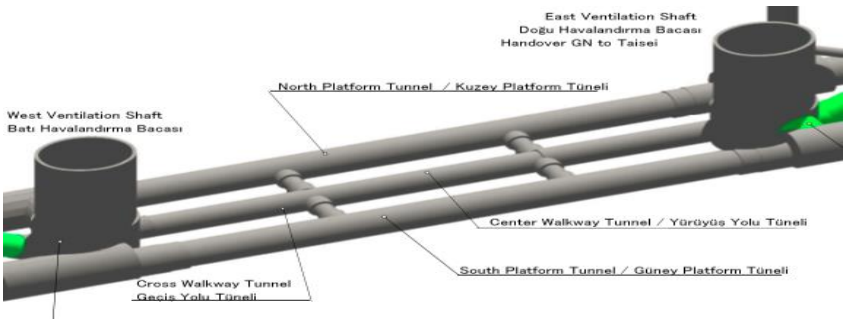

Figure 4. 3D representation of the Sirkeci station

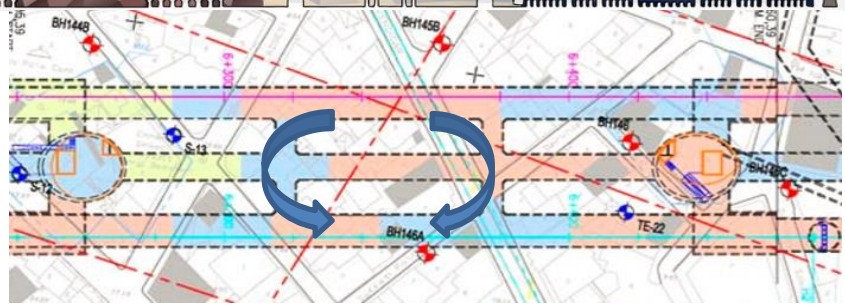

Figure 5. The region where the deformation measurements were made

Several drilling wells have been opened along the route. After examining the ground with laboratory and field tests, the ground parameters for the top fill zone, middle layer and main rock were extracted according to the critical values. Thus the 1st and 2nd layer floors are defined identically on the whole project. 3. The base rock is defined as the floor in 6 different properties (B, CI, CII, DI, DII, and E) in the whole project.

Table 1. Parameters for the first and second soils

Symbol	Soil Type	N_{45}	N_{60}	γ t (kN/m^2)	γ sat (kN/m^2)	γ sub (kN/m^2)	ϕ (°)	c (kN/m^2)	E1 (kN/m^2)	E2 (kN/m^2)	ν
F	Manmade	16	12	18	19	9	30	0		33,600	0.3
SM5/SC5	Silty, Clayey sand	24	18	18	19	9	34	0		50,400	0.3

Table 2. Parameters of the main rock

Rock classification	Deformation modulus E (N/mm^2)	Poisson's ratio ν	Cohesion C (N/mm^2)	Internal friction angle ϕ (°)	Unit weight γ t (kN/m_3)
B	5,000	0.25	4.0	50	25
CI	2,000	0.30	2.0	45	24
CII	1,000	0.30	1.0	40	23
DI	500	0.35	0.4	35	22
DII	150	0.35	0.2	30	21
E	80	0.40	0.1	30	20

The investigated Sirkeci station is a district with CI, DI and DII flooring characteristics. In the study, deformations in the DII section were investigated.

2.4. Modelling

In this study, deformation of a real tunnel constructed by New Austrian Tunneling Method is examined. The correlation of the various variables is analyzed. The model has been made by using the finite element method in the Plaxis 2D program. Below are the actual observations from the project data which are used in our model.

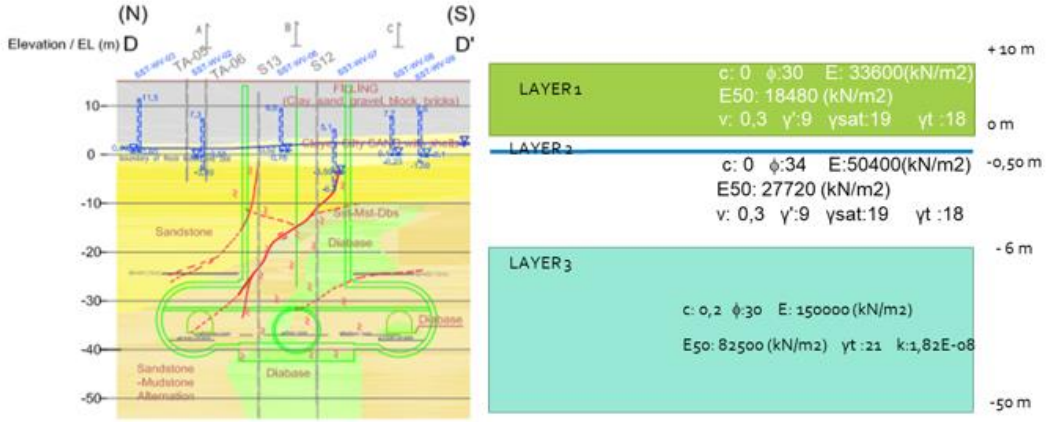

Figure 6. The modeled soil properties of the region where the deformation measurement is to be performed

The Modelling Steps

1 – Preconstruction area analysis

2 – Boring and support of the upper half of the tunnel

3 –Boring and support of the lower half of the tunnel

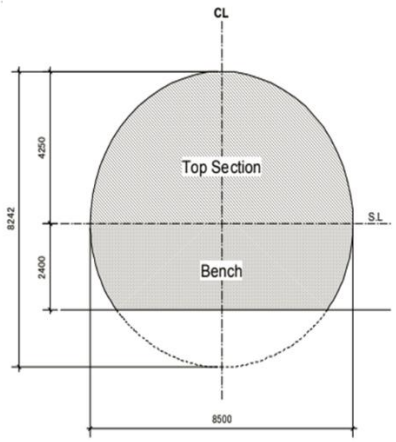

Figure 7. Dimension of the modeled section

2.5. Analysis steps

Preconstruction Analysis;

Total Displacements: 0,00 m

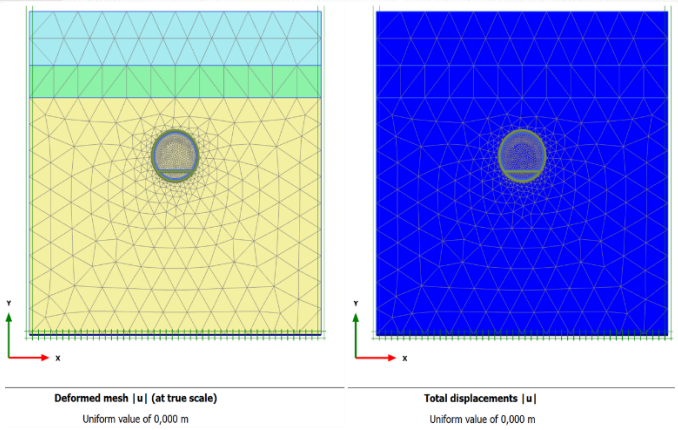

Figure 8. Preconstruction situation

Boring and support of the upper half of the tunnel;

Total Displacements: 2.622E-03 m

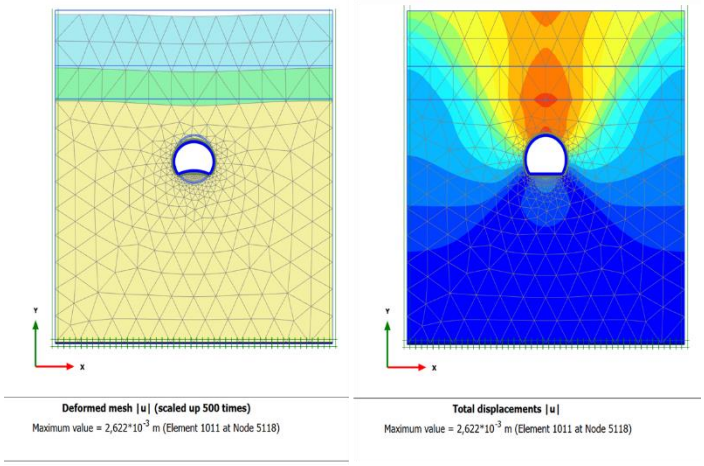

Figure 9. Boring and support of the upper half of the tunnel

Boring and support of the lower half of the tunnel;

Total Displacements: 3.010E-03 m

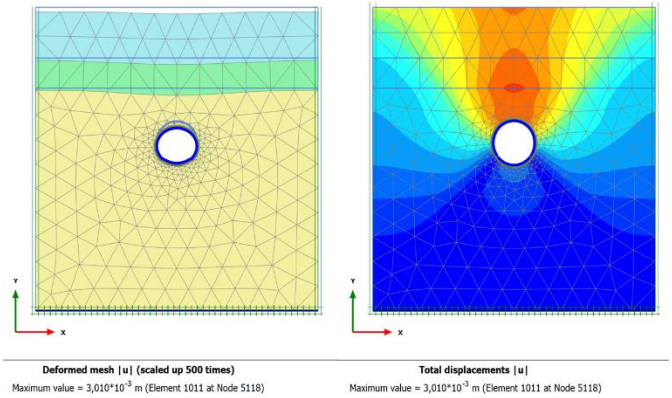

Figure 10. Boring and support of the lower half of the tunnel

At the surface of the tunnel, the maximum deformation was measured as 3 mm.

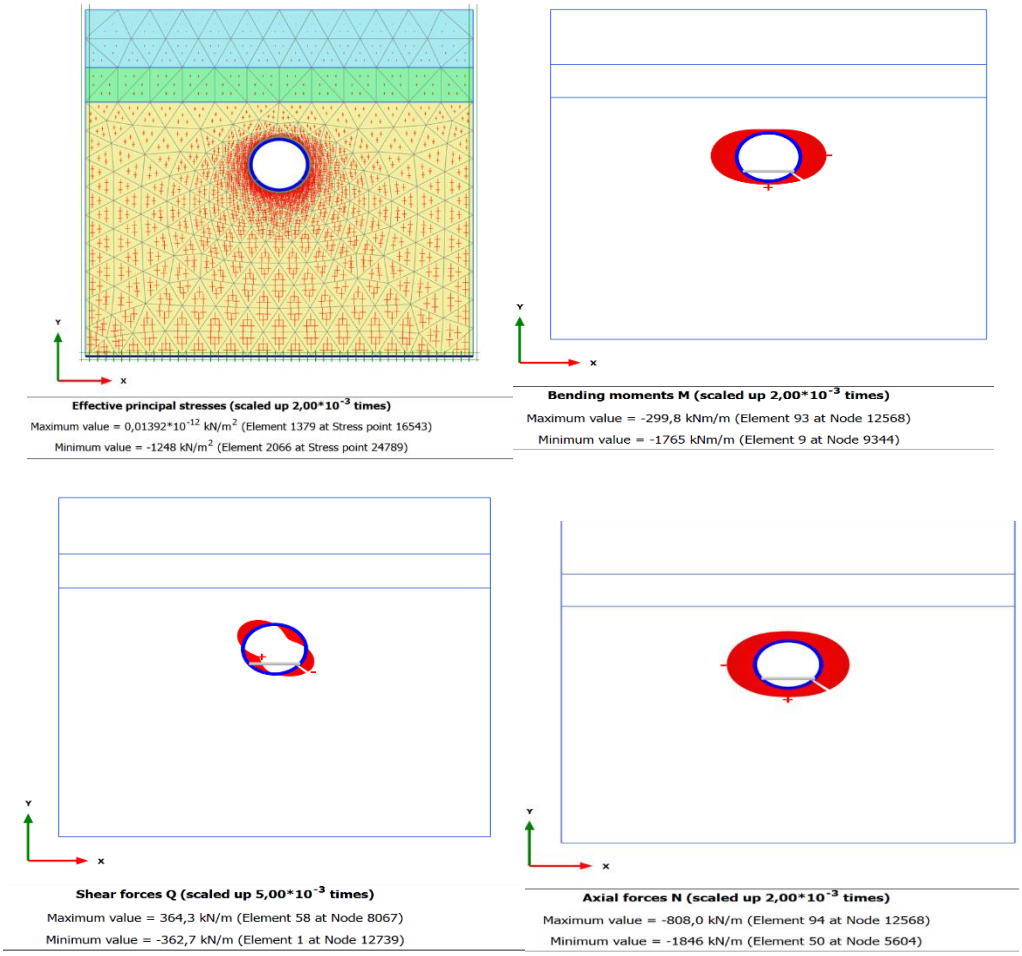

Figure 11. Program analysis results

3. RESULTS AND DISCUSSION

In the modelled tunnel, the value of maximum bending moment was 1765 kNm/m, the value of maximum shear force was 364,3 kN/m, the value of maximum axial forces was 1846 kN/m and the value of maximum deformation was approximately 3 mm.

In the real project, the deformations were measured of between 4 mm – 22 mm. The maximum allowed value for the real project was 24 mm.

4. CONCLUSIONS

During the modelling the deformation was calculated to be around 3mm, however deformations of up to 22 mm were actually encountered in the real world project. This difference indicates the existence of natural conditions that cannot be modeled in the calculations. This is due to errors in obtaining the ground parameters used in the calculations. This study also highlighted the importance of the accuracy of the ground survey that will be used in the model.

At the continuation of this work, the tunnel shape, dimensions, type of support used and soil parameters values will be changed to investigate their effects on the deformation.

REFERENCES

[1]. I. Ocak, "Metro tunellerinde, kayac ozelliklerinin tasman ve konverjansa etkilerinin arastirilmasi", *Istanbul Universitesi Muhendislik Fakultesi Yer bilimleri Dergisi*, vol. 18, pp. 45-46, 2005
[2]. Kahyaoglu T., "TAG otoyolu uzerinde tunel isleri ve Yeni Avusturya Tunel Acma Yontemi, *IV. Ulastirma Kongresi*, 1998, paper 49-50
[3]. Karakus M., Fowell R.J., "An insight into the New Austrian Tunneling Method (NATM)", *KAYAMEK'2004-VII Bolgesel Kaya Mekanigi Sempozyumu*, 2004.
[4]. Kalkan Y., "Alkan R. M., Muhendislik yapilarinda deformasyon olcmeleri", *2. Muhendislik Olcmeleri Sempozyumu*, 2005.
[5] (2017) The Marmaray website. [Online] Available: http://www.marmaray.gov.tr/icerik/marmaray/Marmaray-Teknik-%C3%96zellikleri/56
[6]. Topal, "Marmaray projesi Sirkeci Istasyonu pilot tunel kazilarina bagli gelisen yuzey deformasyonlarinin degerlendirilmesi", M. Eng. Thesis, ITU, Istanbul, Turkey, May 2014.

ICETI 2018 07-11 MARCH BUDAPEST HUNGARY www.iceti.org
II. INTERNATIONAL CONFERENCE ON ENGINEERING TECHNOLOGY AND INNOVATION

Influence of Different Si Levels on Mechanical Properties of Aluminium Casting Alloys

Onur Ozaydin[1] and Alper Kaya[1]

Abstract

AlSi7 and AlSi11 are the most commonly used materials in aluminum alloy wheel production. The main difference is the heat treatment application; for wheel production AlSi7 is usually used in heat treated form while AlSi11 is not. Heat treatment processes play a vital role on production costs. More than fifty percent of aluminum wheels are heat treated however the exact value varies between different manufacturers. Additional heat treatment costs directly affect the competitiveness of the manufacturer. In this study the material properties of an alternative Si level between AlSi7 and AlSi11 are examined and the effects of these intermediate Si levels on mechanical properties are compared with that of AlSi7 and AlSi11. The aim of this study to examine the possibility of obtaining mechanical properties of heat treated AlSi7 with a non-heat-treated material differing only in Si content. In this experiment all processes and casting parameters for different material types are the same except for the Si content. In addition to an experimental study, the mechanical properties of the alternative material are simulated by utilizing a material analysis software and these properties are compared with experimental results. Thus, correlation between simulation and experimental study results can also be examined. As a conclusion, the alternative non-heat-treated material is presented to manufacturers. These results may be used to bypass the heat treatment process and to decrease the cost of final product.

Keywords: Aluminum, Heat Treatment, Mechanical Properties, Simulation of Material Properties

1. INTRODUCTION

In the last decades, the importance of weight reduction is growing dramatically in the automotive industry. Not only fuel efficiency, but also emission values which is regulated by rule-maker lead the automotive manufacturer to use lightweight materials. Considering the low density, better mechanical properties, easier machinability, corrosion resistance and recyclability, Al-Si based alloys are widely used in automotive components. Especially, AlSi7 and AlSi11 dominate the Al-Si based alloys as a main material in wheel production. The main difference is the heat treatment application; for wheel production AlSi7 is usually used in heat treated form while AlSi11 is not. The primary reason of heat treatment is improving the mechanical properties. Many authors investigate the optimization of heat treatment to get better mechanical properties [1],[2],[3]. Main purpose of these optimization studies is cost reduction because the heat treatment processes play a vital role on production costs. The exact value varies between different wheel manufacturers, but more than fifty percent of products are heat treated and heat treatment costs directly affect the competitiveness of the wheel manufacturer. In this study the properties of an alternative Si level between AlSi7 and AlSi11 is examined and the effects of these intermediate Si levels on mechanical properties are compared with that of AlSi7 and AlSi11. The aim of this study to examine the possibility of obtaining mechanical properties of heat treated AlSi7 with a non-heat-treated material differing only in Si content.

2. MATERIALS AND METHODS

In addition to two main materials, the alternative Si level material was produced by mixing 50% percentage of each two main material ingots. Thus, AlSi9Mg which is known as hypoeutectic silumin is obtained as an alternative alloy. The alternative alloy was melted in a SiC crucible furnace and all serial production procedures such as grain refinement, modification and degassing were applied in accordance with related regulations. Grain refinement was provided by Al-5Ti-1B rods, alloys were modified by Strontium (AlSr15) and degassed by nitrogen. Quantity of Al-5Ti-1B rods and Strontium (AlSr15) were calculated and added according to chemical content which was measured by OES (Optical Emission Spectrometry) (As shown in Table 1.). [5],[6],[7]

[1] *Corresponding author: Cevher Wheels, R&D Department, 35411, Gaziemir/Izmir, Turkey. oozaydin@cevherwheels.com*

Table 9. Chemical composition [7]

	Si	Fe	Cu	Mn	Mg	Zn	Ti
AlSi7	6,5-7,5	0,15	0,02	0,10	0,30-0,45	0,07	0,10-0,18
AlSi9	9,0-10,0	0,15	0,02	0,05	0,30-0,45	0,07	0,15
AlSi11	10,0-11,8	0,15	0,02	0,05	0,1-0,45	0,07	0,15

The first step of casting process is mold preparation. In mold preparation step, wheel mold was coated and preheated to minimize the casting defects such as shrinkage, cracks and metal flow problems. Directional solidification leads to an increase in mechanical properties and a decrease of casting defects. The directional solidification can be controlled by utilizing the cooling channels in the mold. All casting process parameters such as pouring temperature, mold coating type, preheating mold temperature and cooling channels properties were the same as in serial production.

The second step of casting process is the die casting. 36 Wheel specimens were casted by LPDC (Low Pressure Die Casting) method at 720 ± 20 °C for each 3 samples sets (AlSi7 – AlSi9 – AlSi11) to investigate differences in metallurgical and mechanical tests.

Table 10. Specimen configuration

	Metallurgical Tests				Mechanical Tests	
	As Cast	With HT* Without Wheel Base Coating	Without HT* With Wheel Base Coating	With HT* With Wheel Base Coating	Without HT* With Wheel Base Coating	With HT* With Wheel Base Coating
AlSi7	1	1	1	1	16	16
AlSi9	1	1	1	1	16	16
AlSi11	1	1	1	1	16	16

**HT: Heat Treatment*

Production process was finished with heat treatment application. Heat treatment starts with solution treatment and continues with water quenching and is finalized with artificial aging. The next step of production process is machining. Machining parameters depend on the technical drawing, tolerances, wheel types and milling tools. To minimize these complexity, all wheel specimens were casted into same mold and machined with same machining program and parameters. Machined wheels were deburred and inspected, all specimens were also controlled by a helium-based leakage detector to detect cracks in rim section.

The final step of wheel production process is painting. This process contains three phases; first phase is primary coating; second phase is the color coating and third phase is clear coating. All coatings are applied in an oven since a certain curing temperature is required. Curing temperature is between 100 °C - 210 °C. In a sense, the wheel base coating can be called as secondary artificial ageing. In this study, two different sets, one with wheel base coating and one without wheel base coating were investigated with regarding to metallurgical properties to understand the effect base coating.

In addition to tensile test specimens obtained by machining of wheels, some tensile test specimens were produced by gravity casting method. Figure (1.a) shows LPDC (Low Pressure Die Casting) method and Figure (1.b) shows permanent mold for gravity casting tensile test specimens.

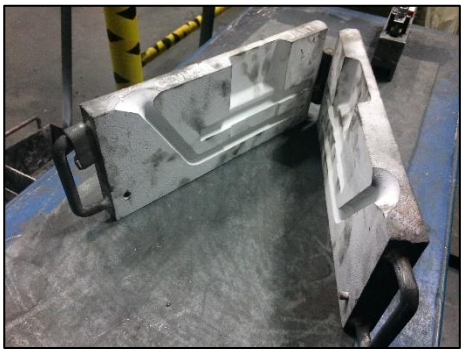

Figure 14. (a) LPDC (Low Pressure Die Casting) method (b) Permanent mold for tensile specimen

All microstructure samples were prepared in accordance with standard metallographic techniques. First, samples were grinded with SiC paper and polished. Second, samples were etched with 0.5% HF solution and examined with an optical microscope. Thermal analysis was conducted by an IDECO thermal analyser that can measure with ±0,1 °C accuracy and can report the grain size. Both types of tensile test specimens were machined and finalized according to DIN 50125 [9] and tested according to EN ISO 6892-1:2016 [10] with a Zwick Z100 model test machine.

Impact tests are applied to verify the wheel shock loading resistance. The impact test can simulate a curb stone or pothole hit and the impact load is dependent on axle load of the car.

Damage on wheels is evaluated in accordance with related specifications and standards. [11],[12]The wheel is considered to fail when the following are observed: visible fractures / cracks, separation of the centre from the rim and air pressure loss in 1 min. [12]

Finally, all metallurgical and mechanical tests are completed in laboratory environment at room temperature.

3. RESULTS AND DISCUSSION

Specimens were investigated with regards to metallurgical and mechanical properties. First, microstructure and macrostructure were obtained. Differences between the samples were examined. Second, UTS (Ultimate Tensile Strength), YS (Yield Strength) and Elongation (ε%) and hardness values were measured. Finally, impact tests were applied to final product. All these steps play a vital role in validation of a wheel.

Chemical contents of the samples are shown in Table 3.

Table 11. Chemical composition of samples

	Si	Fe	Cu	Mn	Mg	Zn	Ti
Sample Group #1	10,765	0,1113	0,0013	0,0029	0,173	0,0031	0,1206
Sample Group #2	9,000	0,1076	0,0012	0,0027	0,304	0,0039	0,1166

Sample Group #3	7,151	0,1070	0,0011	0,0025	0,302	0,0033	0,1203

3.1. Microstructure Analysis

The microstructures of the alloys with different Si level are shown below. All microstructures in Figure 2 are as cast and before heat treatment. Figure 2 (a) shows the sample with highest Si level and higher amount of Al-Si eutectic structures may be observed. Figure 2 (b) shows intermetallic phases and structure. Figure 2 (c) shows lowest Si level and a higher amount of α-Al dendrite may remarked.

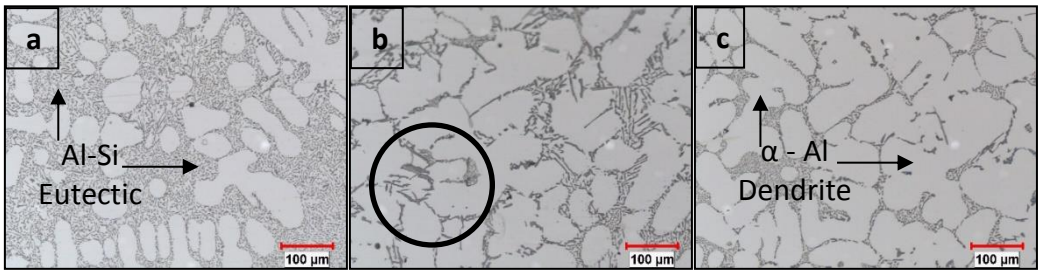

Figure 15. Microstructure of (a) Sample Group #1 as cast (b) Sample Group #2 as cast (c) Sample Group #3 as cast

All microstructures in Figure 3 are obtained from the final product, i.e. after heat treatment and base coating. Figure 3 (a) shows globular structures which are more invisible after heat treatment. Figure 3 (b) shows a decrease in intermetallic phases. Figure 3 (c) shows that Si particles are distributed in the Al matrix uniformly.

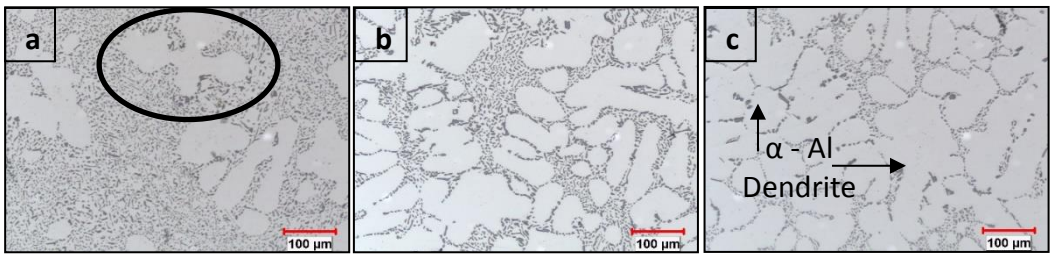

Figure 16. Microstructure of (a) Sample Group #1 as final product (b) Sample Group #2 as final product (c) Sample Group #3 as final product

3.2. Tensile Test Results

Tensile specimens are obtained by two different approaches. Firstly, by gravity casting into a permanent mold and secondly by obtaining from wheel spoke directly with machining. Elongation values of sample group #2 are at the lowest level. On the other hand, UTS and YS are better as sample group #3. As expected, heat treatment plays an important role.

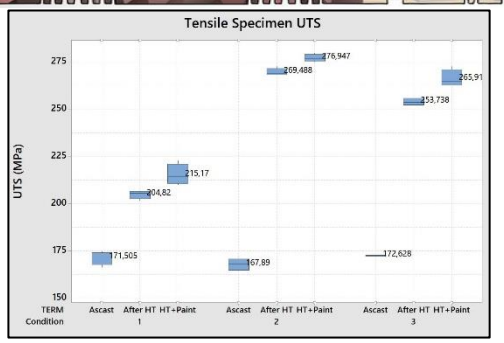

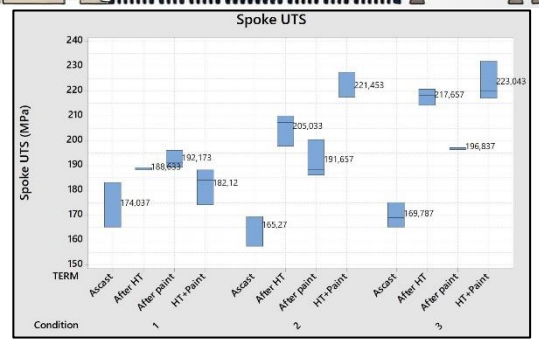

Figure 17. (a) UTS of Tensile Test Specimen (Permanent Mold)

(b) UTS of Wheel Spoke

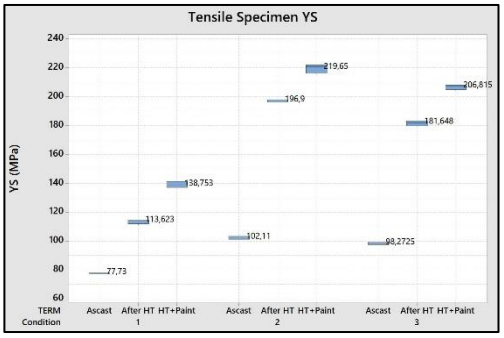

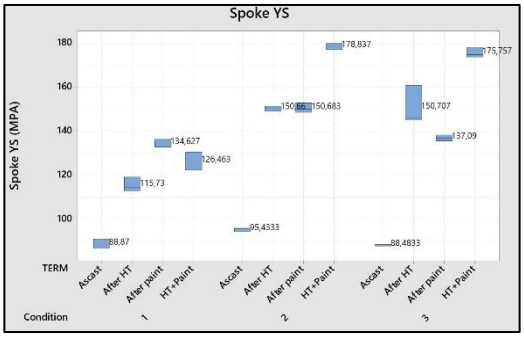

Figure 18. (a) YS of Tensile Test Specimen (Permanent Mold)

(b) YS of Wheel Spoke

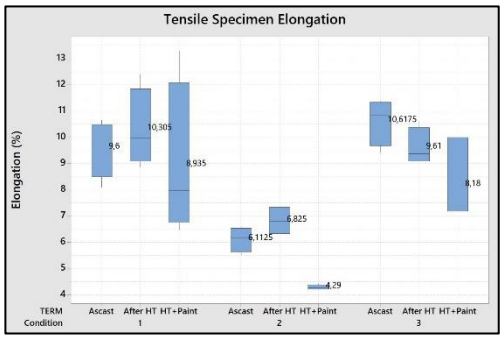

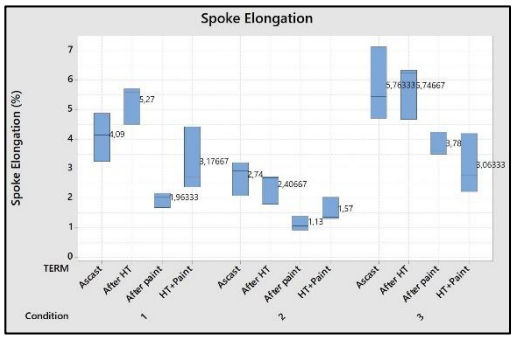

Figure 19. (a) Elongation of Tensile Test Specimen (Permanent Mold)

(b) Elongation of Wheel Spoke

3.3. Hardness Results

Hardness Brinell values were measured for (Sample group #1, Sample group #2, Sample group #3) at 3 stages: After heat treatment, after base coating and after heat treatment + base coating.

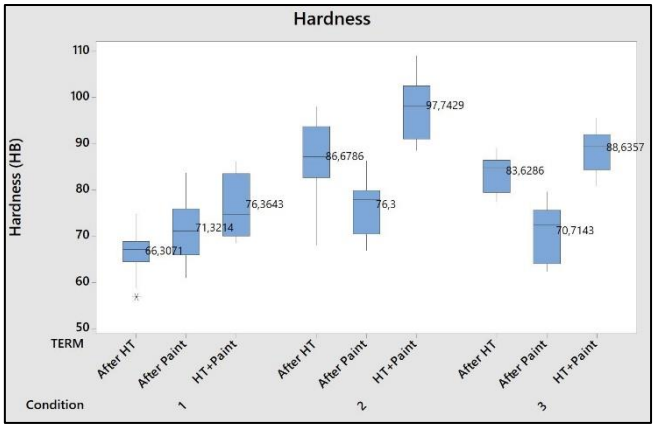

Figure 20. Hardness values

As seen figure above, sample group #2 (AlSi9 set) shows a higher average hardness at all 3 stages. The hardness may affect the impact values negatively.

3.4. Charpy Impact Test Results

Six test specimens which are prepared according to 'ISO 148-1: Metallic materials – Charpy pendulum – Impact Test' have been used to evaluate the toughness. [14] The results for all specimens are tabled below:

Table 12. Charpy Impact Test Results

	Sample Group #1		**Sample Group #2**		**Sample Group #3**	
	Heat Treated	**Non – Heat Treated**	**Heat Treated**	**Non – Heat Treated**	**Heat Treated**	**Non – Heat Treated**
	J (Joule)					
Specimen #1	4	4	2	2	3	3
Specimen #2	4	4	2	2	3	2,5
Specimen #3	4,5	3	3	2	4	3
Specimen #4	4	3	2	2	3	2
Specimen #5	4	3	2,5	2	3	3
Specimen #6	4	3	2	2	4	3
Average	4,08	3,33	2,25	2,00	3,33	2,75

According to results, the worst Charpy impact values are obtained from sample group #2. In addition to this, heat treatment helps to improve the impact values. Standard deviation is max. 0,5 for all measurements.

3.5. 13° Impact Test Results

Conducted according to 'Light alloy wheels – Impact test / ISO – 7141' Standard.

Table 13. 13° Impact Test Results

		OK	NOK
Sample Group #1	Heat Treated	650 Kg.	675 Kg.
	Non – Heat Treated	600 Kg.	625 Kg.
Sample Group #2	Heat Treated	-	450 Kg.
	Non – Heat Treated	-	450 Kg.
Sample Group #3	Heat Treated	575 Kg.	600 Kg.
	Non – Heat Treated	500 Kg.	525 Kg.

The weight is calculated according to wheel model. In this study, the weight is 450 Kg. and stopped with failure. The load is increased with extra 25 kg and the load reach final value which cause failure. As a result, sample group #2 failed with 13° impact tests, on the other hand, sample group #1 and #3 show better result from %11 to %44 according to calculated wheel load. Clearly, heat treated samples give better impact values, these results are actually in agreement with Charpy impact tests.

4. CONCLUSION

The chemical contents of all samples are in good agreement with literature. Microstructures and macrostructures were evaluated according to related specifications and results are approved. Al-Si eutectic, α-Al dendrite, modified Si structures may be observed.

'Permanent Tensile Specimen Mold' specimens of sample group #2 display almost same UTS and YS values with sample group #3 and better values than sample group #1. But, elongation (%ε) is lower than others. Chemical content differences –especially higher Mg- may lead these low elongation values.

Similarly, sample group #2 obtained by machining of 'wheel spoke' have similar UTS and YS values to sample group #3 and are better than sample group #1. Elongation (%ε) is lower than sample group #1 and #3.

The results of specimen obtained by machining 'wheel outer flange' displays the same trend with previous specimens; better UTS and YS, lower elongation (%ε).

The highest hardness (Brinell) results are obtained from sample group #2.

ACKNOWLEDGMENT

The authors would thank to all colleagues, especially A. Oktem, Z. Gokcen, E. Armakan, O. Beyter and Y. Sagnak from Cevher Alloy Wheels for their collaboration and Assoc. Dr. O. Culha for academic support.

REFERENCES

[1]. J. Pezda and A. Jarco, Effect of T6 Heat Treatment Parameters on Technological Quality of the AlSi7Mg Alloy, Arcihes of Foundry Engineering Volume 16, Issue 4 / 95 – 100, 2016
[2]. L.Y. Pio, Effect of T6 Heat Treatment on the Mechanical Properties of Gravity Die Cast A356 Aluminium Alloy, Journal of Applied Sciences 11 (11): 2048-2052, 2011
[3]. V. Grubisic, Air Tightness Control of Passenger Car Wheels, Scientific Research Publishing, 171-180, 2017
[4]. T. LIPIŃSKI, Double Modification of $AlSi_9$ Mg Alloy with Boron, Titanium and Strontium, Archives of Metallurgy and Materials, Volume 60 Issue 3: 2415-2419, 2015
[5]. AlSiMg Alloy, Sr-Refined, Artificially Aged, Cevher Inner Standard – Specification, 2014
[6]. Sr-Refined Eutectic AlSi Alloy, Cevher Inner Standard – Specification, 2004
[7]. Rheinfelden, Primary Aluminium Casting Alloys, Datasheet L 2.06/3-KH
[8]. Y. Birol, Effect of solution heat treatment on the age hardening capacity of dendritic and globular AlSi7Mg0.6 Alloys, International Journal of Materials Research (formerly Zeitschrift fuer Metallkunde): 439-444, March 2010
[9]. Testing of metallic materials – Tensile test pieces, Prufung metallischer Werkstoffe – Zugproben Deutsche Norm DIN 50125, 2016
[10]. Metallic materials - Tensile testing - Part 1: Method of test at room temperature, Metalik malzemeler - Cekme deneyi - Bolum 1: Ortam sicakliginda deney metodu, TS EN ISO 6892-1:2016, 2016
[11]. Road vehicles — Wheels/rims for commercial vehicles — Test methods, Karayolu tasitlari - Ticari tasitlar icin tekerlekler/jantlar - Deney yontemleri, TS ISO 3894, 2015
[12]. Road vehicles — Light alloy wheels – Impact test, ISO 7141, 2005
[13]. R.B. Thakare, Stress Analysis in Wheel Rim by using Dynamic Cornering Fatigue Test Under Different Conditions, IJARIIE: International Journal of Advance Research and Innovative Ideas Vol-3 Issue-2, 2017
[14]. Metallic materials — Charpy pendulum impact test — Part 1: Test method, ISO 148-1 2009

ICETI
www.iceti.org
2018
07-11 MARCH
BUDAPEST
HUNGARY
II. INTERNATIONAL CONFERENCE ON ENGINEERING TECHNOLOGY AND INNOVATION

Performance Comparison of Levy Flight Mechanism in Dragonfly Optimization and Gravitational Search Algorithm

Hakan Gulcan[1], Cigdem Aci[2]

Abstract

Dragonfly Optimization Algorithm (DOA) and Gravitational Search Algorithm (GSA) are heuristic optimization methods which inspired by animals' social behaviors and gravitational force. However, these optimization algorithms cannot get good results for some benchmark functions. Some random flight methods have been applied to these algorithms to solve this problem. In this paper, the performance of classical random flight and Levy Flight mechanism is compared to DOA and GSA algorithms to prevent the algorithms from sticking to local minimum of benchmark functions. The comparison is done total of 15 benchmark functions. After applying Levy Flight mechanism to DOA, 12 out of 15 benchmark functions have at least 50% certain success, while 1 is the same as original. After applying Levy Flight mechanism to GSA, 13 out of 15 benchmark functions (with various dimensions and agent counts), at least 60% had a definite success, while 1 had the same result as the original. The results showed that Levy Flight mechanism significantly reduced the problem of premature convergence of flying swarms and the number of sticks to local minimums. Levy Flight has a good ability to expand the field of exploration and to screen the area of exploitation.

Keywords: dragonfly optimization; gravitational search; levy flight; random flight.

1. INTRODUCTION

Some of the artificial intelligence algorithms have been developed inspired by the behavior of swarm creatures living in nature. These algorithms are also called swarm intelligence-based algorithms. The basic behavior modeled in these algorithms is the food. In some algorithms, avoiding from the enemy is also modeled. These behavioral models in algorithms today have also made great strides in solving many real-life problems. These algorithms are tested on a set of benchmark functions before they are applied to real-life problems. In benchmark functions, the goal is to reach the minimum point of the function, which can also be maximum. For this purpose, modeled swarm behaviors are developed in the function model in accordance with the randomness which is the basic principle of artificial intelligence. This randomization has 2 basic tasks in the function. The first is to increase the possibility of optimizing by increasing the range of motion and the second is to avoid sticking the local minimums of the function by making sudden movements. While this classical random behavior has been successful in most benchmark functions, our research has shown that it can sometimes be inadequate. The Levy flight mechanism has brought a new solution to the researchers at this point.

The Levy flight mechanism, as an alternative to the classical randomness, has achieved great successes over the cases where the solutions of the classical random are blocked.

In this work, we have studied two swarm-based optimization algorithms used by the Levy Flight mechanism. These algorithms are Dragonfly Optimization Algorithm (DOA) and Gravitational Search Algorithm (GSA). Comparisons were made on the MATLAB program with 15 benchmark functions.

In Section 2, DOA and GSA algorithms are introduced with nature-inspired swarm intelligence-based optimization technique. In Section 3, randomization and levy flight mechanism are discussed. Detailed comparisons were made in Section 4 and the results of study in Section 5 were evaluated.

[1] *Corresponding author: Mersin University, Department of Electrical and Electronics Engineering, 33343, Yenisehir, Mersin, Turkey.* hgulcan333@gmail.com

[2] *Mersin University, Department of Computer Engineering, 33343, Yenisehir, Mersin, Turkey.* caci@mersin.edu.tr

2. NATURE INSPIRED SWARM INTELLIGENCE BASED OPTIMIZATION TECHNIQUE

Sometimes, individuals who cannot do any work alone can behave very cleverly when they act collectively. Individuals belonging to a community make use of the best individual's behavior or behavior of other individuals and their own experiences and make use of this information as a tool for solving the problems that they will face in the future. For example, when one of the individuals who make up a living swarm reacts to this danger when it perceives a danger, this reaction moves in the swarm and allows all the individuals to behave in common to the danger. Observing these movements in the swarm, the swarm-based optimization algorithms have been developed [1]. Some of them are ant colony optimization, artificial bee optimization, particle swarm optimization, elephant herd optimization, dragonfly optimization algorithm.

Another method of optimization is also nature-based, but techniques based on natural motions, not based on animal behaviors. The most important example of these is the gravitational search algorithm.

2.1. Dragonfly Optimization Algorithm

This algorithm was discovered in 2014 by Seyedali Mirjalili from Griffith University [2]. It is a technique based on herd intelligence. It is inspired by the static and dynamic behaviors of dragonfly swarms in nature. Optimization has two basic stages: Exploration and Exploitation. These two stages have been modeled by watching dragonflies dynamically or statically in search of food or avoiding enemies.

Dragonflies behave in swarms only in two cases: Feeding and Migration. Feeding is modeled as a static swarm. Migratory is modeled as a dynamic swarm. The algorithm is as follows:

According to C. Reynolds, swarms have three basic behaviors: Separation / Division, Sorting / Alignment, Cohesion / Merging. S. Mirjalili adds two additional behaviors to this algorithm: Go to the food, run away from the enemy. Separation: means that an individual avoids the static collision of an individual with its neighbor. Sorting / Alignment: Indicates the speed at which individuals match neighboring to other individuals. Cohesion: Individuals tend towards the center of the neighborhood.

The reason for the 2 added behavior that is added to the algorithm: Every swarm is the main goal to survive. In dynamic swarming dragonflies tend to align their flight. In a static swarm, the cohesion is very high to attack the food, while the alignment is very low.

2.2. Gravitational Search Algorithm

Gravitational search algorithm (GSA) is a population search algorithm proposed by Rashedi et al. in 2009 [3]. The GSA is based on the low of gravity and mass interactions. The solutions in the GSA population are called agents, these agents interact with each other through the gravity force. The performance of each agent in the population is measured by its mass.

Each agent is considered as an object and all objects move towards other objects with heavier mass due to the gravity force. This step represents a global movement (exploration step) of the object, while the agent with a heavy mass moves slowly, which represents the exploitation step of the algorithm. The best solution is the solution with the heavier mass.

3. RANDOMIZATION

Randomization plays an important role in both exploration and exploitation. The essence of such randomization is the random walk. A random walk is a random process which consists of taking a series of consecutive random steps [4].

Randomization is the process of doing something random. For example:

- Creation of a random permutation of an index;
- Choosing a random sample of a population;
- Generate random numbers; or
- Converting a data stream.

Randomization is not arbitrary. For example, a random sample of individuals from a population is found in a sample where each individual has a known likelihood of sampling. This can be compared to the likelihood sampling of arbitrary individuals [5].

A random walk is a process by which randomly-moving objects wander away from where they started. In a subdivision, we will examine the Levy Flight Mechanism, which is a random walk.

3.1. Levy Flight Mechanism

Lévy flight, named for French mathematician Paul Lévy. The characteristic of Levy flights is that the step lengths are chosen from a "heavy-tailed" probability distribution which means the decreasing probabilities of longer lengths are not small enough to overpower the increasing lengths. Technically, a heavy-tailed distribution has infinite variance (possible length). Figure 1 shows an example of Levy Flight in 1000 steps:

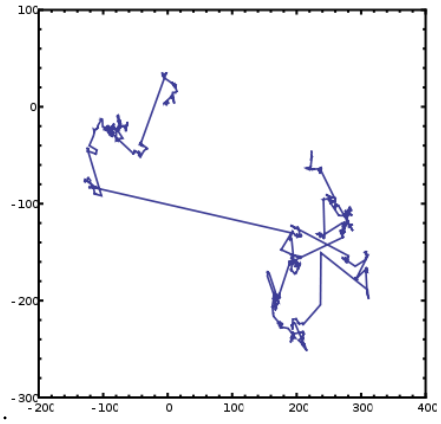

Figure 1. An example of 1000 steps of a Lévy flight in two dimensions. The origin of the motion is at [0,0].

The adaptation of the Levy flight mechanism to the algorithm of the mathematical formulation is as follows:

$$X_{t+1} = X_t + Levy(d) * X_t \quad (1)$$

Where d is the dimension and X is the position of agent. The Levy flight is calculated as follows:

$$Levy(x) = 0.01 * \left(\frac{r_{1*}\sigma}{|r_2|^{\frac{1}{\beta}}}\right) \quad (2)$$

Where r_1 and r_2 are the random numbers between [0,1], β is the constant value and σ is calculated as follows:

$$\sigma = \left[\frac{\Gamma(1+\beta)*\sin\left(\frac{\pi\beta}{2}\right)}{\Gamma\left(\frac{1+\beta}{2}\right)*\beta*2^{\frac{\beta-1}{2}}}\right]^{1/\beta} \quad (3)$$

Where $\Gamma(x) = (x-1)!$

4. COMPARISON OF LEVY FLIGHT MECHANISM IN DOA AND GSA

In comparison, 15 benchmark functions were used. We used Levy Flight in original way and with Step Size Controlled(SSC). SSC means how one solution deviates from its position after applying Levy function. This can be tuned based on the range of your variables. We used the Levy steps by multiplying 0,01 in this study as Mirjalili. The results were initially evaluated according to the minimum values. Secondly, evaluations were made based on mean values according to 200 iterations. The progress recorded are calculated as a percentage, compared with the results given by the classical randomness.

4.1. Levy Flight Mechanism with Dragonfly Optimization Algorithm

In Dragonfly Optimization Algorithm, classical randomness first applied. Then the Levy Flight mechanism was applied both step size controlled and originally. All the results are shown in Table 1 below:

Table 14. Numerical results for DOA

FUNCTIONS	WITHOUT LEVY	LEVY (WITH 0.01)	LEVY	SSC SUCCESS (%)	NORMAL SUCCESS (%)
F1 (BEST)	6,55E-05	5,56E-06	5,32E-06	91,51	91,87
AVG	5,612	4,588	4,623	18,25	17,62
F2	0,00953	0,012931	0,010326	-35,69	-8,35
AVG	1,9733	1,2632	1,9654	35,99	0,40
F3	0,98265	0,083867	1,065235	91,47	-8,40
AVG	180,132	138,4496	170,2356	23,14	5,49
F4	0,65332	0,034473	0,035684	94,72	94,54
AVG	3,9232223	1,9093	1,8562	51,33	52,69
F5	12,000326	5,5642	5,0265	53,63	58,11
AVG	1532,623	1742,4351	1654,2654	-13,69	-7,94
F6	9,10E-07	4,10E-07	3,93E-07	54,96	56,77
AVG	3,0323	5,4863	5,5953	-80,93	-84,52
F7	0,0235	0,0014141	0,001365	93,98	94,19
AVG	0,6532	0,19505	0,03658	70,14	94,40
F8	-4331,4562	-1891,5994	-4326,2654	56,33	-0,12
AVG	-1326,32	-2815,1938	-1328,6596	-112,26	0,18
F9	6,26523	2,9921	7,6599	52,24	-22,26
AVG	270,32	25,63	45,26985	90,52	83,25
F10	6,34E-14	4,44E-15	5,63E-15	93,00	91,12
AVG	2,32623	2,2751	2,03263	2,20	12,62
F11	2,65E-03	3,94E-03	4,37E-03	-48,62	-64,66
AVG	0,55265	0,46969	0,400794	15,01	27,48
F12	4,57E-04	1,63E-04	1,93E-04	64,38	57,69
AVG	1,8772	1,1918	2,0234	36,51	-7,79
F13	1,92E-04	6,70E-05	3,66E-05	65,10	80,96
AVG	1,262	0,83522	2,65326	33,82	-110,24
F14	2,6226	0,998	2,52482	61,95	3,73
AVG	2,6592	1,2509	1,92367	52,96	27,66
F15	0,00034105	0,00034105	0,00034105	0,00	0,00
AVG	0,0024521	0,0024521	0,0024521	0,00	0,00

According to the results, the Levy Flight mechanism implemented with step size controlling achieved at least 50% success in 12 of the 15 benchmark functions compared to the results from the classic random in the problem of reaching the minimum value. When the Levy Flight mechanism was applied in its original form, it succeeded in 10 out of 15 benchmark functions according to the classic randomness (as shown in Figure 2).

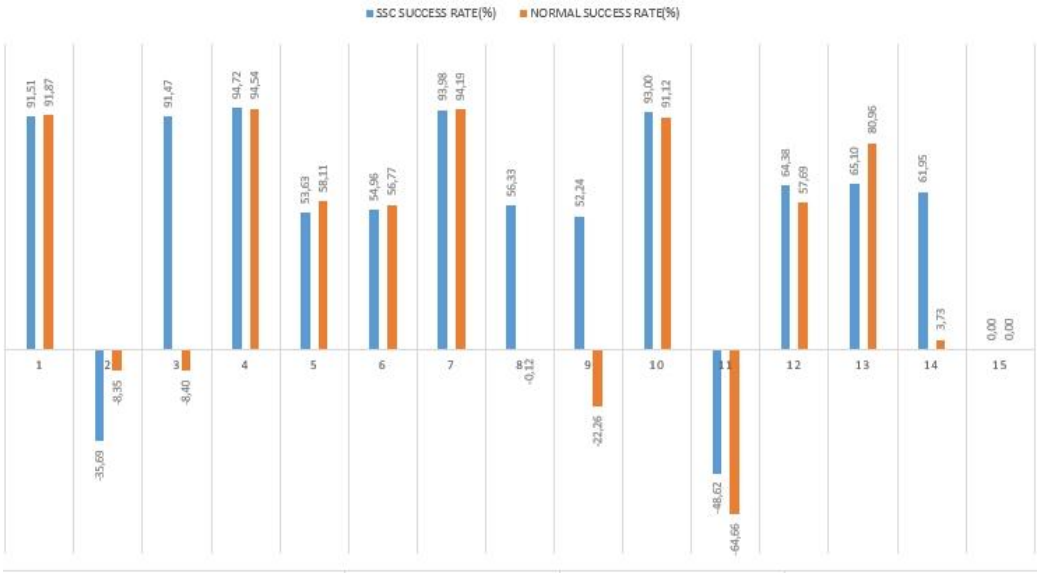

Figure 2. DOA Success rate for minimum values

If we look at the mean values of the results, not the minimum values resulting from the 200 iterations, it will be seen that in the 2nd and 11th benchmark functions that fail step size controlling, success is achieved according to the mean values in the classical randomness (as shown in Figure 3).

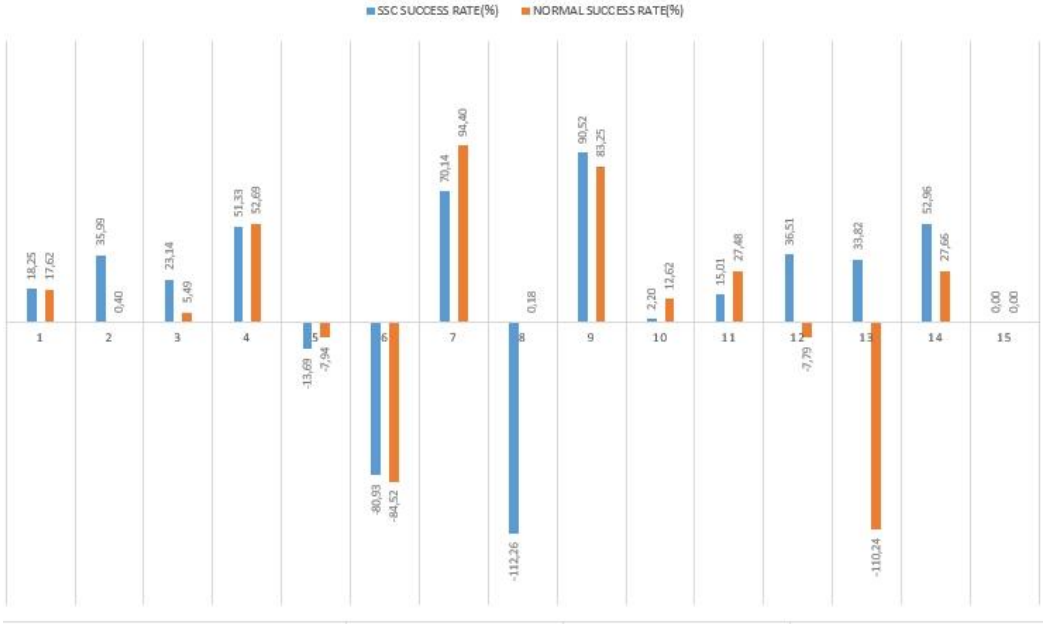

Figure 3. DOA Success rate for mean values

4.2. Levy Flight Mechanism with Gravitational Search Algorithm

In the Gravitational Search algorithm, the Levy Flight mechanism is implemented in the same way as DOA. All the results are shown in Table 2 below:

According to the results, the Levy Flight mechanism implemented with step size controlling achieved at least 60% success in 13 of the 15 benchmark functions (1 is same with original) compared to the results from the classic random in the problem of reaching the minimum value. When the Levy Flight mechanism was applied in its original form, it succeeded in 12 out of 15 benchmark functions according to the classic randomness (as shown in Figure 4).

If we look at the mean values of the results, it will be seen that in the 11th benchmark function that fail with step size controlling, success is achieved according to the mean values in the classical randomness (as shown in Figure 5).

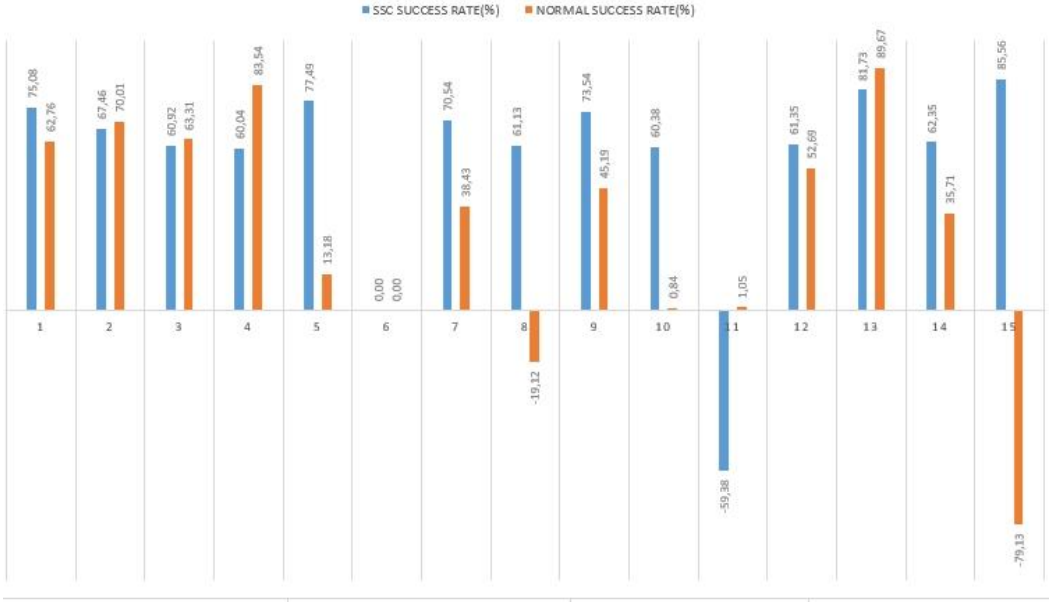

Figure 4. GSA Success rate for minimum values

Table 2. Numerical results for GSA

FUNCTIONS	ORIGINAL	LEVY (WITH 0.01)	LEVY	SSC SUCCESS (%)	NORMAL SUCCESS (%)
F1 (BEST)	4,06E-19	1,01E-19	1,51E-19	75,08	62,76
AVG	1,61E-18	5,88E-19	1,08E-18	63,50	33,18
F2	2,35E-09	7,66E-10	7,0612E-10	67,46	70,01
AVG	3,70E-09	1,003E-09	6,256E-09	72,91	-68,94
F3	8,37E-19	3,27E-19	3,07E-19	60,92	63,31
AVG	9,10E-05	0,000099021	1,01021E-05	-8,79	88,90
F4	4,25E-10	1,70E-10	7,001E-11	60,04	83,54
AVG	8,93E-10	5,33E-10	1,3256E-09	40,36	-48,45
F5	5,0592	1,1388	4,3926	77,49	13,18
AVG	6	6,3893	7,9233	-1,45	-25,81
F6	0,00E+00	0,00E+00	0,00E+00	0,00	0,00
AVG	0	0	0	0,00	0,00
F7	0,00031145	9,18E-05	1,92E-04	70,54	38,43
AVG	0,004308	0,0021929	0,0011929	49,10	72,31
F8	-2491,3615	-4014,3648	-2014,9486	61,13	-19,12
AVG	-1607,3275	-1567,9737	-2408,53	-2,45	49,85
F9	0,99496	0,263233	0,545345	73,54	45,19
AVG	3,2883	2,3311	2,97989	29,11	9,38
F10	8,62E-10	3,42E-10	8,55E-10	60,38	0,84
AVG	1,79E-09	9,29E-10	1,59E-09	48,07	11,19
F11	9,12E-02	1,45E-01	9,02E-02	-59,38	1,05
AVG	0,083963	0,06505	0,04557	22,53	45,73
F12	7,30E-21	2,82E-21	3,45E-21	61,35	52,69
AVG	0,00039014	1,30E-06	2,42E-05	99,67	93,79
F13	4,89E-20	8,93E-21	5,05E-21	81,73	89,67
AVG	1,72E-19	3,38E-19	3,01E-19	-96,40	-74,82
F14	2,90035	1,0921	1,8645	62,35	35,71
AVG	4,21321	4,2208	5,21354	-0,18	-23,74
F15	0,0126	0	0	85,56	-79,13
AVG	0,0045326	0,0045769	0,001000008	-0,98	77,94

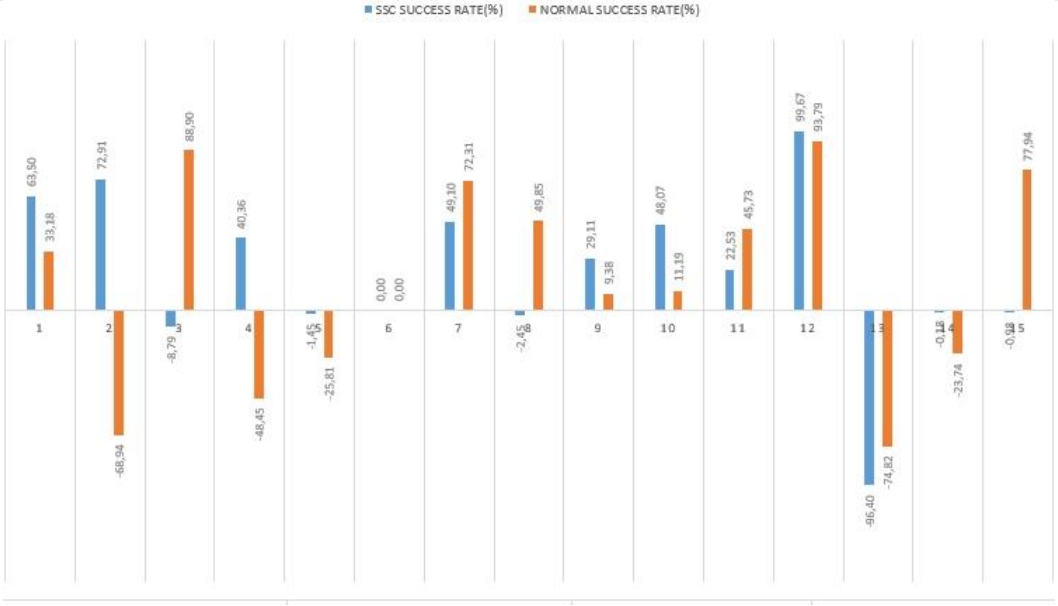

Figure 5. GSA Success rate for mean values

5. CONCLUSION

When the results of the two algorithms are considered, it is clear that the Levy Flight mechanism has achieved successful results when compared to the classical randomness. In particular, when the Levy Flight mechanism was implemented in conjunction with step size control, the success of this random flight method proved to be a definite success in the problem of reaching the minimum point in both algorithms.

The average values obtained as a result of 200 iterations showed compensatory results for some of the benchmark functions' failure to reach the minimum point. However, the average value results are not as satisfactory as the minimum point results. This can also lead us to a future study.

REFERENCES

[1]. S. Akyol and B. Alatas, "Guncel Suru Zekasi Optimizasyon Algoritmalari," Nevsehir Universitesi Fen Bilimleri Enstitu Dergisi 1 p. 36-50, 2012.
[2]. S. Mirjalili, "Dragonfly algorithm: a new meta-heuristic optimization technique for solving single-objective, discrete, and multi-objective problems," Neural Comput & Applic 27: p. 1053–1073, 2016.
[3]. E. Rashedi, H. Nezamabadi-pour, S. Saryazdi, "GSA: A Gravitational Search Algorithm," Information Sciences 179, p. 2232–2248, 2009.
[4]. X. Yang, *Nature-Inspired Metaheuristic Algorithms*, 2nd ed., Luniver Press, United Kingdom, July 2010.
[5]. Wikipedia. "Randomization." Last ed: 27 Feb 2018. Available: https://en.wikipedia.org/wiki/Randomization/

BIOGRAPHY

HAKAN GULCAN born in 1993 in Mersin. Graduated in Computer Engineering Department from Cukurova University, Adana, in 2016. Since 2016, he is a MSc student in Electrical and Electronics Engineering Department at Mersin University.

CIGDEM ACI received her BSc. degree in Computer Engineering from Firat University, Elazig, in 2007. MSc. and Ph.D. degrees in Computer Engineering from the University of Cukurova, Adana, in 2009 and 2013. From 2008 to 2013, she was a Research Assistant with the Department of Computer Engineering at Cukurova University. Between 2013-2015 years, she worked as an Assistant Professor in the Computer Engineering Department, Cukurova University. Since 2015, she has been an Assistant Professor and Deputy Dean in the Faculty of Engineering, Mersin University. Her research areas are Machine Learning, Data Mining, and High-Performance Computing.

ICETI
www.iceti.org
2018
07-11 MARCH
BUDAPEST
HUNGARY
II. INTERNATIONAL CONFERENCE ON ENGINEERING TECHNOLOGY AND INNOVATION

Performance Improvement of an Intelligent Material Handling System

Ridvan Ozdemir[1] Omer Faruk Argin[2]

Abstract

Industry 4.0 technologies represent high-level intelligent manufacturing strategies that increase production efficiency and decrease production time. For an instance, one of the most useful Material Handling System (MHS) is Automated Storage and Retrieval System (ASRS), which allows factory owners to enhance operational efficiency and increase productivity. The main aim of this study is to create a simulation platform of a MHS serviced by Rail Guided Vehicles (RGV) to measure possible performance improvements on the MHS. MHS serviced by RGV, which we used in this study, is in the class of Discrete Event Systems (DES). One of the most commonly used method in modeling and analysis of the DES is Petri nets. Petri nets are very efficient for modeling the MHS's dynamic behaviors, especially convenient for real time control implementation. In this study, Petri nets are used for modeling framework. The model is constructed and implemented in MATLAB's Simulink Stateflow environment. An interface is designed in MATLAB's GUI tool for setting system's specific parameters, choosing the type of input load, demonstrating the performance graphs, monitoring the system online and real-time controlling. The RGV's route is divided into 2 zone with an interlocking application for reducing unnecessary movements after the simulation of system was completed and these changes were implemented on the simulation. Finally, the performance of the system for with/without interlocking application are compared with each other according to the performance indices in literature under three different type load inputs which are low, medium and high frequency.

Keywords: Material Handling Systems, Rail Guided Vehicles, Simulation of a Manufacturing System

1. INTRODUCTION

High-level intelligent production strategies increase the production efficiency and safety and shorten the production time. The applications of modern railway systems in factories and warehouses has a history more than a century. Nowadays railway system vehicles which powered by electricity are commonly used in industry. These vehicles distribute almost every size of components from large ones to subassemblies to manufacturing operation areas. One of the most useful Material Handling System (MHS) is Automated Storage and Retrieval System (ASRS), which allows factory owners to enhance operational efficiency and increase productivity. Railway system vehicles are generally integrated to an **A**utomated **S**torage and **R**etrieval **S**ystem. ASRS has been widely used in distribution and production industries since 1950's. Nevertheless, developments in the electronics and computer industries have made a successful development period for ASRS in the last 35 years. The material handling cost can be up to 30% of the total production costs. The usage of ASRS has many benefits according to manual systems. For example: labor costs and floor space savings, increased reliability of production, decrease of production error rates, lower decrease of energy consumption, reduced product damage, and improved customer service. The most obvious disadvantages are less flexibility and higher investments in automation systems [1].

The problems encountered in the material handling systems and their possible causes are gathered under the 5 main topics in literature. The problem is under the "Delivery Precision" topic that we will work on. *Delivery Precision:* Products can be in right place just in time, only if unnecessary movements are removed during the processes of production. These unnecessary movements lead to problems if they are not removed. Another problem is production delays and longer production time resulting from a deficient material handling system. [2], [3], [4] *Inventory Levels:* Keeping the quantities of materials in both production and distribution at the correct levels. This

[1] *Corresponding author: Bilecik Seyh Edebali University, EDMEM, 11230, Bilecik, Turkey. ridvan.ozdemir@bilecik.edu.tr*

[2] *Istanbul Technical University, Mechatronic Engineering, 34469, Maslak/Istanbul, Turkey. oargin@itu.edu.tr*

problem can be solved with just in time production, inventory management and reducing the number of semi-finished products. [3], [4] *Operation Costs:* The system should be designed to maximize profit rather than increase costs by guaranteeing the lowest possible operating costs. [2], [3], [4] *Delivery Quality:* Quality standards on the market floor should be able to get right materials, on right conditions and with right methods. [3], [4] *Information Flow:* Providing appropriate material and information flow, accurate material identification systems, real time information. [2]

Some systems can have uncertainty characteristics such as automated manufacturing systems, communication networks, various transportation and transportation systems and they can be affected by other events. We call them Discrete Event Systems (DES) [5]. Discrete event systems become more complex day by day so controlling of these systems are getting harder. As a result of this some methods are developed to control DES. One of the most preferred method for controlling DES is Petri nets [6], [7].

The products can be in right place just in time only if unnecessary movements are removed in manufacturing process. These unnecessary movements may cause problems. This paper focuses to solve the problems caused by unnecessary movements in manufacturing process. The monorail line consisting of a single loop is divided into two parts by the interconnection in order to avoid unnecessary movements. The new version of monorail line, which is divided into two loops, allows the RGVs to use shortest route to drop the parts without traveling the entire line. In this way, unnecessary movements are eliminated. The obtained new system was compared with old version according to the performance indices, which are used in literature, and the numerical difference was shown.

Cycle time estimates are an appropriate analytical tool for comparing control methods [8]. Simulation can lead to more extensive experiments under random conditions [9]. There are many systems that work together in material distribution and transfer systems and ASRS is one of them. While Performance of ASRS is affected by performance of the other systems, also performance of ASRS is affected by other system's performance [10].

Various performance indices can be used when assessing the design and control rules of material handling systems. Based on several studies following performance indices can be considered: Travel time per request, number of requests handled per time period [11],[12], total time required to handle a certain number of requests, number of requests waiting to be stored/retrieved [13]. This paper uses number of requests handled per time period and total time required to handle a certain number of requests as performance indices.

The remainder of this paper is structured as follows. The next section outlines the characteristics of the system, definition of problem and proposal of the solution and works to improve the system. The proposed method is simulated and performance of old and new version of the system is compared with obtained simulation model in the following section. Finally, obtained results were evaluated and future work was given in section 5.

2. MATERIAL HANDLING SYSTEM SERVICED BY RAIL GUIDED VEHICLES

ASRS, which is discussed in this study, has an event flow like this: first, ASRS brings the part to material loading point from storage department. Rail guided vehicle (RGV) collect this part and drops it to unloading station on the relevant production line. And after that RGV goes to the material loading station to collect new material. RGV can move only forward because the system has one direction.

Before the system was modeled it had been divided into 4 main groups for considering in more detail. These groups are listed as follows:

- One material loading station
- Four material unloading station
- Four RGV to handling materials
- One monorail loop

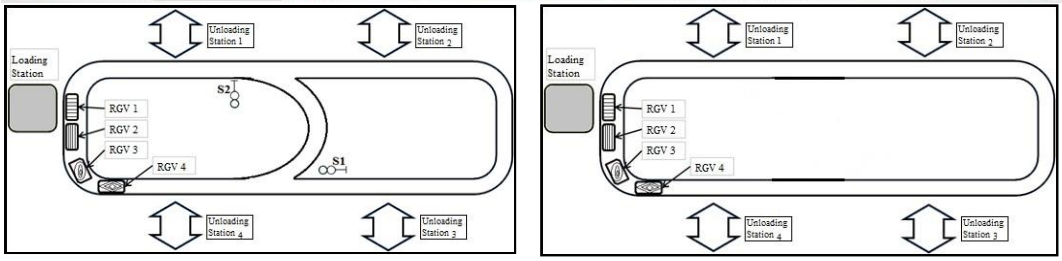

Figure 1. (a) Representation of monorail line. *(b) Interlocking application on monorail.*

2.1. Features of Ray-Guided Vehicles

RGV is a vehicle which is driven by an electric motor and energized from the bar which is located on monorail loop. It has electronic equipments such as PLC, inverter, color sensor, optical communication sensor, photocell and RFID. RGV's average speed is 1,2 m/s.

2.2. Definition of Problem and Proposal of Solution

RGVs have to travel the whole monorail line when they are traveling to the unloading stations in the first half of the loop because the monorail line is in form of a single loop. These unnecessary movements cause some problems, which is called the delivery precision problems, in the literature.

Cycle time can be reduced without chancing RGV's speed if the distance can be shorten. An interconnection and an interlocking system application can be made in the middle of the loop for having shorter routes. Therefore, we can increase the number of parts to be distributed at the same time. For illustrating the interlocking application proposal on a simple example, consider the monorail line consisting of the two loops like in Figure 1(b). There are four unloading stations where RGV drops the parts. Two of them are in the first half of loop and other two are in the second half of the loop. RGV is have to travel the second half of the loop even it is not necessary when parts need to drop first or fourth unloading stations in no interlocking application case. However, it can prevent that RGV is traveling the second half of loop unnecessarily when materials are being distributed the first and fourth unloading stations in interlocking application case. Nevertheless, an interlocking application and investment are needed in order to provide this situation.

2.3. Signalization Application

There are four situations for signaling application because the current system operates in one direction. These four cases will be examined in Figure 2. The signal lights are labeled as S1 and S2 that is used in interlocking application. If the signaling lights are green that means the railroad is empty and RGV can access the railroad but if the signaling lights are red that means the railroad is not empty, RGV cannot access the railroad and it has to stop.

If there is no RGV on the road, then S1 and S2 signals turn green. This is the first case. And the second case is there is a RGV between A2 and D2. Both of signals S1 and S2 turn red in this case. In the third case, RGV is between D2 and D3 and both of signals S1 and S2 turn red in this case. There is a RGV between D1 and D2 in last case that means A2-D2 zone is close to access but D2-D3 zone is open so S2 signal turn red and S1 signal turn green.

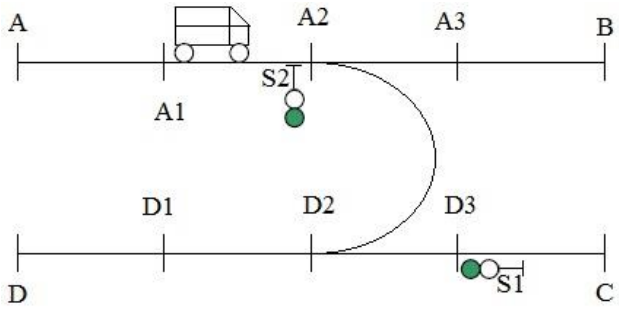

Figure 2. Interlocking application.

3. SIMILATION OF THE SYSTEM

3.1. Modelling of the System and Introduction to Simulation

In order to be able to simulate the DES in question, it needs to be modeled first and Petri Nets method is used for that. When modeling is carried out, not only the classical Petri nets but also the timed Petri nets and the prohibited petri nets are used too. While delays of flow and transport events in the system were being modeled by timed petri nets, also anti-collision situations have been created in the system using prohibited arrow Petri nets. The modeled monorail line was divided into 24 separate regions, and a separate place was created for each region. Delay times between regions are determined according to RGV's speed, the transition is triggered when this time expires and moves of RGV from one place to another is completed. If a place is active, it means that there is a RGV in the region it represents, so positioning is also provided with Petri Nets. An overview of the system, which is modeled by Petri nets, is given on Figure 3.

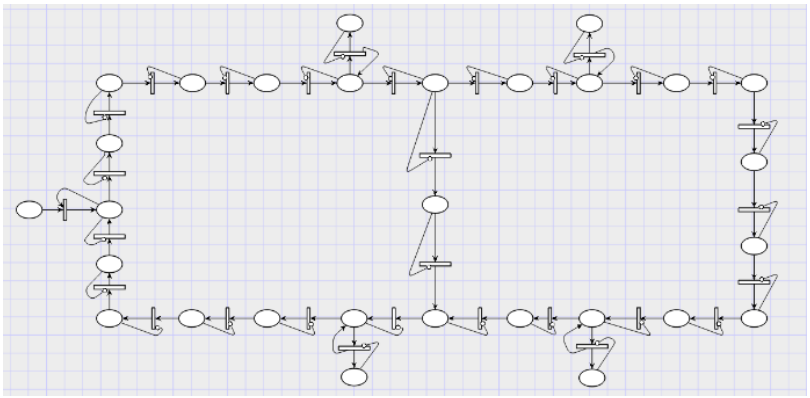

Figure 3. Petri nets model of the system.

The system is transferred to MATLAB \ Simulink environment with stateflow method after it is modeled by Petri Nets. An interface, which belongs to this created system, is shown at Figure 4.

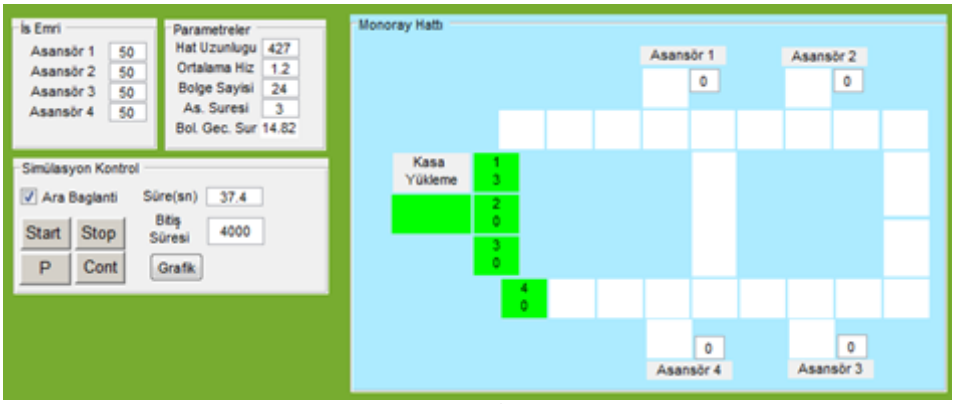

Figure 4. GUI of simulation.

With this interface, users can enter some parameters to the system, which are given below:

- length of loop
- average speed,

- number of regions,
- lift loading time
- load

In addition to these, the user can also specify a period for the simulation so it can be possible to reach the number of parts that will handle in unit time. If the background of the box is green, that means there is a RGV in this region. The number on the top of the box shows the number of RGV and the number at the bottom of the box shows the number of the unloading station where the parts will be distribute. If this number is "0", it means that the RGV is unloaded. There is 3 different type of load inputs can be applied to the modeled system, these are:

- Low frequency load
- Medium frequency load
- High frequency load

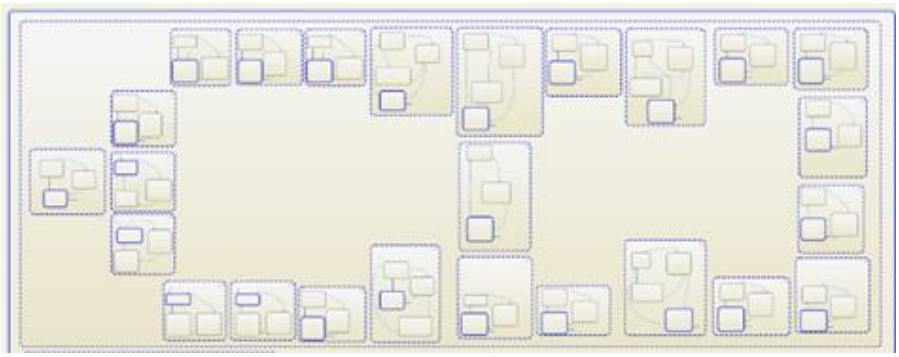

Figure 5. Representaion of monorail block.

The flow of the simulation can be controlled with the commands "Start, Pause, Continue, Stop" in the simulation control section on the interface module. The total number of parts handled can be seen in this graph. Figure 5 shows the internal structure of the monorail block prepared with stateflow commands. The material handling system's loop is divided into 24 sections while It is modeling, and the situations which can occur for each section are handled separately. These situations are divided into sub-states within themselves too like On, Off, Next. These sub-states can be seen at Figure 6. There are three information parameters in each state, these are: number of RGV, status of load and unloading station's number. This information which state has, transfer to next state with a trigger if the conditions are appropriate. This flow continues in a loop to maintain the continuity of the system.

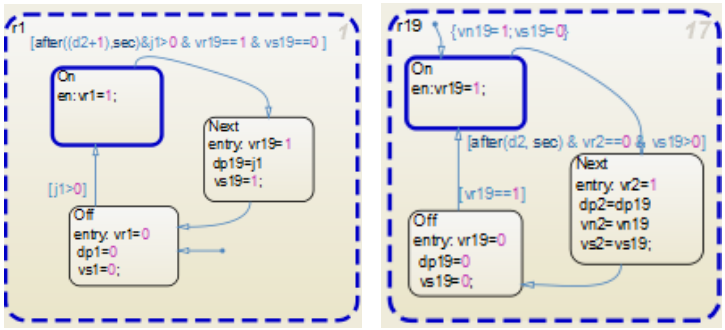

Figure 6. Blocks of material loading station and first RGV.

As mentioned earlier, there are some indices, which provide performance measurement in material handling systems. The indices that we can use for this study are as follows:

- Number of requests handled per time period
- Total time required to handle a certain number of requests

Three type of load will be used for each performance indices and same parameters will be used for each test, which are given below:

Length of monorail loop: 427 meter

Average speed: 1,2 m/s

Region number: 24

Unloading time: 3 second

3.2. Performance Measurement

The monorail systems, which are given in Figure 1 (a) and Figure 1 (b), were compared with low, medium and high frequency load input. The distribution characteristics of three different type load input that based to unloading station is given in Table 1.

Table 1. Load input characteristics.

	Low Frequency Load Input				Medium Frequency Load Input				High Frequency Load Input			
Time (minute)	A1	A2	A3	A4	A1	A2	A3	A4	A1	A2	A3	A4
0	2	2	2	2	3	3	3	3	4	4	4	4
16	2	2	2	2	3	3	3	3	4	4	4	4
32	2	2	2	2	3	3	3	3	4	4	4	4
48	2	2	2	2	3	3	3	3	4	4	4	4
...	...	...	...	...	...	...	...	...	...	...	...	...
464	2	2	2	2	3	3	3	3	4	4	4	4
Total	240				360				480			

3.3. Number of requests handled per period

Low frequency load input: The summary of comparison of the results under the low frequency load input is given in Table 2. And this results show us there is no difference between interconnected and non-interconnected systems when it is working with low frequency load input. In both cases, the entire 240 materials that need to be dispensed are distributed. Therefore, we can say there is no need to improvement if the system will always work under low frequency load input.

Table 2. Number of requests handled per period under the low frequency load input.

Line State	Cycle Time	Unloading Station 1	Unloading Station 2	Unloading Station 3	Unloading Station 4	Difference
No Interconnection	480	**60**	**60**	**60**	**60**	**%0**
With Interconnection	480	**60**	**60**	**60**	**60**	

Medium frequency load input: The summary of comparison of the results under the medium frequency load input is given in Table 3. The entire 360 materials that need to be dispensed are distributed in interconnected state but some of amount cannot be distributed in non-interconnected state. And according to this results there is an increase of %11,11 in total number of distributed materials between interconnected and non-interconnected systems when it is working with medium frequency load input.

Table 3. Number of requests handled per period under the medium frequency load input.

Line State	Cycle Time	Unloading Station 1	Unloading Station 2	Unloading Station 3	Unloading Station 4	Difference
No Interconnection	480	**81**	**81**	**81**	**81**	**%11,11**
With Interconnection	480	**90**	**90**	**90**	**90**	

High frequency load input: The summary of comparison of the results under the high frequency load input is given in Table 4. A total of 480 materials to be distributed could not be completed in either case. And according to this results there is an increase of % 23,76 in total number of distributed materials between interconnected and non-interconnected systems when it is working with high frequency load input.

Table 4. Number of requests handled per period under the high frequency load input.

Line State	Cycle Time	Unloading Station 1	Unloading Station 2	Unloading Station 3	Unloading Station 4	Difference
No Interconnection	480	**81**	**81**	**81**	**81**	**%23,76**
With Interconnection	480	**101**	**100**	**100**	**100**	

3.4. Total time required to handle a certain number of requests

Low frequency load input: The summary of comparison of the results under the low frequency load input is given in Table 5. And this results show us there is no difference between interconnected and non-interconnected systems when it is working with low frequency load input. Therefore, we can say there is no need to improvement if the system will always work under low frequency load input.

Table 5. Total time required to handle a certain number of requests under the low frequency load input.

Line State	Cycle Time	Unloading Station 1	Unloading Station 2	Unloading Station 3	Unloading Station 4	Difference
No Interconnection	**796**	100	100	100	100	**%0,18**
With Interconnection	**795**	100	100	100	100	

Medium frequency load input: The summary of comparison of the results under the medium frequency load input is given in Table 6. And according to this results there is a reduction of %9,89 at total operation time between interconnected and non-interconnected systems when it is working with medium frequency load input.

Table 6. Total time required to handle a certain number of requests under the medium frequency load input.

Line State	Cycle Time	Unloading Station 1	Unloading Station 2	Unloading Station 3	Unloading Station 4	Difference
No Interconnection	**591**	100	100	100	100	**%9,89**
With Interconnection	**533**	100	100	100	100	

High frequency load input: The summary of comparison of the results under the high frequency load input is given in Table 7. And according to this results there is a reduction of %19,08 at total operation time between interconnected and non-interconnected systems when it is working with high frequency load input.

Table 7. Total time required to handle a certain number of requests under the high frequency load input.

Line State	Cycle Time	Unloading Station 1	Unloading Station 2	Unloading Station 3	Unloading Station 4	Difference
No Interconnection	**591**	100	100	100	100	**%19,08**
With Interconnection	**479**	100	100	100	100	

Figure 7 shows the required operation times all together for low, medium and high frequency load input cases. It seems that the interlocking application does not provide an improvement in the case of low frequency load input, when the graph is examined but we can see that there is an increase of improvement rate from medium frequency load input sate through high frequency load input state.

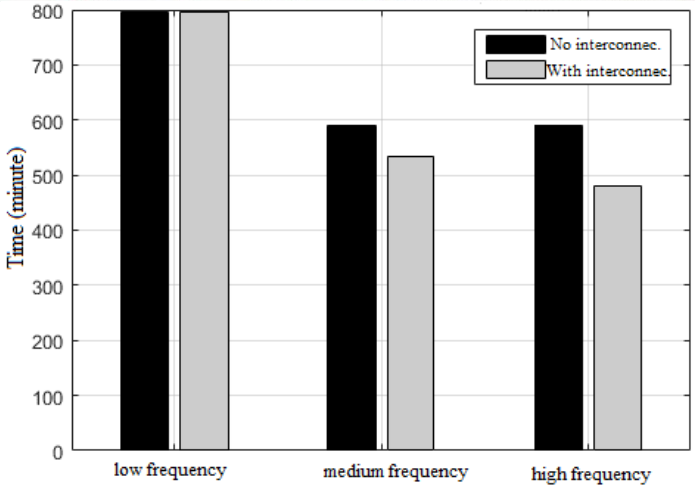

Figure 7. Total time required to handle a certain number of requests under the low, medium and high frequency load inputs.

4. CONCLUSION

This paper shows it is possible to feasibility a MHS serviced by a RGVs before it is implemented with a simulation which is modeled using Petri nets. The performance changes can be compared with the relevant performance indices thanks to this simulation.

According to result of performance tests an interlocking application which will adapted to material handling system serviced by rail-guided vehicles can perform %20 better performance of the system. The expected improvement rate can be estimated before the investment is realized with this simulation application, and it is possible to make an investment decision according to the income to be obtained.

Simulation of different material handling systems can be done with this simulation program in progressive studies. Future work is an empty material box collection station can be created and a simulation can be developed which can collect empty material boxes from unloading stations.

REFERENCES

[1] Zollinger, H., AS/RS application, benefits and justification in comparison to other storage methods: A white paper. Automated Storage Retrieval Systems Production Section of the Material Handling Industry of America, 1999.
[2] Mulcahy, D.E., Materials Handling Handbook, McGraw-Hill, 1998.
[3] Hassan, M.M.D., Engineering supply chains as systems, Systems Engineering, 9 (1), 73-89, 2006.
[4] Tompkins, J. A, White, J. A, Bozer, Y. A, Frazella, E.H, Tanchoco, J. M. A. & Trevino, J. Facilities Planning. 2nd ed. USA: John Wiley & Sons, Inc, 1996.
[5] Cassandras C.G. ve Lafortune S., "Introduction to Discrete Event Systems", Kluwer Academic Publishers, 1999.
[6] Murata T., "Petri Nets: Properties, Analysis and Applications", Proc. of IEEE, Vol: 77, No: 4, pp. 541-580, 1989.
[7] Petri C.A., "Kommunikation mit Automaten Schriften des Rheinisch", Westfalischen Inst. fur Instrumentelle Mathematik und der Universitat Bonn, Ingilizce ceviri, C.F. Green, Applied Data Research Inc., Suppl 1 to Tech report RADC-TR-65-337, NY, 1962.
[8] Hausman, W.H., Schwarz, L.B., Graves, S.C., Optimal storage assignment in automatic warehousing systems. Management Science 22 (6), 629-638, 1976.
[9] Schwarz, L.B., Graves, S.C., Hausman, W.H, Scheduling policies for automatic warehousing systems: Simulation results. AIIE Transactions 10 (3), 260-270, 1978.
[10] Roodbergen, K. J., Iris F.A. Vis., A survey of literature on automated storage and retrieval systems. European Journal of Operational Research 194, 343–362, 2009.
[11] Azadivar, F., Maximization of the throughput of a computerized automated warehousing system under system constraints. International Journal of Production Research 24 (3), 551–566, 1986.
[12] Foley, R.D., Frazelle, E.H., Park, B.C., Throughput bounds for miniload automated storage/retrieval systems. IIE Transactions 34, 915-920, 2002.

[13] Hur, S., Lee, Y.H., Lim, S.Y., Lee, M.H., A performance estimation model for ASRS by M/G/1 queuing system. Computers & Industrial Engineering 46, 233-241, 2004.

ICETI
www.iceti.org
2018
07-11 MARCH
BUDAPEST
HUNGARY
II. INTERNATIONAL CONFERENCE ON ENGINEERING TECHNOLOGY AND INNOVATION

Fabric Based Plain Heaters as an Innovative Approach for Vehicle Heating: A Theoretical Research on Comparative Performance

Volkan Kirmaci[1], Mustafa Erol[2], Hayri Eren [1,3], Ahmet Yavas[4], Huseyin Duran[1], Yavuz Ozturk[3]

Abstract

Traditionally, almost in all vehicle types, convectional heating method has been used to warm-up passenger compartment air so as to provide a comfortable aurora for the passengers. However, this traditional method has some disadvantages in its own. The major disadvantage of the system may be cited as its cascaded structure. In order to warm up a passenger, system sequentially requires some steps as; burning the fuel, warming up the coolant, heating coils through pumping coolant and conditioning the cabin air using heated coils. This cascaded and low efficient proses is take longer times owing to the steps of operation. Against traditional heating system, a heating system which located on the interior surfaces of the vehicle interior trim components may provide significant difference on heating performance as well as efficiency and comfort. In this study, an electrical heating system with fabric based plain heating elements with conductive yarns are theoretically investigated as a part of an experimental research project and thermal performance comparison studies are presented.

Keywords: Fabric heating, public transport vehicle heating, innovative heating, novel heating, vehicle electrical heating

1. INTRODUCTION

Regardless from the size or types a traditional heating method, which uses the warmed up engine coolant as heat source, has been used to warm up passenger compartment and to provide a comfortable aurora for the passenger as well as driver. The basic heating system can be described as shown in Figure 1. [1,2]

The system uses coolant from the engine and circulates the coolant using an additional circulation pump depending on the size of the system. The coolant is firstly pumped to a fuel burner heater if available, in order to increase its temperature and provide quicker warm-up in the cabin. After fuel burner heater, the warmed up coolant has been sent to heat exchangers which are located on the floor and/or in the roof via coolant pipes. After passing through heating coils, cooled down coolant has been sent back to the engine in order to complete the circuit. Meanwhile cabin heat exchangers heats up the cabin air using hot coolant, in to warm-up passengers. This traditional heating method is called as convectional heating method with a very well-known name [3,4,5].

The heating system has some advantages and disadvantages. While its design wise flexibility, affordable price, being a well-known technology, commonality are the advantages; its weight, part count, non-homogeneous temperature distribution and cascaded heating structure can be listed as disadvantages. Because the available heating system is based on a very old technology (tube and fin heat exchangers, metal pipes and coolant as heat source) its weight is relatively high and overall system is a combination of too many parts.

[1]*Corresponding author: Bartin University, Mechanical engineering dept. Bartin, Turkey. volkan.kirmaci@bartin.edu.tr*

[2] *Dokuz Eylul University, Metallurgical and Materials Science Engineering dept, Izmir, Turkey*

[3] *Anadolu Isuzu Otomotiv, R&D department*

[4] *Izmir Katip Celebi University, Materials Science and Engineering Dept, Izmir, Turkey*

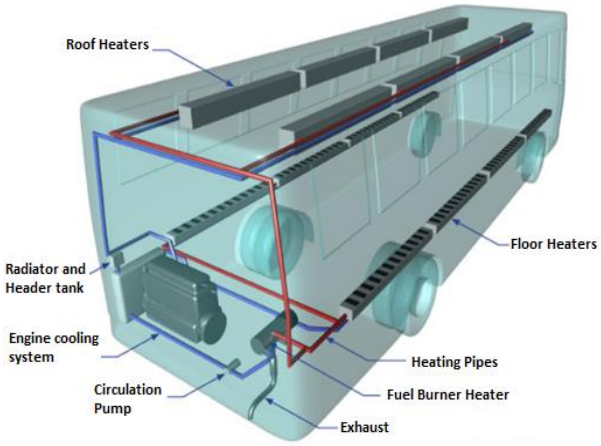

Figure 1. Vehicle heating system [2]

In addition, vertical temperature differences is mainly caused by the nature of heating method, convective heating (See Figure 2). While heated air along the heating coils moving upwards as a result of its density change, it pushes down the cold air in the cabin thru down wards. This air movement in the cabin causes head-roof level temperature stays always above the average room temperature while the foot level temperature is always below the average.

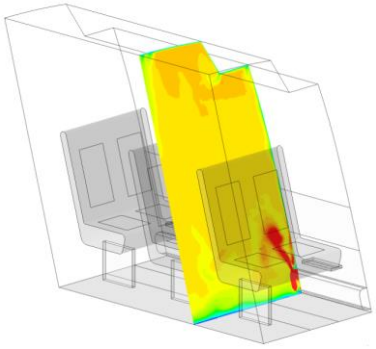

Figure 2. Vehicle cabin vertical temperature difference with convector heating

Beyond that, a cascaded heating structure is one of the major disadvantage of system especially when new technology vehicles are considered (See Figure 3). There are many heat and mass transfer steps from first step up to last step - passenger warm-up - and every step has its own inefficiency. So that, overall efficiency of the total system is considerably low and hence the consumption is high [6]

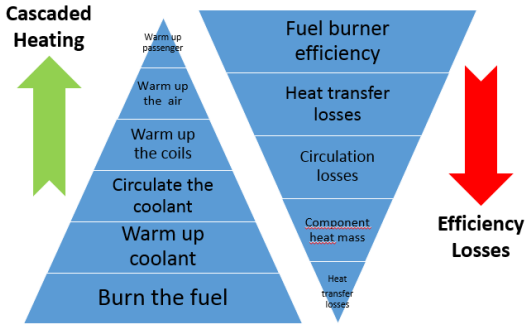

Figure 3. Cascaded heating structure and efficiency losses

At this point, radiant heating method, which heats the components and human directly, rather than convectional heating may provide a significant difference (See Figure 4) [7, 8]. In this research, infrared heating methods, which heats the components and human by infrared radiation, is studied for commercial passenger vehicles. In order to provide heating, fabric based heating elements, with infrared radiating capability as well as convection and conduction heating future, has been used on the interior surfaces of interior trim parts (see Figure 5).

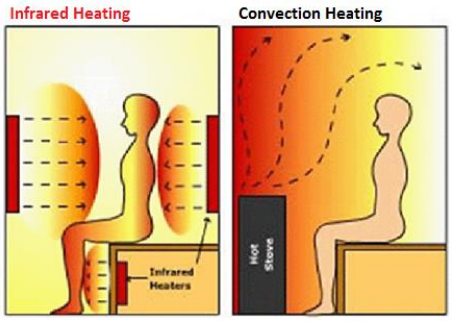

Figure 4. Radiant heating vs. convectional heating [9]

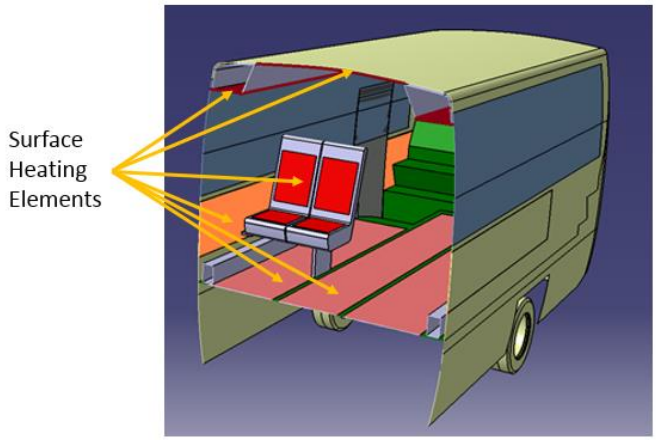

Figure 5. Surfaces with surface heating elements

2. MATERIALS AND METHODS

A fabric based heating elements, with infrared heating capability had been already studied, produced and explained in a former study [2]. In this study, the fabric heating elements has been used as a vehicle interior heating elements and vehicle level CFD analysis has been conducted.

In order to find the optimum heating surface layout and to compare the different heating techniques, problem modelled in a commercial CFD code Fluent. Since the solution of whole vehicle would have too much computational cost, it is decided to study on a model which could be assume as periodically repeated in the vehicle (See Figure 6).

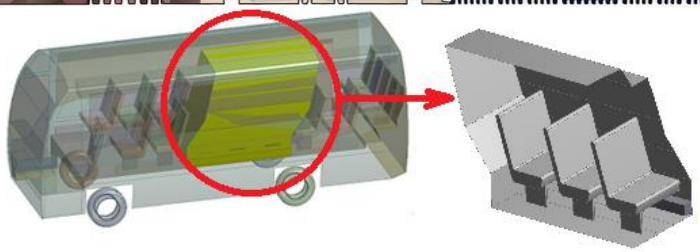

Figure 6. Selected cabin section for CFD

Eight millions of elements are created for the mathematical model. All wall surfaces inflated with continues wedge multi layers to minimize numerical errors while solving thermal and viscous boundary layers. Because solution domain is geometrically complex, rest is filled with tetrahedral elements.

3. RESULTS AND DISCUSSIONS

To compare convectional and fabric heating elements, two CFD models had been prepared. One of the models corresponds to the convectional heating. A convectional heating with a capacity of 6kW has been applied to the model and the results are provided as base system reference results. (See Figure 7)

Second model has been prepared using fabric based heating element instead of convector heaters and solved for more than one option to optimize the locations and effective areas of heating surfaces. Three different heating capacities has been applied. “Option 1” is conducted with 3 kW fabric based heating elements, “Option 2” is with 4 kW fabric based heating elements and “Option 3 is with 5.5 kW fabric based heating elements. (See Figure 7) All analysis has been conducted at steady state conditions.

Analysis results clearly showed that rather than having a localized larger capacity heating power in the cabin, it can be more efficient to provide as much homogeneous heating power as possible in all surfaces of the cabin. Therefore heating power and hence energy consumption can be reduced.

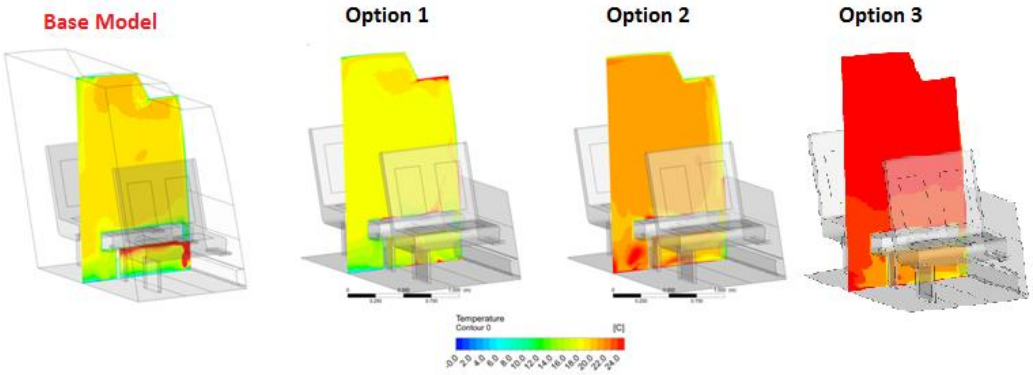

Figure 7. Different heating options analisys results

4. CONCLUSION

Performance comparison of a conventional heating system with an innovative fabric based heating system for vehicles was performed by means of CFD technique. As the results of the analysis pointed out the heating quality of the fabric based heating system was found to be better than the conventional one. Additionally it is important to note that using the new light weight technique instead of the conventional heating systems will provide a significant decrease in the fuel consumption and an increase in the travel range. Furthermore new system can be a good candidate for the hybrid and electric vehicles in which the energy source is electrical energy

ACKNOWLEDGMENT

This research is financially supported by Scientific and Technological Research Council of Turkey (TUBITAK) with project code 1010.STZ.2016 and Anadolu Isuzu Otomotiv AS. (AIOS).

REFERENCES

[1]. H. Eren., V. Kirmaci, "Infrared Heating System Design on Commercial Passenger Vehicles", IMSTEC'16, pp. 745-748, Nevsehir, Turkey, April 2016.

[2]. M. Erol, V. Kirmaci, H.Eren, A. Yavas, H. Duran, Y. Ozturk, "*Yolcu Tasimaciligi Yapan Tasitlarda Isinimla Isitma Sistemininde Kullanilan Tekstil Kumasinin Tasarimi",* International Turkish World Enginering and Science Congress in Antalya, Turkey, December 2017

[3]. H.Eren, V. Kirmaci, M. Erol, A. Yavas, H. Duran, Y. Ozturk, "*New Generation Fabric Based Electrical Heating Systems: A Case Study For Public Transport Vehicles"*, ICSTEM, Prague, Czech Republic, 2017.

[4]. F.P.Incorpera, D.P.Dewitt, T.L.Bergman, A.S.Lavine, Fundamentals of Heat and Mass Transfer, 6th ed.

[5]. .Eren, V. Kirmaci, M. Erol, A. Yavas, H. Duran, "*Tasitlarda Iletken Karbon Lif Kullanimiyla Isinimla Isitma Sisteminin Tasarimi*", International Congress on Engineering, Architecture and Design, Kocaeli, Turkey, May 2017.

[6]. D.Leighton, "*Combined Fluid Loop Thermal Management for Electric Drive Vehicle Range Improvement"*, SAE Int. J. Passeng. Cars - Mech. Syst. / Volume 8, Issue 2, July 2015.

[7]. T. Bauml,D. Dvorak, A. Frohner, and D. Simic, "*Simulation and Measurement of an Energy Efficient Infrared Radiation Heating of a Full Electric Vehicle*", AIT Austrian Institute of Technology, Vienna, Austria 2014.

[8]. BMW Group Innovation Day, "Efficient Dynamics, Intelligent Energy Management: heat pump, infrared heating surfaces and the second generation of the air vent control help to save energy", 2012.

[9]. (2018), Available: http://etat-du-monde-etat-d-etre.net/du-reste/sante/saunas-infrarouges-une-maniere-facile-de-perdre-du-poids-de-reduire-la-tension-arterielle-de-se-detoxifier-et-dameliorer-la-fonction-cerebrale

ICETI
www.iceti.org
2018
07-11 MARCH
BUDAPEST
HUNGARY
II. INTERNATIONAL CONFERENCE ON ENGINEERING TECHNOLOGY AND INNOVATION

Improving Cluster Analysis Using K-means Based and Weighted Clustering Ensembles

Pelin Yildirim[1], Derya Birant[2]

Abstract

Clustering ensemble integrates multiple clustering models to improve the quality of the results of individual clustering algorithms. The study presented in this paper demonstrates the ability of obtaining consistent, reliable and accurate clustering results provided by this paradigm. Considering this motivation, it investigates different K-means based clustering ensembles to determine the best way for building an ensemble (i.e., ensemble size, the diversity of the ensemble members, setting the weights). As a result of researches, this study proposes a novel clustering ensemble approach that use k-means algorithm with different parameters, named wEKDIM (weighted Ensemble K-means with Distance and Initialization Methods). wEKDIM runs K-means algorithm many times with different distance metrics (Euclidean and Manhattan) and different initializations (Random, K-means++, Canopy and Farthest first) and then combines all of the available clustering partitions to get the final clustering result using a weighted consensus function. We believe that our approach is the first attempt to design a cluster ensemble in such a way. In the experimental studies, the proposed K-means based clustering ensemble was tested on 18 different real-world datasets which are well-known and broadly used in machine learning. The results show that the proposed k-means based ensemble approach (wEKDIM) achieves better clustering performance on average than an individual k-means clustering algorithm in terms of accuracy.

Keywords: clustering ensemble, distance metrics, initialization methods, K-means, unsupervised machine learning.

1. INTRODUCTION

Cluster analysis is an unsupervised learning method that groups a set of objects into clusters based on a similarity criterion. Clustering algorithms can be basically categorized into three groups: partitioning, hierarchical and density-based methods. In partitioning clustering, objects are divided into non-overlapping subsets with a goal to group similar objects together. K-means is the most widely used and easily implemented partitioning clustering algorithm that groups objects in dataset into *k* clusters by considering their similarities. In this study, K-means clustering algorithm has been used for building the clustering ensembles.

Ensemble learning is an important sub-field of machine learning, which combines a set of individual learning models and aggregates the outputs obtained from each model using a consensus function to produce a single final output. The ensemble approach was firstly proposed for supervised learning (i.e., classification), but in recent years this paradigm commenced to be applied on unsupervised learning applications as clustering ensemble. The principle of the clustering ensemble is to generate a set of different clustering models and then aggregate them into one model. Clustering ensemble has been proven to obtain better clustering performance than could be obtained from a model individually [1] [2]. Considering this motivation, the study presented in this paper investigates different K-means based clustering ensembles to determine the best approach for building an ensemble such as the dimension of the ensemble, the diversity of the ensemble members, and optimal weight values.

The novelty and main contributions of this paper are four-fold as follows. First, this paper provides a brief survey of clustering ensemble, which has been emerged to improve the clustering performance of unsupervised learning algorithms. Second, it constructs and compares four different K-means based clustering ensembles:
(i) EKIM (**E**nsemble **K**-means with **I**nitialization **M**ethods,
(ii) wEKIM (**w**eighted **E**nsemble **K**-means with **I**nitialization **M**ethods),

[1] *Corresponding author: Manisa Celal Bayar University, Department of Software Engineering, 45400, Manisa, Turkey.* *pelin@cs.deu.edu.tr*

[2] *Author: Dokuz Eylul University, Department of Computer Engineering, 35390, Izmir, Turkey.* *derya@cs.deu.edu.tr*

(iii) EKDIM (**E**nsemble **K**-means with **D**istance and **I**nitialization **M**ethods) and
(iv) wEKDIM (**w**eighted **E**nsemble **K**-means with **D**istance and **I**nitialization **M**ethods).
These ensembles were generated by using different initialization methods (Random, K-means++, Canopy and Farthest first), different distance metrics (Euclidean and Manhattan) and different ensemble member weights. Third, as a result of comparisons, this paper proposes a novel ensemble approach, named wEKDIM, which runs K-means algorithm eight times with different initial settings and then combines clustering outputs to obtain the final clustering result using a weighted consensus function. We believe that our approach is the first attempt to design a cluster ensemble in such a way. Fourth, this paper presents experimental studies conducted on 18 well-known benchmark datasets to demonstrate that the proposed ensemble approach often gives better results than an individual clustering in terms of accuracy.

This paper is structured as follows: In the following section, related literature and previous studies on the subject are summarized briefly. Section 3 gives background information about clustering ensemble and K-means algorithm with its alternative initial settings: initialization methods and distance metrics. In section 4, four novel K-means based clustering ensembles are described. Section 5 explains the application of the different ensemble approaches on the datasets and presents the obtained results with discussions. Finally, Section 6 gives some concluding remarks and future directions.

2. RELATED WORK

In recent years, ensemble learning commenced to be used widely in clustering task [1] as well as classification task. Different types of combinations of clusterings have been explained in detail [2]: sequential clustering, cooperative clustering and collaborative clustering. The potential benefits of clustering ensemble have been recognized by previous studies [3]; robustness, consistency, novelty, and stability. Clustering ensemble has been utilized in a very broad range of areas such as chemistry [3], biology [4], web usage mining [5], intrusion detection [6], electricity power consumption [7] and health [8]. The most preferred clustering algorithm to construct a clustering ensemble is *K*-means due to its simplicity and easy implemented structure [5] [6] [9] [10] [11]. Cheriyan and Chembath [5] suggested a modified K-means algorithm which determines initial points of centroid automatically, obtains *k* value using ensemble method and reduces the computational complexity of distance evaluation. Wankhade et al. [6] presented a new hybrid approach for clustering ensemble that consists of six stages (feature selection, filtering, K-means clustering, divide & merge techniques, cluster formation, and intrusion detection) to improve the detection rate and decrease the false alarm rate of intrusion. In the another study, Abbasian et al. [11] proposed a new method, named Inner Ensemble K-means (IEK-m), that selects a random subset of features for each ensemble member.

In addition to K-means based clustering ensemble studies, there are several researches that focuses on other clustering algorithms such as density-based [7], fuzzy c-means [8] [12], hierarchical [13] [14] algorithms. Suguna and Selvi [15] developed an ensemble fuzzy clustering framework that combines the results of two different fuzzy clustering algorithms (Fuzzy C-Means and Fuzzy C-Modes) and achieved better results than traditional clustering algorithms. The other study [16] proposed a novel hierarchical ensemble clustering framework that naturally combines both partitional clustering and hierarchical clustering results.

There are several clustering ensemble studies [4] [17] that combines different clustering algorithms to generate various clustering solutions based on different perspectives. Yu et al. [17] proposed a clustering ensemble approach that randomly selects the K-means algorithm or the spectral clustering algorithm as the basic clustering algorithm to increase the diversity of the ensemble. Pirim and Seker [4] implemented an ensemble clustering framework that aggregates results obtained from K-means, hierarchical clustering and C-means algorithms.

Differently from the existing studies, the research presented in this paper focuses on the application of alternative K-means based ensembles constructed by using different initialization methods (Random, K-means++, Canopy and Farthest first), different distance metrics (Euclidean and Manhattan distances) and weight values.

3. CLUSTERING ENSEMBLE

Clustering ensemble is the process that combines multiple clustering models to provide more accurate clustering results compared to individual clustering algorithms. It consists of two main steps: the ensemble generation and consensus function. In the *ensemble generation* step, the main aim is to generate *m* clustering models as the members for building an ensemble. In the literature [1] [2], the principal diversity mechanisms applied for building an ensemble are: (i) different subsets of features, (ii) different clustering algorithms, (iii) different parameters initialization, (iv) different subsets of objects and (v) projection to subspaces. *Consensus function* step finds the final clustering result C^* by combining the outputs of multiple clustering models $\{C_1, C_2, ..., C_m\}$. It can be grouped under two main types: approaches based on object co-occurrence and approaches based on median partition. In the approaches based on object co-

occurrence, the occurrence of an object in one cluster is identified and the final clustering result is determined by an aggregation mechanism such as relabeling, voting and co-association method. Voting is an easy implemented consensus method in which cluster labels are assigned to data points by considering majority vote.

In our study, the diversity in the ensemble generation step was provided by different initialization methods and different distance metrics. We used weighted majority voting mechanism as consensus function.

3.1. K-Means

K-means is one of the simplest and most popular unsupervised learning algorithms, which divides given dataset into *k* clusters based on a specific similarity measure. First, initial centroids are determined for each cluster and each data point is assigned to the closest centroid based on the similarity metric. When all data points have been assigned, *k* centroids are recalculated. These steps are repeated until the centroids no longer move. The algorithm aims to minimize the distances between the points within the same cluster. The commonly used similarity measures to calculate the distance between the data point and the centroid are Euclidean and Manhattan distances.

- **Euclidean distance:** It gives the root of square difference between pair of objects *x* and *y* with *n* dimensions and it is calculated as in Equation 1.

$$D(x,y) = \sqrt{\sum_{i=1}^{n}(x_i - y_i)^2} \quad (1)$$

- **Manhattan distance:** It gives the absolute difference between pair of objects *x* and *y* with *n* dimensions and it is calculated as in Equation 2.

$$D(x,y) = \sum_{i=1}^{n}|x_i - y_i| \quad (2)$$

In the literature, there are several variants to determine initial centroids for *k* clusters: Random, K-Means++, Canopy and Farthest first.

- **Random:** *k* centroids are determined randomly.
- **K-Means++:** *D(x)* denotes the distance between the data point *x* and the closest centroid.
  1. Centroid c_1 is randomly selected.
  2. The new centroid c_i is selected using probability $\frac{D(x)^2}{\sum_{x \in X} D(x)^2}$
  3. Repeat Step 2 until all *k* centroids have been selected.
- **Canopy:** T_1 and T_2 denote two threshold distances, where $T_1 > T_2$.
  1. Initialize a new pre-cluster by selecting a data point randomly.
  2. All data points at a distance < T_1 in the data set are assigned to the corresponding cluster.
  3. If any data point is unassigned to a pre-cluster, go to Step 1.
- **Farthest first:** $x_1, x_2, \ldots, x_n$ are data points and c_i is centroid.
  1. Centroid c_1 is randomly selected.
  2. The new centroid c_i is selected as $c_i = min\{maxDist(x_i, x_1), maxDist(x_i, x_2), \ldots, maxDist(x_i, x_n)\}$.
  3. Repeat Step 2 until all *k* centroids have been selected.

4. PROPOSED CLUSTERING ENSEMBLE

This study builds and compares four different K-means based clustering ensembles, named EKIM, wEKIM, EKDIM and wEKDIM, using the combination of different initialization methods and different distance measures with/without weight values. Finding optimal ensemble generation and consensus function are rather time-consuming problems.

4.1. EKIM: Ensemble K-means with Initialization Methods

Generally, four alternative initialization methods are used for K-means clustering algorithm to determine initial placement of the centroids: Random, K-means++, Canopy and Farthest First. EKIM model consists of four members and each member runs K-means algorithm with a different initialization method. In other words, in the first ensemble member initial centroids are generated randomly; in the second ensemble member initial values of the cluster centroids are selected using K-means++ method, and so on.

4.2. wEKIM: weighted Ensemble K-means with Initialization Methods

Weighted clustering ensemble is a quite recent research topic in machine learning. The earlier works on ensemble clustering assumed equal contribution of each member to the consensus function ($w_i = 1$). However, it is possible to increase cluster validity by the assessment of significance values to ensemble solutions: the method with higher accuracy obtains greater weight in the resultant partition. In the literature, different ensembles use different techniques for setting the weights. In our study, we used weighted majority voting mechanism because of its good empirical success.

In EKIM model, some initialization methods give more accurate results on a specified data rather than the others. So it is required to determine an objective measure of member's contribution into the collective decision. wEKIM is an extended version of EKIM, which uses a weight vector associated with each ensemble member. Optimal weights are specified by the analysis of individual ensemble member solutions.

4.3. EKDIM: Ensemble K-means with Distance and Initialization Methods

Euclidean and Manhattan distances are the most preferred measures for K-means clustering algorithm when finding the distance between data points and centroids. Another alternative clustering ensemble, named EKDIM, runs K-means clustering algorithm by using different distance metrics and different initialization methods.

4.4. wEKDIM: weighted Ensemble K-means with Distance and Initialization Methods

The last ensemble approach proposed in this paper is wEKDIM, which is the weighted version of EKDIM. It is the weighted combination of K-means algorithm with distance metrics and different initialization methods. Only one parameter was changed at each time, while other parameter was kept constant.

Some weak clustering models in the ensemble structure can lead to incorrect clustering results and reduce the ensemble approach's clustering success. To solve this drawback, weighted majority voting function as given in Equation (3) was used in our study and the most voted cluster label was selected as a final cluster result.

$$C^*(x) = max_{j=1}^{k} \sum_{i=1}^{m} \omega_i C_{i,j} \qquad (3)$$

where C is a set of cluster models, m is the ensemble size (the dimension of the ensemble, in other words the number of cluster models), k is the number of clusters, ω is the weight value assigned for each ensemble member $w_i = \{1,2, ..., m\}$ and x is a sample to be clustered. The decision of the i^{th} ensemble member (cluster model) on j^{th} cluster for the sample x is denoted by $C_{i,j}$. The value of $C_{i,j}$ is 1 if the sample x is clustered to j^{th} cluster by i^{th} ensemble member, otherwise 0.

In our study, each ensemble member is weighted according to its individual performance on the specified dataset. The weight values are specified as rank-based and ranged from 1 to 8. The most successful ensemble member is weighted by 8, the next one by 7, and so on.

Table 1 presents novel K-means based ensembles that are built by different combinations of initialization methods, distance metrics and weights. Euclidean distance versions of EKIM and wEKIM approaches are denoted by EKIM-E and wEKIM-E respectively, while their Manhattan versions are indicated by EKIM-M and wEKIM-M.

Table 15. Alternative K-means based clustering ensembles

Initialization Methods				Distance Metrics		Weight	Ensemble Methods	
Random	K-means++	Canopy	Farthest first	Euclidean	Manhattan			
✓				✓			EKIM-E	EKDIM
	✓			✓				
		✓		✓				
			✓	✓				
✓					✓		EKIM-M	
	✓				✓			
		✓			✓			
			✓		✓			
✓				✓		✓	wEKIM-E	wEKDIM
	✓			✓		✓		
		✓		✓		✓		
			✓	✓		✓		
✓					✓	✓	wEKIM-M	
	✓				✓	✓		
		✓			✓	✓		
			✓		✓	✓		

The general structure of the weighted clustering ensemble presented in this study is shown in Figure 1. In this ensemble, input dataset *D* is given to the *m* different ensemble members, each member runs K-means clustering algorithm with different initial settings and the final clustering result is determined by the weighted majority vote of clustering outputs (partitions) that are obtained from each member.

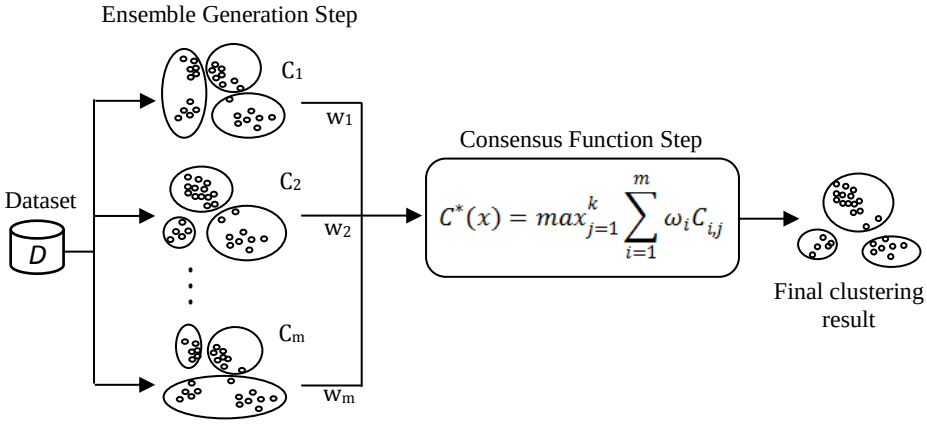

Figure 1. General structure of the weighted clustering ensemble

5. EXPERIMENTAL STUDY

In this study, the traditional K-means clustering algorithm and the alternative clustering ensembles (EKIM-E, wEKIM-E, EKIM-M, wEKIM-M, EKDIM, wEKDIM) were applied on 18 different benchmark datasets. Each solution was compared to each other in terms of accuracy. To evaluate clustering results, final cluster labels obtained from the ensemble are compared with the previously known class labels. The application was developed by using Weka open source data mining library in C# programming language on Visual Studio IDE.

5.1. Dataset Description

In the experimental study, 18 different real-world datasets that are well-known and broadly used in machine learning were selected to compare the alternative K-means based clustering ensembles. The datasets that are available for public use were obtained from UCI Machine Learning Repository [18]. Basic characteristics of the utilized datasets in this study are given in Table 2.

Table 2. Dataset description

Dataset	# of attributes	# of clusters	# of instances
blogger	6	2	100
breast-w	10	2	699
dermatology	35	6	366
diabetes	9	2	768
ecoli	8	8	336
heart-statlog	14	2	270
hepatitis	20	2	155
ionosphere	35	2	351
iris	5	3	150
labor	17	2	57
lung-cancer	57	3	32
seeds	8	3	210
segment	20	7	2310
seismic-bumps	19	2	2584
sick	30	2	3772
spambase	58	2	4601
wine	14	3	178
zoo	17	7	101

5.2. Experimental Work

The alternative clustering ensembles (EKIM-E, wEKIM-E, EKIM-M, wEKIM-M, EKDIM, wEKDIM) were applied and compared on 18 different datasets. These novel ensembles were constructed by running K-means algorithm with different initialization methods (Random, K-means++, Canopy and Farthest first), different distance metrics (Euclidean and Manhattan distances) and different weight values. Each ensemble member is weighted according to its individual performance on the current dataset. While the weight values of wEKIM-E and wEKIM-M range from 1 to 4 by increment 1, wEKDIM takes varying weight values from 1 to 8 by increment 1 in accordance with the number of ensemble members.

The graph given in the Figure 2 shows the average accuracy rates obtained by the application of the individual K-means algorithms and the K-means based clustering ensembles on 18 real-world datasets. Since the labels of the data are known, we checked whether the class label and cluster labels match. The accuracy of the results is calculated using the formula: accuracy = (TP + TN) / (TP + FN + TN + FP), where TP, FP, TN, and FN denote the number of true positives, false positives, true negatives, and false negatives, respectively. The results indicate that the weighted methods are generally provides higher accuracy values (wEKDIM 78.69%, wEKIM-E 77.87% and wEKIM-M 76.4%). In addition, the results specify that wEKDIM approach (78.69%) gives more accurate clustering results than the other K-means based ensemble approaches on average. As a result of comparisons, we propose wEKDIM to improve clustering quality, which runs K-means algorithm eight times with different initial settings and then combines clustering outputs to obtain the final clustering result using a weighted consensus function.

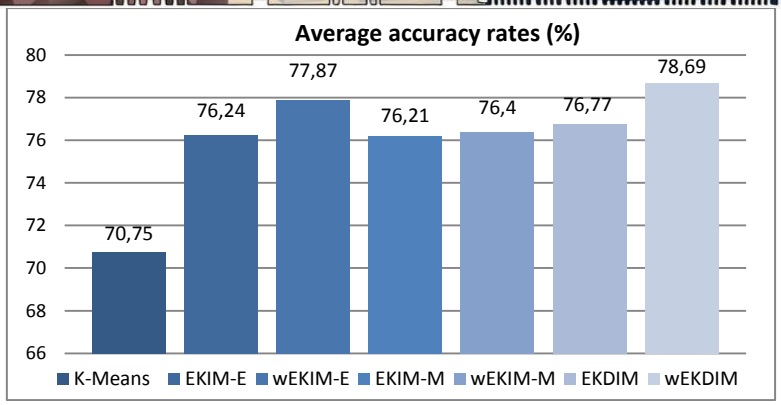

Figure 2. Comparison of individual K-means algorithm and alternative K-means based clustering ensembles

First, the traditional K-means clustering algorithm with different initialization methods (Random, K-means++, Canopy and Farthest first) and different distance metrics (Euclidean and Manhattan distances) were applied on the datasets separately. After that, their results were compared with the proposed wEKDIM approach in terms of accuracy. The weight values of wEKDIM range from 1 to 8 by increment 1 on the basis of giving low values to weak cluster models. The comparative results are given in Table 3. The experimental results show that the proposed wEKDIM approach is equal or more successful than others when considering the number of datasets (12 times for the18 datasets). In addition, it is clearly seen from the average accuracy rates that wEKDIM provides better clustering performance than individual methods.

Table 3. Comparison of individual K-means and wEKDIM in terms of accuracy rates

		Accuracy rates (%)								
	Distance Metrics →	**Euclidean Distance**				**Manhattan Distance**				**wEKDIM**
	Initialization Methods →	**Random**	**K-means++**	**Canopy**	**Farthest first**	**Random**	**K-means++**	**Canopy**	**Farthest first**	
Datasets	blogger	53	54	63	**64**	53	54	63	**64**	62
	breast-w	95.71	95.71	95.71	95.71	94.13	94.13	94.13	94.13	**95.71**
	dermatology	43.17	66.39	70.22	56.56	42.62	56.83	70.22	56.56	**76.5**
	diabetes	66.8	66.8	66.8	66.8	65.23	65.49	65.49	65.23	**66.8**
	ecoli	61.31	61.31	61.9	80.65	55.65	60.71	72.02	59.23	**82.44**
	heart-statlog	59.26	78.52	79.63	78.89	80.74	80.74	80.74	78.15	**80.74**
	hepatitis	73.55	71.61	70.32	71.61	52.26	71.61	65.16	71.61	**73.55**
	ionosphere	71.23	71.23	71.23	70.94	66.1	65.81	66.1	65.81	**71.23**
	iris	88.67	88	88	88.67	89.33	**90**	**90**	89.33	88.67
	labor	77.19	77.19	61.4	75.44	77.19	**87.72**	61.4	75.44	78.95
	lung-cancer	**56.25**	**56.25**	53.12	46.88	**56.25**	**56.25**	53.12	46.88	53.12
	seeds	**89.05**	88.57	88.57	88.57	88.57	88.1	88.1	88.1	88.57
	segment	58.87	66.54	51.17	62.08	48.4	67.32	43.29	61.86	**67.36**
	seismic-bumps	59.75	60.33	**72.99**	51.39	57.7	53.75	67.03	72.64	72.83
	sick	71.13	68.32	87.62	68.32	63.36	72.75	87.62	68.32	**91.65**
	spambase	79.92	79.92	59.92	59.92	77.07	56.94	59.86	60.01	**80.07**
	wine	94.38	94.94	94.94	94.94	96.07	96.07	96.07	96.07	**96.07**
	zoo	74.26	66.34	90.1	72.28	74.26	80.2	90.1	72.28	**90.1**
	Average	70.75	72.89	73.7	71.87	68.77	72.13	72.97	71.42	**78.69**

The matrix given in Table 4 presents all pairwise combinations of the methods. Each cell contains the number of wins, losses, and ties between the method in that row and the method in that column. For example, 2-15-1 indicates that K-means algorithm with Farthest first initialization is better than wEKDIM only in 2 domains, while wEKDIM is better than the other 15 times. Their accuracies are equal for 1 dataset. When the first column is examined, it is clearly seen that our proposed method (wEKDIM) outperforms all other methods.

Table 4. Comparison of individual K-means and wEKDIM in terms of wins - losses - ties on datasets

			Euclidean Distance				Manhattan Distance		
		wEKDIM	**Random**	**K-means++**	**Canopy**	**Farthest first**	**Random**	**K-means++**	**Canopy**
Manhattan Distance	**Farthest first**	2-15-1	7-11-0	5-11-2	7-11-0	4-7-7	7-7-4	3-10-5	6-9-3
	Canopy	2-12-4	9-9-0	9-9-0	6-8-4	8-10-0	9-5-4	8-4-6	
	K-means++	3-13-2	9-8-1	7-8-3	7-11-0	10-7-1	10-4-4		
	Random	2-13-3	3-11-4	4-11-3	6-11-1	8-9-1			
Euclidean Distance	**Farthest first**	1-13-4	6-9-3	5-7-6	6-7-5				
	Canopy	2-10-6	8-7-3	7-5-6					
	K-means++	1-13-4	6-5-7						
	Random	2-11-5							

6. CONCLUSION & FUTURE DIRECTIONS

Clustering ensemble, also known as consensus clustering or clustering aggregation, is an important type of ensemble learning that combines multiple clustering models to improve the quality of individual data clustering. Finding optimal ensemble generation and the best consensus function are rather time-consuming problems. This study investigates different K-means based clustering ensembles to determine the best way for building an ensemble (i.e., ensemble size, the diversity of the ensemble members, setting the weights). It compares different ensembles (EKIM, wEKIM, EKDIM, wEKDIM) that are constructed by running K-means algorithm using different initialization methods (Random, K-means++, Canopy and Farthest first), different distance metrics (Euclidean and Manhattan distances) and different weight values. An application was developed by using Weka open source data mining library in C# programming language on Visual Studio IDE. In the experimental study, the alternative ensemble approaches were compared on 18 different UCI datasets in terms of accuracy. The results indicates that wEKDIM method provides more accurate clustering results than both the individual K-means algorithm and other K-means based ensemble approaches.

As further work, a clustering ensemble framework can be developed using different ensemble generation mechanisms such as different object representations, different clustering algorithms or different subsets of objects. In addition, multiple clustering model outputs can be combined using different consensus functions (i.e. median partition, relabeling, and co-association) for better cluster analysis.

REFERENCES

[1]. T. Alqurashi and W. Wang, "Clustering ensemble method," *International Journal of Machine Learning and Cybernetics*, pp. 1-18, Jan. 2018.
[2]. A. Cornuejols, C. Wemmert, P. Gancarski, and Y. Bennani, "Collaborative clustering: Why, when, what and how", *Information Fusion*, vol. 39, pp. 81-95, 2018.
[3]. F. Saeed, N. Salim, and A. Abdo, "Voting-based consensus clustering for combining multiple clusterings of chemical structures," *Journal of Cheminformatics*, vol. 4, pp. 1-8, Dec. 2012.
[4]. H. Pirim and S.E. Seker, "Ensemble Clustering for Biological Datasets", Bioinformatics, InTech publisher, pp. 287-298, 2012.
[5]. S. Cheriyan and J. Chembath, "Comprehensible predictive system model using parameter less Fast K-Means (EPFK-Means) for web usage data," in *Proc. ICACC*, 2017, p. 243.

[6]. K. Wankhade, S. Patha, and R. Thool, "An efficient approach for intrusion detection using data mining methods," in *Proc. ICACCI*, 2013, p. 1615.
[7]. I. Khan, J. Z. Huang, and K. Ivanov, "Incremental density-based ensemble clustering over evolving data streams," *Neurocomputing*, vol. 191, pp. 36-43, Feb. 2016.
[8]. J. Zou, L. Chen, and C. L. P. Chen, "Ensemble fuzzy c-means clustering algorithms based on KL-Divergence for medical image segmentation," in *Proc. BIBM*, 2013, p. 291.
[9]. R. Paithankar and B. Tidke, "A H-K clustering algorithm for high dimensional data using ensemble learning," *International Journal of Information Technology Convergence and Services*, vol. 4, pp. 1-9, Dec. 2014.
[10]. F. Yang, T. Li, Q. Zhou, and H. Xiao, "Cluster ensemble selection with constraints", *Neurocomputing*, vol. 235, pp. 59–70, 2017.
[11]. H. Abbasian, C. Drummond, N. Japkowicz, and S. Matwin, "Inner Ensembles: Using ensemble methods inside the learning algorithm," in *Proc. PKDD*, 2013, p. 33.
[12]. X. Wan, H. Lin, H. Li, G. Liu, and M. An, "Ensemble clustering via Fuzzy c-Means", in *Proc. ICSSSM*, 2017, p. 291.
[13]. E. Rashedi and A. Mirzaei, "A hierarchical clusterer ensemble method based on boosting theory", *Knowledge-Based Systems*, vol. 45, pp. 83-93, June 2013.
[14]. W. Xiao, Y. Yang, H. Wang, T. Li, and H. Xing, "Semi-supervised hierarchical clustering ensemble and its application", *Neurocomputing*, vol. 173, pp. 1362-1376, 2016.
[15]. J. Suguna and M. A. Selvi, "Ensemble fuzzy clustering for mixed numeric and categorical data," *International Journal of Computer Applications*, vol. 42, pp. 19-23, Mar. 2012.
[16]. L. Zheng, T. Li, and C. Ding, "A framework for hierarchical ensemble clustering," *ACM Transactions on Knowledge Discovery from Data*, vol. 9, pp. 1-23, Nov. 2014.
[17]. Z. Yu, L. Li, Y. Gao, J. You, J. Liu, H-S. Wong, and G. Han, "Hybrid clustering solution selection strategy", *Pattern Recognition*, vol. 47, pp. 3362-3375, 2014.
[18]. (2018) UCI Machine Learning Repository. [Online]. Available: https:// archive.ics.uci.edu/ml/datasets.html

Pelin Yildirim received her B.Sc. and M.Sc. degrees in computer engineering at Dokuz Eylul University, Izmir, Turkey in 2013 and 2015 respectively. She has started Ph.D. in computer engineering at the Dokuz Eylul University in 2015 and she still continues her education. She is currently working as a research assistant in the Department of Software Engineering at Manisa Celal Bayar University. Her research interests include data mining, machine learning and intelligent learning systems.

ICETI
www.iceti.org
2018
07-11 MARCH
BUDAPEST
HUNGARY
II. INTERNATIONAL CONFERENCE ON ENGINEERING TECHNOLOGY AND INNOVATION

Blended of New Generation Regenerated Cellulosic Fibers with Polyester and Cotton: Thereof Knitted Fabrics Air Permeability

Deniz Vuruskan[1], Esin Sarioglu[1]

Abstract

Regenerated cellulosic fibers are mainly used to impart comfort properties of knitted fabrics with blending of natural and synthetic fibers. Thanks to technological progress, it can be said that there are various types of new generation cellulosic fibers in textile sector under several brands and these all have their own properties. The scope of this study is about the investigation on the air permeability of blended knitted fabrics of new generation regenerated cellulosic fibers with polyester and cotton, individually. Bamboo, ProModal® and Viloft® fibers were chosen as regenerated cellulosic fibers in order to evaluate their own functional properties. These fibers were blended with most commercially used fibers as cotton and polyester at different ratios as 67%/33%, 50%/50% and 33%/67% to produce 19.7 tex ring spun yarns. Furthermore, 100% regenerated cellulosic fibers, 100% cotton and 100% polyester ring spun yarns were also manufactured for comparison the differences. Blending of regenerated/cotton and regenerated/polyester yarns are preferred in the production of knitted fabrics so all yarn samples obtained from these yarns were knitted as single jersey at the same production parameters. The permeability of fabric to air tests were performed in accordance with the related standard at 100 Pa pressure drop by using 20 cm^2 test surface area. Variance analysis was carried out using statistical package program to put forward the whether there was an effect of regenerated type (Bamboo, ProModal® and Viloft®), blend type (cotton and polyester) and blend ratio (100%, 67%/33%, 50%/50% and 33%/67%) on air permeability of fabrics at 95% confidence interval or not. As a consequence, it was determined that these parameters have statistically significance on air permeability of single jersey fabrics.

Keywords: *Air permeability, knitted fabric, new regeneration cellulosic fiber, ring spun yarn.*

1. INTRODUCTION

In accordance with the quality and cost effective importance of fibers used in textile sector, there are various studies about the use of regenerated cellulosic fibers. The use of regenerated cellulosic fibers with different proportions enhances some characteristics of fabric such as comfort ability, durability, wickability etc. In textile sector, there are various regenerated cellulosic fibers are available and with technological progress new ones are placed nowadays. Thus, it is important the evaluation of the properties of yarns and fabrics from regenerated cellulosic fibers and some researchers took this investigating area from consideration.

Kilic et al., compared the structural, physical and mechanical properties of cotton-Tencel and cotton-ProModal® blended ring, compact and vortex spun yarns with different blend ratios. It was stated that increasingthe ratio of regenerated cellulosic fiber, unevenness, imperfections, and diameter and roughness values decreased whereas tenacity, elongation, density and shape values increased. It was found that cotton-ProModal® blended yarns had better structural and physical properties than cotton-Tencel® blended yarns [1].

[1] *Corresponding Author: Gaziantep University, Faculty of Fine Arts, Department of Fashion and Textile Design, 27310 Sehitkamil/Gaziantep, Turkey.* vuruskan@gantep.edu.tr

Demiryurek et al., studied about the thermal properties of Viloft®-cotton and Viloft®-polyester single- jersey and 1x1 rib knitted fabrics. They concluded that fabrics made from higher blend ratio of Viloft® had more air gaps and it's an indicative property for detecting the thermal characteristics of the fabrics [2].

Atasagun et al., analyzed physical, mechanical and transfer properties of 1x1 rib fabrics made by blending Viloft® fiber, natural, synthetic, and functional fibers [3]. North compared the comfort and fabric performance of single-jersey fabric containing Viloft® fibers as pure and blending with cotton, viscose, modal and other cellulosic fibers. It was stated that fabrics containing Viloft® fibers contributed the thermal insulation and wearer comfort properties [4].

Bamboo fiber is also a kind of regenerated cellulosic fiberis used as pure or blended with natural/synthetic fibers in order to match required quality of the products such as thermal conductivity, perspiration adsorption, tenacity etc. ProModal® is another important regenerated cellulosic fiber that consists of a blend of Modal® and Tencel® fibers with good moisture absorption, skin-sensitive properties and strength [5-7]. Viloft® fiber is mainly used with blends of polyester and cotton fibers and it has unique flat cross-section with a crenellated surface which yarn from this fiber finally contains approximately 70% air [8].

In this study the effect of blend type, regenerated cellulosic fiber type and blend ratio on air permeability of single jersey knitted fabrics.

2. MATERIALS AND METHOD

As regenerated cellulosic fiber to be used, bamboo, ProModal® and Viloft® fibers were selected because these are commonly used fibers in textile industry. As a blend type, cotton and polyester fibers were used. The physical properties of fibers used are illustrated in Table 1.Cotton fiber used in this study has 4.5 micronaire fineness and 30 mm length.

Table 1. Properties of raw materials

Raw Material	Linear density (dtex)	Staple Length (mm)
Polyester	1.3	32
Bamboo	1.5	38
Promodal®	1.3	38
Viloft®	1.9	38

In order to determine the optimum proportion, these fibers were blended at 67%/33%, 50%/50% and 33%/67% ratios. Besides, pure regenerated cellulosic yarns, cotton and polyester yarns were manufactured by means of ring spinning system. In the yarn production, all production parameters were kept constant in order to eliminate the effect of these parameters. Fibers were blended at drawframe according to desired blend ratio to be obtained. Eight doublings and eight drafts were performed in all drawing passages in order to make blends more homogeneous. Roving with 656tex linear density was used to produce 19.7 tex ring spun yarn at 10.000 rpm spindle speed and 797 turns/m twist value. By using these yarns single jersey knitted fabric were produced by laboratory knitting machine at the same parameters. Totally, 26 single jersey knitted fabrics were manufactured.

The air permeability tests were carried out after the samples had been conditioned under standard laboratory conditions (20 ± 2 ºC and 65 ± 4 %) for 24 h. Yarn diameters were measured by means of Uster® Tester to investigate the relationship between yarn diameter, density and air permeability of fabrics. Air permeability tests were performed in accordance with ISO 9237: 1995-Textiles- Determination of the permeability of fabrics to air standard at 100 Pa pressure drop by using 20 cm^2 test area. Ten tests for each fabric sample were achieved.

To analyze the correlation between air permeability and predicted area of free space in 1 cm^2, stitch (loop) length, stitch density and then free space area in 1 cm^2 are calculated, respectively. Stitch length was calculate in accordance with the Eq. (1) given below [9].

$$l = {}^{2}/_{c} + {}^{1}/_{w} + 5.94.d \quad (1)$$

Where:

l = Length of yarn in one loop;

c= Number of courses per cm;

w = Number of wales per cm;

d = Diameter of yarn in one cm.

S, the number of stitches/cm^2 of fabrics or stitch density is calculated as follows in which c is number of courses per cm and w is number of wales per cm [10]:

$$S = c\ x\ w \quad (2)$$

Area of free space in one cm^2 of the fabric is expressed as Eq. (3) given below [10].

$$Area\ of\ free\ space\ in\ 1cm^2\ of\ the\ fabric\ (Porosity) = \frac{t - S\ l\ \pi\ R^2}{t} \quad (3)$$

Where:

t = Fabric thickness (cm);

S = Stitch density in one cm^2;

l = Stitch length (cm);

R = Radius of yarn.

The porosity in 1 cm^2 obtained from Eq. (3) explains the inter-yarn porosity including pores between the yarn from which the fabric is made [11].

Statistical analysis was achieved in order to determine the significant effect of regenerated cellulosic fiber type, blend type and blend ratio on air permeability of knitted fabric samples at 95% confidence interval. In addition, the effect of sub groups of regenerated cellulosic fiber type and fiber blend ratio on air permeability, Tukey HSD multiple comparison test was performed at 95% confidence interval. Moreover, correlation between air permeability and porosity of fabric was also determined.

3. RESULTS AND DISCUSSION

Diameter yarn samples and fabric structural properties are illustrated in Table 2. As indicated in Table 2 stitch length and stitch density given is calculated by using Eq. (1) and Eq. (2).

Table 2. Yarn diameter and structural properties of fabric samples

Blend Type	Regenerated Cellulosic Fiber Type	Blend Ratio (%)	Yarn Diameter 2DØ (mm)	Areal Density (g/m^2)	Fabric Thickness (mm)	Courses per cm	Wales per cm	Stitch Length in cm	Stitch Density in cm^2	Porosity in 1 cm^2
Cotton (CO)	Bamboo	100	0.241	119.62	0.70	17	12	0.344	204	0.543
		67/33	0.229	120.76	0.65	15	12	0.353	180	0.598
		50/50	0.221	116.69	0.62	15	13	0.342	195	0.588
		33/67	0.219	109.86	0.60	15	13	0.340	195	0.584
		0	0.214	109.07	0.51	13	14	0.352	182	0.548
		100	0.241	119.62	0.70	17	12	0.344	204	0.543

	ProModal®	67/33	0.226	114.18	0.65	14	13	0.354	182	0.603
		50/50	0.222	110.82	0.60	14	13	0.352	182	0.587
		33/67	0.224	109.19	0.59	14	12	0.359	168	0.597
		0	0.217	110.93	0.54	15	13	0.339	195	0.547
	Viloft®	100	0.241	119.62	0.70	17	12	0.344	204	0.543
		67/33	0.233	111.44	0.61	14	13	0.358	182	0.545
		50/50	0.235	112.17	0.64	15	13	0.350	195	0.538
		33/67	0.235	111.77	0.61	15	13	0.350	195	0.515
		0	0.239	110.18	0.59	15	13	0.352	195	0.478
Polyester (PET)	Bamboo	100	0.212	116.51	0.67	17	14	0.315	238	0.605
		67/33	0.214	116.57	0.58	14	14	0.341	196	0.585
		50/50	0.213	112.96	0.58	14	14	0.341	196	0.590
		33/67	0.215	115.97	0.58	14	14	0.342	196	0.581
		0	0.214	109.07	0.51	13	14	0.352	182	0.548
	ProModal®	100	0.212	116.51	0.67	17	14	0.315	238	0.605
		67/33	0.219	115.52.	0.59	14	13	0.350	182	0.594
		50/50	0.218	114.04	0.61	14	13	0.349	182	0.611
		33/67	0.218	109.72	0.60	15	13	0.340	195	0.588
		0	0.217	110.93	0.54	15	13	0.339	195	0.547
	Viloft®	100	0.212	116.51	0.67	17	14	0.315	238	0.605
		67/33	0.232	143.18	0.80	22	12	0.312	264	0.565
		50/50	0.229	116.76	0.59	14	13	0.356	182	0.548
		33/67	0.236	115.05	0.59	14	13	0.360	182	0.515
		0	0.239	110.18	0.59	15	13	0.352	195	0.478

Air permeability plays an important role in comfort properties of fabric that enables transportation of moisture vapor from the skin to the outside atmosphere. So higher value of air permeability of fabric, therefore, makes fabric more suitable to hot and humid climate [10]. Besides, cross-section of the fiber has already important influence on air permeability such as Viloft® has crenulated surface that maintains air gaps in the yarns which makes the fabric from this fiber resistance to air flow and improve thermal properties of the fabric. Air permeability of single jersey knitted fabric samples is shown graphically in Figure 1.

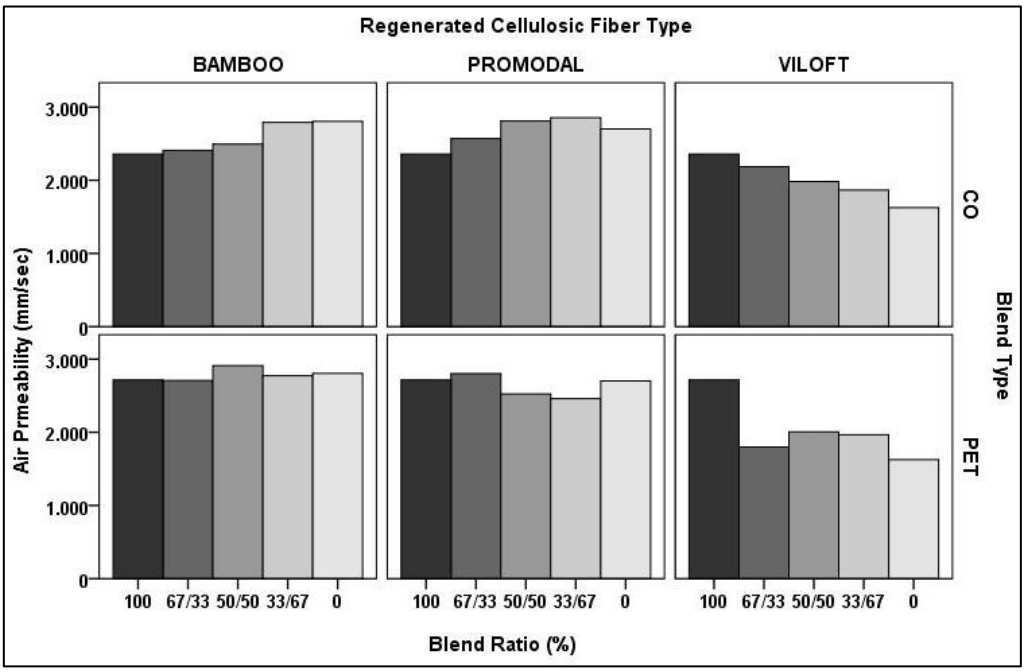

Figure1. Air permeability of single jersey knitted fabric samples

According to the regenerated cellulosic fiber type used, air permeability of fabrics changes adversely with the order of Bamboo>Promodal®>Viloft®. Here, it can be that the cross sectional shapes of the fibers enables whether permit the flow of the air or not which makes them permeable with high porosity. When blend type is taken into consideration, 100% PET fabric has higher air permeability properties than that of 100% CO yarn. And the value is similar to 100% Bamboo and 100% Promodal® fabric. If the air permeability of the fabric is good, the temperature of the air circulating around the body and overflows out of the body, while the fabric with low air permeability prevents the loss of heat by interrupting the air movement.

In statistical analysis, the effect of regenerated cellulosic fiber type, blend type and blend ratio parameters on air permeability were determined by performing ANOVA test in which results are illustrated in Table 3.

Table 3. ANOVA results of single jersey fabric samples for air permeability

Source	**Sum of Squares**	**df**	**Mean Square**	**F**	**Sig.**
Corrected Model	43969994.667[a]	29	1516206.713	193.956	0.000*
Intercept	1795559745.333	1	1795559745.333	229691.723	0.000*
Blend type	378785.333	1	378785.333	48.455	0.000*
Regenerated cellulosic fiber type	28206644.667	2	14103322.333	1804.126	0.000*
Blend ratio	853781.333	4	213445.333	27.304	0.000*
Blendtype * Regenerated cellulosic fiber type	755616.667	2	377808.333	48.330	0.000*
Blend type * Blend ratio	1783048.000	4	445762.000	57.023	0.000*
Regenerated cellulosic fiber type * Blend ratio	9408218.667	8	1176027.333	150.440	0.000*
Blend type * Regenerated cellulosic fiber type * Blend ratio	2583900.000	8	322987.500	41.317	0.000*
Error	2110660.000	270	7817.259		
Total	1841640400.000	300			
Corrected Total	46080654.667	299			
a. R Squared = 0.954 (Adjusted R Squared = 0.949)					

*statistically significant at $p<0.05$.

According to the ANOVA results, blend type, regenerated cellulosic fiber type and blend ratio had significant effect on air permeability with *p value=0.000.* When examining which independent parameter has the highest significant effect on air permeability, regenerated cellulosic fiber type was found with the highest *F* value. In addition, the intersection of these three parameters was also found to be statistically significant. R^2 explains the correlation between independent variable and dependent variable and it was found as 95.4 %. On the other hand all independent parameters explain the air permeability with a highest correlation value.

Tukey HSD multiple comparison test results for regenerated cellulosic fiber type and blend ratio for air permeability are shown in Table 4 and Table 5, respectively.

Table 4. Tukey HSD multiple comparison results of regenerated cellulosic fiber type for air permeability

Regenerated Cellulosic Fiber Type	N	Subset	
		1	2
Viloft®	100	2013.1000	-
ProModal®	100	-	2649.8000
Bamboo	100	-	2676.5000
Sig.		1.000	0.085

Table 5. Tukey HSD multiple comparison results of blend ratio for air permeability

BlendRatio (%)	N	Subset		
		1	2	3
0	60	2377.6667	-	-
67/33	60	2411.6667	2411.6667	-
33/67	60	-	2451.6667	-
50/50	60	-	2454.3333	-
100	60	-	-	2537.0000
Sig.		0.220	0.066	1.000

As seen in Table 4, there is no difference between ProModal® and Bamboo fiber blended fabrics air permeability properties at 0.05 level. Fabric samples made of Viloft® have the lowest air permeability. Furthermore, for 0% blend ratio or pure regenerated cellulosic fabrics have the lowest air permeability than pure PET and CO fabrics. It was seen that the differences between 67%/33%, 33%/67% and 50%/50% blend ratios was found to be insignificant that is these fabrics have similar air permeability.

The correlation analysis between predicted porosity in 1 cm^2 and air permeability of knitted fabrics is given in Table 6. According to the correlation results, it was found that there was a strong relationship between these two parameters with 76.4%. However, the cross-sectional shape of the fiber should be taken into consideration to determine the intra-yarn porosity including pores within yarns. In this study, inter-yarn porosity analysis was performed by using Eq. (3). For the further study, including both intra-yarn porosity and inter-yarn porosity prediction, estimation of air permeability and correlation between predicted and measured values are planned to investigate for weft knitted fabrics.

Table 6. Correlation between air permeability and predicted porosity in 1 cm^2

		Air Permeability (mm/sec)	Porosity in 1 cm^2
Air Permeability (mm/sec)	Pearson Correlation	1	0.764**
	Sig. (2-tailed)	-	0.000
	N	300	30

Porosity in 1 cm^2	Pearson Correlation	0.764**	1
	Sig. (2-tailed)	0.000	-
	N	30	30
**. Correlation is significant at the 0.01 level (2-tailed).			

4. CONCLUSION

This study was conducted to determine the influence of regenerated cellulosic fiber type, blend type and blend ratio on air permeability of single jersey knitted fabric. For this purpose, three types of regenerated cellulosic fiber were selected and blended with PET and CO fiber with different proportion in the yarn production stage. Single jersey fabrics were manufactured by using these yarn types. Besides the measurement of air permeability of fabric samples, porosity in 1 cm^2 of the fabrics are estimated in accordance with the reference taken equations. Results showed that all three parameters and their intersections had a significant effect on air permeability with $p=0.000$. However, multiple comparison test results showed that there is no difference between ProModal® and bamboo containing fabric just for air permeability properties analyzed. In the correlation analysis, it was determined that there was good and positive relationship between air permeability and predicted porosity of the fabric with the value of 76.4%. In other word, higher the porosity enables higher permeability properties to air flow.

ACKNOWLEDGEMENTS

Authors would like to thank to SANKO Textile Industries for their contribution in the production of yarn samples and measurement of yarn characteristics.

REFERENCES

[1]. M. Kilic and A. Okur, "The properties of cotton-Tencel and cotton-promodal blended yarns spun in different spinning systems", *Textile Research Journal*, , vol.81, no.2, pp.156-172, 2011.
[2]. O. Demiryurek and D. Uysalturk, "Thermal comfort properties of viloft/cotton and viloft/polyester blended knitted fabrics", *Textile Research Journal*, vol.83, no.83, pp.1740-1753, 2013.
[3]. H.G. Atasagun, E. Oner, A. Okur and A.R. Beden, "A comprehensive study on the general performance properties of viloft-blended knitted fabrics", *The Journal of Textile Institute*, vol.106, no.5, pp.525-535, 2015.
[4]. M. North, "Engineered viscose fibres delivering enhanced wearer comfort and fabric performance", *Lenzinger Berichte*, vol.89, pp.37-42, 2011.
[5]. F. Sekerden, "Investigation on the unevenness, tenacity and elongation properties of bamboo/cotton blended yarns", *Fibres & Textiles in Eastern Europe*, vol.19, no.3 (86), pp.26-29, 2011.
[6]. I. Ahmad, A. Farooq, S.A. Baig and M.F. Rashid, "Quality parameters analysis of ring spun yarns made from different blends of bamboo and cotton fibres", *Journal of Quality and Technology Management*, vol.8, no.1, pp. 1-12, 2012.
[7]. K. Saravan and C. Prakash, "Bamboo fibres & their application in textiles", *The Indian Textile Journal*, vol.117, pp.33-36, 2007.
[8]. http://www.kelheim-fibres.com/produkte/vi_te_uk.php, 30.01.2018.
[9]. F.T. Peirce, "Geometrical principles applicable to the design of functional fabrics", *Textile Research Journal*, vol.17 pp.123–147, 1947.
[10]. B. Karaguzel, "Characterization and role of porosity in knitted fabrics", M.S. Thesis, North Carolina State University: Raleigh, NC, USA, 2004.
[11]. M. Havlova and J. Spankova, "Porosity of knitted fabrics in the aspect of air permeability – discussion of selected assumptions", *Fibres & Textiles in Eastern Europe*, vol.25, no.3 (123), pp.86-91, 2017.

ICETI
www.iceti.org
2018
07-11 MARCH
BUDAPEST
HUNGARY
II. INTERNATIONAL CONFERENCE ON ENGINEERING TECHNOLOGY AND INNOVATION

Optimization of MR Fluid Polishing Condition for Improving the Shape Accuracy of Cover-Glass Edge

Byung-Chan Kim[1], Ki-Hyeok Song[1], Jae-Hwa Chung[1], Myeong-Woo Cho[1]

Abstract

According to the minimization of the electronic devices, thickness of cover-glass becomes thinner and the strength of that is stronger. In this reason, the research for the cover-glass that has high strength is ongoing. Generally, the break of glass by external force is occurred from the edge because it is the stress by external force is concentrated. The PV (Peak and Valley) value, which is one of the parameter in surface roughness, can affect to the strength of cover-glass. It is important for high edge strength of cover-glass to develop the grinding and polishing technology for cover-glass edge.

MR fluid is used to polishing cover-glass edge for high-precise surface roughness. MR fluid in magnetic field acts as a polishing pad in MR fluid polishing system, not a general grinding or polishing process. For the high-precise surface roughness of cover-glass edge, optimum polishing condition is essentially deducted. To deduct the optimum MR fluid polishing condition, response surface method (RSM) that one of the design of experiment (DOE) is used. Factors in response surface method are abrasive size, federate and polishing depth and the PV value is a dependent variable. Also, the effect of each factor to the PV value is analyzed using analysis of variance (ANOVA). It is confirmed that each factor affects to the PV value in 95% confidence interval and it can be found that precise surface roughness can be obtained by optimum polishing condition in MR fluid polishing.

Keywords: Analysis of variance (ANOVA), Cover-glass, MR fluid polishing, Response surface method (RSM)

1. INTRODUCTION

An optical device is used for controlling a light source to suit the purpose of use and is widely used in industrial fields from ultra-precision instruments to display devise. In addition, demand for optical glasses is increasing as electronic products with optical glasses, such as tablet PCs or smart phones, are widely used recently. The optical glass attached to such a smart device is called cover-glass. The thickness of the cover-glass is minimized for reducing the weight of the smart device and research is actively conducted for this reason.

Generally, the cover-glass is manufactured in order through processes such as design, cutting or molding, grinding, polishing and inspection. The grinding and polishing during the process of the cover-glass is an important step which has the greatest influence on the shape and optical performance of the cover-glass. Also, the strength of cover-glass is determined according to the polishing state of the cover-glass edge. Most of the grinding and polishing process of the cover-glass is done by mechanical machining. In this process, the tool contacts the cover-glass directly. Unlike metal, cover-glass with high brittleness causes scratches, chipping, notch or cracks on the surface even small impact due to the vibration of the tool during the process. This causes optical defects of the cove-glass and it can be easily damaged even by a small external impact. As a result, the strength of the cover-glass can be increased through the polished surface of the cover-glass edge.

In this study, the polishing cover-glass edge using MR (Magneto-rheological) fluid, which is a super precision polishing method that overcomes limitations of mechanical polishing and minimizes surface defects, was studied.

[1] *Corresponding author: Inha University, Department of Mechanical Engineering, 22212, Incheon, South Korea.*
chomwnet@inha.ac.kr

2. PRINCIPLE OF MR FLUID POLISHING

MR (Magneto-rheological) fluid is a fluid whose properties vary in a magnetic field, and is a materials whose viscosity changes with the strength of the magnetic field. The main components of the MR fluid are micro ferromagnetic particles that react with the magnetic field and fluids such as water or oil. In the magnetic field, micro ferromagnetic particles in the MR fluid that are magnetized induce magnetic dipoles and the interaction becomes active [1]-[3]. As shown Fig. 1, particles become chain-shaped and become semi-solid with viscosity.

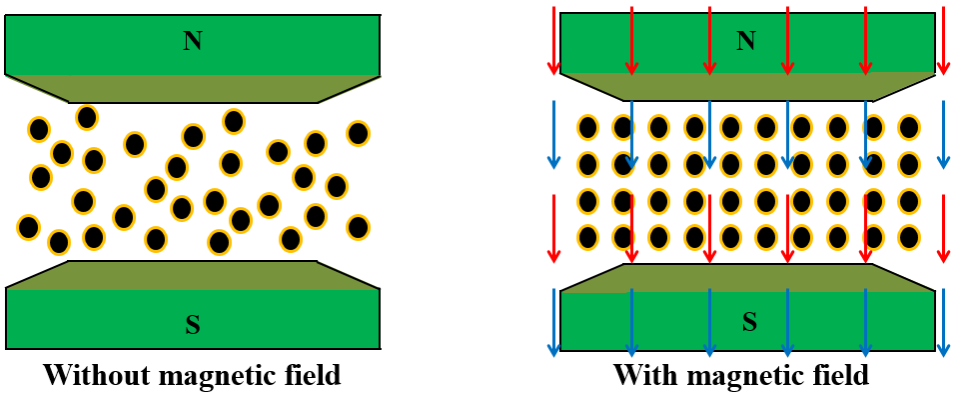

Fig. 1 Schematic diagram of chain phase of MR fluid

The formed chain shape has a shear force between the objects moving relative to each other, and when the shear force is greater than the yield stress in magnetic field, the shear stress appears as Bingham expression as Eq. 1 [4].

$$\tau = \eta_c \dot{\gamma} + \tau_0(\mathrm{H})\mathrm{sgn}(\dot{\gamma}) \quad (|\tau| \geq |\tau_0(H)|) \tag{1}$$

In the above equation, τ be shear stress, η_c be plastic viscosity, $\dot{\gamma}$ be shear rate, $\tau_0(\mathrm{H})$ be shear force by magnetic field (yield stress). MR fluid changes to Bingham plastic fluid, which is in Newtonian fluid without magnetic field but changes in yield strength and viscosity in the magnetic field [5]~[8]. In other words, MR fluid is a smart material that can control the flow characteristics in real time according to the change of magnetic field.

MR fluid polishing is performed using MR fluid which is changed to semi-solid state in magnetic field. The semi-solid MR fluid acts as a soft polishing pad and the workpiece is polished by shear force generated by contact [9]. As a result, the removal rate and the quality of the surface are significantly influenced by variables that can change the viscosity, such as the intensity of magnetic field. The material removal rate by MR fluid polishing can be expressed as Eq. 2. The material removal rate is divided by normal stress using Preston equation which is the material removal rate by conventional polishing and the characteristics of material is applied in Eq. 2 [10].

$$MRR_{MRF} = C_{P,MRF(\tau,FOM)} \frac{E}{K_C H_V^2} \cdot \tau \cdot V \tag{2}$$

In the above equation, $C_{P,MRF(\tau,FOM)}$ be new Preston constant for shear force, E be Young's modulus, H_V be Vickers hardness, K_C be fracture toughness, τ be shear force. While scratch, chipping or micro cracks occur in the polishing process using general solid tools, MR fluid polishing reduces surface defects such as SSD(Sub-surface damage) because low forces are applied to the workpiece relatively [10]-[12]. Therefore, it is possible to obtain a surface superior to the conventional polishing process when cover-glass is polished using MR fluid.

In this study, MR fluid used in the MR fluid polishing consists of DI(Deionized) water CI(carbonyl iron) particles, Na_2CO_3 and glycerin. CI particles are sensitive to magnetic field, and are spherical Fe particles having a diameter of 2 to 6 ㎛ which are produced by thermally decomposing iron pentacarbonyl. The reason why DI water was used as the base of MR fluid is that the water molecule breaks the Si-O-Si bond of the glass, and it can form the hydration layer on the glass surface. And the hydration layer formed on the glass surface can improve the material removal rate during polishing [13]. The CI particles mixed with the DI water are oxidized and these have different physical and chemical properties from those of conventional MR fluid. Therefore, the pH of MR fluid was increased to about

10~12 by adding Na_2CO_3 to reduce the oxidation rate of the CI particles in MR fluid. Also, CI particles sink over time because of a higher density than that of DI water. For this reason, glycerin, which acts as dispersion stabilizer, was added to increase the viscosity of DI water and to produce a stable MR fluid [14]. The abrasive used in this experiment was Al_2O_3 powder of 0.3 ㎛.

Fig. 2 shows the schematic diagram of MR fluid polishing used in this study. MR fluid is supplied onto the rotating wheel, which becomes a semi-solid state in the magnetic field and act as a soft polishing pad. The abrasive is supplied separately on the MR fluid and it can improve the polishing efficiency.

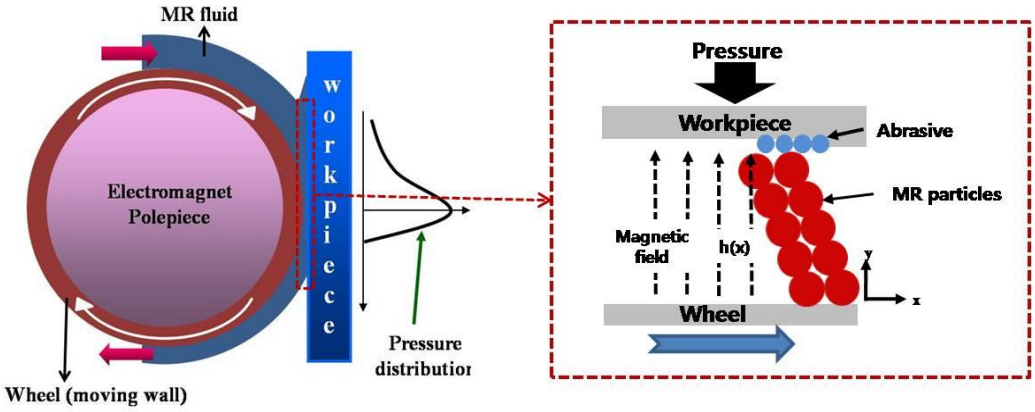

Fig. 2 Schematic diagram of MR fluid polishing

Fig. 3(a) shows an electromagnet module used in MR fluid polishing system. The magnetic field is formed by the coils and the magnetic field is transmitted to the pole-piece by the inside the coil. In this module, the magnetic field is maximized in the air gap between the pole-piece. To confirm this, Fig. 3(b) is the result of magneto static analysis. The magnetic field generated by the coil is concentrated and transmitted through the core located inside the coil. It can be seen that the magnetic field is the most concentrated between the pole-piece.

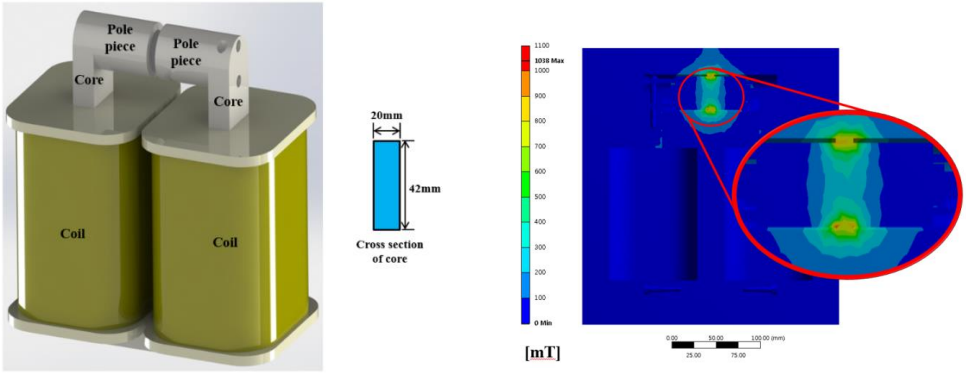

Fig. 3 (a) Modeling of electromagnet *(b) Result of magneto static analysis*

Based on the above design of electromagnet and the result of analysis, the MR fluid polishing system for polishing cover-glass edge was designed and fabricated as Fig. 4.

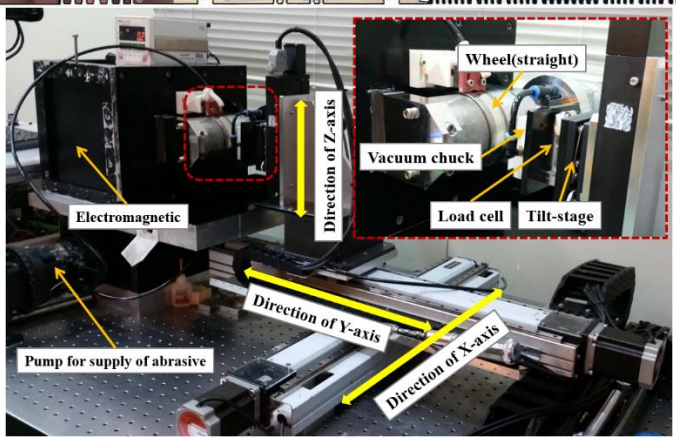

Fig. 4 Experimental system of MR fluid polishing

3. DERIVATION OF OPTIMUM PROCESS CONDITIONS USING RESPONSE SURFACE METHOD (RSM)

Response surface method (RSM) is an experimental design method used to identify the relationship between response variables and quantitative experimental variables, which is used to find the conditions of factors that can optimize response variables. Particularly, it is a method to visually confirm the reaction value which changes according to the acceptance different variables by 2, 3D surface. In this study, central composite design(CCD) was used to determine the process conditions of MR fluid polishing that minimizes the PV value of cover-glass edge affecting the bending strength of the cover-glass. Polishing depth, Feedrate of cover-glass and abrasive size are selected as the factors used in the RSM. The above mentioned variables are referred to as X1(abrasive size), X2(Feedrate) and X3(Polishing depth). The magnetic field, rotational speed of the wheel and the content of CI particle, which do not affect to the material removal rate in MR fluid polishing, are determined as fixed variables.

PV value of cover-glass edge was specified as the objective function in the RSM. This is because the strength of cover-glass has the greatest influence on the PV value of the edge roughness [15]. The surface roughness of the cover-glass edge was measured using non-contact surface profiler (Newview 7200, Zygo). Fig. 5~7 show the results of the experiment based on the RSM and the analysis of variance (ANOVA) was applied for the effect of each factor on PV value. The correlation between the each factor and the independent variable is shown by the second-order polynomial as Eq. 3.

$$Y = 1838 - 1992 * X1 - 23.8 * X2 - 195 * X3 + 1852 * X1\text{^}2 + 0.379 * X2\text{^}2 \quad (3)$$

The surface plot is shown for each factor and it can be seen that the optimum value can be derived from the fact that the three plots have a curvature.

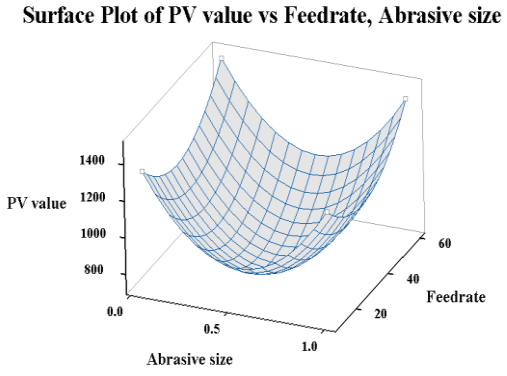

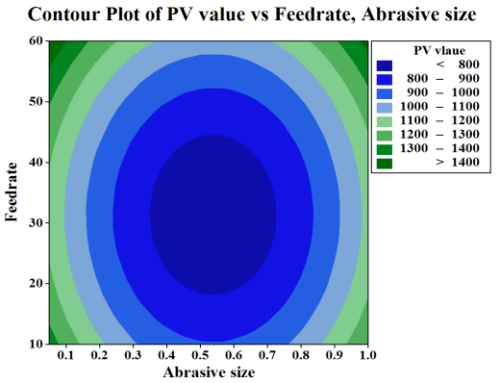

Fig. 5 (a) 3D surface plot when polishing depth is fixed at 1.0mm

Fig. 5 (b) 2D contour plot when polishing depth is fixed at 1.0mm

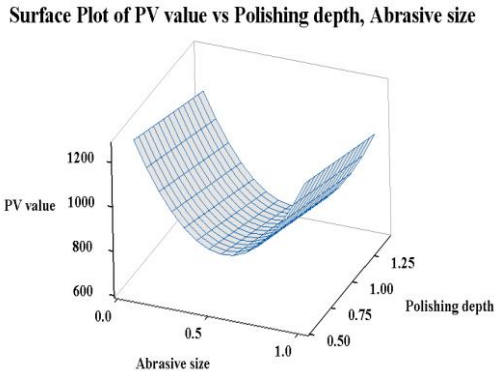

Fig. 6 (a) 3D surface plot when feedrate is tixed at 35mm/min

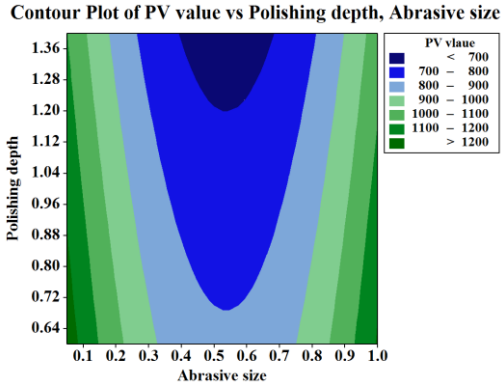

Fig. 6 (b) 2D contour plot when feedrate is tixed at 35mm/min

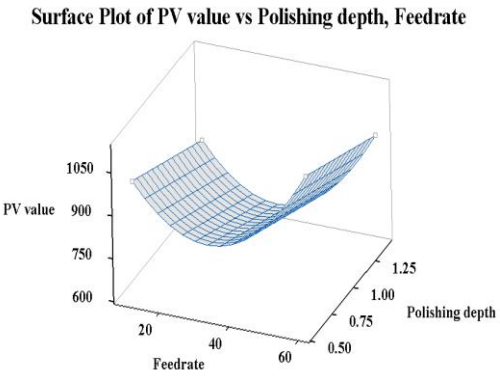

Fig. 7 (a) 3D surface plot when abrasive size is fixed at 0.3 ㎜

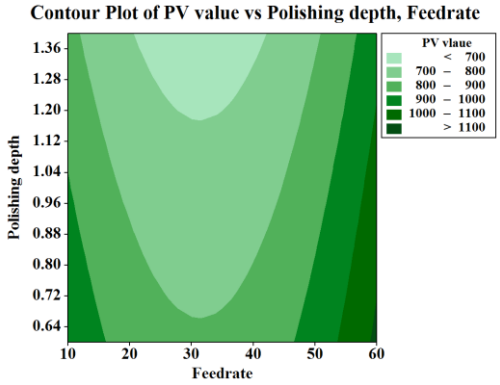

Fig. 7 (b) 2D contour plot when abrasive size is fixed at 0.3 ㎜

Also, Table 1 shows the results for the ANOVA, which is the result of a 95% confidence interval. P value is used as a value to confirm the importance of each coefficient. If P value is less than 0.05, it means that the result is meaningful. If it is more than 0.10, it is considered to be meaningless[16]. P value of each factor is larger than 0.05 and it is not significant. However P value of the square each factor is smaller than 0.05, which is highly significant. Also, if P value of lack-of-fit has a value less than 0.05, there is a problem with the predicted model. On the contrary, if the value is greater than 0.05, the assumed model is appropriate. The P value of lack-of-fit calculated in this study is 0.075, which means that the model obtained in the ANOVA is appropriate.

Table 1 Analysis of variance of the experimental results of the BBD

Source	DF	Sum of Square	Mean of Square	F value	P value
Model	5	1254808	250962	2.76	0.042
Abrasive size	1	8023	8023	0.09	0.769
Feedrate	1	75224	75224	0.83	0.372
Polishing depth	1	97523	97523	1.07	0.311
Abrasive size^2	1	706656	706656	7.76	0.010
Feedrate^2	1	417382	417382	4.59	0.043
Lack-of-fit	7	1064595	152085	2.31	0.075

4. CONCLUSION

In this study, MR fluid polishing was used to obtain excellent surface roughness of cover-glass edge for improving the strength of the cover-glass edge. Among the process parameters of MR fluid polishing, factors affecting the surface roughness were selected. The correlation between surface toughness and CCD method of RSM was used. The P value of the determination coefficient is smaller than 0.056, indicating a small error range and it means that the fit of this model is high. Therefore, this study can be used as the basis of many studies that predict the optimized process conditions or utilize the predicted values.

ACKNOWLEDGMENT

This work was supported by the National Research Foundation of Korea (NRF) grant funded by the Korea government (MSIP) (NRF-2015R1A2A2A01005811)

REFERENCES

[1] M. T. Lopez-Lopez, P. Kuzhir, S. Lacis, G. Bossis, F. Gonzalez-Caballero, J. D. G. Duran, “Magnetorheology for suspensions of solid particles dispersed in ferrofluids”, J. Phys.: Condens. Mater 18, (2006), pp2803–2813.
[2] C. Rinaldi, A. Chaves, S. Elborai, X. He, M. Zahn, “Magnetic fluid rheology and flows”, Curr. Opin. Colloid Interface Sci.10, (2005), pp141–157.
[3] Harvey P, Don G. “Deterministic manufacturing processes for precision optical surfaces”, Key Engineering Materials, (2003), 238 – 239.
[4] E. C. Bingham, Fluidity and Plasticity. New York: McGraw-Hill, 1922.
[5] M. Kciuk, R. Turczyn, “Properties and application of magnetorheological fluids”, Journal of Achievements in Materials and Manufacturing Engineering, Volume 18, Issue 1-2, (2006), pp127-130.
[6] G. R. Iglesias, M.T. López-López, J.D.G. Durán, F. González-Caballero, A.V. Delgado, “Dynamic characterization of extremely disperse magnetorheological fluids”, Journal of Colloid and Interface Science, Volume 377, Issue 1, (2012), pp153-159
[7] Hall Christopher, Donohue Stephen, Dumas Paul. “Correcting transmitted wavefronts using magnetorheological finishing (MRF)”, Proceedings of the SPIE [C]. 2005. 76.
[8] Huang Jin , Zhang Junqian, Yang Yan , Wei Yuqing . “Analysis and design of a cylindrical magneto-rheological fluid brake”, Journal of Materials Processing Technology, 2002, 129: 559
[9] W. Kordenski, S. Gorodkin, “Material removal in magnetorheological finishing of optics”, Optical Society of America, (2011), pp1984-1994.
[10] DeGroote JE, Marino AE, Wilson JP, Bishop AL, Lambropoulos JC, Jacobs SD. Removal rate model for magnetorheological finishing of glass. Applied Optics 2007;46(32):7927–41.
[10] Hallock B, Dumas P, Shorey A, Tricard M. Recent advances in deterministic low-cost finishing of sapphire windows. Proceedings of SPIE 2005;5786: 154–64.
[12] Bulsara VH, Ahn Y, Chandrasekar S, Farris TN. Mechanics of polishing. Transaction of ASME, Journal of Applied Mechanics 1998;65:410–6.
[13] Cook L. M. “Chemical processes in glass polishing.” Journal of Non-Crystalline Solids 1990;120:152–71.
[14] Genc S. Phule PP. Rheological properties of magnetorheological fluids. Smart Materials and Structures 2002;11:140–6
[15] Maria Lindqvist, Marc Vandebroek, Christian Louter, Jan Belis, “Influence of edge flaws on failure strength of glass”, Glass Performance Days 2011, 2011, pp. 126-129
[16] H. Xu, L. P. Sun, Y. Z. Shi, Y. H. Wu, B. Zhang, and D. Q. Zhao, Biochem. Eng. J., 39, 66 (2008).

BIOGRAPHY

Byung-Chan Kim 2014~2016 M.S. Mechanical Engineering, Inha University
2016~present Doctor's course in Inha University

Ki-hyeok Song 2013~2015 M.S. Mechanical Engineering, Inha University
2015~present Doctor's course in Inha University

Jae-Hwa Chung 2017~present Master's course in Inha University

Myeong-Woo Cho 1983~1985 M.S. Mechanical Engineering, Seoul University
1989~1992 Ph.D. Mechanical Engineering, Illinois University in Chicago
1993~1997 Head of the Department of System, Deawoo Inc.
1997~present Associate Professor, Inha University

ICETI
www.iceti.org
2018
07-11 MARCH
BUDAPEST
HUNGARY
II. INTERNATIONAL CONFERENCE ON ENGINEERING TECHNOLOGY AND INNOVATION

Preparation and Application of APEO-Free Surface Active Agents for Soaking Process of Leather

Ali Yorgancioglu[1], Ersin Onem[1], Bahri Basaran[1]

Abstract

Surface active agents have been widely used in leather industry for soaking, degreasing, fatliquoring and dyeing processes. Soaking is the first step and very important process that surface active agents are applied. For this step, anionic and nonionic surface active agents with high wetting ability have been used to enhance the rehydration process. Ethoxylated alkylphenols and their residuals in the final leather products were banned and restricted due to the environmental and health risks in the recent times. Demands and social sensivity on the ecological products and new technical approaches based on functional properties for the surface active agent applications make to develop the APEO-free surfactants having good wetting and emulsification ability and without any environmental problem.

In this study, APEO-free surface active agents were synthesized and applied for the efficient wetting of fibers of sheepskins in soaking process. They were also compared with the conventional APEO containing surfactants. The results of the research showed that APEO-free surface active agents for soaking application provided the similar properties with the APEO containing agents. Thus, a considerable progress will be able to provided to achieve the production of ecologically benign leather goods and sustainability in the industry.

Keywords: Leather, Soaking, Rehydration, Wetting, APEO, Eco-Surfactant.

1. INTRODUCTION

New eco-benign systems, either using non-hazardous compounds or developing new production methods have become the raising trend in global industrial activities, due to the increasing health and environmental regulations and restrictions. Researchers have adopted various approaches to minimize the environmental impact of leather processes taking into consideration the use of chemicals having less toxicity or less environmental impact, recovery and/or reuse of water, floats and chemicals in leather processing steps and innovation of processes and products [1-4].

Soaking is the first process of leather manufacturing. Hides and skins, when received from tannery, are in a condition of preservation based on dehydration. Therefore, the purpose of soaking is to make skins wet back and bring them to a flaccid condition for subsequent operations. On the other hand, it is better to remove non-collagen components in the skins in the soaking process. Common soaking agents are alkali, sodium sulphide, salt and some surfactants. However, these materials often lead to environmental pollution. Especially APEO-based soaking agents occur big problems for tanneries. In modern technology, APEO-free soaking agents should be applied to facilitate the skin soaking process [5].

Most known nonionic emulsifiers include addition compounds of ethylene oxide and of propylene oxide with alkylphenols, alcohols or fatty acids. Alkylphenol ethoxylates have been the most widely used nonionic surfactants for decades, especially nonylphenol ethoxylate having on average 10 EO (ethylene oxide) units. APEOs are surface active agents synthesized by the reaction of alkylphenol with branched chain and ethylene oxide. Commonly used APEOs in the industry are nonylphenols (NP), nonylphenol ethoxylates (NPEO), octylphenols (OP) and octylphenol

[1] *Corresponding author: Department of Leather Engineering, Faculty of Engineering, Ege University, 35100 Bornova-Izmir, Turkey.* bahri.basaran@ege.edu.tr

ethoxylates (OPEO). APEO and derivates have been used in the soaking, degreasing and finishing processes of leather industry for many years [6].

Despite the advantages of APEOs, they cause the reproduction, growth and vital problems on the terrestrial and aquatic livings as a result of the industrial wastes charging to the environment. It was reported that these auxiliaries or their degradation products have carcinogenic and/or toxic properties [7,8]. In addition to low biodegradability, the use of alkylphenol ethoxylates, which are reported to be harmful to human health, has been restricted due to the potential conversion to alkyl phenols and mono- or di ethoxy alkyl phenols known to be estrogenic. The most influential legislations relating to APEOs are the European Union (EU) Directive 2003/53/EC and 2009/563/EC which especially restrict the use of NPEOs in substance or preparations for leather processing. Eco-labels like EU flower and Oeko-Tex 1000 banned the using of APEO (limit value: 100 mg/kg) [9]. Although the Directive 2003/53/EC has been followed for many years, APEOs are still possibly applied in the tannery because of their low cost and excellent characteristics.

APEO-based surface active agents are indispensable auxiliaries because of the above-mentioned properties for soaking process of leather production. On the other hand, requests on the ecological criteria and sustainability of the processes increased in the industries. In our study, the mixtures of APEO-free surface active agents having high wetting ability were synthesized to soak the sheepskins in an effective and homogeneous way. The synthesized surface active mixtures were also compared with the conventional APEO-based surface active agents in terms of their soaking efficiency.

2. MATERIALS

Crust leathers were used as the leather material for soaking tests. All chemicals used in the experiments were of analytical reagent grade and purchased from Sigma-Aldrich.

3. METHODS

3.1. Production of Ecological APEO-Free Soaking Agents (SAs)

Production of ecological APEO-free soaking agents were carried out according to the given in below mixtures (Table 1).

Table 1. Contents of the produced surfactants

Surfactants	Contents
SA1	Alcohols, C12-18, ethoxylated + Lauryl-, myristyl alcohol, ethoxylated, propoxylated + Ethylene glycol monobutyl ether
SA2	Alcohols, C12-14, ethoxylated + Lauryl-, myristyl alcohol, ethoxylated, propoxylated + Ethylene glycol monobutyl ether
SA3	Alcohols, C12-14, ethoxylated + Alkyl ether sulfate C12-14 with EO, sodium salt.+ 2-methyl-2,4-pentandiol
SA4	Alcohols, C12-14, ethoxylated + Sulfuric acid, mono-C12-16-alkyl esters, ammonium salts + 2-methyl-2,4-pentandiol
SA5	Secondary alkane sulphonate, sodium salt + Isotridecanol,ethoxylated+Ethylene glycol monobutyl ether + Alcohols, C12-18, ethoxylated

3.2. Determination of Product Properties

APEO content, refractometer value, pH, solid content, viscosity, appearance, blurring point and ionic charge analyses were carried out to put forward the product properties of soaking agents.

3.3. Sampling of Leathers

Sampling from leathers for the analyses was realized in accordance with the TS EN ISO 2418 standard test method.

3.4. Soaking Test

Test samples were weighed about 0.5 g in a beaker (600 mL). Water was added up to 500 mL and homogeneous mixed. 2.5x2.5 cm of test samples were hung to the pin (V shape) and sunk to the beaker. When test samples touch the water, time recorder starts. When test samples reach to the bottom, time recorder stops and the soaking time notes. Analyses were repeated two times and the averages were calculated.

3.5. Production of Leathers in Lab-Scale

Shoe upper crust leathers were processed using the recipes given in Table 2.

Table 2. Leather production recipe

Process	**%**	**Chemicals**	**Temp. (ºC)**	**Time (min)**	**Remarks**
Soaking	500	Water	35		
	3	Soaking agent		60	Drain
Washing	200	Water	35	10	Drain
	200	Water	35		
	2	Neutralizing agent		60	pH 5,5
Dyeing	100	Water	35		
	3	Dyestuff		60	
	+150	Water	60		
	3	Emulsified oils and modified lecithin			
	2	Mixture of synthetic emulsifiers with neutral oils			
	2	Paraffin oil and hydrophobic emulsifiers		60	
	1	HCOOH		45	pH 3,8
Washing x 3	200	Water	30	30	Drain

3.6. Determination of APEOs in Leather Samples

The leather sample was firstly extracted. The extract was analyzed with combined high performance liquid chromatography and mass spectrometry according to standard procedure (Moralesa et al., 2009).

4. RESULTS AND DISCUSSIONS

4.1. Properties of Apeo-Free Soaking Agents

Product properties of soaking agents were given at Table 3.

Table 3. Surfactants product properties

	pH	Solid content	Refractometer value	Viscosity	Blurring point	Ionic charge	Appearance
SA1	7.25	46.81	39.84	59.4	40 ºC	Nonionic	Opaque, clear liquid
SA2	6.48	23.90	22.32	43.6	48 ºC	Nonionic	Opaque, clear liquid
SA3	5.53	44.46	35.28	51.5	31 ºC	Nonionic	Opaque, clear liquid
SA4	5.25	29.27	26.75	48.5	Blurry	Nonionic	Blurry
SA5	5.23	32.05	29.35	51.8	39 ºC	Nonionic	Opaque, clear liquid
CSA	7.75	60.07	28.86	69.0	12	Nonionic	Opaque, clear liquid

4.2. Soaking Efficiency

Soaking test results by different soaking agents were presented in Figure 1.

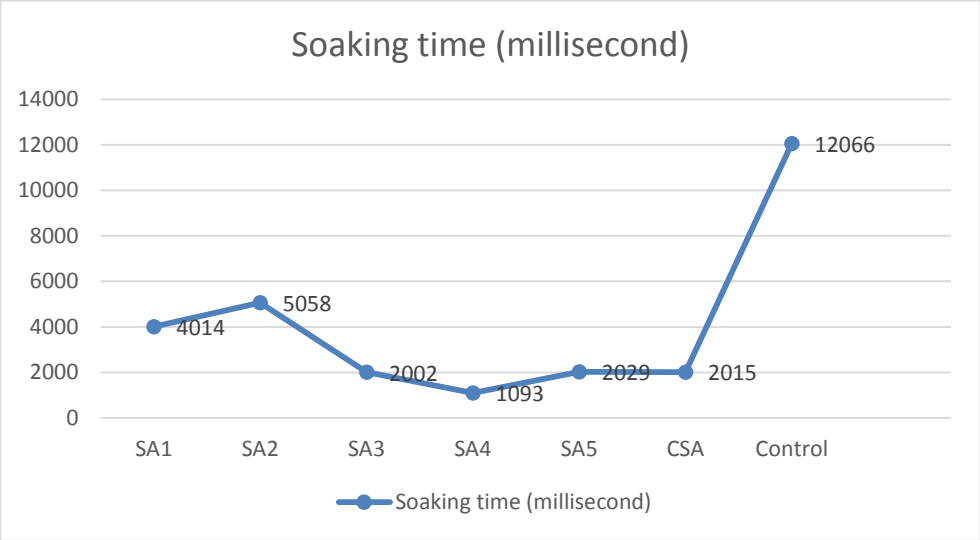

Figure 1. Soaking efficiency of the surfactants

The wetting of a fibrous material such as leather is complex since it has a chemically and physically heterogeneous surface. The problem is further complicated by the simultaneous spreading of the liquid on the surface and absorption of the liquid into the pores of the material. Besides, the wettability of a surface depends on the surface tension of the liquid that goes into contact with the same. Water has a very high surface tension (72.8 mN/m), so it tends to wet only surfaces bearing highly polar groups. In the tanneries, rewetting of crust leathers could create a problem when it is too dried. In this situation surface active agents can be used for improving the wetting properties of leather by lowering the surface tension of water. Upon the examination of Figure 1; leathers processed with APEO-free soaking agents indicated a significant decrease in soaking time (millisecond) when compared to the control sample. However the quickest soaking was obtained with SA4. APEO contented commercial soaking agent shows similar wwtting efficiany as SA3 and SA5.

4.3. APEO Contents of Soaking Agents and Leather Products

Produced soaking agents and commercial soaking agents APEO content was given in Table 4. Leathers processed with the commercial soaking agents and APEO-free soaking agents were also screened for APEO content was given in the Table.

Table 4. APEO contents

	APEO content in product (mg/kg)	**APEO content in leather (mg/kg)**
SA1	< 10	248
SA2	< 10	160
SA3	< 10	325
SA4	< 10	186
SA5	< 10	127
CSA	9870	1150

When Table 3 is examined, it is observed that the highest APEO content was obtained from commercial soaking agent processed leather. The lowest APEO content was, on the other hand, obtained from SA5 processed leather. Moreover, results showed that APEO contents of the shoe upper leathers were lower than the described limit values (1000 ppm) except CSA processed leather.

5. CONCLUSION

APEO derivative surface active agents became considerable matter after the awareness of restricted substances in leather industry. This matter decrease the quality of leather and it's marketability. For these reasons, the studies on the development of new innovative surface active agents were accelerated to eliminate the current problems in the sector. Our study indicates that APEO-free surfactants have a good effect on the wetting properties and provides a similar wetting efficiency on the leathers compared to APEO-based surfactants. The above findings revealed that soaking with produced surfactants will provide an environmentally friendly soaking process. Besides, produced APEO-free surfactants can be used also in double-face production as wool cleaning, wetting, emulsifying and degreasing agents in leather production.

REFERENCES

[1]. A.C.A. Zengin, S.M. Colak, G. Zengin and E. Kilic, "Eco-friendly soaking process using tannic acid as an alternative bactericide", Archives of Environmental Protection, vol. 40, pp. 3-12, 2014.
[2]. J.M. Morera, E. Bartolí, R. Chico, C. Solé, and L.F. Cabeza, "Minimization of the environmental impact of chrome tanning: A new process reusing the tanning floats", Journal of Cleaner Production, vol. 19, pp. 2128-2132, 2011.
[3]. M. Gutterres, P.M. Aquim, J.B. Passos, and J.O. Trierweiler, "Water reuse in tannery beamhouse process", Journal of Cleaner Production, vol. 18, pp. 1545-1552, 2010.
[4]. M.M. Mutlu, B.H. Cadirci, H. Ozgunay, A.C. Adiguzel, O. Sari, "Ozone as a biocide in soaking", Journal of the Society of Leather Technologists and Chemists, vol. 93, pp. 18-20, 2009.
[5]. J. Ma, X. Hou, D. Gao, B. Lv and J. Zhang, "Greener approach to efficient leather soaking process: role of enzymes and their synergistic effect", Journal of Cleaner Production, vol. 78, pp. 226-232, 2014.
[6]. H.F. Smyth and J.C. Calandra, "Toxicologic studies of alkylphenol polyoxyethylene surfactants", Toxicology and Applied Pharmacology, vol. 14, pp. 315–334, 1969.
[7] A.M. Warhurst, "An environmental assessment of alkylphenol ethoxylates and alkylphenols", Friends of the Earth, Edinburgh, 1995.
[8]. P. Voogt, O. Kwast, R. Hendriks and N. Jonkers, "Alkylphenol ethoxylates and their degradation products in abiotic and biological samples from the environmen"t, Analysis, vol. 28, pp. 776-782, 2000.
[9]. T.V. Moralesa, M.E.T. Padróna, Z.S. Ferreraa and J.J.S. Rodríguez, "Determination of alkylphenol ethoxylates and their degradation products in liquid and solid samples", Trends Analytical Chemistry, vol. 28, pp. 1186-1200, 2009.

ICETI
www.iceti.org
2018
07-11 MARCH
BUDAPEST
HUNGARY
II. INTERNATIONAL CONFERENCE ON ENGINEERING TECHNOLOGY AND INNOVATION

An Optimization Model for Production Planning in an International Chemical Company

Sema Demiray Kirmizi[1], Murat Colak[2], Gulsen Aydin Keskin[3]

Abstract

Conventional production planning aims to provide effective usage of resources such as manpower, material and machine in order to satisfy customer demand. It is aimed to minimize the costs and maximize profit in the production planning process. At this point, inventory and backorder quantities constituting cost items have become significant in this process. On the other hand, since each production environment has its own constraints, it is necessary to develop solution approaches according to these constraints. Mathematical programming models are effectively utilized to solve optimization problems like determination of production quantity and inventory level. This study was realized in an international company operating in the chemical industry. A mathematical model with maximization objective was developed to solve production planning problem for a product group and 6 months period considering production constraints of this company. This model includes 4 decision variables and 8 constraints and has been solved by means of IBM ILOG CPLEX 10.0 in order to find optimal solution for this production planning problem. As a result, optimal production, inventory and backorder quantities have been determined through mathematical programming model.

Keywords: *Production planning, integer programming, mathematical modelling, inventory level, backorder.*

1. INTRODUCTION

Production planning is the organization of production activities in order to meet customer demands and use resources such as machinery, equipment and workforce in the production environment in line with the institution's performance targets. Production planning is a very critical process for manufacturers. That is why producers need a production planning process that is designed and responsive in line with both customer expectations and their own corporate objectives. The designed production plan is a projection showing the quantity and timing of the outputs of the production. Demand/sales quantities, inventory levels, resource capacities, cost items and safety stock levels have to be taken into consideration as outputs in the production planning process.

When a customer demand occurs there are two possibilities in terms of stocking out according to inventory theory. These possibilities are defined as 'loss of profit' and 'backorder'. If the customer wait until the demand is met, this case is referred as backorder. Since this concept is a cost item, compaines aim to decrease costs rooted from this event. For this purpose, they desire to keep safety stock meant minimum stock level that allowed [1].

In this study, it is aimed to maximize the profit of an international chemical company by optimizing production, inventory, backorder and sales quantities during a planning period. For this reason, a mathematical programming model was developed with regards to constraints of production environment. The rest of paper is organized as follows. A brief literature review has been presented in Section 2. A mathematical model developed for this study has been given in Section 3. The study has been concluded with conclusions and future suggestions in Section 4.

[1] *Author: Kocaeli University, Department of Industrial Engineering, 41380, Izmit/Kocaeli, Turkey. semademiray@gmail.com*

[2] *Author: Kocaeli University, Department of Industrial Engineering, 41380, Izmit/Kocaeli, Turkey. colak.murat@kocaeli.edu.tr*

[3] *Corresponding author: Kocaeli University, Department of Industrial Engineering, 41380, Izmit/Kocaeli, Turkey. gaydin@kocaeli.edu.tr*

2. LITERATURE REVIEW

There are many articles related to inventory planning in the literature. Inventory planning includes terms such as capacity, material, order, production, safety stock and backorder. Some of studies regarding production planning are briefly summarized as follows:

Mousavi et al. [2] researched an inventory control problem considering the backorder quantities in a multi-product industry under a budget constraint. They aimed to optimize two objectives as minimizing the inventory costs and warehouse volume needs under fuzzy environment. They compared the results of harmony search algorithm and particle swarm algorithm. As a result, they decided that harmony search algorithm was more promising. San-José et al. [3] focused on analysis of the economic order quantity model considering two different costs related to keeping inventory. One of them is the fixed cost derived from keeping the item in the warehouse, second is the variable cost related to the time over that kept in stock. An economic order quantity model is developed to establish optimal inventory policy in order to minimize the whole inventory cost which includes the fixed and variable cost functions. Kumar and Evers [4] discussed the unreliability of determining the safety stocks with random sums approach and its impact on inventory management and suggested a new method based on multiplication approach, which considers the data quality issues, demand and lead time correlation, and computational simplicity. They demonstrated the effectiveness of the multiplication approach via simulation. Zoysa and Rupasinghe [5] aimed to minimize the high stock quantities and to optimize the safety stock level in winery supply chains and they obtained promising results using a mixed integer programming model. Boulaksil [6] modeled customer demand utilizing the Martingale Model of Forecast Evolution. The safety stocks were determined under demand uncertainty and supply chain risk through simulation. As a result of the simulation study, the safety stock quantities have been measured according to customer satisfaction and low backorder quantities. Srivastav and Agrawal [7] focused on an inventory problem for the products of monopolistic and captive markets. They used a hybrid backorder inventory model to compare the results of particle swarm optimization and genetic algorithm. Sadeghi et al. [8] handled vendor managed inventory model with fuzzy demand for a single-vendor multi-retailer supply chain. They aimed to minimize the total inventory by considering the warehouse capacity and number of orders as constraints. They used hybrid imperialist competitive algorithm (HICA) to find a near-optimum solution and compared the result of this algorithm with simulated annealing algorithm. Kundu et al [9] suggested an economic production quantity (EPQ) model under fuzzy environment. They obtained this model by combining fuzzy differential equation and α-cut of the total profit. They utilized an integrated algorithm including particle swarm optimization and genetic algorithm in order to find optimal solution. Keizer et al. [10] studied on relationship between inventory planning and maintenance planning. They mentioned that inventory control of the spare parts is related to effectiveness of the maintenance. So, they applied joint optimization of condition-based maintenance and spares planning for multi-component systems in order to minimize the unit average costs. Prak et al. [11] discussed efficiency of the safety stock inventory models determined in the environment of demand variety. They suggested batch ordering policies combined with moving average and exponential smoothing forecasts.

3. MATERIALS AND METHODS

This study was realized in an international company operating in the chemical industry. The company aims to maximize its profit by optimizing production, inventory, backorder and sales quantities during its planning period. For this reason, it is initially aimed to realize this study for a group of products before generalized it to all product groups. Therefore, the products shown similar production characteristics are divided into sub-groups at this paper.

Since, each production environment has its own constraints, it is necessary to develop solution approaches according to these constraints. Mathematical programming models are effectively utilized to solve optimization problems like determination of production quantity, sales quantity, inventory and backorder levels. The production plan is revealed as daily, weekly or monthly according to production constraints using some data such as demand, sales and production capacity. In our study, the demand of each product is shown in Table 1.

Table 1. The demand of each product for 6 months period

Products	Month 1	Month 2	Month 3	Month 4	Month 5	Month 6	Month 7

Product 1	8434	9784	9446	10186	9291	9758	10168
Product 2	1596	1077	1337	1142	1246	999	1041
Product 3	84	221	0	91	71	149	155
Product 4	130	0	39	13	117	0	0
Product 5	32	6	6	32	0	0	0
Product 6	1427	1687	2050	1285	1739	1531	1595
Product 7	1920	2141	1894	2790	1959	2829	2948
Product 8	7863	9148	9291	10679	12041	11756	12250
Product 9	52	19	78	26	32	47	49
Product 10	0	26	6	32	19	32	34

The other variables considered in the scope of production-sales-inventory balance are presented in Table 2.

Table 2. Price, cost, inventory and production capacity data for each product

		Cost			**Quantity**		
Products	**Unit Selling Price**	**Unit Holding Cost**	**Unit Backorder Cost**	**Unit Production Cost**	**Production Capacity**	**Beginning Backorder**	**Beginning Inventory**
Product 1	1137	10	253	631	10734	0	8036
Product 2	1200	145	316	568	1515	0	3186
Product 3	1137	158	253	568	631	0	144

Product 4	1263	164	379	631	379	0	76
Product 5	1263	139	379	606	379	0	40
Product 6	1515	208	505	783	2526	0	6169
Product 7	3157	442	884	1263	2526	0	1134
Product 8	101	25	38	57	8840	0	1528
Product 9	1768	170	631	985	253	0	117
Product 10	1642	177	631	909	253	0	23

Parameters and decision variables:

Parameters:

i= 1,2,….,10 number of products

m= 1,2,…,6 months

SP_i : Unit selling price of product i ($\forall i = 1, \dots ,10$)

HC_i : Holding cost of product i for one period ($\forall i = 1, \dots ,10$)

BC_i : Backorder cost of product i for one period ($\forall i = 1, \dots ,10$)

PC_i : Production cost of product i ($\forall i = 1, \dots ,10$)

D_{im} : Demand of product i at month m ($\forall i = 1, \dots ,10;\ \forall m = 1, \dots ,6$)

Cap_i : Production capacity of product i ($\forall i = 1, \dots ,10$)

W_{cap} : Warehouse capacity

SS_{im} : the safety stock quantity of product i at month m ($\forall i = 1, \dots ,10;\ \forall m = 1, \dots ,6$)

Decision variables:

S_{im}: the sold quantity of product i at month m ($\forall i = 1, \dots ,10;\ \forall m = 1, \dots ,6$)

P_{im} : the quantity of production of product i at month m ($\forall i = 1, \dots ,10;\ \forall m = 1, \dots ,6$)

B_{im} : the backorder quantity of product i at month m ($\forall i = 1, \dots ,10;\ \forall m = 1, \dots ,6$)

EP_{im} : the ending period inventory of product i at the end of month m ($\forall i = 1, \dots ,10;\ \forall m = 1, \dots ,6$)

Mathematical Model

$$\text{MaxZ}=\sum_{i=1}^{10}\sum_{m=1}^{6} S_{im} * SP_i - \left(\sum_{i=1}^{10}\sum_{m=1}^{6} P_{im} * PC_i + \sum_{i=1}^{10}\sum_{m=1}^{6} EP_{im} * HC_i + \sum_{i=1}^{10}\sum_{m=1}^{6} B_{im} * BC_i\right) \quad (1)$$

Subject to:

$$S_{im} \le D_{im} \qquad \forall i, m \qquad (2)$$

$$P_{im} \leq Cap_i \qquad \forall i,m \qquad (3)$$

$$P_{im} \leq D_{im} \qquad \forall i,m \qquad (4)$$

$$EP_{im} \geq SS_{im} \qquad \forall i,m \qquad (5)$$

$$EP_{im} = EP_{i(m-1)} + P_{im} - S_{im} - B_{i(m-1)} + B_{im} + SS_{im} \qquad \forall i,m \qquad (6)$$

$$\sum_{i=1}^{10} EP_{im} \leq Wcap \qquad \forall m \qquad (7)$$

$$S_{im}, P_{im}, B_{im}, EP_{im}, SS_{im} \geq 0 \qquad \forall i,m \qquad (8)$$

$$S_{im}, P_{im}, B_{im}, EP_{im}, SS_{im} \in Z^+ \qquad \forall i,m \qquad (9)$$

Equation (1) is the objective function and aims to maximize the profit. Constraint (2) ensures that the sold quantity of product cannot exceed the demand of the product. Constraints (3) and (4) guarantee that production quantity cannot exceed production capacity and demand, respectively. Constraint (5) ensures that ending period inventory should be higher or equals to safety stock quantity. Safety stock quantity is determined as the quartile of the demand of next month. Constraint (6) gives the inventory balance equations of each product. Constraint (7) ensures that the total amount of ending period inventory cannot exceed the capacity of the warehouse. Finally, constraints (8) and (9) provide not being negative and being integer, respectively

In this section, production programming problem at the chemical company was modeled as integer linear programming and solved by IBM ILOG Cplex 10.0 to find the optimum quantities of production, sales, backorder and ending period inventory of each product for 6 months period.

4. RESULTS AND DISCUSSION

Several optimization models could be applied in production, material planning and supply chain management successfully. The production planning model should be dynamic and enables to obtain new results according to current demand values. In this study, we aimed to develop a mathematical model to maximize the profit by determining the optimal production, sales, ending inventory and backorder levels. By the result of solver program the objective function value was obtained as 28.362.045 TRY. Besides, monthly stock amounts were calculated as 26.572, 40.299, 30.286, 34.140, 37.923 and 45.000 tons according to warehouse capacity constraint, separately. As a result, the optimization model will be extended for all groups of products and for whole year.

REFERENCES

[1]. Aydin Keskin, G., Ilhan Omurca, S., Aydin, N., Ekinci, E., A comparative study of production–inventory model for determining effective production quantity and safety stock level, Applied Mathematical Modelling, vol. 39, pp. 6359-6374, 2015.
[2]. Mousavi, S.M., Sadeghi, J., Niaki, S.T.A., Alikar, N., Bahreininejad A., Metselaar, H.S.C., Two parameter-tuned meta-heuristics for a discounted inventory control problem in a fuzzy environment, Information Sciences, vol. 276, pp. 42–62, 2014.
[3]. San-José, L.A., Sicilia, J., García-Laguna, J., Analysis of an EOQ inventory model with partial backordering and non-linear unit holding cost, Omega, vol. 54, pp. 147–157, 2015.
[4]. Kumar, A., Evers, P.T., Setting safety stock based on imprecise records, Int. J. Production Economics, vol. 169, pp. 68–75, 2015.
[5]. Zoysa, D.C.L.D., Rupasinghe, T.D., Development of a Safety Stock Optimization Model with High Demand Uncertainties for Winery Supply Chains (WSCs), Proceedings of the 1st Manufacturing & Industrial Engineering Symposium 22 October 2016, Colombo, Sri Lanka.
[6]. Boulaksil, Y., Safety stock placement in supply chains with demand forecast updates, Operations Research Perspectives vol. 3, pp. 27–31, 2016.
[7]. Srivastav, A., Agrawal, S., Multi-objective optimization of hybrid backorder inventory model, Expert Systems With Applications vol. 51, pp. 76–84, 2016.
[8]. Sadeghi J., Mousavi S.M., Niaki, S.T.A., Optimizing an inventory model with fuzzy demand, backordering, and discount using a hybrid imperialist competitive algorithm, Applied Mathematical Modelling vol. 40, pp. 7318–7335, 2016.
[9]. Kundu, A., Guchhait P., Pramanik, P., Maiti, M.K., Maiti, M., A production inventory model with price discounted fuzzy demand using an interval compared hybrid algorithm, Swarm and Evolutionary Computation vol. 34, pp. 1–17, 2017.
[10]. Keizer, M.C.A.O., Teunter, R.H., Veldman, J., Joint condition-based maintenance and inventory optimization for systems with multiple components, European Journal of Operational Research vol. 257, pp. 209–222, 2017.
[11]. Prak, D., Teunter, R., Syntetos, A., On the calculation of safety stocks when demand is forecasted, European Journal of Operational Research vol. 256, pp. 454–461, 2017.

ICETI
www.iceti.org
2018
07-11 MARCH
BUDAPEST
HUNGARY
II. INTERNATIONAL CONFERENCE ON ENGINEERING TECHNOLOGY AND INNOVATION

Comparison of Color Values of Polyester Fabrics Woven from Conventional and Microfilament Yarns

Halil Ibrahim Icoglu[1], Hatice Kubra Kaynak[2]

Abstract

In this study, determination and comparison of color properties of satin weave polyester dyed fabrics woven from conventional filaments and microfilaments with different weft sett values is aimed. 5 end Satin polyester woven fabrics with different weft yarns of 3 different filament fineness values (0.33 dtex, 0.76 dtex, 3.05 dtex) and three different weft sett values (45 wefts/cm, 47 wefts/cm and 49 wefts/cm) were dyed with a disperse blue dye by exhaust dyeing method in three different depth of shades (0.5% owf, 1.5% owf, 3% owf) at 130 °Cin the same bath. Color measurement was carried out using a reflectance spectrophotometer (Datacolor 650) under illuminant D65/10° standard observer with the specular component included. The average of four measurements for each fabric was taken by rotating 90° clockwise after each measurement. For all dyed samples, CIELAB coordinates (L, a*, b*, C*, h), total color difference (ΔE*) and K/S values were determined according to the reflectance values by the software of the spectrophotometer. K/S values were recorded at wavelength of maximum absorption. It is observed that L* values decrease and K/S values increase when filament fineness values decrease. It is also seen that ΔE* values of the fabric with 0.33 dtex microfilament are higher than that of 0.76 dtex microfilament according to that of 3.05 dtex filament. L* and K/S values of the fabrics with three weft sett construction are similar.*

Keywords: microfilament, woven fabric, color values, polyester, disperse dye

1. INTRODUCTION

Synthetic fiber industry has been enforced to make developments due to the increasing performance demand for textile products. One of the most important developments in synthetic fiber industry, is absolutely producing extremely fine fibers which are named as microfibers and nanofibers. Until today, there is no exact definition for microfibers. But common opinion is defining a fiber finer than 1 dtex or 1 denier as microfiber. Fabrics produced from microfilaments are superior to conventional fiber fabrics, due to their properties such as light weight, durability, waterproofness, windproofness, breathability and drapeability [1-8]. Since microfibers have an increased surface area, resulting in a dyeing rate four times higher than that of normal which can cause unlevelness in dyeing. They require more dyestuff than normal fibers to attain a given shade depth [6,9,10].

Understanding the differences of dyeing mechanisms between microfibers and conventional fibers is an important issue for textile dyers. So that, in the literature studies are available that define the dyeing behavior and dye diffusion mechanism of microfibers [11-13]. On the other hand, some researchers studied on the effects of filament fineness on dyeing, color strength, color difference and color reflectance properties of polyamide [14] and polyester [15-18] fabrics to understand this topic in a detailed manner. Also there are some studies on the prediction of percentage reflectance of microfiber fabrics comprising the different yarn counts, filament fineness, weft density and weave pattern [19,20].

[1] *Gaziantep University, Metallurgical and Materials Engineering Department, Gaziantep / TURKEY*

[2] *Gaziantep University, Textile Engineering Department, Gaziantep / TURKEY*

2. MATERIALS AND METHODS

2.1. Materials

Sample fabrics were produced with 4/1 (five end) Satin weave type. Different weft sett values were applied as 45, 47, 49 wefts/cm. The warp sett was constant for all samples as 85 warps/cm. For weft, polyester textured yarns of 110 dtex linear density with 0.33 dtex, 0.76 dtex and 3.05 dtex filament linear density were used. For warp 82.5 dtex polyester yarn with 1.14 dtex filament fineness was used. By this way 9 different woven fabric samples were produced.

2.2. Fabric Production

Sample fabrics were woven by a conventional loom with an electronic dobby shedding mechanism and rapier weft insertion at a loom speed of 420 rpm. Warp sheet was prepared with a 185 cm reed width. Before desizing process, sample fabrics were treated thermal fixation process to obtain dimensional stability. Thermal fixation process was done with a stenter which has 8 chambers at 195ºC with 25 m/min process speed.

Structural properties namely, weft sett, fabric weight and fabric thickness of sample fabrics were determined according to TS 250 EN 1049-2 (1996), TS EN 12127(1999) and TS 7128 EN ISO 5084 (1998), respectively. Cover factor of samples were determined as the proportion of covered area of the fabric to the total area. The structural properties of fabric samples are given in Table 1.

Table 1. The structural properties of satin woven fabrics

Weave type	Weft yarn filament fineness, dtex	Adjusted weft sett, wefts/cm	Actual weft sett, wefts/cm	Warp sett, warps/cm	Fabric weight, g/m²	Fabric thickness, mm	Cover factor
4/1 Satin	3.05	44	**45**	85	132	0.23	0,857
	0.76	44	**45**	85	132	0.22	0,857
	0.33	44	**45**	85	133	0.23	0,857
	3.05	46	**47**	85	133	0.23	0,862
	0.76	46	**47**	85	134	0.23	0,862
	0.33	46	**47**	85	136	0.23	0,862
	3.05	48	**49**	85	136	0.23	0,867
	0.76	48	**49**	85	138	0.23	0,867
	0.33	48	**49**	85	138	0.23	0,867

According to Table 1, there is no thickness difference among the samples. Also there is an increase of fabric weight and cover factor with increasing of weft sett value.

2.3. Dyeing Operation

The sample fabrics were dyed with a disperse blue dye (Setapers Blue CE3R®) by exhaust dyeing method in three different depth of shades (0.5% owf, 1.5% owf, 3% owf) at 130 ℃ in the same bath. Reductive washing was applied after dyeing. Termal IR Lab dyeing machine was used for dyeing operations. The recipe and dyeing program are given in Table 2 and Figure 1.

Table 2. The dyeing recipe

Disperse dye, %	**0,5-1,5-3**
Dispersing agent, g/L	1
Acetic acid, g/L	1
Liquor ratio	1:15
pH	4-5

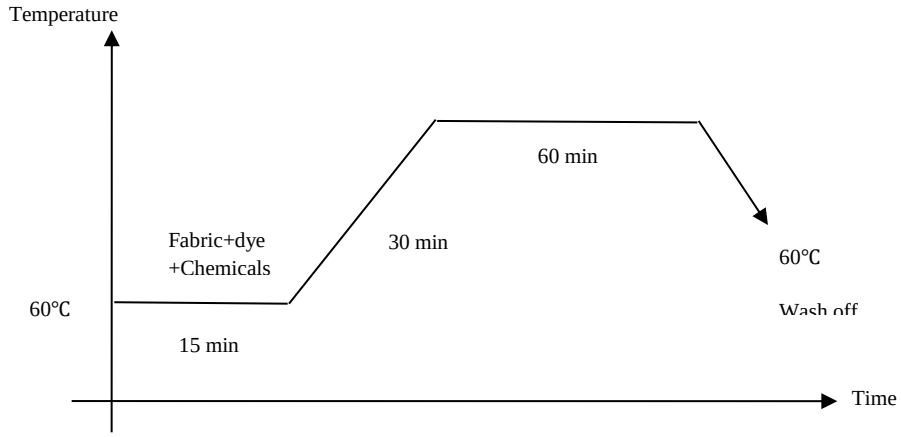

Figure 1. The dyeing program

2.4. Color Measurement

Color measurement was carried out using a reflectance spectrophotometer (Datacolor 650®) under illuminant D65/10º standard observer with the specular component included. The average of four measurement for each fabric were taken by rotating 90º clockwise after each measurement. For all dyed samples, CIELAB coordinates (L*, a*, b*, C*, h), total color difference (ΔE*) and K/S values were determined according to the reflectance values by the software of the spectrophotometer. K/S values were recorded at wavelength of maximum absorption.

3. RESULTS AND DISCUSSION

The coding system is applied for the samples in the following tables. “S” is used for satin, “45/47/49” are used for weft sett, and “36/144/333” are used for “3,05dtex / 0,76dtex / 0,33dtex”, respectively. Since, 36 filaments in 110 dtex yarn cross section provide 3.05 dtex filament linear density, while 144 filaments provide 0.76 dtex linear density and 333 filaments provide 0.33 dtex linear density. Also L/M/D are used for depth of shade as 0,5%owf / 1,5%owf / 3%owf, respectively. Table 3 shows the all color measurement results of the samples with 45 and 49 weft sett values. Table 4 shows lightness (L*), color strength (K/S) and total color difference (ΔE*) values of the samples according to weft sett.

Table 3. Color values of the dyed samples

Sample Fabrics	**L***	**a***	**b***	**C***	**h**	**K/S**	**ΔE***
S4536L	48,78	-1,57	-37,34	37,37	267,59	5,3501	

S45144L	48,61	-2,24	-37,07	37,14	266,54	5,5411	0,74
S45333L	47,73	-2,66	-36,78	36,88	265,86	5,9698	1,61
S4536M	35,8	4,92	-39,87	40,17	277,03	12,16	
S45144M	34,87	5,52	-40,58	40,96	277,75	13,25	1,32
S45333M	33,93	5,95	-40,92	41,36	278,28	14,401	2,38
S4536D	34,59	3,93	-37,19	37,39	276,03	12,465	
S45144D	33,55	4,85	-38,05	38,36	277,26	13,587	1,64
S45333D	32,21	5,85	-38,59	39,03	278,62	15,03	3,37
S4936L	50,64	-2,52	-36,59	36,68	266,06	4,7409	
S49144L	48,23	-2,19	-37,06	37,13	266,62	5,697	2,48
S49333L	48,1	-2,78	-36,65	36,75	265,66	5,7979	2,56
S4936M	36,08	4,72	-39,71	39,99	276,78	11,889	
S49144M	34,68	5,79	-40,73	41,14	278,1	13,36	2,04
S49333M	33,81	6,25	-41,15	41,62	278,63	14,484	3,09
S4936D	34,95	3,69	-36,98	37,16	275,7	12,107	
S49144D	33,3	4,98	-37,89	38,21	277,49	13,591	2,28
S49333D	32,21	5,72	-38,32	38,75	278,49	14,815	3,67

Table 4. L, K/S and ΔE* values of the dyed samples according to weft sett*

Sample Fabrics	**L***	**K/S**	**Sample Fabrics**	**L***	**K/S**	**ΔE***	**Sample Fabrics**	**L***	**K/S**	**ΔE***
S4536L	48,78	5,35	S45144L	48,61	5,54	0,74	S45333L	47,73	5,97	1,61
S4736L	49,03	5,25	S47144L	48,52	5,61	0,85	S47333L	48,54	5,65	1,57
S4936L	50,64	4,74	S49144L	48,23	5,70	2,48	S49333L	48,10	5,80	2,56
S4536M	35,8	12,16	S45144M	34,87	13,25	1,32	S45333M	33,93	14,41	2,38
S4736M	35,93	11,99	S47144M	35,29	13,04	1,47	S47333M	33,85	14,49	2,88
S4936M	36,08	11,89	S49144M	34,68	13,36	2,04	S49333M	33,81	14,48	3,09
S4536D	34,59	12,47	S45144D	33,55	13,59	1,64	S45333D	32,21	15,03	3,37
S4736D	34,96	12,27	S47144D	33,31	13,6	2,26	S47333D	32,01	15,09	3,92
S4936D	34,95	12,11	S49144D	33,3	13,60	2,28	S49333D	32,21	14,82	3,67

According to Table 3 and Table 4, it can be seen that lightness and color strength values of the dyed fabrics are not affected by weft sett difference due to they have similar results. However, weft sett increases from 45 to 49, total color difference values increase. Also, it is seen that total color difference values (ΔE*) of 0,33dtex filaments are higher than that of 0,76dtex filaments for all shades. Figure 2 and Figure 3 show lightness and color strength values results according to fiber fineness, respectively.

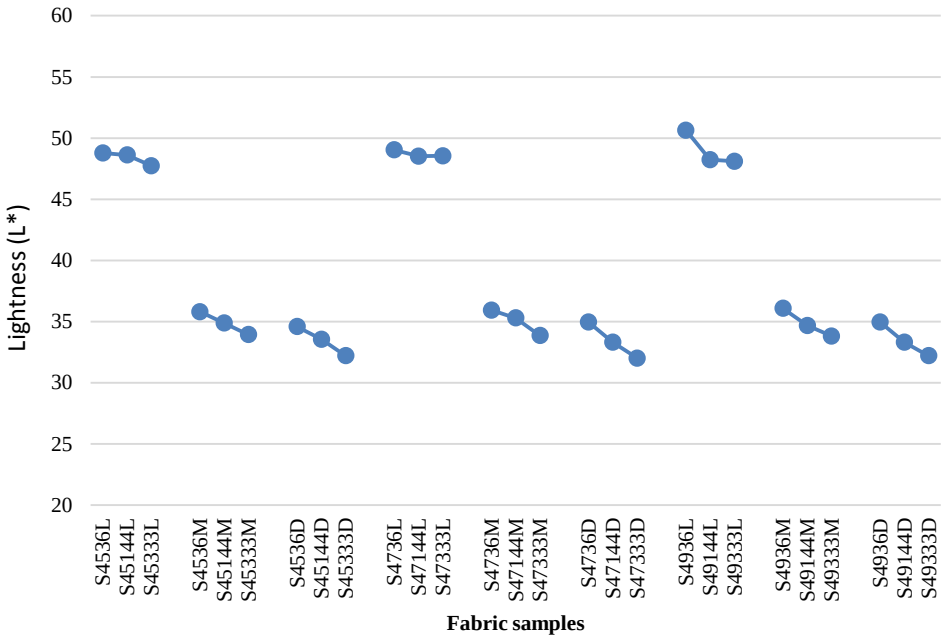

Figure 2. Lightness values of the samples according to filament fineness

According to Figure 2, it can be said that when fiber fineness increases, lightness values decreases. It can be related the difference of number of filaments for the same diameter of yarn. There is higher number of filaments for microfilament yarn than conventional yarn. So, surface structure will be different for microfilament yarns. Due to the fact that lightness are depended on surface characteristics instead of chemical structure, microfilament yarns show lower lightness values than conventional filament yarn.

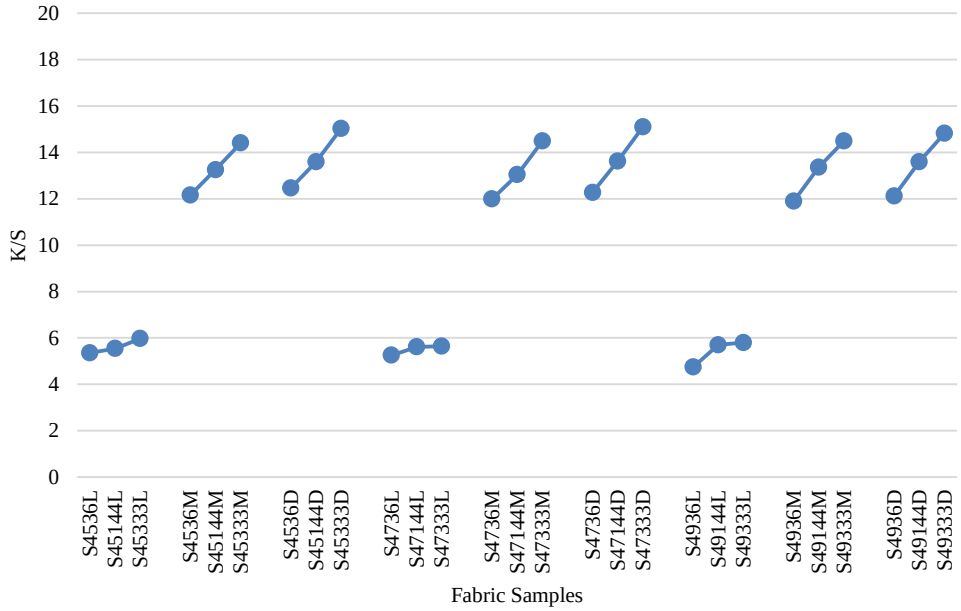

Figure 3. K/S values of the samples according to filament fineness

According to Figure 3, it can be said that when fiber fineness increases, K/S values increases. It may be related the difference of surface area of filaments with different fineness values. When filament diameter decreases, total fiber surface area in fabric structure increases. This situation may lead to increase dyeing property. That means it can be obtained same color strength by using lesser amount of dye for microfilament yarns than conventional yarns.

4. CONCLUSIONS

In this study, color properties of polyester Satin dyed fabrics woven from conventional filament and microfilaments with different weft sett values were determined. 5 end Satin polyester woven fabrics with different weft yarns of 3 different filament fineness values (0.33 dtex, 0.76 dtex, 3.05 dtex) and three different weft sett values (45 wefts/cm, 47 wefts/cm and 49 wefts/cm) were dyed with a disperse blue dye by exhaust dyeing method in three different depth of shades (0.5% owf, 1.5% owf, 3% owf), and color values were measured by a spectrophotometer. It was seen that, change in weft sett values has no effect on color values for both conventional filament and microfilament polyester fabrics. Also, microfilament fineness values affected lightness, color strength and total color difference values at all dyeing shades.

REFERENCES

[1]. P. Leadbetter, S. Dervan, "The microfiber step change", *Journal of the Society of Dyers and Colourists*, 1992, Vol. 108, No. 9, pp.369–371.
[2]. R. Bianchi, R. Maglione, "Manufacturing of fine denier filaments", In: *Polyester: 50 Years of Achievement*, Tomorrow's Ideas and Profits, D. Brunnschweiler & J. Hearle (Eds), 1993, pp.196-198, Stanley Press, Dewsbury, England.
[3]. S.V. Purane, N.R. Panigrahi, "Microfibers, microfilaments and their applications", *AUTEX Research Journal*, 2007, Vol.7, No.3, pp.148-158.
[4]. A. Basu, "Microfibers: Properties, processing and use", *Asian Textile Journal*, 2001, Vol.10, No.4.
[5]. S. Mukhopadhyay, "Microfibers – An Overview", *Indian Journal of Fiber & Textile Research*, 2002, Vol.27, No.3, pp.307-314,
[6]. B.V. Falkai, "Production and properties of microfibers and microfilaments", *The Indian Textile Journal*, 1991, No.2, pp.62-70.

[7]. J. Rupp, A. Yonenaga, "Microfibers-The new man made fiber image", *International Textile Bulletin*, 2000, No.4, pp.12-24.
[8]. H.K. Kaynak, O. Babaarslan, "Polyester Microfilament Woven Fabrics". In Han-Yong Jeon (Ed.) *Woven Fabrics*, 2012, (pp.155-178). InTech Publishing, Croatia.
[9]. G. Jerg, J. Baumann, "Polyester microfibers: A new generation of fabrics", *Textile Chemists and Colorists*, 1990, Vol.22, No.12, pp.12-14.

[10]. Anonymous, "Recent advancements in man-made textiles", *New Cloth Market*, 2000, Vol.14, No.4, pp.13-14.
[11]. C. Keqiang, C. Zhongxun, X. Jianwei, "Analyzing the dyeing behavior and chromaticity characteristics of polyester microfibers", *Textile Research Journal*; Apr 2002; 72, 4; ProQuest Science Journals p. 367-371.
[12]. M. Casetta and V. Koncar, "Modeling of the diffusion during polyester dyeing - a survey", Proceedings 14th European Simulation Symposium
[13]. K. H. Park and V. Koncar, "Diffusion of disperse dyes into supermicrofibres", *AUTEX Research Journal*, Vol. 4, No1, 2004.
[14]. C. Makhlouf, C. Kacem, S. Roudesli and F. Sakli, "Dyeing Behaviour of Unmodified and Modified Polyamide 6.6 Fibers of Different Levels of Fineness", 2008, *Journal of Applied Sciences*, 8: 77-85.
[15]. A. S. Young, T. L Hyeong, P. H.Jin, K. K. Tae, "Indigo adsorption properties to polyester fibers of different levels of fineness", 2005, *Dyes and Pigments* 65:137-143.
[16]. M. Akgun, B. Becerir, H. R. Alpay, "Assessing the Relationship among Fabric Constructional Parameters, Fractional Reflectances and Cover Factors of Polyester Fabrics by Experimental and Mathematical Methods", 2010, *Fibers and Polymers*, Vol.11, No.2, p. 291-302.
[17]. M. Akgun, B. Becerir, H. R. Alpay, "Effect of sample layer numbers and fabric constructional parameters on colour strength, colour difference and colour matching properties of polyester woven fabrics", 2017, *The Journal of The Textile Institute*, 108:1, p. 102-109.
[18]. M. Akgun, B. Becerir, H. R. Alpay,, "The effect of fabric constructional parameters on percentage reflectance and surface roughness of polyester fabrics", 2012, *Textile Research Journal* 82(7):700–707.
[19]. M. Akgun, B. Becerir, H. R. Alpay,, "Reflectance Prediction of Colored Polyester Fabrics by a Novel Formula", 2014, *Fibers and Polymers*, Vol.15, No.1, 126-137.
[20]. M. Akgun, B. Becerir, H. R. Alpay,, "Usage of proportions method for predicting percentage reflectance of woven structures in fabric design", 2015, *Indian Journal of Fibre & Textile Research*, Vol 40, No 3.

ICETI
www.iceti.org
2018
07-11 MARCH
BUDAPEST
HUNGARY
II. INTERNATIONAL CONFERENCE ON ENGINEERING TECHNOLOGY AND INNOVATION

Bursting Strength of Knitted Fabrics Produced from of Polybutylene Terephthalate (PBT) Yarns with Different False-Twist Texturing Parameters

Halil Ibrahim Celik[1], Esin Sarioglu[1], Hatice Kubra Kaynak[1]

Abstract

Polybuthylene Terephtalate (PBT) is a semi-aromatic polyester. It provides advantages such as high elasticity, ease of dyeing at lower temperatures. Due to its especially high elasticity property, PBT fiber became popular in textile industry with an increasing rate and used for the production of many textile applications such as; underwear, sport cloths, carpet, hosiery etc. In this study, it is intended to reveal the effect of temperature of heating zone and draw ratio on bursting strength and distension performances of the knitted fabric samples produced form PBT yarns. For this aim, partially oriented (POY) 110 dtex/24 filament PBT yarn samples were applied to false-twist texturing process with three different heating temperatures (175, 200, 225 0C) and three different draw ratios (1.2, 1.4, 1.6). Totally, 9 false-twist textured stretch PBT yarn samples were produced. Then, knitted fabric samples were prepared under same conditions and with same fabric structural parameters. In order to obtain bursting strength and bursting distension values, the knitted fabric samples were applied bursting strength test. It was concluded that temperature parameter has a significant effect only on bursting distension performance and draw ratio has significant effect on both bursting strength and distension performances.

Keywords: Bursting strength, Bursting distension, Polybuthylene terephtalate, Texturing, False-twist

1. INTRODUCTION

Polybuthylene Terephtalate (PBT) is a semi-aromatic polyester. The polymer production of PBT is similar to Polyethylene Terephtalate (PET) synthesis and involves direct esterification and ester interchange polymerization (Figure 1). During the condensation reaction of the dihydric alcohol with terephthalic acid, ethylene glycol is replaced by butanediol with four methylene groups [1]. PBT had a lower Tdi (initial degradation temperature) value, lower tensile strength and similar surface characteristics compared to regular PET. On the other hand, PBT has higher stretch and recovery performance than standard PET. Besides, PBT provides a good form fitting property to the fabric and chlorine resistance [2,3]. These performance properties make PBT fibers suitable for swimsuits. Due to their especially high elasticity property, PBT fibers became popular in textile industry with an increasing rate and used for the production of many textile applications such as; underwear, sport cloths, carpet, hosiery etc.

In order to introduce more softness, bulk, warmth and extensibility, synthetic continuous filaments yarns are exposed to some mechanical, thermal or chemical processes. These processes are called as texturing. The texturing process parameters have significant effects on physical and mechanical characteristics of the filament yarns. Since the yarn properties have important influence on fabric performance, it is considered that the texturing parameters may affect the fabric mechanical properties.

[1] *Gaziantep University, Textile Engineering Department, Gaziantep / TURKEY*
Corresponding author:tuluce@gantep.edu.tr

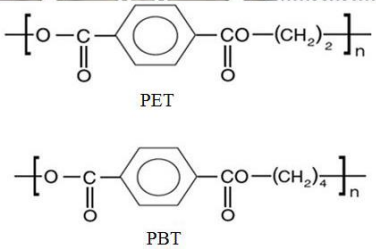

Figure 1. Molecular formula of PET and PBT [4]

In literature, there are some studies on PET and PBT fiber properties and also influence of texturing parameters of these fibers on yarn and fabric performance properties [3-9].

In this study, it is intended to reveal the effect of temperature of heating zone and draw ratio on knitted fabric bursting strength performance. For this aim, partially oriented (POY) 110 dtex/24 filament PBT yarn samples were applied false-twist texturing process with three different heating temperatures (175, 200, 225 ^{0}C) and three different draw ratios (1.2, 1.4, 1.6). Totally, 9 false-twist textured stretch PBT yarn samples were produced. Then, knitted fabric samples were prepared under same conditions and with same fabric structural parameters. In order to obtain bursting strength and bursting distension values, the knitted fabric samples were applied bursting strength test in accordance with BS EN ISO 13938-1:1999 standard. The effect of texturing parameters (heating zone temperatures, draw ratios) on knitted fabric bursting strength was investigated by performing ANOVA. The statistical software package SPSS 21.0 was used to interpret the experimental data. All test results were assessed at 95% confidence interval.

2. MATERIAL AND METHOD

In this study, 110 dtex/ 24 filaments PBT POY yarn was used as material. The yarn sample is applied false-twist texturing process with three different temperatures; 175, 200, 225 ^{0}C and three different draw ratios; 1.2, 1.4, 1.6. Totally, 9 false-twist textured PBT yarn samples were obtained. Texturing process was carried out by Oerlikon Barmag brand false-twist texturing machine. All texturing parameters given in Table 1 were kept constant during the sample manufacturing. Yarn strength and elongation was done according to the standard of ASTM D 2256-02. 110dtex/24 filament PBT POY yarn strength was 41.7 cN/tex and elongation was 116%. Single jersey structure knitted fabric samples were then produced by using PBT yarn samples via a 3.5" gauge, 22 fein and one feeder sample circular knitting machine at 20±2 rev/min production speed. The fabric structural properties are submitted in Table 2.

The course and wale densities were measured according to TS EN 14971:2006 [10]. The fabric thickness and fabric mass were determined in accordance with the standards TS 7128 EN ISO 5048:1998 [11], TS EN 12127:1999 [12], respectively. The yarn loop lengths were measured according to the standard TS EN 14970:2006 [13]. All the fabric samples were conditioned in standard atmosphere according to TS EN ISO 139 [14] (65±4% relative humidity and 20±2 0C temperature) for 24 h before the tests.

Table 16. Texturing parameters

Texturing speed, m/min	450
Disc surface speed / Yarn speed	1.90
% Spin Finish	1.2
Friction disc configuration	1+5+1

Table 2. Fabric structural properties

Samples	Thickness, mm	Fabric mass, g/m²	Loop density, loops/cm²	Loop length, mm
1	0.62	98	323	3.5
2	0.62	78	305	3.4
3	0.59	72	323	3.3
4	0.62	94	318	3.2

5	0.65	83	293	3.1
6	0.63	81	368	3.3
7	0.6	83	337	3.2
8	0.65	89	294	3.2
9	0.66	86	378	3

In order to obtain bursting strength and bursting distension values, the knitted fabric samples were applied bursting strength test in accordance with BS EN ISO 13938-1:1999 standard [15]. James Heal Truburst pneumatic bursting strength test device was used at 7.3 cm^2 test area. The test sample was laid over diaphragm and clamped by means of a circular clamping dome. Increasing compressed air pressure was applied to the underside of the diaphragm and so the diaphragm and fabric was forced to distention. The pressure was increased smoothly until the test specimen burst. The bursting strength and distension are measured. The measurements were repeated five times from different parts of the samples. After five bursting measurements were completed, diaphragm correction procedure was applied. In this procedure, the diaphragm was distended without the presence of the specimen with the same test area and same rate of increase in volume to burst the previous specimen tests. Then, the pressure at this distension was noted as diaphragm pressure and subtracted from the initial pressure values.

3. RESULTS AND DISCUSSION

Bursting strength results of the knitted fabric samples are given in Figure 2. It is observed that, as the draw ratio of the filament during texturing process is increased, the bursting strength of the fabrics decreased for all texturing temperatures. When the effect of temperature change is investigated for each draw ratio, it can be said that there is no consistency or general trend for all draw ratios. For all draw ratio values, the bursting strength values at 175 and 200 ^{0}C temperatures are close to each other. However, some difference is observed for 225 ^{0}C values and other two temperature levels for all draw ratios.

Bursting distention results of the knitted fabric samples are given in Figure 3. Any remarkable difference is not determined in relation to temperature and draw ratio changes.

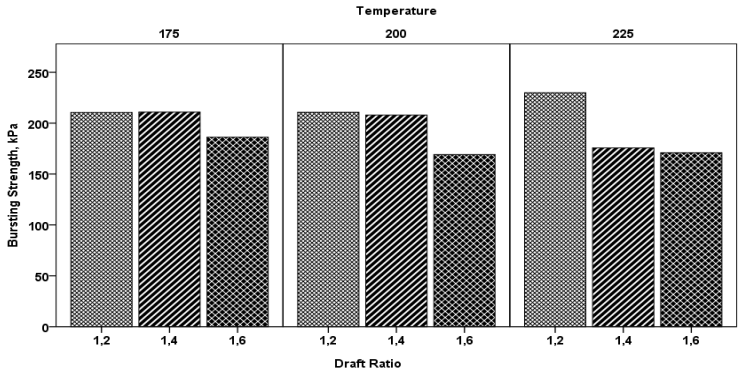

Figure 2. Bursting strength results of fabric samples

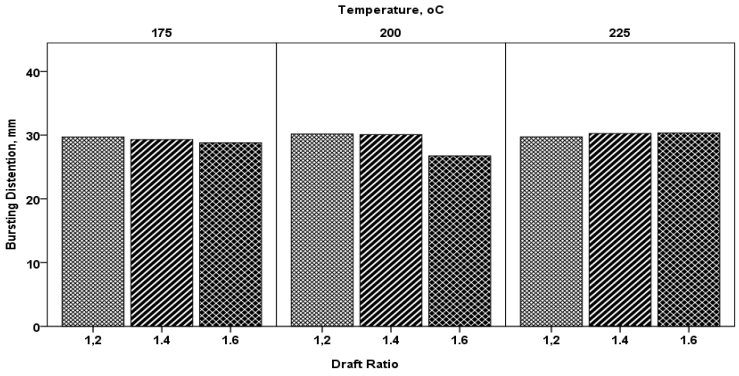

Figure 3. Bursting distension results of fabric samples

In order to determine the effect of independent variables; texturing temperature and draw ratio on fabric bursting strength and distension, AVONA was applied in %95 confidence level. As it can be followed from Table 3, temperature parameter has a significant effect only on bursting distension performance. Draw ratio has significant effect ($p<0.05$) on both bursting strength and distension performances. When the interaction between temperature and draw ratio are considered, there is a statistically significant interaction between these independent variables for both bursting strength and distention.

In order to determine which temperature level provide statistically significant difference on bursting distention, multiple comparison test was done (Table 4). It is seen that 225 ^{o}C temperature has a statistically significant difference from 200 ^{o}C temperature level by providing higher bursting distention values.

Table 3. ANOVA for bursting strength and distention

Source	Dependent Variable	Type III Sum of Squares	df	Mean Square	F	Sig.
Corrected Model	burstingstrength	18960,607[a]	8	2370,076	15,818	,000
	Bursting distention	51.510[b]	8	6.439	5.319	.000
Intercept	Bursting strength	1744002.427	1	1744002.427	11639.279	.000
	Bursting distention	39049.230	1	39049.230	32257.281	.000
Temperature	Bursting strength	830.646	2	415.323	2.772	.076
	Bursting distention	10.007	2	5.004	4.133	.024
Draftratio	Bursting strength	13029.448	2	6514.724	43.479	.000
	Bursting distention	15.543	2	7.772	6.420	.004
Temperature * Draftratio	Bursting strength	5100.513	4	1275.128	8.510	.000
	Bursting distention	25.960	4	6.490	5.361	.002
Error	Bursting strength	5394.156	36	149.838		
	Bursting distention	43.580	36	1.211		
Total	Bursting strength	1768357.190	45			

	Bursting distention	39144.320	45
Corrected Total	Bursting strength	24354.763	44
	Bursting distention	95.090	44

a. R Squared = .779 (Adjusted R Squared = .729)

b. R Squared = .542 (Adjusted R Squared = .440)

Table 4. Multiple comparison of bursting distention performance with regard to temperature effect

Dependent Variable	(I) Temperature	(J) Temperature	Mean Difference (I-J)	Std. Error	Sig.	95% Confidence Interval Lower Bound	95% Confidence Interval Upper Bound
bursting distention	175	200	.2667	.40176	.786	-.7153	1.2487
		225	-.8400	.40176	.106	-1.8220	.1420
	200	175	-.2667	.40176	.786	-1.2487	.7153
		225	-1.1067*	.40176	.024	-2.0887	-.1247
	225	175	.8400	.40176	.106	-.1420	1.8220
		200	1.1067*	.40176	.024	.1247	2.0887

Based on observed means.

The error term is Mean Square(Error) = 1.211.

*. The mean difference is significant at the .05 level.

In order to compare the bursting strength and distension performances of the fabric samples in relation to the draw ratio changes, multiple comparison test was applied (Table 5). According to multiple comparison test (Table 5), it is determined that there is significant difference between each draw ratio values in terms of bursting strength performance. As the draw ratio value increases, the bursting strength value decreases. This situation can be explained with the effect draw ratio on polymer crystallinity. As the draw ratio increases, it will cause higher orientation between monomers and higher crystallinity. The higher crystallinity of polymer results in higher strength and rigidity. On the other hand, higher crystallinity will decrease the polymer elongation. It can be concluded that this lower elongation value makes the fabric material less resistive to bursting strength under multi-directional tensile forces. In accordance with the bursting distension comparison, it is determined that there is significant difference between 1.6 draw ratio and other two draw ratios of 1.2 and 1.4. There is no significant difference between the bursting distention performances of fabric samples 1.2 and 1.4 draw ratios.

Table 5. Multiple comparison of bursting strength and distention performance with regard to draw ratio effect

Dependent Variable	(I) Draftratio	(J) Draftratio	Mean Difference (I-J)	Std. Error	Sig.	95% Confidence Interval

						Lower Bound	Upper Bound
bursting strength	1.2	1.4	18.8667*	4.46972	.000	7.9414	29.7920
		1.6	41.6200*	4.46972	.000	30.6947	52.5453
	1.4	1.2	-18.8667*	4.46972	.000	-29.7920	-7.9414
		1.6	22.7533*	4.46972	.000	11.8280	33.6786
	1.6	1.2	-41.6200*	4.46972	.000	-52.5453	-30.6947
		1.4	-22.7533*	4.46972	.000	-33.6786	-11.8280
bursting distention	1.2	1.4	-.0133	.40176	.999	-.9953	.9687
		1.6	1.2400*	.40176	.011	.2580	2.2220
	1.4	1.2	.0133	.40176	.999	-.9687	.9953
		1.6	1.2533*	.40176	.010	.2713	2.2353
	1.6	1.2	-1.2400*	.40176	.011	-2.2220	-.2580
		1.4	-1.2533*	.40176	.010	-2.2353	-.2713

Based on observed means.

The error term is Mean Square(Error) = 1.211.

*. The mean difference is significant at the .05 level.

4. CONCLUSION

As a result of the study, it is concluded that texturing temperature parameter has significant effect only on bursting distension performance. Draw ratio of the filaments has significant effect ($p<0.05$) on both bursting strength and distension performances. However, it can be revealed that the bursting strength values of the fabric samples decreases with the temperature increases. On the other hand, there is significant difference between each draw ratio values in terms of bursting strength performance. As the draw ratio increases, the bursting strength decreases. In accordance with the bursting distension comparison, it is determined that there is only significant difference between 1.6 draw ratio and other two draw ratios of 1.2 and 1.4.

ACKNOWLEDGMENT

Authors are grateful to Ozkaya Group and Kasim GULLU for their cooperation and contribution.

REFERENCES

[1]. J. Hu , J. Lu, Y. Zhu, "New developments in elastic fibers", *Polymer Reviews*, vol. 48:2, pp. 275-301, 2008.
[2]. F.F. Yildirim, A. Yavas, O. O. Avinc, "Polibutilen tereftalat liflerine genel bakis", *Tekstil ve Muhendis*, vol. 19: 87, pp. 29-42, 2012.
[3]. H. Kadoglu, K. Dimitrovski, A. Marmarali, P. Celik, G. B. Bayraktar, T. B. Ute1, G. Ertekin, A. Demšar, K. Kostanjek, "Investigation of the characteristics of elasticised woven fabric by using pbt filament yarns", *AUTEX Research Journal*, vol. 16:2, pp. 109-117, 2016.
[4]. S. K. Koc, S. Duzyer, A. Hockenberger, "A new approach to determination of the instability of air-jet textured yarns", *Journal of Engineered Fibers and Fabrics*, vol. 10:1, pp. 152-157, 2015.
[5]. R. Tomisawa, T. Ikaga, K.H. Kim, Y. Ohkoshi, K. Okada, H. Masunaga, T. Kanaya, M. Masuda, Y. Maeda, "Effect of draw ratio on fiber structure development of polyethylene terephthalate", *Polymer*, vol.116, pp. 357-366,2017.

[6]. R. Tomisawa, T. Ikaga, K.H. Kim, Y. Ohkoshi, K. Okada, H. Masunaga, T. Kanaya, M. Masuda, Y. Maeda, "Effect of melt spinning conditions on the fiber structure development of polyethylene terephthalate", *Polymer*, vol.116, pp.367-377,2017.
[7]. B. Arik, E. Bozaci, A. Demir, E. Ozdogan,"Thermogravimetric, microscopic and mechanical analyses of PBT and PET yarns", *Tekstil ve Konfeksiyon*, vol.23(2), pp. 101-106,2013.
[8]. D. Štrukelj, K. Dimitrovski, "Study of cotton woven fabrics with added polybutylene terephthalate yarns", *Tekstil*, vol. 61:(1-6), pp. 18-24, 2012.
[9]. E. Sarioglu, O. Babaarslan, H. K. Kaynak, H. I. Celik, "Yalanci bukum teksture parametrelerinin Polibutilen Tereftalat (PBT) ipliklerin yorulma sonrasi mekanik ozellikleri uzerindeki etkilerinin incelenmesi", *II. Lif Ve Polimer Arastirmalari Sempozyumu*, pp. 85-86, 27-28 April, Bursa, 2017.
[10]. TS EN 14971:2006 Textiles - Knitted fabrics - Determination of number of stitches per unit length and unit area.
[11]. TS 7128 EN ISO 5048:1998-Textiles - Determination of thickness of textiles and textile products.
[12]. TS EN 12127: 1999 Textiles- Fabrics - Determination of mass per unit area using small samples.
[13]. TS EN 14970:2006 Textiles – Knitted fabrics - Determination of stitch length and yarn linear density in weft knitted fabrics.
[14]. TS EN ISO 139: 2008 Textiles-Standard atmospheres for conditioning and testing.
[15]. BS EN ISO 13938-1:1999 Textiles. Bursting properties of fabrics. Hydraulic method for determination of bursting strength and bursting distension

BIOGRAPHY

H.Ibrahim CELIK was born in 1981 in Gaziantep Turkey. He graduated from Gaziantep University Textile Engineering Department in 2004. He received M.Sc. degree in 2007 from Gaziantep University Textile Engineering Department and Ph.D. degree in 2013 from Gaziantep University Mechanical Engineering Department. In 2005, he joined Gaziantep University Textile Engineering Department as a research assistant and became Assistant Professor in 2014. His current research interests include weaving technology, woven fabrics, textile quality, image processing, machine vision systems, neural network.

ICETI
www.iceti.org
2018
07-11 MARCH
BUDAPEST
HUNGARY
II. INTERNATIONAL CONFERENCE ON ENGINEERING TECHNOLOGY AND INNOVATION

The Effect of Preform Preheating on Microstructural and Mechanical Features of 80% CP-Ti Reinforced A356 Matrix Composite

Ridvan Gecu[1], Ahmet Karaaslan[1]

Abstract

Commercially pure titanium (CP-Ti) reinforced A356 aluminum matrix composites were fabricated by melt infiltration casting. Nearly same sized CP-Ti sawdusts were assembled under 440 MPa pressure to procure one-piece preforms with 20% porosity. The vacancies of the preforms were filled by molten A356 alloy in a plaster mould at 700°C under 10^{-5} Pa vacuum atmosphere. CP-Ti preforms were preheated in a plaster mould for 0, 30, 60 and 240 minutes before infiltration to determine the effects of preform preheating on microstructural and mechanical features of manufactured composites. A356 alloy was melt at 790°C in an electrical furnace for casting operation. After melt infiltration casting, A356 matrix composites containing 80% CP-Ti reinforcement were successfully manufactured. Produced specimens were characterized by light optical microscopy and micro-Vickers hardness measurements. $TiAl_3$ intermetallic phase was obtained at Al/Ti interfaces of 0 and 240 min preheated samples. Oxide film formed during preheating acted as a barrier to Al diffusion and only mechanical bonding was observed for 30 and 60 min preheated specimens. Excessive preheating caused thicker oxide film which was broken because of its increasing brittleness when it was exposed to molten A356 alloy during casting. Due to broken oxide film, Al alloy diffused in Ti part and $TiAl_3$ phase was formed for 240 min preheated sample. The average $TiAl_3$ hardness of 0 and 240 min preheated samples was calculated 474 and 507 HV0.01, respectively.

Keywords: A356 alloy, commercially pure titanium, melt infiltration casting, composite

1. INTRODUCTION

Aluminum has been attracted attention for a long time due to increased demand for lightweight materials. Al alloys have several advantageous properties including low density, low thermal expansion coefficient and good corrosion resistance [1]. Besides, under favour of its relative low melting temperature, Al alloys can be manufactured by many processing techniques. Because of its widespread availability of production methods, Al alloys have been widely used as a matrix in the composite structure [2]. Mainly, ceramic reinforcements have been used to strengthen Al matrix owing to high specific strength, high hardness and good wear resistance of ceramics [3]. However, reinforcing with ceramic particles adversely affects on the original ductility and toughness of Al alloy. Undesired phase formations at the interface and wettability failure between ceramic and Al alloy are the main problems of the Al matrix composite (AMC) production with ceramic reinforcements [4].

Metal reinforcements have huge potential to replace ceramic reinforcements with environmentally friendly and lower cost production techniques, without sacrificing worthwhile mechanical or tribological properties. Titanium especially have a promising future to be used for strengthening Al matrix due to its low density, high elastic modulus, high strength/density ratio and good fatigue strength [2]. The applied load during operating conditions can be transferred from Al matrix to Ti reinforcement thanks to the plastic deformation ability of Ti particles [5].

Wu et al. [6] studied Al matrix composites reinforced with the mixture of graphite fibers and Ti particles. At about 700 °C, the formation of $TiAl_3$ phase was proved by DSC curve. When the reaction temperature was set at 1000 °C, in addition to $TiAl_3$ formation, Ti_3Al, TiC and Al_2O_3 were also formed. At the temperature of 1300 °C, TiO_2 diffraction

[1] *Yildiz Technical University, Department of Metallurgical and Materials Engineering, 34220, Esenler/Istanbul, Turkey. gecur@yildiz.edu.tr, karaas@yildiz.edu.tr*

peaks were also detected while $TiAl_3$ peaks were weakened. It was understood from this study that the temperature must be controlled so that undesired phases have not been occurred.

$TiAl_3$ is the most promising intermetallic compound (IMC) compared to other IMCs formed at the Al/Ti interface. This phase has low density, good oxidation resistance, high modulus of elasticity and high temperature strength [7]. Guo et al. [8] revealed that $TiAl_3$ prevented the propagation of nucleated cracks by transferring externally applied load from the softer Al matrix to the reinforcement.

It is not possible to produce metal-metal composite production by every method. For example, according to Karthik et al. [9], conventional stir casting method is not suitable for metal-metal composite manufacturing. Instead, Hassan and Gupta [10] proposed a process called Disintegrated Melt Deposition (DMD) and some other researchers [5, 11] use powder metallurgy (PM) to fabricate metal-metal composites. Another way to produce AMCs with Ti reinforcements is melt infiltration casting. By this method, very high volume fraction of reinforcement phase in composite structure can be possible. Method is based on the infiltration of Al melt into porous preforms consisting of reinforcement shavings, under vacuum atmosphere [12].

In this work, commercially pure Ti (CP-Ti) reinforced A356 Al matrix composites were manufactured via melt infiltration casting with several CP-Ti preform preheating times (0, 30, 60 and 240 min). Pouring temperature of A356 alloy was 790 °C for all composites. Light optical microscopy and micro-Vickers hardness examinations were carried out for the characterization of the final products.

2. EXPERIMENTAL

In melt infiltration casting method, wax was used as a pattern and the mixture of investment powder and water at the ratio of 40% was used as a mould. Wax pattern was made by pouring of molten wax into silicon mould at 85 °C and holding there until solidification was completed. The sprue was attached to the wax pattern (25 mm in diameter and 50 mm in height) and they were placed in stainless steel perforated flask. Castable plaster slurry was prepared by the mixture of 500 g investment powder and 200 g water. Investment powder was composed of silica and calcium sulphate. The plaster slurry, obtained by mixing of investment powder and water for 3 min, was poured in perforated flask and held under vibration for 20 min. After the hardening of plaster mould, dewaxing process was carried out at 110 °C and the mould cavity was obtained.

CP-Ti shavings taken from turning machine were combined together under 440 MPa pressure to get a monoblock preform with 20% porosity. 440 MPa was a result of trial and error method. This pressure provided 80% of the theoretical density of CP-Ti preforms experimentally. In further process, the remaining 20% was infiltrated by A356 Al melt under vacuum atmosphere.

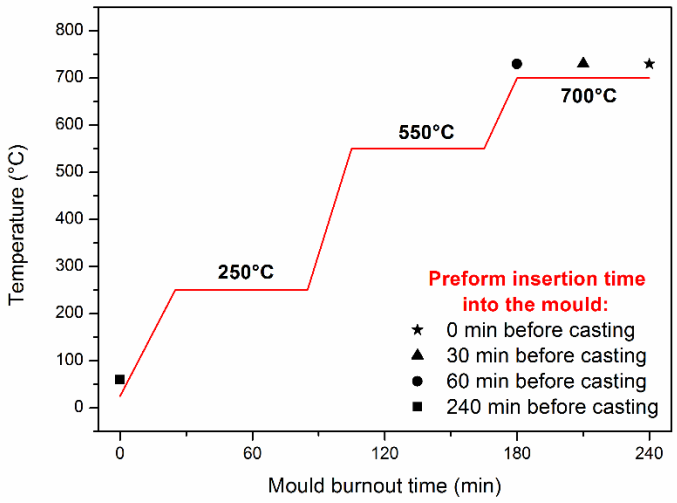

Figure 21. Burnout process for plaster mould used in melt infiltration casting

CP-Ti preforms were settled in mould cavity before melt infiltration casting for preheating process. Preheating prevents rapid solidification of liquid Al alloy and increases the solid/liquid interaction time. While one of the preforms were settled in the mould at the same time with casting, the other preforms were preheated for 30, 60 and 240 min in the

mould. Burnout regime of the plaster mould was given in Fig. 1 schematically. As pointed out, plaster mould was gradually heated up to 700 °C in three steps. Samples preheated for 0, 30 and 60 min were settled in the mould when the temperature was 700 °C in furnace. Sample preheated for 240 min was placed in the mould at the initial stage of burnout regime.

When the mould burnout process was finished, perforated flask was placed in vacuum chamber and molten A356 alloy was poured into the mould immediately. A356 alloy was melt at different furnace at 790 °C during burnout process. Under 10^{-5} Pa vacuum pressure, Al infiltration into the vacancies of CP-Ti preform was carried out. The mould was water-cooled after solidification was done and the composite production was accomplished. Chemical compositions of A356 Al and CP-Ti were reported in Table 1. The illustration of melt infiltration casting process was given in Fig. 2.

Table 17. Chemical compositions of A356 matrix and CP-Ti reinforcement

Alloy	C	Si	Mn	Cr	Mg	Cu	Zn	Ni	O	Fe	Ti	Al
A356	-	7.0	0.1	-	0.35	0.2	0.1	-	-	0.2	0.2	Bal.
CP-Ti	0.1								0.2	0.3	Bal.	-

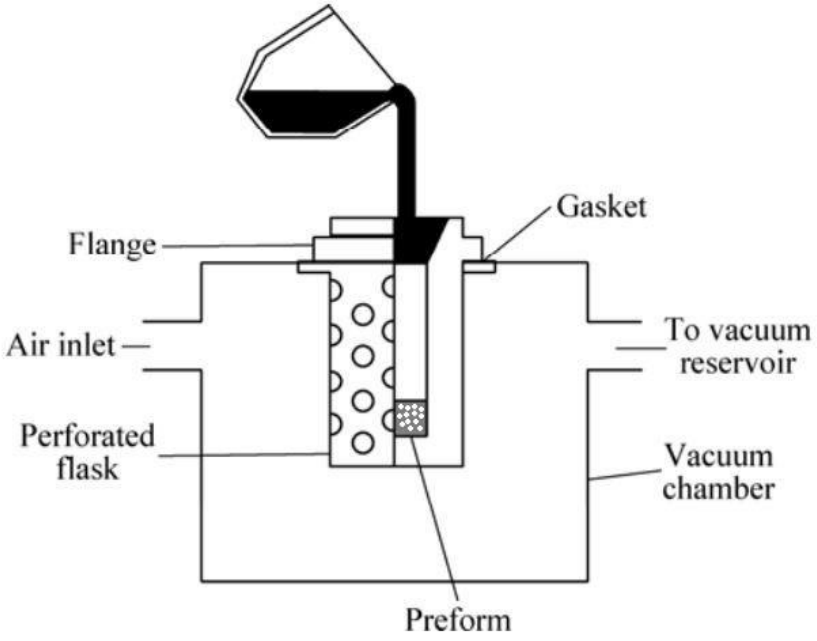

Figure 2. Illustration of melt infiltration casting

Cross sections of manufactured composite samples were embedded in a cold resin and their microstructures were examined via light optical microscope following to grinding and polishing. Micro-Vickers hardness tester was used to measure the hardness of formed phases individually. 100 mN load was applied in 120 steps with the interval of 1 s. Samples were held for 10 s under 100 mN following by removing applied load as it was indented. The average results of 10 random measurements were given for each formed phase and each specimen. Microstructures and hardness results of composite structures were discussed as functions of preform preheating times.

3. RESULTS AND DISCUSSION

A356 matrix composites reinforced with CP-Ti were successfully produced by melt infiltration casting without any infiltration problem although CP-Ti preform included just 20% emptiness in its structure. Vacuum assistance allowed Al alloy to infiltrate in even the narrowest regions of CP-Ti. Fig. 3 shows low-magnification micrographs of CP-Ti reinforced A356 matrix composites with varied preform preheating times. Formed intermetallic compounds (IMCs) at

the interfaces were indicated in Fig. 3(a) and Fig. 3(d), with the help of red arrows. For 30 min and 60 min preheated specimens, it was observed that just mechanical bonding was occurred at the interface between Al and Ti. For 0 and 240 min preheated sample, in addition to strong mechanical bond, metallurgical bond was also obtained. Al matrix must hold CP-Ti shavings together and transfer the applied load during operating conditions to the reinforcement phase. A356 alloy was constituted 20% of the composite structure. This amount was sufficient to transmit applied load from Al matrix to more strength CP-Ti phase.

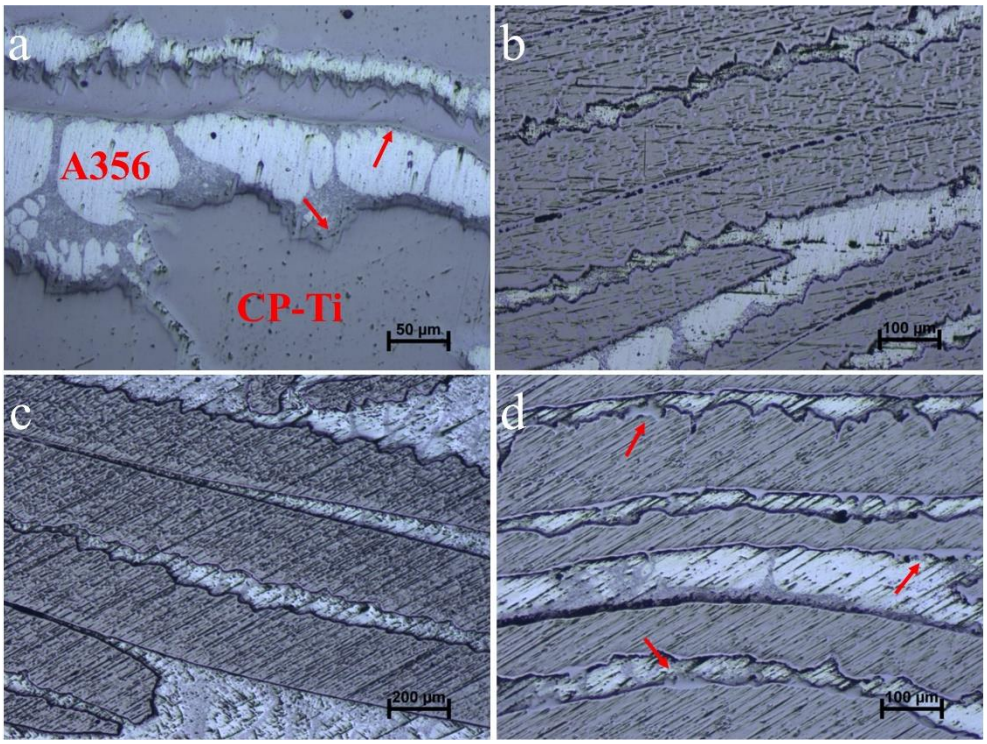

Figure 3. Low-magnification micrographs of CP-Ti reinforced A356 matrix composites for (a) 0, (b) 30, (c) 60 and (d) 240 min preform preheating times

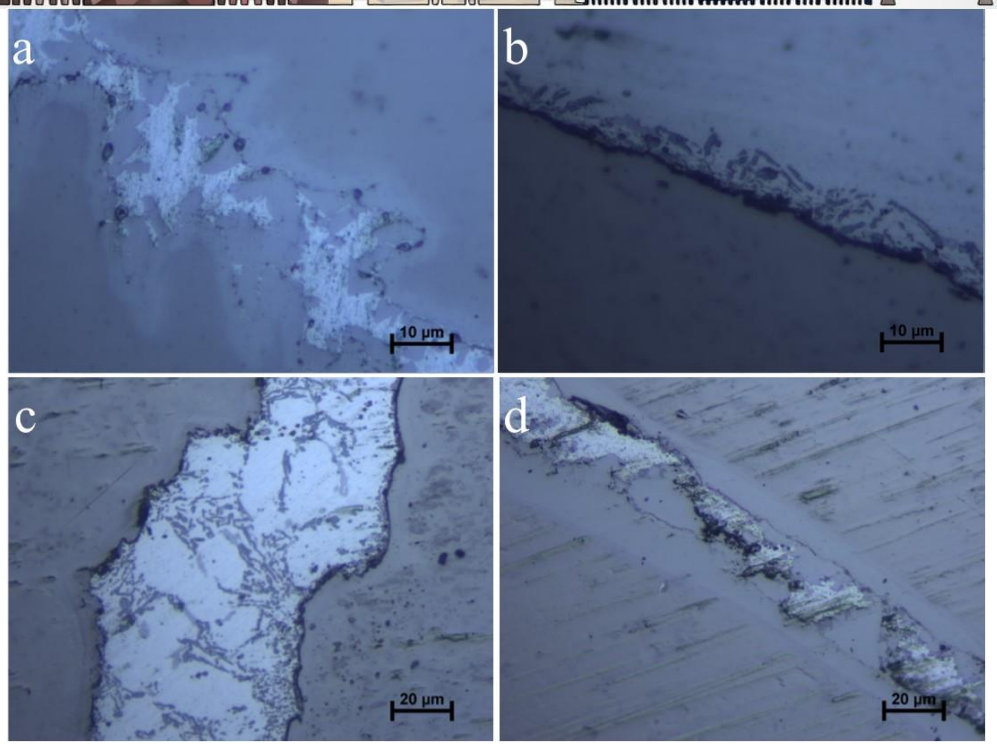

Figure 4. High-magnification micrographs of CP-Ti reinforced A356 matrix composites for (a) 0, (b) 30, (c) 60 and (d) 240 min preform preheating times

High-magnification optical microscope images were demonstrated in Fig. 4. IMCs were seen much more clearly for 0 and 240 min preheated samples in Fig. 4(a) and Fig. 4(d), respectively. Although IMC was not occurred in specimens preheated for 30 and 60 min, their interfaces were still strong due to the strong mechanical bonding at the interface. In non-preheated sample, temperature gradient between CP-Ti and A356 alloy was huge. Considering all produced composites, it can be surely said that solidification time of A356 alloy was the lowest in this sample. Still, composite components found sufficient time to diffuse in each other until solidification was completed and thusly IMC was formed at the interface. Since CP-Ti preforms were not preheated, this sample was not exposed to oxidative environment in the furnace. For 30 and 60 min preheated samples, it can be obviously seen that the black oxide layer was covered the interface. This oxide layer was grown on CP-Ti preforms in the furnace prior to casting and prevent the diffusion of the composite components during infiltration process. On the other hand, when preheating time was reached up to 240 min, oxide layer thickness was increased excessively and it became very brittle. When A356 melt was poured, thick oxide layer was ruptured and diffusion became possible again. For this time, solid/liquid interaction time between A356 alloy and CP-Ti was increased due to slight difference in temperature gradients. Increasing diffusion rate provided thicker IMC layer at the interface. The average layer thickness of non-preheated sample was measured 4.67 µm while it was 10.51 µm for 240 min preheated sample.

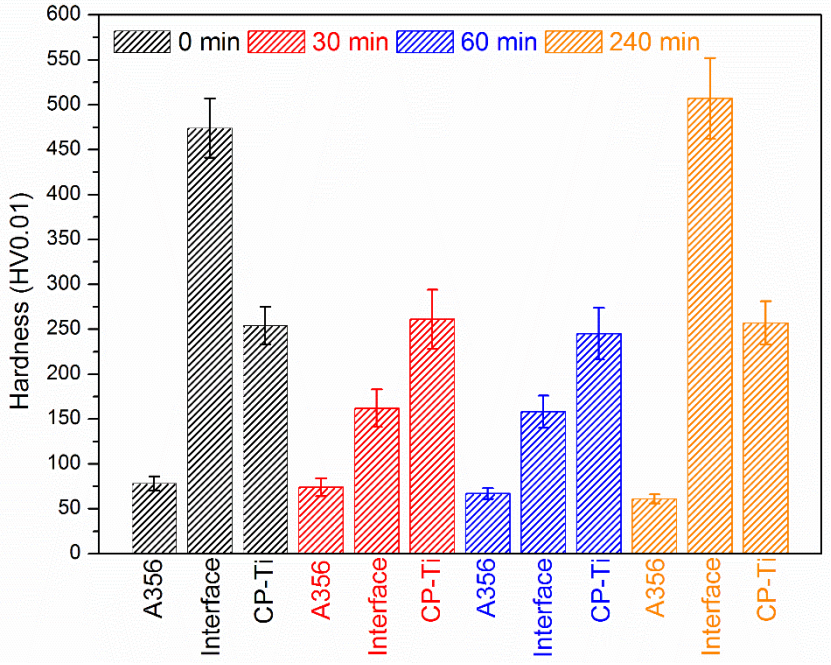

Figure 5. Hardness results of phases formed in composite structure produced with varied preform preheating times

Hardness measurements were also performed following to microstructural investigations. The results of the micro-Vickers hardness of manufactured composites were given in Fig. 5 for Al-sides, interfaces and CP-Ti sides individually. Considering standard deviations, it can be said that the matrix and the reinforcement hardness values did not significantly changed with the preform preheating times. The average hardness of A356 matrix was varied from 61 to 78 HV0.01 whereas the average CP-Ti hardness was measured between 245 and 261 HV0.01. Calculated interface hardness of 30 and 60 min preheated samples was approximately the average of matrix and reinforcement hardnesses. This was an evidence of strong mechanical bond between A356 alloy and CP-Ti. For 0 and 240 min preheated samples, the average hardness of the interface was measured 474 and 507 HV0.01, respectively. These values point out that the chemical composition of IMC is $TiAl_3$ phase. According to Al-Ti phase diagram, when the molten Al interacts with Ti, the first formed reaction phase is $TiAl_3$. Hardness results were matched with Al-Ti phase diagram.

Increase in solidification time provided increasing diffusion of the composite components. Al and Ti atoms were diffused in $TiAl_3$ layer during infiltration and changed the coherent structure to incoherent structure. These atoms caused distortion in $TiAl_3$ layer and consequently $TiAl_3$ hardness was increased with increasing preform preheating times.

4. CONCLUSION

CP-Ti reinforced A356 alloy matrix composite was successfully manufactured by melt infiltration casting at several preform preheating times between 0 and 240 min. Mechanical bonding was observed at all interfaces whereas the metallurgical bonding was obtained in only samples produced with 0 and 240 min preform preheating. In 30 and 60 min preheated samples, formed oxide layer in a furnace during preheating prevented IMC formation at the interface. Non-preheated sample was not exposed to oxidative environment and thusly narrower IMC layer was formed at its interface. In 240 min preheated sample, oxide layer was excessively enlarged and during pouring of A356 alloy, it was demolished by the pressure of liquid Al. Due to its increased solidification time, Ti and Al were much more interacted with each other and thicker IMC layer was formed, by comparison with non-preheated sample. Interface hardnesses of these samples were directly related to IMC thicknesses and it was determined 474 and 507 HV0.01 for non-preheated and 240 min preheated specimens, respectively.

ACKNOWLEDGMENT

This study was supported by Yildiz Technical University Scientific Research Projects Coordination Department with the project number of FBA-2017-3052.

REFERENCES

[1]. D.L. Zalensas, Aluminum Casting Technology, 2nd ed., American Foundry Society, 1997.
[2]. S.K. Thakur, M. Gupta, "Improving mechanical performance of Al by using Ti as reinforcement", *Compos. Part A Appl. Sci. Manuf.*, vol. 38 pp. 1010–1018, 2007.
[3]. V.K. Patel, S.D. Bhole, D.L. Chen, D.R. Ni, B.L. Xiao, Z.Y. Ma, "Solid-state ultrasonic spot welding of SiCp/2009Al composite sheets", *Mater. Des.*, vol. 65 pp. 489–495, 2015.
[4]. K. Landry, S. Kalogeropoulou, N. Eustathopoulos, "Wettability of carbon by aluminum and aluminum alloys", *Mater. Sci. Eng. A.*, vol. 254 pp. 99–111, 1998.
[5]. P. Pérez, G. Garcés, P. Adeva, "Mechanical properties of a Mg–10 (vol.%)Ti composite", *Compos. Sci. Technol.*, vol. 64, pp. 145–151, 2004.
[6]. G. Wu, Y. Liu, Z. Xiu, L. Jiang, W. Yang, "Reaction procedure of a graphite fiber reinforced Ti-Al composite produced by squeeze casting-in situ reaction", *Rare Met.*, vol. 29, pp. 98–101, 2010.
[7]. T. Ai, F. Liu, X. Feng, Q. Yu, N. Yu, M. Ruan, X. Yuan, Y. Zhang, "Processing, microstructural characterization and mechanical properties of in situ $Ti_3AlC_2/TiAl_3$ composite by hot pressing", *Mater. Sci. Eng. A.*, vol. 610, pp. 297–300, 2014.
[8]. B. Guo, S. Ni, R. Shen, M. Song, "Fabrication of Ti–Al_3Ti core–shell structured particle reinforced Al based composite with promising mechanical properties", *Mater. Sci. Eng. A.*, vol. 639, pp. 269–273, 2015.
[9]. G.M. Karthik, G.D.J. Ram, R.S. Kottada, "Friction deposition of titanium particle reinforced aluminum matrix composites", *Mater. Sci. Eng. A.*, vol. 653, pp. 71–83, 2016.
[10]. S.F. Hassan, M. Gupta, "Development of a novel magnesium–copper based composite with improved mechanical properties", *Mater. Res. Bull.*, vol. 37, pp. 377–389, 2002.
[11]. Y.L. Xi, D.L. Chai, W.X. Zhang, J.E. Zhou, "Titanium alloy reinforced magnesium matrix composite with improved mechanical properties", *Scr. Mater.*, vol. 54 pp. 19–23, 2006.
[12]. R. Gecu, H. Atapek, A. Karaaslan, "Influence of preform preheating on dry sliding wear behavior of 304 stainless steel reinforced A356 aluminum matrix composite produced by melt infiltration casting", *Tribol. Int.*, vol. 115, pp. 608–618, 2017.

ICETI
www.iceti.org
2018
07-11 MARCH
BUDAPEST
HUNGARY
II. INTERNATIONAL CONFERENCE ON ENGINEERING TECHNOLOGY AND INNOVATION

The Tensile and Bursting Strength Evaluation of Linear Low Density Polyethylene (LLDPE) Spunbond Fabrics

Esin Sarioglu[1], Hatice Kubra Kaynak[2], Halil Ibrahim Celik[2] and Deniz Vuruskan[1]

Abstract

In the production of the spunbond nonwovens, polypropylene (PP) is the most widely used polyolefin class polymer. PP spunbond nonwovens have many field of use such as agriculture, automotive, household, hygiene and medical, packaging etc. Polyethylene is one of the polyolefins and spunbond nonwovens from this polymer exhibits excellent properties, particularly hand softness and drape. Among the polyethylene group, linear low density polyethylene (LLDPE) has advantages such as good spinnability at lower temperature in comparison with PP. Present study was conducted to evaluate tensile and bursting strength properties of LLDPE spunbond nonwovens and to investigate alternative usage areas instead of PP in the medical textile sector. For this purpose, LLDPE spunbond nonwovens were produced at different weights (40 gsm, 50 gsm, 60 gsm, 80 gsm and 100 gsm). Tensile and bursting strength tests were performed on both wet and dry state spunbond nonwovens samples. Statistical analysis was achieved in order to determine the effect of the weight on bursting and tensile performance of the samples at 95% confidence interval. Results showed that LLDPE spunbond nonwoven fabric with higher weight has higher bursting and tensile properties.

Keywords: *linear low density polyethylene, bursting strength, tensile strength, spunbond nonwoven.*

1. INTRODUCTION

Spunbond nonwovens are widely used all over the world. Today, it has the largest share in various nonwoven fabric manufacturing techniques and finds use in diverse fields such as baby diapers and incontinence products, automotive, geotextiles, civil engineering, medical and packaging [1]. There are various polymers, polypropylene, polyester, polyethylene, polyamide, polyurethane, etc., used for the manufacture of spunbond nonwovens. Among these, polypropylene is the most widely used polymer due to its lower price and higher yield [2]. Meanwhile, polyethylene has excellent chemical resistance; good fatigue behavior, wear resistance and higher impact strength. Lower working temperature is needed than polypropylene polymer and LLDPE polymer has low moisture absorption rates [3]. But, it has been put forward that it is difficult to produce spunbond nonwovens of LLDPE which have more than about 50% of tensile properties manufactured from polypropylene polymers. This advantage makes LLDPE desirable in diaper cover stock, medical and hygiene products [4].

This study provides important contribution to the spunbond nonwovens field such as medical and hygiene by using LLDPE spunbond nonwovens. So, it was focused on tensile and bursting properties of LLDPE spunbond nonwovens with different weights in dry and wet state. LLDPE spunbond nonwovens with 40 gsm, 50 gsm, 60 gsm, 80 gsmand 100 gsmwere manufactured. LLDPE spunbond nonwovens samples were determined in dry and wet state and the results

[1] *Corresponding author: Gaziantep University, Faculty of Fine Arts, Department of Fashion and Textile Design,27310 Sehitkamil/Gaziantep, Turkey,sarioglu@gantep.edu.tr*

[2]*Gaziantep University, Faculty of Engineering, Textile Engineering Department, 27310 Sehitkamil/Gaziantep, Turkey, tuluce@gantep.edu.tr, hcelik@gantep.edu.tr*

were compared.

2. MATERIALS AND METHOD

LLDPE was used with 11.6 g/10 min melt flow index value. The index value was determined at 190 °C temperature and under 2.16 kg load. Nonwoven fabrics with different weights were produced with spunbond technology illustrated in Figure 1.

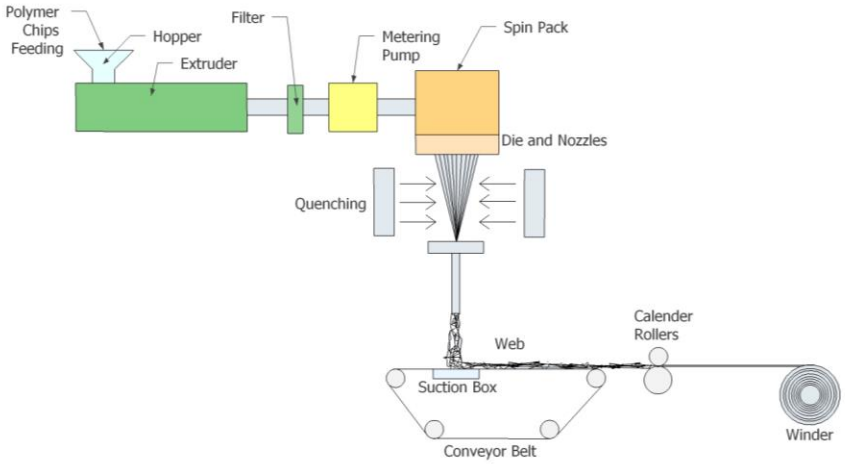

Figure 1. Schematic representation of spunbond nonwoven production

In the production of LLDPE spunbond nonwoven fabrics, some important machine parameters were adapted and determined after several trials. Some important parameters to obtain nonwoven fabrics with different weights are given in Table 1.In order to determine the effect of weight parameter on tensile and bursting performance in wet and dry state, five different weight LLDPE spunbond nonwoven samples were manufactured; 40 gsm, 50 gsm, 60 gsm, 80 gsm and 100 gsm.

Table 1.Main production settings

Production Settings	**Value**
Extrusion Temperature, °C	210-250
Die Temperature, °C	200-240
Die hole diameter, mm	0.043
Calendar Speed, m/min	50-300
Calendar Bonding Temperature, °C	135
Nip Point Pressure, bar	80-90

The nonwoven samples tests were carried out under standard laboratory conditions (20 ± 2 °C and 65 ± 4 %) after the samples had been conditioned for 24 h. Physical properties of fabric samples are given in Table 2. The weight per unit area of LLDPE spunbond nonwovens is expressed in grams per square meter. It was determined by cutting test pieces with 100 cm^2 cutting areas from a nonwoven fabrics by means of dies, and weighing them using a precision scale. The weight of nonwoven samples were determined in accordance with NWSP 130.1.R0 (15) standard in g/m^2 [5]. Thickness of the samples was determined in mm according to NWSP 120.1.R0 (15) standard by using a digital thickness instrument [6].

Table 2. Physical properties of LLDPE spunbond nonwovens

LLDPE Spunbond Nonwoven Samples	Thickness, mm	Weight, gsm
40	0.30	40.3
50	0.35	50.1
60	0.41	61.3
80	0.56	80.2
100	0.67	101.1

Tensile tests were achieved according to NWSP 110.4.R0 (15)-Option B standard in which samples were prepared as 50×200 mm strip [7]. Tensile force was applied at a speed of 100 mm/min for wet and dry nonwovens both in machine direction (MD) and cross direction (CD). The specimens to be tested in the wet state were prepared by immersing in distilled water for 1 hour at a temperature of 20 ± 2 °C until thoroughly wetted. Titan 2 Universal Tester was used to determine tensile properties of nonwovens. When the bursting properties of nonwovens are taken into consideration, samples were tested according to NWSP 030.2.R0 (15) standard by using 50 cm^2 test area in wet and dry condition [8]. Averages of five measurements for all tests from each specimen were taken. To determine and evaluate the significance of weight of LLDPE spunbond nonwovens in wet and dry state on tensile and bursting performances, analysis of variance (ANOVA) was achieved at 95% confidence interval.

3. RESULTS AND DISCUSSION

In Figure 2, breaking force of dry and wet specimens in MD and CD directions are shown.

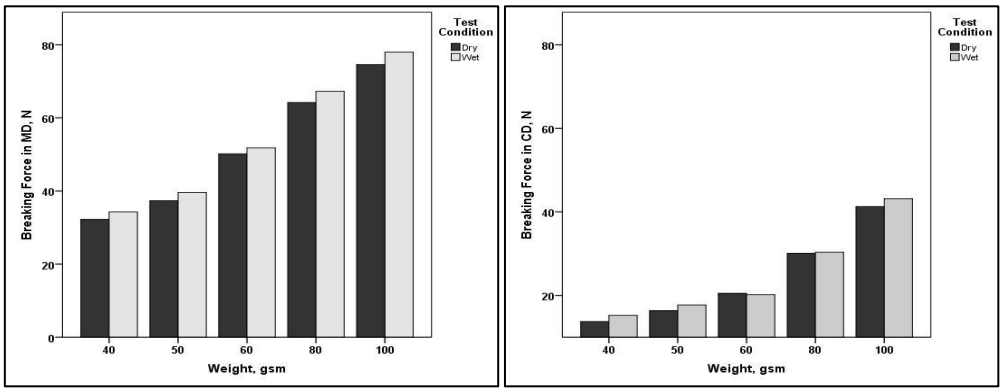

Figure 2. Breaking force of LLDPE spunbond nonwovens in MD and CD

With increase in the fabric weight, more filaments presence within unit square area of the fabric and so, more filaments react efficiently against the tensile force than the lower weight of LLDPE spunbond nonwovens. It can be seen from Figure 2 that the breaking force in MD is higher than that of CD for all fabric weights. MD breaking forces are approximately two times higher than that of CD. As observed from Figure 2, breaking forces of wet fabrics are higher than dry ones in both directions. Since the polyethylene fiber is hydrophobic, this result can be attributed to the fact that the water penetrated and migrated between fibers cause sticking the fibers to each other and so provide a contribution to the breaking force. On the other hand, the difference between wet and dry state breaking forces is not higher. They are close to each other. The breaking elongation changes of LLDPE spunbond nonwovens in both dry-wet states were given in Figure 3.

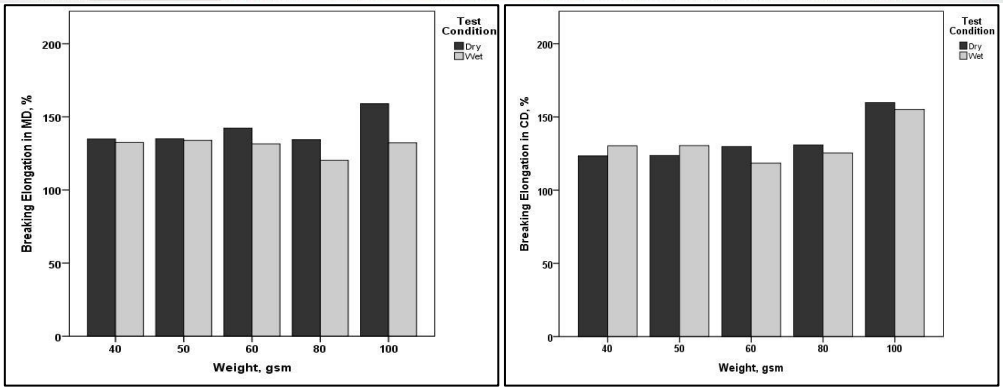

Figure 3. Breaking elongation of LLDPE spunbond nonwovens in MD and CD

There is no increasing or decreasing trend between fabric weights when breaking elongation is considered. In MD, there is only low breaking elongation difference between wet and dry state samples. It seems that the break elongation increase of LLDPE spunbond is not clear in relation to increase in fabric weight. In addition, for CD samples, the breaking elongation of spunbond nonwovens increases with increase in fabric weight for both dry states.

The bursting strength and distention in wet and dry states of spunbond nonwovens are shown in Figure 4 and Figure 5, respectively.

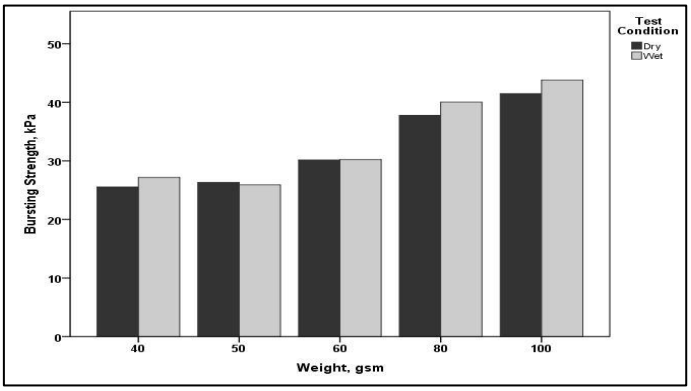

Figure 4. Bursting strength of LLDPE spunbond nonwovens

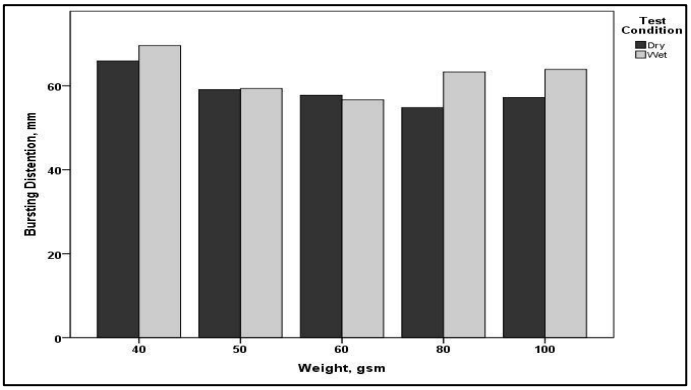

Figure 5. Bursting distention of LLDPE spunbond nonwovens

Similarly to breaking force, bursting strength of LLDPE spunbond nonwovens increase with the increase in fabric weight. According to the orientation of the filament, fabric with more filaments reacts more against multiaxial forces until it burst. Bursting strength of LLDPE spunbond nonwovens obtained in wet state are higher than dry ones except

50 gsm nonwoven. It can also said that penetration of water within the inner structure of the nonwoven contribute also to the bursting strength. On the other hand, bursting distention of nonwovens decreases until 80 gsm then increases for both dry and wet state samples. Highest bursting distention value was obtained with lowest weight i.e. 40 gsm.

In order to determine the importance of fabric weight and wet/dry test state on strength and elongation performances against tensile and multiaxial forces, analysis of variance (ANOVA) was achieved at 0.05 level. ANOVA test result is illustrated in Table 3. The effect of fabric weight was found to be significant ($p<0.05$) on breaking force in both MD and CD, breaking elongation in CD, bursting strength and distention. In addition, test condition has significant effect on breaking force and elongation in MD and bursting distention at 95% confidence interval.

Table 3. ANOVA results for fabric weight and test condition

Independent Parameters	Breaking Force in MD, N	Breaking Elongation in MD, %	Breaking Force in CD, N	Breaking Elongation in CD, %	Bursting Strength, kPa	Bursting Distention, mm
Fabric Weight	0.000*	0.218	0.000*	0.000*	0.000*	0.000*
Wet/Dry State	0.006*	0.028*	0.060	0.742	0.089	0.000*

*statistically significant at $p<0.05$.

4. CONCLUSION

The scope of this study is to produce LLDPE spunbond nonwovens with suitable production parameters and to determine the tensile, bursting properties in wet and dry conditions. The limited production parameters were given because of the company's privacy policy. Results showed that fabric weight has a significant effect on breaking force in both MD and CD, breaking elongation in CD, bursting strength and bursting distention performances of LLDPE spunbond nonwovens. Bursting strength of LLDPE spunbond nonwovens increase with the increase in fabric weight. Bursting strength values obtained in wet state are higher than dry ones except 50 gsm nonwoven. For the further study, it is planned that different form of LLDPE nonwoven fabrics such as spunbond-meltblown-spunbond (SMS)will produced systematically. And also meltblown nonwoven fabrics will be manufactured from LLDPE raw material and optimum system parameters will be determined by several trials.

ACKNOWLEDGEMENTS

This research was supported by Bayteks Teknik Tekstil Company and all samples production was held in this company which is located in Kilis/Turkey. Authors would like to thank to Gokhan Selcuk Gerlikhan and his team for their contribution to this study. Authors would also thank to Super Film Packaging Company for their test analysis contribution.

REFERENCES

[1]. V. K.Midha and A.Dakuri,"Spun bonding technology and fabric properties: aReview", Journal of Textile Engineering & Fashion Technology, vol.1, no.4, pp. 1-9, 2017.
[2]. H.Lim, "A review of spun bond process",Journal of Textile and Apparel, Technology and Management**,** vol. 6, no.3, pp. 1-13, 2010.
[3]. Y.Yesil and G.S.Bhat,"Structure and mechanical properties of polyethylene melt blown nonwovens",International Journal of Clothing Science and Technology, vol.28, no.6, pp. 780-793, 2016.
[4]. S.P. Krupp, E.N. Knickerbocker and J.O. Bieser, "Polyethylene fibers and spunbonded fabric or web", US Patent Number 4,842,922, 1989.
[5]. NWSP 130.1.R0 (15)- Mass per Unit Area.
[6]. NWSP 120.1.R0 (15)-Thickness of Nonwoven Fabrics.
[7]. NWSP 110.4.R0 (15)-Breaking Force and Elongation of Nonwoven Materials (Strip Method)-Option B
[8]. NWSP 030.2.R0 (15)-Nonwovens Burst.

ICETI
www.iceti.org
2018
07-11 MARCH
BUDAPEST
HUNGARY
II. INTERNATIONAL CONFERENCE ON ENGINEERING TECHNOLOGY AND INNOVATION

Applications development for easy learning of Geographical Information Systems

***Abdurrahman Eymen*[1]**

Abstract

There are many methods in literature for ensuring higher level of learning efficiencies of students. There is no study on the learning of spatial analysis used in Geographical Information Systems (GIS) in the literature. Therefore in this paper, it is aimed to visualize spatial analyses with animations made in ArcGIS software in order to especially ensure that students understand better spatial analyses used in GIS. Learning of spatial analysis methods used in GIS are difficult issue for both lecturers and students. As a solution method in this study, in order to overcome these difficulties in the teaching of spatial analysis, animations are created in ArcGIS software. For this purpose, "Animation" module was developed in ArcGIS. The effects of these educational animations made for spatial analysis to successes of students are assessed by using Likert type surveys. According to the evaluation of the results, it is seen that the interests of the students to the spatial analysis increase thanks to the proposed method and the students perform the spatial analysis by reaching current data.

Keywords: Geographical Information System, Spatial Analysis, Animation-Based Learning, Digital Elevation Model

1. INTRODUCTION

One of the main aim of educational study is to identify strategies and conditions that improve learning for all students [1]. Two educational strategies that have received considerable attention in recent years are use of animations and Geographical Information System (GIS). The emergence of new technologies has made them easily accessible. Animations and geographic information systems are used very effectively in spatial analysis. Because these technologies are satisfactory in terms of motivation and learning [2]. At the same time, they accurately reflect changing situations over time. In fact, dynamic representations (animations) were found to be more effective than traditional methods of learning. Animations can be expressed in many forms as dynamic representations of motion generated from different sources, such as video recordings [2, 3].

The main aim of the training is to define new methods that improve learning for all students [4]. Several methods have been developed in the literature for this purpose. These developed methods have been developed to help the learning process of the students. The most commonly used methods are animation based, web based and computer aided learning methods [4, 5].

Animation based learning helps students imagine abstract concepts. In this way, students are informed consciously [6]. This method allows students to get more attention to the lesson [7, 8, 9]. Thus, students have direct access to basic information and prevent learning unnecessary information [9]. Animation based learning is also a positive contribution to visual and auditory learning processes. In previous studies, it has been determined that 10% of students learn by reading, 20% by hearing, 30% by sight, and 50% by hearing and sight [10, 11]. The use of traditional methods distracts the attention of the student after a while [12, 13]. It has been determined that this negative effect can be solved with educational animations [14, 15, 16]. One of the most important reasons for choosing Geographical Information Systems as a decision-making tool is to allow the analysis of graphical and non-graphical data [17]. Spatial analysis is defined as representation of graphical and attribute data on a defined coordinate system and interpretation of data as interpretation of spatial relations [17, 18]. Animations are also effectively used in GIS, where the technology is intensely used. The main aim of the study was to investigate the effects of spatial analysis on learning from animations.

[1] *Corresponding author: Erciyes University, Department of Geomatics Engineering, 38039, Kayseri, Turkey.*
ageymen@erciyes.edu.tr

2. MATERIALS AND METHODS

Digital Elevation Model, Proximity, Extract Operations, Grid, Overlay and Network Analyzes are defined as spatial analyzes. In these analyzes raster and vector data are used together. The spatial analysis and animation processes used in this study were carried out using ArcGIS software. The animation process was performed using the "Animation Module" included in ArcGIS software. The operations performed in ArcGIS software are automatically combined to create animations.

3. RESULTS

In the first example, Digital Elevation Model data will be used. In this example, it is aimed to find places to be affected from natural disasters such as floods, earthquakes and tsunami. Risky regions are calculated using "Raster Calculator" tool of ArcGIS software's.

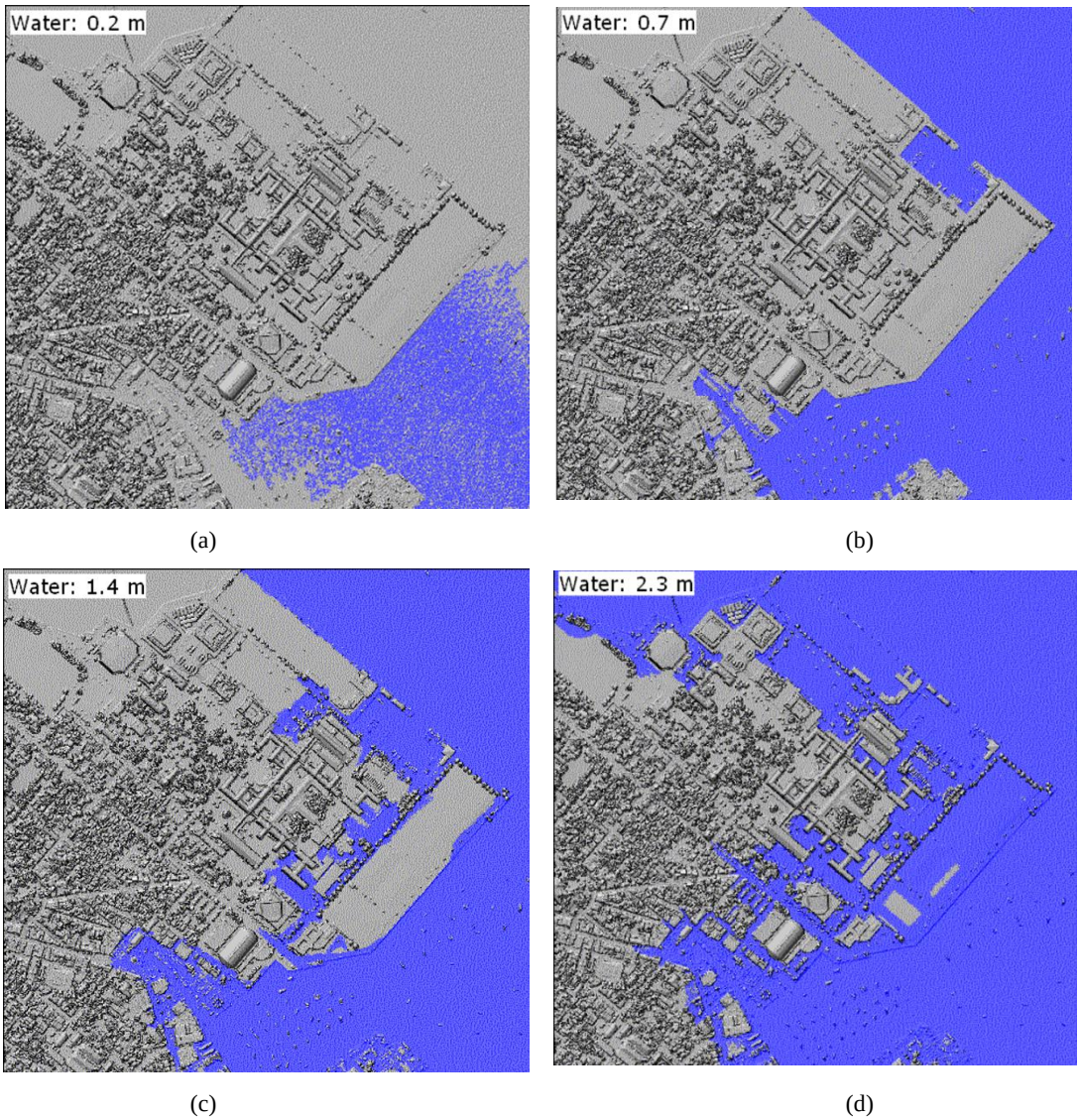

Figure 1. The risky zones will be affected from a periodic increase in water level from sea level

The second example of spatial analysis is an animation of earthquakes from 1903 to 2005. Data on earthquakes from 1903 to 2005 in Turkey were stored in the database. In ArcGIS software, time intervals are calculated using the "Time Slider" tool. In the next step, animations are obtained.

(1903)

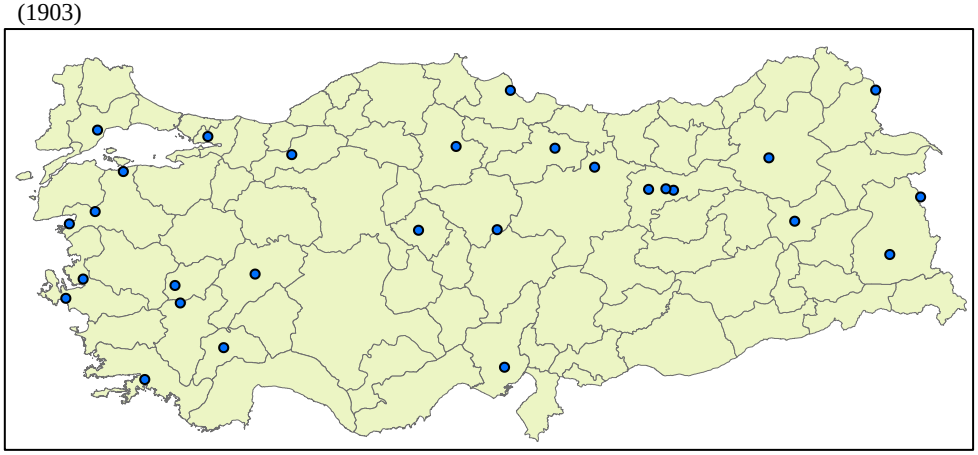

(1957)

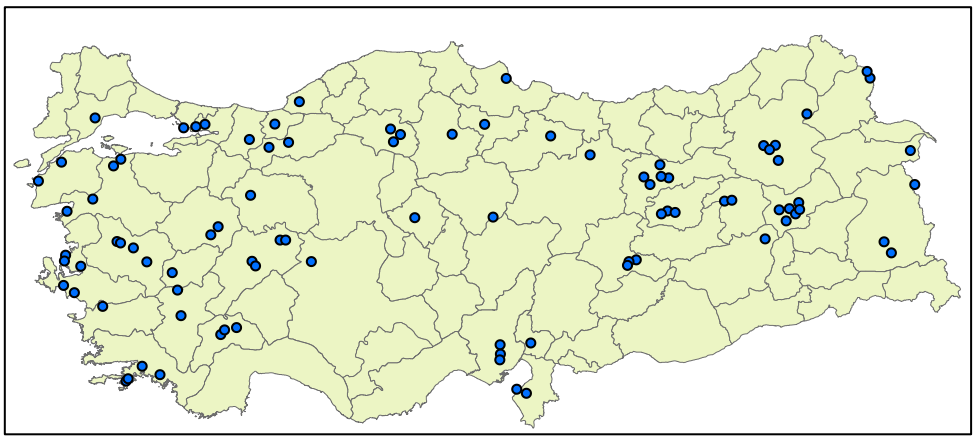

(2005)

Figure 2. Animation example of an earthquake

The effects of these educational animations made for spatial analysis to successes of students are assessed by using Likert type surveys. According to the evaluation of the results, it is seen that the interests of the students to the spatial analysis increase thanks to the proposed method and the students perform the spatial analysis by reaching current data.

4. CONCLUSION

In this study, animations were prepared to provide students with better understanding of spatial analysis. To accomplish this, the "Time Slider" and "Animation" modules were first used in ArcGIS software. The main purpose of this study is to visualize educational animations and spatial analyzes prepared. Technological methods must be utilized to overcome the disadvantages of Geographic Information System Software. Thus, the content of the lesson needs to be enriched to increase the imagination of the students on the spatial analysis in order to be more successful. For this reason, in favor of a 3D visual and interactive learning environment in the digital elevation model, spatial analysis will become more interesting for the students.

REFERENCES

[1]. Lajevardi N, Narang NS, Marcus N, Ayres P. Can mimicking gestures facilitate learning from instructional animations and static graphics? Computers & Education 2017;110:64-76. DOI:10.1016/j.compedu.2017.03.010.
[2]. Chandler, P. (2009). Dynamic visualizations and hypermedia: Beyond the "wow" factor. Computers in Human Behavior, 25, 389-392.
[3]. Chandler, P., & Sweller, J. (1991). Cognitive load theory and the format of instruction. Cognition and Instruction, 8, 293-332.
[4]. Gunal AY, Guven A. Determination of geomorphological parameters of Damlica Basin using GIS, Acta Physica Polonica A 2015;128 (1):B-222-B224. DOI: 10.12693/APhysPolA.128.B-222.
[5]. Yildiz A. Prospective teachers' comprehension levels of special relativity theory and the effect of writing for learning on achievement. Australian Journal of Teacher Education 2012;37:551-556. DOI:10.14221/ajte.2012v37n12.1
[6]. Clausen T. May Teaching Math's to pupils with different learning styles. Paul Chapman Publishing, London; 2005.
[7]. Castejón C, Blanco D, Moreno L. Friendly interface to learn stereovision theory. Computer Application Engineering Education 2009;17:180–186. DOI:10.1002/cae.20170.
[8]. Christel MG. The role of visual fidelity in computer-based instruction. Human Computer Interaction 1994;9:183–223. DOI: 10.1207/s15327051hci0902_2.
[9]. Gunal AY, Guven A. Synthetic unit hydrograph of small catchments by using GIS. Acta Physica Polonica A 2016;130:130-132. DOI: 10.12693/APhysPolA.130.130.
[10]. Xhafka E, Teta J, Agastra E. Mobile environmental sensing and sustainable public, transportation using ICT tools. Acta Physica Polonica A 2015;128:B-122-B124. DOI: 10.12693/APhysPolA.128.B-122.
[11]. Gunal M, Kosen A. Application of GIS for predicting quality of underground water for drinking. Acta Physica Polonica A 2015;128:B107- B109. DOI: 10.12693/APhysPolA.128.B-107.
[12]. Al-Seghayer, K. (2001). The effect of multimedia annotation modes on L2 vocabulary acquisition: A comparative study. Language Learning & Technology, 5(1), 202-232.
[13]. 202e232.Castro-Alonso JC, Ayres P, Paas F.Animations showing Lego manipulative tasks: Three potential moderators of effectiveness. Computers &Education 2015;85;1-13. DOI:10.1016/j.compedu.2014.12.022.
[14]. Garland TB, Sanchez CA. Rotational perspective and learning procedural tasks from dynamic media. Computers & Education 2013;69:31-37. DOI:10.1016/j.compedu.2013.06.014.
[15]. Hoffler TN, Leutner D.Instructional animation versus static pictures: a meta-analysis Learning and Instruction. 2007;17:722–738. DOI: 10.1016/j.learninstruc.2007.09.013.
[16]. Gunal M, Ay M, Gunal AY. Cross-drainage culvert design by using GIS. Acta Physica Polonica A 2017;132:595-598. DOI: 10.12693/APhysPolA.132.595.
[17]. Yomralioglu T. Cografi bilgi sistemleri temel kavramlar ve uygulamalar. Secil Ofset, Istanbul; 2000.
[18]. Aranoff S. Geographical information systems: a management perspective. WDL Publications, Ottawa, Canada; 1989.

ICETI
www.iceti.org
2018
07-11 MARCH
BUDAPEST
HUNGARY
II. INTERNATIONAL CONFERENCE ON ENGINEERING TECHNOLOGY AND INNOVATION

A Study on Line Rate Neighboring for MLR WDM Optical Networks

Gul Boztok Algin[1], E. Turhan Tunali[2]

Abstract

Due to their high transmission capability, mixed-line-rate (MLR) optical network employing wavelength-division-multiplexing (WDM) on fibers is one of the best candidates to support the increasing traffic volume of communication networks. Since different line rates coexist on different wavelengths of a fiber in MLR networks, in addition to other physical impairments, cross-phase modulation (XPM) effect arises. Studies show that a significant performance penalty occurs for 100 Gbps and 40 Gbps coherent DP-QPSK wavelengths due to XPM induced by adjacent 10 Gbps OOK wavelengths. This problem must be handled during wavelength assignment process. By measuring the performance of a signal by its transmission reach, in order to keep the signal's quality of transmission (QoT) in adequate level, the effective transmission reach of the underlying line rate must be adapted according to other line rates used in adjacent wavelengths of the same fiber. In this work, we study the assignment of neighboring line rates in MLR WDM optical networks. Simulations are carried out to demonstrate the effect of constraining line rate neighboring over routing performance in terms of communication cost and resource utilization. As simulation test bed, Survivable Routing with Rate and Wavelength Assignment (SRRWA) using shared backup path protection algorithm for dynamic traffic model that has been previously developed by the authors is used. The results of constrained strategies are compared with unconstrained wavelength assignment method. Simulation results show that constraining the wavelengths to be assigned for each line rate increases traffic blocking and/or transmission cost of the network.

Keywords: MLR, Optical WDM networks, Rate Assignment, Survivable communication, SRRWA

1. INTRODUCTION

The need for high speed communication networks has emerged with the significantly growing network traffic and diversifying data sharing patterns. The required bandwidth increases each day due to the wide usage of applications with intensive traffic volume. Communication networks must meet these diverse variety of traffic requests with efficient resource allocation and high-speed data transmission. Optical networks employing WDM on fibers are suitable candidates to support this need by the help of their high transmission capability.

With dynamic traffic model in single-line-rate (SLR) networks, during network design, it is difficult to decide which line rate to employ, due to lack of knowledge about future demands. Optical networks with MLR support relax this design limitation by their ability to choose appropriate line rate dynamically for each traffic request according to the network's current state. MLR support offers flexibility in routing traffic requests cost effectively [1] by decreasing the overall transmission cost using the volume discount [2] of high bit rate transponders. MLR networks can support 10/40/100 Gbps capable transponders. Experimentally 400 Gbps and 1 Tbps line rates are also achieved and expected to be industrially used within several years [3].

Signal encounters various physical layer impairments during its lifetime. Some of them are optical impairments, such as chromatic dispersion, polarization-mode dispersion, linear crosstalk and four-wave mixing, all of which can degrade an optical signal [3]. Beside these, since different line rates coexist on different wavelengths of a fiber in MLR networks, in addition to other physical layer impairments, cross-phase modulation (XPM) effect arises also. XPM is a nonlinear optical effect distorting the pulse, where the interaction of two signals causes the phase of the optical signal to vary with time [3]. XPM is more likely to occur when signals are closely packed together in the spectrum. Studies show that a significant performance penalty occurs for 100 Gbps and 40 Gbps coherent dual-

[1] *Corresponding author: Ege University, International Computer Institute, 35100, Bornova/Izmir, Turkiye. gul.boztok@ege.edu.tr*

[2] *Izmir University of Economics, Department of Computer Engineering, Balcova/Izmir, Turkiye. turhan.tunali@ieu.edu.tr*

polarization quadrature phase-shift keying (DP-QPSK) wavelengths due to XPM induced by adjacent 10 Gbps on–off keying (OOK) wavelengths [3,4,5,6]. This problem emerges the XPM awareness as new aspects to the resource allocation problem and must be handled during wavelength assignment process.

It is possible to keep the signal's QoT in adequate level by constraining the maximum allowed transmission distance according to the underlying line rate. The effective transmission reach of a line rate may be estimated by considering some major factors like physical impairment, modulation scheme, crosstalk impairment, network traffic and alike [7]. In this study, the transmission reach of each line rate is taken from the results of a crosstalk and impairment-aware study [7] and the candidate paths for a lightpath are constrained to be shorter than or equal to the transmission reach of the chosen rate. Furthermore, to simulate the XPM effect of MLR networks, the effective transmission reach of a line rate is adapted according to other line rates used in adjacent wavelengths of the same fiber.

In this work, we study the neighboring effects of different line rates generated by DPQPSK and OOK modulation formats and propose a strategy that aims to minimize the XPM effect. Through simulations, we compare the routing performance of line rate neighboring constrained wavelength assignment strategy to the conventional first fit (FF) wavelength assignment heuristic, in terms of communication cost and resource utilization.

2. PLI-AWARE SRRWA STRATEGY

The routing and wavelength assignment process performs dynamic resource allocation for traffic requests, considering the current state of the physical network. The underlying physical network is a transparent optical WDM network with MLR ability. Transponders capable of 10-40-100 Gbps line rates are deployed. To keep the simplicity, it is assumed that all nodes have adequate number of transponders for each line rate. By using the opportunity to dynamically choose the most suitable line rate, offered by MLR networks, known as rate assignment problem, and the aspect of ensuring the robustness of provisioned requests, which is called survivability, the problem becomes the well-known survivable routing, rate and wavelength assignment (SRRWA) problem. There are numerous well-known solutions to SRRWA problem in literature [2,8,9,10].

In this work, we used the SRRWA algorithm [11] using least used (LU) path first heuristic and shared backup path protection scheme for dynamic traffic model. To briefly mention, the first stage of the algorithm is performed offline, where the network is examined, and all simple paths are explored between node pairs. For each simple path, maximum feasible line rate is calculated using the transmission reach constraint. There are many factors like physical impairment, modulation scheme, crosstalk impairment, network traffic and alike [7] affecting the signal reach. For the sake of simplicity, while we consider only the physical lengths of the paths, to ensure the physical layer impairment (PLI) awareness of the strategy, the transmission reach of each line rate is taken from the results of a crosstalk and impairment-aware study [7] as used in [12]. The transmission reach is 2000 km for 100 Gbps, 2500 km for 40 Gbps and ∞ for 10 Gbps. The maximum line rate whose transmission reach is greater than or equal to the physical length of the path is chosen as the maximum feasible line rate of that path. We assume that all nodes have adequate number of transponders for each line rate.

The second stage of the algorithm is performed online. This stage is where the dynamic traffic requests $R(s,d,B,h_t)$ are provisioned; with s and d are source-destination nodes, B is the bandwidth requirement and h_t is the holding time of the traffic. All traffic requests are handled one by one with first in first served strategy according to their arrival time. For the request under consideration, all the working path alternatives, whether end-to-end or multi hop, to be groomed or newly established lightpaths, are evaluated and the one with optimum performance is assigned. After provisioning the working resources of a traffic request, backup resource assignments are done through a reverting protection-at-lightpath (PAL) shared backup path protection scheme. Assigned network resources remain active during the h_t of the connection. At the end of h_t, the connection is torn down and the resources assigned are freed.

The performance of an alternative resource is calculated by a mixed strategy evaluating the metrics of the resource such as the number of busy wavelengths of that resource, the transponder cost, and alike. This strategy is called optimal resource allocation (OPT) method [11]. OPT method is an adaptive routing algorithm. For wavelength assignment problem, the well-known low complexity heuristic of FF wavelength assignment strategy is used.

A link's usage value is equal to the number of busy wavelengths at this link. Respectively, a path's usage value is equal to the number of busy wavelengths at the most used link along that path (P), as formulated in (1). The main reason of this formulation is to find the bottle neck of the path under consideration. By choosing the least used alternative, algorithm tries to select lightly loaded paths and to ensure the load balancing in network.

$$path\_usage_P = max\{\forall(ij \in P)\ link\_usage_{ij}\} \quad (1)$$

In MLR networks, line rate selection of a path has direct influence over routing performance. The communication cost is calculated according to the number of transponders, using their normalized costs. Besides, the transmission reach is calculated according to the modulation format thus line rate of a lightpath. Therefore, line rate selection is a crucial problem for dynamic lightpath provisioning and is deeply investigated in literature [1, 2, 7, 10-14]. In this work, to simplify the process and to bring forward the effect of line rate neighboring, we used the maximize grooming line rate assignment method [7], which assigns the higher feasible line rate to the lightpaths. Maximize grooming method exploits volume discount [2] in total transponder cost and ensures more traffic to be provisioned leading to savings of more resources.

3. CONSTRAINING THE LINE RATE NEIGHBORING APPROACH

In this work, we try to minimize the negative effect of XPM over routing performance. To reduce the performance penalty of XPM, a number of inactive wavelengths may be placed between the DP-QPSK and OOK wavelengths. For an acceptable level of performance penalty, needed guard bands are of roughly 300 GHz between the 40 and 10 Gbps wavelengths; and 150 GHz between the 100 and 10 Gbps wavelengths [6]. In this study, to minimize the wasted capacity, we do not consider the guard bands. Instead, we propose to partition the spectrum into frequency intervals to be assigned to DP-QPSK and OOK wavelengths via constraining the wavelength assignment process as seen in [13,14]. We predetermine frequency intervals for each line rate. To establish a lightpath, available optical frequencies within appropriate interval are assigned in FF manner. A possible placement of wavelengths of a fiber according to their line rates is shown in Figure 1.

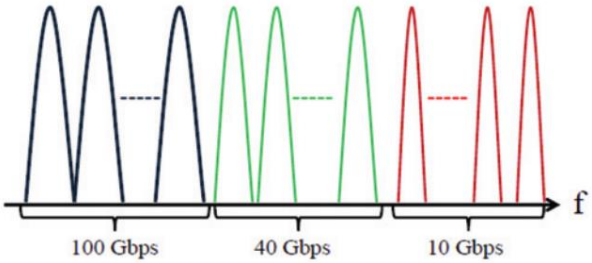

Figure 1. Placement of wavelengths of a fiber according to their line rates [14].

To keep the signal's QoT in adequate level, instead of measuring the QoT of each signal, we constrain the maximum allowed transmission distance of the line rates. With the fact that the effective transmission reach of a line rate is affected by various factors like physical impairment, modulation scheme, crosstalk impairment, network traffic and alike [7], in this study, the transmission reach of each line rate is taken from the results of a crosstalk and impairment-aware study [7]. For the proposed constrained wavelength assignment strategy, the transmission reach is assumed to be 3000 km for 100 Gbps, 3500 km for 40 Gbps and ∞ for 10 Gbps. On the other hand, to demonstrate the XPM of adjacent signals, we adapt the transmission reach of line rates according to neighboring wavelengths used in adjacent frequencies of the same fiber. For the conventional wavelength assignment strategy, for the sake of simplicity we consider the worst case and the transmission reach is assumed to be 2000 km for 100 Gbps, 2500 km for 40 Gbps and ∞ for 10 Gbps as used for MLR networks in [12]. Through simulations, we compare the results of the proposed line rate neighboring constrained wavelength assignment strategy to the conventional FF wavelength assignment heuristic.

The number of frequencies reserved for each line rate is an important parameter possibly affecting the routing performance in low resource availability. To observe the effect of spectrum partitioning with various proportions, we designed several scenarios. Assuming total 80 wavelengths per fiber, Table 1 shows the details of each scenario. Mixed scenario is our conventional FF wavelength assignment strategy where all frequencies are available to be used by all line rates. Ptr_i scenarios present spectrum partitioning with various proportions, e.g. in prt_1 one end frequencies of the spectrum between 1 to 30 are reserved for 10 Gbps signals, while 31 to 60 are reserved to 40 Gbps and last end frequencies 61 to 80 are reserved for 100 Gbps signals. Noting that adjacent co-propagating 40 and 100 Gbps DP-QPSK wavelengths suffer little performance penalty [3], we designed ptr_4 and ptr_5 where one end of the spectrum may be used by both 40 and 100 Gbps signals in mixed manner.

Table 18. Details of the simulation scenarios.

Scenario id	*Frequency Intervals reserved for*		
	10 Gbps	*40 Gbps*	*100 Gbps*
mixed	1 .. 80		
prt_1	1 .. 20	21 .. 50	51 .. 80
prt_2	1 .. 30	31 .. 60	61 .. 80
prt_3	1 .. 30	31 .. 50	51 .. 80
prt_4	1 .. 40	41 .. 80	
prt_5	1 .. 50	51 .. 80	

We performed simulations on NSF and EON networks shown in Figure 2 (a) and (b) respectively. The main difference between the two networks is their average link length. With average 487 km EON network has comparatively shorter links than NSF network having 1.086 km mean link length. This difference enables EON to support higher line rates without need for regeneration. Hence, in EON, lightpaths are generally established at higher line rates which results in more grooming opportunities and high resource availability for subsequent traffic requests.

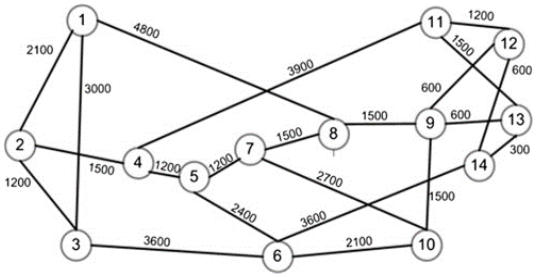

Figure 2. (a) NSF Network [1].

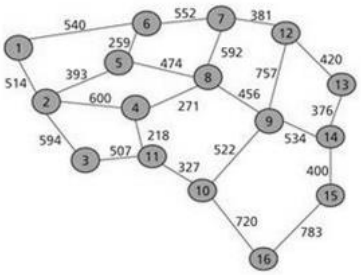

(b) EON Network [15].

For each scenario, 500 Erlangs to 1100 Erlangs total dynamic traffic requests are generated with uniformly distributed source and destination node pairs. The bandwidth requirement of each request is uniformly chosen between 1 to 10 Gbps. The arrival process is characterized as a Poisson process with average 20 requests/unit time and the holding time of each established connection is characterized as an exponential distribution. Each scenario is performed thirty times and average results are reported.

Performance metrics used in this work are bandwidth blocking ratio (BBR), total communication cost and lightpath utilization ratio (LUR). BBR is the ratio of blocked traffic bandwidth over serviced bandwidth. Communication cost is calculated according to the number of transponders employed to establish both working ($W_{ij,k}^{l}$) and backup ($B_{ij,k}^{l}$) lightpaths regarding their normalized costs as shown in (2). In (2) $W_{ij,k}^{l}$ symbolizes the existence of k^{th} working lightpath established between physical nodes *i* and *j* at rate *l*. Respectively, $B_{ij,k}^{l}$ symbolizes the existence of k^{th} backup lightpath established between physical nodes *i* and *j* at rate *l*. D_l is the normalized cost of transponder at rate *l*; which is considered as $D_{10}=1$, $D_{40}=2.5$, $D_{100}=3.75$ in this study. The objective is to minimize the total communication cost and the BBR.

$$cost = \sum_{ij}\sum_{k}\sum_{l}\left(W_{ij,k}^{l} + B_{ij,k}^{l}\right).D_l \qquad [2] \qquad (2)$$

LUR is another metric which gives idea about the resource utilization efficiency. It is the ratio of non-idle capacity of all the lightpaths over total capacity. The objective is to maximize the utilization ratio. For dynamic traffic model, lightpath utilization is calculated periodically while the provisioning continues and presents snapshots of network resource utilization efficiency.

Figure 3 shows the BBR values for all scenarios in NSF network. From the results, it is observed that a fixed partitioning of spectrum among the line rates leads to higher blocking. Our conventional FF wavelength assignment strategy presents lowest blocking, while BBR increases with the number of frequencies reserved for 10 Gbps line rate decrease. The main reason of this tendency is the mostly needing to establish 10 Gbps lightpaths since the NSF network, possessing long links, dramatically minimizes the possibility of establishing lightpaths with higher line rates.

Figure 4 shows the cost values of various scenarios. The results show that, even on lower traffic volumes, where BBR is zero for mixed scenario and minimal for prt_i scenarios, mixed presents lowest communication cost per traffic serviced. It is remarkable that the cost difference is very high between mixed and prt_5, which has the second smallest BBR value. For line rate neighboring constrained wavelength assignment scenarios, the cost is proportional to the

traffic amount successfully serviced. For all scenarios, with the increase in traffic load, cost decreases. This is due to high grooming in case of higher load. If the load is low, connections are setup and teared down quickly leading to increase in cost with new lightpath establishments for subsequent traffic requests. At higher loads, connections remain active longer, leading to increase in grooming opportunity for subsequent requests and decrease in total communication cost.

Traffic requests may be groomed to a lightpath iff the available capacity of that lightpath is sufficient for the new request. Generally, the available capacities are very low on lightpaths established with low line rate. To give an example, there will remain only 2 Gbps capacity to be groomed on a 10 Gbps lightpath established for a 8 Gbps traffic request. This low capacity negatively affects grooming capability, leading to unused capacities on network. On the other hand, new lightpath establishment becomes necessary leading to early wavelength exhaustion. This is the main reason of low resource utilization efficiency and high BBR presented by constrained prt_i scenarios. Evaluating the LUR values shown in Figure 5, it is observed that unconstrained conventional FF wavelength assignment strategy presents higher resource utilization with average 0,43 where constrained scenarios present similar LUR values within 0.23 to 0.35 range.

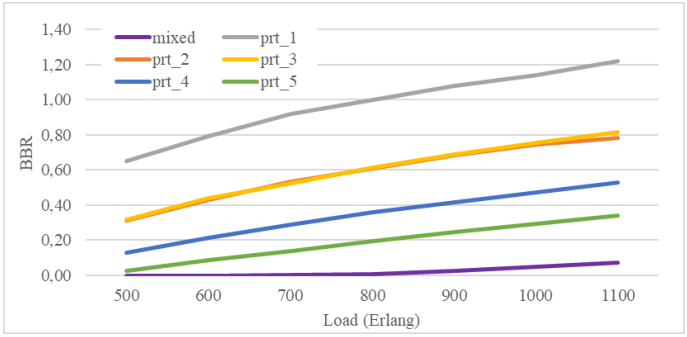

Figure 3. BBR values of scenarios in NSF network.

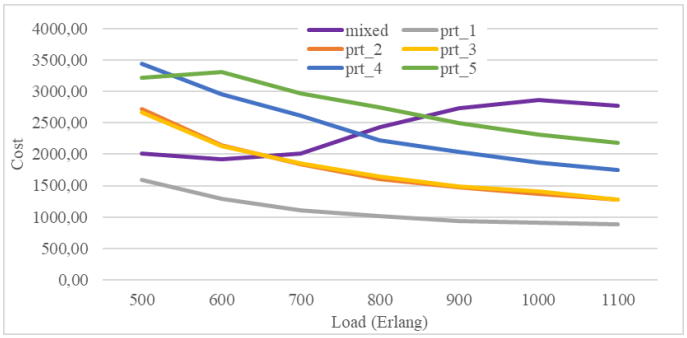

Figure 4. Cost values of scenarios in NSF network.

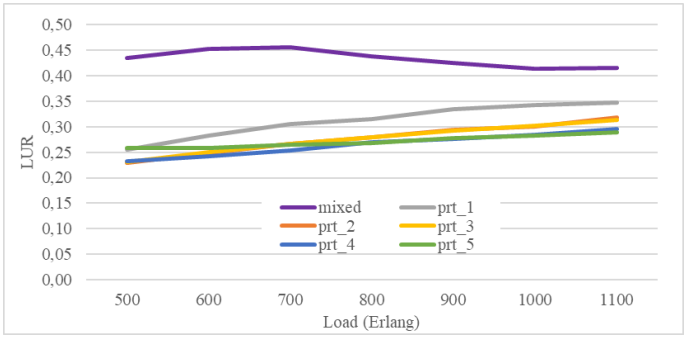

Figure 5. LUR values of scenarios in NSF network.

To observe the scenarios on a different network, all simulations are reperformed on EON network, which has comparably shorter links than NSF network. From the results, it is observed that all scenarios provision the requests with no blocking. This is due to the shorter links of EON enabling the establishment of higher line rate lightpaths,

which results in high grooming opportunities and high resource availability. It would not be inaccurate to presume that most of the lightpaths communicates at 100 and 40 Gbps line rates since most possible simple path's lengths are shorter than their transmission reaches.

Figure 6 shows the cost values for all scenarios with various traffic loads in EON network. Keeping in mind that all scenarios presents no blocking, it is observed that our conventional FF wavelength assignment strategy presents lowest communication cost. At higher loads, since connections remain active longer, grooming opportunity for subsequent requests increases and total communication costs decrease for all scenarios. This is the reason of constrained scenarios begin to present lower costs. The performances on constrained and unconstrained scenarios are very similar in EON network. This is because, the high line rate lightpaths are sufficiently available for all traffic requests in all scenarios.

Figure 7 presents the LUR values of all scenarios in EON network. First observation is that the resource utilization, within 0,1 to 0,2 range, is very low for all scenarios. This is an expected result of establishing high line rate lightpaths at all cases. There remain dramatically high unused capacities on all lightpaths leading to decrease in resource utilization efficiency. However, it is observed that unconstrained conventional FF wavelength assignment strategy presents nearly 80% higher resource utilization for all loads.

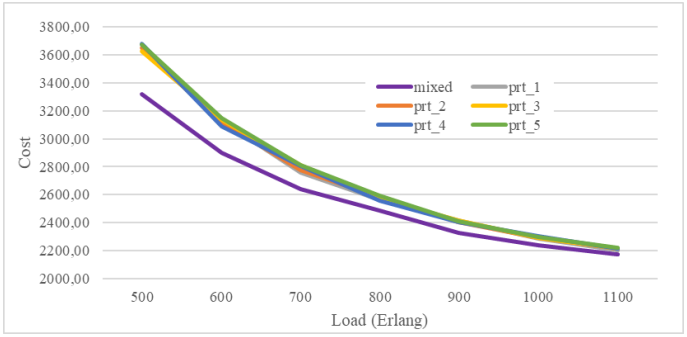

Figure 6. Cost values of scenarios in EON network.

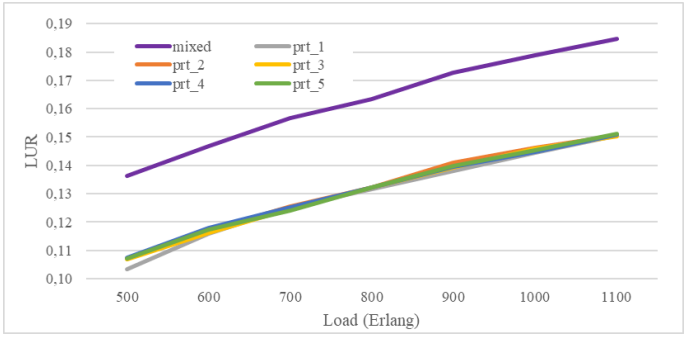

Figure 7. LUR values of scenarios in EON network.

4. CONCLUSION

In this work, we studied the neighboring effects of different line rates generated by DPQPSK and OOK modulation formats and proposed a strategy that aims to minimize the negative effect of cross-phase modulation (XPM) over routing performance. We proposed to partition the spectrum into frequency intervals to be assigned to DP-QPSK and OOK wavelengths via constraining the wavelength assignment process as seen in [13,14].

We transformed the measurement of the QoT of signals into limiting their transmission distances. To satisfy the physical layer impairment (PLI) awareness of the strategy, the transmission reach of each line rate is taken from the results of a crosstalk and impairment-aware study [7] as used in [12]. To ensure the QoT, we assured that the physical lengths of the candidate paths are shorter than the line rate's transmission reach. We presented the XPM effect by decreasing the transmission reach of line rates, in presence of different modulation formats neighboring on the same fiber.

From the simulation results, it is observed that a fixed partitioning of spectrum among the line rates leads to higher blocking and/or communication cost. Partitions must be arranged according to the network's physical properties as well as to the requirement patterns of the traffic requests. It is not feasible to limit the number of frequencies to be assigned to lower rates, if the underlying network could not support high line rates broadly. This unbalanced usage of line rates leads to increased blocking while reserved frequencies' capacities remain idle. On the other hand, it merits to remark that, even in networks having shorter links and enabling higher line rates, it is not feasible to always establishing high line rate lightpaths if bandwidth requirements of the traffic requests are low. This leads to inefficient resource utilization with increased cost. For future work, we plan to expand our work towards more intelligent XPM awareness solutions which may include dynamic partitioning of the spectrum.

REFERENCES

[1]. A. Nag, and M. Tornatore, "Transparent optical network design with mixed line rates," Int. Symp. on Advanced Networks and Telecommunication Systems (ANTS), India, 2008.
[2]. M. Liu, M. Tornatore and B. Mukherjee, "New strategies for connection protection in mixed-line-rate optical WDM networks", J. Opt. Comm. Net., vol.2 no.9, pp.641-650, 2011.
[3]. Simmons, Jane M., *Optical Network Design and Planning*, 2nd ed., B. Mukherjee, Opt. Net. Series Edit., Springer, 2008.
[4]. G. Charlet, J. Renaudier, P. Brindel, P. Tran, H. Mardoyan, O. Bertran Pardo, M. Salsi, and S. Bigo, "Performance comparison of DPSK, P-DPSK, RZ-DQPSK and coherent PDM-QPSK at 40 Gb/s over a terrestrial link", In Proc., OFC/NFOEC'09, Mar 2009, San Diego, CA, paper JWA40.
[5]. A. Bononi, M. Bertolini, P. Serena, and G. Bellotti, "Cross-phase modulation induced by OOK channels on higher-rate DQPSK and coherent QPSK channels," J. Lightwave. Technol. vol. 27 no.18, pp. 3974–3983, Sept 2009.
[6]. O. Bertran-Pardo, J. Renaudier, G. Charlet, H. Mardoyan, P. Tran, M. Salsi, and S. Bigo, "Overlaying 10 Gb/s legacy optical networks with 40 and 100 Gb/s coherent terminals," J. Lightwave. Technol. vol.30 no.14, pp.2367–2375, July 2012.
[7]. M. Batayneh, D.A. Schupke, M. Hoffmann, A. Kirstaedter, and B. Mukherjee, "On routing and transmission-range determination of multibit-rate signals over mixed-line-rate WDM optical networks for carrier ethernet", IEEE/ACM Transactions on Networking, vol.19 no.5, pp.1304-1316, 2011.
[8]. C. S. Ou, B. Mukherjee, *Survivable Optical WDM Networks*, Optical Networks Series, Springer, 2005.
[9]. C. Gao, H.C. Cankaya, A.N. Patel, J.P. Jue, X. Wang and Q. Zhang, "Survivable impairment-aware traffic grooming and regenerator placement with connection-level protection", J. Opt. Comm. Net., vol.4 no.3, pp.259-270, 2012.
[10]. G. Boztok Algin and E.T. Tunali, "Dedicated path protection in mixed-line-rate optical WDM networks", 21th Signal Processing and Communications Applications Conference (SIU), Cyprus, 2013.
[11]. G.B. Algin and E.T. Tunali, "A Dynamic Line Rate Assignment Strategy for MLR WDM Optical Networks", in Proc. of IEEE Int. Black Sea Conf. on Comm. and Netw. (BlackSeaCom), 2017.
[12]. X. Wang, M. Brandt-Pearce, and S. Subramaniam, "Grooming and RWA in translucent dynamic mixed-line-rate WDM networks with impairments - OSA Technical Digest," OFC 2012, paper OTh1A.7.
[13]. S. Iyer, S.P. Singh, "Physical Layer Impairment-Aware Routing and Wavelength Assignment (PLI-RWA) Strategy for Mixed Line Rate (MLR) Wavelength Division Multiplexed (WDM) Optical Networks," 12th Int. Conf. Wireless and Opt. Comm. Net. (WOCN 2015), Bangalore, India, Sept. 2015.
[14]. S. Iyer, "A Novel Dynamic Physical Layer Impairment-Aware Routing and Wavelength Assignment (PLI-RWA) Algorithm for Mixed Line Rate (MLR) Wavelength Division Multiplexed (WDM) Optical Networks", J. Opt. Comm. vol.37 no.4, pp.349-356, Feb. 2016.
[15]. A. Morea, J. Perello, S. Spadaro, D. Verchere, and M. Vigoureux, "Protocol enhancements for 'greening' optical networks," Bell Labs Tech. J., vol.18, no.3, pp.211–230, Dec. 2013.

BIOGRAPHY

Gul Boztok Algin received her B.Sc. degree in 2004 in Computer Engineering from Dokuz Eylul University, Izmir, Turkiye. She earned M.Sc. and Ph.D. degrees in Computer Science from International Computer Institute of Ege University in Izmir, Turkiye, in 2007 and 2017 respectively. She is with International Computer Institute of Ege University since 2005. Her research interest includes information and video security. She's currently working on communication networks especially in optical routing and survivable design.

E. Turhan Tunali earned a B.Sc. Degree in Electrical Engineering from Middle East Technical University and M.Sc. Degree in Applied Statistics from Ege University, both in Turkey. He then earned a D.Sc. Degree in Systems Science and Mathematics from Washington University in St. Louis, U.S.A. in 1985. After his doctorate study, he joined Computer Engineering Department of Ege University as an assistant professor where he became an associate professor in 1988. During the period of 1992-1994, he worked in Department of Computer Technology of Nanyang Technological University of Singapore as a Visiting Senior Fellow. He then joined International Computer Institute of Ege University as a Professor where he was the director. In the period of 2000-2001, he worked in Department of Computer Science of Loyola University of Chicago as a Visiting Professor. In 2009, he joined Department of

Computer Engineering of Izmir University of Economics where he is currently working as a Professor. His current research interests include computer networking and Internet performance measurements.

ICETI
www.iceti.org
2018
07-11 MARCH
BUDAPEST
HUNGARY
II. INTERNATIONAL CONFERENCE ON ENGINEERING TECHNOLOGY AND INNOVATION

Design and Optimization of Amorphous Compact Microstrip Antenna using Artificial Bee Colony Algorithm for Microwave Imaging Applications

Mustafa Berkan Bicer[1], Ali Akdagli[1]

Abstract

In this study, a compact microstrip antenna with a relatively small in size and a non-symmetrical shape that can be used alone or as a part of an antenna array in ultrawideband microwave imaging applications is designed and optimized using the artificial bee colony algorithm to perform a good ultrawideband bandwidth characteristics. The design and simulations of the microstrip-fed monopole antennas, with outer size of 40 x 50 mm^2 on an FR4 substrate with permittivity of 4.3 and a thickness of 1.5 mm, are utilized with the use of a full-wave electromagnetic simulation software based on the moment method (MoM). As a result of the optimizations made by using the artificial bee colony (ABC) algorithm, two different antenna designs with broadband performance were obtained. The return loss (S_{11}) results show that the characteristics of the obtained antennas meet the bandwidth requirements and offer good performance for microwave imaging applications, operating between 3.1 GHz and 10.6 GHz, covering the entire ultrawideband frequencies.

Keywords: antenna, design, microstrip, microwave imaging, ultrawideband

1. INTRODUCTION

With the rapid development of technology, imaging technologies using microwaves have begun to be used in many areas such as medical, defense and security industries. Microwave-based imaging techniques are used extensively in providing border security, protection of places such as airports and shopping centers, rescue of people under the rubble, search of precious metals, and screening and diagnosis of various diseases, especially cancer. Medical imaging systems require compact and small antennas because of the small size of the tissue to be measured. Conventional microstrip antennas (MA) have small dimensions in high frequencies, but as the frequency decreases, the antenna size also increases. Small-size and compact microstrip antennas (CMA) that can operate in the ultrawideband frequencies are obtained by modifying the ground plane and/or the radiating patch of the conventional microstrip antennas. Various antenna designs are available in the literature [1]–[6] for use in ultrawideband microwave imaging applications. Adnan et. al. [5] designed a compact microstrip antenna consist of air substrate and two parallel copper plates with the thickness of 0.5 mm for breast cancer imaging operating from 4 GHz to 8 GHz. Nasir et. al. [4] designed an ultrawideband antenna operating between 2.01 GHz and 7.64 GHz frequencies. The proposed microstrip-fed monopole antenna [4] has a modified ground plane and a slot loaded radiating patch. Ustun et. al. [1] also designed a dual-band microstrip antenna for UMTS, WLAN and WiMAX applications by using artificial bee colony algorithm to optimize the antenna.

In this study, a microstrip-fed compact microstrip antenna with tree-like shape is designed and the physical parameters of the radiating patch and the ground plane is optimized by utilizing artificial bee colony (ABC) optimization algorithm [7]–[9]. The return loss results of the simulated antenna satisfy the desired performance of the ultrawideband imaging applications.

[1] *Corresponding author: Mersin University, Department of Electrical and Electronics Engineering, 33343, Yenisehir/Mersin, Turkey. akdagli@mersin.edu.tr*

2. ANTENNA DESIGN

An antenna, capable of operating at ultrawideband frequencies between 3.1 GHz to 10.6 GHz frequencies, having a rectangular shaped ground plane and a microstrip-fed symmetrical tree-like radiating plane, is designed using FR4 substrate with dielectric constant of 4.3 and height of 1.5 mm. The initial geometry of the designed antenna is shown in Figure 1.

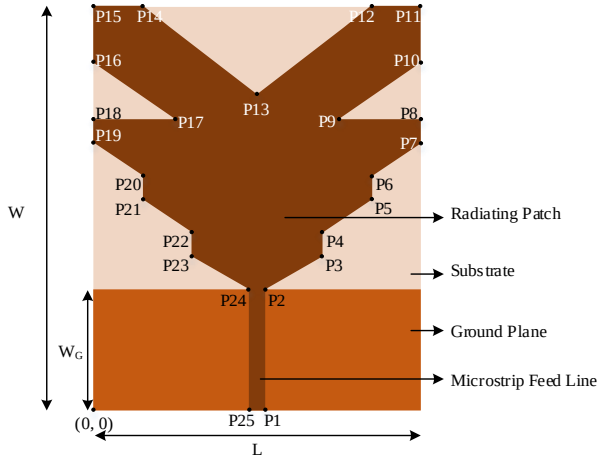

Figure 1. Initial design of the compact microstrip antenna

The size of the antenna is determined, as given in Table 1, considering the wavelengths of the ultrawideband frequencies. A microstrip feed line with a width of 2 mm and a length of 15 mm is used to feed the radiating patch. W_G and L_G parameters are the width and the length of the ground plane, respectively, with values of 15 mm and 40 mm.

Table 19. Initial values of the parameters ((x, y) in mm)

P1	**P2**	**P3**	**P4**	**P5**	**P6**	**P7**	**P8**	**P9**
(21, 0)	(21, 15)	(28, 19)	(28, 22)	(34, 26)	(34, 29)	(40, 33)	(40, 36)	(30, 36)
P10	**P11**	**P12**	**P13**	**P14**	**P15**	**P16**	**P17**	**P18**
(40, 43)	(40, 50)	(34, 50)	(20, 39)	(6, 50)	(0, 50)	(0, 43)	(10, 36)	(0, 36)
P19	**P20**	**P21**	**P22**	**P23**	**P24**	**P25**	***W_G***	***L_G***
(0, 33)	(6, 29)	(6, 26)	(12, 22)	(12, 19)	(19, 15)	(15, 0)	*15*	*40*

The antenna, shown in Figure 1, is simulated with the use of a full-wave electromagnetic simulation tool and the return loss result between 3 GHz and 11 GHz are given in Figure 2. It is seen from the Figure 2 that the performance of the proposed antenna is insufficient to satisfy the bandwidth requirements of the entire ultrawideband frequency range. The return loss of the antenna needs to be below the reference value of -10 dB in order to work efficiently in ultrawideband frequencies. To achieve the ultrawideband performance, the physical parameters of the radiating patch or the ground plane should be optimized.

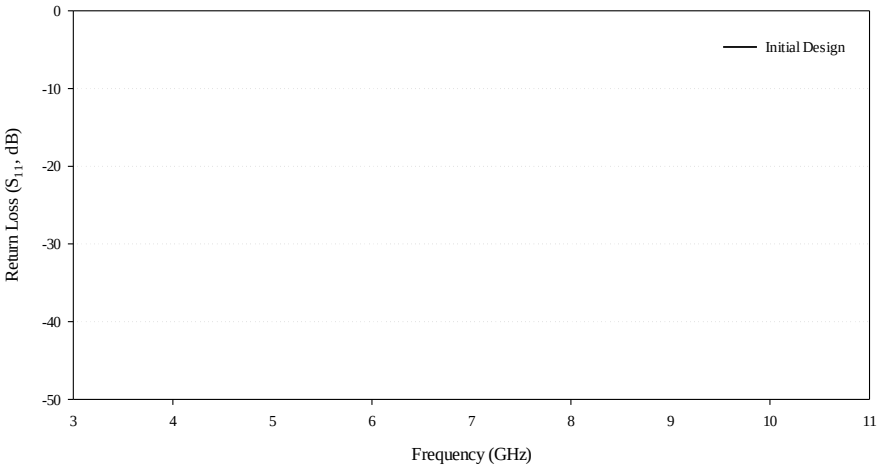

Figure 2. The return loss (S_{11}) result of the antenna before optimization process

As seen from the Figure 1, the radiating plane is designed to consist of 25 optimization points, but the points of P1 and P25 are excluded from the optimization process in order to avoid connection problems with feed line. The length of the feed line is kept constant but the width is included in the optimization process. Each of the points, chosen as optimization parameters, between P2 and P24 is set to change within certain limits in both x and y directions. Also, the width and the length of the ground plane is chosen as additional optimization parameters.

3. OPTIMIZATION USING ARTIFICIAL BEE COLONY ALGORITHM

As seen from the return loss results given in Figure 2, the physical sizes of the initial design of the antenna should be optimized to achieve the bandwidth and frequency coverage requirement of the entire ultrawideband range. In this study, artificial bee colony (ABC) algorithm is chosen to optimize the variables of the antenna due to its having higher performance than the other algorithms for finding global minima at the end of the iterative search process. The ABC algorithm, which tries to find a global minimum in solution space iteratively, is based on the food search behavior of the bee swarms [7]–[9].

In order to achieve the ultrawideband performance of the antenna design shown in Figure 1, the return loss results of the antenna should be less than -10 dB between 3.1 GHz and 10.6 GHz frequencies. Accordingly, the cost function to be used in optimization can be selected as given in Equation (1) and Equation (2),

$$C(f_n)=\begin{cases} 0 & S_{11,O}(f_n) < S_{11,D}(f_n) \\ \left|S_{11,D}(f_n)-S_{11,O}(f_n)\right| & otherwise \end{cases} \quad (1)$$

$$CF=\frac{1}{N}\sum_{n=1}^{N} C(f_n) \quad (2)$$

where CF, N, f_n, $S_{11,D}$ and $S_{11,O}$ represent the cost function to be minimized, the number of the frequencies, each frequencies, desired and obtained return loss results, respectively. The flowchart of the optimization process of the antenna is given in Figure 3.

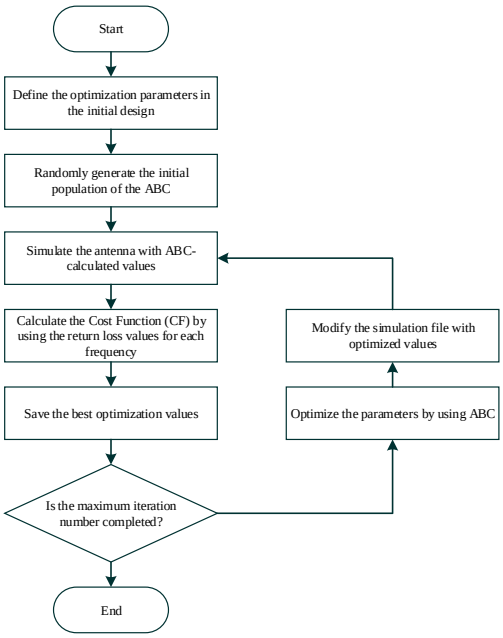

Figure 3. The flowchart of the optimization process of the antenna

The iterative optimization process is terminated when the return loss falls below -10 dB for all frequencies between 3.1 GHz and 10.6 GHz.

4. NUMERICAL RESULTS

The optimized antenna design is presented in Figure 4. It is understood from the figure that after the optimization process, two of the optimization variables are taken out from the structure.

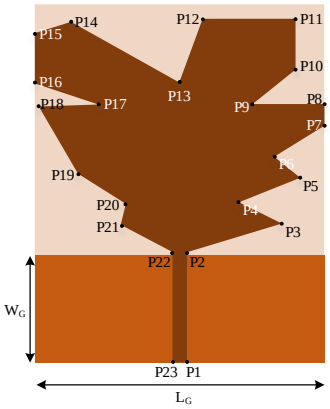

Figure 4. Optimized compact microstrip antenna

The optimized cartesian coordinate values of the optimization parameters are given in Table 3.

Table 3. Values of the parameters for optimized antenna ((x, y) in mm)

P1	**P2**	**P3**	**P4**	**P5**	**P6**	**P7**	**P8**	**P9**
(21, 0)	(21, 15.5)	(34.15, 19.43)	(28.23, 22.45)	(36.63, 25.83)	(33.03, 28.83)	(39.95, 33.08)	(39.95, 36.08)	(30.05, 36.08)
P10	**P11**	**P12**	**P13**	**P14**	**P15**	**P16**	**P17**	**P18**
(36, 40.95)	(36, 47.95)	(23.13, 47.95)	(20, 39.15)	(5, 47.63)	(0.05, 46)	(0.05, 39)	(9, 36)	(0.63, 35.75)
P19	**P20**	**P21**	**P22**	**P23**	W_G	L_G		
(6.13, 26.35)	(12.55, 22.25)	(11.85, 19.25)	(19, 15.5)	(19, 0)	*14.9*	*40*		

The parameters of the antenna are changed with the optimized values and the simulation is done. A comparative graph of the return loss results for the initial antenna and the optimized antenna is given in Figure 5.

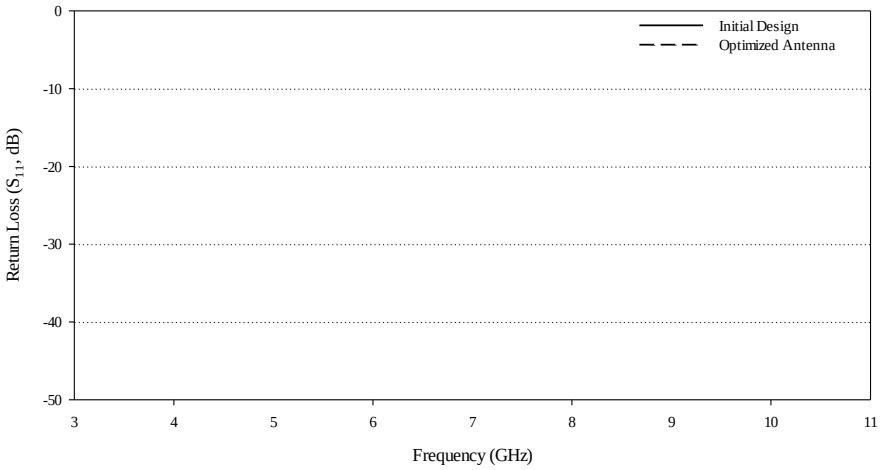

Figure 5. Return loss results of the proposed and optimized antennas

As shown in Figure 5, the return loss results of the optimized antenna are below -10 dB for the ultrawideband frequency range. The simulated radiation patterns of the optimized antenna for $\theta = 90°$, $\phi = 0°$ and $\phi = 90°$ at 3 GHz, 6.61 GHz and 10.3 GHz are given in Figure 7.

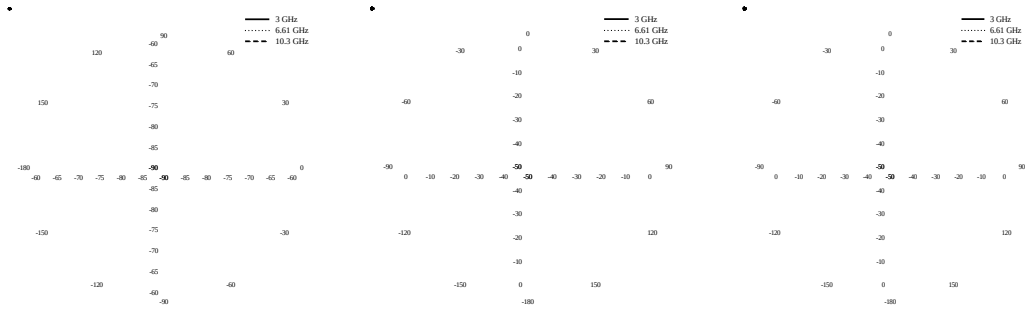

(a) *(b)* *(c)*

Figure 7. The simulated radiation patterns of the optimized antenna (a) θ=90°, (b) ϕ=0° and (c) ϕ=90° at 3 GHz, 6.61 GHz and 10.3 GHz

Figure 7(a) shows that the radiation pattern for $\theta = 90°$ is nearly omnidirectional in lower frequencies while the shape of the pattern is distorted by the increasing frequency. Also, according to Figure 7(b) and Figure 7(c), the elevation pattern is nearly 8-shape.

5. CONCLUSION

In this study, a microstrip-fed monopole compact microstrip antenna is designed for use in ultrawideband applications. Since the initially designed antenna is insufficient in providing the desired performance at some frequencies, the physical dimensions of the radiating patch and the ground plane of the antenna are optimized with the use of the ABC algorithm. The shape of the initially designed symmetrical and tree-shaped antenna has been transformed into a complex shaped antenna as a result of optimization. Although the design of the antenna is not symmetrical and good-looking, the simulation results show that the proposed antenna can be used for ultrawideband microwave imaging applications.

ACKNOWLEDGMENT

This study was supported by the Research Fund of Mersin University in Turkey with Project Number: 2017-1-TP3-2190.

REFERENCES

[1]. D. Ustun and A. Akdagli, "Design of a dual-wideband monopole antenna by artificial bee colony algorithm for UMTS, WLAN, and WiMAX applications," *Int. J. Microw. Wirel. Technol.*, vol. 9, no. 5, pp. 1197–1208, 2017.

[2]. A. Toktas, M. B. Bicer, A. Akdagli, and A. Kayabasi, "Simple formulas for calculating resonant frequencies of C and H shaped compact microstrip antennas obtained by using artificial bee colony algorithm," *J. Electromagn. Waves Appl.*, vol. 25, no. 11–12, pp. 1718–1729, 2011.

[3]. A. Akdagli, M. B. Bicer, and S. Ermis, "A novel expression for resonant length obtained by using artificial bee colony algorithm in calculating resonant frequency of C-shaped compact microstrip antennas," *Turkish J. Electr. Eng. Comput. Sci.*, vol. 19, no. 4, pp. 597–606, 2011.

[4]. N. Iqbal and S. Karamzadeh, "UWB microstrip antenna design for microwave imaging systems," *Int. J. Electron. Mech. Mechatronics Eng.*, vol. 7, no. 2, pp. 1411–1417, 2017.

[5]. S. Adnan, R. A. Abd-Alhameed, H. I. Hraga, I. T. E. Elfergani, and M. B. Child, "Compact microstrip antenna design for microwave imaging," in *2010 Loughborough Antennas & Propagation Conference*, 2010, pp. 389–392.

[6]. M. B. Bicer and A. Akdagli, "A novel microstrip-fed monopole antenna for WLAN/WiMAX applications," *J. Electromagn. Waves Appl.*, vol. 26, no. 7, pp. 904–913, 2012.

[7]. D. Karaboga and B. Basturk, "A powerful and efficient algorithm for numerical function optimization: artificial bee colony (ABC) algorithm," *J. Glob. Optim.*, vol. 39, no. 3, pp. 459–471, 2007.

[8]. D. Karaboga and B. Akay, "A comparative study of artificial bee colony algorithm," *Appl. Math. Comput.*, vol. 214, no. 1, pp. 108–132, 2009.

[9]. D. Karaboga and B. Basturk, "On the performance of artificial bee colony (ABC) algorithm," *Appl. Soft Comput.*, vol. 8, no. 1, pp. 687–697, 2008.

ICETI
www.iceti.org
2018
07-11 MARCH
BUDAPEST
HUNGARY
II. INTERNATIONAL CONFERENCE ON ENGINEERING TECHNOLOGY AND INNOVATION

3D Imaging and Visualization of Engineering Materials with Optical Metrology

Anil Akdogan[1], Ali Serdar Vanli[1]

Abstract

Optical imaging and visualization techniques are based on some classical optical techniques by using novel devices and instrumentation. Researchers can analyze structures, associated electronic systems, materials, specifications and manufacturing marks with help of optical systems. Innovative optical measurement devices and microscopes combine the speed and accuracy requirements of the researchers and industry. The invention of non-contact type techniques is in a sense due to the drawbacks of the contact type stylus measurement techniques. These non-contact measurement methods have unique ability to measure not only in laboratory conditions but also in-process of different types of materials like metals or polymers. This research is about the use of innovative optical techniques in 3D imaging and visualization of engineering materials performance analysis experimentally. In the conducted experiments the surface conditions of the brand new milling tool qualities are visualized. After milling operations at different process parameters, worn mills were analyzed with optical metrology, as well. The results are profitable not only about life predictions of the tools but also useful for coating conditions of the work-piece surfaces.

Keywords: 3D Imaging, Optical Metrology, Visualization

1. INTRODUCTION

Advances and innovations in measurement techniques and quality control tools are crucial in supporting many kinds of industrial developments [1]. New experimental techniques were being advanced during the last decade about innovative measurement techniques. Those techniques may be applied to solve fundamental problems especially in surface science with growing demands. Measurement techniques that are applied during the processes have mostly the aim to control the quality of the work by monitoring and imaging of the tools and/or workpieces. Real-time visualization of the measured parameters is a very helpful tool to assure the quality of the workpiece. Optical imaging and visualization base on classical optical techniques by using novel devices and instrumentation. Researchers can analyze structures, associated electronic systems, materials, specifications and manufacturing marks with help of optical systems.

The main advances in modern optics have been driven by the principles of quantum physics. Probably, one of the most significant breakthroughs was the inventions of the Microwave Amplification by Stimulated Emission Radiation (MASER) and the Light Amplification by Stimulated Emission Radiation (LASER) at the beginning of the second half of 1900s [2]. These devices were capable of producing coherent electromagnetic waves, namely microwaves and light, based on a quantum phenomenon called stimulated emission. Optical 3D measurements based on digital data are a versatile tool as they have a number of advantages. They can be applied at a wide variety of scales and contactless data acquisition prevents damage of objects. In addition, increasing variety of sensors, data, products, and processing and analysis tools have become available in recent years. Besides the unique properties of light as a sensing element, optical methods also stand out for their high versatility, sensitivity and spatial resolution. In the early 1870s, the German physicist Ernst K. Abbé formulated a rigorous criterion for being able to resolve two objects in a light microscope. According to his equation, the best resolution achievable with visible light is about a few hundreds of nanometers. This theoretical resolution limit of conventional optical imaging methodology was the primary factor motivating the development of recent higher-resolution scanning probe techniques [3].

[1] *Corresponding author: Yildiz Technical University, Department of Mechanical Engineering, 34349, Besiktas/Istanbul, Turkey.* svanli@yildiz.edu.tr

The most important experimental and technical configurations employed in optical microscopy have naturally been transferred to near-field optical microscopy. In a near-field optical microscope, a nanoscale optical probe is raster scanned across a surface much similar as in Atomic Force Microscope (AFM) or Scanning Tunneling Microscope (STM). There have been numerous variations on the types of microscopy. Acoustic microscopy involves the reflection of sound waves off a workpiece; x-ray microscopy involves the transmission of x-rays through the workpiece; near field optical microscopy involves shining light through a smaller opening than the wavelength of light; and atomic force microscopy is similar to scanning tunneling microscopy but can be applied to materials that are not electrically conducting. Optical microscopy is the traditional form of microscopy involves viewing a sample closely through magnifying a lens with visible light, in general. It is used across several research areas such as microbiology, nanophysics, pharmaceutical research, microelectronics, and biotechnology. It is also used to view biological samples for diagnosis of medical conditions. Particularly, optical microscopes are used to view very small objects. An optical microscope can produce a micrograph with the help of standard light-sensitive cameras [4].

In this experimental work, in order to show the important usage of optical metrology in manufacturing environment, different end milling tool tip geometries and milled workpiece surface qualities were analyzed in 3D and visualized by optical measurement techniques and methods. In addition, it is aimed to determine the optimal process parameters and tool radius by using design of experiment methodology resulting fine surface roughness in workpieces.

2. EXPERIMENTAL WORKS

This work experimentally researches end milling parameters such as the cutting speed, the feed rate, the depth of cut and also various coatings to indicate the effects of surface quality of the machined parts. It focuses on the effects of tip radius of the tools on the machined surface quality with modern and precise visualization techniques. Taguchi, design of experiments method, was used to determine the optimum processing parameters. L27 orthogonal array was designed for the experiments. The selected solid carbide cutting tools for end milling Aluminum alloys coated by 3 different material types by “Plasma Vapor Deposition” technique. Each tool has four flutes and 10 mm nominal diameter. The tests were performed on a vertical CNC machining center, Mori Seiki, MillTap 700, Japan. Manufacturers should test functional geometry and wear characteristics of tools to ensure that only the functionally capable tools are used in the production process as well as by the users or customers. For these purposes, the initial geometrical and surface characteristics of the brand new tools are examined in high precise optical microscopic methods [5]. After milling processes, surface roughness values of machined parts were confirmed by the Taylor Hobson UK, Form Talysurf Intra, surface roughness profilometer also in 2D to determine surface quality considering the related standard [6]. Edge radii of the brand new and end mill-processed tools are measured by a Zoller - Venturion 450 - 3D laser scanner, Germany. Images were captured by a Keyence - optical microscope, US, and a Schut - stereo microscope, The Netherlands, considering the related standard [7].

3. RESULTS AND DISCUSSIONS

This work researches end milling parameters such as the cutting speed, the feed rate, the depth of cut and also various coatings to indicate the effects of surface quality of the machined parts. It especially focuses on the effects of tip radius on the milled surface quality with modern and precise measurement techniques and methods. Taguchi design of experiments method is used to determine the optimum processing parameters and the best coating material which combined with different tool radiuses to obtain high surface quality for the end milling process of Al 7075 alloy.

Figure 22. 3D laser scanning radius measurements (Operation is on the left, calculation the results is on the right)

3D laser scanning radius measurement examples are given in Figure 1. Tool geometries and radius measurements are verified with optical microscope measurements, as well. As the example of all conducted measurement experiments, optical microscopic images of AlTiN coated 0.5 mm (tip radius) brand new tools are shown in Figure 2. 3D laser scanning radius measurements and radius measurements on optical images are determined almost the same.

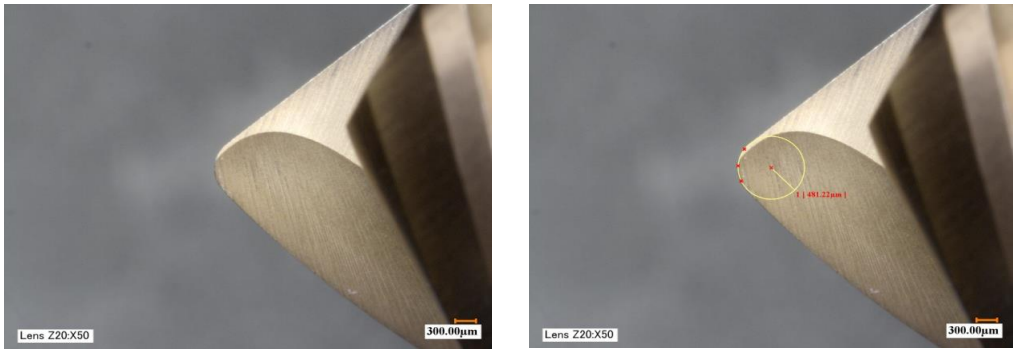

Figure 2. 3D Optical Microscope image of AlTiN coated 0.5 mm (tip radius) brand new tool on the left and radius measurement on the right

Manufacturers need to ensure that, only the functionally capable tools are being used in production process as well as by the customers. Both can be aware about functional geometry deviations and wear characteristics of tools at the end of the machining processes precisely only by this way. ZrN coated 0.5 mm nominal tip radiused brand new tool's optical microscopic images are given in Figure 3 as an example of all conducted image captures.

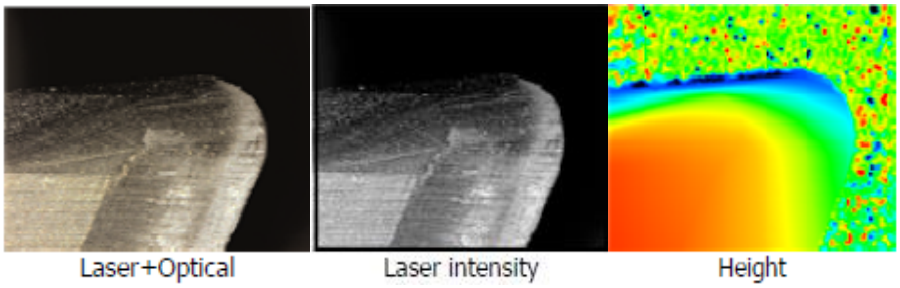

Figure 3. ZrN coated (0.5 mm nominal tip radii) brand new tools' optical microscopic images

ZrN coated 1.0 mm nominal tip radius tools optical microscopic images before and after end milling operation are given in Figure 4 respectively, as an example of all conducted image captures. Optical images give data about wear mechanism of the used tools. Wear volume of the materials can be measured by image processing applications. Images help to find out the type of the wear mechanism, as well.

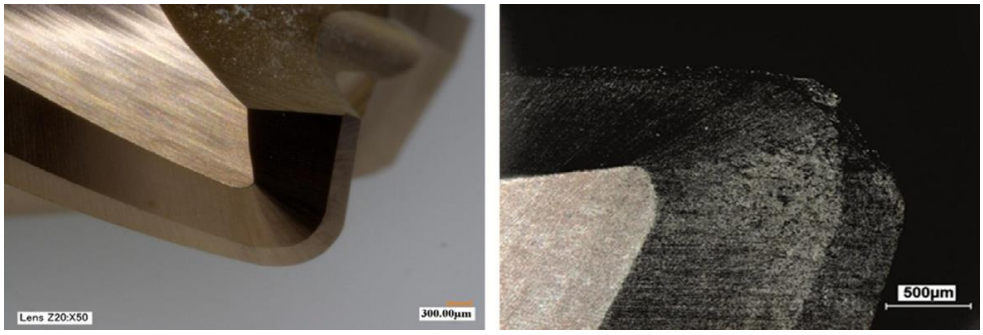

Figure 4. ZrN coated (1.0 mm nominal tip radii) tools' optical microscopic images before (on the left) and after (on the right) end milling operation

We not only visualize the tools but also examine the milled surfaces by optical microscopes. End milled Al 7075 surfaces "laser and optical", "optical", "laser intensity" and "height" images are given in Figure 5 respectively. These images show the surface conditions of the milled surfaces. When the manufacturing marks of the surfaces are examined researchers can find valuable clues about the conditions of tools, as well.

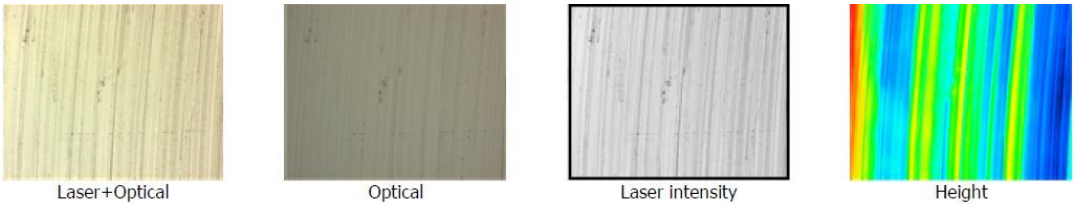

Figure 5. Captured images of end milled Al 7075 surface

The conducted ANOVA (Analysis of Variance) test results indicate 0.75 mm depth of cut recorded the best surface roughness means the minimum "Arithmetical Average Surface Roughness" (R_a) value as 0.274 µm. 50 m/min, minimum cutting speed is resulted the minimum surface roughness. The experiments in this study also confirmed that the minimum feed rate leads to the minimum surface roughness of end milled products. The analyses show that ZrN provides the best surface quality with the lowest surface roughness of the aluminum workpieces.

4. CONCLUSIONS

This work is about the use of innovative optical techniques in 3D imaging and visualization of materials performance analysis experimentally. It also focuses on optimization of process parameters and different coating materials which combined with different tool tip radiuses to obtain the high surface quality for end milling processed Al 7075 alloy parts in dry cutting conditions. As a result of the conducted experimental works 0.75 mm depth of cut recorded the best surface roughness. Additionally, 50 m/min cutting speed is resulted the minimum surface roughness. The experiments in this study also confirmed that the minimum feed rate leads to the minimum surface roughness of end milled products.

Surely, measurement processes should be analyzed and all operation should be reported according to the related international standards in optical measurements. For continuous improvement of products and processes as well as a successful process control system, measurement equipment must be calibrated and verified. Only by this way the procedure can be traceable.

REFERENCES

[1]. *Quality Management Systems – Requirements*, ISO Std. 9001, 2008.
[2]. A.T. Rosell, *New Measurements Techniques: Optical Methods for Characterizing Sound Fields*, PhD Thesis, Technical University of Denmark: 2014.
[3]. M. Berger. (2007) "Nanoscopy - Nanoscale Resolution in Light Microscopy" Available: https://www.nanowerk.com/spotlight/spotid=2358.php
[4]. *Optische Messtechnik an Mikrotopografien Kalibrieren von konfokalen Mikroskopen und Tiefeneinstellnormalen fur die Rauheitsmessung*, VDI Std. 2655 - Blat 1.2, 2010.
[5]. M. N. Durakbasa, A. Akdogan, A.S. Vanli, A. Gunay, "Determination of Cutting Tool Geometries with High Precise Measurement Techniques and Investigation of Their Effects on Workpiece Surface Properties", *12th IMEKO TC10 Workshop on Technical Diagnostics New Perspectives in Measurements, Tools and Techniques for Industrial Applications.*, Florence, Italy, 2013.
[6]. *Geometrical Product Specifications (GPS)- Surface texture: Profile method, Calibration of contact (stylus) instruments*, ISO Std. 12179, 2000.
[7]. *Geometrical product specifications (GPS)- Surface texture: Areal: Part 6: Classification of methods for measuring surface texture*, ISO Std. 25178-6, 2010.

ICETI
www.iceti.org
2018
07-11 MARCH
BUDAPEST
HUNGARY
II. INTERNATIONAL CONFERENCE ON ENGINEERING TECHNOLOGY AND INNOVATION

A Cfd Study Of Separating Reattaching Flows

Taner Cosgun[1], Ahmet Yurtseven[1], Nurten Vardar[1]

Abstract

Separation and reattachment of turbulent flows can be seen in many engineering applications and play an important role. Diameter change in internal flows like pipes, combustion chambers or chemical reactors or separation in external flows around cars, foils or buildings create a recirculation region and changes the flow characteristics. The benchmark configuration to observe these type of flows called backward facing step flow. In this study, turbulent flow over backward facing step is numerically investigated via computational fluid dynamics. Expansion ratios are changed for same inlet conditions to examine the variation of separation zone. Velocity fields in different locations are reported as a result of separating behavior in different conditions. Pressure coefficients on the bottom wall are also presented.

Keywords: *Separating Flows, Computational Fluid Dynamics, Backward Facing Step Flow*

1. INTRODUCTION

Flow separation and reattachment mechanism occurs in many practical engineering applications. External flows like flow around vehicles, buildings and foils and internal flows like sudden diameter change in pipes and passages in turbo machinery are some of the common examples. In these kind of flows, flow separation from solid boundary creates a recirculation zone and cause a complicated turbulent zone. Because of the industrial importance and being an importance area of fluid mechanic research, separating-reattaching flows are focused by many researchers for many years.

The simplest case to investigate the flow separation reattachment behavior is the backward facing step flow. Because of the geometrical simplicity and involving many of the characteristics of the separating reattaching flows, backward facing flow is studied in many research. Jovic and Driver [1] experimentally investigate the turbulent flow over backward facing step and report the features of the flow field. in their wind tunnel experiment, Adams [2] examine the separating shear layer and its effect on the recirculation region. Vogel [3] investigates the heat transfer behavior on the backward facing step flow reports the heat transfer characteristics.

along with the experimental affords, many numerical studies about the separating reattaching flows can be found in the literature. Erturk [4] investigates 2d backward facing step flow with finite difference approach and presents high Reynolds numbers solutions. Nie and Armaly [5]studied the effects of step high on the flow over backward facing step and revealed the heat transfer characteristics. besides, more complicated numerical approaches like large eddy simulation [6, 7, 8] and direct numerical simulation [9,10] were used to enlighten the details of the turbulent field.

In this study, turbulent flow over backward facing step is numerically investigated via computational fluid dynamics to examine the effect of expansion ratio on the flow characteristics. By this manner, inlet conditions are kept constant and 3 different expansion ratio were tested. Results are presented in terms of reattachment lengths, velocity distributions and pressure coefficients.

2. COMPUTATIONAL APPROACH

Turbulent flow over backward facing step is modeled numerically. The geometry of the problem is schematically shown in figure 1. Overall length of the geometry is L_x=30h. inlet length is L_i =3h and width l_z= 4h. the height

[1]*Corresponding author: Yildiz Technical University, Department of Naval Architecture and Marine Engineering - 34349 Besiktas - Istanbul, Turkey. tcosgun@yildiz.edu.tr*

from the expansion to top of the geometry is l_y=5h. here, h is the smallest step size(step 1). behind this size, 1.5 h (step 2) and 2 h (step 3) step heights were also tested.

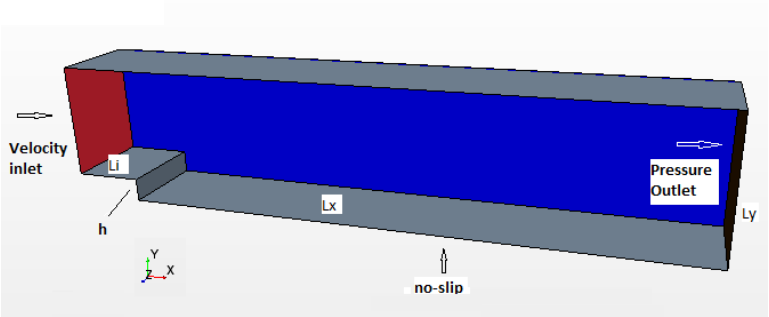

Figure 1. Geometry of the problem

Developed velocity profile is imposed through the inlet. Reynolds number at the inlet is Re_h=5000. Reynolds number is defined as $\mathrm{Re} = U_b h / \nu$. Here, U_b is the axial velocity at the inlet, ν is the kinematic viscosity and h is the smallest step size. Numerical simulations are performed with StarCCM+ commercial code. Also, turbulent field is modeled with Reynolds Stress turbulence model [11].

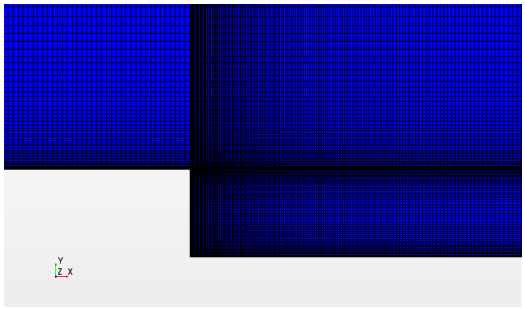

Figure 2. Mesh Structure Near the Step

Computational grid was created using structural hexahedral elements. Detailed view of the mesh structure near the step can be seen in figure 2. To clearly identify the flow characteristics near the walls, wall y+ on the wall boundaries were kept below the value of 1. Here, wall y+ was defined as y+=uy/v, where u is the stream wise velocity, y is the wall distance of the first grid and v is the kinematic viscosity.

3. RESULTS

Numerical results of the effect of expansion ratio on the general futures of the flow field are presented below. Figure 3 shows the variation of the recirculation bubble for different expansion ratios.

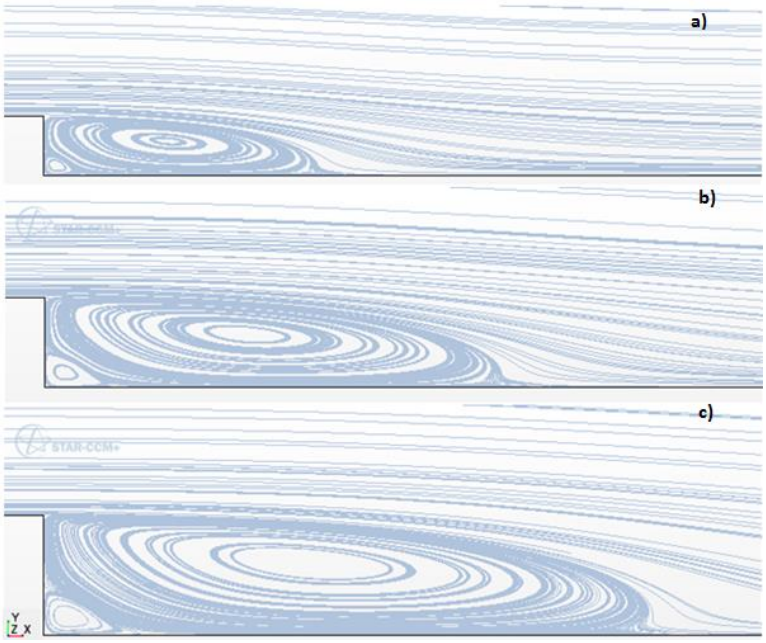

Fig.3 Variation of the recirculation bubble for different expansion ratios.

Streamlines showing the change of the shape of recirculation bubble for different step heights. Fig.3 a), fig 3 b) and fig.3 c) represents the results of step 1, 2 and 3 respectively. A main recirculation bubble develops downstream of separation point. Also, a counter rotating secondary corner eddy occurs for all step heights. The size of the main recirculation bubble increases with the increase of the expansion ratio. So, reattachment length increase for higher expansion ratios, as well. Recirculation lengths are determined by examining the shear stress at the bottom wall. The point where the shear stress going to zero chosen as the reattachment point.

Table 1 presents the results of normalized recirculation lengths.

Table 1. normalized reattachment lengths

	h(m)	X_r/h
step_1	0.0096	5.416667
step_2	0.0144	5.368056
step_3	0.0216	5.023148

If we normalize the recirculation length with the step height, recirculation lengths are decreasing with the increase of the step height (i.e. expansion ratio). Otugen [12]suggests that it may be the result of faster development of separating shear layer. Figure 4 shows the normalized velocity profiles in different locations.

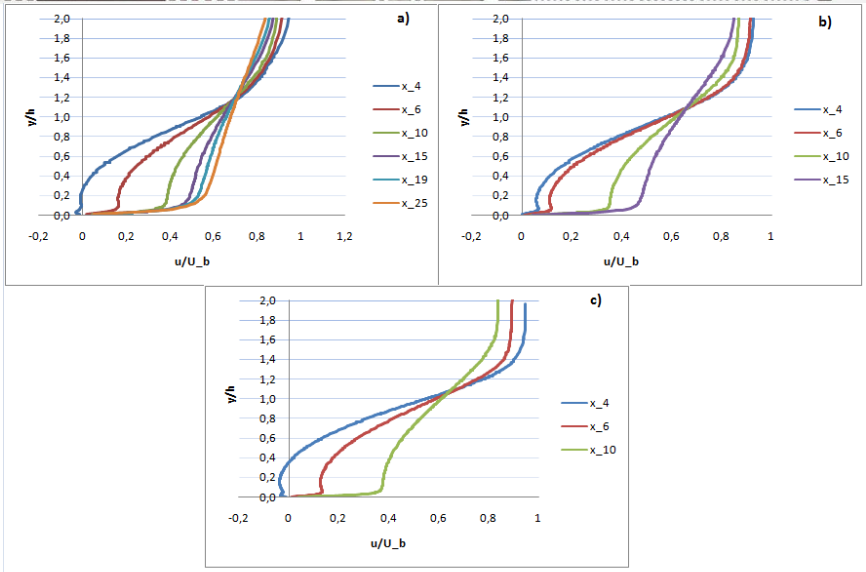

Figure 4 Normalized velocity profiles in different locations.

To seek the reason of this rapid development of recirculation region, the velocity profiles in different locations are investigated. Fig.4 a), fig 4 b) and fig.4 c) represents the results of step 1, 2 and 3 respectively. Also, in legend, x_4 represents the location of 4 times of step height from the separation edge in streamwise direction. Velocity values are normalized with the bulk velocity at the inlet. Wall normal location is normalized with the step height, too. Effect of recirculation can be seen in each expansion ratio. It is also more apparent in closer locations to the step. Figure 5 presents the normalized velocity profiles in different locations of the recirculation bubble for each expansion ratio.

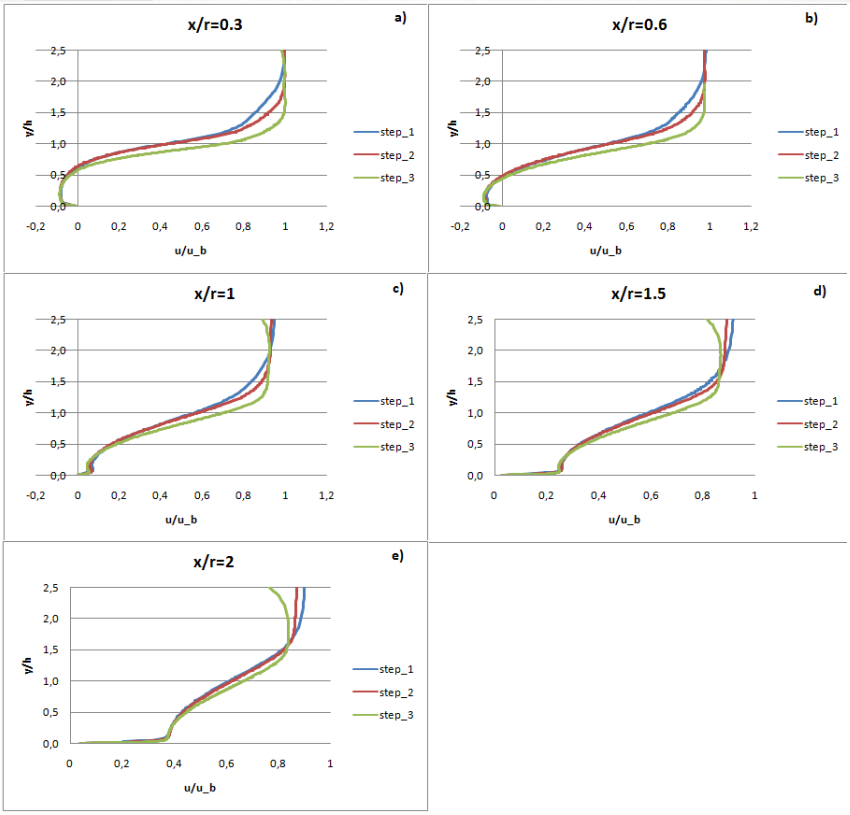

Figure 5 Normalized velocity profiles in different locations of the recirculation bubble

To make a better comparison, velocity profiles in the same locations of recirculation bubble are investigated for each expansion ratio. . Fig.5 a), fig 5 b).fig.5 c)...etc. represents the different locations of the recirculation bubbles. In headings of the figures, x represents the streamwise location from the corner of the step and r represents the recirculation length. For every location, velocity profiles shows a similar behavior in the lower parts of the domain. However, at the upper portions, higher expansion ratios exhibit a flatter profile, while lower expansion ratios, for example step 1, shows a parabolic one. This situation may be the results of more turbulent behavior of the flow with the increase in the expansion ration. Figure 6 shows the turbulence intensities in different locations for each expansion ratio.

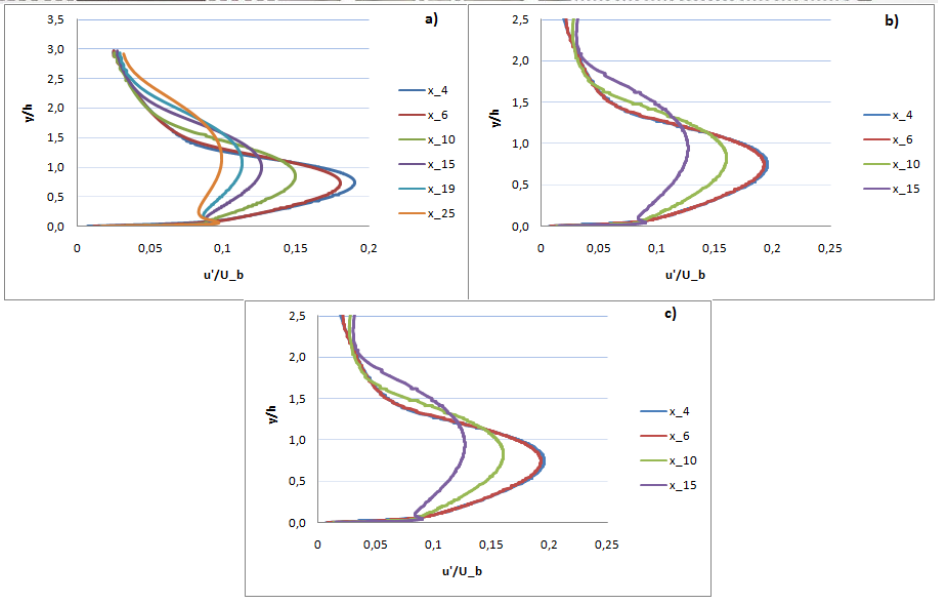

Figure 6. Turbulence intensities in different locations

Turbulence stresses are normalized with the bulk velocity at the inlet, to obtain the turbulence intensity. Legend is similar to the figure 4. Turbulence intensities are higher in closer locations to the step for every expansion ratio. However, peak of the turbulence intensity is higher for higher step heights. This may be the reason for the rapid development of the flow, which is observed at the streamlines and reattachment lengths.

Pressure coefficients along the bottom wall for each expansion ratio can be seen in figure 7.

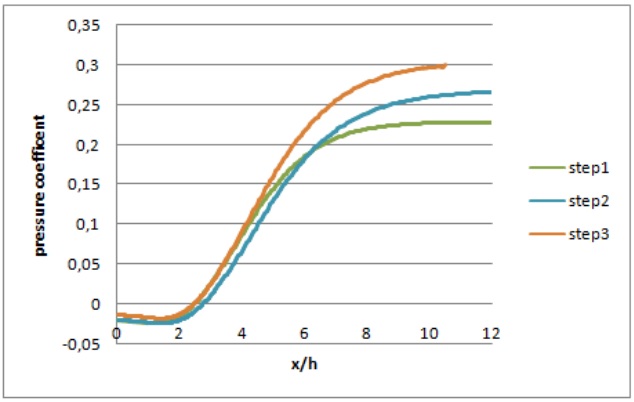

Figure 7. Pressure coefficients along the bottom wall

Inside the recirculation region, magnitudes of the peak pressure coefficient are close to each other for every expansion ratio. However, higher expansion ratios results in higher pressure coefficients in the recovery region. Recovery lengths are also higher for larger expansion ratios. Fully recovered portions are cannot be seen in the figure for the largest expansion ratio because of the limited dimensions of the solution domain.

4. CONCLUSIONS

This study aims to distinguish the effect of expansion ratio on the flow characteristics of separating reattaching flows. Primary findigs are listed below:

- A main recirculation bubble develops downstream of separation point. Also, a counter rotating secondary corner eddy occurs for all step heights. The size of the main recirculation bubble increases with the increase of the expansion ratio. However, if we normalize the recirculation length with the step height, recirculation lengths are decreasing with the increase of the step height.

- Velocity profiles in the same locations of recirculation bubble are investigated for each expansion ratio. For every location, velocity profiles shows a similar behavior in the lower parts of the domain. However, at the upper portions, higher expansion ratios exhibit a flatter profile, while lower expansion ratios, shows a parabolic one.

- Turbulence intensities are higher in closer locations to the step for every expansion ratio. Peak of the turbulence intensity is higher for larger expansion ratios.

- Higher expansion ratios results in higher pressure coefficients in the recovery region. Recovery lengths are also higher for larger expansion ratios.

REFERENCES

[1]. Jovic S., Driver M.V., 1994. "Backward-facing step measurements at low Reynolds number, Re(sub h)=5000", *Nasa Technical Report*, NASA-TM-108807

[2]. E. W. AdamsJ. P. Johnston, "Effects of the separating shear layer on the reattachment flow structure Part 1: Pressure and turbulence quantities" *Experiments in Fluids*, Volume 6, Issue 6, pp 400–408. 1988

[3]. Vogel JC, Eaton JK. "Combined Heat Transfer and Fluid Dynamic Measurements Downstream of a Backward-Facing Step". ASME. *J. Heat Transfer*.;107(4):922-929. 1985

[4]. E. Erturk, "Numerical solutions of 2-D steady incompressible flow over a backward-facing step, Part I: High Reynolds number solutions". *Computers & Fluids* 37(6):633-655. 2008

[5]. J. Nie, B. F. Armaly, "Three-dimensional convective flow adjacent to backward-facing step - Effects of step height." *International Journal of Heat and Mass Transfer* 45(12):2431-2438.2002

[6]. B.Panjwani, I. S. Ertesvåg, A. Gruber,K. E. Rian. Large eddy simulation of backward facing step flow. *In 5th National Conference on Computational Mech*.2009

[7]. X. Han, S. Krajnović. "Validation of a novel very large eddy simulation method for simulation of turbulent separated flow". *International Journal for Numerical Methods In Fluids*. 73:436–461. 2013

[8]. M. L.Shur,P. R.Spalart,M. Kh.Strelets,A. K.Travin. "A hybrid RANS-LES approach with delayed-DES and wall-modelled LES capabilities". *International Journal of Heat and Fluid Flow*.Volume 29, Issue 6, 2008

[9]. H. Le,P. Moin,J. Kim. "Direct Numerical Simulation of Turbulent Flow over a Backward-Facing Step". *Journal of Fluid Mechanics* 330. 1997

[10]. D.Y. Ding, S.Q. Wu. "Direct numerical simulation of turbulent flow over backward-facing at high Reynolds numbers". *Science China Technological Sciences*. Volume 55, Issue 11, pp 3213–3222.2012

[11]. CD-ADAPCO star ccm+ manual

[12]. Otugen M. V. "Expansion ratio effects on the separated shear layer and reattachment downstream of a backward-facing step". *Experiments in Fluids*. Volume 10, Issue 5, pp 273–280. 1991

ICETI
www.iceti.org
2018
07-11 MARCH
BUDAPEST
HUNGARY
II. INTERNATIONAL CONFERENCE ON ENGINEERING TECHNOLOGY AND INNOVATION

IoT and Arduino Based Mobile Accessible Smart Parking System

Fatih Kayaalp[1], Sultan Zavrak[1], Huseyin Bodur[1], Murat Oflezer[1]

Abstract

Because of the many facilities provided by the use of the vehicles, many people prefer to buy and use their own cars today. This results a great number of cars registered to traffic both in Turkey and the world. Although there are many facilities provided by vehicles, many problems arise because of the huge number of vehicles in traffic such as increasing the carbon emissions and triggering global warming, time loss due to traffic congestion, stress on drivers, vital and financial losses caused by accidents. Because of these problems, many researchers have focused on this area with many studies. The Internet of Things (IoT), which has emerged in recent years as a branch of the field of computer engineering, also contributes to the solution of some of these problems, especially by applications like smart homes or smart cities. The presented work also describes a Smart Parking System, which can be considered as a smart city application, using IoT, Arduino, Mobile platform and Cloud technologies together. With this solution, it is contributed to find available parking lot locally in the parking area for the drivers. Besides that, the parking area can be accessed and monitored on the internet via mobile application by drivers and the parking lots can be reserved before accessing the parking area, navigation route to the reserved parking area is shown in the mobile application, parking fee collection management can be calculated according to the parking records and shown on the mobile application, parking area management for both member and non-member drivers are taken into considerations. The implemented system results as saving time and fuel, decreasing the traffic congestion caused by the vehicles during the time for searching parking place, simplifying the management of parking area.

Keywords: IoT, Arduino, Mobile, Smart Parking System, Cloud

1. INTRODUCTION

Because of the technological developments in automobile industry, improvements of the financial conditions of the people, growth of the cities that does not allow people going on foot for long distances; many people prefer to buy and drive their own cars.

As seen in Figure 1, the number of vehicles has exceeded 1 billion and according to another statistic from TUIK, the total number of registered vehicles to the traffic was 20456000 at May 2016 in Turkey and 53% of this number was passenger vehicles [1].

[1] *Corresponding author: Duzce University, Department of Computer Engineering, 81620, Duzce, Turkey.* fatihkayaalp@duzce.edu.tr

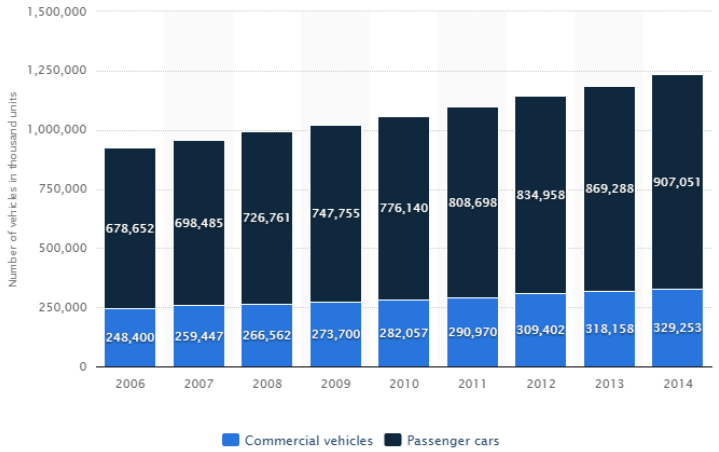

Figure 1: Changing in the number of commercial and passenger cars from 2006 to 2014 worldwide [2]

In the light of the given statistics above, number of cars both for Turkey and world has reached big numbers. Some authorities predict this number to exceed 2 billion cars by the year 2035 [3]. Even though the cars provide many facilities to human daily life, they also have potential to create many problems. Some of these are:

- Triggering global warming because of the carbon emission rates created by using fossil fuels for energy sources of the cars.
- Traffic congestions occurring on the roads at specific hours of the days as the infrastructures of the roads are not good enough to handle these huge numbers of cars.
- Loss of time and work caused by traffic congestions
- Stress and phycological problems caused by traffic congestions on drivers
- Traffic accidents resulting as financial losses or death caused by stress, rush or carelessness

Many problems have focused on this common problem and presented many studies by using technologies on their own sciences. IoT [4] which is one of the branches of computer science has provided some flexibilities that can be used to solve this problem in many ways. IoT can be defined as communicating sensors over internet or Wi-Fi that send measured data to a base station for monitoring a remote environment. As the sensors have small physical dimensions, capable to sense and measure data over Wi-Fi or internet, have easy installation, IoT can be deployed to many environments easily and getting so popular on recent years.

Physical Objects + (Sensor / Controller / Actuator) + Internet = Internet of Things (IoT)

Smart cities or smart homes are two of the areas that IoT has been deployed. Light, humidity, noise, temperature, air pollution, and motion are some of the popular cases that have been monitored at these smart home/city applications. Most projects have same structure including transferring of sensed data over internet/Wi-Fi, insertion into the databases and analysis of the data in order to understand the abnormal changes in the data.

2. RELATED WORKS

There are many smart home/city studies in literature based on IoT from many scientists all over the world. As traffic is a common problem and smart parking areas management contributes to the solution of this problem, many researchers have paid attention and presented different architectures. Some of these are given below.

Huang and colleagues presented a smart parking application that is being observed with cameras. The system has features such as allowing users to find free parking spaces, reminding the driver when the parking place is forgotten, remotely monitoring the parking area with the camera, and facilitating the work of the security officer [5]. Pham and colleagues presented a study to solve the problem of finding a parking space with a new cloud-based algorithm that helps the user to find a vacant lot in a parking lot and redirects to a vacant place in another car park nearby if there is no parking space [6]. In the study proposed by Ramaswamy, an IoT-based intelligent parking system

application was introduced to reduce the effect of atmospheric greenhouse gases on climate change. Thanks to this application, a system has been realized to prevent the vehicles from finding extra parking spaces and excess CO_2 emissions in the meantime [7].

Depending on the number of vehicles in use, there is a problem of finding parking spaces during the use of these vehicles in everyday life. Finding parking space can become a major problem, especially when you are looking for a place to park in crowded residential areas or the parked position (the locations close to the main streets fill up very early). In order to solve this problem, people either must park their vehicles farther away and have to walk, or have to search for vacancies by taking extra rounds to find a parking lot. Obviously, unnecessary fuel wastage occurs in this process, more CO_2 is emitted and time is lost.

Since this problem is experienced in almost all countries, it is necessary to have solutions in various forms. Alternative solutions such as the construction of underground parking garages, the prohibition of vehicle access to specific areas at certain times, the compulsory prohibition of public transportation, the payment of parking at certain hours or the efficient use of existing parking areas with different management techniques should be designed.

3. ARCHITECTURE OF THE PROPOSED MODEL

In the light of the presented problems above, there is a need for smart parking areas by using the latest technologies. We have designed a smart parking application to contribute to these studies with IoT, Arduino [8] and Cloud Technologies with the capabilities listed below:

- Determining the free parking lots in a car park, informing and directing the driver about the available parking lots,
- Listing the parking areas around his location before reaching the parking area by a mobile application,
- Displaying the occupancy status of the parking lot selected from the parking lots listed in the mobile application, and reserving the parking lot in case of availability,
- Showing the navigation route to the user through the mobile application to be followed for the transportation to the reserved parking lot,
- Providing facilities in general management issues such as tracking vehicles parked in the parking lot and the collected fees,
- Keeping a database of parked vehicles and parking spaces in a cloud environment and, if necessary, providing immediate or retrospective reporting.
- Helping drivers find empty parking spaces, contributing to reduced fuel consumption, waste of time, reduced traffic complexity, and unnecessary reduction of atmospheric carbon emissions.

The proposed model as seen in Figure 2 has been based on two main parts which are hardware and software. The detailed information about these subjects are given in below subsections.

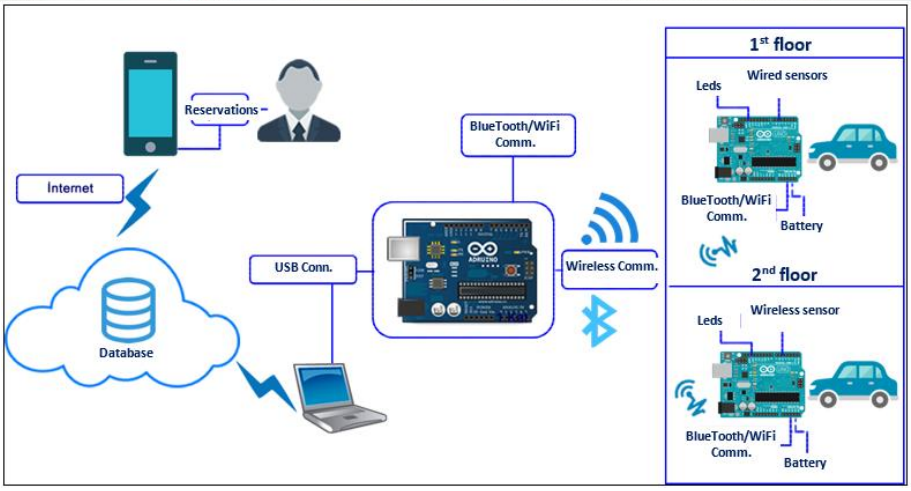

Figure 2: Architecture of the proposed model

4.1. 3.1. Hardware Architecture

Hardware consists of Arduino cards, Wi-Fi and Bluetooth communication modules, led lights with different colors meaning Free/Reserved/Occupied for each park lot, distance sensors.

4.2. 3.2. Software Architecture

Software consists of Android operating system [9], the application that runs on Android written with Java by using Android Studio IDE [10], Firebase [11] as a cloud based NoSQL database to store the information about the parked cars.

4. IMPLEMENTATION OF THE MODEL

4.3. 4.1. Database Design

The "Settings" table in "Otopark" database in Figure 3, stores *maxKilometer*, *memberHourFee* and *NonMemberHourFee* data values.

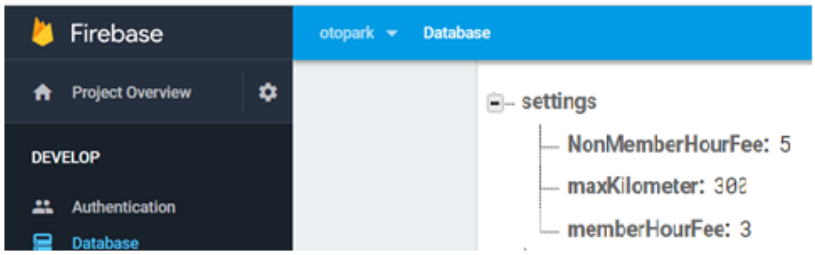

Figure 3: Settings table

The "Parking" table in "Otopark" database in Figure 4 stores data for each parking areas such as "Duzce Municipality Parking, KremPark Parking". Each parking area has its GPS (Global Positioning System) coordinates (latitude and longitude) as *X* and *Y*. Each parking lot in a parking area has been defined with location details, state (0: parked, 1: available, 2: reserved,), entry date and ID of the driver reserved when the driver enters the parking area.

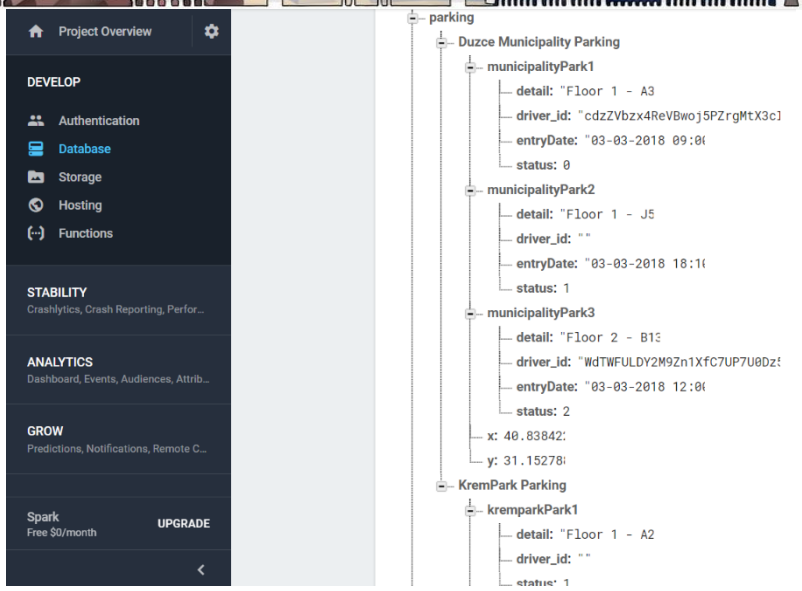

Figure 4: Parking table

4.4. 4.2. Mobile Parking Application Screens

4.5. 4.2.1. Register/Login Screen

The mobile application initially requires the users to register to the system as seen in Figure 5. After the registration of the user with an e-mail and a password, a unique id for the user is created and stored in database. After registration, the user can login to the system by using the form in Figure 6. The necessary information about the registered users are stored in database as seen in Figure 7.

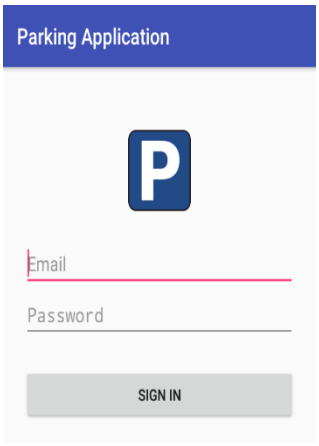

Figure 5: Registration Form Screen

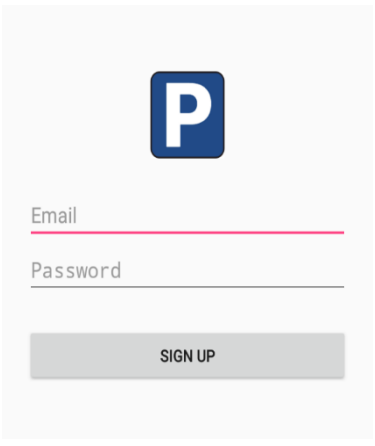

Figure 6: Login Screen

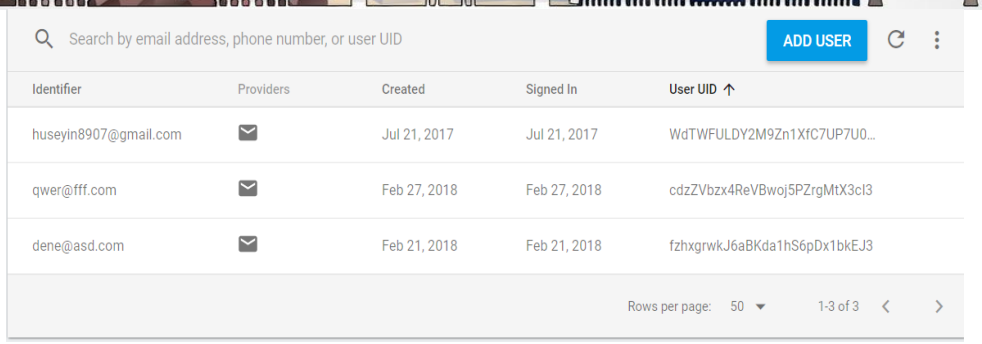

Figure 7: User Information Details

4.6. 4.2.2. Parking Lot Reservation Screen

After logging in, a list of the available parking areas in the range of max distance are shown to the user as seen in Figure 8. In order to notify the user about the distances to the alternative parking areas, the distances from the location of the user to each parking area are also written in the list which are calculated after getting the permission for using user's the location data as seen in Figure 9.

If the user location couldn't be detected, the distance of the parking area is assigned to *maxKilometer* value so that the user can reserve a parking lot.

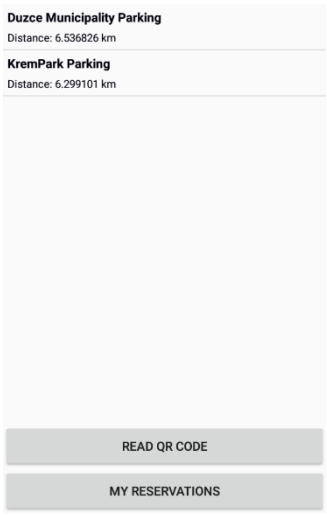

Figure 8: The list of available parking areas

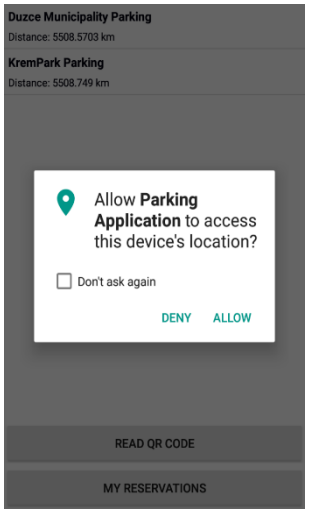

Figure 9: Permission for getting user's location

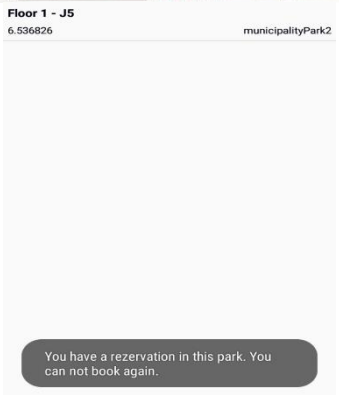

Figure 10: Warning message for the second reservation at same parking area

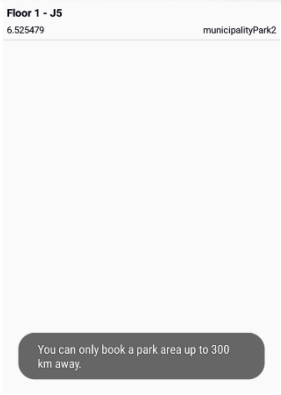

Figure 11: Warning message for max reservation distance

The user can reserve one of the available parking lots in selected parking area. If a user tries to reserve a second parking lot, the system warns the user that second reservation is not allowed as seen in Figure 10. And if the user tries to reserve a parking lot in a parking area that has a higher distance value defined as *maxKilometer* for reservation, the system warns the user that max distance is exceeded and not allowed as seen in Figure 11.

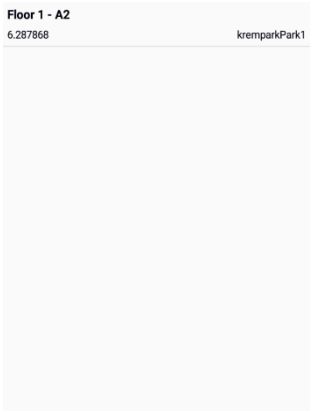

Figure 12: Making a reservation

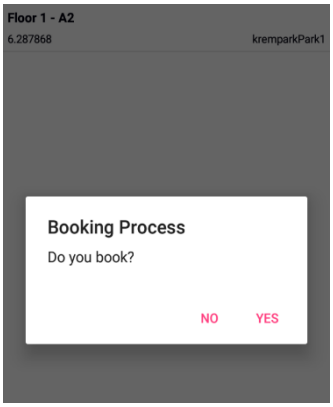

Figure 13: Confirming reservation

When the user clicks on the available parking lot seen in Figure 12, a message is displayed on the screen asking for the parking lot to reserve or not. If "Yes" is clicked, the parking lot becomes reserved (state=2) which is seen in Figure 13. The user can list his reservations on the by clicking on "Reservations" on Home screen.

By clicking Reservations button, the user's reservations are listed in Figure 14. If the user clicks on "Open In Map", the route from the current location to location of the parking area will be shown on Google Maps as seen in Figure 15. The reservation can be cancelled by "Cancel Reservation" and can return back to the previous screen by "Cancel".

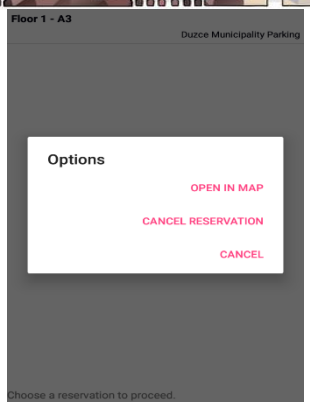

Figure 14: Reservation options

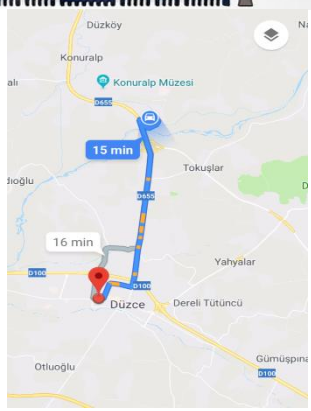

Figure 15: Navigation to parking area

4.7. 4.2.3. Entering/Leaving Parking Area Screen

After reaching the parking area, the user is required to read the QR (Quick Response) code through the mobile application at the entrance as seen in Figure 16. By reading the QR code, the date and time values are inserted into the database and the lighting system on the floor helps the user to find the reserved parking lot by him.

Figure 16: QR code reading at the entrance

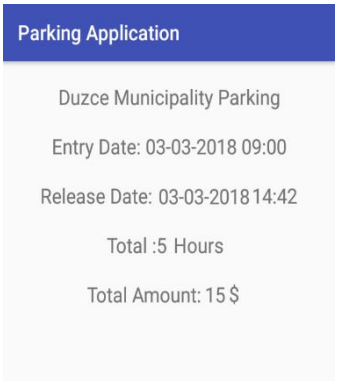

Figure 17: Parking fee calculation report when exiting the parking area by reading QR code

When the user wants to leave the parking area, the user again reads the QR code through mobile application. Then exit date and time values are inserted into the database for calculating the total parking price and listed on the screen as seen in Figure 17. The same total parking fee information is also displayed on the parking stuff's display.

By storing the entry and exit date and time data, total income for the parking area can be reported for a defined day or time period easily.

4.8. 4.2.4. Parking Area Management for Nonmember Users

The drivers who want to park a car into the parking area are not required to use only the mobile application. But, in order to encourage the users to use mobile application, the parking price for an hour for a member is less than for the parking price for a nonmember driver.

There are some alternative methods in general use for detecting the entry and exit date/time values and parking total prices for cars by using car plate detection systems or printing a ticket at the entry for each car and calculating the total parking price according to the time difference. Another method to be used for integration to our proposed method is waiting the driver to read the QR code for a specified time period. When timeout occurs, an available

parking slot information with the current date and time value is printed on a ticket and given to the driver. The lighting system on the floor helps him to find the parking lot. After routing the driver to that parking lot, the parking lot record on the database is updated with entry date/time and "quest" value for the ID of the driver. When a quest driver wants to exit from the parking area, total parking fee is calculated according to the time difference due to the given ticket information by using nonmember price. The electronic prototype of the designed system is shown in Figure 18.

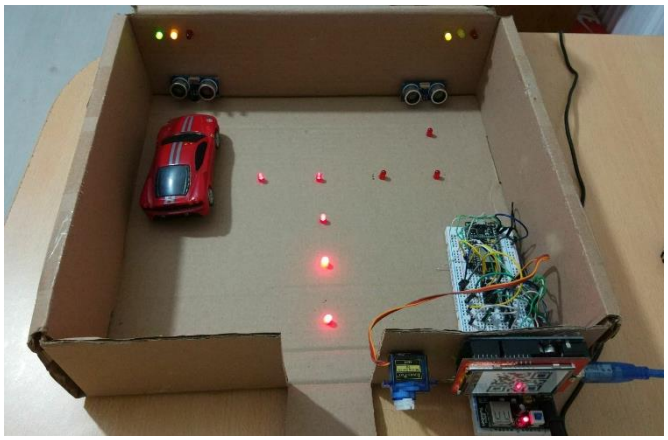

Figure 18: Prototype of the parking area

5. CONCLUSIONS

An IoT and Arduino based mobile accessible smart parking system storing the parking data in a NoSQL database (Firebase) has been designed, implemented and presented. Contributions to the solution of problems like CO_2 emission rates, time losses during searching for parking places, stress on drivers are aimed. By the proposed method, management of parking areas and finding available parking spaces problems can be easily solved.

Managing more parking areas in different cities, cancelling the reservations after a defined latency time, disabling drivers that makes reservations but don't park his car for more than 3 times, listing the available parking areas in an ascending distance order are planned for future works.

ACKNOWLEDGMENT

This study has been funded by Duzce University Research Fund Project Number: 2017.06.01.548.

REFERENCES

[1]. Turkiye Istatistik Kurumu, "Turkiye Istatistik Kurumu, Motorlu Kara Tasitlari, Mayis 2016," 2016. [Online]. Available: http://www.tuik.gov.tr/PreHaberBultenleri.do?id=21605. [Accessed: 21-Feb-2017].

[2]. Statista, "Number of passenger cars and commercial vehicles in use worldwide from 2006 to 2014 in (1,000 units)," 2015. [Online]. Available: https://www.statista.com/statistics/281134/number-of-vehicles-in-use-worldwide/.

[3]. J. Voelcker, "1.2 Billion Vehicles On World's Roads Now, 2 Billion By 2035: Report," *Green Car Reports*, 2014. [Online]. Available: https://www.greencarreports.com/news/1093560_1-2-billion-vehicles-on-worlds-roads-now-2-billion-by-2035-report. [Accessed: 21-Feb-2017].

[4]. L. Atzori, A. Iera, and G. Morabito, "The internet of things: A survey," *Comput. networks*, vol. 54, no. 15, pp. 2787–2805, 2010.

[5]. C.-H. Huang, H.-S. Hsu, H.-R. Wang, T.-Y. Yang, and C.-M. Huang, "Design and management of an intelligent parking IOT system by multiple camera platforms," in *Networking, Sensing and Control (ICNSC), 2015 IEEE 12th International Conference on*, 2015, pp. 354–359.

[6]. T. N. Pham, M.-F. Tsai, D. B. Nguyen, C.-R. Dow, and D.-J. Deng, "A Cloud-Based Smart-Parking System Based on Internet-of-Things Technologies," *IEEE Access*, vol. 3, pp. 1581–1591, 2015.

[7]. P. Ramaswamy, "IoT smart parking system for reducing green house gas emission," in *Recent Trends in Information Technology (ICRTIT), 2016 International Conference on*, 2016, pp. 1–6.

[8]. "Arduino - Home," 2018. [Online]. Available: https://www.arduino.cc/. [Accessed: 21-Feb-2018].

[9]. "Android," 2018. [Online]. Available: https://www.android.com/%0A. [Accessed: 21-Feb-2018].

[10]. "Download Android Studio and SDK Tools | Android Studio," 2018. [Online]. Available: https://developer.android.com/studio/index.html. [Accessed: 21-Feb-2018].

[11]. "Firebase," 2018. [Online]. Available: https://firebase.google.com/. [Accessed: 21-Feb-2018].

ICETI
www.iceti.org
2018
07-11 MARCH
BUDAPEST
II. INTERNATIONAL CONFERENCE ON ENGINEERING TECHNOLOGY AND INNOVATION

Microstructural Characterization and Heat Treatment Effect on Photoluminescence of $BaTa_2O_6:Sm^{3+}$ Phosphor

Mustafa Ilhan[1]*, Zarif Catalgol[1], Seyyid Abdulkadir Ilhan[2], Ramazan Samur[1]

Abstract

Trivalent samarium ion (Sm^{3+}) doped (2.5 mol%) $BaTa_2O_6$ phosphors were sintered by solid state reaction route at temperatures between 1150 and 1425°C for 20 hours in order to determine temperature effect on structural and luminescence properties. Structural and luminescence properties of the ceramic powder samples were investigated by X–ray diffraction (XRD), scanning electron microscopy (SEM), energy dispersive spectroscopy (EDS) and photoluminescence (PL) analyses. In XRD analysis, while Sm^{3+} doped $BaTa_2O_6$ structure has single phase tetragonal tungsten bronze (TTB) structure above 1350°C, small amount orthorhombic $BaTa_2O_6$ phase appeared at temperatures of 1150 and 1250°C. SEM analysis revealed that size of Sm^{3+} doped $BaTa_2O_6$ grains increased with increasing the heat treatment temperature. In the PL analysis, depending on the increase in heat treatment temperature, the intensity of emission reached maximum at 1425°C. Increase of the emission intensities of $^4G_{5/2}\rightarrow{}^6H_{5/2}$ and $^4G_{5/2}\rightarrow{}^6H_{7/2}$ transitions may have been attributed to the improving crystallinity and growing symmetry, with increasing of temperature.

Keywords: XRD; SEM; Heat treatment; Luminescence; Rare earth ion

1. INTRODUCTION

Materials with the tetragonal tungsten bronze (TTB) crystal structure can exhibit different physical properties (dielectric, ferroelectric, piezoelectric etc.) depending on their chemical composition [1]. Among the phosphor materials, trivalent rare earth ion (RE^{3+}) doped oxide phosphors can be promising candidates being part of many applications in many fields due to their having useful and versatile properties. RE^{3+} doped oxide phosphors have exhibit the energy saving, long life, improved physical stability, smaller size, faster switching, significant efficiency, environmental properties [2], [3]. For trivalent samarium (Sm^{3+}) ion, which is one of the RE^{3+} ions, the emission bands can be listed as; one of these bands present in the green region (550–570 nm) because of $^4G_{5/2}\rightarrow{}^6H_{5/2}$ transition, others exist in the orange-red region (590–620 nm, 630–660 nm and 690–720 nm) due to $^4G_{5/2}\rightarrow{}^6H_{7/2}$, $^4G_{5/2}\rightarrow{}^6H_{9/2}$ and $^4G_{5/2}\rightarrow{}^6H_{11/2}$ transitions respectively [4].

Barium tantalate ($BaTa_2O_6$) compound have been investigated in terms of dielectric, photo-catalytic and optical properties in recent years [5]-[8]. $BaTa_2O_6$ has three types of crystal structure, as orthorhombic, hexagonal and tetragonal which have tetragonal tungsten bronze (TTB) symmetry [9]. TTB structure for oxide compounds having $A_2BC_2M_5O_{15}$ general formula where A, B and C correspond to cationic sites with 15, 12 and 9 C.N. (coordination number), respectively [10], [11].

[1]* *Corresponding author: Marmara University, Department of Metallurgical and Materials Engineering, 34722, Kadikoy/Istanbul, Turkey. mustafa.ilhan@marmara.edu.tr*

[2]*Department of Metallurgical and Materials Engineering, Sakarya University, Serdivan Campus, 54187, Sakarya, Turkey. seyyid.ilhan@gmail.com*

In this study, structural and photoluminescence properties of $BaTa_2O_6:Sm^{3+}$ phosphor were investigated depending on heat treatment temperature. On the other hand, photoluminescence of $BaTa_2O_6:Sm^{3+}$ phosphor has been previously reported in the literature in which the highest luminescence was obtanied for 2.5 mol% Sm^{3+} doped sample [12]. Therefore, we investigated the heat treatment effect on the photoluminescence by using 2.5 mol% Sm^{3+} doped $BaTa_2O_6$ phosphor. Microstructural and photoluminescence characterizations were performed by using XRD, SEM–EDS and PL analyses.

2. MATERIALS AND METHODS

2.5 mol% Sm^{3+} doped $BaTa_2O_6$ materials were synthesized by solid state process. Ta_2O_5 (99.9%, Alfa Aesar, Ward Hill, MA) and $BaCO_3$ (99.9%, Sigma-Aldrich, St. Louis, MO) were used as starting materials. Sm_2O_3 (99.9%, Alfa Aesar) used as dopant material. $BaCO_3$ and Ta_2O_5 powders weighted considering $BaTa_2O_6$ stoichiometry then mixed and ground in an agate mortar in the presence of acetone for 20 minutes to obtain a homogeneous mixture. Subsequently, 2.5 mol% Sm_2O_3 dopant was added to the first mixture. Resultant powder was mixed accompanied by acetone about 10 min for further homogenization. After the elimination of acetone, homogenized powder was sintered at temperatures 1150, 1250, 1350 and 1425°C for 20 hours in an electric furnace in order to investigate temperature dependent structural and luminescence properties.

The sintered powders were characterized by X-ray diffractometer (XRD, Rigaku, Tokyo, Japan, D-MAX 2200) using Cu-K_α radiation between 2θ=20–60° at 2°/min and Ni filter. Morphologic properties and elemental compositions of sintered powders were analyzed by SEM (JEOL, Tokyo, Japan, JSM–5910LV) which is equipped with EDS (OXFORD Instruments, Abingdon, England, INCAx-Sight 7274; 133-eV resolution 5.9 keV). The electron microscope was operated at 20 kV accelerating voltage for both SEM and EDS analyses. Excitation and emission spectra were monitored by Scinco fluoromaster-FS/2 model fluorometer with a Xe-arc lamp (150 W). PL analysis were carried out under room temperature.

3. RESULTS AND DISCUSSIONS

4.9. X-ray diffraction and SEM-EDS analyses

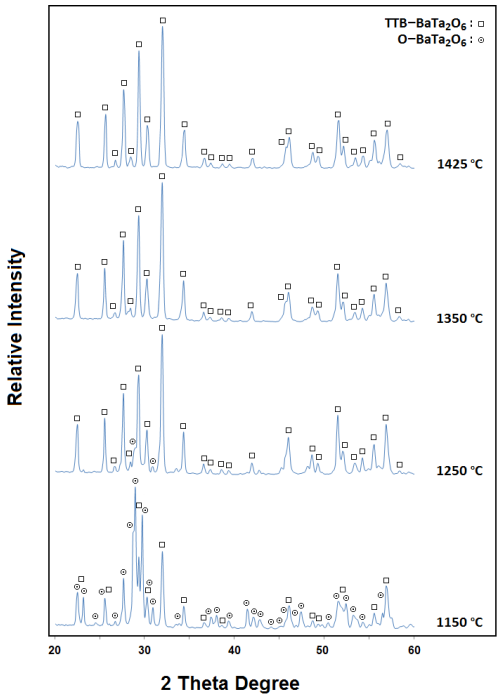

Figure 23. X-ray diffraction patterns for 2.5 mol% Sm^{3+} doped $BaTa_2O_6$ samples sintered between 1150 and 1425°C.

Figure 1 shows XRD patterns of 2.5 mol% Sm^{3+} doped $BaTa_2O_6$ samples which were sintered between 1150 and 1425°C for 20 h in order to observe the phase development, crystallization and luminescence behavior. As seen from the XRD patterns, the phase transformation started at from 1150°C low temperature orthorhombic polymorph (JCPDS card No.20–0146) to tetragonal polymorph (JCPDS card No.17–0793) of $BaTa_2O_6$. Depending on the heat treatment temperature, orthorhombic phase mostly disappeared at 1250°C and then only tetragonal phase formed between 1350 and 1425°C. Although the single phase structure was obtained at 1350°C, it's clear from the XRD results that the crystallization at temperature of 1425°C gave the desired result. The narrowing of diffraction peaks and the flatness of background for 1425°C has clearly demonstrated this effect. Also, no any secondary phase was observed depending on the temperature increase. XRD results showed that 2.5 mol% Sm^{3+} doped $BaTa_2O_6$ single phase (JCPDS card No.17–0793) crystallized in tetragonal symmetry with space group *P4/mbm* having (no.127) TTB type structure.

When TTB structure is considered in terms of cationic occupy (based on the ion's radius and coordination number), cation-site distribution can be predicted as; Ba^{2+} ions locate in the larger pentagonal (A) sites whereas they partially locate in the square (B) sites, while small triangular (C) sites remain empty. For Sm^{3+} ion doped TTB–$BaTa_2O_6$ structure, the partially full square (B) sites may be occupied by smaller Sm^{3+} ions which have an ionic radius of 1.24 Å (for 12 C.N.) compared to 1.61 Å (12 C.N.) for Ba^{2+}. Samarium cations might also enter into the larger pentagonal (A) sites in case of empty from Ba^{2+} cations in which Sm^{3+} ions can be replaced by some Ba^{2+} lead ions due to the barium evaporation during high heat treatment process [13]. But, the vacant triangular (C) sites are too small for such occupation. Moreover, the charge compensation of TTB structure may be ascribed to the evaporation of Ba^{2+} cations. Therefore, the continuation of the charge balance and the improved crystallinity could be attributed to mostly heat treatment effect of 1425°C.

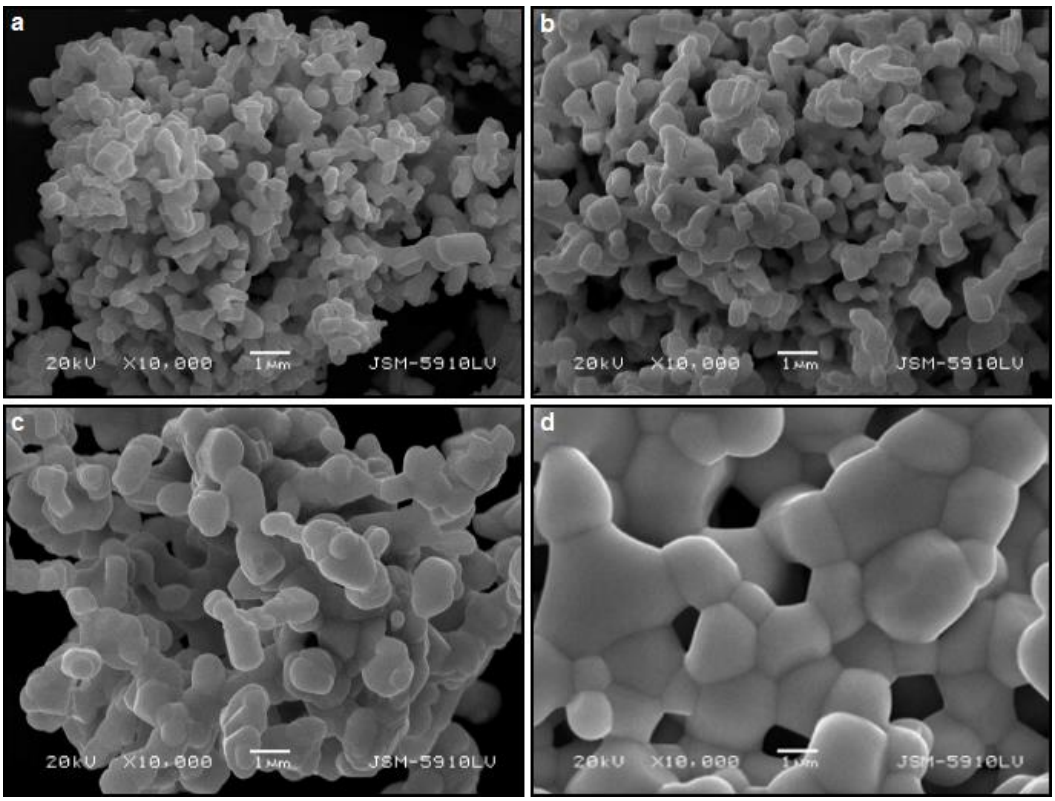

Figure 2. SEM micrographs of 2.5 mol% Sm^{3+} doped $BaTa_2O_6$ phosphors sintered at (a) 1150°C, (b) 1250°C, (c) 1350°C and (d) 1425°C at 10.000× magnification.

Effect of heat treatment temperature on the grain growth and phase development were investigated by SEM. Figure 2 (a–d) gives the SEM micrographs of 2.5 mol% Sm^{3+} doped $BaTa_2O_6$ powders which were sintered between 1150 and 1425°C. From the SEM observations, small grains formed at 1150°C then transformed into large grains due to heat treatment effect 1425°C. Depending on the increase of temperature from 1150 to 1425°C, the grain size increased

from 0.2-1.2 μm to 0.9-7 μm respectively. Grain size growth can be interpretable by a phase transformation from orthorhombic to tetragonal between 1150°C and 1350°C [13], [14]. SEM examination also showed that heat treatment has no effect on the grain shape. As seen from SEM micrographs, oval-roundish grain shape continued at all the sintering temperatures.

Phase determination and elemental composition have been carried out by SEM-EDS analysis. EDS analysis revealed that the elemental composition of 2.5 mol% Sm^{3+} doped $BaTa_2O_6$ grains were in agreement with the XRD results and theoretical composition. EDS spectrum of 1425°C doped sample were given in Figure 3.

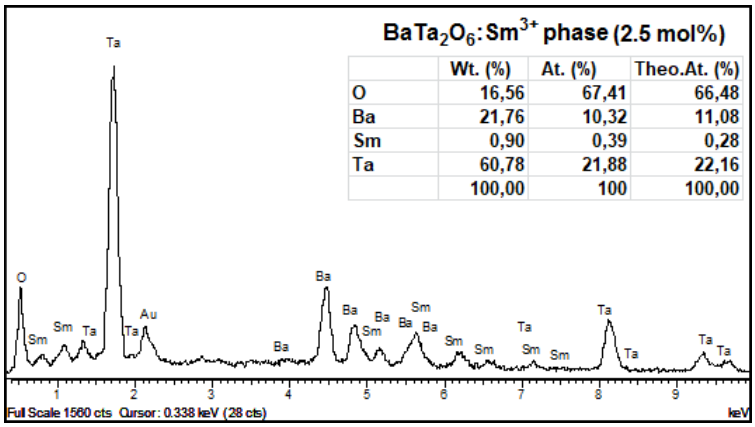

Figure 3. EDS spectrum TTB-$BaTa_2O_6$:Sm^{3+} phase.

a. Photoluminescnce Analysis

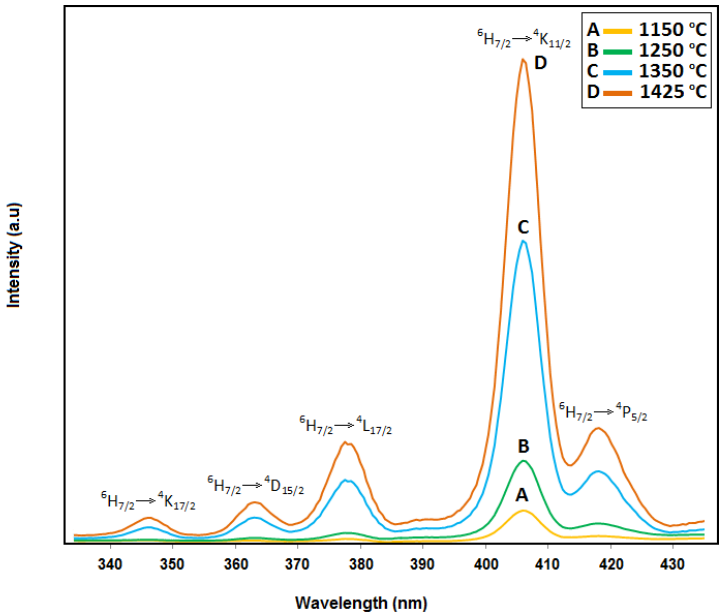

Figure 4. Excitation spectra of $BaTa_2O_6$:Sm^{3+} phosphors monitored at λ_{em}=597 nm.

Figure 4 shows the excitation spectra of 2.5 mol% Sm^{3+} doped $BaTa_2O_6$ phosphors were monitored under 597 nm emission that synthesized at 1150 (A), 1250 (B), 1350 (C) and 1425°C (D) respectively. Five excitations bands were identified as $^6H_{7/2}\rightarrow{}^4K_{17/2}$, $^4L_{17/2}$ (347 nm), $^6H_{7/2}\rightarrow{}^4D_{15/2}$, $^6P_{15/2}$ (364 nm), $^6H_{7/2}\rightarrow{}^4L_{17/2}$ (377 nm), $^6H_{7/2}\rightarrow{}^4K_{11/2}$ (406 nm) and $^6H_{7/2}\rightarrow{}^4P_{5/2}$, $^6P_{5/2}$ (420 nm). Figure 5 shows the emission spectra of 2.5 mol% Sm^{3+} doped $BaTa_2O_6$ samples excited under 406 nm. The emissions of $BaTa_2O_6$:Sm^{3+} phosphors exhibited two emission bands at 563 nm (green emission) and 597 nm (orange-reddish

emission) under 406 nm excitation. Green and orange-reddish emissions of Sm^{3+} attributed to the $^4G_{5/2}\rightarrow{}^6H_{5/2}$ and $^4G_{5/2}\rightarrow{}^6H_{7/2}$ transitions respectively. In the previously conducted $BaTa_2O_6:Sm^{3+}$ study [12], emission intensity increased by increasing of Sm^{3+} concentration up to 2.5 mol% that is the critical concentration value. Then emission intensity decreased due to concentration quenching effect. In the $BaTa_2O_6:Sm^{3+}$ study, Sm^{3+} doped $BaTa_2O_6$ samples have been excited with excitation source at 406 nm [12].

Depending on the increase of temperature from 1150 to 1425 °C, the emission intensities of $^4G_{5/2}\rightarrow{}^6H_{5/2}$ and $^4G_{5/2}\rightarrow{}^6H_{7/2}$ transitions increased due to phase development and improved crystallinity as structrul section mentioned before. The heat treatment effect of at 1425°C may had been improved the symmetry of between Sm^{3+} and ligand ions.

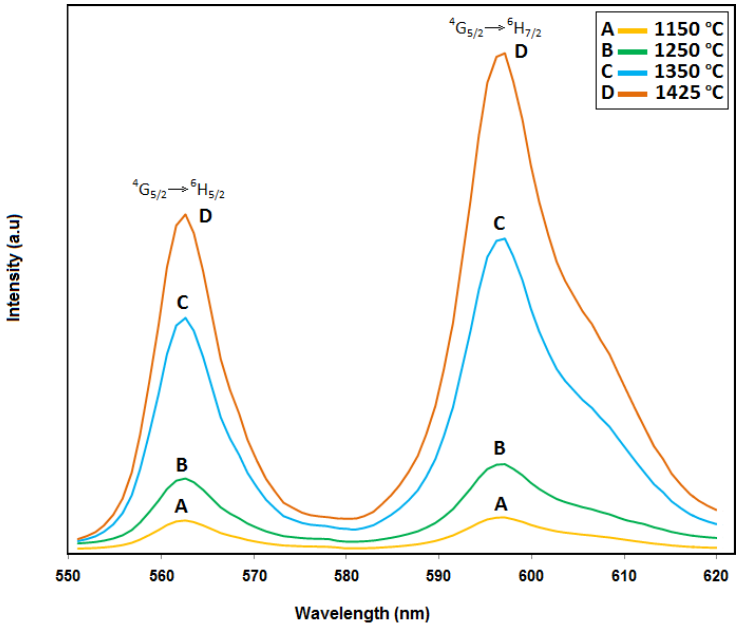

Figure 6. Emission spectra of $BaTa_2O_6:Sm^{3+}$ phosphors excited at λ_{ex}=406 nm.

In the Figure 6 show the changing in photoluminescence depending on temperature and colored pictures. The colored pictures of 2.5 mol% Sm^{3+} doped $BaTa_2O_6$ phosphors which were taken under 366 nm UV-light excitation by using CAMAG Model UV lamp in a dark room. As seen from the colored pictures, enhanced crystallinity obtained for 2.5 mol% Sm^{3+} doped $BaTa_2O_6$ phosphor at 1425°C has led to reddish emission, while 1350°C have earth color emission and the others have a weak luminescence. On the other hand, the Sm^{3+} ion has some other characteristic emissions in the red region. Some of these emissions are assigned to the $^4G_{5/2}\rightarrow{}^6H_J$ (J = 9/2 and 11/2) transitions, respectively [15]. Depending on the developed crystallization, the red emission of color picture may be partly attributable to the presence of these emissions.

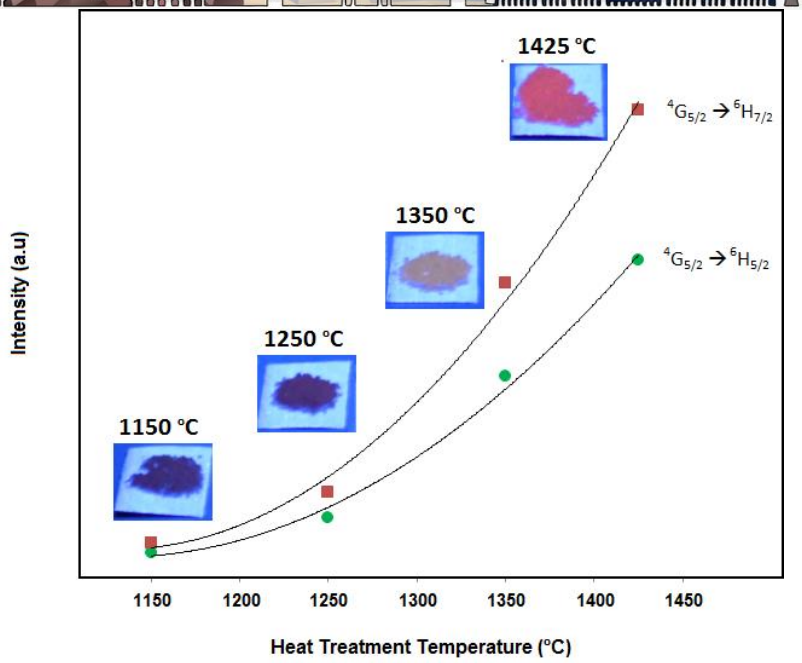

Figure 6. Depend on heat treatment temperature, emission spectra of 2.5 mol% Sm^{3+} doped $BaTa_2O_6$ phosphors sintered between 1150 and 1425°C at λ_{ex}=406 nm. Colored pictures of 2.5 mol% Sm^{3+} doped $BaTa_2O_6$ phosphors taken under 366 nm UV-light excitation.

4. CONSLUSIONS

Having high luminescence or 2.5 mol% Sm^{3+} doped $BaTa_2O_6$ phosphors were synthesized between 1150 and 1425°C in order to determine temperature effect on structural and photoluminescence properties. Depending on the heat treatment temperature, orthorhombic phase mostly disappeared at 1250°C and tetragonal phase has formed between 1350 and 1425°C. From the SEM results, grains have small size at 1150°C, while they became larger due to the heat treatment effect 1425°C. SEM analysis also showed that $BaTa_2O_6$:Sm^{3+} grain size decreased with the increasing Sm^{3+} concentration. Increase of temperature from 1150 to 1425°C led to an increase in the emission intensities due to phase development and improved crystallinity. $BaTa_2O_6$:Sm^{3+} phosphors exhibited $^4G_{5/2} \rightarrow {}^6H_{5/2}$ at 563 nm and $^4G_{5/2} \rightarrow {}^6H_{7/2}$ at 597 nm transitions. Depending on the increase of temperature, the emission intensities increased due to phase transformation and improved crystallinity. In the UV lamp pictures, the emission of 1425°C has the reddish color emission.

ACKNOWLEDGMENT

The conducted study was economically supported by Scientific Research Projects Unit of Marmara University with the grant number: FEN A-080715-0339

REFERENCES

[1]. M. Albino, P. Veber, E. Castel, M. Velázquez, K. Schenk, G. Chapuis, M. Lahaye, S. Pechev, M. Maglione and M. Josse, "Growth and characterization of centimeter-sized $Ba_2LaFeNb_4O_{15}$ crystals from high-temperature solution under a controlled atmosphere", *Eur J Inorg Chem*., vol. 2013, pp. 2817–2825, 2013.

[2]. M. Ilhan, "Synthesis, structural characterization, and photoluminescence properties of TTB-type $PbTa_2O6:Eu^{3+}$ phosphor", *Int J Appl Ceram Technol*., vol. 14, pp. 1144-1150, 2017.

[3]. J.S. Garciá, L.E. Bausá, and D. Jaque, *An introduction to the optical spectroscopy of inorganic solids*, John Wiley & Sons Ltd, England, 2005.

[4]. G. Annadurai, S. M. M. Kennedy and V. Sivakuma, "Photoluminescence properties of a novel orange-red emitting $Ba_2CaZn_2Si_6O_{17}$:Sm^{3+} phosphor", *J Rare Earth.*, vol. 34, pp. 576–582, 2016.

[5]. G. K. Layden, "Dielectric and structure studies of hexagonal $BaTa_2O_6$", *Mater Res Bull.*, vol. 3, pp. 349, 1968.

[6]. N. Ichinose, and T. Shimada, "Effect of grain size and secondary phase on microwave dielectric properties of $Ba(Mg_{1/3}Ta_{2/3})O_3$ and $Ba([Mg, Zn]_{1/3}Ta_{2/3})O_3$ systems", *J Eur Ceram Soc.*, vol. 26, pp. 1755–1759, 2006.

[7]. Y. H. Lee, Y. S. Kim, D. H. Kim, and M. H. Oh, "Conduction mechanisms in barium tantalates films and modification of interfacial barrier height", *IEEE T Electron Dev.*, vol. 47, pp. 71–76, 2000.

[8]. H. Kato, and A. Kudo, "New tantalate photocatalysts for water decomposition into H_2 and O_2", *Chem Phys Lett.*, vol. 295, pp. 487–492, 1998.

[9]. G. K. Layden, "Polymorphism of $BaTa_2O_6$", *Mater Res Bull.*, vol. 2, pp. 533–539, 1967.

[10]. A. Magneli, "The crystal structure of tetragonal potassium tungsten bronze", *Ark Kemi.*, vol. 1, pp. 213–221, 1949.

[11]. A. Simon, and J. Ravez, "Solid-state chemistry and non-linear properties of tetragonal tungsten bronzes materials", *C R Chimie.*, vol. 9, pp.1268–1276, 2006.

[12]. M. K. Ekmekci, M. Ilhan, A. S. Basak, and S. Deniz, "Structural and luminescence properties of Sm^{3+} doped TTB - Type $BaTa_2O_6$ ceramic phosphors", *J Fluoresc.*, vol. 25, pp. 1671–1678, 2015.

[13]. M. Ilhan, A. Mergen, and C. Yaman, "Removal of iron from $BaTa_2O_6$ ceramic powder produced by high energy milling", *Ceram Int.*, vol. 39, pp. 5741–5750, 2013.

[14]. P. Zeng, K. Wang, R. L. Falkenstein-Smith and J. Ahn, "Effects of sintering temperature on the performance of $SrSc_{0.1}Co_{0.9}O_{3-\delta}$ oxygen semipermeable membrane", *Braz J Chem Eng.*, vol. 32, pp. 757–765, 2015.

[15]. W. Zhang, and H. J. Seo, "Luminescence and structure of a novel red-emitting phosphor Eu^{3+}-doped tellurate garnet $Li_3Y_3Te_2O_{12}$", *J Alloy Compd*, vol. 553, pp. 183–187, 2013.

Investigation of dissimilar laser welded joint properties of TRIP and DP steels

F. Hayat[1], C.K. Ovali[2]

Abstract

Theaim of the study is analyzing TRIP 800 / DP600 steels which are bought for commercial purpose intercourse of dissimilar welded joint of each other. For this aim there sultsac quired by welding TRIP 800 steeland DP800 of mechanic and microstructure results were compared. Composite steels were applied strength tensile test and the value of hardness of weld zone was taken. As a result of strength tensile test, fractured surface's SEM photographs were taken. It was seen that the most solided part of the welding material is welding metal. It has been determined that the welded parts are broken from the DP600 sheet side.

Keywords*: Automotive Steel, TRIP steel, DP steel, laser welding*

1.INTRODUCTION

The automotive industry is one of the industries most affected by the energy, oil, and financial crises experienced in recent years. The fluctuations experienced in fuel prices, in the last 30–40 years, due to crises have compelled countries to take economic precautions. In this respect, the increase in taxes and decrease in purchasing power make saving fuel a current issue for consumers [1,2]. Steel is widely used in automotive industry. It is important for its performance features as a material used either for automobile body constructural pieces such as chassis and wheels [3,4]. Dual phase (DP) steel is one of them ostimportant advanced high-strength steels (AHSS). This steel has particular characteristics such as its microstructure and superior mechanical properties [5,6]. DP steels provide very valuable economic and technologicbenefits such as easy forming, even more strength after process of forming, low and delayed deformation osculation [7].

Laser welding at sub atmospheric pressures possesses unique bene fits, such as sub stantially improved penetration depth and noshield gas requirement. Unlike electron beam welding, ultra-high vacuum conditions are not require deither. In recent years, there fore, a great deal of effort has been made by researchers in investigating the effect of decreased pressures on laser welding processes and weld quality [8].

The laser beam welding is mainly used for joining components that need to be joined with high welding speeds, thin and small weld seams and low thermal distortion. The high welding speeds, an excellent automatic operation and thepossibility to control the quality online during the process make the laser welding a common joining method in the modern industrial production The application range covers finest welding of non-porous seams in medical technology toprecision spot welding in electronic sorth ejewelry industry, todeposit welding in too land mold-making and welding complete car bodies in automobile construction [9]. The use of lasers in automotive manufacture has increased dramatically over recent years to a position where about 15% of all industrial processing lasers are installed in production. Although the lasers are devoted mainly to cutting applications, a significant and growing proportion of lasers is being applied to welding. In a survey in 1992, about 20% of the lasers installed in the automotive industry

[1] *Department of metallurgy and Materials Engineering, Karabuk University,Karabuk, 78100, fhayat@karabuk.edu.tr*

[2] *Department of metallurgy and Materials Engineering, Karabuk University,Karabuk, 78100, cemkadirovali@karabuk.edu.tr*

were used in welding applications. [10] Since that time, there has been an explosion of growth in welding applications, particularly involving steel manufacturers, for tailored blank manufacture and in body-in-white welding applications.

TRIP800 and DP600 steel material sused in this study are automobile steels. Galvanized DP and TRIP steels heets are widely used in automotive industry for their beter corrosion resistan ceproperty. In this study, welded joint of TRIP 800 and DP 600 steel with electron beam welding was investigated. These two steel plates joined by laser welding were photographed with an optical microscope and SEM. Hardness values were examined by micro hardness test and by applying tensile test, tension and strain values were analyzed.

2. EXPERIMENTAL

2.1 Materials

In this study, 1,4 mm thickness DP600 and 1,5 mm thickness TRIP 800 galvanized (coated) automotive steels were used. Chemical compositions of the sesamples are given in Table1.

Table 1. Chemical composition of base metals (wt.%).

Spec.	C	Mn	Al	Cr	Si	Ti	V	W	Fe
TRIP800	**0.205**	**2.21**	**0.43**	**0.321**	**0.48**	**0.019**	**0.011**	**0.19**	**Kalan**
DP600	**0.131**	**1.82**	**0.29**	**0.274**	**0.39**	**0.011**	**0.027**	**0.120**	**Kalan**

The TRIP800 / DP600 steels are joined together by laser welding method. On these steels, which are to be welded, the light energy is turned into thermal energy on the surface by targeting the center point. For welding, the beam energy is kept below the evaporation temperature of the work piece. The parameters used in the TRIP800 / DP600 steels to be welded are shown in Table 2 and the drawing of welded joints is shown in Fig.1.

Tablo2.Parameters used in the laser welding machine.

Weld Speed	Beam Diameter	Wavelength	Protective Gas
3000mm/dk	200 micron	1000W Fiber Lazer/1065 micron	10 lt./dk Argon

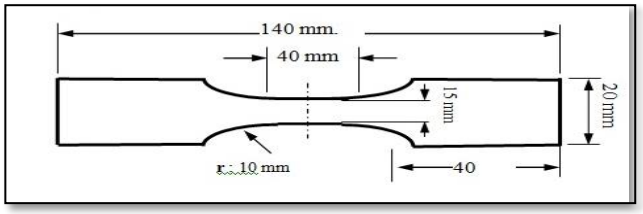

Fig.1. Welded samples.

For applying mechanical tests, the test samples were cut from the welded part by wire erosion. Materials were tested in the 40-ton LANDMARK brand tensile testing device at the Karabuk University Iron and Steel Institute Laboratory according to TSEN ISO 6892-1 standard, at a drawing speed of 2 mm / min. The microhardness test was carried out

in 15 zones as 2 primary metals, 3 heat-affected zones (ITAB), 5 weld metals, 3 ITAB and 2 base metals. The distance between each point is set as 0.4 mm and the applied load is 200 grams. Vickers detected the hardness results.

The sample was taken into hot bakalite to obtain images with an optical microscope. The sample was sanded in the order of 240-400-600-800-1200-2000-3000 mesh water abrasive. Then the whole sample was polished with 3 μm diamond paste. The sample was prepared for the microstructure examination by performing the etching process. The etching process was carried out with a mixture of 2% nital and 98% methanol. The sample was left in this mixture for 12 seconds.

3. RESULTS AND DISCUSSION

3.1. Microstructure and SEM Analiyses

As seen in Fig. 2, grain growth was observed in weld metal and heat affected zones.

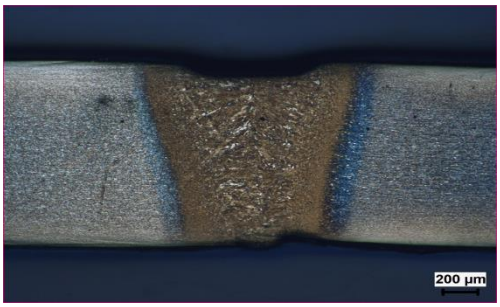

Fig. 2. Microstructures of welded samples (50x).

The optical microstructure photographs of the combined DP600 / TRIP800 samples are shown at 2000 magnification in FIG. 3 below.

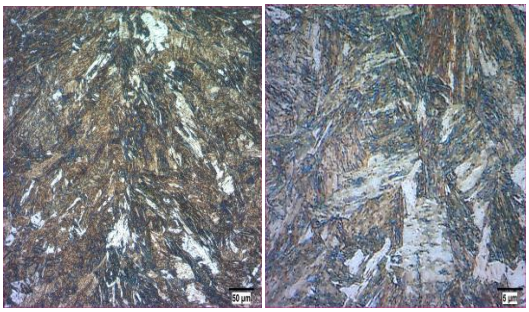

Fig. 3. Micro structures of weld metal

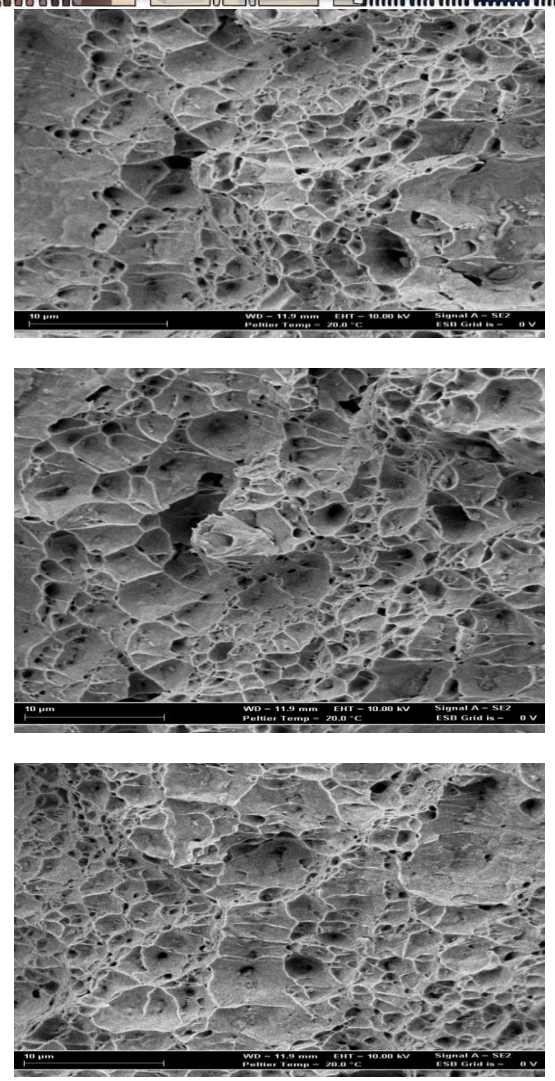

Figure 6. 5000x SEM images of the TRIP800 / DP600 joint.

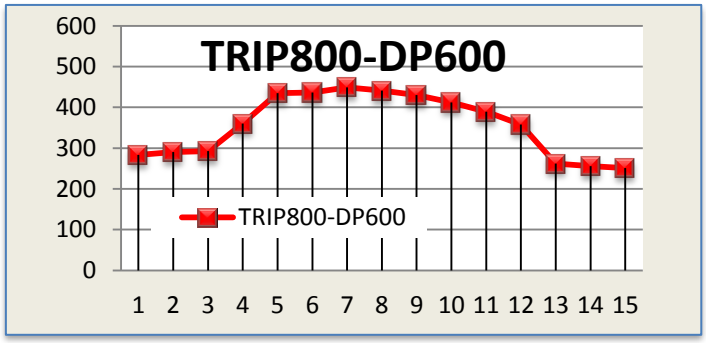

Fig.4. Typical micro hardness profile sof dissimilar welded,

According to the SEM images shown in Fig. 6, it is determined that there are dimple structures in the fracture zone and a partially ductile fracture also occurs in that zone.

As shown in the figure, it appears that the rupture occurred in the ITAB region. It has been determined that the clipping in this region is more brittle.

3.2Micro hardness

Table3 and Figure 4 shows hardness profiles of laser welded galvanized TRIP800 and DP600 auto steels.

Table3.Hardness results.

Specimen	Hardness (HV 0.2)														
	Base metal TRIP			HAZ			Weld Metal			HAZ			Base metal DP		
	1	2	3	4	5	6	7	8	9	10	11	12	13	14	15
TRIP800-DP800	283	290	293	360	435	436	449	441	430	412	389	358	262	256	251

In Figure 4, it has been detected that the hardness values at the horizontal axis of the samples taken from welded joints differ in the base material, ITAB and welded zones. When we look at the main materials, the TRIP800 sample is measured as 284 ± 10 HV and the DP800 sample is measured as 256 ± 10 HV.
G. Shi and S. A. Westgate have investigated the point resistance welding capabilities of TRIP700 steels in their study. Micro hardness test of welded joints reported that the hardness value of the base metal was about 250 HV1. It has been mentioned that hardness increases up to 600 HV1 in the weld metal [8].
Rajashekbar S. Sharma and Pal Molion have studied about the laser welding of TRIP 780 alloy with a thickness of 1 mm. Micro hardness tests have reported that the main metal is 250 HV0.3 and the weld metal is 500 HV0.3 [9].

3.3. Tensile tests

The drawing test results of the TRIP 800 / DP 600 steel joined with the laser weld are given in Fig 5.

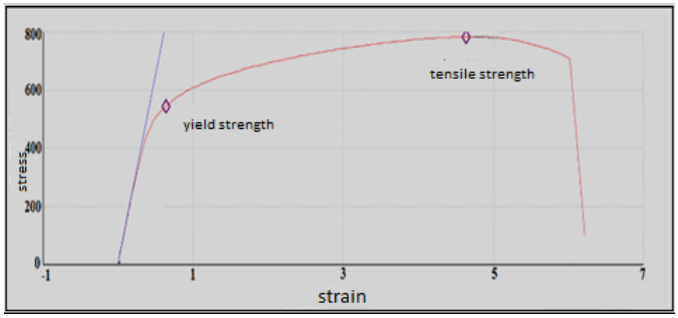

Fig.5 MPa stress -% elongation curve of

DP600 / TRIP800 sample.

SEM images of the broken samples at the end of the drawing test are given in Fig.6

4. CONCLUSIONS

a) According to the results of the pull test in the study carried out; The TRIP 800-DP 600 connection was seen to be broken by the DP 600.

b) Tension test according to fracture surface SEM images; it is seen that all the samples have fibrous structures in which the fractures of the base metal usually show ductility and the fracture surfaces are in the same direction.

c) According to hardness value results; The TRIP 800 sample was measured at about 257 ± 10 HV and the DP600 sample at about 256 ± 10 HV. In weld metal, hardness values were found to increase to about 450 ± 10 HV.

d) No rupture was observed in welded joints. This shows that the weld parameters are selected correctly and that the weld process is done properly.

Thanks

This study was supported by Karabuk University Scientific Research Projects Coordination Unit. Project Number: ***KBUBAP-17-YD-275****.*

REFERENCES

[1.] Hayat Fatih, The effects of the welding current on heat input nugget geometry and the mechanical and fractural properties of resistance spot welding on Mg Al dissimilar materials. Materials & Design, 32(4), 2476-2484. (2011).
[2] Hayat Fatih, Effect of aging treatment on the microstructure and mechanical properties of the similar and dissimilar 6061 T6 7075 T651 RSW joints. Materials Science and Engineering: A, 556, 834-843. (2012).
[3] Cem Kadir OVALI, TRIP800 / DP800 / DP600 Celiklerinin Lazer Kaynak Kabiliyetinin Incelenmesi, Yuksek Lisans Tezi Fen Bilimleri Enstitusu, Karabuk Universitesi, (2014).
[4] Speich G R 1997 ASM Handbook (ASM International) 5th ed.,p. 424.
[5] Hayat F., and Sevim I., 2012 Int. J. Adv. Manuf. Technol. 43 1050.
[6] Fatih Hayat, TRIP Celiklerinin Otomotiv Endustrisinde Kullaniminin Incelenmesi, Journal of The Faculty of Engineeringand Architecture of Gazi University 25 (4), 701-712, (2010).
[7] Erdogan M 2002 J. Mater. Sci. 37 3623.
[9] Jaehun K., Sehyeok O., Myeonggyun S., Hyungson K., A study of keyhole behavior and weldability in zero-gap laser welding of zinc-coated steels heets at sub atmospheric pressures Journal of Materials Processing Technology, Volume 249, November 2017, Pages 135-148. 9. https://www.rofin.com/en/applications/laser-welding/ "2017".
[10] Roessler D et al., Laser Materials Processing in General Motors Corporation, Proc ISATA 92, June 1992, pp37-51
[11] Shi G. And Westgate S. A.,"Techniques for improwing the weldability of TRIP steel using resistance spot welding", 1st International Conference Super-High StrengthS teels, Rome, Italy, (2005).
[12] Rajashekbar S. S. and Pal M., "YAG laser welding of TRIP780 steel with dual-phase and mild steels foruse in tailor welded blanks", Materials and Design, 30: 4146-4155 (2009).
[13] Kim C. H., Choi J. K., Kang M. J. and Park Y. D., " A study on the CO2 laser welding characteristics of high strength steel up to 1500 MPa for automotive application", Journal of Achivements in Materials and Manufacturing Engineering, 39(1): 80-85 (2010).

ICETI
www.iceti.org
2018
07-11 MARCH
BUDAPEST
HUNGARY
II. INTERNATIONAL CONFERENCE ON ENGINEERING TECHNOLOGY AND INNOVATION

Determination of Turbidity in Filyos Stream Water by Artificial Neural Network

Berna Aksoy[1], Ismail Hakki Ozolcer[1], Emrah Dogan[2], Onur Dundar[1]

Abstract

Water is in an endless cycle, which is source of life for human beings. During this cycle, substances that are contaminated in water cause physical, chemical or biological alteration of the water's natural features, that leads to water pollution and therefore causes the environmental balance to deteriorate over time. This quality changes cause deteriorations in ecosystem. For this reason, it is important to investigate the water quality in rivers and water reservoirs which are close to settlement areas. In this study, surface water quality measurements were carried out at downstream of the Filyos stream, which forms the largest sub-basin in the Western Karadeniz Basin, at intervals of thirty days in one year period between September 2015 and August 2016. In the scope of the study, zinc, chromium, calcium, aluminium, manganese and turbidity parameters measured in the laboratory and estimation of the turbidity parameter basaed on parameters of zinc, chromium, calcium, aluminium, manganese was performed by artificial neural networks.

Keywords: Filyos Stream, Heavy Metal, Turbidity, Artificial Neural Networks, Western Blacksea Basin

1. INTRODUCTION

Rivers and streams are used in many parts of the world for drinking water, agricultural irrigation and industrial purposes. Today, rapidly growing population, developing infrastructural deficiencies resulting from the expansion of industrial and residential areas and the inadequacy of treatment plants cause pollution of rivers and freshwater resources. The increasing rate of pollution destroys the balance of nature and reaches the dimensions that threaten human life.

Water quality changes cause the animal and plant species that exist in nature to change, thus causing the ecosystem to change. Therefore, investigations of water quality in rivers and water reservoirs close to their habitat are important.

Make observations and measurements over the river, prodives information to researchers and planner. When these researches are planned on a basin basis, sustainable management of water resources has considerable precaution.

A better understanding of the hydrodynamic properties of reservoirs has also gained momentum with advances in computer technology in recent years. Measurements in water quality models, such as mathematical and artificial neural network, can also be analyzed with methods. In this study, artificial neural networks were used and data obtained from water quality studies were estimated in this method.

In this study, surface water quality measurements were made at the observation station selected at the Filyos Stream (228 km), the largest sub-basin of the Western Black Sea Basin, at intervals of thirty days in one year period. Water quality parameters (turbidity, calcium, aluminium, manganese, chromium and zinc) measured and analysis were

[1] *Bulent Ecevit University, Civil Engineering Department, Zonguldak/Turkey*

[2] *Sakarya University, Civil Engineering Department, Sakarya/Turkey*

performed in the laboratory according to standart methods, After, estimation of the turbidity parameter based on parameters of calcium, aluminium, manganese, chromium and zinc was performed by artificial neural networks.

Figure 24. Subbasin of Western Blacksea Basin (URL-6)

2. MATERIALS AND METHODS

Surface water quality measurements were carried out at downstream of the Filyos stream, which forms the largest sub-basin in the western Karadeniz Basin, at intervals of thirty days (September 2015- August 2016) in one year period. (Figure 2).

Figure 25. Filyos downstream satellite image (Google Earth, 2017)

The collection, storage and delivery of water samples in accordance with standard methods has been carried out. During sampling, the sample containers of the water samples to be taken were rinsed with water, filled with no gaps and tightly closed. +4 °C prodected samples brought to the laboratory in six hours. Turbidity and ion analysis were performed in the laboratory according to the standart methods. Nexion 300D model ICP-MS was used in the analysis.

Figure 26. Nexion 300D model ICP-MS

An artificial neural network (AAN) model was prepaered for the samples which taken from downstream to estimate the turbidity according to month. MATLAB-based artifical neural network (ANN) toolbox was used for model analysis. AAN topology analysis was performed to determine the number of AAN hidden layer neurons in the

preparation phase. AAN performances for different hidden layer neuron numbers, R^2 (Determination coefficient) and MSE (Mean Squared Error) statistical performance analysis criteria were used. The hidden layer neuron counts were taken as 3, 4, 6, 8 and 10, respectively, and the AAN topologies were trained and tested.

The AAN analysis method used for estimating the turbidity parameter in the water is the multi-layered sensor (MDA) model; input layer, intermediate layers and output layer. In the models, Ca^{+2} Al^{+3} Mn^{+2} Cr^{+3} Zn^{+2} parameters are input and turbidity is used as output parameter.

3. RESULTS AND DISCUSSION

The results of the parameters analyzed in the laboratory according to standard methods are given in Table 1.

Table 20.Laboratory Analysis Results

Months	Turbidity	Ca^{+2}	Al^{+3}	Mn^{+2}	Cr^{+3}	Zn^{+2}
1	98.6	52.31	7.65	0.217	0.087	0.246
2	86.4	50.68	10.96	0.147	0.135	0.547
3	95.6	51.64	12.8	0.351	0.426	0.372
4	78.4	52.31	17.5	0.438	0.258	0.254
5	68.3	54.86	25.4	0.372	0.324	0.212
6	69.1	55.16	15.24	0.371	0.355	0.127
7	46.7	55.13	4.327	0.326	0.132	0.59
8	28.12	55.23	4.641	0.108	0.033	0.658
9	63.25	55.25	2.142	0.642	0.284	0.392
10	35.72	55.31	5.526	0.02	0.114	0.587
11	17.09	53.48	4.434	0.093	0.05	0.286
12	64.12	51.68	8.61	0.154	0.074	0.097

. According to the obtained analysis results, the models in Table 2 for different input layers in AAN have been established. Weights, number of hidden layers and number of nodes were found by trial and error to obtain the most appropriate result between 1 input and 1 output while the model was being created.

Table 21. Models created for different input layers

Model No	Input Layer Variables	Output Layer
1	Ca^{+2}	Turbidity
2	Al^{+3}	Turbidity
3	Mn^{+2}	Turbidity
4	Cr^{+3}	Turbidity
5	Zn^{+2}	Turbidity

In this study, each parameter was tried as an input data value, and the turbidity as the output value was estimated.. The data were normalized between 0-1 before being given to the network. Accordingly, the YSA results will remain between 0-1. The model results are shown in tables for each parameter separately and the topologies with the best performance is charted.

Table 22. Zn^{+2}topology analysis for parameter

Model No	Number of Hidden Layer Neurons	R^2	MSE
1	3	0.9667	0.0021
2	4	0.9264	0.0047
3	6	0.9900	0.0006431
4	8	0.9030	0.0062
5	10	0.9821	0.0008031

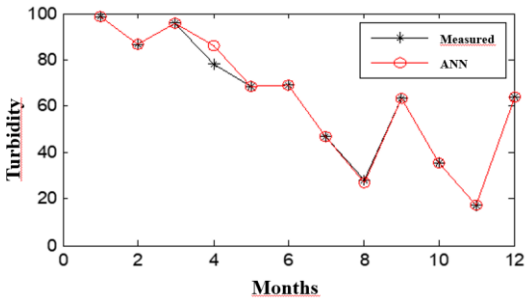

Figure 27. Zn^{+2}parameter AAN performance

Table 23. Cr^{+3}topology analysis for parameter

Model No	Number of Hidden Layer Neurons	R^2	MSE
1	3	0.9409	0.0038
2	4	0.9115	0.0057
3	6	0.9643	0.0023
4	8	0.9759	0.0016
5	10	0.9874	0.0008133

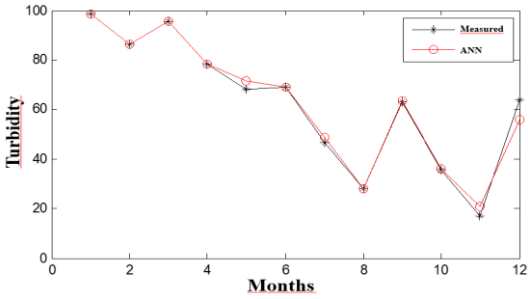

Figure 28. Cr^{+3}parameter AAN performance

Table 24. Ca^{+2}topology analysis for parameter

Model No	Number of Hidden Layer Neurons	R^2	MSE
1	3	0.9563	0.0028
2	4	0.8747	0.0081
3	6	0.9776	0.0021
4	8	0.9231	0.0052
5	10	0.9570	0.0028

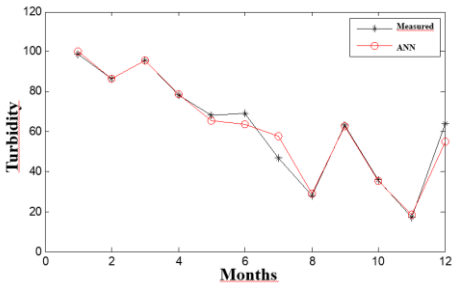

Figure 29. Ca^{+2}parameter AAN performance

Table 25. Al^{+3}topology analysis for parameter

Model No	Number of Hidden Layer Neurons	R^2	MSE
1	3	0.9426	0.0037
2	4	0.8761	0.0080

3	6	0.9722	0.0018
4	8	0.9473	0.0034
5	10	0.9608	0.0025

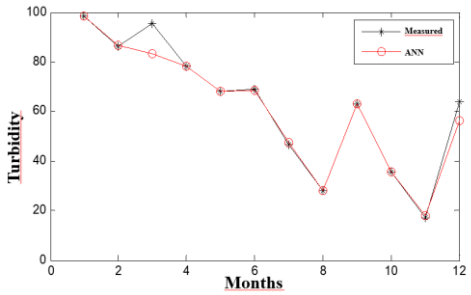

Figure 30. Al^{+3}parameter AAN performance

Table 26. Mn^{+2}topology analysis for parameter

Model No	Number of Hidden Layer Neurons	R^2	MSE
1	3	0.9642	0.0061
2	4	0.9198	0.0052
3	6	0.8762	0.0080
4	8	0.9642	0.0023
5	10	0.9335	0.0043

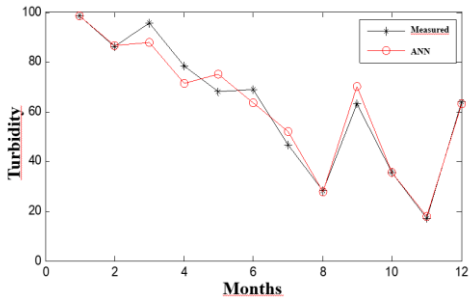

Figure 31. Mn^{+2}parameter AAN performance

4. CONCLUSIONS

Clarity is a magnitude that determines the natural structure of water Organic and inorganic materials etc. causes turbidity in the waterThe strength of the sulfur contaminant causes water turbidity. For this reason, the turbidity level of surface waters is measured as the degree of pollution. The measurement of the turbidity parameter in the surface

water can be used to follow the pollution test in the water and the natural cleansing of the river. For this reason, the studies in which the pollution dimension is searched are the investigations that should be done routinely.

However, since turbidity depends on many parameters changing over time, it is difficult to be formulated For this reason, artificial neural networks come into play here. In this study, considering the ions affecting the turbidity, AAN models were established and the parameters giving the best test performance were determined. As a result of the analyzes made, it has been observed that the Zn parameter has the best test performance. This is followed by the parameters Cr, Ca, Al, Mn, respectively. As it is clear from the graphs, it is determined that there are not very big differences between the results obtained from AAN and the measured values. It has been demonstrated that YSA can be successfully implemented and produces safe estimates.

REFERENCES

[1]. APHA Standart Methods for the Examination of Water and Waste Water, 20th Ed., APHA, AWWA, WEF, Washington , D. C., 1998.
[2]. Ay M, Su Kalitesi Parametrelerinin Yapay Zeka Yontemleri Ile Degerlendirilmesi, Doktora Tezi, Erciyes Universitesi, Fen Bilimleri Enstitusu, Insaat Muhendisligi Anabilim Dali, Kayseri, 117, 2014.
[3]. Bayram A, Harsit Cayi Su Kalitesinin Mevsimsel Degisiminin Incelenmesi Ve Aski Madde Konsantrasyonunun Yapay Sinir Aglari Yontemi Ile Tahmin Edilmesi, Doktora, Karadeniz Teknik Universitesi, Fen Bilimleri Enstitusu, Insaat Muhendisligi Anabilim Dali, Trabzon, 163, 2011.
[4]. Bayram A ve Kenanoglu M, Temporal Variation of Total Nitrogen and Total Phosphorus in Surface Waters from the Lower Coruh River Basin, Turkey, 3rd International Conference on Computational and Experimental Science and Engineering, 19-24 Ekim 2016, Antalya, Turkiye, 132(3): 712-716, 2017.
[5]. Dogan E, Sengorur B ve Koklu R, Modeling Biological Oxygen Demand of the Melen River in Turkey Using An Artificial Neural Network Technique, Journal of Environmental Management, 90, (2): 1229-1235, 2009.
[6]. Icaga Y, Bostanoglu Y ve Kahraman E, Akarcay Havzasi Su Kalitesi Istatistikleri. Yapi Teknolojileri Elektronik Dergisi, 2(1): 43-50, 2006.
[7]. Kajiya T, Schellenberger F, Papadopulos P, Vollmer D and Butt H J, 3D Imaging of Water-Drop Condensation on Hydrophobic and Hydrophilic Lubricant-Impregnated Surfaces. Nature, 6: 1-10, 2016.
[8]. Minarecioglu N, Dogal Akarsularda Tasinan Kati Madde Miktarinin Yapay Zeka Yontemleri Kullanilarak Tahmin Edilmesi, Yuksek Lisans, Erciyes Universitesi, Fen Bilimleri, Insaat Muhendisligi Anabilim Dali, Kayseri, 68, 2008.
[9]. Oztemel E, Yapay Sinir Aglari, 3. Baski, ISBN: 9756797396, Papatya Bilim, Istanbul, 232,2016.
[10]. Sonmez A Y, Hisar O ve Yanik T, Karasu Irmaginda Agir Metal Kirliliginin Tespiti ve Su Kalitesine Gore Siniflandirilmasi. Ataturk Universitesi Ziraat Fakultesi Dergisi, 43(1): 69-77, 2012.

ICETI
www.iceti.org
2018
07-11 MARCH
BUDAPEST
HUNGARY
II. INTERNATIONAL CONFERENCE ON ENGINEERING TECHNOLOGY AND INNOVATION

Numerical Simulation of Single Bubble Nucleation Flow Boiling Both From an Artificial Cavity and From a Flat Surface and Pool Boiling From a Flat Surface In Horizontal Channel

Mehmetcan Donertas[1],Benjamin Franz[2], Axel Sielaff[3], Sabiha Yildiz[4], Peter Stephan[5]

Abstract

In this study, Volume of Fluid (VOF) method with extended interfoam solver in OpenFoam software was used to numerically simulate superheated FC-72 single bubble nucleation during flow boiling both from an artificial cavity and flat surface and also single bubble nucleation during pool boiling from a flat surface. All simulations were performed in 3D. FC-72 was used as a working fluid and BaF_2 was used for channel and cavity walls. The studies of the pool boiling on the flat surface were carried out on 0.01g 0.1g, 1g, 10g gravity magnitudes. Bubble detachment diameter, bubble detachment time, velocity and temperature magnitudes in bubbles were investigated on different earth gravities . The studies of flow boiling from a flat surface in horizontal channel were conducted for several bulk fluid velocities on constant Earth gravity. The range of the bulk fluid velocities investigated from 0.01 m/s to 0.6 m/s. In this study bubble detachment diameter, bubble detachment time, velocity and temperature magnitudes in bubbles were examined and also were compared to each other. First and Second studies were compared on superheated bulk fluid (5K) and superheated solid domain (10K). The results of study which was conducted in pool boiling section on constant Earth gravity were taken and compared with results of flow boiling from a flat surface. The studies of flow boiling from an artificial cavity in horizontal channel were conducted for four different cavity depths on 1g gravity magnitude. Flow boiling from an artificial cavity studies were examined in saturated and superheated bulk fluid temperature seperately. Cavities diameters were defined as 30 micrometers for 3, 12, 25 and 50 micrometers cavities depths. Each cavity depth simulation was investigated in both bulk fluid temperature. Bulk fluid velocity magnitude was constant and defined as 10m/s in flow boiling from a cavity studies.

Keywords: *Flow boiling from an artificial cavity, Nucleate flow boiling in horizontal channel, Pool boiling, volume of fluid method (VOF)*

1. INTRODUCTION

As well as the fact that boiling is a frequent phenomenon in daily life, it has a broad and wide range of use in the industry. Chemical industry, cooler and steam boilers are the most common among these. As boiling process involves high transfer rates, it is usually deployed in the cooling processes of relatively smaller devices. In addition, it is also deployed in steam boilers at a greater scale and in various practices in the chemical industry. Because of the common deployment of the boiling phenomenon in the industry, it has been a hot topic of research for many research groups for the last ten years throughout the world. The boiling phenomenon is still yet to be fully understood despite the current high density of the existing and ongoing pile of research. For the sake of getting a full of grasp of the boiling phenomenon, there has been a growing rate of numerical and simulation studies recently.

[1] *Corresponding author: Yildiz Technical University, Department of Mechanical Engineering, Besiktas/Istanbul, Turkey. mmehmetcan786@gmail.com*

[2] *Darmstadt Technical University, Department of Mechanical Engineering, Darmstadt,Germany. franz@ttd.tu-darmstadt.de*

[3] *Darmstadt Technical University, Department of Mechanical Engineering, Darmstadt,Germany. sielaff@ttd.tu-darmstadt.de*

[4] *Yildiz Technical University, Department of Mechanical Engineering, Besiktas/Istanbul, Turkey. syildiz@yildiz.edu.tr*

[5] *Darmstadt Technical University, Department of Mechanical Engineering, Darmstadt ,Germany. pstephan@ttd.tu-darmstadt.de*

Kunkelmann (2011) examined the single bubble formation, bubble coalescence in pool boiling, flow boiling at different velocities and flow boiling in modified microchannels. In his studies, he developed a model which can carry out the simulation of boiling processes in complex geometries with highest accuracy. During the simulations, heat transfer and flux at micro and macro levels were investigated thoroughly. He determined the time required for bubble formation, detachment and re-formation. He also observed that the growth rate of the dimeter of the bubble foot during the bubble growth was greater than the rate of the shrinking of the bubble foot during the bubble detachment. He obtained the diameter of the bubble detachment in his experiments 30% higher than the previous experiments as 2.5 mm. In another study, he found out that the density of the frequency of the bubble formation was reversely correlated with the diameter of the bubble detachment in a pool boiling study. In an experiment for a heat transfer mechanism, the latent heat flux read 0,4 W. This value was seen to be in quick increase during the bubble growth and in slow decrease during the bubble detachment. The heat flux along the length of the contact line increased during the bubble formation and decreased during the bubble growth. In an experiment where 3 different mesh resolutions were used for one single bubble cycle period to observe the effects of the mesh resolution on the diameter of the bubble, heater flux and the heat flux along the contact line. The simulations yielded that increasing mesh resolution enabled approximation and that inaccurate mesh resolution produced faulty results.

In his study, Dietl (2015) studied the simulations of the boiling processes on surfaces with cavities using the volume-of-fluid (VOF) method. In his experiments, he studied the effects of the cavity geometries on the heat transfer. In the study carried out with round cavities, the effect of the amount of the fluid film in the cavity on the heat transfer. The study yielded that the heat transfer with fluid film both at the bottom line and top line of the cavity was eight times better than the heat transfer with dry cavity. A similar experiment was applied to the square-shaped cavity. Also, the fluid film in the square-shaped cavity increased the heat transfer. The effect of the depth of cavity on the flooding and drying. The flooding took place in the shallow cavity whereas the drying occurred in the deep cavity. The deeper the cavity gets, it was observed that the drying occurred. The studies on cavities with different diameter holes deployed constant heat flux as the boundary layer condition. The fluid diffusion levels in the cavities were investigated. Lower fluid volume diffusions were observed in the cavities with greater diameter holes at lower heat fluxes. The higher bubble detachment diameters were observed in higher diameter holes.

Christian Kunkelmann and Peter Stephan (2009) studied bubbles in flow boiling on OPENFOAM software using VOF. They mainly studied the evaporation on the contact line between the fluid-solid zones caused by the combined heat transfer. The heat consumed by the evaporation increased gradually during the bubble growth. Later, that value decreased gradually until bubble detachment.

Liu et al. (2016) studied the single bubble pool boiling on COMSOL software using the Level Set method. They examined the shifts in velocity and pressure for the phenomena of bubble growth and detachment. According to the results of the study, there was an increased difference of pressure between the bubble and the mass fluid during the bubble growth. However, it was concluded that this difference of pressure decreases and becomes constant during the bubble detachment. For a whole bubble cycle period, the velocity values inside the bubble were higher than the velocity values of the mass fluid.

Kunkelmann et. al. (2011) studied experimentally and numerically the effect of the three-phase contact line at the area of contact line during the evaporation of the meniscus and pool boiling on local heat transfer. As a result of their study, they identified the heat transfer along the contact line with the temporary heat conduction and evaporation on the micro-solid area during the bubble detachment while it was only identified with the evaporation on the micro area during the bubble growth.

For both cases, the amount of evaporation from the micro area and the amount of heat transfer were determined as a constant. Moreover, it was concluded that the amount of the heat transfer from the micro area was independent of the velocity of the contact line. The temporary heat conduction is highly dependent on the velocity of the contact line and it was seen that the velocity of the contact line increased with the heat transfer rate. According to the results of the experiment for the moving meniscus case, the regressing meniscus is independent of the heat flux contact line while for the progressing meniscus case, as the velocity of the contact line increased, the heat flux increased. For the comparison of both cases, the maximum local heat transfer rate on the three-phase contact line area for the progressing meniscus was greater than that of the regressing meniscus.

In a study carried out by Ding Li et. al. (2007), single bubble flow boiling was investigated numerically along

horizontal, vertical, angled surfaces at different gravitational accelerations. In simulation experiments, to maintain the fluid-vapor interface, the Level Set method was used. In the studies where the gravitational acceleration was reduced it was found out that the bubble growth time and the diameter of the bubble detachment increased at greater levels. In the studies where the mass fluid has velocity it was discovered that the velocity of the mass fluid decreased the effect of the gravitational acceleration. In other words, at constant gravity, when the velocity of the mass fluid is increased, the diameter of bubble detachment and the bubble growth time decreases.

2. NUMERIC MODEL

FC-72 was used as a bulk fluid and BaF_2 was used as solid domain and cavity walls for all simulations. In this section, underlying equations of the numerical model were described. In the first section conservation equations for mass, momentum and energy were investigated. In the second section, particular equations for micro scale heat transfer were described.

2.1. Governing Equations

The fallowing assumptions were used in order to simplify the set of equations.

- The material properties are constant
- Flow is uncompressible
- Fluid is Newtonian
- Viscous Dissipation can be neglected

$$\nabla . u = \frac{\dot{\rho}}{\rho} \tag{2.1}$$

$$\rho\left(\frac{\partial u}{\partial \tau} + (u\,.\nabla).u\right) = \mathrm{f} - \nabla p + \nabla\left(-\frac{2}{3}\mu\nabla.u\right) + \nabla.\left(\mu(\nabla u + (\nabla u)^T)\right) \tag{2.2}$$

$$\rho c\left(\frac{\partial T}{\partial \tau} + u.\nabla T\right) - \nabla.(k\nabla T) = \dot{h} \tag{2.3}$$

In the solid domain, the convective term is zero. Therefore energy equation for solid domain can be written with diffusive and transient term.

$$\frac{\partial(\rho c T)}{\partial \tau} = \nabla(k\nabla T) \tag{2.4}$$

Equation (2.5) denotes the transport of volume of fluid parameter. This equation can be solved by using MULES scheme in OpenFoam software. F denotes liquid partial volume in a particular cell. Value of F parameter equals to unity for liquid phase and equals to zero for vapor phase.

$$\frac{\partial F}{\partial \tau} + \nabla.(uF) + \nabla.\left(u_r F(1-F)\right) = \frac{\dot{\rho}}{\rho} F$$

(2.5)

2.2. Micro Region Equations

The fallowing assumptions were used in order to simplify the set of equations.

- The liquid layer is thin.
- Heat transfer is one – dimensional in micro region and perpendicular to the wall
- The wall temperature within the micro zone is uniform.

$$\frac{\mathrm{d}\delta}{\mathrm{d}\xi} = \delta' \tag{2.6}$$

$$\frac{\mathrm{d}\delta'}{\mathrm{d}\xi} = \frac{\left(1+\delta'^2\right)^{1.5}}{\sigma}\left(p_{\mathrm{cap}} - \frac{A}{\delta^3} + \frac{1}{\Delta h_{\mathrm{v}}^2}\left(\frac{T_{\mathrm{w}} - T_{\mathrm{sat}}\left(1+\frac{p_{\mathrm{cap}}}{\Delta h_{\mathrm{v}}\rho_l}\right)}{\sqrt{1+\delta'^2}\,\frac{\delta}{k_{\mathrm{l}}} + R_{\mathrm{int}}}\right)^2\left(\frac{1}{\rho_{\mathrm{v}}} - \frac{1}{\rho_{\mathrm{l}}}\right)\right)$$

(2.7)

$$\frac{\mathrm{d}p_{\mathrm{cap}}}{\mathrm{d}\xi} = -\frac{3\nu_{\mathrm{l}}}{\delta^3 \Delta h_{\mathrm{v}}}\left(\dot{Q}_{\mathrm{cl}} + \rho_l \Delta h_{\mathrm{v}} u_{\mathrm{cl}}(\delta - \delta_{ad})\right) \tag{2.8}$$

$$\frac{\mathrm{d}\dot{Q}_{\mathrm{cl}}}{\mathrm{d}\xi} = \frac{T_{\mathrm{w}} - T_{\mathrm{sat}}\left(1+\frac{p_{\mathrm{cap}}}{\Delta h_{\mathrm{v}}\rho_{\mathrm{l}}}\right)}{\frac{\delta}{k_{\mathrm{l}}} + \frac{R_{\mathrm{int}}}{\sqrt{1+\delta'^2}}} \tag{2.9}$$

3. NUMERIC ANALYSIS

In this section, studies have been examined under 3 main subtitles.

3.1. Single Bubble Pool Boiling From a Flat Surface Simulations

Pool boiling studies were carried out in 5K superheated bulk fluid domain and 10K superheated solid domain. Adaptive mesh refinement was fulfilled at liquid-vapor interface. Initial bubble radius was defined as 0.15 milimeter and hemispherical for all studies. Simulations were conducted on 0.01g, 0.1g, 1g and 10g gravity magnitudes separately. Finest mesh resolutions were obtained at liquid vapor interface and equal to 6.25 micrometers. Coarsest mesh resolutions equals to 0.1 milimeter in computational domain. In the pool boiling studies, velocity profile and temperature distribution in the bubble were examined besides bubble detachment time and bubble detachment diameter.

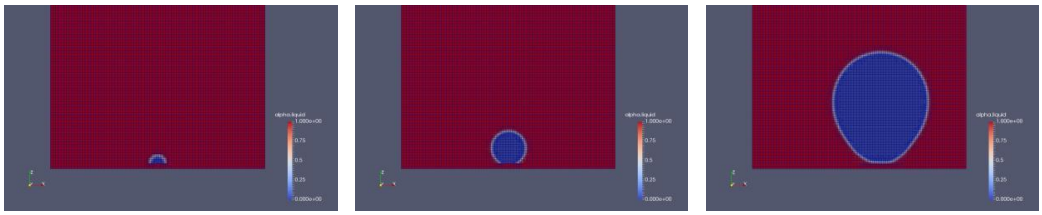

Figure 1. Bubble growing period in pool boiling study

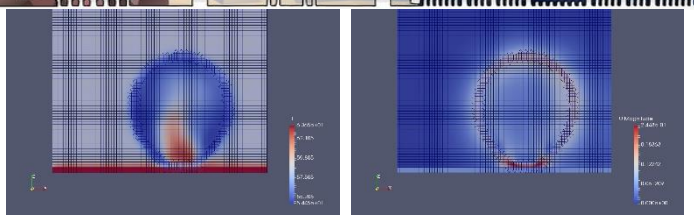

Figure 2. Temperature (left) and velocity distribution (right) in pool boiling study

3.2. Single Bubble Flow Boiling From a Flat Surface Simulations

Flow boiling studies were carried out in 5K superheated bulk fluid domain and 10K superheated solid domain. Adaptive mesh refinement was fulfilled at liquid-vapor interface. Initial bubble radius was defined as 0.15 milimeter and hemispherical for all studies. Simulations were conducted on constant earth gravity with different bulk fluid velocities. The range of the bulk fluid velocities investigated is from 0.01 m/s to 0.6 m/s. In flow boiling studies channel height was defined as 5 milimeter. But simulations were performed on real nucleation site in order to obtain better computational effort and time.Finest mesh resolutions were obtained at liquid vapor interface and equal to 1.56 micrometers. Coarsest mesh resolutions equals to 0.1 milimeter in computational domain. In the pool boiling studies, velocity profile and temperature distribution in the bubble were examined besides bubble detachment time and bubble detachment diameter.

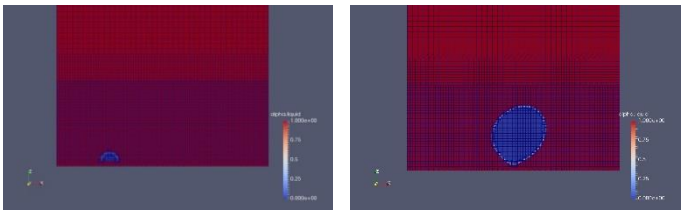

Figure 3. Bubble growing period in flow boiling study

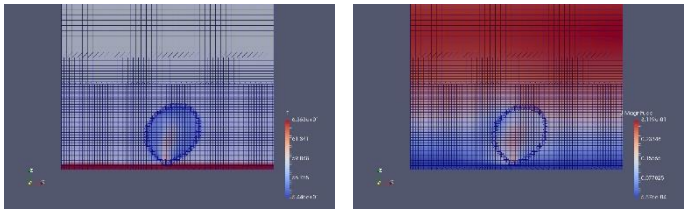

Figure 4. Temperature (left) and velocity distribution (right) in flow boiling study

3.3. Flow Boiling From a Cavity Simulations

Flow boiling from a cavity studies were carried out in 10K superheated solid domain. Simulations were performed in 5K superheated bulk fluid temperature and saturated bulk fluid temperature seperately. Gravity magnitude was defined as Earth gravity magnitude and also bulk fluid velocity was defined as 10m/s for all simulations. Flow boiling frm a cavity studies were conducted with 3, 12, 25 and 50 micrometers depth cavities in both bulk fluid temperature seperately. Cavity pore diameter was defined 30 micrometers for all studies. Initial bubble radius was defined as 0.15 milimeter and hemispherical for all simulations. Moreover simulations were performed on real nucleation site such as flow boiling from a flat surface case. Finest mesh resolutions were obtained at liquid vapor interface and equal to 0.25 micrometers. Coarsest mesh resolutions equals to 20 micrometers in computational domain. Besides, 1 micrometer chamfer was defined at the top of the cavity and in the vicinity of the cavity unstructured mesh was defined in order to obtain smooth transition of contact line.

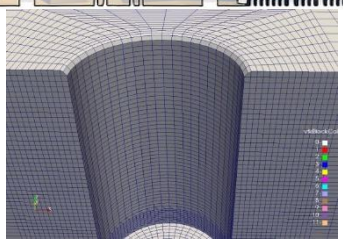

Figure 5. Cavity geometry and chamfer

Results were investigated under 2 main subtitles for flow boiling from a cavity simulations.

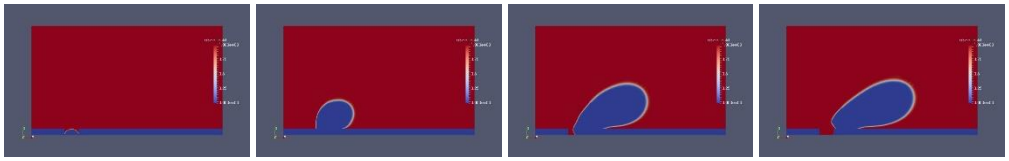

Figure 6. Bubble growing and detachment period for 3 and 12 micrometers depth cavities in both bulk fluid temperature

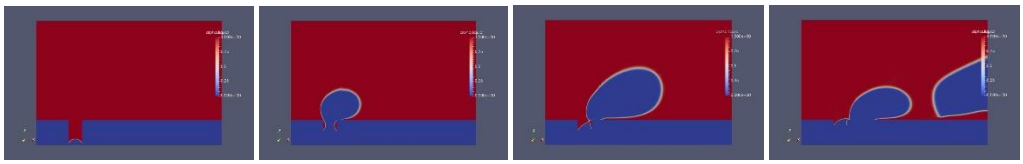

Figure 7. Bubbles growing and detachment periods for 25 and 50 micrometers depth cavities in 5K superheated bulk fluid temperature

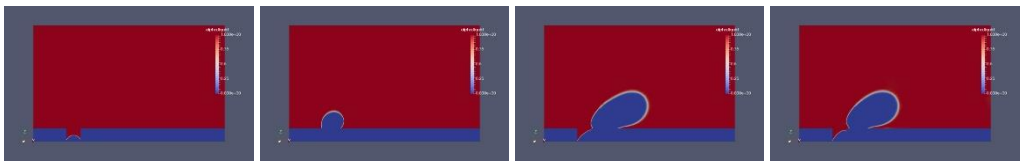

Figure 8. Bubbles growing and detachment periods for 25 and 50 micrometers depth cavities in saturated bulk fluid temperature

4. RESULTS AND DISCUSSION

4.1. Results for Pool Boiling

Studies (g=9,81 m/s²)	Initial Bubble Radius (milimeter)	Detachment Diameter (milimeter)	Detachment Time (second)
10g	0.15	0.32	0.001325367
1g	0.15	0.5	0.0081703
0.1g	0.15	1.74	0.0773541
0.01g	0.15	3.39	0.2223272

Table 1. Pool boiling results

As a result of pool boiling studies, gravity magnitude has important influence on bubble growing and detachment periods. As the gravity magnitude decrease, bubble detachment time and bubble detachment diameter increase. The highest temperature profiles were obtained in the vicinity of the contact line during bubble growing and detachment periods. Moreover the highest velocity profiles were obtained at contact line during bubble growin period. In the bubble detachment period highest velocity profiles were obtained at the bubble hull and bottom of the bubble while bubble was rising.

4.2. Results for Flow Boiling From a Flat Surface

Bulk Fluid Velocities (m/s)	Initial Bubble Radius (milimeter)	Detachment Diameter (milimeter)	Detachment Time (second)
0.6	0.15	1.02	0.01442734
0.3	0.15	0.953	0.01381226
0.07	0.15	0.914	0.01348432
0.035	0.15	0.897	0.01337803
0.01	0.15	0.875	0.01318347
0	0.15	0.5	0.0081703

Table 2. Flow boiling from a flat surface results

Many flow boiling from a flat surface studies were carried out in subcooled bulk fluid temperature in the literature. On the contrary of the results of subcooled studies, as the bulk fluid velocity increase, bubble detachment time and bubble detachment diamater increase. In addition last data was taken from pool boiling on constant Earth gravity simulations. It has been observed that as bulk fluid velocity incrase, effects of the gravity magnitude on bubble growin and detachment periods decrease. Furthermore the highest velocity profiles were obtained at contact line during bubble growin period. In the bubble detachment period highest velocity profiles were obtained at the bubble hull and bottom of the bubble while bubble was rising.

4.3. Results for Flow Boiling From a Cavity

Studies (Cavity Depth, Micrometer)	Initial Bubble Radius (micrometer)	Detachment Diameter(micrometer)	Detachment Time (micrometer)	Any Vapor Remained
3	15	123	0.000160593	No
12	15	166	0.0002362	No

Table 3. Results for 3 and 12 micrometers depth cavities in 5K superheated bulk fluid

Studies (Cavity Depth, Micrometer)	Initial Bubble Radius (micrometer)	Detachment Diameter(micrometer)	Detachment Time (micrometer)	Any Vapor Remained
3	15	123	0.000160593	No
12	15	166	0.0002362	No

Table 4. Results for 3 and 12 micrometers depth cavities in saturated bulk fluid

Studies (Cavity Depth, Micrometer)	Initial Bubble Radius (micrometer)	First Bubble Detachment Diameter(micrometer)	First Bubble Detachment Time (micrometer)	Second Bubble Detachment Diameter(micrometer)	Second Bubble Detachment Time (micrometer)	Detachment Time Difference (second)
50	15	163	0.0001671	124	0.0003991	0.000232
25	15	197	0.000220828	154	0.00065511	0.000434282

Table 5. Results for 25 and 50 micrometers depth cavities in 5K superheated bulk fluid

Studies (Cavity Depth, Micrometer)	Initial Bubble Radius (micrometer)	First Bubble Detachment Diameter(micrometer)	First Bubble Detachment Time (micrometer)	Second Bubble Detachment Diameter(micrometer)	Second Bubble Detachment Time (micrometer)	Detachment Time Difference (second)
50	15	112	0.0002866	102	0.0006699	0.0003833
25	15	120	0.00032	108	0.000803	0.000483

Table 6. Results for 25 and 50 micrometers depth cavities in saturated bulk fluid

Bubble growing in the cavity period could not be observed for 3 micrometers depth cavity in both bulk fluid temperature due to the fact that initial bubble size were defined 15 micrometers and cavity was completely filled with vapor phase. Although top of the bubble hull growth faster than the bubble feet for 12 micrometer depth cavity case in 5K superheated bulk fluid due to higher evaporation rate, any neck formation could not be observed. Top of the bubble hull and bubble feet growth with the same rate in saturated bulk fluid. For 25 and 50 micrometers depth cavity cases bubble growing in the cavity periods shows the same behaviour with 12 micrometers depth cavity case in 5K superheated bulk fluid. But when the bubble reached top of the cavity, a neck formation was observed in the cavity for 25 and 50 micrometers depth cavity cases in 5K superheated bulk fluid. Indeed this neck formation can be observed more specifically for 50 micrometers depth cavity case.

Top of the bubble hull and bubble feet growth with the same rate for 25 and 50 micrometers depth cavity case in saturated bulk fluid. A small neck formation occured at the top of the cavity for 50 micrometer depth cavity case in saturated bulk fluid. As the bubble kept growing, the small neck formation completely vanished. For 3 and 12 micrometers cavity depth cases bubble completely detached from the bottoms of the cavities in both bulk fluid temperature. After the detachments no vapor remained in the cavities. Therefore second bubble growin and detachment periods could not be observed. As the bubble kept growing neck formations became thinner and bubble detached through neck formation in superheated bulk fluid for 25 and 50 micrometers cavity dept cases. After the detachments some vapor remained in the cavities. Therefore second bubble growing and detachment periods could be observed.

Results of the bubble growing in the cavity periods have been examined.It has been observed that bubble showed the same behaviour for 3 and 12 micrometer depth cavity cases. On the other hand bubbl growing and detachment periods were completely same for 25 and 50 micrometers depth cavity cases. Therefore results of bubble detachment periods were investigated seperately.

Results showed that 12 micrometers depth cavity case had bigger bubble detachment diameter and bigger bubble detachment time than 3 micrometers depth cavity case in both bulk fluid temperature. Another result is, as the bulk fluid temperature decrease bubble detachment time increase but bubble detachment diameter decrease due to the higher evaporation rate.

It has been observed that 25 micrometers depth cavity case had bigger bubble detachment time and bigger bubble detachment diameter than 25 micrometer depth cavity case in both bulk fluid temperature. Time difference between first and second bubble detachment times denotes second bubble growing and detachment period. 25 micrometer depth cavity case had almost two times bigger than 50 micrometer depth cavity case. Another result is, first bubble detachment diameter obtained bigger than second bubbles detachment diameters.

REFERENCES

[1]. Kunkelmann, C., (2011). “Numerical Modeling and Investigation of Boiling Phenomena”, Phd Thesis, Dartmstadt Technical University, Darmstadt.

[2]. [2] Dietl, J., (2015).“Numerical Simulation of Pool Boiling from Reentrant Type Structured Surfaces”, Phd Thesis, Technical University, Darmstadt.
[3]. Kunkelmann, C. ve Stephan, P., (2009). “CFD Simulation of Boiling Flows Using The Volume of Fluid Method within OPENFOAM”, Numerical Heat Transfer, Part A: Applications, 56:8, 631-646.
[4]. Liu, J., Wang, G., Zhang, L., Shi, Y., Zhang, H. ve Yao, S., (2017). “Numerical Simulation of Single Bubble Behaviour”, Propulsion and Power Research, 6(2):117-125.
[5]. Kunkelmann, C., Ibrahem, K., Schweizer, N., Herbert, S., Stephan, P. ve Gambaryan-Roisman, T,. (2011). “The Effect of Three-Phase Contact Line Speed on Local Evaporative Heat Transfer: Experimental and Numerical Investigations”, International Journal of Heat and Mass Transfer, 55:1896-1904.
[6]. Stephan, P., Sielaff, A., Fischer S., Dietl, J. ve Herbert, S., (2012). “A Contribution to The Basic Understanding of Nucleate Boiling Phenomena: Generic Experiments and Numerical Simulations”, Processing of the 3rd International Forum on Heat Transfer, 3-15 November 2012, Nagasaki, Japan.
[7]. Li, D. and Dhir, V.K., (2007). “Numerical Study of Single Bubble Dynamics During Flow Boiling”, Journal of Heat Transfer, 129/ 864-876.
[8]. Carey, V.P., (1992). “Liquid-Vapor Phase-Change Phenomena”, 2. Edition, Hemisphere Pub. Corp., Washington, D.C., 1997.

BIOGRAPHY

Mehmetcan Donertas. Received his diploma from Yildiz Technical University and is currently studying as master student in Yildiz Technical University. Interesting areas are numerical study of heat and fluid flow.

ICETI
www.iceti.org
2018
07-11 MARCH
BUDAPEST
HUNGARY
II. INTERNATIONAL CONFERENCE ON ENGINEERING TECHNOLOGY AND INNOVATION

Comparison of the Multi Line Anchor System and Bored Pile Wall System Under Earthquake Effect

Pinar Sezin Ozturk Kardogan [1] Mehmet Inanc Onur [2]

Abstract

In the recent times, using the excavation support systems has very important role for deep excavations. In the excavation support system design, the multi line anchor systems and the bored pile wall systems are frequently preferred. In this study, behavior of the anchor supported system and the bored pile wall system were modelled under the seismic load. For this purpose; firstly, the depth of excavation is chosen as 15 meters and then, safe design parameters were determined for both systems. The essential number of anchors and the length of anchors were calculated in the anchor supported systems. The diameter and length of pile were designated in the bored pile wall system. After the static analyzes were completed, two ground motion records were applied to understand the behavior of the supported systems under the seismic load by using Plaxis program. Stresses and deformations were determined by the Plaxis program for both systems. It has been observed that the multi line anchor system gives smaller displacements under earthquake loading.

Keywords: Deep excavations, Earthquake effects, Plaxis.

1. INTRODUCTION

Increasing world population and developing urbanization policies have required to design areas in the most ergonomic way for construction sector. Increasing number of tall buildings and decreasing available areas for construction in city centers have caused to use underground spaces. Deep excavation support systems are now being constructed in order to make safe excavations and foundations. Especially in the city centers due to the construction concentration, there is no area boundaries to sloping excavation therefore excavations should be supported by temporary or permanent excavation systems [1]. Deep and large excavations change the balance of the foundation soil and groundwater and also may have a great effect on the neighboring structures [2]. Deep excavation applications must be performed based on the external loads and the lateral earth pressures. Excavation support methods can differ depending on the type of soil and the site conditions.

Soil investigation must be performed before deep excavation [3]. On the other hand, ground water table is an important factor when preparing deep excavation support system projects. Alkaya and Cobanoglu (2007) provided a checklist for deep excavation applications and emphasized the importance of excavation support system selection. Damages caused by displacements and settlements before and after the applications should be distinguished.

Excavation support systems are structural elements for safe construction to support deep excavations. The failure mechanism in the excavation is usually due to the weak support systems and movement of the back soil to the excavation area [4]. Foundation pit should be safe against all negativities such as lateral movements or settlements in the neighboring structures [5]. Support systems can be categorized under six groups:

Diaphragm Walls

[1] *Corresponding author: Gazi University,Faculty of Technology, Department of Civil Engineering sezinozturk@gazi.edu.tr*

[2] *Assist. Prof. Dr., Anadolu University, mionur@anadolu.edu.tr*

This is one of the geotechnical applications to support the excavation that is commonly used in recent years. The diaphragm walls are the types of supports that can be used under water effect because they are impervious to water as well as providing excavation support. Diaphragm walls and anchor systems are generally used to support seaside piers and port structures [6]. The diaphragm walls function as an impervious layer is to prevent leakage of clean or dirty underground water or other liquids into the excavation when the hydraulic permeability of the soil is high [7].

Bored Pile Walls

Bored pile is a vertical member obtained by opening a hole with specific diameter and depth and then pouring concrete before or after the reinforcing [8]. The wall are called bored pile wall obtained by intermittently or side by side pile applications. If the excavation depth is small and the pile diameters are large, the pile wall works cantilever and the pile system is connected with a continuous beam from the top. If the pile diameters are small, the excavation depth is large or the support system is designated with no horizontally deformation, the pile wall is anchored to backwards [9].

Sheet-Pile Walls

Vertical continuous walls formed by individual steel elements to hold a soil mass are called sheet-pile walls [10]. The sheet-pile walls are generally used as water resistant structures, to keep water away from the construction site during the construction, or when other retaining structure is inadequate to support the back soil [10]. The sheet-pile walls are used when the water level is high and the load is low.

Braced Cuts

It is one of the structural elements used to support deep excavations similar to anchors [5]. The supports are structural elements that try to carry soil mass located behind the wall with the material rigidity properties of the element. Supports that can be used in multiple line, such as in anchor applications, are usually applied using with steel tubes [11].

Anchors

Anchors is the structural element located behind the active wedge and transferring to the applied tensile load to hard soil / rock layer [8]. It is an application to prevent stability problems by using the pre-stressing ropes. Before the anchor application, it is necessary to find out the project properties according to the soil properties and behavior. In addition, the anchors should be subjected to load tests to check whether they are compatible with the calculated bearing capacities. Akbas (2010) reported the intended uses of soil and rock anchors. In addition, he mentioned that anchors could be used for different purposes such as preventing vertical displacement.

Multi Line Anchor Systems

The elements of the multi-line anchorage system (supporting system) are dimensioned according to the earth pressure. In the system design, it is necessary to determine the total load and soil pressure distribution, and to estimate the deformations [12]. The followings are important in anchor design; total failure check, depth of anchor embedment, group effect, size of the anchor tie back.

This study models the behaviors of multi-line anchor system and bored pile wall system under earthquake conditions. For this purpose, safety design parameters were defined for both excavation support systems for an excavation depth of 15 meters. Stress and deformations were estimated for both systems by using Plaxis software. In addition, the behaviors of excavation support systems were analyzed using Plaxis software for two historically recorded earthquakes.

2. APPROACHES FOR DEEP EXCAVATION SYSTEMS

2.1. Limit Equilibrium Method

Limit equilibrium method is an approach used for situations where sliding resistance occurs. Although limit equilibrium methods use linear load distribution on the excavation support system that is increasing with the depth, the actual load distribution behind the anchorage/support systems with multiple line differs widely from the estimations [13].

2.2. Beams on Elastic Foundation

In this simple analysis method based on soil-structure interaction, retaining wall is designed as a beam and soil is modeled with springs [13]. Beams on elastic foundation uses a model in a way spring coefficients are defined that soil rigidity and spring rigidity have similar behavior. Because of the analyses, it is possible to calculate wall bending moments, shear forces, anchorage/support forces and wall displacement, however, it is not possible to calculate the movements of neighboring structures and soil [13].

2.3. Semi-Analytical Finite Element Method

Similar to the lateral subgrade reaction method, the soil around the wall is modeled as an elastic medium instead of a spring [13]. It is possible to model the soil-structure interaction and calculate wall bending moments, shear forces, anchorage/support forces and wall displacement, however, it is not possible to calculate the movements of neighboring structures and soil [13].

2.4. Finite Element Method

Superior features of this method are that it can provide the equilibrium, suitability and material conditions needed in the solution, and that it can model the geometry and limit conditions [12]. The most commonly methods in engineering problem modeling are finite elements and finite differences methods. Many engineering software use these methods [14].

3. MODELING

Plaxis software is used to compare multi line anchor system and bored pile wall supported system under the effects of earthquake. Plaxis software, uses finite element method, is commonly preferred in the solution of geotechnical engineering problems.

First, multi-line anchor system and bored pile wall supported system were statically analyzed for an excavation depth of 15 meters. The number and length of anchors needed for the multi-line anchor system and the *embedment* length of bored pile wall system were defined. Lateral deformation values were limited at (δ/H), 1.05 % level as reported by Clough and O'Rourke (1990). The screenshots of the analyses are given in Figure 1.

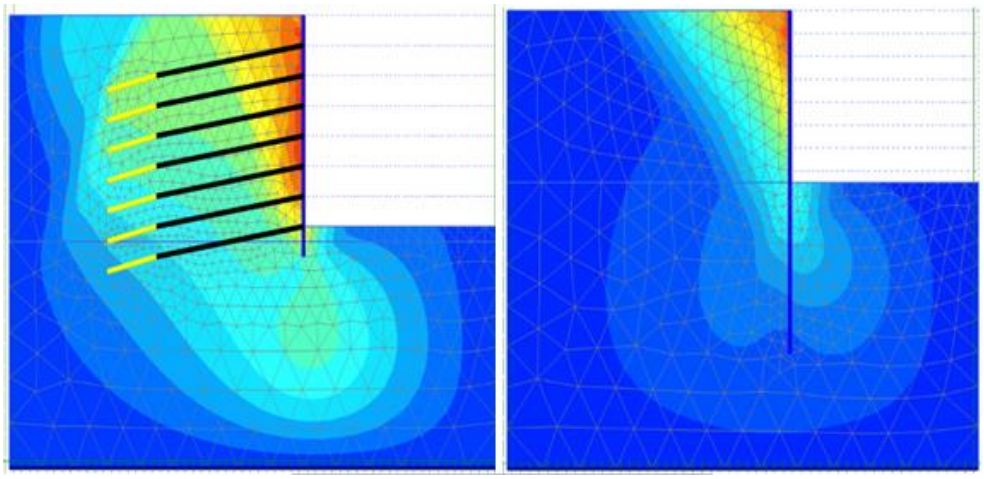

Figure. 1. Results of the static analysis

Pile having 65 cm diameter and 16 m length were sufficient for the safe service with 7 line anchors in the multi-line anchor systems. In the bored pile wall system, pile length were founded as 30 m. Table 1 shows the pile sizes used in this study and their structural properties. Table 2 shows the soil properties.

Table 27. Pile sizes mechanical properties

Pile Diameter (cm)	Pile Length (m)	Pile Elasticity Module (kPA)
65	16	$28x10^6$
100	30	28x106

Table 2. Soil properties

Unit Volumetric Weight (kN/m3)	Cohesion (kN/m2)	Angle of Friction (°)	Material Model
17.8	0.01	31	Mohr-Coulomb

Using the historical data from two different earthquakes, these two models were analyzed in the second section of the study. These earthquakes were 1971 San Fernando (Mw=6.6) and 1995 Kobe (Mw=7.2) earthquakes. Figure 2 and 3 show the acceleration-time graphs of these earthquakes.

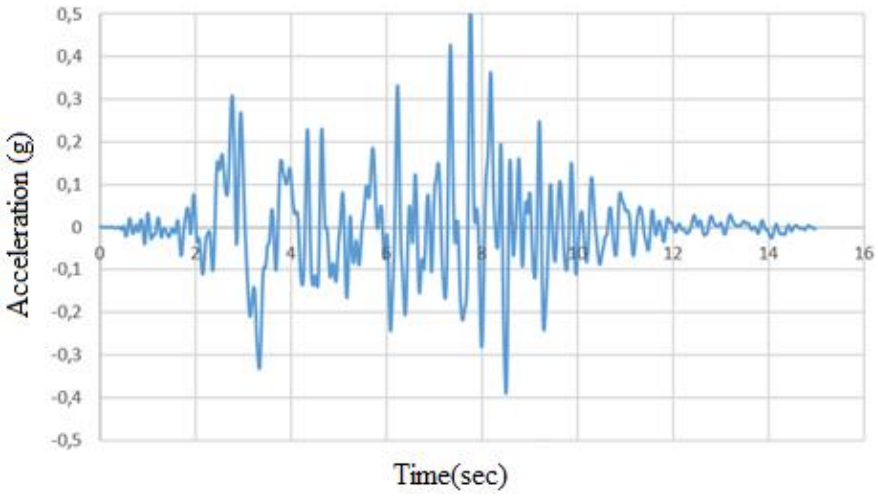

Figure. 2. Earthquake records of 1971 San Fernando Earthquake

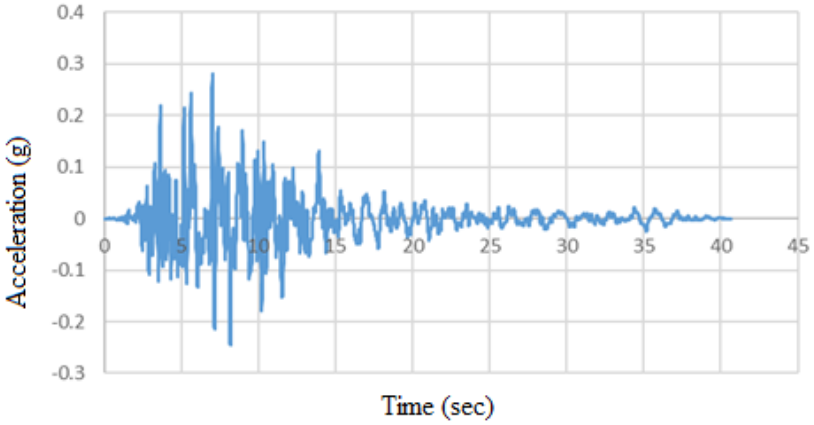

Figure. 3. Earthquake records of 1995 Kobe Earthquake

4. RESULTS

According to the analyses, it was found that pile behavior differs under different earthquake loads and Table 3 shows the lateral displacement values.

Table 3. Results of the analysis

Excavation Support System	Lateral Displacement (cm)	Earthquake Record
Multiline Anchor System	11	1995 Kobe
Multiline Anchor System	19	1971 San Fernando
Excavation Support System	**Lateral Displacement (cm)**	**Earthquake Record**
Bored Pile Wall System	32	1995 Kobe
Bored Pile Wall System	49	1971 San Fernando

The analysis showed that the multi-line anchor system results in smaller displacement when compared to the bored pile wall system. The displacements were increased for 1971 San Fernando Earthquake due to increased acceleration. Behavior of the deep excavations under both static and earthquake loads should be estimated. The selection of excavation support system depends on factors such as soil properties, water pressure, external loads and cost. Today, multi-line anchor systems and bored pile wall systems are commonly used for deep excavation projects. Previous studies comparing these two systems reported that the use of ground anchors is economical with increasing excavation depth [12]. It should be remembered that these results depends on the data used in this study and that it will be necessary to analyze each design separately.

ACKNOWLEDGMENT

This study was supported by Anadolu University Scientific Research Projects Commission under the grant no: 1705F331. The second author of this study would like to thank the Directorate of Scientific Research Projects Commission of Anadolu University.

REFERENCES

[1] Dadasbilge, O., (2015), "Ankrajli Iksa Sistemlerinin Tasarim Esaslari ve Proje Uygulamalarindan Ornekler", TMH - 485, 2015/2, 31-43.
[2] Alkaya, D., Cobanoglu, I., "Derin Kazilar ve Destekleme Yapilari", 2. Geoteknik Sempozyumu, 22-23 Kasim 2007, Bildiriler Kitabi, s. 163 – 173, Adana.
[3] Ergun,U. (2014), "Derin Kazi Projelerinin Ilkeleri: Bir Ozet", ODTU Basim Isligi.
[4] Do, T., Ou, C. Y., Chen, R., (2016), "A Study Of Failure Mechanisms of Deep Excavations in Soft Clay Using The Finite Element Method" Computers and Geotechnics, Vol 73, 153-163.
[5] Altun, G., (2013). "Ankrajli ve Ankrajsiz Derin Kazi Iksa Sistemlerinin Sayisal Yontemler Ile Analizi" Eskisehir Osmangazi Universitesi, Fen Bilimleri Enstitusu, Yuksek Lisans Tezi.
[6] Holla, Y., Ranjan, H.S., Rao, S., (2015), "Analysis of the Effect of Anchor Rod on the Behavior of Diaphragm Wall Using Plaxis 3d" Aquatic Procedia, Vol 4, 240-247,
[7] Uk, M., (2009), "Derin Kazilar ve Derin Kazilara Bir Ornek: Flame Towers Projesi Iksa Sistemi" Istanbul Teknik Universitesi, Fen Bilimleri Enstitusu, Yuksek Lisans Tezi,.
[8] Kose, K., H., (2011), "Derin Kazilar Ve Derin Kazi Uygulamasina Bir Ornek: Hilton Garden Inn Sutluce Derin Temel Kazisi" Istanbul Teknik Universitesi Fen Bilimleri Enstitusu, Yuksek Lisans Tezi.
[9] Akbas, M., (2010), "Derin Kazilarin Numerik Analizi" Yildiz Teknik Universitesi Fen Bilimleri Enstitusu, Yuksek Lisans Tezi.
[10] Saglam, A., (2006), "Derin Kazilarda Gorulen Stabilite Problemleri Ve Ilgili Cozum Kriterlerinin Belirlenmesi" Sakarya Universitesi Fen Bilimleri Enstitusu, Yuksek Lisans Tezi.
[11] Terzaghi, K. Peck, R.B., (1967), "Soil Mechanics in Engineeering Practice" John Wiley and Sons, New York,
[12] Arslan, B, Oztoprak, S., "Derin Kazilarda Cok Sira Ankrajli Iksa Sistemleri Ile Ankastre Fore Kazik Iksa Sistemlerinin Tasarimi Ve Maliyet Karsilastirmasi" II. Muhendislik Bilimleri Genc Arastirmacilar Kongresi, 17-19 Kasim 2005, Istanbul.
[13] Aslan, V., (2017), "Derin Kazilarin Sayisal Analizi Icin Parametrik Bir Calisma" Balikesir Universitesi, Fen Bilimleri Enstitusu, Yuksek Lisans Tezi,
[14] Cetin, Z., (2012), "Derin Kazi Yuzeyi Desteklenmesinin Sonlu Eleman Modelleriyle Analizi" Anadolu Universitesi Fen Bilimleri Enstitusu, Yuksek Lisans Tezi.
[15] Clough, G.W. ve O'Rourke, T.D. "Wall Deflection and Ground Surface Settlement Induced by Excavation", In Proceedings of the 4th National Geotechnical Conference, Hawlin, Taiwan, 1990.

ICETI 2018 07-11 MARCH BUDAPEST HUNGARY www.iceti.org
II. INTERNATIONAL CONFERENCE ON ENGINEERING TECHNOLOGY AND INNOVATION

Effects of Elliptical Condenser on the Performance of a Vapor Compression Refrigeration System

Fatih Selimefendigil[1], Hakan F. Oztop[2]

Abstract

In this study, effects of an elliptical condenser on the performance of vapor compression refrigeration system was examined. Reference configuration was obtained from a refrigerator with having a circular condenser. Thermodynamic analysis by using first and second law of thermodynamics was utilized. Performances were tested on an experimental test rig for various ambient temperatures and for different flow rates of air of the condenser fan. Coefficient of performances (COP) values were found to be higher when elliptical condensers were used instead of circular ones. When the ambient temperature increases, the discrepancy between the elliptic and circular condensers enhances. The difference between two condenser types results in COP enhancements of 2.15%, 17.3% and 20.2% for the ambient temperatures of 25 ºC, 32 ºC and 40 ºC, respectively. When the elliptic condenser fan air mass flow rate increases, first law efficiencies were also enhancing. A 15% enhancement in the condenser fan air flow results in 6.94% performance enhancement. Second law analysis of the system with circular and elliptic condensers reveal that total irreversibilities can be reduced for a refrigeration system by using elliptic type condensers. It was observed that a component based improvement in the vapor compression refrigeration system results in energy and exergy performance improvements.

Keywords: elliptic condenser, thermodynamics analysis, coefficient of performance, irreversibility

1. INTRODUCTION

Nowadays many attempts were made to develop energy efficient systems in power generation and refrigeration applications. The environmental side effects are also considered in order to have the least impact of those systems. Many novel design techniques are offered for various components of the refrigeration systems to achieve higher coefficient of performance. In some applications, also various types of refrigerants are used for the best performance and for the lowest impact on the environment.

Designs based on increasing the heat transfer capacity of condensers is a possible approach to increase the overall performance of a refrigeration system [1-5]. In general, it is possible to improve the overall performance of a system by component-wise improvement of the design. Air-cooled condensers which are composed of wire on tube bundles can be optimized to have higher heat transfer capacities. The fins can be made wavy and the heat transfer surface area of the tube bundles can be increased. Tube bundles of circular cross-section can be made elliptic to have higher heat transfer surface area.

In this study, we performed thermodynamic analysis of air cooled condenser with elliptic cross-section and comparisons were made against the reference circular cross-section. Energetic and energetic performances were compared by using the first and second law of thermodynamics.

[1] *Corresponding author: Department of Mechanical Engineering, Celal Bayar University, 45140 Manisa,Turkey.* *fthsel@yahoo.com*

[2] *Department of Mechanical Engineering, Technology Faculty, Firat University, 23119 Elazig, Turkey*

hfoztop1@gmail.com

2. METHODOLGY

In this study, a condenser composed of an elliptical cross-section was produced. The diameter of reference configuration of the circular tubes within the condenser is 4.76 mm and it is shown in Figure 1. Due to the difficulties in the production process of the elliptic condenser that is made of stainless steel, copper was used instead of stainless steel material. The circular cross sections were made elliptic in the ratio of 1.5 to 1 in the air flow direction. Thermodynamic analysis was performed both for vapor-compression refrigeration system with circular and elliptic condensers. The test stand of the refrigeration system with circular condensers that is made of copper is demonstrated in Figure 2.

In the analysis, R290 refrigerant was used and a P-h diagram of this refrigerant is given in Figure 3.

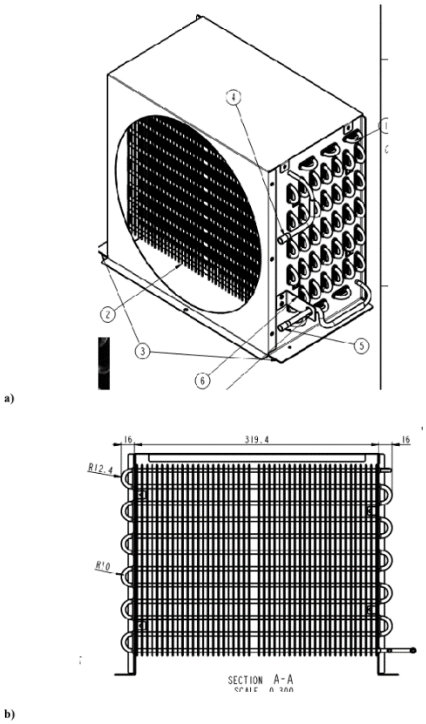

Figure 1 – Condenser with circular tube bubdles with fins (wire on tube)

Energy and Exergy Analysis

For a steady flowing device, energy conservation and entropy generation equations are given as:

 (1)

 (2)

Kinetic energy, potential energy and pressure loss in the connecting elements were neglected.

Physical specific exergy can be defined as:

 (3)

From the exergy balance, the rate of irreversibility cab ne obtained as:

 (4)

In Table 2, a compact notation of energy and exergy balance for each of the component in the vapor-compression refrigeration system is given.

Figure 2 – Vapor compression refrigeration system used in the experiment with condenser made of copper circular tubes

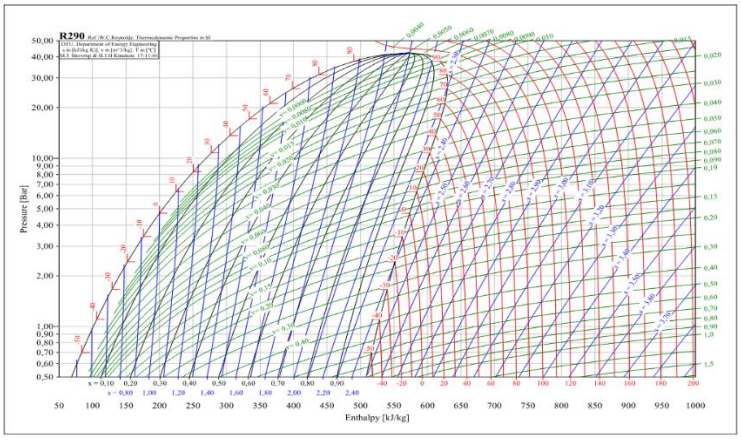

Figure 3 – P-h diagram of refrigerant R290

Table 1. Energy and exergy balance for each of the component in a vapor-compression refrigeration system

Component	Energy balance	Exergy balance
Compressor	$\dot{W}_c = \dot{m}(h_2 - h_1)$	$\dot{I} = \dot{m}(\psi_1 - \psi_2) + \dot{W}_c$
Condenser	$\dot{Q}_c = \dot{m}(h_2 - h_3)$	$\dot{I} = \dot{m}(\psi_2 - \psi_3) + \dot{Q}_c\left(1 - \frac{T_0}{T_c}\right)$
Expansion valve	$h_3 = h_4$	$\dot{I} = \dot{m}(\psi_3 - \psi_4)$
Evaporator	$\dot{Q}_e = \dot{m}(h_1 - h_4)$	$\dot{I} = \dot{m}(\psi_1 - \psi_4)$

3. RESULTS AND DISCUSSIONS

Thermodynamic analysis tests were performed for three different ambient temperatures both for circular and elliptical condensers. Energy and exergy balance equations that were given in Table 1 were used. Figure 4 and Figure 5 show the COP comparison for the refrigeration systems with circular and elliptical condensers. COP values deteriorates for higher values of ambient temperatures as it is expected. When the ambient temperature increase from 25ºC to 40ºC, COP value reduces by about 37.94% for circular condenser and 27% for elliptical condensers. For all temperature values, COP of elliptic condenser is higher than that of circular condenser but using an elliptic condenser is advantageous especially for higher values of ambient temperatures. The discrepancy between the COP values are 2.15%, 17.3% and 20.2% at 25 ºC, 32 ºC and 40 ºC, respectively.

In another test, condenser fan airflow capacity was changed for elliptic condensers. The result of COP comparison is shown in Table 2. When the condenser fan capacity was increased by 15%, COP increases by 6.94%, while 15% less fan capacity results in reduction of 15.97% of the COP value.

Exergy analysis was performed to show the potential for the system for further improvement in order to obtain an energy efficient system. Component-wise exergy balance was performed for each of the vapor-compression refrigeration system as it is given in Table 1. Total exergy destruction was computed from summing up all the exergy destruction for each of the component. Figure 6 and Figure 7 show the total exergy of refrigeration systems with circular and elliptic condensers. Total exergy destruction is higher for circular condensers and as the temperature increases, discrepancy between the total exergy destruction values become higher between circular and elliptic condensers. At the highest value of ambient temperature using elliptic condensers results in 20% reduction in the total exergy destruction.

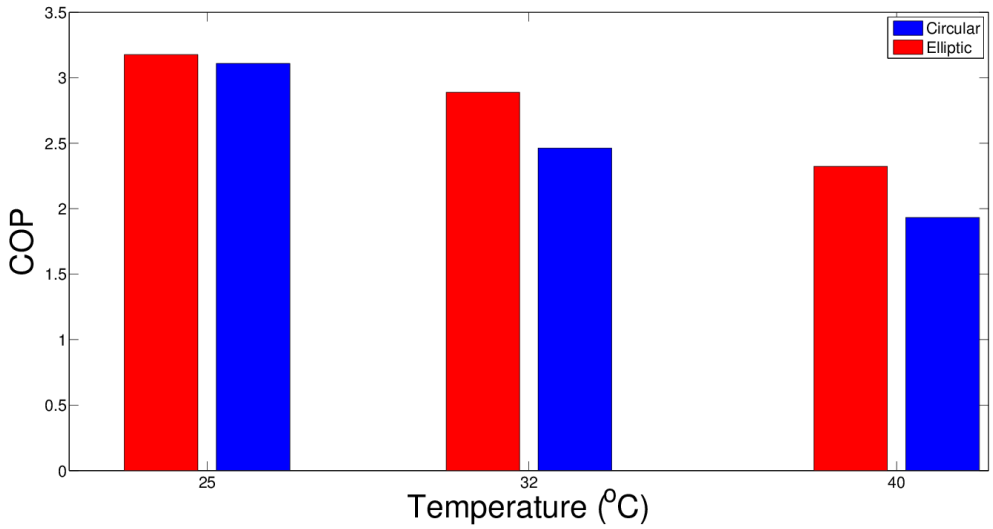

Figure 4 - Comparison of coefficient of performances for circular and elliptic condensers for three values of ambient temperatures

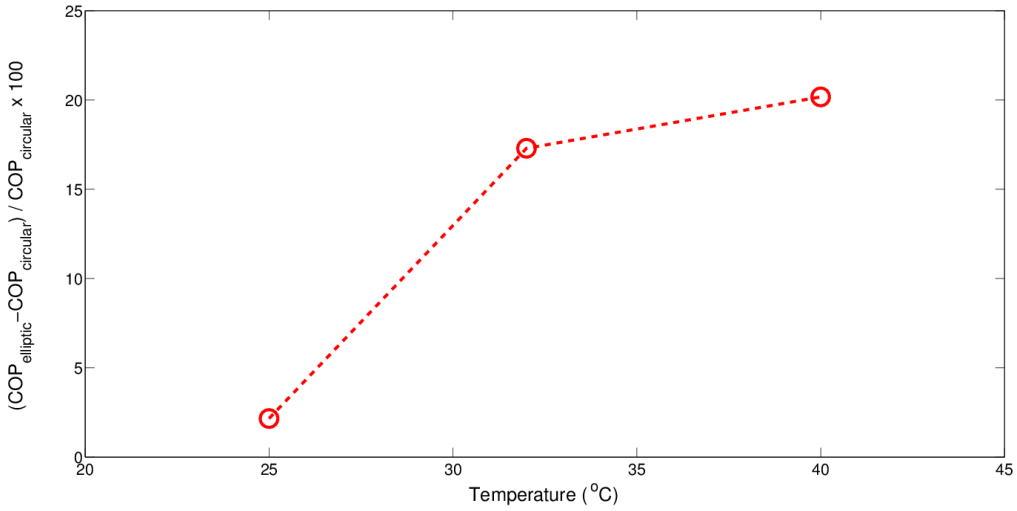

Figure 5 - Enhancement of COP value in percentage between a circular and elliptical condenser

Table 2 – COP values for various condenser fan airflow for elliptic condensers

Elliptic configuration	**COP**	**Change**
Reference (32ºC)	2.88	0 %
Fan air low rate %15 more	3.08	6.94%
Fan air low rate %15 less	2.42	-15.97%

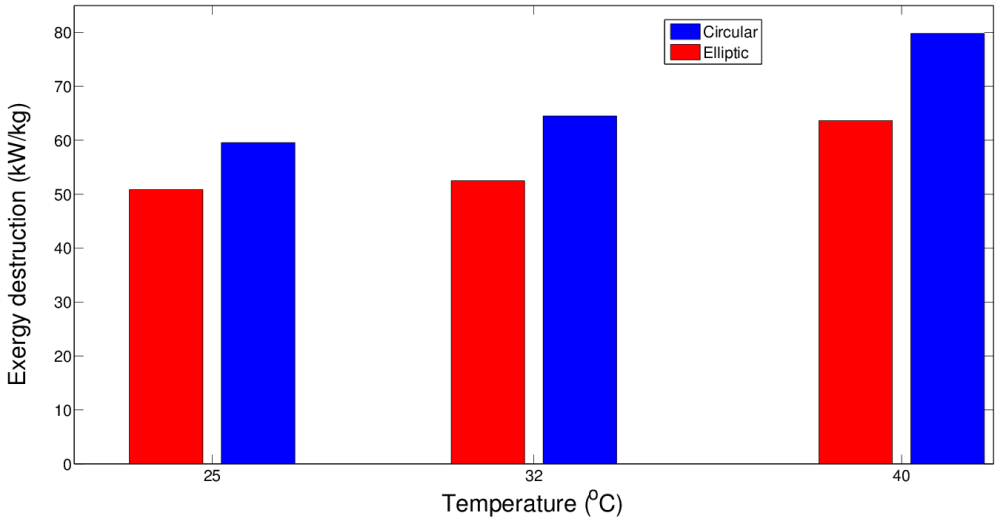

Figure 6 - Total exergy destruction of various components for systems with circular and elliptic condensers

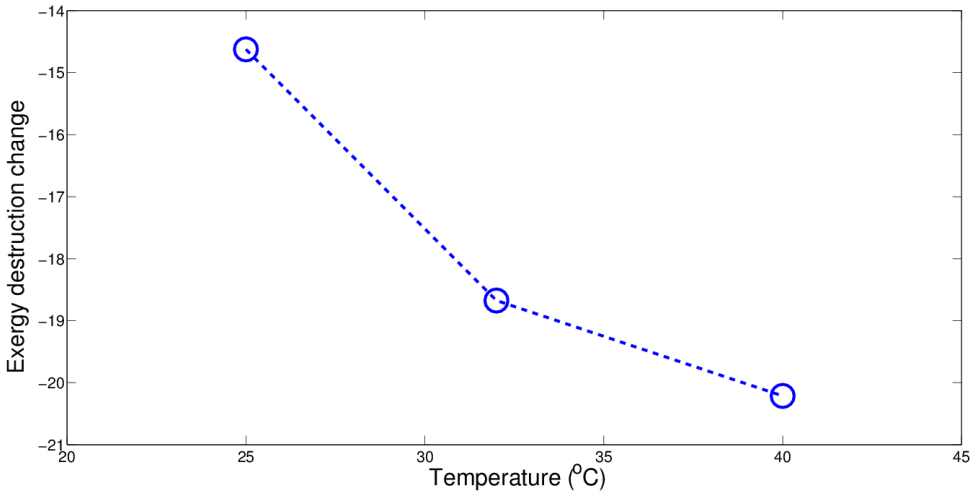

Figure 7 - Difference in the percentage for the total exergy destruction of circular and elliptic condensers

4. CONCULSIONS

Thermodynamic analysis of a vapor compression refrigeration system with circular and elliptic condenser was performed. It was observed that COP values enhance and total exergy destruction deteriorates for the system with elliptic condensers which is very effective for higher ambient temperatures.

ACKNOWLEDGMENT

This study is supported by The Scientific and Technological Research Council of Turkey (**TUBITAK**) for the project no: **5150047** whose support is gratefully acknowledged.

REFERENCES

[1] P.K. Bansal and T.C. Chin, T.C., 2002, ‘’Design and modelling of hot-wall condensers in domestic refrigerators’’, *Applied Thermal Engineering*, vol. 22, pp. 1601–1617, 2002.
[2] C.C. Wang, J.S. Liaw, and B.C. Yang, ‘’Airside performance of herringbone wavy fin and-tube heat exchangers - data with larger diameter tube’’, *International Journal of Heat and Mass Transfer*, vol. 54, pp.1024–1029, 2011
[3] B. Youn and N. H. Kim, ‘’An experimental investigation on the airside performanceof finand-tube heat exchangers having sinusoidal wave fins’’, *Heat and Mass Transfer*, vol. 43, pp.1249–1262, 2007.
[4] R. Bassiouny, 2009, ‘’Evaluating the effect of the space surrounding the condenser of a household refrigerator’’, *International Journal of Refrigeration*, vol. 32, pp. 1645-1656, 2009.
[5] T. Lee, W. Wu, Y.K. Chuah and S. K. Wang, ‘’An improvement of airflow and heat transfer performance of multi-coil condensers by different coil configurations’’, *International Journal of Refrigeration*, vol. 33, pp. 1370-1376, 2010.

ICETI
www.iceti.org
2018
07-11 MARCH
BUDAPEST
HUNGARY
II. INTERNATIONAL CONFERENCE ON ENGINEERING TECHNOLOGY AND INNOVATION

The Characterization of Pack Boronized W-Cu Based Tungsten Alloy

Ibrahim Gunes[1], Tayfun Uygunoglu[2]

Abstract

In the present study, effect of the boriding heat treatment process on surface properties of 80W- 20Cu Tungsten alloy has been investigated. Boriding was performed in a pack medium consisting of Ekabor-II powders at 1073 and 1173K for 3 and 7 h. The boride layer was characterized by optical microscopy, X-ray diffraction technique and the micro-Vickers hardness tester. X-ray diffraction analysis of boride layers on the surface of the steels revealed the existence of CuO, Cu_2O, WB2, and WB_3 compounds. Depending on the chemical composition of substrates, the boride layer thickness on the surface of the only parameter that changes is boronizing temperature and time. Thus, thickness of boride layer changes with boronizing time and temperatire. Boride layers ranged in thickness from 7 to 24 μm. The hardness of the boride compounds formed on the surface of the Tungsten alloy ranged from 980 to 2342 $HV_{0,1,}$ whereas Vickers hardness values of the untreated Tungsten alloy were 258 $HV_{0,1}$.

Keywords: Tungsten Alloys, Boride layer, XRD, Micro-hardness

1. INTRODUCTION

Surface properties of materials are currently being developed with coating using different methods. Boriding is a thermo-chemical surface treatment, in which boron is diffused into, and combines with, the substrate, forming a single or double phase metal boride layer on the surface. The boriding process improves the hardness, fatigue, corrosion, and wears properties of the surface. Industrial boriding processes can be applied to a wide range of steel alloys including carbon steel, low alloy-steel, tool-steel and stainless-steel. The boriding process involves heating the material in the range of different temperature and times, in contact with a boronaceous solid, liquid, gaseous, or plasma boriding. Industrial boriding processes can be applied to a wide range of steel and non-metallic alloys including. Thermal diffusion treatments of boron compounds used to form iron and metal borides typically require process temperatures of higher temperratures. The process can be carried out in solid, liquid, gaseous or plasma media. Because of their relatively small size and very mobile nature, boron atoms, can diffuse into substrate materials. The diffusion of B into steel results in the formation of iron borides (FeB and Fe_2B) and the thickness of the boride layer is determined by the temperature and treatment time. The characteristics of this boride layer depend on the physical state of the boride source used, boriding temperature, treatment time, and properties of the borided material [1-9].

In the present study, effect of the boriding process on surface properties of 80W- 20Cu Tungsten alloy has been investigated. For this reason, structural properties of each sample were investigated using optical microscopy, XRD, SEM, EDS, micro hardness tests.

2. EXPERIMENTAL STUDIES

This study uses 80W- 20Cu Tungsten alloy. The samples were sized to 20x8 mm and polished progressively with 1000-grit emery paper before boronizing process. The boriding heat treatment was carried out in solid medium containing a B_4C and KBF_4 powder mixture placed in an electrical resistance furnace operated at temperatures of 1073 and 1173 K for 3 and 7 h under atmospheric pressure.

The microstructures of polished and etched cross-sections of the specimens were observed under a Nikon MA100 optical microscope. The X-ray diffractograms were obtained by using a copper tube source as dictated by the

conventional bragg-brentano (θ-2θ) technique having symmetric geometry with monochromatized radiation (Cu Kα, λ=0.15418 nm). The thickness of the layers formed on the steels was measured by an optical micrometer attached to the optical microscope. The hardness of the boride layers was measured on the cross-sections using the Micro-Vickers indenter (Shimadzu HMV-2) with 50 g loads.

Figure 1. Boriding heat treatment of Tungsten alloys

3. RESULTS AND DISCUSSIONS

The cross-sections of optical micrographs of the borided 80W- 20Cu Tungsten alloy at temperatures of 1073 and 1173 K for 3 and 7 h are shown in Figures 1a-d. It is seen that the formed boride layers on the borided 80W- 20Cu Tungsten alloy appear to be compact and regular and having a smooth interface. Depending on the boriding parameter (temperature), the boride layer thickness on the surface of borided Tungsten alloy ranged from 7 μm and 24 μm.

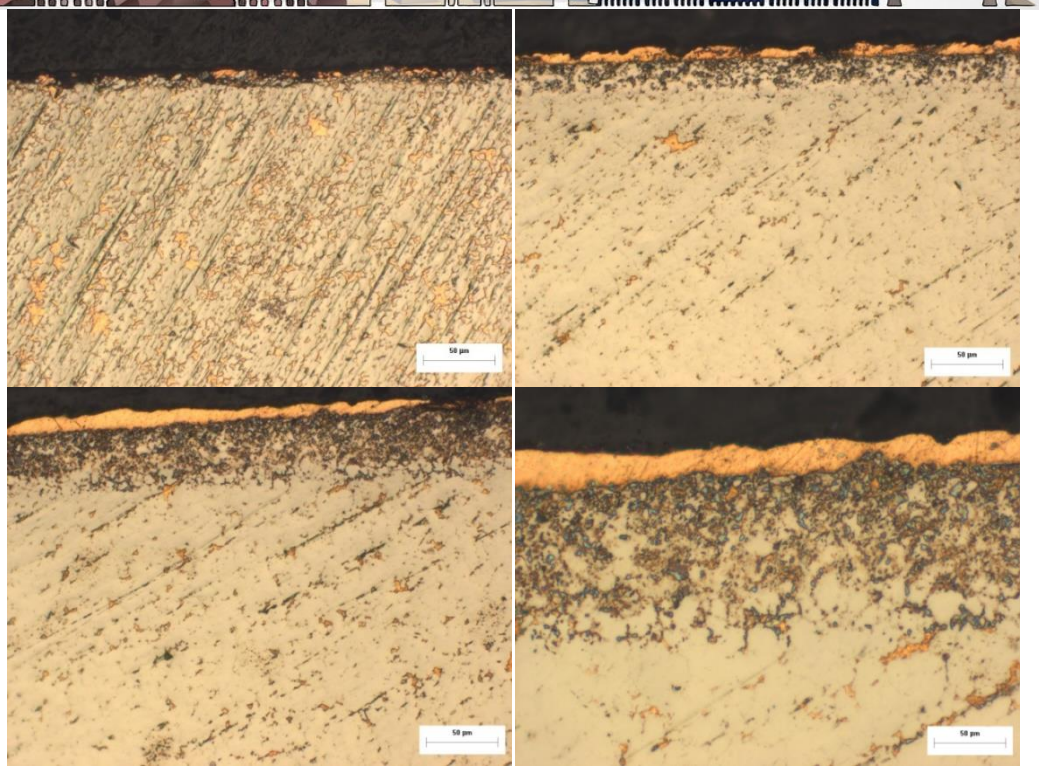

Figure 2. The SEM micrograph of the cross-sections of the borided tungsten alloys a) 1073 K - 3h, b) 1073 K - 7h, c) 1173 K - 3h, d) 1173 K - 7h.

XRD results showed that the boride layers formed on the Tungsten alloys contained WB, WB_2, WB_3, CuO, Cu_2O and W_2B_5 phases in Fig. 3. Micro-hardness measurements were carried out on the cross-sections from the surface to the interior along a line, as can be seen in Figure 3. The hardness of the borided Tungsten alloys varied between 980 and 2342 $HV_{0,05}$.

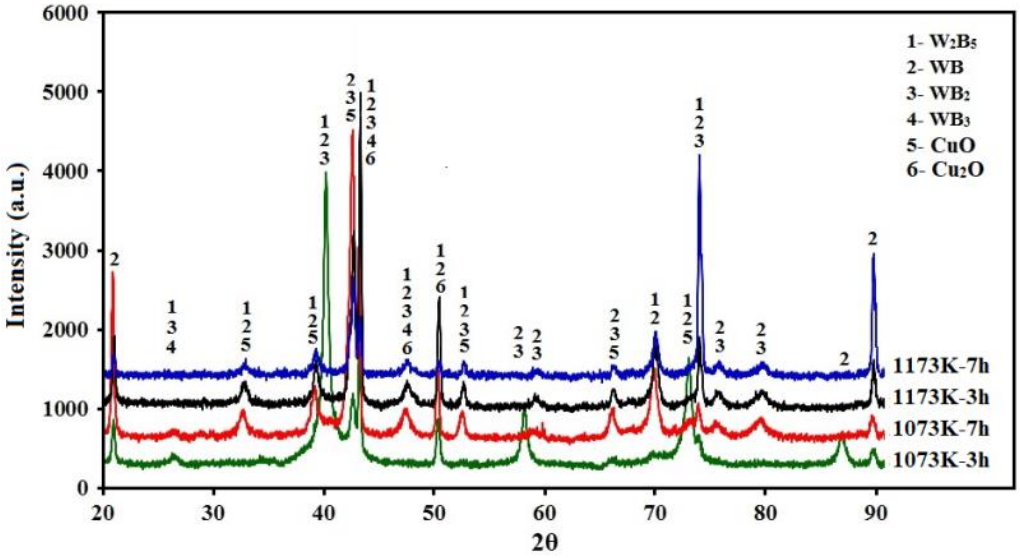

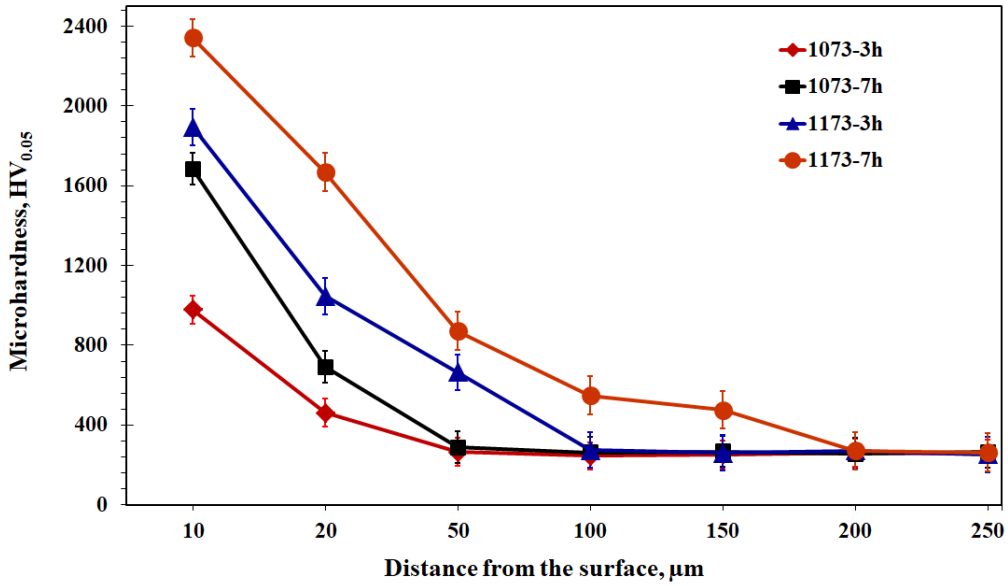

Figure 3 gives the XRD pattern and hardness recorded at the surface of borided Tungsten at the two temperatures 1073 and 1173 K for 3 and 7 h.

4. CONCLUSIONS

The following conclusions may be derived from the present study.

- Boride types formed on the surface of the tungsten alloy has a smooth and flat morphology.
- The multiphase boride coatings that were thermo chemically grown on the tungsten alloy were constituted by the W_2B_5 WB, W_2B, W_3B, CuO and Cu_2O phases.
- Depending on the boriding parameters, the boride layer thickness formed on the borided tungsten alloy was ranged from 7.3 µm to 24.5 µm.
- Depending on the boriding temperature and time, the hardness of the boride layer formed on the tungsten alloy varied between 980 and 2342 $HV_{0.05}$, whereas Vickers hardness value of the untreated tungsten alloy was 258 $HV_{0.05}$.
- As a result of boriding, the high surface hardness of the tungsten alloy was improved.

ACKNOWLEDGEMENT

The authors are grateful to the Scientific Research Project (16.KARIYER.37) Council of Afyon Kocatepe University. The authors wish to express their gratitude to the AKU-BAPK for its financial assistance.

REFERENCES

[1] A. K. Sinha: Boriding (Boronizing). ASM Int. Handbook, Vol 4, The Materials International Society, 437–447, 1991.
[2] A. G. Von MATUSCHKA: Boronizing. Heyden and Son Inc., Philadelphia, 1980.
[3] M. Usta, I. Ozbek, C. Bindal, A. H. Ucisik, S. Ingole, H. Liang: A comparative study of borided pure niobium, tungsten and chromium. *Vacuum*, 80, 1321, 2006.
[4] Uslu, I.; Comert, H.; Ipek, M.; Ozdemir, O.; Bindal, C. Evaluation of borides formed on AISI P20 steel. *Mater. and Des.* 28, 55-61, 2007.

[5] M. Usta, I. Ozbek, C. Bindal, A. H. Ucisik, S. Ingole, H. Liang: A comparative study of borided pure niobium, tungsten and chromium. *Vacuum*, 80, 1321, 2006.
[6] I. Ozbek., C. Bindal., Kinetics of borided AISI M2 high speed steel, *Vacuum*, 86, 391-397, 2011.
[7] I. Gunes., Kinetics of borided gear steels", *Sadhana*, 38, 527-541, 2013.
[8] L.G. Yu., X.J Chen,. K.A. Khor,. G. Sundararajan, FeB/Fe_2B phase transformation during SPS pack-boriding: boride layer growth kinetics. *Acta. Mater*. 53, 2361-2368. 2005.
[9] I. Campos, G. Ramirez, U. Figueroa, J. Martinez, O. Morales, et al. Evaluation of boron mobility on the phases FeB, Fe_2B and diffusion zone in AISI 1045 and M2 steels, *Applied Surface Science*, No. 253, 3469-3475, 2007.

ICETI
www.iceti.org
2018
07-11 MARCH
BUDAPEST
HUNGARY
II. INTERNATIONAL CONFERENCE ON ENGINEERING TECHNOLOGY AND INNOVATION

Breakfast Plate Design with Step Motor Control

Irem Senyer Yapici[1], Rukiye Uzun[1], Emrah Demir[1]

Abstract

In this application study, it was aimed that the individuals within the food departments of big corporations could get the food they wished at their own direction without walking round the table. A breakfast plate, which would be conveniently used in daily life, was designed with this aim. Designed breakfast plate comprised of four segments and four buttons were placed at each edge of the table on behalf of these four zones. Thus, when the button is pressed, the desired part of the plate is brought to the front of the individual. Step motor was used for performing rotational movement of breakfast plate at an intended direction. The control of step motor was carried out with Arduino. Apart from Arduino, ULN2003 integrated unit was used for motor driving step. Therefore, desired segment was brought right to the individual by pressing the button from any edge of the table at an intended direction.

Keywords: *Arduino; Breakfast plate; Step motor*

1. INTRODUCTION

Depending on the developments in technology, the studies making our lives easy are increasing day by day [1]. In these studies, the area including the ones based on service has a big share [2]. Within this context, developing service quality of food departments of big hotels and corporations in service sector was considered. A system bringing the food at an intended direction for the individuals was designed. The system includes a breakfast plate comprising of four segments. There are four buttons representing the segments at an each edge of the table. Therefore, the person at any edge of the table can request the food up to his direction by pressing the button on his side.

Step motor was used for operating the rotation of the disk used as the breakfast plate. The location and speed control of the disk can be carried out precisely thanks to the use of step motor. When the first energy was given to the step motor, QTR-1A infrared sensor was used to find reference point of the plate. The control of the values like the direction of the motor, spinning speed and rotational speed was performed with Arduino. ULN2003 integrated unit was also used as Arduino wasn't solely enough to operate the motor directly. In addition, PROTEUS simulation program was used for modeling of the program.

Similar smart breakfast plate study is also available in Yilanci's research. In this study, Pic16F28A micro controller was used instead of Arduino [3].

2. MATERIAL AND METHOD

2.1. Step Motor

Step motors are the systems converting electrical energy into rotational movement. They are often used in various areas from computer hardware to industrial systems. Step motors can rotate in multiple angle intervals such as 7, 5, 18, 45 and 90 degrees according to the structure of the motor. Depending on the change of impact rate, one step movement of the motor can be accelerated as it can be also slowed [4], [5].

[1] *Corresponding author: Bulent Ecevit University, Department of Electrical and Electronics Engineering, 67100, Zonguldak, Turkey.* senyerirem@gmail.com

Step motors were used in this study due to the fact that they are special motors used for precise control of the location and the movement. The step motor used in this study rotates in 7, 5 degree angle intervals. The step motor used in this study was shown in Figure 1.

Figure 1. The step motor used in this study

2.2. ULN2003A Integrated Unit

ULN2003A integrated unit gives driving information coming from Arduino to the step motor by increasing it to 12 DC volts [3]. If this integrated unit isn't used, Arduino will not be enough to operate step motors. Therefore, the use of this integrated unit was necessitated.

Figure 2. Step Motor Driver Integrated Circuit

2.3. Arduino Uno

Arduino is a platform providing the use of open source codes. It consists of a simple microprocessor circuit. Also, it includes software programs that are useful for programming the circuit [6], [7]. Arduino has 14 digital in/out pins. 6 out of these can be used as PWM outputs.

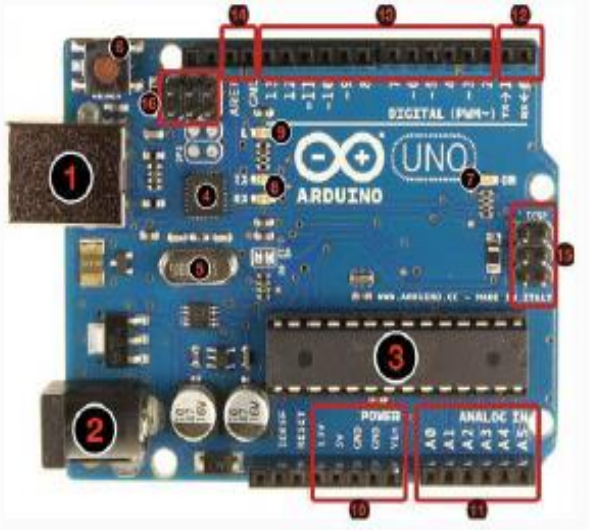

Figure 3. Arduino Uno Circuit

In Arduino Uno Circuit shown in Figure 3, there are [3]:

1.USB Jack

2.Power Jack (7-12 V DC)

3.Microcontroller ATmega38

4.Communication Chip

5.16 MHz Crystal

6.Reset Button

7.Power Led

8.TX / NX Led

9.Led

10.Power Pins

11.Analogue Inputs

12.TX / RX Pins

13.Digital in/out pins (pins having ~ sign with them. They can be used as PWM outputs)

14.Ground and AREF Pins

15.ICSP for ATmega328

16.ICSP for USB Interface

2.4. QTR-1A Infrared Sensor

This sensor is a sensor used for making contrast distinction in electronic and robotic projects. The sensor used in the circuit was shown in Figure 6. QRE111E was used in this study and it includes infrared led over the sensor and photo transistor sensor. Analogue voltage output is carried out by measuring the distance of photo transistor to the substance or line. This sensor was shown in Figure 4.

Figure 4. QTR-1A Infrared Sensor

2.5. Modelling of the System

The system was operated with Proteus before it was applied practically. Therefore, possible mistakes will be prevented. Proteus that was put into practice to control rotational direction and location of the step motor was shown in Figure 5.

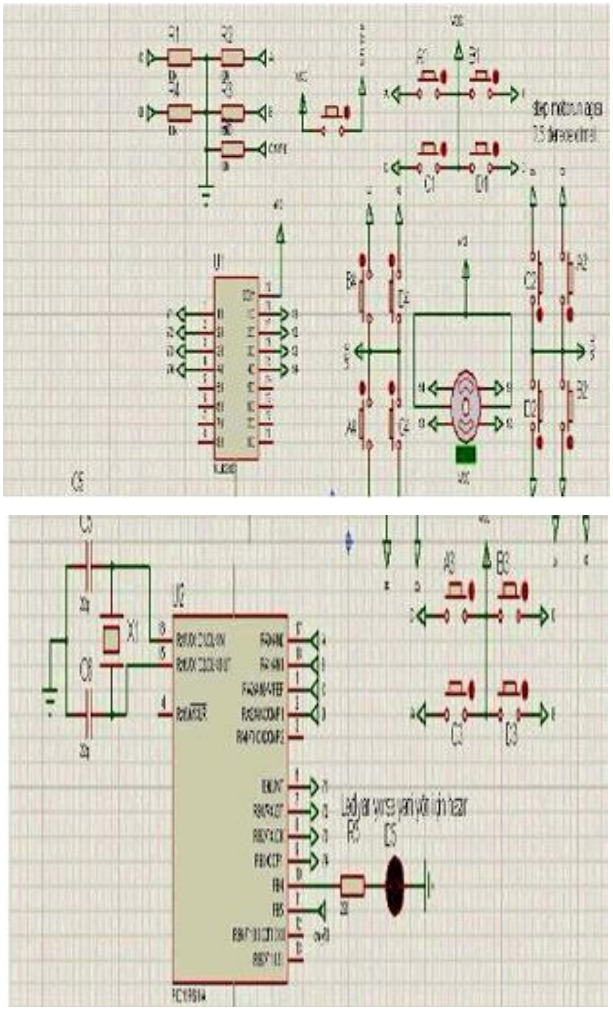

Figure 5. Step Motor Control Circuit in Proteus

2.6. Operation of the System

There is a disk used as a breakfast plate in the system. This disk consists of four equal parts. Each disk was placed into the motor shaft. There are four buttons at the edges and they represent these four disks. Therefore, desired segment will be brought right to the individual by pressing the button at the desired edge. Schematic demonstration of the system was given in Figure 6.

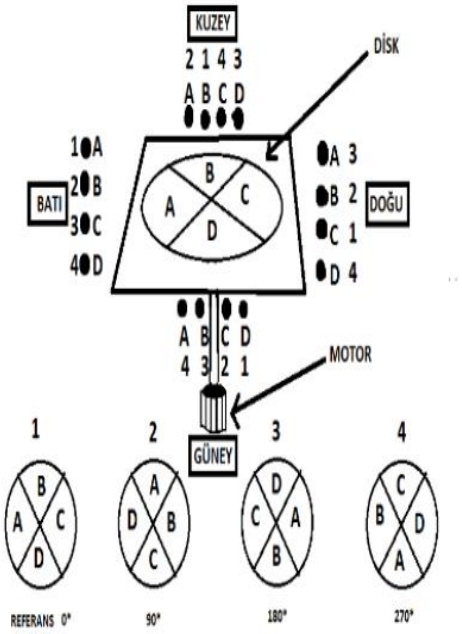

Figure 6. Schematic Demonstration of the System

3. CONCLUSION

In this study, by taking into consideration the food departments of big hotels and corporations, it was aimed that the individuals could easily reach the food at the remotest distance. Accordingly, a breakfast plate that could be practically used in daily life was designed. The movement of the breakfast table was performed with the step motor and the control of the motor was carried out with Arduino. Thanks to this study, it is thought that it will benefit us in visual and presentational aspects in the future.

REFERENCES

[1]. P. Basanta-Val, and M. García-Valls, "A library for developing real-time and embedded applications in C.," *Journal of Systems Architecture*, vol. 61, pp. 239–255, 2015.
[2]. D. L. McKee, "Services, growth poles and advanced economies," *Service business*, vol. 2, pp. 99–107, 2008.
[3]. Yilanci, "Akilli Kahvalti Tabagi," M. Eng. thesis, Electrical and Electronics Engineering Department, Trabzon, Turkey, 2011.
[4]. V. I. Nizhankovskii, and L. B. Lugansky, "Vibrating sample magnetometer with a step motor," *Measurement Science and Technology*, vol. 18, pp. 1436-1447, 2007.
[5]. Yilmaz, and Kucuk, "Akilli Gunes Takipleyici Sistem," M. Eng. thesis, Electrical and Electronics Engineering Department, Istanbul, Turkey, 2009.

BIOGRAPHIES

RUKIYE UZUN was born in Zonguldak, Turkey in 1983. She received the B.S. degree from Cumhuriyet University Electric and Electronic Engineering Department, in 2004. She completed her M.Sc. in 2010 at Bulent Ecevit University, Electric and Electronic Engineering Department and Ph.D. in 2014 at Bulent Ecevit University, Electric and Electronic Engineering Department. She is currently Assist. Prof. Dr. at Bulent Ecevit University, Electric and Electronic Engineering Department.

IREM SENYER YAPICI was born in Zonguldak, Turkey in 1990. She received the B.S. degree from Bulent Ecevit University Electric and Electronic Engineering Department, in 2012. She completed her M.Sc. in 2016 at Bulent Ecevit University Electric and Electronic Engineering Department. She is currently Research Assistant with the Bulent Ecevit University Electric and Electronic Engineering Department.

EMRAH DEMIR was born in Zonguldak, Turkey in 1994. He received the B.S. degree from Bulent Ecevit University Electric and Electronic Engineering Department, in 2017.

ICETI
www.iceti.org
2018
07-11 MARCH
BUDAPEST
HUNGARY
II. INTERNATIONAL CONFERENCE ON ENGINEERING TECHNOLOGY AND INNOVATION

Investigation of the Effects of Solution Heat Treatment Time on Eutectic Silicon for A356 Alloy

Serhat Acar [1], Ridvan Gecu[1], Alptekin Kisasoz[1], Kerem A. Guler[1], Ahmet Karaaslan[1]

Abstract

In this research microstructural variations for A356 aluminum casting alloy were examined with different casting methods and different solution heat treatment time. Permanent and green sand moulds were used for casting processes which were carried out at 730°C. Effects of different cooling rate which arised from different mould type, and solution heat treatment time have been investigated with the variations on microstructures and hardness values. Cast samples were solution heat treated at 525 °C for 3, 6 and 12 hours to observe the effects of solution heat treatment time on different casting methods. All specimens including as-casts were undergone metallographic preparation and all microstructures were evaluated in terms of determining secondary dendritic arm spacing (SDAS) for as-cast specimens and differentiations on aspect ratio of eutectic silicon for heat treated samples. Brinell hardness tests were carried out on each sample in order to relate the hardness property with microstructural variations. SDAS values were found higher in specimen cast into green sand mould than the other specimen cast into permanent metal mould due to slower cooling rate and thusly displaying lower hardness value. Maximum hardness and the lowest aspect ratio values were obtained with solution treatment time of 3 hours for both mould type.

Keywords: A356, eutectic modification, solution heat treatment

1. INTRODUCTION

A356 alloy has been widely used in automotive and aeronautical industries for numerous applications due to its low density, excellent castability and heat treatability [1]. On the other hand heat treatments on aluminum alloys are both time and energy consuming processes. During solution heat treatment process, which is the first step of precipitation hardening, secondary phases dissolve in aluminum matrix. Upon the quenching step, dissolved phases precipitate from super-saturated solid solution after final ageing step. Beside of finer morphology of precipitates, morphology of eutectic silicon also matters for final mechanical properties for Al-Si-Mg alloys. More globular and refined form of silicon particles is always desired [2–4].

In this study solution heat treatment for 3, 6 and 12 hours was applied to A356 samples cast in both permanent (metal) and green sand moulds in order to determine optimum duration. Effects of heat treatment time were investigated with evaluating eutectic morphology and hardness properties for all samples.

2. EXPERIMENTAL

In this study, A356 alloy, with chemical composition as given in Table 1, was cast at 730 °C in both sand and metal moulds. Obtained casts were machined and produced specimens were solution heat treated at 525° C for 3, 6 and 12 hours. All specimens were ground up to 2000, polished with 1 µm diamond solution and etched with % 0.5 HF solution. After metallographic preparation, micrographs of all samples were taken by Nicon Eclipse MA100 optical microscope. Effect of the cooling rate on secondary dendrite arm spacing (SDAS) and relation between heat treatment time and aspect ratio of silicon particles were investigated through taken micrographs. Hardness

[1] *Corresponding author: Yildiz Technical University, Department of Metallurgical and Materials Engineering, 34210, Esenler/Istanbul, Turkey.* seacar@yildiz.edu.tr

measurements were taken via Brinell hardness device with 62.5 kg force load and 2.5 mm tip diameter in order to associate the microstructural properties with a mechanical feature.

Table 1. Chemical composition of A356 alloy

Alloying Element	**Si**	**Fe**	**Cu**	**Mn**	**Mg**	**Zn**	**Cr**	**Ni**	**Ti**	**Pb**	**Al**
% Content	7.288	0.144	0.011	0.028	0.354	0.008	0.003	0.0031	0.123	0.0117	Bal.

3. RESULTS AND DISCUSSION

The as-cast microstructures of the metal mould and sand mould samples are shown in Figure 1 which consist of the dendritic α(Al) phase and the dark grey plate-like silicon phase. In terms of dendrite spacing depending on cooling rate, it can be found that the α(Al) and the eutectic silicon phases of the metal mould sample were composed in finer morphology due to a higher cooling rate comparing to the microstructure of the sand mould sample.

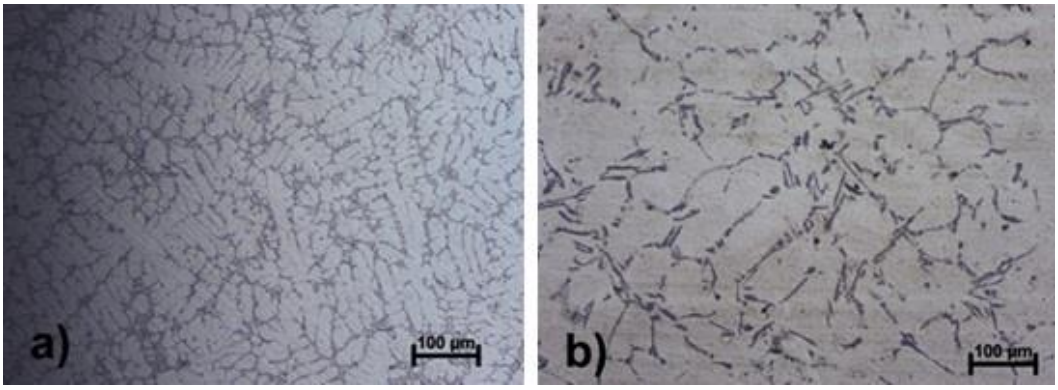

Figure 32. Optical microstructures of as-cast A356 aluminum alloy: (a) metal mould sample, (b) sand mould sample

Microstructures of solution heat treated samples are given in Figure 2. It can be seen that secondary dentritic arm spacings in sand mould samples are wider than metal mould samples. The slower cooling rate in sand mould results in coarser Si particles and also increased SDAS. High cooling rate restricts the dendrite coarsening, thus reducing the SDAS and consequently changing eutectic Si morphologies from coarse plate-like to short-rod shape even spherical shape. The SDAS values were found for the metal mould and sand mould as-cast samples 16.44 µm and 69.00 µm respectively.

Aspect ratio of the particles were measured in order to precisely describe the morphological changes in eutectic silicon. The aspect ratio is the ratio of length to width for specific particle, which can be useful for understanding the degree of transformation of plate-like morphology to more rounded one. As the aspect ratio value approaches to 1 it means more rounded the particle is. Aspect ratios were found by taking 20 different measurements from each sample for silicon particles and the results are given in Figure 3. Aspect ratio values of as-cast specimens were found for metal and sand mould samples 6.1285 µm and 7.1662 µm respectively. According to this results, as cast metal mould value is closer to 1 and the sphericity of eutectic silicon is higher for the metal mould sample. It can be seen that optimum solution heat treatment time is 3 hours for both mould types among the selected durations in order to obtain minimum aspect ratio.

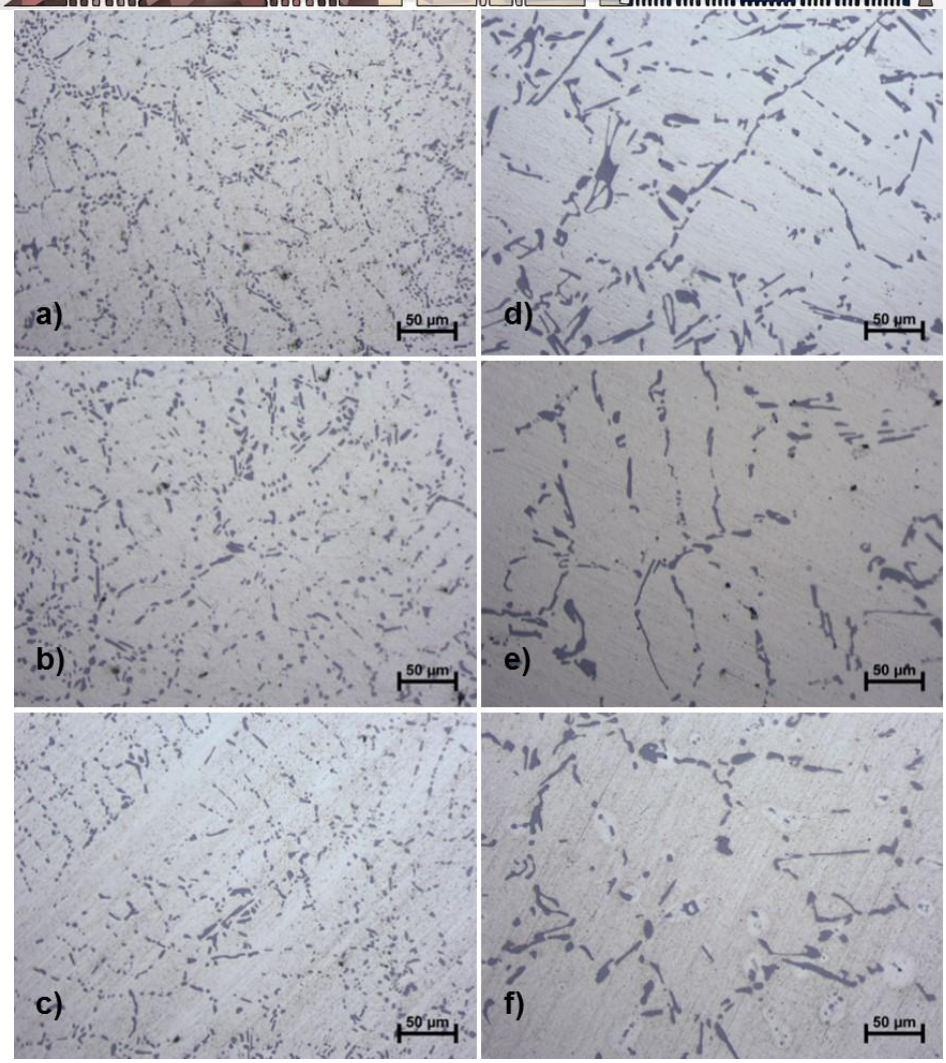

Figure 2. The microstructure of the metal and sand mould samples after solution heat treatment for different times; a) 3h metal mould, b) 6h metal mould, c) 12h metal mould, d) 3h sand mould, e) 6h sand mould, d)12 h sand mould

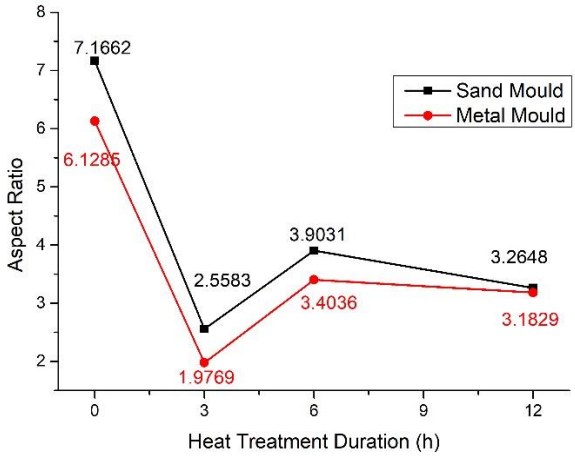

Figure 3. Aspect ratio of eutectic silicon particles as function of solution heat treatment

Figure 4 shows the hardness properties of as-cast and solution heat treated specimens. Samples cast in metal mould were shown higher hardness results for each duration because of higher heat transfer coefficient of metal mould. With fast solidification grain size and distribution of α Al and eutectic silicon particles became finer and more uniform. SDAS also effects on the hardness property, with increasing SDAS values resistance to indentation decreases. Microporosities, intergranular and impurity segregations occurs less with decreasing SDAS.

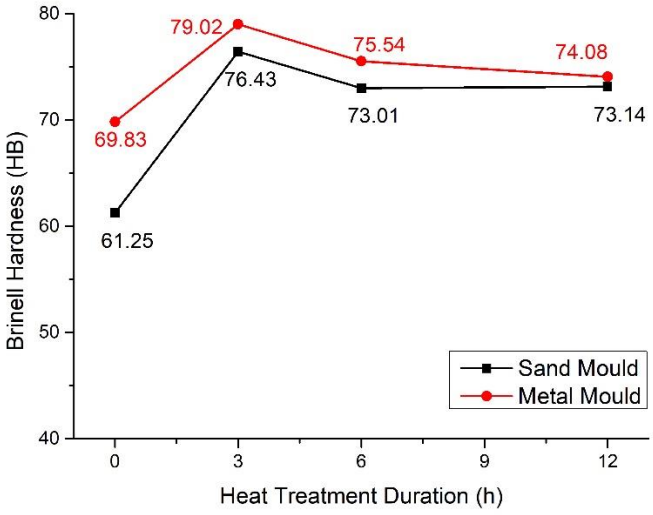

Figure 4. Hardness values of all specimens

Metal mould as-cast sample hardness was measured 69.83 HB and it was 61.25 HB for sand mould sample. After 3 hours of solution heat treatment, strong increase was observed in hardness values for both sample. Calculated hardnesses after 3 hours was 79.02 HB for metal mould and 76.43HB for sand mould samples. More than 3 hours

of solution heat treatment hardness slow decrease in hardness values were observed for both mould type. Because excessive solution treatment time effected α Al and eutectic silicon particles poorly, secondary particles became coarsened and less spheroidized.

4. CONCLUSION

Permanent (metal) and green sand mould casting methods were employed in this study for A356 alloy. Cast samples were solution heat treated for 3, 6 and 12 hours, obtained results can be highlighted as;

1) Obtained grain structure was finer in metal mould casting due to higher heat transfer coefficient also SDAS values were measured as 69.00 µm for green sand mould and 16.44 µm for metal mould as-cast specimens.

2) The lowest aspect ratio and the maximum hardness values were obtained with 3 hours of solution heat treatment duration for both mould kind. Excessive time of solution heat treatment coarsens the microstructure and causes high cost of energy.

REFERENCES

[1] L. Y. Zhang, Y. H. Jiang, Z. Ma, S. F. Shan, Y. Z. Jia, C. Z. Fan, and W. K. Wang, "Effect of cooling rate on solidified microstructure and mechanical properties of aluminium-A356 alloy," *J. Mater. Process. Technol.*, vol. 207, no. 1–3, pp. 107–111, Oct. 2008.

[2] B. Dang, C.-C. Liu, F. Liu, Y.-Z. Liu, and Y.-B. Li, "Effect of as-solidified microstructure on subsequent solution-treatment process for A356 Al alloy," *Trans. Nonferrous Met. Soc. China*, vol. 26, pp. 634–642, 2016.

[3] D. Ferdian, J. Lacaze, I. Lizarralde, A. Niklas, and A. I. Fernandez-Calvo, "Study of the Effect of Cooling Rate on Eutectic Modification in A356 Aluminium Alloys," *Mater. Sci. Forum*, vol. 765, pp. 130–134, Jul. 2013.

[4] D. Dioni, S. Cecchel, G. Cornacchia, M. Faccoli, and A. Panvini, "Effects of artificial aging conditions on mechanical properties of gravity cast B356 aluminum alloy," *Trans. Nonferrous Met. Soc. China*, vol. 25, no. 4, pp. 1035–1042, Apr. 2015.

ICETI 2018 07-11 MARCH BUDAPEST HUNGARY www.iceti.org
II. INTERNATIONAL CONFERENCE ON ENGINEERING TECHNOLOGY AND INNOVATION

Investigation of Wickability Properties of Microfilament Woven Fabrics

Hatice Kubra Kaynak[1], Osman Babaarslan[2], Esin Sarioglu[1], Halil Ibrahim Celik[1]

Abstract

Synthetic fiber industry has been enforced to make developments due to the increasing performance demands from textile products. One of the most important developments in synthetic fiber industry, is absolutely producing extremely fine filaments which are named as microfilaments. A microfilament can be defined as a filament finer than 1 dtex or 1 Denier and 1dtex polyester fiber has a fiber diameter of approximately 10 µm. It is an important factor of having a good thermophysiological comfort for textile fabrics for a comfortable and healthy use of textiles. As an aspect of thermophysiological comfort, transferring the liquid perspiration to the outer surface of the garment is an important issue. Wicking can be defined as spontaneous flow of the liquid in a porous substance, driven by capillary forces. In this study, it is aimed to determine the effects of filament fineness, weft sett and weave type on the wickability of filament woven fabrics. For this aim, 3/2 Twill and 5 end Satin polyester filament woven fabrics with different weft yarns of 3 different filament finenesses (0.33 dtex, 0.76 dtex, 3.05 dtex) and two different weft sett values (45 wefts/cm and 47 wefts/cm) were tested according to AATCC Test Method 197-2011, Vertical Wicking of Textiles. For comparison of the wickability of sample fabrics, the wetted height of the samples for different time intervals are determined.

Keywords: filament linear density, liquid transport, microfilament, wickability, woven fabric

1. INTRODUCTION

Synthetic fiber industry has been enforced to make developments due to the increasing performance demand for textile products. One of the most important developments in synthetic fiber industry, is absolutely producing extremely fine fibers which are named as microfibers and nanofibers. Until today, there is no exact definition for microfibers. But common opinion is defining a fiber finer than 1 dtex or 1 denier as microfiber. Fabrics produced from microfilaments are superior to conventional fiber fabrics, due to their properties such as light weight, durability, waterproofness, windproofness, breathability and drapeability [1-8]. A spontaneous transport of a liquid driven into a porous system by capillary forces is termed wicking. Capillary forces are caused by wetting and then wicking occurs a result of spontaneous wetting in a capillary system [9]. The wetting and wicking behaviors affect the moisture and thermal comfort of clothing systems. A clothing system with high wicking ability can hold the liquid perspiration quickly from skin area and transfer it to top side of fabric, providing a good level of comfort to wearer due to evaporating cooling. There are some factors that affect wicking property of a textile structure namely; fibre content, fibre cross-section, number of filaments, fabric structure, spinning system, the topogragraphy structure and etc. [10]. A polyester filament which has a linear density of 1 dtex, has a fiber diameter of approximately 10 µm. These extremely fine filaments in fabric structure are expected to serve good capillary forces and enhance the wickability of the fabrics. In this study it is aimed to investigate the effects of filament fineness, weft sett and weave type on wickability of polyester woven fabrics.

[1] *Gaziantep University, Textile Engineering Department, Gaziantep / TURKEY*

[2] *Cukurova University, Textile Engineering Department, Adana / TURKEY Corresponding author: tuluce@gantep.edu.tr*

2. MATERIALS AND METHODS

In this study it is aimed to investigate the effects of filament fineness, weft sett and weave type on wickability of polyester woven fabrics. For this aim polyester textured yarns of 110 dtex linear density which has three different filament linear densities (0.33 dtex, 0.76 dtex, 3.05 dtex), were applied merely in weft direction. The cross-sectional SEM views of the sample yarns are seen in Figure 1. For warp direction, 82.5 dtex polyester yarn with 1.14 dtex filament fineness was used in all samples.

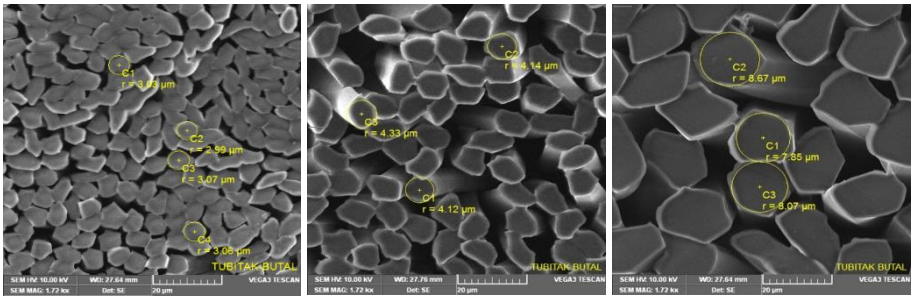

Figure 1. SEM views of filament yarns with different filament linear densities from left to right 0.33 dtex, 0.76 dtex, 3.05 dtex, respectively.

Sample fabrics were woven by a conventional loom with an electronic dobby shedding mechanism and rapier weft insertion at a loom speed of 420 rpm. Warp sheet was prepared with a 185 cm reed width. Before desizing process, sample fabrics were treated thermal fixation process to obtain dimensional stability. Thermal fixation process was done with a stenter which has 8 chambers at 195ºC with 25 m/min process speed. Sample fabrics were produced with two different weave types; Twill 2/3 (Z) and Satin 4/1 (five end satin). The warp sett value was constant for each weave type as 85 warps/cm. Two different weft sett values were applied to twill and satin weave samples as 45 weft/cm and 47 wefts/cm.

Structural properties namely, weft sett, fabric weight and fabric thickness of sample fabrics were determined according to TS 250 EN 1049-2 (1996), TS EN 12127(1999) and TS 7128 EN ISO 5084 (1998), respectively. Cover factor of samples were determined as the proportion of covered area of the fabric to the total area. The structural properties of fabric samples are given in Table 1.

Table 1. Structural properties of twill weave sample fabrics

Weave type	Weft yarn filament fineness, dtex	Weft sett, wefts/cm	Warp sett, warps/cm	Fabric weight, g/m²	Fabric thickness, mm	Cover factor
2/3 Twill (Z)	**3.05**	45	85	131	0.22	0.857
	0.76	45	85	132	0.22	0.857
	0.33	45	85	137	0.23	0.857
	3.05	47	85	134	0.23	0.862
	0.76	47	85	136	0.22	0.862
	0.33	47	85	141	0.23	0.862

Table 2. Structural properties of satin weave sample fabrics

Weave type	Weft yarn filament fineness, dtex	Weft sett, wefts/cm	Warp sett, warps/cm	Fabric weight, g/m²	Fabric thickness, mm	Cover factor
4/1 Satin	**3.05**	45	85	132	0.23	0.857
	0.76	45	85	132	0.22	0.857
	0.33	45	85	133	0.23	0.857
	3.05	47	85	133	0.23	0.862
	0.76	47	85	134	0.23	0.862
	0.33	47	85	136	0.23	0.862

Vertical wicking test was applied to determine the wickability. The height of rise (in cm) of water is taken as an indication of the wickability of the test fabric in different time intervals namely; 2, 3, 4, 5, 15, 30 minutes. Water-soluble ink is used to mark dots to indicate distance on the fabric. Higher rise of height indicates higher wickability. Wicking test apparatus is seen in Figure 1.

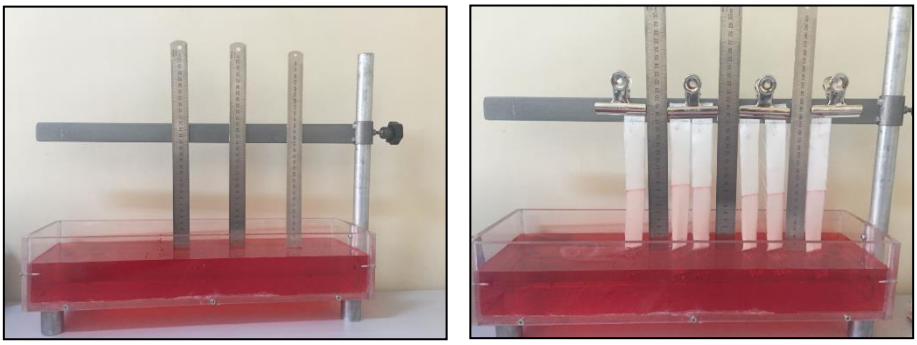

Figure 1. Wicking test apparatus

3. RESULTS

3.1. The Effect of Filament Linear Density on Wicking

Wicking results of satin weave fabrics are given in Figures 2 and 3 and twill weave fabrics in Figures 4 and 5.

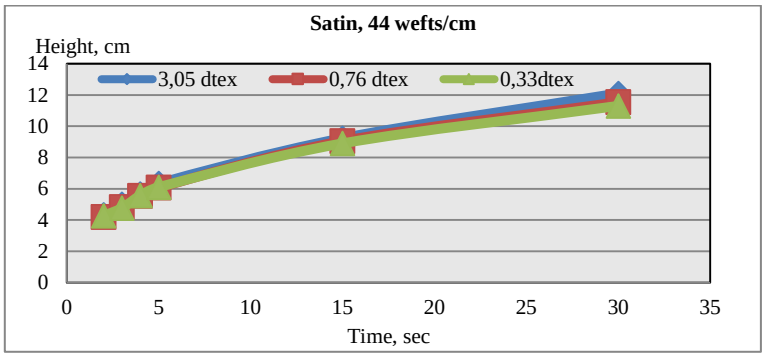

Figure 2 . Wicking of satin weave fabrics with 44 wefts/cm

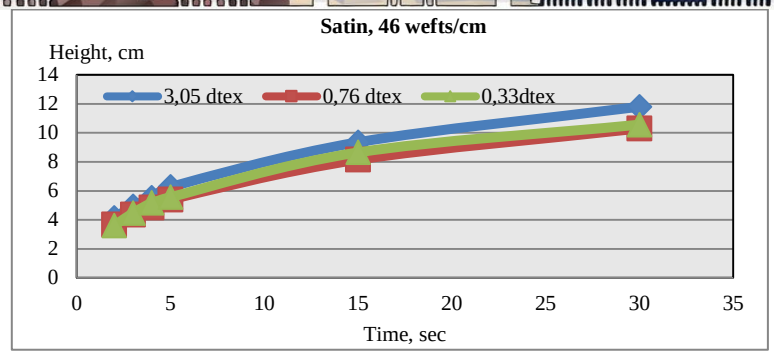

Figure 3. Wicking of satin weave fabrics with 46 wefts/cm

As seen in Figures 1 and 2, there is no obvious effect of filament linear density on wicking for satin weave samples which has a weft sett value of 44 wefts/cm. On the other hand, for 46 wefts/cm a minor increase of wickability is seen for 3.05 dtex filament linear density.

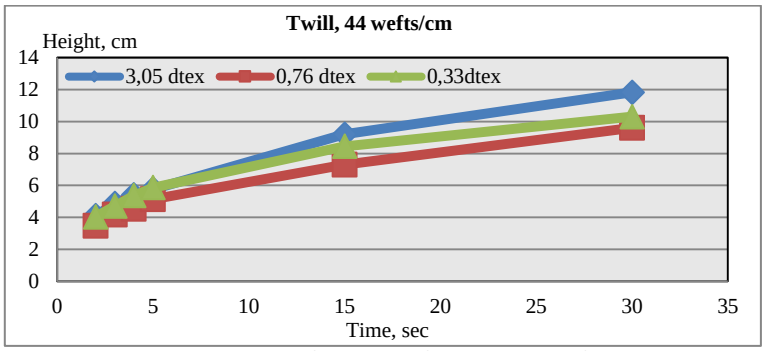

Figure 4. Wicking of twill weave fabrics with 44 wefts/cm

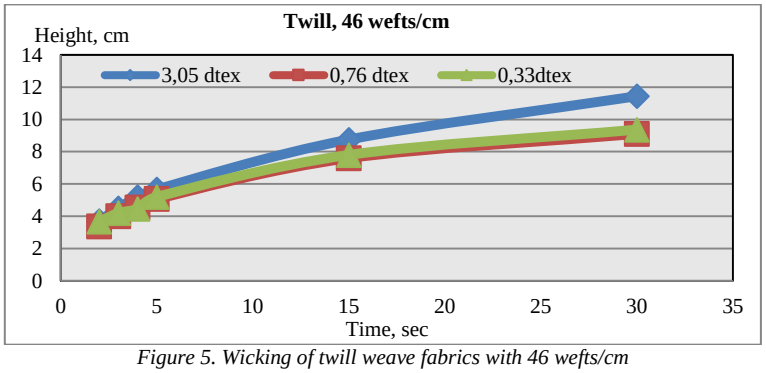

Figure 5. Wicking of twill weave fabrics with 46 wefts/cm

It is obvious from Figures 4 and 5 that, twill weave fabrics behave differently from satin ones, that 3.05 dtex sample has a more considerable increase in water height than 0.76 dtex and 0.33 dtex samples.

3.2. The Effect of Weft Sett on Wickability

Figures 6, 7 and 8 exhibit the effects of weft sett on wickability for 3.05 dtex, 0.76 dtex and 0.33 dtex filament linear densities, respectively.

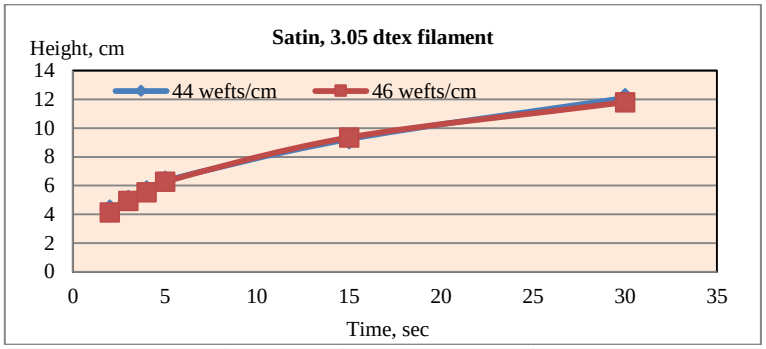

Figure 6. Wicking of satin weave fabrics with 3.05 dtex filament linear density

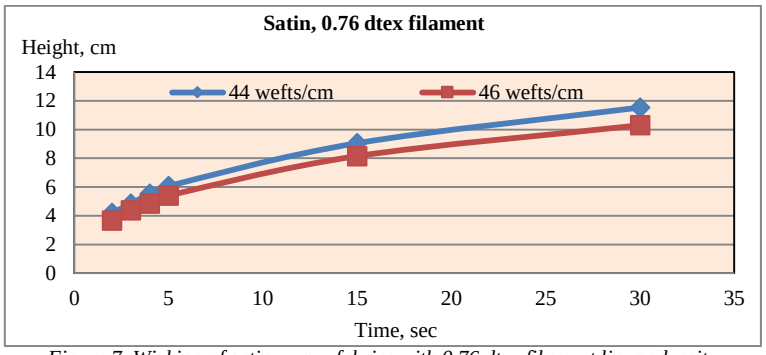

Figure 7. Wicking of satin weave fabrics with 0.76 dtex filament linear density

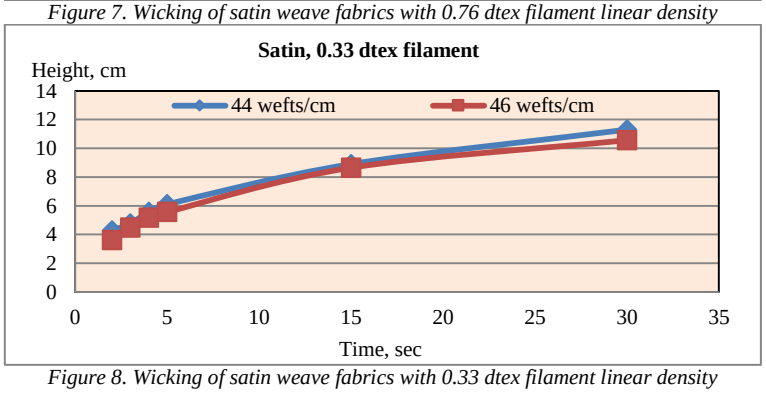

Figure 8. Wicking of satin weave fabrics with 0.33 dtex filament linear density

As it is seen from Figures 6, 7 and 8, weft sett has no considerable effect on wickability for 3.05 dtex conventional filament linear density whereas there is a minor increase in wickability for lower weft sett values for microfilament fineness levels

3.3. The Effects of Weave Type on Wickability

The effects of weave type on wickability for 44 wefts/cm are seen in Figures 9, 10 and 11.

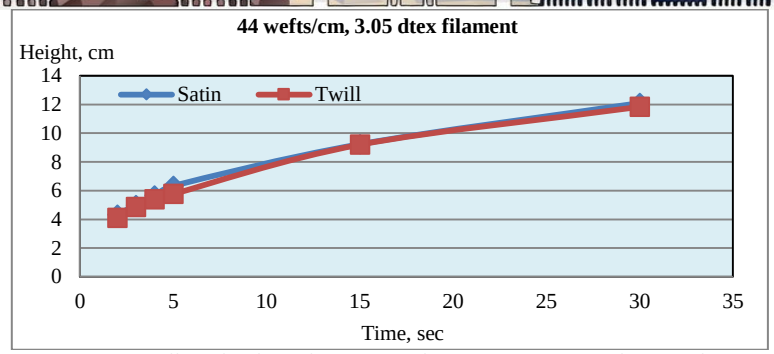

Figure 9. The effect of weft sett for 3.05 dtex filament linear density for 44 wefts/cm

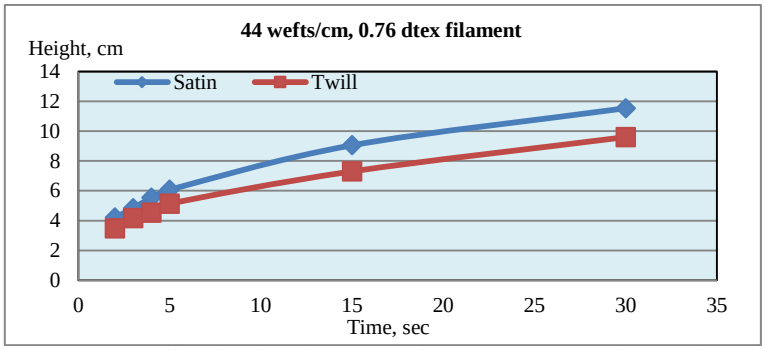

Figure 10. The effect of weft sett for 0.76 dtex filament linear density for 44 wefts/cm

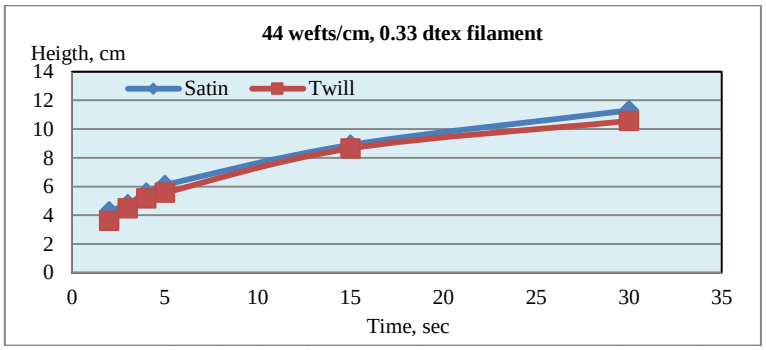

Figure 11. The effect of weft sett for 0.33 dtex filament linear density for 44 wefts/cm

As it is obvious from Figures 9, 10 and 11, there is a minor increase in wickability for satin weave samples. But this increase is negligible. The effects of weave type on wickability for 46 wefts/cm are seen in Figures 12, 13 and 14.

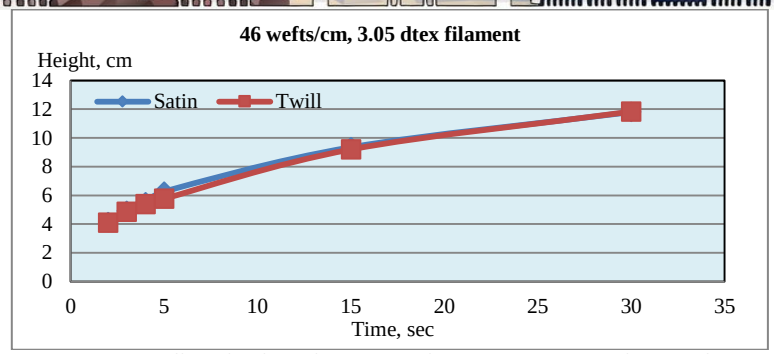

Figure 10. The effect of weft sett for 3.05 dtex filament linear density for 46 wefts/cm

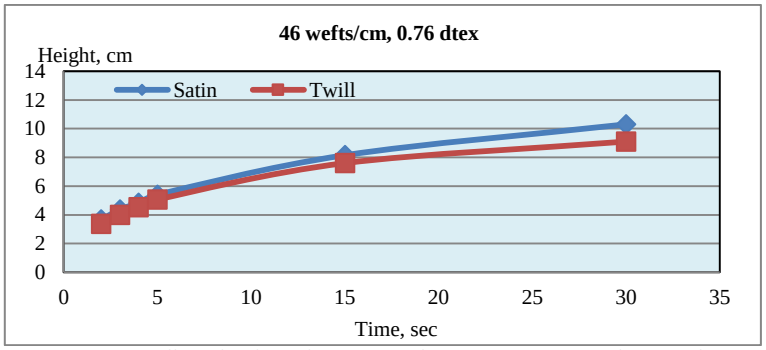

Figure 11. The effect of weft sett for 0.76 dtex filament linear density for 46 wefts/cm

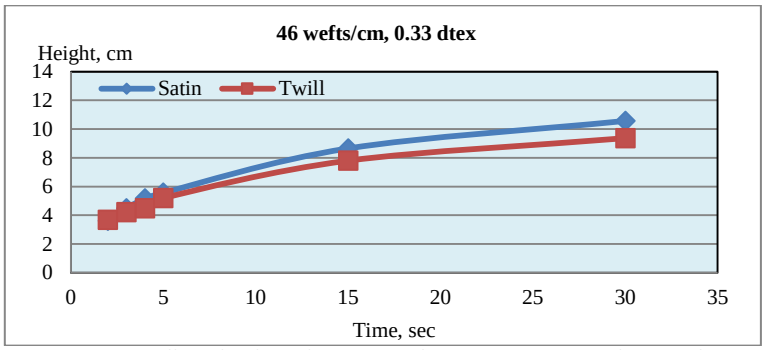

Figure 12. The effect of weft sett for 0.33 dtex filament linear density for 46 wefts/cm

Similar with samples that have 44 weft/cm weft sett, among samples with 46 wefts/cm satin weave type provided little increase in wickability property in comparison to twill weave samples.

4. CONCLUSIONS

The wetting and wicking behavior of the fibrous structure is a critical aspect of performance of products such as sports clothes, hygiene disposable materials, and medical products. Capillarity of the fibrous structure is very important on wickability. So, higher wickability is expected from microfilament samples. But, in contrary to the expectations, different results were obtained. Since, capillarity may not be the foremost factor that affect wickability. There are some other factors such as drying rate, water holding capacity, total porosity, pore size and pore distribution that affect the wickability.

For a better wickability in filament woven fabrics following issues should be kept in mind;

- Coarser filaments in yarn cross section *(for larger pores providing a higher water holding capacity)*
- Longer floats in weave type *(for a continuous transport of liquid)*
- Lower fabric density (by lower warp and weft sett values) (*for a higher porosity and water holding capacity)*
- Also, it is seen that microfilaments provide a very high drying rate that restricts the wickability of the fabric.

ACKNOWLEDGMENT

Authors are grateful to Korteks for supplying the yarn samples and Derhan Textile for producing the woven fabrics used in the study.

REFERENCES

[1]. P. Leadbetter, S. Dervan, "The microfiber step change", *Journal of the Society of Dyers and Colourists*, 1992, Vol. 108, No. 9, pp.369–371.
[2]. R. Bianchi, R. Maglione, "Manufacturing of fine denier filaments", In: *Polyester: 50 Years of Achievement*, Tomorrow's Ideas and Profits, D. Brunnschweiler & J. Hearle (Eds), 1993, pp.196-198, Stanley Press, Dewsbury, England.
[3]. S.V. Purane, N.R. Panigrahi, "Microfibers, microfilaments and their applications", *AUTEX Research Journal*, 2007, Vol.7, No.3, pp.148-158.
[4]. A. Basu, "Microfibers: Properties, processing and use", *Asian Textile Journal*, 2001, Vol.10, No.4.
[5]. S. Mukhopadhyay, "Microfibers – An Overview", *Indian Journal of Fiber & Textile Research*, 2002, Vol.27, No.3, pp.307-314,
[6]. B.V. Falkai, "Production and properties of microfibers and microfilaments", *The Indian Textile Journal*, 1991, No.2, pp.62-70.
[7]. J. Rupp, A. Yonenaga, "Microfibers-The new man made fiber image", *International Textile Bulletin*, 2000, No.4, pp.12-24.
[8]. H.K. Kaynak, O. Babaarslan, "Polyester Microfilament Woven Fabrics". In Han-Yong Jeon (Ed.) *Woven Fabrics*, 2012, (pp.155-178). InTech Publishing, Croatia.
[9]. A. Patnaik , R. S. Rengasamy , V. K. Kothari, A. Ghosh, "Wetting and Wicking in Fibrous Materials", *Textile Progress*, 2006, 38:1, 1-105.
[10]. M. Gorji, R. Bagherzadeh, " Moisture management behaviors of high wicking fabrics composed of profiled Fibres", *Indian Journal of Fibre & Textile Research*, 2016, Vol 41, , pp. 318-324.

BIOGRAPHY

Hatice Kubra KAYNAK is an Associated Professor in Textile Engineering Department of Gaziantep University, Turkey. She was born in 1980. She received her BSc degree from Kahramanmaras Sutcu Imam University, Textile Engineering Department (2002), Turkey, MSc degree from Gaziantep University, Textile Engineering Department (2005), Turkey and PhD degree from Cukurova University, Textile Engineering Department (2013), Turkey. She is now working nearly fifteen years as an academic staff of the Textile Science Division in Textile Engineering Department in Gaziantep University. She has authored over 40 peer reviewed publications and congress articles published in English and Turkish, 2 book chapters in English. Her current research interests include Weaving Technology, Technical Textiles, Textile Testing and Quality Control.

ICETI
www.iceti.org
2018
07-11 MARCH
BUDAPEST
HUNGARY
II. INTERNATIONAL CONFERENCE ON ENGINEERING TECHNOLOGY AND INNOVATION

Technical and Economical Approaches in Designing of Antifoaming Emulsions For Leather And Textile Industry

Bahri Basaran[1], Tayfun Barisik[1], Ahmet Aslan[1]

1. INTRODUCTION

The functionality of various surfactants based on their unique physicochemical properties has prompted considerable interest in their usage onto chemical processes. Surfactants have a very large number of applications by altering the properties of surfaces and interfaces due to their balanced structure having amphiphilic and amphipathic properties. Their characteristic chemical structure consists of some molecular components having little attraction for one surrounding phase, which is called lyophobic group, and some moieties adjacent to the chemical skeleton having a strong attraction for that phase; so called the lyophilic group form oriented monolayers in the interfaces. They come into prominence with their surface activity characterized by lowering the surface and interfacial tension in the medium in which they are dissolved. These compounds are termed surfactant relevantly. The function of a surfactant might have on a interfacial region between two liquids or between a liquid and a solid. Surface active agents play an important role as cleaning, wetting, dispersing, emulsifying, foaming and anti-foaming agents in many practical applications and products included in paints, emulsions adhesives, inks, biocides (sanitizers), shampoos, toothpastes, firefighting (foams), detergents, insecticides, deinking of recycled papers, ski waxes and spermicides etc.

The leather and textile industry is of the prominent industries in where excessive surfactant usage is required. For example, surface active additives such as wetting and cleaning agents, degreasing emulsifiers, dispersants, leveling agents and so on are extensively used in leather beamhouse and textile finishing processes. Due to the fact that their effectivity on the surfaces and functionality in two immiscible phases, while lowering surface tensions, foam arises on the surface. Foaming is a phenomena caused by the mixing of the air into liquid phase with mechanical action onto the destroyed layer of surface where these additives localized.

Nowadays, in the viewpoint of both social sensitivity about ecological production and new technical approaches based on functional properties in surfactant applications; for efficient knock-down of foams, elimination of defined and technically proven foam problems, and the elimination of deficiencies resulting from antifoaming agents, it is necessary to design and develop a variety of silicone polymer-containing antifoaming emulsions.

The paper comprises a consideration of the different variables affecting on the design of antifoam. Firstly; solid particles was experimented into a dispersion of solid in oil. Subsequently, the dispersion is brought in through water phase by conversion into emulsions. The paper is about the basics of these complex emulsification and their properties effecting the antifoaming ability. After some performance tests and evaluations the emulsion 2 prepared by 6.5 % of solid particle has a satisfactorily good in terms of antifoaming ability and durability.

2. FOAMING AND ITS IMPACTS

Foam is simply considered to be a gaseous mixture on the aqueous surface and mechanically dispersed air in the water phase to form physicochemical formation. In case of intensive formation this phenomena leads to both the prevention of mechanical effect; namely lower rinsing and the deposition of the dispersed phase ingredients in the foam layer, thereby; the chemicals can not be taken up adequately and uniformly by the substrate. In both cases foam layer causes physical and chemical disorders and also quality deficiencies such as uneven distribution of chemicals, and especially inhomogenous dyeing in the products. Due to the lower exhaustion of additives and their deposition on the aqueous phase surface give rise to the ecological problems based on the increasing pollution loads in the effluent. In addition, intensive foam reduces the equipment capacity and increases process time and costs; the foam volume also accumulates on the equipment, causing the lower pumping, reducing the functionality and blocking the pipes and prevent discharge (16, 21).

[1] *Department of Leather Engineering, Faculty of Engineering, Ege University, P.O. Box 35100, Bornova, IZMIR, TURKEY,bahri.basaran@gmail.com, ahmet.aslan@gmail.com, tafo1907.1@gmail.com*

The leather and textile processing are two phase systems in which the physicochemical effect of liquid phase on solid one yields in the final leather product. The all well being in this interaction is the more relevant reactions occurs and thereby; obtaining technical and quality requirements. For this purpose many surface modifications are necessarily practised by imposing some surfactants considering the process parameters. Foaming refers to functionality for a surfactant and when used more than required some technical deficiencies and complications arises. In the process steps used those stuffs the coarse mixture of water and gase (air) with mechanical action produces foam. The properties of this mixture are dependant on the surfactant amount and types, two phases characteristics and shaking times and intensity and so on.

The main foaming problem to be faced with in leather processing exists during the degreasing and rinsing for washing out for extracted fatty substances which is necessary to make the skins up to further processing. Both of these processes are of high foaming features due to excessive surfactants usage. In addition, intense foam formation occurs in the dyeing process which is carried out at high temperature and intensive rinsing as it is in double-face processing. The main importance of antifoaming emulsions being used for knock-down effect for the fact is to have high termal and mechanic stability for its emulsions. Otherwise; the uneven deposition of silicon polimer can result in staining problems in the substrate. For this reason and; chosing the appropriate antifoaming agents is crucial from technical point of view including both effectivity in the process and quality in the end product.

3. MECHANISM OF ANTIFOAMING

In order to successfully displace foam, an antifoam must be insoluble in the foam system, have a lower surface tension than the foam, disperse well in the foam system, possess none of the foam stabilizing properties, produce no secondary effects such as oil spotting or fisheyeing.

It has been known for many years that the presence of oil droplets and hydrophobic solid particles in the aqueous foaming solutions can strongly reduce the foaminess and foam stability, which might be a problem in various applications.

The effect of antifoaming is a phenomena happenning physicochemically. Antifoaming agents are dispersed throughout the liquid/air interface and are effective in reducing the surface tension by providing drainage of liquid from the foam surface (lamella wall) (4, 13, 21). At the same time antifoaming agent particles prevent the foam surface (lamella walls) to revert back and thereby providing for carrier oil to displace the film layers produced by surface active agents and thus decreasing the foam stability. The success in defoaming depends upon the foam liquid, antifoam surface tensions, and foam/antifoam interfacial tension. The most important factor determining spreading, however, is that the surface tension of the antifoaming agent must be less than the foaming liquid (10, 13, 21).

4. COMPOSITION OF ANTIFOAMING AGENTS

A typical antifoam or defoamer emulsion consists of oil, hydrophobic solid particles, or a mixture of both and some additives. Antifoams are the substances which are predispersed in the foaming solution as solid particles, oil drops, or mixed oil-solid globules by the aids of surfactants. The functionality of these emulsions is to distract the mixture of the two phase.

The use of oil-based antifoaming agents causes technical problems for applications in aqueous media as homogeneously distribution of the oil components is very difficult in the system. As a solution to this problem, the use of antifoaming emulsions prepared by using emulsifiers, dispersants and various other auxiliary substances is a priority (9).

As per the general requirements the basic elements of an antifoaming agent is probable to be as follows:

a) Carrier Oils: Silicone, mineral, vegetable, etc.

b) Activating Components: Hydrophobic solid particles (e.g. SiO_2, TiO_2, Al_2O_3), metal soaps (e.g. aluminium distearate), waxes (e.g. EBS), PPG etc.

c) Emulsion Auxiliaries: Emulsifiers (lipophilic - hydrophilic), stabilizers (e.g. PVA, HPMC), drainage enhancers (e.g. hydroxyalkyl acrylate containing polymers), preservatives (biocides).

Silicone-based antifoaming agents do not dissolve in liquid systems duly, but they are very well and homogeneously dispersed. Because of these properties, they can eliminate the negative effect on foam formation caused by surfactants used during processing.

In order to prevent the physicochemical effects and foam formation at the air/water interface, it is an important requirement that the antifoaming particles penetrate into this surface and spread through the interface like a film. Polydimethyl siloxanes are auxiliary materials which are formed by the repetition of silicon-oxygen bonds (Si-O) along the main chain and which act

by spreading at the air/water interface with low surface tensions of about 20-22 mN/m. Thus they can provide knocking-down of foam layer with lipophilic properties as indicated in the figure 5. (15, 16, 20).

5. STABILITY OF THE ANTIFOAMING EMULSIONS

The effectivity of antifoaming agents is dependant on emulsion properties and stability in the process conditions, which are based on parameters included in emulsification method and temperature, agitation speed and time, additional sequences of the oil and water phase, particle size, viscosity of carrier oil, emulsifier type and HLB values etc. (7).

Many of the auxiliary antifoaming emulsions found in the market do not have effectivity in leather beamhouse and textile finishing operations performed at high temperatures and high speed agitations because they do not have sufficient stability. These products, which are not well emulsified and have no mechanical and thermal stability, become destabilized under extreme process conditions, and consequently leading to quality defects in the product such as stain problems. At high temperatures and speedy agitations antifoaming emulsions become unstabil and uneffective.

6. MATERIAL AND METHOD

This research was based on some experiments which are the oil-in-water (o/w) types antifoaming emulsions composed of oils, solid particles, surfactants and other auxiliaries etc. Emulsification was carried out in a homogenizer equiped with a 3 necked glass container, electrical heater and a stirrer.

6.1. Material

As raw material components for dispersion phase of antifoaming emulsions; polydimethyl siloxane oil (Pmx – 350 cSt) and hydrophilic silica (Aerosil 200) particles, and subsequently; tridecyl alcohol 5 EO and Tween 60 emulsifiers, polypropylene glycol were used for emulsification.

6.2. Method

In the manufacturing of antifoaming emulsions, a dispersion of oils and solid particles should be prepared firstly. The oil and solid particles are mechanically mixed at 150 °C until obtaining the homogeneous dispersion for 4 hours. In order to evaluate the effects of the solid particle amount in our study, dispersions which contain solid particles of 5%, 6.5% and 8%, were prepared and then these dispersions were emulsified.

In our study; the formulations of the emulsion 1,2 and 3 as shown in the tables in below two charts, the three dispersions with different solid particle contents were studied in an antifoaming emulsion prototypes and the effects of solid particle content were evaluated as antifoamer.

Table 1. *Formulations of Dispersion*

	Oil ratio	**Solid particle ratio**
Dispersion 1	95 %	5 %
Dispersion 2	93,5 %	6,5 %
Dispersion 3	92 %	8 %

Table 2. *Formulations of Emulsion*

Formulation 1	**Formulation 2**	**Formulation 3**
20 % Dispersion 1	20 % Dispersion 2	20 % Dispersion 3
7 % emulsifier combination	7 % emulsifier combination	7 % emulsifier combination
3,5 % PPG	3,5 % PPG	3,5 % PPG
69,5 % water	69,5 % water	69,5 % water

Dispersions having different amounts of solid particles were used in the emulsions prepared as Formulation 1, Formulation 2 and Formulation 3 shown in Table 2, and their effects on characterization of emulsions and performance evaluations were investigated.

6.3. Tests

After emulsification, some tests were carried out for evaluation if the antifoaming efficiency were satisfactorily accomplished and particle size of emulsions. According to the results differenciation between the emulsions was assessed.

6.3.1. Particle Size of Emulsions

Particle size analysis of the emulsions was performed with a Malvern particle size analyzer and its effects on the defoaming were defined.

6.3.2. Antifoaming Performance

Three parameters are considered in evaluating the performance of antifoaming emulsions:

a) Knock-down ability or shock effect (defoaming): Bursting rate of the existing foam.

b) Persistence or Hold-down (antifoaming): The change in foam height depending on the time.

c) Durability: The change in collapse time depending on the total shaking time.

To evaluate the antifoaming performance; 0.1 g of antifoaming emulsion is weighed. Then 2 gram Nonylphenol 10 EO is added. Beaker is completed with pure water to 1000 ml and mixed. Then, the solution mixed to a level of 150 ml is put into a 250 ml graduated cylinder and mixed rapidly for 1 minute. This process is repeated 5 times. Collapse rate depending on the time (knock-down ability) and initial foam height, residual foam height are recorded and the durability of the emulsion is evaluated.

7. RESULTS AND DISCUSSIONS

7.1. Characterization of Emulsions

7.1.1. Particle Size of Emulsions

The particle size distributions of the antifoaming emulsions are practically critical for the reason of bursting foams. In most foam systems, the thickness of foam lamella varies from 0.01 to 1 µm. On the other hand, the average particle sizes of effective antifoaming emulsions are around 0,5 – 40 µm. So the particle size of emulsions should be as close as to lamella thickness for penetration and replacement. Our emulsions have particle sizes of up to 1.5 µm as shown Figure 1, Figure 2 and Figure 3.

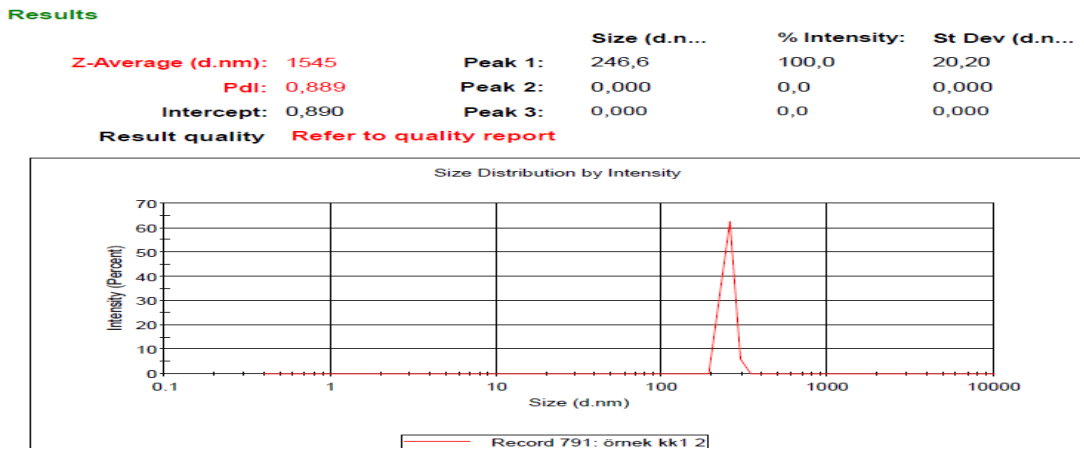

Figure 1. Particle size of Formulation 1

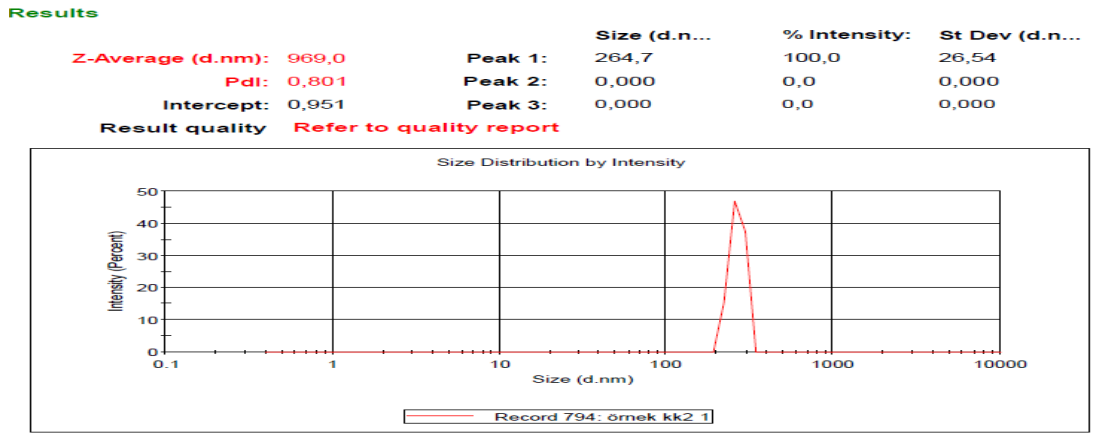

Figure 2. Particle size of Formulation 3

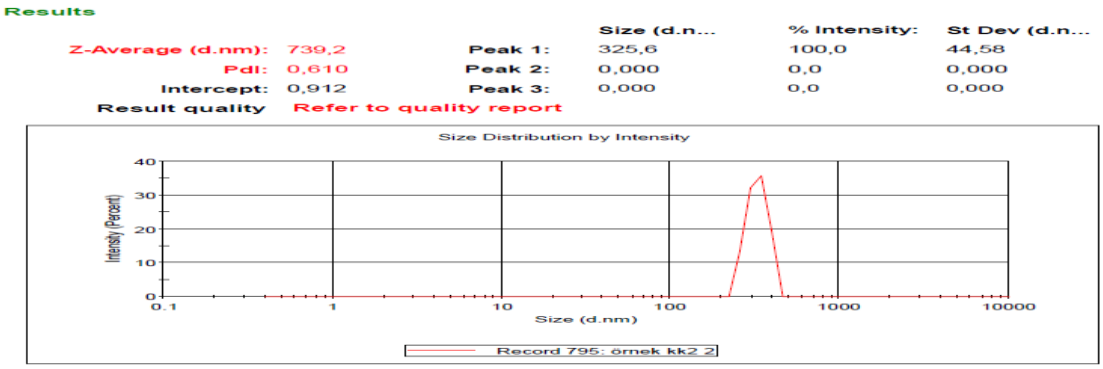

Figure 3. Particle size of Formulation 2

7.2. Evaluation of Performance

7.2.1. Antifoaming Performance

All the emulsions had a antifoaming performance, especially formulation 2 According to the accomplish studies on the influence of the solid particle contents.

Analyzing Figure 4; it is possible to see that the antifoaming performance of the emulsion 2 was the desired one. After 7 seconds of testing unwanted foam disappeared. Also, observing Figure 4 it is possible to notice that all formulations worked very well in terms of durability.

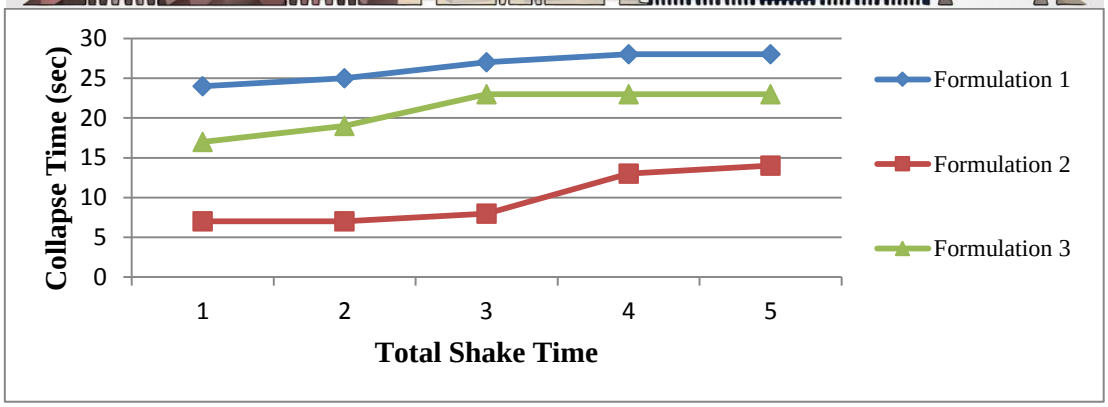

Figure 4. Evaluation of durability of antifoaming emulsions

It is possible to verify in Figure 5 that formulation 2 with 6.5 % solid particle had a lowest initial foam height and left no residual foam.

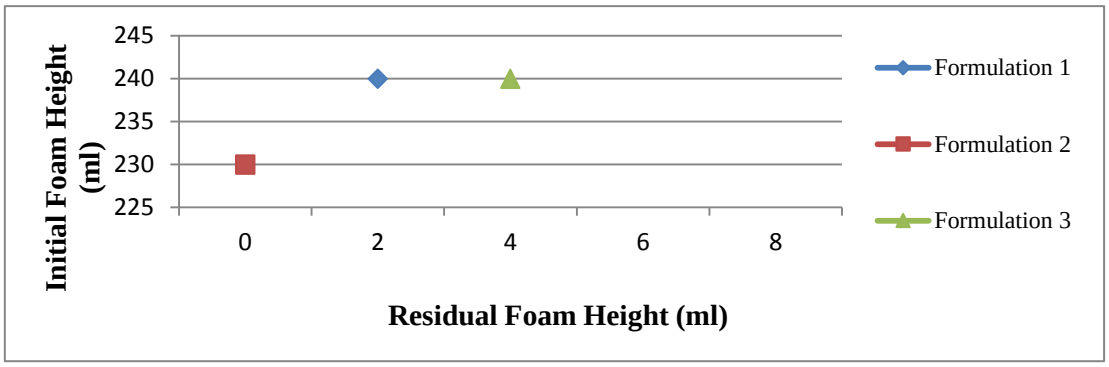

Figure 5. Evaluation of antifoaming performance of emulsions

It can be seen from particle size and antifoaming analyses that as particle size of emulsions decreases, antifoaming performance of emulsions increases.

8. CONCLUSION

Different kind of surface active agents are used during the production process for numerous industrial products which are used for many different applications and all surface active agents, however, tend to foam in aqueous systems.

Foam, one of the basic problems arising in industrial processes, is of immediate concerns, because they can rapidly lead to serious economic consequences. Foam itself or the use of inappropriate antifoaming agent might lead to quality problems and surface irregularities in end products thereby facing with economical losses.

A basic knowledge about surface active agents used in process line and their functional properties; namely foaming, will yield a cost effective compensation when encountered with their problems. At the same time this knowledge might cause the antifoaming phenomena which is oppositely function to foam formation. All are so important basics for leather and textile industry with respect to economic, ecologic and technology based production.

ACKNOWLEDGEMENT

This study was financially supported by Ege University Scientific Research Projects Coordination Unit for Financial Support (Project Number: 17-MUH-005).

REFERENCES

[1]. Afcona Additives technical team. Last access date: 13.04.2017, "Defoamer", ''www.afcona.com.my/pdf/Defoamer.pdf''.
[2]. Aylin, B. and Oya, K., ''Deterjan Sektorunde Kullanilan Kopuk Kesiciler'', Uluslararasi Katilimli Yuzey Aktif Maddeler, Sabun ve Deterjan Sempozyumu ve Sergisi, Izmir, Turkiye, 2011, 64-81.
[3]. Denkov, N.D. and Marinova, K.G., ''Antifoam effects of solid particles, oil drops and oil-solid compounds in aqueous foam''. Colloidal Particles at Liquid Interfaces. Editor: Bernard, B.P., Tommy, S.H. Cambridge: Cambridge University Press, 2006.
[4]. DOW CORNING CORPORATION TECHNICAL TEAM. LAST ACCESS DATE: 05.04.2017, "FOAM AND ANTIFOAM THEORY", ''HTTP://WWW.DOWCORNING.COM/CONTENT/PUBLISHEDLIT/22-0160-01.PDF''.
[5]. Evonik Industries technical team. Last access date: 08.03.2017, "SIPERNAT® Specialty Silica and AEROSIL® Fumed Silica for Defoamer'', ''https://www.aerosil.com/sites/lists/RE/DocumentsSI/TI-1313-SIPERNAT-and-AEROSIL-for-Defoamer-EN.pdf''.
[6]. Farn, R.J., Chemistry and Technology of Surfactants, 1. Edition, Oxford; Blackwell Publishing Ltd., 2006.
[7]. Fengyan, L., Wenli, Z., Tianbo, Z., Danghui, D. and Fang, Y., "Factors influencing droplet size of silicone oil emulsion with high solid content". China Petroleum Processing and Petrochemical Technology, 2011, 13, 21-26.
[8]. Holmberg, K., Jonsson, B., Kronberg, B. and Lindman, B., Surfactants and Polymers in Aqueous Solution, 2. Edition, Chichester: John Wiley & Sons, Ltd., 2002.
[9]. Koczo, K. and Kircher, J. 1998, ''Water Dispersible Antifoam Concentrates''. U.S. Patent. 5,846,454.
[10]. Kulkarni, R.D., Goddard, E.D. and Rosen, M.R. 1979,''Antifoams'', Journal of the Society of Cosmetic Chemists, 30, 105-125.
[11]. Mark H. Last access date: 28.07.2017, ''Defoamers and Air Release Additives'', ''https://ebooks.byk.com/fileadmin/pdf/BYK_L-DI_1_EN_Online.pdf''.
[12]. Munzing chemie technical team. Last access date: 06.04.2017, "Defoamer Technologies", ''http://www.munzing.com/fileadmin/_migrated/content_uploads/AGITAN-Defoamer-Technologies.pdf''.
[13]. Myers, D., Surfactant Science and Technology, 3.Edition, ABD: John Wiley & Sons, Inc., 2005.
[14]. Naresh, M.S. and Deepak, V.A., '' Defoamers – Bursting The Bubble – Foam Killers'', International Dyer, 2007, 34-36.
[15]. O'Neil, V., Zeng, J. and Perry D. Last access date: 06.04.2017, "New silicone foam control agents for waterborn coatings", dowcorning, ''http://www.dowcorning.com.cn/zh_CN/content/publishedlit/26-1159-01.pdf?DCWS=Paints''.
[16]. PUGH, R.J., ''BUBBLE AND FOAM CHEMISTRY", IN: EDITOR: HILSENRATH, J., ANTIFOAMING AND DEFOAMING, CAMBRIDGE: CAMBRIDGE UNIVERSITY PRESS, 2016.
[17]. Rainer, H. and Franz, J., ''Foams and Foam Control'', Ullmann's Encyclopedia of Industrial Chemistry, 2000, Volume: 15, 572.
[18]. Randal M. Hill and Kenneth C. Fey., ''Silicone Surfactants in Surfactant Science Series'', 1999, Vol. 86, 159-181.
[19]. Sawicki, G.C, Renauld, F.A.D. and L'Hostis, J. 1997, ''Foam Control Agent''. U.S. Patent. 5,693,256.
[20]. Schramm, L.L., Emulsions, Foams, and Suspensions-Fundamentals and Applications, 1.Edition, Weinheim: WILEY-VCH Verlag GmbH & Co., 2005.
[21]. Sohl, K., "Foam Happens", Textile Chemist and Colorist / American Dyestuff Reporter, 1999, 1, 31-3
[22]. SNF S.A. technical team. Last access date: 05.04.2017, "Flofoam™ Defoamer", ''www.snf.us/wp-content/.../08/FLOFOAM-Defoamer.pdf''.

ICETI
www.iceti.org
2018
07-11 MARCH
BUDAPEST
HUNGARY
II. INTERNATIONAL CONFERENCE ON ENGINEERING TECHNOLOGY AND INNOVATION

The Mechanical Properties of Sr Modification on Aluminium Casting Alloys

Onur Ozaydin[1], Elvan Armakan and Alper Kaya[1]

Abstract

Al-Si based alloys are commonly used in aluminium alloy wheel production. Inoculant materials such as Antimony (Sb), Sodium (Na) and and Strontium (Sr) modify the structure from a course structure to a finer one. Antimony (Sb) and Sodium (Na) may cause occupational health and safety and holding time problems. On the other hand, Strontium (Sr) is commonly used in industry as an inoculant material in Al-Si based alloys and Sr modifies not only silicon particles but also transforms phases in morphology, hence Sr modification leads to better mechanical properties. On the other hand, high amount of Sr causes porosity in the structure and the average grain size is increased proportionally with higher Sr levels. In this study different Sr levels are examined to obtain an optimum result regarding mechanical properties and chemical composition. After the calculation, the correlations between mechanical properties and material characterization are examined. Holding time after the modification affects the mechanical properties. In the second part of this study different Sr holding time levels are evaluated to see the effect on mechanical properties. As a conclusion the optimum Sr modification level and optimum holding time after modification are presented. Optimization of process parameters may be helpful to researchers working on modification in aluminum alloys.

Keywords: AlSi7Mg0.3, Holding Time, Material Characterization, Metallurgical Properties, Sr Modification.

1. INTRODUCTION

Aluminium is widely used in automotive industry due to its low density, castability, good mechanical properties and corrosion resistance. Al-Si based alloys are widely used the automotive industry for weight savings. Especially AlSi7Mg0.3 is the most popular material for aluminium alloy wheels. There are many different methods to get better mechanical properties. One of them is modification with inoculant materials; antimony (Sb), sodium (Na) and strontium (Sr). Antimony (Sb) and sodium (Na) may cause occupational health and safety and holding time problems respectively. In addition to this some studies note that *'antimony caused no change in eutectic silicon morphology of AlSi7Mg0.3'* [5]. Thus, strontium (Sr) modification is the most popular method to transform a coarse and extended grain to a finer morphology which leads to improved mechanical properties. Also, a better material feeding may be obtained with Sr modification. [1]

Sr modification additionally decreases the detrimental effects of Fe inter metallics. For example, β-Al_5 Fe-Si inter metallic decreases the mechanical properties due to a high stress concentration. Sr modifies the needle structure morphology of β-phase inter metallic to Chinese script morphology and increases the mechanical properties. [2]

On the other hand, previous studies shown that porosity may increase with higher Sr proportion in the structure. Moreover, a Boron based grain refiner may introduce SrB_6 inter metallic phases in the structure and effect on the Si performance negatively. [2]

The present work investigates the effects of strontium level limited between 450 ppm and 140 ppm approximately and a holding time between 0 to 45 hours. The mechanical properties and micro-macrostructures are examined.

[1] *Corresponding author: Cevher Wheels, R&D Department, 35411, Gaziemir/Izmir, Turkey.* oozaydin@cevherwheels.com

2. MATERIALS AND METHODS

In this study, AlSi7Mg0.3 aluminium alloy (A356) was used. First, liquid metal was transferred from melting furnace to transfer ladle. Second, Sr modification (with AlSr15 master alloy) and degassing (with nitrogen) were completed. After modification and degassing, liquid metal was transferred and held in the holding furnace at 720 ± 10 °C between 0 to 45 hours. All casting procedures were same as serial production. Holding time was selected as an experiment parameter and pouring period was determined according to time intervals (Figure 2).

Specimens were poured from holding furnace to a tensile specimen mold (Figure 1.a) at different time intervals for chemical analysis, thermal analysis and tensile test.

Tensile specimen mold was stabilized at 360 ± 40 °C to minimize the effects of mold temperature on the specimens since the mold temperature may affect solidification rate and the mechanical properties directly. (Figure 1.b)

Figure 33. (a) Tensile Specimen Mold *(b) Mold Temperature*

Chemical analysis was conducted with a spectrometer and results are shown in Table 1.

Table 28. Chemical composition before modification

	Si	Fe	Cu	Mn	Ti	Al	Sr
AlSi7Mg0.3 (Before modification)	7,21	0,08	0,001	0,002	0,12	92,26	0,0144

Thermal analysis was completed by a IDECO Thermal Analyzer. IDECO Thermal Analyzer can measure the grain size with 0,1 °C accuracy.

Microstructures were examined with an optical microscope. Specimens were etched and prepared according to related specifications and analyzed at a 500x magnification. The samples for microstructural analysis were extracted from with machining from wheel spokes, outer or inner flanges. Cast samples were mounted and prepared with standard metallographic practices with SiC paper and polished with diamond paste to a 0.25-micron finish. Microstructures were examined using an Nikon Eclipse LV150N model optical microscope after etching with a 0.5% HF solution. Macrostructures were examined after etching in a solution of % 30 $FeCl_3$.

Tensile tests were applied according to EN ISO 6892-1:2016 and tensile specimens were machined according to DIN 50125 [3-4]. At least 3 specimens were used for each tensile test. Specimens were tested by Zwick Z100 model (100 kN) tensile test machine.

Finally, all metallurgical and mechanical tests are completed in a laboratory environment at room temperature.

3. RESULTS AND DISCUSSION

Metallurgical and mechanical tests were conducted on gravity cast specimens. First, microstructure and macrostructure are examined. Secondly, UTS (Ultimate Tensile Strength), YS (Yield Strength) and Elongation (ε%) were measured.

3.1. Chemical Analysis

Chemical content is measured by OES (Optical Emission Spectrometry) as shown in Table 2. Strontium is the only meaningful variable parameter effecting on test results.

Table 29. Chemical composition

	Si	Fe	Cu	Mn	Ti	Al	Sr
Specimen #1	7,22	0,09	0,002	0,002	0,11	92,22	0,0449
Specimen #2	7,21	0,09	0,002	0,002	0,11	92,26	0,0425
Specimen #3	7,16	0,09	0,002	0,002	0,11	92,30	0,0400
Specimen #4	7,17	0,09	0,002	0,002	0,11	92,30	0,0372
Specimen #5	7,21	0,09	0,002	0,002	0,11	92,27	0,0222
Specimen #6	7,21	0,08	0,001	0,002	0,12	92,27	0,0139

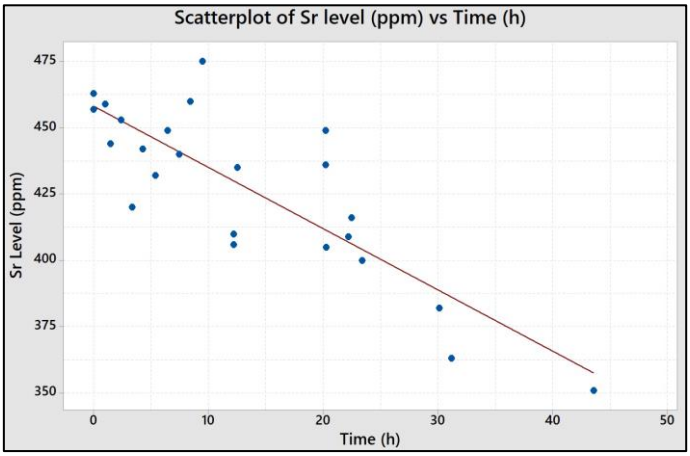

Figure 34. Sr Level (ppm) vs Time (h)

3.2. Thermal Analysis

Grain size has increased with Sr modification as verified by the thermal and macrostructure analysis. Literature also confirms these results. [2]

The results show an increasing grain size with increasing Sr level (Figure 3).

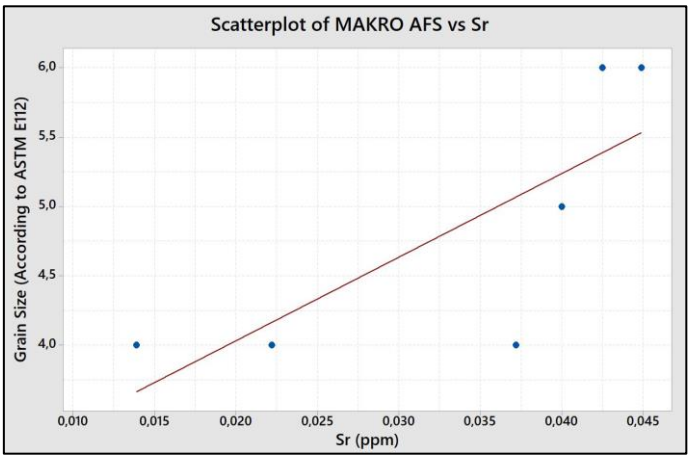

Figure 35. Grain Size (ASTM E112 Macro AFS) vs. Sr Level (ppm)

3.3. Macrostructure Results

An increasing porosity level may be observed with increasing Sr amount. Specimen #1 which has the highest Sr level displays a very course macrostructure. Specimen #6 which has the lowest Sr level displays a very fine macrostructure and specimen #6 displays uppermost mechanical properties. This prediction is confirmed with 'Tensile Test Results' section in this study.

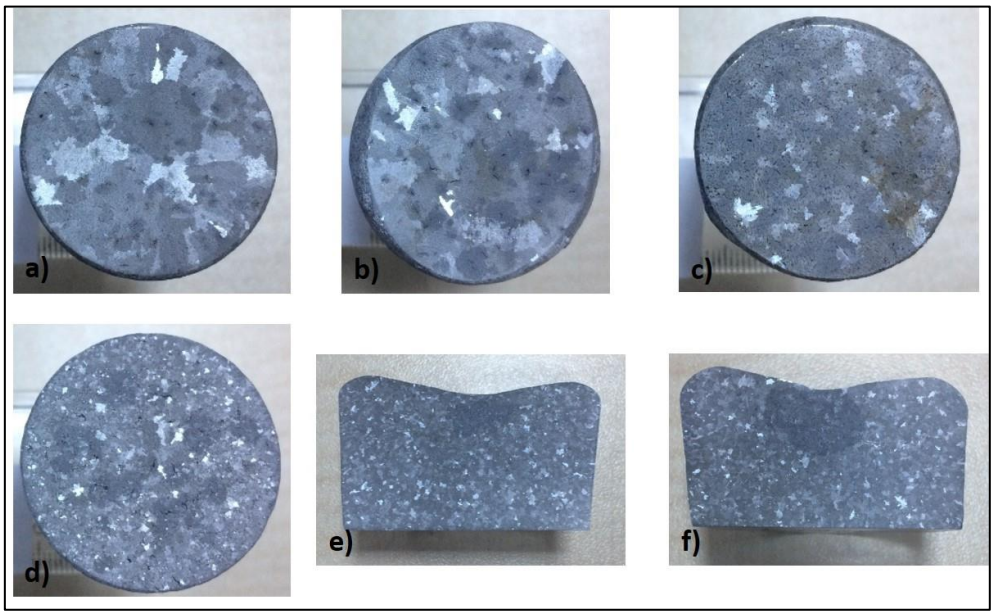

Figure 36. Macrostructure of (a) Specimen #1 (b) Specimen #2 (c) Specimen #3 (d) Specimen #4 (e) Specimen #5 (f) Specimen #6

3.4. Microstructure Results

Modified microstructures with different Sr levels are shown below. (Figure 5.) All specimens have a finer structure in comparison to unmodified structures.

The lowest level Si is appr. 140 ppm in this study and it is sufficient to modify the structure from the needle structure morphology to Chinese script morphology. Comparing the microstructures of samples, the effect of holding time on the microstructure may be observed. Strontium modification shows diminishing returns.

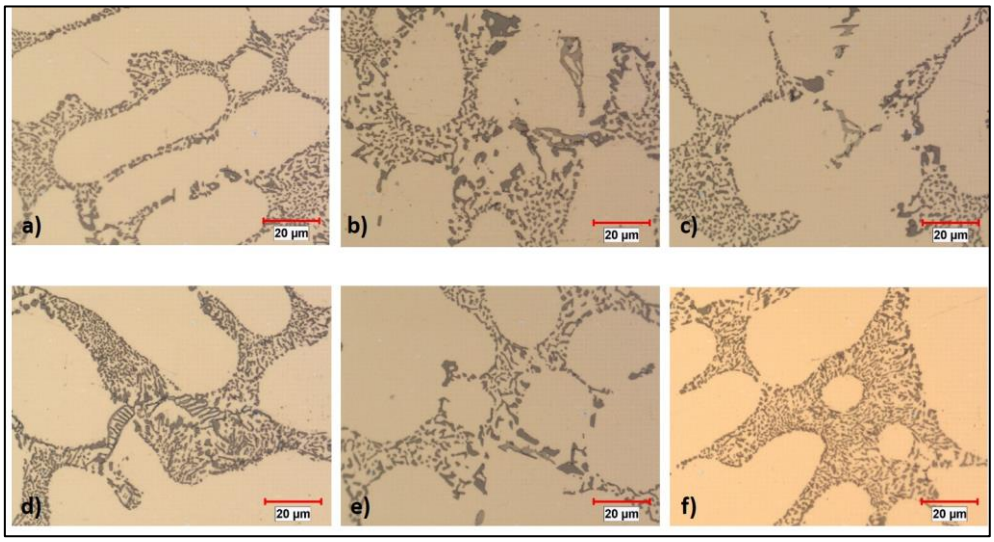

Figure 37. Microstructure of (a) Specimen #1 (b) Specimen #2 (c) Specimen #3 (d) Specimen #4 (e) Specimen #5 (f) Specimen #6

3.5. Tensile Test Results

Mechanical properties i.e. ultimate tensile strength (UTS), yield strength (YS) and elongation (ε%) are given in Figures 6., 7. and 8 respectively.

UTS decreases with higher Sr levels in a standard tensile test. As stated before, higher Sr level leads to porosity, shrinkage and a bigger grain size.

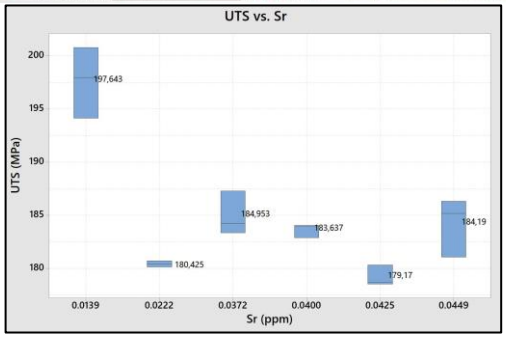

Figure 38. (a) UTS (MPa) vs. Sr Level (ppm)

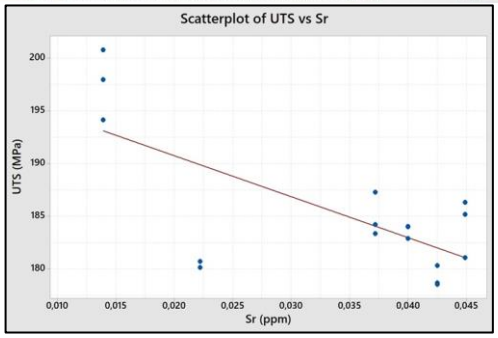

(b) Scatterplot of UTS (MPa) vs. Sr Level (ppm)

Similar to UTS results, elongation (%ε) decreased with higher Sr levels.

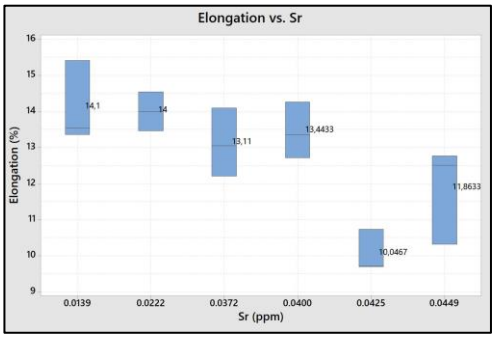

Figure 39. (a) Elongation (%) vs. Sr Level (ppm)

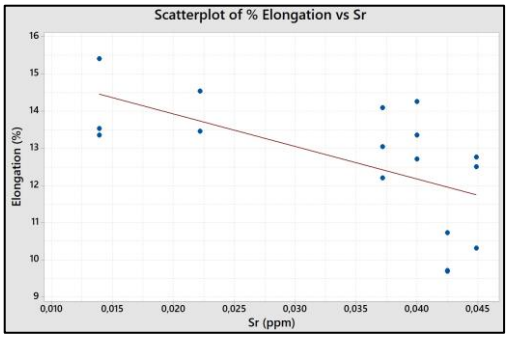

(b) Scatterplot of Elongation (%) vs. Sr Level (ppm)

YS displays a downtrend with increasing Sr level. Please note that, a strong correlation cannot be obtained between YS and Sr level. (Correlation Value: 0,564)

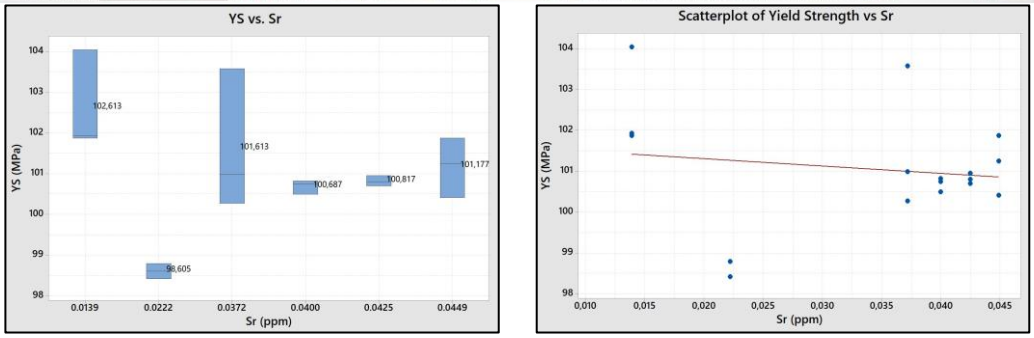

Figure 40. (a) YS (MPa) vs. Sr Level (ppm) *(b) Scatterplot of YS (MPa) vs. Sr Level (ppm)*

It can therefore be concluded that the modification of AlSi7Mg0,3 alloy by Sr has positive effects when compared to unmodified examples as stated in the literature. Beside this, over modification may lead to negative effects on mechanical properties.

4. CONCLUSION

Sr modifies the needle structure morphology of β-phase inter metallics to Chinese script morphology and increases the mechanical properties.

On the other hand, porosity may increase with higher Sr proportion in the structure which results in decreased mechanical properties. Shrinkage can be detected visually at 400 ppm and more Sr level.

Literature shows decreasing effects of Sr with extended holding time. The trend shows a nearly 50 ppm decrease at 24 hours (3 Shifts). The trend may show differences for different casting parameters and materials.

Higher grain size and increasing porosity-shrinkage may cause lower UTS and elongation. Although a downtrend is obtained, there is no strong correlation between YS and Sr. (Correlation Value: 0,564)

In the microstructure analysis, the modification effects of Sr are clearly observed. Optimum Sr modification level is determined to lie between 100-200 ppm and more than 200 ppm may cause a deterioration in mechanical properties.

ACKNOWLEDGMENT

The authors would thank to all colleagues, especially A. Oktem, Z. Gokcen and I. Icli, from Cevher Alloy Wheels for their collaboration.

REFERENCES

[1]. M. Uludag, L. Gemi and D. Dispinar, A356 Alasiminda katilasma hizi ve sivi durumda bekletme suresinin mekanik ozellikler uzerine etkisi, 4th International Symposium on Innovative Technologies in Engineering and Science 1752 – 1758, 2016
[2]. S. Derin, U. Aybarc and Y. Birol, Optimization of Strontium Addition for the Modification of AlSi7Mg0.3 Alloy, 18th International Metallurgy & Materials Congress UCTEA Chamber of Metallurgical & Materials Engineers 626 – 629, 2016
[3]. Testing of metallic materials – Tensile test pieces, Prufung metallischer Werkstoffe – Zugproben Deutsche Norm DIN 50125, 2016
[4]. Metallic materials - Tensile testing - Part 1: Method of test at room temperature, Metalik malzemeler - Cekme deneyi - Bolum 1: Ortam sicakliginda deney metodu, TS EN ISO 6892-1:2016, 2016
[5]. S. Derin, U. Aybarc and Y. Birol, Effect of Strontium Addition on Microstructure and Mechanical Properties of AlSi7Mg0.3 Alloy, International Journal of Metalcasting / Volume 11, Issue 4, 688 – 695, 2017

ICETI
www.iceti.org
2018
07-11 MARCH
BUDAPEST
HUNGARY
II. INTERNATIONAL CONFERENCE ON ENGINEERING TECHNOLOGY AND INNOVATION

Dry Sliding Wear Properties of AA7075 Aluminum Matrix Hybrid Composites

Ridvan Gecu[1], Serhat Acar[1], Alptekin Kisasoz[1], Kerem Altug Guler[1], Ahmet Karaaslan[1]

Abstract

304 stainless steel (SS) and commercially pure titanium (CP-Ti) reinforced AA7075 aluminum matrix hybrid composites were manufactured by melt infiltration casting under vacuum atmosphere. Various SS and CP-Ti contents (at the ratios of 3:1, 1:1 and 1:3) in AA7075 alloy were studied and the effects of SS/CP-Ti ratio on wear resistance of produced composites were investigated. All casting operations of Al alloy were performed at 830˚C. Produced composites were characterized by light optical microscope and pin-on-disc type tribometer with using 6 mm diameter Al_2O_3 counterpart under 10 N load during 100 m sliding distance. Reaction phases were formed at both Al/CP-Ti and Al/SS interfaces. Double-layered intermetallic compound (IMC) was formed between AA7075 and 304 SS alloys whereas monolayer IMC was obtained at Al/CP-Ti interface. Formation of hot cracks in SS/Al interface was occurred while good metallurgical and mechanical bonding was observed between Al matrix and CP-Ti reinforcement. With increasing SS amounts in composite structure, wear rates were slightly decreased. In spite of increased hot crack formation at the interface, the best wear resistance was obtained in 75% 304 SS and 25% CP-Ti reinforced AA7075 matrix hybrid composites because double-layered IMC between AA7075 and 304 SS was more resistant to wear than that of monolayer IMC at Al/CP-Ti interface.

Keywords: AA7075 alloy, commercially pure titanium, 304 stainless steel, melt infiltration casting, hybrid composite, wear

1. INTRODUCTION

Metal matrix composites (MMCs) have been widely used in automotive, aerospace, aviation and medical industries due to their high strength/density ratio [1]. MMCs have been developed to improve elastic modulus, wear resistance and tensile strength of the unreinforced alloys. The incorporation of ceramic reinforcement into metal matrix provides advantageous features and Al alloys have been attracted attention as a matrix material owing to their lightweight and good corrosion resistance [2]. Al matrix composites (AMCs) can be fabricated by various method thanks to low melting temperature of Al alloys. Ceramic reinforced AMCs become prominent and have been investigated extensively. However, high-cost production of these composites restricted their commercial applications considerably [3]. The use of metal reinforcements has a potential to allow for the production of low-cost AMCs. Moreover, metal reinforcements do not destroy the original ductility and toughness of the matrix, unlike the ceramic reinforcements.

Iron and titanium based reinforcements come to the forefront to improve mechanical and tribological properties of monolithic Al alloy. Undesired phase formation at the interface and wettability failure between reinforcement and matrix phase can be achieved by metal usage instead of ceramics [4]. Titanium has beneficial features including low density, high elastic modulus and high specific strength [5]. These properties make Ti and Ti alloys usable as a composite component. Fe based alloys have also been preferred as reinforcements due to their excellent corrosion resistance, in addition to good mechanical features. When Cr amount exceeds about 12%, corrosion resistance of Fe based alloys are improved significantly [6].

Environmentally friendly and low cost production is possible for composites provided that using molten metal routes. Melt infiltration casting is one of the molten metal manufacturing technique that based on the infiltration of the liquid

[1] *Yildiz Technical University, Department of Metallurgical and Materials Engineering, 34220, Esenler/Istanbul, Turkey. gecur@yildiz.edu.tr, seacar@yildiz.edu.tr, akisasoz@yildiz.edu.tr, kguler@yildiz.edu.tr, karaas@yildiz.edu.tr*

matrix into solid reinforcement with hollow structure. By this method, matrix material can be reinforced with high volume fraction of reinforcement [7].

In this study, 304 stainless steel (SS) and commercially pure titanium (CP-Ti) reinforced AA7075 aluminum matrix hybrid composites were manufactured by melt infiltration casting with varied amounts of 304 SS and CP-Ti. Produced composites were characterized by light optical microscopy and pin-on-disc type tribometer. Dry sliding wear properties of 304 SS and CP-Ti reinforced AMCs were discussed considering friction coefficient and wear rate measurements.

2. EXPERIMENTAL

2.1. Mould making

Wax pattern with the dimensions of 25 mm in diameter and 50 mm in height was obtained by casting of molten wax into the silicon mould at 85 °C. After solidification of molten wax, the sprue was attached to the pattern and they were settled in SS perforated flask.

500 g investment powder and 200 g water was mixed for 3 min to make castable plaster slurry. This slurry was poured into perforated flask under vibration and covered wax pattern completely. When the slurry was solidified, plaster mould was obtained. Wax pattern was removed by dewaxing process which was performed at 110 °C and the mould cavity was attained.

2.2. Casting

304 SS and CP-Ti sawdusts were combined together at the ratios of 3:1, 1:1 and 1:3 with the help of the mechanical press, to obtain porous one-piece preform that was shown in Fig. 1. The vacancies of the preforms were infiltrated by AA7075 Al alloy under vacuum atmosphere in a further process. The chemical compositions of the composite components consisting of AA7075 Al, 304 SS and CP-Ti alloys were given in Table 1.

Figure 1. Porous one-piece preform made by 304 SS and CP-Ti sawdusts

Table 30. Chemical compositions of AA7075 matrix, 304 SS and CP-Ti reinforcements (wt. %)

Alloy	C	Si	Mn	Cr	Mg	Cu	Zn	Ni	O	Fe	Ti	Al
AA7075	-	0.4	0.3	0.23	2.5	1.6	5.6	-	-	0.5	0.2	Bal.
CP-Ti	0.1	-	-	-	-	-	-	-	0.2	0.3	Bal.	-
304 SS	0.08	1.0	2.0	18.0	2.5	-	-	8.0	-	Bal.	-	-

Plaster mould was subjected to burnout process prior to casting. It was gradually heated up to 700 °C in three steps. The heating regime of the plaster mould was given in Fig. 2. Water as moisture escaped through the mould pores at 250 °C, whereas the residual wax in the mould was transformed to black carbon powder at 550 °C. The complete evacuation of this black carbon was occurred at 700 °C.

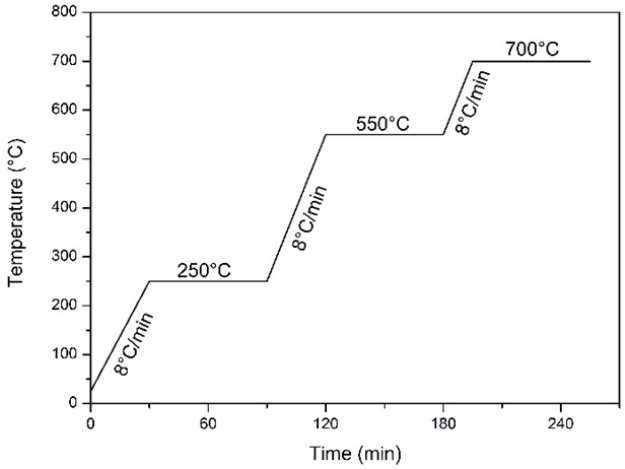

Figure 2. Burnout regime of the plaster mould

Preforms were settled in a plaster mould at the initial stage of the burnout process. This preheating stage prevents rapid solidification of AA7075 alloy. Increasing interaction time between matrix and reinforcement phases allow better metallurgical bonding at the interface.

The casting temperature of AA7075 alloy was chosen as 830 °C for all composites. After burnout process, the flask was placed in a vacuum chamber and molten Al alloy was poured into the mould under 10^{-5} Pa vacuum atmosphere. The snapshot of the casting process was given in Fig. 3. Molten Al alloy was held in the mould and infiltrated into the vacancies of the preforms with the help of the vacuum assistance. The mould was quenched after solidification of AA7075 melt and composite sample was successfully manufactured. The illustration of melt infiltration casting process was given in Fig. 4.

Figure 3. The snapshot of the casting process

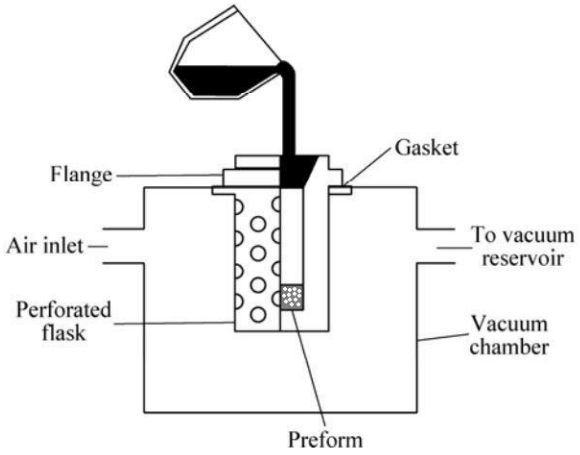

Figure 4. Illustration of melt infiltration casting

2.3. Characterization

The microstructures of manufactured composite samples were examined via light optical microscope (Nikon Eclipse MA100). Pin-on-disc type tribometer (Turkyus) was used to determine tribological behavior of the specimens. 6 mm diameter Al_2O_3 ball was used as a counterface material and 10 N load was applied to the sample surfaces.

$$V = 2\pi R\left[r^2\, sin^{-1}(d/2r) - (d/4)(4r^2 - d^2)^{1/2}\right] \quad (1)$$

formula was used to calculate volume losses. In this equation, V is volume loss, R is wear scar radius, r is ball radius and d is wear track width. Wear track widths were measured via image analyzer software (Zeiss). Wear rates were measured by using volume loss values in

$$W_R = \frac{V}{LP} \quad (2)$$

equation where W_R is wear rate, L is sliding distance and P is applied load. Dry sliding wear behavior of AA7075 matrix hybrid composites were discussed considering sliding distance related friction coefficient and wear rates.

3. RESULTS AND DISCUSSION

Fig. 5 shows the micrograph of formed phases in composite structure. White regions point out AA7075 Al alloy. Two intermetallic compounds (IMCs) were observed at the interfaces of both Al/SS and Al/Ti. IMC 1 is a double-layered compound that includes Fe and Al at different amounts. IMC 2 is a monolayer reaction phase at the Al/Ti interface. It can be obviously seen that fulfilling metallurgical and mechanical bonding was obtained at both interfaces. IMC layers are harder phases and they can carry the applied load better than that of matrix and reinforcements. It can be inferred that the IMC formation provides better mechanical strength in composite structure.

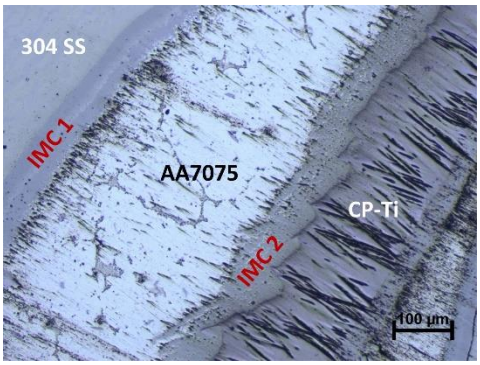

Figure 5. Formed phases in hybrid composite

At some local points at the Al/SS interface, hot crack formation was observed. Fig. 6 shows hot cracks at the interface between AA7075 and 304 SS alloys. These cracks were probably related to AA7075 alloy which is particularly sensitive to hot cracking due to its chemical composition, especially zinc and copper. Solidification shrinking, wide range of solidification and thermal tensions may be also related to this phenomena [8]. Hot cracks were not formed at Al/Ti interface while Al/SS interfaces were suffered from them because austenitic SS alloys are also sensitive to hot cracking failure. The cracking susceptibility of these steels are attributed to the presence of impurities such as sulfur, phosphorus, silicon, and manganese.

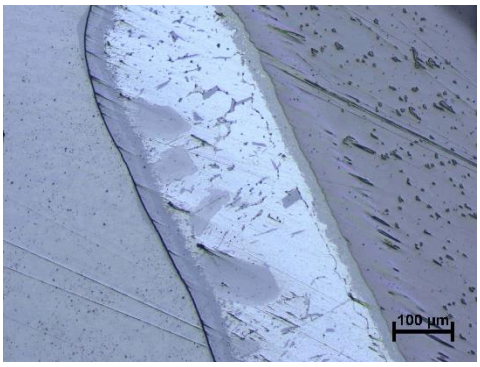

Figure 6. Hot crack formation at Al/SS interface

Sliding distance dependent friction coefficient values of hybrid composites were given in Fig. 7 as a function of 304 SS / CP-Ti ratio. These values were recorded by tribometer during sliding instantaneously. The average values were given at the bottom of the graph. The lowest mean friction coefficient was obtained at the SS/Ti ratio of 3:1 (75%). With increasing Ti and decreasing SS contents, friction coefficient values were increased.

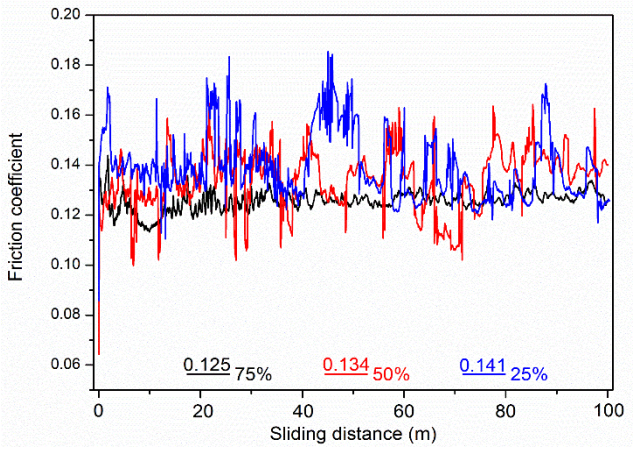

Figure 7. Sliding distance dependent friction coefficient values of hybrid composites as a function of 304 SS / CP-Ti ratio

Fig. 8 shows the volume losses and wear rates of the composite samples after they were exposed to dry sliding contact under 10 N load for 100 m distance. Both volume losses and wear rates were decreased with increasing SS ratio in the composite structure. Although hot cracked area was enlarged with increasing SS, the best wear resistance was still obtained in 75% 304 SS and 25% CP-Ti reinforced composite. Double-layered IMC between AA7075 and 304 SS was harder than that of monolayer IMC at Al/Ti interface [9, 10]. It is well-known fact that there is a direct relationship between hardness and wear resistance [11]. More hardness provides more resistance to wear process and accordingly, more SS ratio provides better wear resistance in hybrid composite specimens.

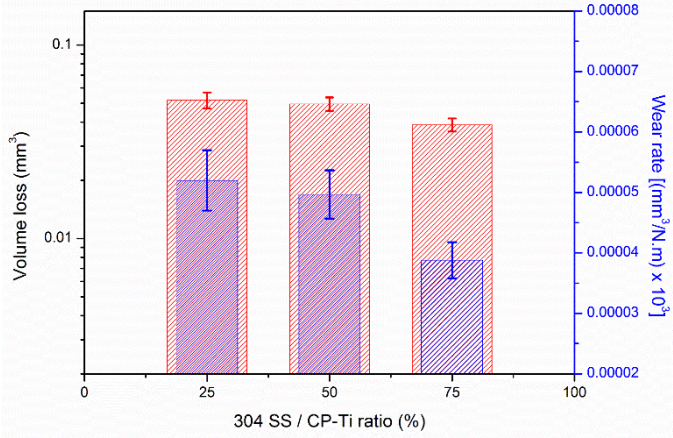

Figure 8. Volume loss and wear rate results of hybrid composites as a function of 304 SS / CP-Ti ratio

4. CONCLUSION

304 SS and CP-Ti reinforced AA7075 alloy matrix hybrid composites were produced by melt infiltration casting at various SS/Ti ratio (3:1, 1:1 and 1:3) in composite structure. Good metallurgical and mechanical bonding were obtained at both interfaces for all specimens. Double-layered IMC was attained at Al/SS interface whereas monolayer IMC was occurred at Al/Ti interface. Due to the nature of 304 SS and AA7075 alloys, hot cracks were formed at the interface between Al and SS, alongside of IMC layer.

With increasing SS and decreasing Ti ratio in composite structure, average coefficients of friction and wear rates were decreased. In spite of hot crack formation at Al/SS interface, increase in SS amount provided better wear resistance against Al_2O_3 ball. It was thought that double-layered IMC with higher hardness at the Al/SS interface was responsible for the increase in wear resistance, considering the direct relationship between hardness and wear resistance.

REFERENCES

[1]. C.S. Ramesh, M. Safiulla, "Wear behavior of hot extruded Al6061 based composites", *Wear*, vol. 263 pp. 629–635, 2007.
[2]. D.L. Zalensas, Aluminum Casting Technology, 2nd ed., American Foundry Society, 1997.
[3]. E. Pagounis, V. Lindroos, "Processing and properties of particulate reinforced steel matrix composites", *Mater. Sci. Eng. A.*, vol. 246 pp. 221–234, 1998.
[4]. K. Landry, S. Kalogeropoulou, N. Eustathopoulos, "Wettability of carbon by aluminum and aluminum alloys", *Mater. Sci. Eng. A.*, vol. 254, pp. 99–111, 1998.
[5]. S.K. Thakur, M. Gupta, "Improving mechanical performance of Al by using Ti as reinforcement", *Compos. Part A Appl. Sci. Manuf.*, vol. 38, pp. 1010–1018, 2007.
[6]. L.H. Hihara, R.M. Latanision, "Corrosion of metal matrix composites", *Int. Mater. Rev.*, vol. 39, pp. 245–264, 1994.
[7]. R. Gecu, H. Atapek, A. Karaaslan, "Influence of preform preheating on dry sliding wear behavior of 304 stainless steel reinforced A356 aluminum matrix composite produced by melt infiltration casting", *Tribol. Int.*, vol. 115, pp. 608–618, 2017.
[8]. E. Cicală, G. Duffet, H. Andrzejewski, D. Grevey, S. Ignat, "Hot cracking in Al-Mg-Si alloy laser welding - Operating parameters and their effects", *Mater. Sci. Eng. A.*, vol. 395, pp. 1–9, 2005.
[9]. R. Gecu, A. Karaaslan, "Relationship Between Nanoindentation and Wear Properties of Stainless Steel-Reinforced Aluminium Matrix Composite", *Tribol. Lett.*, vol. 65, 2017.
[10]. D.M. Fronczek et al., "Structural properties of Ti/Al clads manufactured by explosive welding and annealing", *Mater. Des.*, vol. 91, pp. 80–89, 2016.
[11]. J.D. Lemm, A.R. Warmuth, S.R. Pearson, P.H. Shipway, "The influence of surface hardness on the fretting wear of steel pairs-Its role in debris retention in the contact", *Tribol. Int.*, vol. 81, pp. 258–266, 2014.

ICETI
www.iceti.org
2018
07-11 MARCH
BUDAPEST
HUNGARY
II. INTERNATIONAL CONFERENCE ON ENGINEERING TECHNOLOGY AND INNOVATION

Investigation of Microstructure, Mechanical and Corrosion Properties of AA5754 Aluminum Alloys Coated with Nickel-Copper Based Powder through High Velocity Oxygen Fuel Powder Spraying Method (HVOF) when Combined through Friction Stir Welding

Zarif Catalgol[1], Yavuz Akkas[1], Hasan Kaya[2], Ramazan Samur[1], Mehmet Ucar[3]

Abstract

In this study, AA5754 aluminum plate welding faces to be treated with Friction Stir Welding (FSW) were coated with nickel-copper powder in 100 µm thick by High Velocity Oxy Fuel (HVOF). To use in the FSW, a 20 mm diameter shoulder and an unthreaded conical pin with 1.8 mm length was produced through machining from hot-work tool steel. The effect of HVOF process on the evolution of microstructure, mechanical and corrosion properties of friction stir welded AA5754 aluminum alloy was studied and discussed in detail. The samples were cut with a water jet without being affected by heat. The polished samples were analyzed using a Scanning Electron Microscopy (SEM) equipped with Energy Dispersive Spectroscopy (EDS) analyzer. Microhardness in the stir zone of the sample was measured. FSW welded AA5754 aluminum alloy displayed lower tensile strength value compared to the base metal. The stir zone of AA5754 plate after FSW showed higher hardness than the base metal of AA5754 plate. However, it can be noticed a better corrosion behavior of base metal in comparison with weld region. These results are due to distribution of nickel-copper particles throughout the stir zone as a result of HVOF.

Keywords: Aluminum 5754, Friction stir welding (FSW), High Velocity Oxy Fuel (HVOF), Mechanical properties, Corrosion

1. INTRODUCTION

Friction stir welding (FSW) has proven to be an effective and important method for solid state joining of metallic materials such as aluminum, magnesium and copper. Because welding is performed below the solidification temperature provided in the phase diagram of the material, no melting occurs in FSW process [1]. The friction stir welding (FSW) is one of the most recently discovered solid state welding methods. The combination of similar and different metals and alloys has many advantages over the welded joining methods. In this method, since there is no melting, the generation capacity of intermetallic compounds is low in the welding of dissimilar metals, and the reduction of residual stresses is the most remarkable. For these reasons it is expected that the chemical composition of the weld zones will differ in the chemical, mechanical and physical properties of the weld seam after the friction stir welding process of the aluminum plates modified by the copper-nickel powder coating process. As the nickel-copper ratio in the weld seam is increased, it is possible that the electrical conductivity of the weld zones is increased. Coating 100 microns of weld zones by spraying nickel-copper powder by high-velocity spray method (HVOF) is an easy and economical way of changing the chemical composition of the weld zones. The coating thickness should be

[1] *Department of Metallurgy and Materials,Faculty of Technology,Marmara University,TR-34730 Istanbul, TURKEY, zcatalgol@marmara.edu.tr*
[2] *Department of Machine and Metal Technology,AsimKocabiyik Vocational School of Higher Education, Kocaeli University, TR-41800, Kocaeli, TURKEY*
[3] *Department of Automotive Engineering, Faculty of Technology, Kocaeli University, TR-41380, Kocaeli,*

at the optimum level while changing the chemical composition of the welding site with this method. The melting temperatures of aluminum, copper and nickel are very different [2]. Different researchers have successfully used friction stir welding tips of hardened tool steels HRC 45 to HRC 62 with HSS and heat treatment in friction stir welding applications of Al-Cu materials [3]. It is not advisable to combine Al-Cu alloys with melting welding methods. Because of the solidification and liquefaction cracks, large-sized hard and brittle intermetallic compounds create IMCs and cause welding failures [4].Surface coatings obtained by High Velocity Oxy Fuel (HVOF) are widely used to improve wear or corrosion resistance, and for repair worn parts in various applications. One of the unique features of this technology is the high impact velocity formed during the powder injection molding process. During spraying of powder particles to sub-layers at high-speed powder is melted by accelerating and dense and non-porous coatings are created. Since HVOF method is used in order to obtain dense and homogeneous microstructure formed by plastic deformation of sprayed powder, HVOF coating the aluminum plate with nickel-copper based powder can be improve the binding between the aluminum plates. Because HVOF spray systems operate at atmospheric pressure, investment and operating costs are much lower than other thermal spray processes operated at vacuum [5]. In the present study, microstructure, mechanical and corrosion properties of friction stir welded AA5754 aluminum alloys coated with nickel-copper based powder by HVOF process were investigated.

2. EXPERIMENTAL

In this research, 2 mm-thick rolled AA5754 plates were used. 2x100x300 mm joint configuration was used for the fabrication of friction stir welding (FSW) joints. Before FSW process, the surface of aluminum plate was coated with nickel-copper based powder in a thick of 100 µm using HVOF process (Table 1).The chemical composition and mechanical properties of AA5754 aluminum alloy are given in Table 2 and 3 respectively.

Application view of the FSW and position of sample in fixture are also illustrated in (Fig. 1). The FSW tool had a 20 mm diameter shoulder and an unthreaded conical pin with 1.8 mm length and 3 mm tip diameter. A tool with a conical shoulder diameter of 20 mm was used and pin was tapered from 4.5 to 3 mm as it is shown in (Fig. 2). During the welding process, the angle of tool tilt with respect to the work piece surface was kept constant at 2° (Tab. 4).

Table 1. HVOF process parameters

Powder spray process parameters	**HVOF process**
Spray gun type	Metco Diamond Jet
Spray distance	300 mm
Spraying rate	5.7 kg/h
oxygen pressure	9.35 atm
Nitrogen pressure	3.2 atm
Flammable gas species	Natural Gas
The coating powder	Nickel-Copper based

Table 2. Chemical composition (wt. %) of AA5754 aluminum alloy used in this study

Material	% Fe	%C	% Si	%Cu	%Mn	% Mg	% Zn	%Ti	%Cr	%Al
AA5754	0,312	-	0,23	0,024	0,34	3,2	0,16	0,098	0,26	Remain.

Table 3. Mechanical properties of AA5754 aluminum alloy used in this study

Sample	Tensile Strength (N/mm^2)	% Elongation	Hardness (H_V)

AA5754	232	15	76

Table 4. Selected welding parameters for the welding process

Rotational speed (rpm)	Advance rate (mm/min)	FSW connect tool location	FSW tool profile
2000	125	Derived parts 2 ° angle	Conical

Figure 1. The milling machine used for FSW process

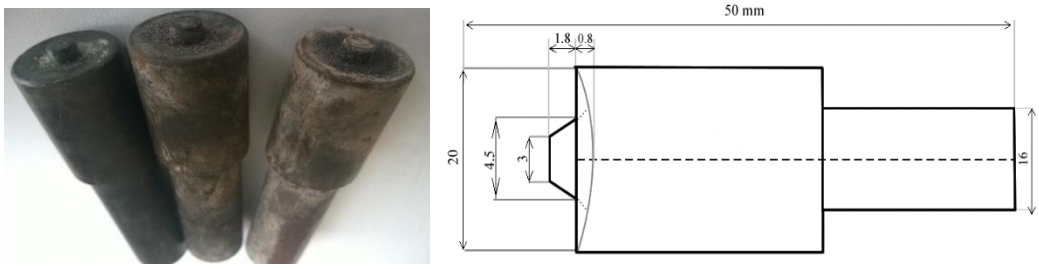

Figure 2. Configuration and typical drawing of used tool

A FLIR A655 brand high-speed camera has been used (Fig. 3). Temperature measuring was done with a thermal imaging camera during the FSW process and it was recorded at 50 fps. The maximum surface temperature achieved in the treatment process was measured as 245 ºC. This temperature is not high enough for structural change of the nickel-copper plating.

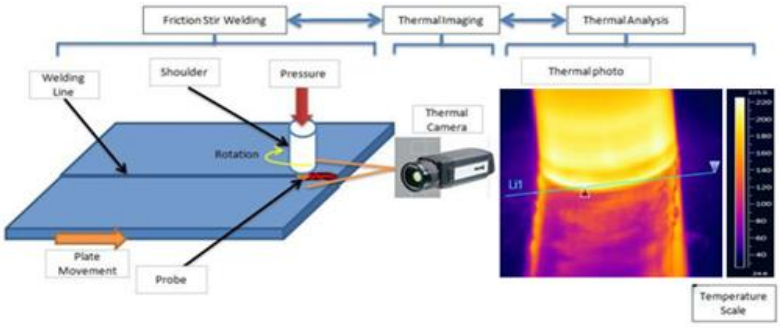

Figure 3. A schematic process of thermal analysis measurement system

Microstructural examination was carried out using an optical microscope (OM). The samples for metallographic examination were polished using various grades of emery sheets. Final polishing was done using diamond paste in the disc polishing machine. The polished samples were etched with standard Keller's reagent. An Electron Dispersive Spectroscopy (EDS) integrated to the Scanning Electron Microscope (SEM) was employed to analyze the microstructure (Fig. 4).

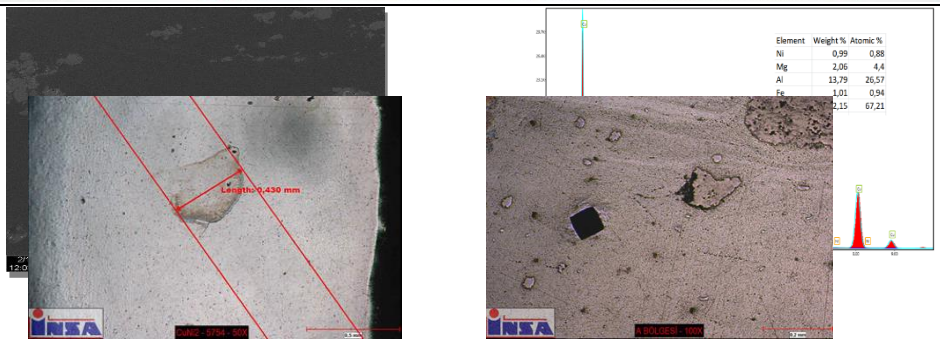

a b

Figure 4. (a) SEM image and (b) EDS analysis results of selected region of the stir zone of an AA5754 aluminum alloy welded by FSW

Microhardness tests were conducted on polished samples from cross section of the BM and weld regions with a Vickers indenter under a load of 200 g for a dwell time of 15 s (Fig.5. a,b ,Fig. 6, Fig 7a,b) For this purpose, the samples were ground to 2000 grit and cleaned by deionized water. The corresponding final values were determined as the average of 3 measurements.

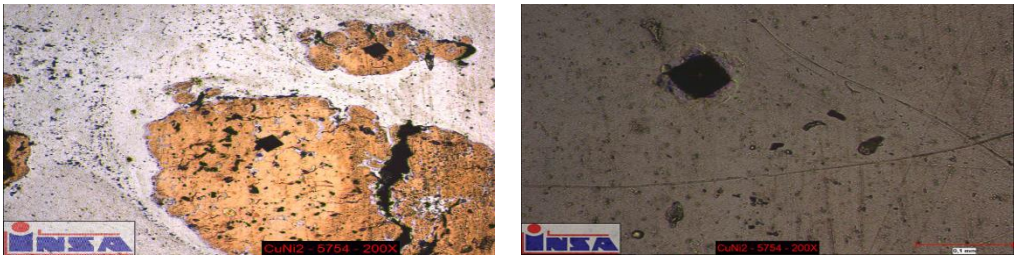

a b

Figure 5. Optical microscope (OM) micrographs and microhardness tests of weld regions of AA5754 aluminum alloy

The tensile tests of the welds were carried out using an Instron-type testing machine with a crosshead speed of 2 mm/min, according to the ASTM E8M-04 standard (Fig. 6).

Figure 6. Standard tensile test samples (ASTM E8M-04) of the welded sheet

a b

Figure 7. Optical microscope (OM) micrographs of weld regions of AA5754 aluminum alloy

The electrochemical corrosion tests of the BM and weld regions were performed utilizing a typical three electrode potentiodynamic polarization test unit in the corroding media of aerated solution of 3.5 wt. % NaCl at room temperature. Calomel and graphite electrodes were used as reference and auxiliary electrode, respectively. The weld regions with a rectangle surface area of 0.24 cm^2 (the working electrode) were embedded in cold resin and were ultrasonically cleaned in distilled water. Before potentiodynamic polarization measurements, an initial delay of 30 min. was employed in order to measure the open circuit potential between working and reference electrodes. Potentiodynamic polarization curves were generated by sweeping the potential from cathodic to anodic direction at a scan rate of 1 mVs^{-1}, starting from – 0.25 up to + 0.25 V. Corrosion potentials (E_{corr}) and corrosion current densities (i_{corr}) were calculated using a Tafel type fit in the software. Finally, the surface images of the corroded samples were examined using an OM.

3. RESULTS AND DISCUSSION

The microstructures of the BM and weld regions are shown in (Fig. 8). Four different zones; BM, HAZ, TMAZ and NZ can be identified in the microstructure of AA5754 joint as shown in (Fig. 8). The onion ring structure that is apparent in the stir zone is characteristic of the FSW. The particles are clearly visible in the stir zone (Fig.12 a,b). In all regions of the welding zones, hardness traces on nickel-copper particles were found to be higher than those of the base material (Fig.8, 9, 10). These particles were confirmed as nickel-copper with EDS analysis as shown in (Fig. 4).

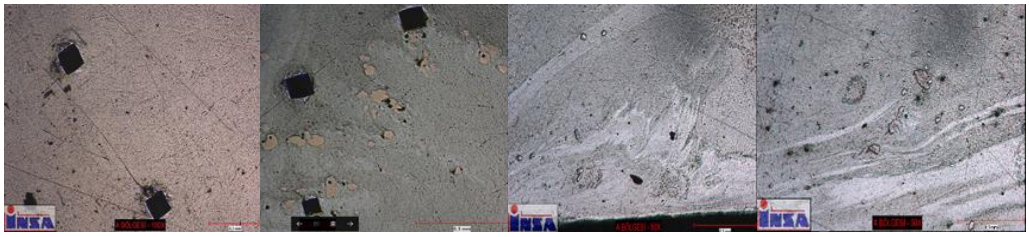

(a) (b) (c) (d)

Figure 8. Cross sectional microstructures of an AA5754 aluminum alloy welded by FSW: (a) BM, (b) HAZ, (c) HAZ/TMAZ and (d) NZ

Figure 9. OM micrograph of Ni-Cu particles observed in the stir zone of an AA5754 aluminum alloy welded by FSW

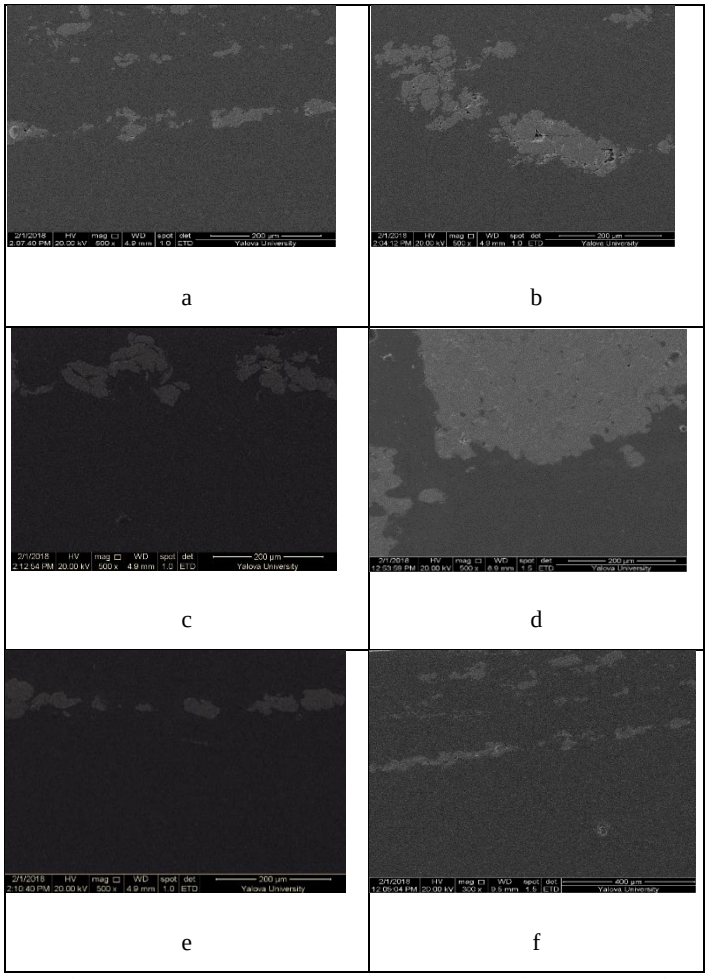

Figure 10. SEM micrograph of Ni-Cu particles observed (a,b) NZ , (c,d) TMAZ, (e,f) TMAZ/ HAZ of an AA5754 aluminum alloy welded by FSW

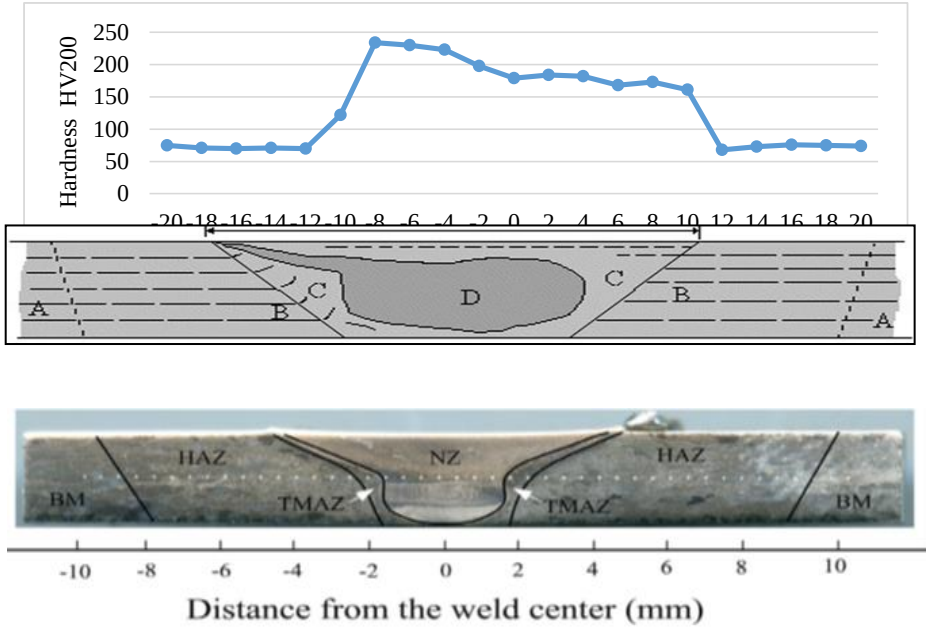

Figure 11. Microhardness profiles along center lines of the weld cross section, appearance of an onion ring in a cross-section and optical macrostructure of an AA5754 aluminum alloy welded by FSW

(Fig. 11) shows the microhardness profiles along center lines of the weld cross section of the FSW joint. Increase in hardness of stir zone-advanced side was reported for coated with nickel-copper on aluminum alloy by HVOF than joined FSW.The highest hardness value occurs in the left side-advanced side of the NZ followed by a gradual decrease across the HAZ until reaching the hardness value of the BM as shown in (Fig. 11). This is attributed to more grain refinement in the NZ due to dynamic recrystallization [6] and the existence of hard nickel-copper particles. The maximum hardness values of nickel-copper particles was measured as 234 $HV_{0.2}$.

Figure 12. Tensile test of coated and welded AA5754 aluminum alloy(ASTM E8M-04)

The tensile strength of AA5754 joint fabricated by FSW was compared to that of the BM (Table 3 and Fig. 11). AA5754 weld produced by FSW displayed lower strength value (Fig. 12) compared to the BM. Higher rotational speed (2000 rpm) fractured in brittle manner due to formation of intermetallic compounds such as AlCu and Al_2Cu (Fig.10a,b ,12a,b, 16a,b). Thick Coating with nickel-copper based powder of AA5754 welding region by HVOF decreased the tensile strength of AA5754 joint (Fig. 13 a,b) (120-152MPa).

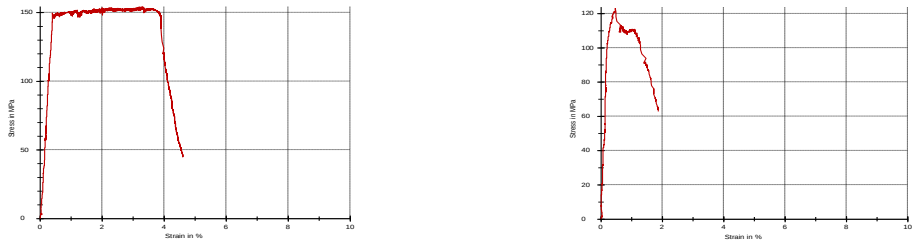

a b

Figure 13. Tensile curves of FSW welded AA5754 aluminum alloy (ASTM E8M-04)

Although the nickel-Cu coating is well wetting the matrix material, large and sufficiently large particle size distribution to the weld zone reduces tensile strength. The nickel-copper particles coated on the weld zones are not uniformly distributed in the welding regions during friction stir welding. Insufficient mixing temperature in the weld zones could not be reached (Fig. 7). It is possible to say that the nickel-copper particle sizes remain large (Figs. 10, 11, 12, 13, 14) and the formation of IMCs by the intermetallic compounds triggers the fornation of ductile brittle fracture (Fig. 14).

Current/(mA.cm^2) Open circuit current density curves

a b

Figure 14. (a) Potentiodynamic polarization curves of NZ, TMAZ and HAZ regions and (b) open circuit current density curves of NZ, TMAZ and HAZ regions

It can be seen from (Fig.14) and (Tab.5) that the corrosion potential (E_{corr}) values of the NZ, TMAZ and HAZ regions value -853mV while that of BM was about -693mV. BM was about 160mV more positive than the NZ, TMAZ and HAZ regions values. As for the corrosion current density (i_{corr}), the samples with welding zones exhibited were similar corrosion current density 2.030, 2.71 (x 10^{-6} A/cm^{-2}) that the BM respectively.

Table 5. Average corrosion potential (E_{corr}) and corrosion current density (i_{corr}) values of BM and weld regions

Material/proces	**E_{corr} (mV)**	**I_{corr} (x 10^{-6} A/cm^{-2})**
BM	-693	2.71
HAZ/ TMAZ/ NZ	-853	2.030

In corrosion behavior, (Fig. 15) shows the OM images of the NZ, TMAZ and HAZ zones after corrosion test. The pitting is due to the local dissolution of the matrix as a result of galvanic coupling between nickel-copper particles and surroundings matrix. The NZ, TMAZ and HAZ regions have terribly corroded and pits are seen throughout the surface. Also in NZ, the rate of attack is very high. In the BM, only a few pits are seen. The anodic reactivity was highest in the weld nugget, particularly towards the higher advanced side. This was shown to correlate with the presence of small and big size precipitates dispersed throughout the matrix of the susceptible regions. It can further be seen that the density and size of pits in TMAZ are higher in comparison to NZ and HAZ weld regions. Galvanic

coupling between nickel-copper particles and surroundings aluminum alloy matrix is the main reason for corrosion in the welding zone of AA5754 alloy. Distribution of nickel-copper particles throughout the advanced side of stir zone increases the sites for galvanic cell and hence decreases the corrosion resistance.

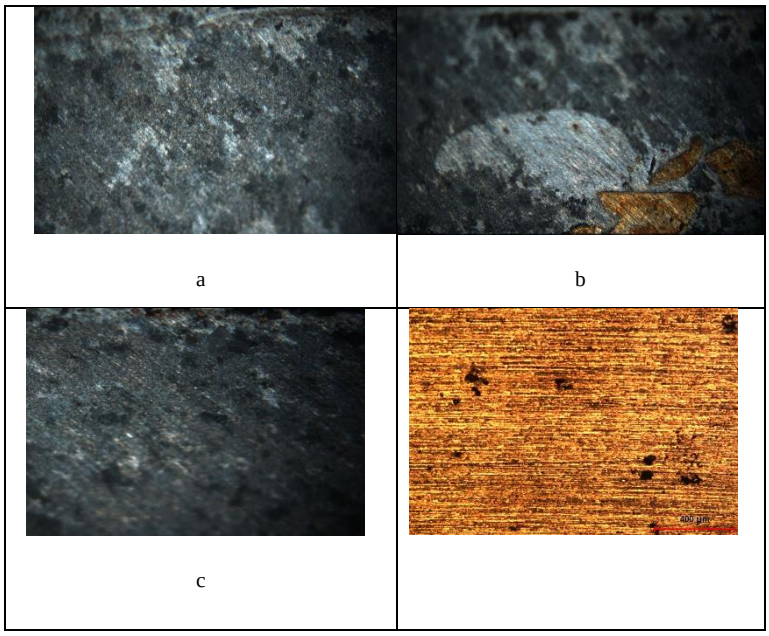

Figure 15. Corrosion surfaces of (a) NZ, (b) TMAZ ,(c) HAZ and (d) BM samples

3. CONCLUSION

Before FSW process, welding edges of AA5754 aluminum alloy sheets were coated with nickel-copper powder in a thick of 100 μm using HVOF process. The microstructure, microhardness, tensile test and corrosion resistance of the BM and weld regions were investigated. Conclusions drawn from the study are as follows:

1. FSW welded AA5754 aluminum alloy displayed lower tensile strength value compared to the BM. Maximum joint strength as high as ~66% of aluminium base metal has been achieved (Figure. 13).

2. The friction stir processing of AA5754 alloy coated with nickel-copper powder by HVOF significantly improved the hardness over those advanced side of the weld regions.

3. Increased peak temperature in the stir zone resulted in the higher dissolution rate of big size Ni-Cu precipitates throughout the stir zone (Figure.9). Moreover, nickel-copper particles sprayed on the welding rigion of aluminum substrate by HVOF process throughout the stir zone increases the number of sites available for galvanic coupling and hence decreases the corrosion resistance (Figure.15 a,b,c).

4. In our next work, it is the reduction of nickel-copper coating thicknesses. Post weld heat treatments will ensure homogeneous distribution of small size particles into the structure. Thus, tensile strength and corrosion resistance are expected to increase.

ACKNOWLEDGMENT

Asst. Prof. Dr. SAMUR acknowledges the support by Marmara University, Scientific Research Projects Department (BAPKO), Project FEN-C-YLP-120917-0539 and FEN-D-150218-0072.

REFERENCES

[1]. P-K. Huang, J-W.Yeh, T-T. Shun, S-K. Chen: Multi-principal-element alloys with improved oxidation and wear resistance for thermal spray coating, Advanced Engineering Materials, 6, 2004, pp. 74-78.

[2]. Mindivan H, Kaya H, Oz A, Yalcinoz Y, Ucar M, Samur R, Microstructure, Mechanical And Corrosion Properties Of Friction Stir Welded AA1050 Aluminum Alloy Coated With Nickel Powder By High Velocity Oxy Fuel (HVOF) Process, 4th International Conference on Welding Technologies and Exhibition (ICWET'16) 11-13 May 2016, Gaziantep-TURKEY

[3]. Mubiayi M, Akinlabi E. Friction stir welding of dissimilar materials between aluminium alloys and copper, An overview [C]//Proceedings of the World Congress on Engineering. San Francisco, USA: IAENG Publications, 2013: 3−5.

[4]. Agarwal S P, Nageswaran P, Arivazhagan N, Ramkumar K D. Development of friction stir welded butt joints of AA 6063 aluminium alloy and pure copper [C]//International Conference on Advanced Research in Mechanical Engineering. Uttarakhand, India: IPM rt. Ltd Naintal, 2012: 46−50.

[5]. E. Lugscheider, C. Herbst, L. Zhao: Parameter studies on high-velocity oxy-fuel spraying of MCrAlY coatings, Surface and Coatings Technology, 108–109, 1998, pp. 16–23

[6]. Mindivan F, Kaya H, Ozer M, Ucar M, Samur R: Investigation of corrosion behavior of the AA5754 aluminum alloy joined using friction stir welding method, CBU Journal of Science, 11, 2015, pp. 413-422.

ICETI
www.iceti.org
2018
07-11 MARCH
BUDAPEST
HUNGARY
II. INTERNATIONAL CONFERENCE ON ENGINEERING TECHNOLOGY AND INNOVATION

Selection of Reinforced Concrete Formwork System with MOORA Multi Criteria Decision Making Method

Latif Onur Ugur[1], Engin Yuksel[2] Mursel Erdal[3]

Abstract

Reinforced concrete formwork systems constitute an important part of rough construction costs. In this study, the MOORA method was used for Multi-Criteria Decision Making approaches in the decision of procurement of reinforced concrete form system for a construction company. In this way, it is aimed to provide a solution to the problem of selecting the mold system. The MOORA method, which is one of the recommended methods for multi-objective optimization with discrete alternatives, is a method that is successfully used in case of importance. Economically cheap in work, long-term use in the opportunity to use, does not create problems in practice and so on it was tried to choose the mold system which provides the best criteria. In the study, both the Odds Method and the Reference Point Approach were used to calculate. In the results of study; it is understood that the decision model of purchasing reinforced concrete formwork system based on MOORA method can be used in the selection and evaluation of reinforced concrete formwork system in construction companies. The applied model can be used in similar production companies by changing the criteria. It should also be emphasized that the subjective assessment given by the decision maker's intuitions, experience and expertise (expert opinion), not only on numerical values, but on the quantification stages gives the process subjectivity.

Keywords: Reinforced concrete formwork system, Multi criteria decision making, MOORA method

1. INTRODUCTION

The auxiliary building elements that provide concrete with necessary form in terms of architecture and aesthetics and carry concrete up to sufficient strength are called formworks. The formworks must be securely sized like the other members of the building, although they are auxiliary building construction tools. Formwork systems must be designed to be used many times. All buildings are made up of horizontal and vertical components. The vertical supports of the constructions are columns and curtains, and the horizontal supports are the upholstery and beams. Formwork systems used in columns, curtains, upholstery and beams should be capable of making economical and rapid construction. The main components of the formwork are the surface and carrier parts. Since formwork surfaces are directly contact with concrete, materials must be resistant to concrete. The formworks must be easy to attach and detach [1].

Since the discovery of reinforced concrete, great progress has been made in construction techniques. Buildings started to be built at heights that cannot be reached with masonry. As the cities get larger, decreasing number

[1] *Corresponding author: Düzce University, Technology Faculty, Department of Civil Engineering, 34220, Düzce, Turkey.* latifugur@duzce.edu.tr

[2] *Düzce University, Technology Faculty, Department of Civil Engineering, 34220, Düzce, Turkey.* enginyuksel@duzce.edu.tr

[3] *Gazi University, Technology Faculty, Department of Civil Engineering, 06500, Ankara, Turkey.* merdal@gazi.edu.tr

of sidewalks and high-rise buildings being seen as prestige indicators. Parallel to the development in construction techniques, concrete quality, formwork, work machinery and equipment, multi-storey high buildings are becoming widespread. It is inevitable to use modern formwork systems with the necessity of finishing these structures generally in a short time, repeating the same floor plan in many numbers, necessity of lowering labor costs [2].

Today, many different formwork systems are used in reinforced concrete structures. It has been understood that the prior art does not give good results due to the wasted and limited use of the wood formwork reuse. Therefore, in recent years, modern formwork systems have been preferred in the constructions where the number of repeating layers is very high and the applications are difficult.

With the development of modern formwork systems covering 40-60 % of the built-in workforce, significant reductions in formwork assembly and disassembly times have been achieved and quality is maintained. Modern formwork systems are at the forefront of material cost, reducing work power and construction time.

According to statistical information, roughly 45% of the rough construction cost is labor, and 55% is the material cost. The ratio of the formwork to the total labor cost is 50% and the ratio of the total material cost to the formwork is about 10%. If these values are taken into consideration, decreasing formwork construction work will be an important factor in reducing the building costs. This can be achieved by designing a healthy formwork suitable for the structure, researching alternative formwork techniques [3].

When choosing a reinforced concrete form, unit cost (m^2), labor cost, required labor force, installation and disassembly periods, number of use of the formwork, work safety, maintenance repairs, and situations need to be considered. When a decision is made to buy such a system, it is obvious that there are multiple criteria for this decision.

Multi-criteria decision-making is the process of achieving the best possible outcome according to established rules. Real-life problems often contain criteria that cannot be expressed on the same scale and conflict with each other. For this reason, it is very difficult to achieve a solution that satisfies the entire selection criteria. In such problems, a conciliatory solution is usually sought in a predetermined rule light [4].

In this study, it is aimed to decide on the selection of the suitable formwork system according to the materials and technology in the projects of a construction company which will be constructed. Sorting and selection were determined using the MOORA method. In MOORA, the normalized matrix is determined using the "linear normalization approach". Expert opinions have been taken into account in the formulation of the criteria.

2. MOORA METHOD

Two applications of this method are given below.

2.1. Ratio Method

MOORA (Multi-Objective Optimization on the Basis of Ratio Analysis) is a process of simultaneous optimization of two or more multi-criteria or multi-criteria overlapping qualities or target specific constraints. The MOORA method starts with the decision matrix in Eq. (1), which shows the performance of different alternatives for different qualities or purposes [5, 6].

$$X = \begin{bmatrix} X_{1,1} & X_{1,2} & . & . & X_{1,n} \\ X_{2,1} & X_{2,2} & . & . & X_{2,n} \\ . & . & . & . & . \\ . & . & . & . & . \\ X_{m,1} & X_{m,2} & . & . & X_{m,n} \end{bmatrix} \quad (1)$$

In this decision matrix,
i = alternative
j = quality criteria
m = total number of alternatives
n = total number of criteria
xij = i. Alternative j. it is expressed as performance measurement value in terms of criteria.

Next, the normalization operation is performed. The methods used for normalization are vector normalization shown in Eq. (2) and linear normalization in Eq. (3) [7].

$$r_{ij} = \frac{x_{ij}}{\sqrt{\sum_{i=1}^{m} x_{ij}^2}}, \; i=1, 2, ..., m; \; j=1, 2, ..., n. \quad (2)$$

$$r_{ij} = \frac{x_{ij}}{\sum_{i=1}^{m} x_{ij}}, \; i=1, 2, ..., m; \; j=1, 2, ..., n. \quad (3)$$

This process is performed by *i*. Alternative n *j*. gives the performance measurement value in terms of criteria. The value of x_{ij} in this case *j* criterion *i*. It is a number that does not have a unit in the range [0,1] representing the normalized performance of the alternative. For multipurpose optimization, these normalized performance values (for useful attributes) are added at maximization, and there is a single value for each alternative, subtracted in minimization case (for useless properties). In this case the problem of optimization occurs as in Eq. (4) [7].

$$y_i = \sum_{j=1}^{g} x_{ij}^* - \sum_{j=g+1}^{n} x_{ij}^* \quad (4)$$

In this equation,
n = the number of attributes or criteria to be ranked
n-g = number of attributes or criteria to be minimized
y_i = in terms of all qualifications or criteria *i*. The normalized value for the alternative.

2.2. Reference Point Theory

In the reference point approach, in addition to the ratio method, for each criterion; (r_j 's) which are the maximum points if the goal is minimization and minimum if the goal is minimization. These points are determined by the distance from x^*_{ij}. So; operation is performed and written as a matrix.

$r_j - x^*_{ij}$ (5)

Here;
i = 1, 2, ..., m is the number of alternatives,
Let $j = 1, 2, ..., n$ be the number of criteria,
x^*_{ij}, i. alternative j. the normalized value in the criterion,
r_j, j. reference point of the criterion.

Constructed matrate "Tchebycheff Min-Max Metric Operation" shown in Eq. (6) is applied

$$Pi = Min_i \, (Max_j \, r_i \, x^*_{ij}) \qquad (6)$$

Thus, sorting is done [8-10].

3. APPLICATION

A large construction company will choose a formwork system for the present and future projects. By conducting researches for the formwork system that they wanted to use in their projects, information was gathered by finding formworks and other construction companies with the company and consulting sector professionals. With the acquisition of the necessary data, company has taken into consideration the different four-formwork systems. It has been decided to use the MOORA method for a ranking and selection exercise. According to the gathered specifications, the characteristics of the formworks will be accepted as the criteria in the ordering. These criteria to be accepted in the evaluation; "K1: Costs (TL/m²)", "K2: Number of Usage", "K3: Labor Costs (TL/hour)", "K4: Number of Workers" (hour) ".

Criteria;
K1: "Cost (TL / m²)"; The concrete system specifies the m² price of the formwork type to be used depending on the required quantity calculations. At this criterion, the unit price is required to be the lowest.

K2: "Number of Usage"; the pattern plays an important role economically in terms of having the ability to reuse after completing the task. Regular maintenance and repairs, in addition to extending the life of the formwork, reduces long-term investment costs. It is desirable that this criterion is at the highest level.

K3: "Labor Cost (TL/hour)"; Labor cost is one of the most important criteria in the sector. The system is so important in workmanship that the highest quality is required, and the cost of the system comes out as a cost. It is desirable that this criterion be the lowest value.

K4: "Number of Workers"; Labor force is required for assembly and disassembly in reinforced concrete formwork systems. Optimization of the number of workers for a formwork job is one of the pioneering rules that must be taken into account in terms of both cost and applicability of work. This criterion is required to be minimum.

K5: "Assembly (hour)"; in the installation of the formworks, the assembly time criterion emerges as a factor. When the installation is done, additional parts are used, the surface of the formwork is lubricated, and the workers perform the installation without damaging the formwork, and so on. It is seen as factors that will completely affect the time and delay the end of the work. It is desirable that this criterion be the lowest value.

K6: "Disassembly (hour)"; It is also important to disassemble as many formworks as possible. During the disassembly process, it is requested that the parts are not broken, the formwork surfaces are not damaged, and the concrete is not damaged. Depending on these, there may be time problems in the works. It is desirable that this criterion be the lowest value.

The decision matrix in which the values of the six criteria specified for the four different options are included is given in Table 1. This matrix will be the basis for the solution.

Table 31. Values of criteria for reinforced concrete formwork systems

	K1	K2	K3	K4	K5	K6
	Cost (TL/m2)	Number of uses	Workmanship cost (TL/h)	Number of workers	Installation (hour)	Dismantling (hour)
Traditional mold	30	5	7,4	8	0,8	0,6
Tunnel mold	41	1000	8,5	4	0,6	0,3
Panel mold	32	30	7	6	0,5	0,4
PVC mold	35	80	7,2	6	0,5	0,3

The values given in Table 1 are normalized using Eq. (2). In this study, linear normalization is used for normalization operations. The values obtained as a result of this process are as in Table 2. In addition, this chart specifies the maximum and minimum required criteria.

Table 2. Values obtained as a result of normalization

	Min	Max	Min	Min	Min	Min
	K1	K2	K3	K4	K5	K6
Traditional mold	0,431665847	0,004981787	0,490238261	0,648885685	0,653197265	0,717137166
Tunnel mold	0,589943325	0,996357499	0,563111516	0,324442842	0,489897949	0,358568583
Panel mold	0,46044357	0,029890725	0,463738896	0,486664263	0,40824829	0,478091444
PVC mold	0,503610155	0,0797086	0,476988578	0,486664263	0,40824829	0,358568583

For two different applications of the MOORA method, these normalized matrix values are taken as basis.

3.1. MOORA Method Application

By setting the criteria with the above scope, it was possible to evaluate qualitative and quantitative criteria as well as the use of certain and uncertain data. According to evaluation criteria; it is desired to reach the highest value at 1 when the lowest values are required at 5 of the criteria. Each criterion was rated equal in weight. Table 3 specifies the maximum and minimum required criteria.

Table 3. Normalized Matrix where maximum and minimum criteria are specified

	Min	Max	Min	Min	Min	Min
	K1	K2	K3	K4	K5	K6
Traditional mold	0,431665847	0,004981787	0,490238261	0,648885685	0,653197265	0,717137166
Tunnel mold	0,589943325	0,996357499	0,563111516	0,324442842	0,489897949	0,358568583
Panel mold	0,46044357	0,029890725	0,463738896	0,486664263	0,40824829	0,478091444
PVC mold	0,503610155	0,0797086	0,476988578	0,486664263	0,40824829	0,358568583

Using the values in Table 3, y_i* *values* were calculated with the help of Eq. (4) and sorted according to the Ratio Method. Table 4 shows the results of this calculation.

Table 4. Sorting by Ratio Method

yi *	Ranking
-2,936142436	4
-1,329606716	1
-2,267295739	3
-2,15437127	2

Reference points are set out from the values in Table 2 to sort using the Reference Point Approach. These values are given in the bottom line of Table 5.

Table 5. Reference points account

	Min	Max	Min	Min	Min	Min
	K1	K2	K3	K4	K5	K6
Traditional mold	0,431665847	0,004981787	0,490238261	0,648885685	0,653197265	0,717137166
Tunnel mold	0,589943325	0,996357499	0,563111516	0,324442842	0,489897949	0,358568583
Panel mold	0,46044357	0,029890725	0,463738896	0,486664263	0,40824829	0,478091444
PVC mold	0,503610155	0,0797086	0,476988578	0,486664263	0,40824829	0,358568583
Reference points	0,431665847	0,996357499	0,463738896	0,324442842	0,40824829	0,358568583

These values were calculated by applying the Eq. (6). These account values are given in Table 6.

Table 6. Calculations using the Eq. (6)

	K1	K2	K3	K4	K5	K6
Traditional mold	0	0,991375711	0,026499365	0,324442842	0,244948974	0,358568583
Tunnel mold	0,158277477	0	0,099372621	0	0,081496658	0
Panel mold	0,028777723	0,966466774	0	0,162221421	0	0,119522861
PVC mold	0,071944308	0,916648899	0,013249683	0,162221421	0	0

The maximum values of the obtained data and the ranking according to the Reference Point Theory are given in Table 7.

Table 7. Sorting by Reference Point Approach

Maximum values	Ranking
0,991375711	4
0,158277477	1
0,966466774	3
0,916648899	2

Thus, the MOORA method was ranked according to two different approaches. According to both approaches, the "Tunnel Formwork System" was chosen as the most suitable option. As a result of the Ratio Method and Reference Method applications, no sequence changes were observed and there was consistency in the selection order of the die system.

4. CONCLUSION

The multi-criteria decision-making approach seeks to select the most appropriate from among the alternatives by evaluating many of the contradictory criteria. Multi-criteria decision making techniques have a considerable use in the literature. The number of multi-criteria decision making methods is also high. Decision makers may choose one or more of these methods, depending on the nature of their work. The criteria set out in some studies are equally preliminary, and in some studies the final weights can be reached by another multi-criteria decision-making method after the criterial weights are determined by one of the multi-criteria decision-making methods within the experts' opinions.

The MOORA method, which is one of the recommended methods for multi-objective optimization with discrete alternatives, is a method that is successfully used in case of importance. It is also possible to use the method as a hybrid with other multi-criteria decision making methods such as Analytic Hierarchy Process (AHP), Analytic Network Process (ANP), VIKOR, TOPSIS, ELECTRE, PROMETHEE, MACBETH, UTA, STEM and PAPRIKA.

In this study, the MOORA method was used for the decision making of multi-criteria decision making of the purchase decision of reinforced concrete formwork system. The implementation of the method is based on the "linear" normalization matrix approach. In Table 8, both the Proportion Method and the Approach to the Reference Point are presented together with the resulting ranking.

Table 8. Reinforced concrete form system order according to Multi Criteria Decision Making Methods

	MOORA Method	
Ranking	Ratio Method	Reference Point
1	Tunnel mold	Tunnel mold
2	PVC mold	PVC mold
3	Panel mold	Panel mold
4	Traditional mold	Traditional mold

When the application results are examined, the MOORA method has the first order for Tunnel Formworking system and the second is PVC Formworking System. The construction company based on this data can select Tunnel Formworking System as the first alternative and PVC Formworking System as the second alternative.

It has been understood that the decision models on which the MOORA method is based can be used in construction companies for the selection and evaluation of reinforced concrete formwork systems. It should also be emphasized that the subjective assessment (expert opinion) given by the decision maker on the basis of his intuitions, experience and expertise, rather than just quantitative analysis, gives the process subjectivity in the quantification stages. Applied models can be used in similar production companies by changing the criteria. It is also possible that the evaluation of the criteria in different organizations is different according to the value judgments of the different experts.

REFERENCES

[1]. N. Türkmenoğlu, "Formwork systems used for reinforced tall buildings", M.Sc. Thesis, İstanbul Technical University, Institute of Science, İstanbul, Turkey, 1999.
[2]. N. Benli, "An evaluation of formwork systems used in multi-storey buildings", M.Sc. Thesis, Dokuz Eylül University, Institute of Science, İzmir, Turkey, 2005.
[3]. İnşaat Mühendisleri Odası Birliği, İzmir Şubesi, http://www.imo.org.tr/resimler/ekutuphane/pdf/12196.pdf , Son erişim tarihi 11.05.2017.
[4]. B. Vahdani, H. Hadipour, J. S. Sadaghiani and M. Amiri, "Extension of VIKOR method based on interval-valued fuzzy sets", *Int. J. Advanced Manufacturing Techno.*, vol. 47, no. (9-12), pp. 1231-1239, 2010.
[5]. W. K. M. Brauers, R. Ginevicius and V. Podvezko, "Regional development in Lithuania considering multiple objectives by the MOORA method" *Techno. Econ. Dev. Econ.*, vol.16, pp. 613–640, 2010.
[6]. S. Chakraborty, "Applications of the MOORA method for decision making in manufacturing environment", *The International Journal of Advanced Manufacturing Technology*, vol. 54, no. (9-12) pp. 1155-1166, 2011.
[7]. A. Özdağoğlu, "The effects of the normalization methods to multi criteria decision making process–MOORA method review", *Ege Academic Review*, vol. 14, no. 2, pp. 283-294, 2014.
[8]. W. K. M. Brauers and E. K. Zavadskas, "The MOORA method and its application to privatization in a transition economy", *Control and Cybernetics*, vol. 35, no. 2, pp. 445-469, 2006.
[9]. W. K. M. Brauers and R. Ginevicius, "Robustness in regional development studies: The case of Lithuania", *Journal of Business Economics and Management*, vol. 10, no. 2, pp.121-140, 2009.
[10]. W. K. M. Brauers and R. Ginevicius, "The economy of the Belgian regions tested with MULTIMOORA", *Journal of Business Economics and Management*, vol. 11, no. 2, pp. 173-209, 2010.

ICETI
www.iceti.org
2018
07-11 MARCH
BUDAPEST
HUNGARY
II. INTERNATIONAL CONFERENCE ON ENGINEERING TECHNOLOGY AND INNOVATION

The Impact of the Use of Different Slabs on the Rough Construction Cost of the Same Architectural Reinforced Concrete Buildings

Latif Onur Ugur[1], Mursel Erdal[2]

Abstract

The floor is divided into floors and walked on; to the structural members carrying the loads and their own weight to the supports. Reinforced concrete carcasses convey the loads from the beams to the beams, the loads coming on the beams to the columns, the columns and all the loads on the foundation. Among these structural elements, the slab can be designed in many types according to the desired characteristics. In this study, it is aimed to compare the rough building costs when four different twenty-storey buildings with the same architectures use different types of slab. For this purpose, the architectural project prepared previously was utilized. Also IDECAD program was used for modeling of buildings. Models are shown in figures. The cost analyzes were compared taking into account the rough construction costs. The costs of rough construction elements are calculated according to 2017 Unit Price Ranges of Turkey. According to the analysis results, the building designed with waffle slab; 21.12% from the design with beam slab, it was found that it was costly 1.08% from the building which was designed with hollow-tile floor slab using hollow block as the filling material and 4.76% from the building which was designed with hollow-tile floor slab which used Styrofoam as filling material. The initial investment cost of the slabs used as the filler hollow block is lower but the time to be spent according to the hollow-tile floor slab will be much higher. It also means that the building is less subject to earthquake effects because it is a lighter material than the hollow block. Styrofoam will be a more appropriate decision to be preferred both in terms of safety and workmanship.

Keywords: Construction cost, Slab, Cost Analyses

1. INTRODUCTION

Reinforced concrete carcasses convey the loads from the beams to the slabs, the loads coming on the beams to the columns, the columns and all the loads to the foundation. Among these structural elements, the slab can be designed in many types according to the desired characteristics.

Firstly, to introduce the slab, the floor separates a building from the storeys and walk on it; to structural members carrying loads and their own weight to the supports [1]. Since thicknesses are negligible compared to the other two dimensions, slab is generally considered two-dimensional. In addition, due to the fact that the same floors have equal displacements and rotations, the rigid diaphragm considered in the analyses are the elements that support the acceptance [2, 3].

[1] *Corresponding author: Düzce University, Technology Faculty, Department of Civil Engineering, 34220, Düzce, Turkey.* latifugur@duzce.edu.tr

[2] *Gazi University, Technology Faculty, Department of Civil Engineering, 06500, Ankara, Turkey.* merdal@gazi.edu.tr

There are different kinds of slab systems; slab with is the most common type of flooring used in Turkey. They transfer loads in one direction or in two directions. The second is the waffle slab. It is designed to work in one or two directions and to make frequent small beams. Waffle slab is called as hollow-tile floor slab type in case of being filled with light material between beams. In addition to the disadvantages of the hollow-tile floor slab, due to the architectural preferences such as easy passage of large openings, reduction of formwork cost, obtaining a flat ceiling without beam protrusions, and thus, partition walls can be made at desired locations. The third type is a beamless slab. The use of this slab model, where horizontal and vertical loads are transferred directly to the carrier elements, is not common in Turkey. It is known that plate systems play a very serious role in the ductility of the structure due to phenomena such as high diaphragm stiffness, required lateral resistance and translational stiffness and affect the results of modal analysis [4].

Hollow-tile floor slab is heavier than the slab with beams and the rigidity is different. Slab is rigid in the direction of small beams, where as there is not enough rigidity at the opposite direction. This may cause structural problems. Care should be taken to create a safe structure in the most economical way while forming the carrier system of the targeted structure. Designers should pay more attention to alternatives in order to avoid having the same safety structure at a higher cost as the type of flooring directly affects the building cost. Since the earthquake loads acting on the structure are applied to the building masses, hollow-tile floor slabs are subjected to more earthquake loads than the slab with beams. For this reason, in order to provide required safety levels to the buildings designed with hollow-tile floor slab against relative floor displacements increased column-reinforced concrete shear wall dimensions are needed. This in turn increases overall cost [4, 5].

As a sense; it is expensive to use hollow-tile floor slab. However, with the temptation of architectural preferences, the cost increase is often foreshadowed. Although the ratio of cost overrun has been expressed in a wide range of forum sites based on the specific experience of the designers, no detailed scientific study has been found [5]. As a result of the horizontal and vertical parametric changes, the financial effect of the slab types is investigated parametrically for the selected regular structure by the authors in the same technical specifications. In this study; it is seen that the cost of the hollow-tile floor slab increases from three times up to three storeys, which is independent of the number of openings in the x and y directions, and is close to its cost in slab with beams [6].

To briefly describe the construction of the slab, the slab formworks are usually prepared together with the joints or beam formworks to be made. It is supported under the floor to carry the weight of the reinforced concrete coming on it. To prevent tensile stresses, the pulling section is provided with a construction steel so that it will be a straight bars. The distribution steels are made up and connected perpendicular to the direction of the main steels. With the dismantling of the formworks within approximately 21 days, the laying process is finished [7]. There are five different types of slabs. These are beam-slab, cantilever slab, ribbed slab, hollow-tile floor slab and waffle slab [8, 9].

Beam-slab: It is a plate with a thickness of 5-20 cm with at least one edge sitting on the beam. Loads and edges are generally preferred in volumes that are not very large (in rooms). The short edge can be 6-7 m. Construction is easy and economical. It is the most commonly used floor type in residential buildings [10].

Cantilever slab: It is a 20-40 cm thick plate without beams, sitting directly on the columns. Formwork work is low. Since there is no dangling beam, a flat ceiling appears when you look up. This type cannot exhibit a good structural behavior. There is a risk of column punching. Collar head is used to prevent punching in heavy floors (industrial buildings, bridges). Earthquake behavior is bad, is not a suitable slab system for Turkey [9].

Ribbed slab: It is a slab formed by placing parallel beams within main beams at 40-70 cm intervals and making

a very thin plate on it. The width of the ribs is 10-15 cm and the height is 25-35 cm. The plate is 5-7 cm, thick. Earthquake behavior is not good [10].

Hollow-tile floor slab: Spaces between ribs (small beams) filled with light material. The ceiling looks flat. Earthquake behavior is not good. Formwork cost is low. It is healthy because there are no indentations to hold the dust. Sound and heat are less transmitted. There is additional block weight. It also increases the additional cost due to the cost of the block [9, 10].

Waffle slab: It is constructed like a ribbed slab. Normal-sized beams are used instead of small beams. Distance between the beams is about 50-150 cm. The opening may be 15-25m [10].

In this study; three model reinforced concrete buildings with different types of slabs were designed, with the same architectural projects, 20 storey, slab classes earthquake zones and basic types. For each design, rough construction quantities and discoveries were made. The rough construction costs of these three buildings were calculated and the effect of the slab type change on the rough building costs was investigated.

2. DIFFERENT SLAB TYPES HAVING SAME ARCHITECTURE

The buildings that were designed as examples in this study were built on the same architectural project. In this architectural project used, one floor is a living room with two floors, the left room is a living room with three rooms, and the right room is a living room with four rooms and a living room with a total floor area of 347.18m^2.

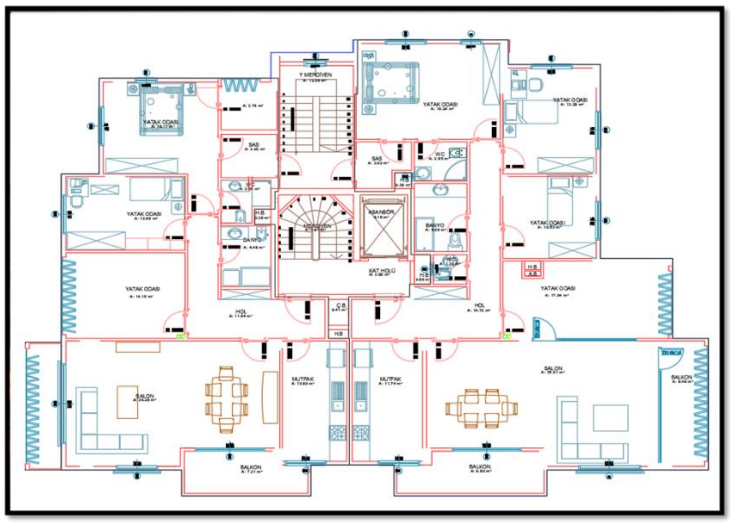

Figure 32. Floor plan used in sample buildings

2.1. Reference Properties of the Building Designed with Beam-Slab

In the structure columns; 30×50 cm, 30×60 cm, 30×70 cm, 30×80 cm, 30×85 cm, 30×90 cm, 40×90 cm, and 50×50 cm sizes were selected for this study. The shear walls that are placed at suitable places are; 25×175 cm, 25×220 cm, 25×280 cm, 25×300 cm, 25×430 cm, 30×210 cm, 30×290 cm and 30×320 cm dimensions. All the beams in the building were selected in dimensions of 25 × 60 cm. The slab thickness is 15 cm, the mat foundation thickness is 50 cm and S420 steel is used in the building elements. C35 class was chosen for concrete in calculations. The structural system type of reinforced concrete ductility is high.

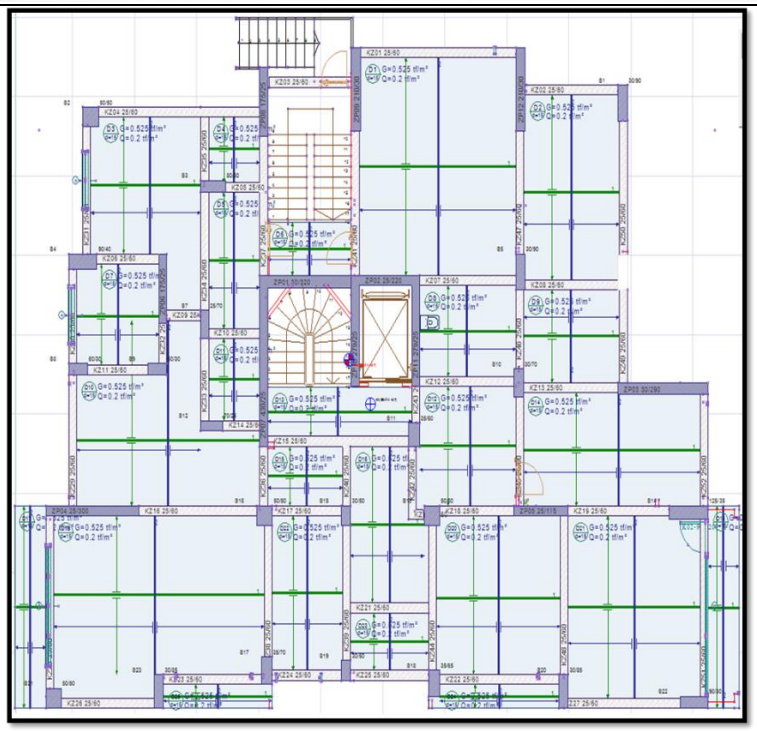

Figure 2. Formwork plan of the building made of beam-slab

Table 1. Features of the designed building (Beam-slab)

Floor heights	3.00 m
Number of floors	20
Building importance coefficient (I)	1
Earthquake Zone	2nd Degree
Effective ground acceleration coefficient (A_0)	0.51
Local Soil Class	Z2
Bearing system behavior coefficient (R)	7
f_{cd} (Concrete strength to be used in the calculation)	23000 kN/m^2 (C35)
f_{yd} (steel yield strength to be used in calculation)	365000 kN/m^2 (S420)
E_c (Elasticity Modulus)	33000 N/mm^2
$\gamma_{concrete}$ (Concrete unit volume weight)	25 kN/m^3

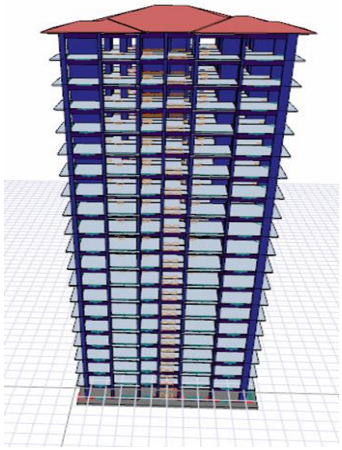

Figure 3. Three-dimensional view of the building

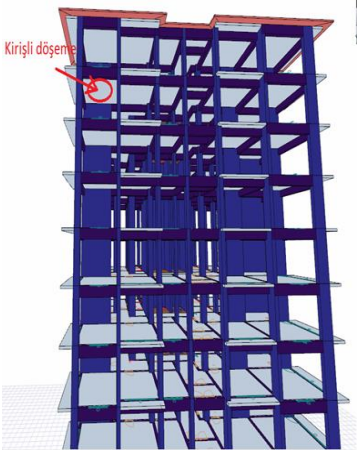

Figure 4. View of beam-slab

2.2. Properties of the Building Designed with Hollow-Tile Floor Slab

In the structure columns; 25×60 cm, 25×100 cm, 30×60 cm, 30×70 cm, 30×90 cm, 40×90 cm, 50×50 cm, 50×70 cm and 50×125 cm have dimensions. The shear walls that are placed at suitable locations are; 25x175 cm, 25x220 cm, 25x280 cm, 25x300 cm, 25x430 cm, 30x210 cm, 30x310 cm, and 30x320 cm dimensions. All the beams in the building were chosen as 50×35 cm and 25×50 cm. The slab thickness is 10 cm, the mat foundation thickness is 50 cm and S420 steel is used in the building elements. C35 class was chosen for concrete in calculations. The structural system type of reinforced concrete ductility is high, earthquake loads are taken as buildings and buildings carried by shear walls.

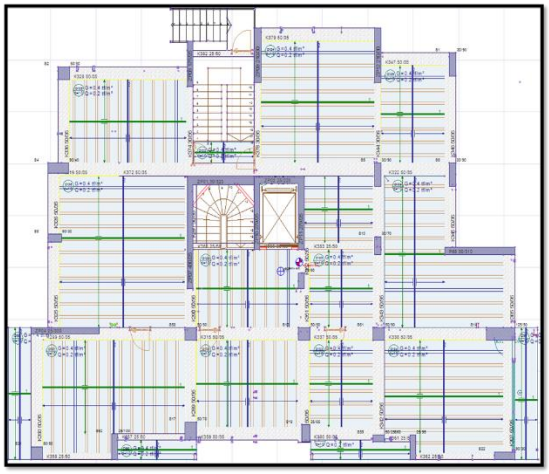

Figure 5. Formwork plan of building made with hollow-tile floor slab

Table 2. Features of the designed building (Hollow-tile floor slab)

Floor heights	3.00 m
Number of floors	20
Building importance coefficient (I)	1
Earthquake Zone	2nd Degree
Effective ground acceleration coefficient (A_0)	0.51
Local Soil Class	Z2
Bearing system behavior coefficient (R)	7
f_{cd} (Concrete strength to be used in the calculation)	23000 kN/m^2 (C35)
f_{yd} (steel yield strength to be used in calculation)	365000 kN/m^2 (S420)
E_c (Elasticity Modulus)	33000 N/mm^2
$\gamma_{concrete}$ (Concrete unit volume weight)	25 kN/m^3

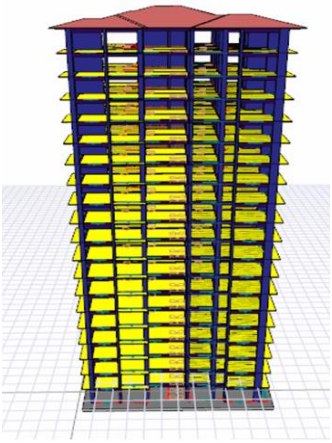

Figure 6. Three-dimensional appearance of the building

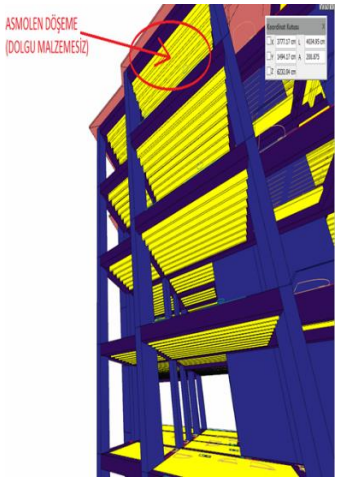

Figure 7. View of hollow-tile floor slab

2.3. Features of the Building Designed with Waffle Slab

In the structure, columns; 25×60 cm, 25×100 cm, 30×60 cm, 30×70 cm, 30×90 cm, 40×90 cm, 50×50 cm, 50×70 cm and 50×125 cm dimensions. The shear walls that are located at suitable places are; 25x175 cm, 25x220 cm, 25x280 cm, 25x300 cm, 25x430 cm, 30x210 cm, 30x310 cm, and 30x320 cm dimensions. All the beams in the building were chosen as 50×35 cm and 25×50 cm. The slab thickness is 10 cm, the mat foundation thickness is 50 cm and S420 steel is used in the building elements. C35 class was chosen for concrete in calculations. The structural system type of reinforced concrete ductility is high.

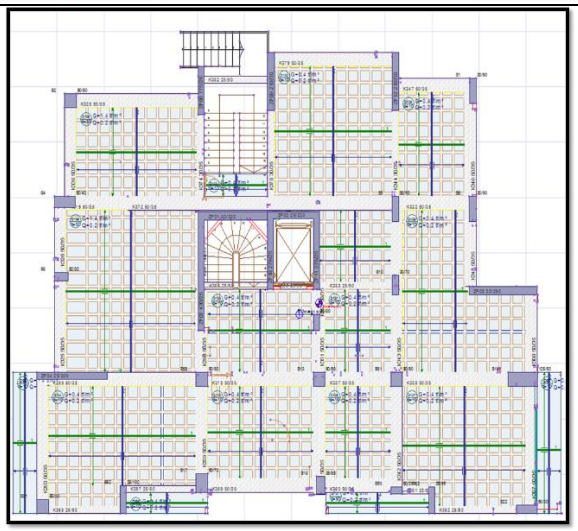

Figure 8. Building plan made with waffle slab

Table 3. Features of the designed building (Waffle Slab)

Floor heights	3.00 m
Number of floors	20
Building importance coefficient (I)	1
Earthquake Zone	2nd Degree
Effective ground acceleration coefficient (A_0)	0.51
Local Soil Class	Z2
Bearing system behavior coefficient (R)	7
f_{cd} (Concrete strength to be used in the calculation)	23000 kN/m^2 (C35)
f_{yd} (steel yield strength to be used in calculation)	365000 kN/m^2 (S420)
E_c (Elasticity Modulus)	33000 N/mm^2
$\gamma_{concrete}$ (Concrete unit volume weight)	25 kN/m^3

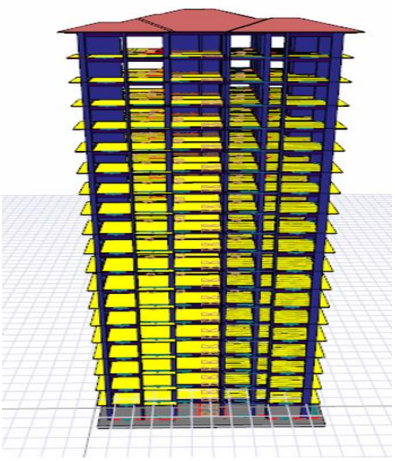

Figure 9. Three-dimensional appearance of the building

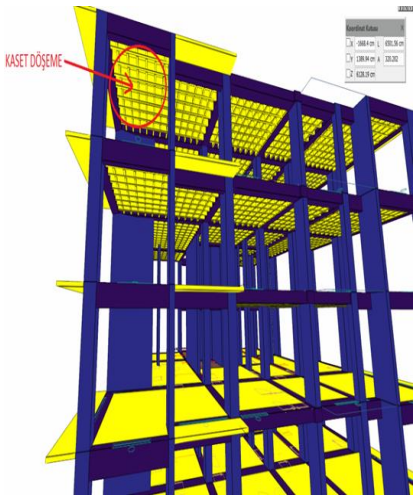

Figure 10. View of hollow-tile floor slab

3. MATERIAL QUANTITIES AND COSTS USED IN BUILDINGS WITH DIFFERENT SLAB TYPES

3.1. Quantity and Cost of Materials used for Building Designed with Beam-slab

The amount of material used in buildings designed with beam slab is given in Table 4 and the cost of rough construction is given in Table 5. All rough construction costs are calculated according to the unit prices of the year 2017.

Table 4. Quantity of materials used for buildings designed with beam-slab

	Unit	Floor	Beam	Shear wall	Column	Raft foundation	Total
Formwork	m^2	4915.70	3368.63	3611.38	2744.97	43.22	14683.90
Concrete	m^3	737.356	430.345	474.285	331.8	231.008	2204.794
Steel reinforcement	ton	51.799	97.711	80.554	84.722	59.727	374.514

Table 5. Cost of rough construction of the building designed with beam-slab

	Unit	Quantity	Unit price (₺)	Cost (₺)
Formwork	m^2	14683.90	39.63	581922.96
Concrete	m^3	2204.794	165.20	364231.97
Steel reinforcement (thin)	ton	107.656	61.65	6636.98
Steel reinforcement (thick)	ton	266.858	75.82	20233.19
Total				973025.09

3.2. Quantity and Cost of Materials used for Building Designed with Hollow-Tile Floor Slab

The amount of material used in buildings designed with hollow-tile floor slab is given in Table 6. In case of using styrofoam as the building material designed with hollow-tile floor slab, the rough construction cost is given in Table 7. In the case of hollow brick, Table 8 is given.

Table 6. Quantity of materials used for buildings designed with hollow-tile floor slab

	Unit	Floor	Beam	Shear wall	Column	Raft foundation	Total
Formwork	m^2	299,49	8293,98	2662,96	3432,33	2358,9	43,22
Concrete	m^3	29,949	620,807	428,383	429,75	302,7	231,008
Steel reinforcement	ton	28,962	44,701	145,136	82,308	79,447	61,733
Hollow block	m^2	-	-	-	-	-	3400,00
Styrofoam	m^3	-	-	-	-	-	1190

Table 7. Cost of rough construction in case of using hollow block as building material which is designed with hollow-tile floor slab

	Unit	Quantity	Unit price (₺)	Cost (₺)
Formwork	m^2	17090.76	39.63	677306.82
Concrete	m^3	2042.596	165.20	337436.86

Steel reinforcement (thin)	ton	131.221	61.65	8089.77
Steel reinforcement (thick)	ton	311.067	75.82	23585.11
Hollow block (35x20x40cm)	m^2 (12.5 number)	3400.00	23.13	78625.00
Total				1125043.56

Table 8. Cost of rough construction in case of using styrofoam as building material which is designed with hollow-tile floor slab

	Unit	Quantity	Unit price (₺)	Cost (₺)
Formwork	m^2	17090.76	39.63	677306.82
Concrete	m^3	2042.596	165.20	337436.86
Steel reinforcement (thin)	ton	131.221	61.65	8089.77
Steel reinforcement (thick)	ton	311.067	75.82	23585.11
Styrofoam (35x100x40cm)	m^3	1190	100.44	119523.60
Total				1165942.16

3.3. Quantity and Cost of Materials used for Building Designed with Waffle Slab

The amount of material used in buildings designed with waffle slab is given in Table 9 and the cost of rough construction is given in Table 10.

Table 9. Quantity of materials used for buildings designed with waffle slab

	Unit	Floor	Beam	Shear wall	Column	Raft foundation	Total
Formwork	m2	299,49	10744,39	2657,96	3656,22	2358,9	43,22
Concrete	m3	29,949	785,167	427,508	429,74	302,7	231,008
Steel reinforcement	ton	28,56822	32,27847	145,89337	86,22573	79,13587	59,72699

Table 10. Cost of rough construction of the building designed with waffle slab

	Unit	Quantity	Unit price (₺)	Cost (₺)
Formwork	m^2	19760.18	39,63	783095.93
Concrete	m^3	2206.072	165,2	364443.09
Steel reinforcement (thin)	ton	119.636	61,65	7375.56
Steel reinforcement (thick)	ton	312,193	75,82	23670.45
Total				1178585,03

4. CONCLUSION

In this study, three types of buildings having same architectures were designed differently and rough building costs were calculated. When the rough construction costs of the structures are examined; the rough construction cost of the building designed with beam slab is 973025.09 ₺, the rough construction cost of the building designed with hollow-tile slab floor using hollow block as filling material is 1125043.56 ₺, the rough building cost of the building designed with hollow-tile slab floor using Styrofoam as filling material is 1165942.16 ₺. The rough cost of the building designed with and waffle slab was calculated as 1178585.03 ₺. According to the results the building, which has the highest cost, is a building designed with waffle slab. Designed with waffle slab; designed with beam slab, was designed with hollow-tile floor slab using hollow block as filling material 21.12%, and it was found to be 1.08% more costly than building designed with hollow-tile floor slab used as stiffener as filling material 4.76%.

Compared to buildings built with hollow-tile floor slab buildings built using styrofoam seem to cost 3.63% more expensive than hollow block. However, the use of styrofoam as a filler material for flooring has many advantages over using hollow blocks. styrofoam is a lighter material than hollow block, so it does not add too much additional weight to the structure. Therefore, the building, which is filled with Styrofoam, is subjected to less earthquake forces than the building which is filled with hollow block. Since styrofoam does not draw water, there is no risk of reducing concrete strength like hollow block. While workmanship of hollow-tile floor slabs is difficult, workmanship of styrofoam is easier and faster. When filling with hollow block is completed, however there is a lot of wastage, if Styrofoam is used, there is not too much material wastage loss. Moreover, the cost of escaping the concrete into the hollow block during the casting of the fill with the hollow block can be increased. Another advantage of filling with styrofoam is heat and shock insulation. On the other hand, direct use of Styrofoam is prohibited according to fire regulations, so it is necessary to use fire resistant plaster on it. As a result, it has been found that the use of beam-slab in residential buildings is more favorable both in terms of cost and security of the building. Moreover, it is suggested to use less strained and lighter styrofoam filler, which is easier to work with than hollow block filler, because the fill of the hollow-tile floor slab fill the void.

REFERENCES

[1]. http://www.insaathaberleri.net/haber/523-doseme-nedir.html, Son erişim tarihi 11.05.2017.
[2]. B. C. Punmia, "Building Construction". Laxmi Publication, New Delhi, pp.847-848, 2005.
[3]. U. Ersoy, "Betonarme 2". Evrim Yayınevi, İstanbul, pp. 253-255, 1995.
[4]. H. Aygün, "Analysis of dynamic attitude of multi-storey reinforced concrete construction through different flooring systems", M.Sc. Thesis, Istanbul Technical University, Institute of Science, İstanbul, Turkey, 2007.
[5]. www.forum.yapisal.net/dosemeler/30472-asmolendoseme-plak-doseme-maliyet-farki, Son erişim tarihi 11.05.2017.
[6]. M. Bikce, B. Akyol, "Comparison of cost structure of ribbed (hollow block) slab/solid plate in the designed building", *Science and Eng. J of Fırat Univ*., vol. 29, no. (1), pp. 133-144, 2017.
[7]. https://emlakkulisi.com/doseme-nedir/168628, Son erişim tarihi 11.05.2017.
[8]. http://abs.mehmetakif.edu.tr/upload/0420_1813_dosya.pdf, Son erişim tarihi 11.05.2017.
[9]. http://insaatmuh.cbu.edu.tr/db_images/site_115/file/d%C3%B6%C5%9Femeler.pdf, Son erişim tarihi 11.05.2017.
[10]. http://www.mimair.com/asmolendos%D0%B5m%D0%B5n%D0%B5dirasmolendosemeler%D1%96n-%D0%B0v%D0%B0nt%D0%B0j-ve-dezavantajlari-nelerdir.html, Son erişim tarihi 11.05.2017.

ICETI

II INTERNATIONAL CONFERENCE ON ENGINEERING TECHNOLOGY AND INNOVATION

www.iceti.org

EUROPE CONGRESS www.europecongress.org

NATIONAL UNIVERSITY OF PUBLIC SERVICE

UNIVERSITY OF Cincinnati

TURKISH AIRLINES

ZENITH GROUP www.zenithgroup.ba

CNR GROUP